

# Stationary properties and dynamical response of few-body systems at low temperatures

Dissertation

zur Erlangung des Doktorgrades

an der Fakultät für Mathematik, Informatik und  
Naturwissenschaften,

Fachbereich Physik,

der Universität Hamburg

vorgelegt von

Georgios Bougas

geboren am 16.01.1993 in Iraklion

Hamburg

2023

Gutachter/innen der Dissertation:

Prof. Dr. Peter Schmelcher  
Prof. Dr. Dieter Jaksch

Zusammensetzung der Prüfungskommission :

Prof. Dr. Peter Schmelcher  
Prof. Dr. Dieter Jaksch  
Prof. Dr. Daniela Pfannkuche  
Priv. Doz. Dr. Tim Laarmann  
Prof. Dr. Henning Moritz

Vorsitzende/r der Prüfungskommission:

Prof. Dr. Daniela Pfannkuche

Datum der Disputation:

19/12/2023

Vorsitzender des Fach-Promotionsausschusses PHYSIK :

Prof. Dr. Günter H. W. Sigl

Leiter des Fachbereichs PHYSIK:

Prof. Dr. Wolfgang J. Parak

Dekan der Fakultät MIN:

Prof. Dr.-Ing. Norbert Ritter

*“I am afraid that our eyes are bigger than our stomachs, and that we have more curiosity than understanding. We grasp at everything, but catch nothing except wind.”*

Michel de Montaigne



*To my parents*



# *Abstract*

Quantum gases at low temperatures provide an ideal testbed for generating, manipulating and imaging strongly interacting systems. This is granted by the ability to tune many parameters, including the effective interatomic interactions as well as the particle number or the dimensionality. Such good grasp over these parameters renders the out-of-equilibrium dynamics of ultracold gases tractable and even controllable. Few-body bound state formation is a fundamental dynamical process of ultracold atoms, and novel phases emerge when a macroscopic number of molecules is generated. Moreover, the out-of-equilibrium properties of few atoms embedded in a many-body medium are crucial for understanding the emergence of quasiparticles.

The present cumulative thesis aims to provide insights on the stationary correlation properties of few-body bound states, as well as their dynamical formation by employing time-dependent protocols. Short-range correlation observables are utilized as signatures for efficiently populating and detecting few-body bound states upon considering several dynamical schemes. The latter involve abrupt ramps (quenches), or modulations of the interaction strengths. Such protocols are also implemented to efficiently control the correlated dynamics of few impurities immersed in a bosonic medium.

Within the first part, analytical formulas are derived for the short-range correlation observables of two and three particles in two dimensions pertaining to all eigenstates at arbitrary interaction strength. We provide a generalized framework for the treatment of three-body correlations of arbitrary three-body binary mixtures in a harmonic trap. These correlation properties are subsequently utilized to assess the dynamical contributions of few-body bound states. For two confined atoms, the two-body bound state is significantly populated following interaction quenches from the repulsive to the attractive regime and vice versa. It is found that the system is perturbed the most when considering quenches from finite values to the vicinity of zero interactions.

For three particle binary mixtures confined in two dimensions, we come up with a dynamical protocol for selectively exciting distinct classes of eigenstates, such as trimers, atom-dimers and atom-atom-atom eigenstates. The mixtures are initialized in a non-interacting state with variable spatial extent. The initial width acts as a control parameter maximizing the dynamical contribution of final eigenstates possessing a comparable spatial extent to the initial state. For initial widths smaller than the oscillator length, trimers and atom-dimers are predominantly populated.

With all the insights on few-body models, we set out to address the association and decay mechanisms of a recently realized protocol that generated a coherent superposition of an Efimov trimer with an atom-dimer in thermal gases. We solve the time-dependent three-boson problem in a three dimensional harmonic trap, upon considering a sequence of modulated interaction strength. It is found that the superposition of the Efimov trimer with the atom-dimer is robust against thermal effects. Moreover, additional superpositions of the two latter states with the first eigenstate describing three interacting atoms in a trap are observed. Furthermore, the manifested interference fringes in the trimer probability display a decay time which is twice as long as the intrinsic lifetime of the Efimov state. In that regard, our results provide a sound theoretical interpretation of the decay mechanisms observed in the experiment.

In the second part of this thesis, we study the out-of-equilibrium response of few interacting impurities embedded in a many-body bosonic environment. The dynamics is initiated by driving the interspecies interaction strength across the miscible-immiscible phase transition. We identify regimes where the impurities are expelled from the bath, or they remain trapped within, performing a breathing motion. These regimes depend

on the initialization of the setup, whether it lies in the miscible or immiscible phase, as well as the driving frequency. The dynamics of the impurities in both scenarios are quite well understood within an effective potential picture, incorporating interspecies correlations induced by the bath.



## *Zusammenfassung*

Quantengase bei niedrigen Temperaturen bieten ein ideales Testfeld für die Erzeugung, Manipulation und Abbildung stark wechselwirkender Systeme. Dies wird ermöglicht durch die Möglichkeit viele Parameter einzustellen, darunter die effektiven interatomaren Wechselwirkungen sowie die Teilchenzahl oder die Dimensionalität. Die gute Beherrschung dieser Parameter macht die Dynamik von ultrakalten Gasen außerhalb des Gleichgewichts nachvollziehbar und sogar kontrollierbar. Die Bildung von gebundenen Zuständen mit wenigen Teilchen ist ein grundlegender dynamischer Prozess bei ultrakalten Atomen, und neue Phasen entstehen, wenn eine makroskopische Anzahl von Molekülen erzeugt wird. Darüber hinaus sind die Eigenschaften von wenigen Atomen, die in einem Vielteilchenmedium eingebettet sind, entscheidend für das Verständnis der Entstehung von Quasiteilchen.

Die vorliegende kumulative Dissertation zielt darauf ab, Einblicke in die stationären Korrelationseigenschaften von gebundenen Zuständen mit wenigen Körpern sowie in deren dynamische Entstehung zu geben, indem durch die Verwendung zeitabhängiger Protokolle. Kurzreichweitige Korrelationsobservablen werden genutzt als Signaturen für die effiziente Besiedlung und Erkennung von gebundenen Zuständen mit wenigen Körpern unter Berücksichtigung verschiedener dynamischer Schemata. Letztere beinhalten abrupte Rampen (Quenches), oder Modulationen der Wechselwirkungsstärken. Solche Protokolle werden auch eingesetzt, um die korrelierte Dynamik von wenigen Verunreinigungen in einem bosonischen Medium effizient zu kontrollieren.

Im ersten Teil werden analytische Formeln für die Kurzstreckenkorrelationsobservablen von zwei und drei Teilchen in zwei Dimensionen für alle Eigenzustände bei beliebiger Wechselwirkungsstärke abgeleitet. Wir stellen einen verallgemeinerten Rahmen für die Behandlung von Dreikörper-Korrelationen beliebiger Dreikörper-Binärgemische in einer harmonischen Falle bereit. Diese Korrelationseigenschaften werden anschließend genutzt, um die dynamischen Beiträge von gebundenen Zuständen mit wenigen Körpern zu bewerten. Bei zwei eingeschlossenen Atomen ist der gebundene Zweikörperzustand nach dem Wechselwirkungsquench vom abstoßenden in den anziehenden Bereich und umgekehrt stark bevölkert. Es zeigt sich, dass das System am stärksten gestört wird, wenn man Quenches von endlichen Werten in der Nähe von Null-Wechselwirkungen betrachtet.

Für binäre Dreiteilchenmischungen, die in zwei Dimensionen eingeschlossen sind, entwickeln wir ein dynamisches Protokoll zur selektiven Anregung verschiedener Klassen von Eigenzuständen wie Trimere, Atom-Dimere und Atom-Atom-Atom-Eigenzustände. Die Gemische werden in einem nicht interagierenden Zustand mit variabler räumlicher Ausdehnung initialisiert. Die Anfangsbreite wirkt als Kontrollparameter, der den dynamischen Beitrag der endgültigen Eigenzustände maximiert, die eine vergleichbare räumliche Ausdehnung wie der Anfangszustand besitzen. Für Anfangsbreiten, die kleiner sind als die Oszillatorlänge, werden überwiegend Trimere und Atom-Dimere besiedelt.

Mit all den Erkenntnissen über Wenig-Körper-Modelle haben wir uns die Assoziations- und Zerfallsmechanismen eines kürzlich realisierten Protokolls zu untersuchen, das eine kohärente Superposition eines Efimov-Trimers mit einem Atom-Dimer in thermischen Gasen erzeugt. Wir lösen das zeitabhängige Drei-Bosonen-Problem in einer dreidimensionalen harmonischen Falle, indem wir eine Sequenz modulierter Wechselwirkungsstärken berücksichtigen. Es zeigt sich, dass die Überlagerung des Efimov-Trimers mit dem Atom-Dimer robust gegen thermische Effekte ist. Außerdem sind

zusätzliche Überlagerungen der beiden letztgenannten Zustände mit dem ersten Eigenzustand der drei wechselwirkende Atome in einer Falle beschreibt, beobachtet werden. Darüber hinaus sind die manifestierten Interferenzstreifen in der Trimer-Wahrscheinlichkeit eine Abklingzeit auf, die doppelt so lang ist lang wie die intrinsische Lebensdauer des Efimov-Zustands ist. In dieser Hinsicht liefern unsere Ergebnisse eine fundierte theoretische Interpretation der im Experiment beobachteten Zerfallsmechanismen.

Im zweiten Teil dieser Arbeit untersuchen wir das Verhalten von wenigen wechselwirkenden Verunreinigungen, die in einer vierteiligen bosonischen Umgebung eingebettet sind, außerhalb des Gleichgewichts. Die Dynamik wird die Wechselwirkungsstärke zwischen den Spezies über den Phasenübergang mischbar-unmischbar Phasenübergang. Wir identifizieren Regime, in denen die Verunreinigungen aus dem Bad ausgetrieben werden, oder sie bleiben darin gefangen und führen eine atmende Bewegung aus. Diese Regime hängen von der Initialisierung des Aufbaus, ob er in der mischbaren oder nicht mischbaren Phase liegt, sowie von der Antriebsfrequenz ab. Die Dynamik der Verunreinigungen in beiden Szenarien ist im Rahmen eines effektiven Potentialbildes recht gut verstanden, wobei durch das Bad Korrelationen, die durch das Bad induziert werden.

# Contents

<b>Preface</b>	<b>xiii</b>
<b>1 Introduction</b>	<b>1</b>
<b>2 Theoretical Framework</b>	<b>7</b>
2.1 Quantum gases	7
2.2 Scattering of two interacting cold atoms	8
2.2.1 s-wave regime	8
2.2.2 Contact Pseudopotential	9
2.2.3 Scattering of neutral cold atoms in low dimensions	9
Two dimensions	9
One dimension	10
Quasi-low dimensional systems	11
2.2.4 Fano-Feshbach resonances	11
2.3 Few cold atoms in a harmonic oscillator trap	12
2.3.1 Two interacting confined atoms	12
2.3.2 Three interacting atoms in a trap	14
Jacobi and Hyperspherical coordinates	14
Potential curves	15
Hyperradial equations and eigenspectra	17
2.4 Short-range correlations	18
2.4.1 Two-body contact and universal relations	19
2.4.2 Three-body contact	21
2.5 Interacting ultracold quantum gases	23
2.5.1 Weakly interacting gases	24
2.5.2 Mesoscopic systems	26
ML-MCTDHX	26
<b>3 Outline of Scientific contributions</b>	<b>29</b>
3.1 Correlations and dynamical response of few-body trapped systems	29
3.1.1 Dynamical response of two particles in two dimensions	30
3.1.2 Correlation and dynamical properties of two atoms in the di- dimensional crossover from two dimensions to one	31
3.1.3 Stationary properties of two-dimensional three-body mixtures	32
3.1.4 Dynamical excitation of distinct eigenstates in three-body two- dimensional mixtures	34
3.1.5 Interferometry of Efimov trimers in thermal gases with modu- lated magnetic fields	35
3.2 Dynamics of few particles in a many-body environment	37
3.2.1 Pattern formation of impurities subjected to driving of the impurity- medium interactions	38

<b>4</b>	<b>Scientific contributions</b>	<b>41</b>
4.1	Correlations and dynamical response of few-body trapped systems . . .	41
4.1.1	Analytical treatment of the interaction quench dynamics of two bosons in a two-dimensional harmonic trap . . . . .	41
4.1.2	Stationary and dynamical properties of two harmonically trapped bosons in the crossover from two dimensions to one . . . . .	60
4.1.3	Few-body correlations in two-dimensional Bose and Fermi ultracold mixtures . . . . .	81
4.1.4	Dynamical excitation processes and correlations of three-body two-dimensional mixtures . . . . .	107
4.1.5	Interferometry of Efimov states in thermal gases by modulated magnetic fields . . . . .	125
4.2	Dynamics of few particles in a many-body environment . . . . .	136
4.2.1	Pattern formation of correlated impurities subjected to an impurity-medium interaction pulse . . . . .	136
<b>5</b>	<b>Conclusions and Outlook</b>	<b>155</b>
	<b>Acknowledgements</b>	<b>161</b>
	<b>Bibliography</b>	<b>163</b>
	<b>Eidesstattliche Versicherung / Declaration of oath</b>	<b>189</b>

# Preface

The present cumulative thesis is based on the following publications:

## List of publications

- [B1] G. Bougas, S. I. Mistakidis, and P. Schmelcher, “Analytical treatment of the interaction quench dynamics of two bosons in a two-dimensional harmonic trap”, *Phys. Rev. A* **100**, 053602 (2019).
- [B2] G. Bougas, S. I. Mistakidis, G. M. Alshalan, and P. Schmelcher, “Stationary and dynamical properties of two harmonically trapped bosons in the crossover from two dimensions to one”, *Phys. Rev. A* **102**, 013314 (2020).
- [B3] G. Bougas, S. I. Mistakidis, P. Giannakeas, and P. Schmelcher, “Few-body correlations in two-dimensional Bose and Fermi ultracold mixtures”, *New J. Phys.* **23**, 093022 (2021).
- [B4] G. Bougas, S. I. Mistakidis, P. Giannakeas, and P. Schmelcher, “Dynamical excitation processes and correlations of three-body two-dimensional mixtures”, *Phys. Rev. A* **106**, 043323 (2022).
- [B5] G. Bougas, S. I. Mistakidis, P. Schmelcher, C. H. Greene, and P. Giannakeas, *Interferometry of Efimov states in thermal gases by modulated magnetic fields*, June 2023, arXiv:2306.01199, **Status: Submitted to Phys. Rev. Lett.**
- [B6] G. Bougas, S. I. Mistakidis, and P. Schmelcher, “Pattern formation of correlated impurities subjected to an impurity-medium interaction pulse”, *Phys. Rev. A* **103**, 023313 (2021).

Note that the reference indices [B1-B6] employed in this thesis refer to the above publications.

## Outline of this thesis

Chapter 1 provides a very general overview to the field of ultracold atoms. It focuses in particular on few ultracold trapped atoms and their dynamical response, addressing processes in gases such as bound state formation. The concept of the contacts is also introduced, establishing a link from few- to many-body physics through the universal relations they satisfy. Finally, the topic of impurities embedded in an ultracold many-body environment is very briefly reviewed. In Chapter 2, we provide the necessary theoretical background for understanding techniques and concepts utilized in our scientific contributions. In particular, a short summary of the basic traits of scattering theory at low energy is outlined. The theoretical treatment of the two- and three-body problem in a trap is also reviewed, along with an outline of the universal relations that the contacts satisfy in arbitrary systems. Subsequently, a brief summary of mean-field theory is given, along with that of a many-body variational method employed in one of our works. In Chapter 3, details are provided regarding

every scientific contribution, which questions are being addressed, as well as which are the main results. In the next chapter (Chapter 4), the scientific contributions [B1–B6] are provided in their published format. Finally, Chapter 5 briefly outlines the main results and conclusions of all of our scientific contributions, suggesting also future extensions of our work.

## Declaration of personal contributions to the publications [B1–B6]

The project [B1] has been conceptualized by Dr. Simeon I. Mistakidis. I have carried out all analytical and numerical computations. For the analytical calculations, substantial feedback was provided by Dr. Georgios M. Koutentakis. Together with Dr. Simeon I. Mistakidis we have discussed about the significance of the two-body contact, which I have subsequently derived for our particular system. The first draft of our work was written by myself, which was subsequently substantially optimized and rewritten by Dr. Simeon I. Mistakidis. The project on the two particle problem in an anisotropic trap [B2] was also conceptualized by Dr. Simeon I. Mistakidis. I have written all the necessary code and performed the analytical calculations. The analytical formula for the overlap of the final states with the initial one was derived by Bsc. Ghadah M. Alshalan, an intern student in our group at the time. Significant feedback came also from the side of Prof. Alexandros I. Karanikas. The first draft was written by myself, subsequently improved and partially rewritten by Dr. Simeon I. Mistakidis.

The project on the correlation properties of three-body binary mixtures [B3] was initiated by Dr. Simeon I. Mistakidis. Subsequent discussions with Dr. Panagiotis Giannakeas helped to better identify the goal of the project as well as the strategy to achieve it. The numerical implementation of the adiabatic hyperspherical formalism in two dimensions was carried out by myself with crucial feedback from Dr. Panagiotis Giannakeas and Dr. Simeon I. Mistakidis. The analytical formulas for the few-body contacts were also derived by myself. Dr. Artem G. Volosniev gave also useful feedback on the structure of one-body densities. The first draft was written by myself, and subsequently Dr. Panagiotis Giannakeas and Dr. Simeon I. Mistakidis substantially improved it and rewrote it. The project on the dynamics of three-body binary mixtures in two dimensions [B4] was conceptualized by Dr. Panagiotis Giannakeas and Dr. Simeon I. Mistakidis. Subsequent discussions helped to set a new interesting direction for the project. The numerical and analytical implementation was carried out by myself. I have written also a first draft, and then Dr. Panagiotis Giannakeas and Dr. Simeon I. Mistakidis substantially improved the presentation of the results and rewrote the manuscript.

The project on the interferometry of Efimov trimers [B5] was conceptualized by Dr. Panagiotis Giannakeas and Prof. Chris H. Greene. I carried out the numerical implementation of the three-body time-dependent problem with substantial feedback from Dr. Panagiotis Giannakeas and Dr. Simeon I. Mistakidis. The three-level model used as an interpretation tool was also implemented by myself. Discussions with Dr. Panagiotis Giannakeas, Dr. Simeon I. Mistakidis, Prof. Chris H. Greene and Prof. Dr. Peter Schmelcher were very helpful in properly interpreting the results. The first draft was written by myself, and then improved and rewritten by all the authors. The project on the correlated dynamics of impurities in a cold bosonic environment was conceptualized by Dr. Simeon I. Mistakidis. I have subsequently carried out the numerical simulations and performed the analysis of the results. Together with

Dr. Simeon I. Mistakidis we interpreted them and decided upon the optimal way to present them. I have written the first draft, subsequently improved and turned into a manuscript by Dr. Simeon I. Mistakidis. The progress of all projects was supervised on a regular basis by Prof. Dr. Peter Schmelcher.





## Chapter 1

# Introduction

Advances in laser cooling of atoms [1–6] granted access to the quantum degeneracy limit and the formation of Bose-Einstein condensates [7, 8] initially, and degenerate Fermi gases later on [9–11]. These milestones were followed by improved techniques for loading, cooling, imaging and controlling gases, further establishing the field of ultracold quantum gases [12–14]. The key advantage of such settings is the ability to control a plethora of parameters. First and foremost, the effective interatomic interactions can be arbitrarily tuned by means of external electromagnetic fields, taking advantage of Fano-Feshbach resonances [15–17]. This remarkable technique allowed the creation of strongly interacting Bose and Fermi gases [18–23].

Moreover, the control over external electromagnetic fields [2] leads to the realization of arbitrary trapping geometries, such as harmonic oscillator traps and optical lattices [24–26]. By tuning the electromagnetic fields, different trapping frequencies along the three spatial dimensions can be generated. For sufficiently high trapping frequencies, the cold atoms are essentially confined kinematically in two or one spatial direction [27]. In this way, low dimensional ultracold quantum systems can be realized [28, 29], exhibiting novel phases [30] and strong correlations [31, 32].

The manipulation of different atomic species as well as the control of their particle number is nowadays state of the art. Indeed, advances in trapping techniques have led to the realization of binary mixtures of any quantum statistics, i.e. bosons and fermions [33–37]. In these setups, the interplay between inter- and intraspecies interactions leads to phase separation phenomena [38, 39], coexistence of non-linear soliton structures in both components [40–44], and stabilization due to quantum fluctuations [45–50]. Furthermore, novel methods [51] allowed the observation of phenomena such as the formation of degenerate Fermi sea [52], Cooper pairing [53], and superfluidity [54] from a few-to-many particles bottom-up approach. At the few-atom limit, the advent of optical tweezers [55–58] provided reliable trapping schemes down to single atoms [59–62], leading to the controllability of quantum states with very high fidelity [63–65].

Given all of this progress, understanding the properties of few cold atoms serves a twofold goal. First, their scattering aspects are crucial for describing resonance mechanisms [15], recombination processes [66], and determining regimes where few-body bound state formation occurs [67, 68]. Second, the small number of degrees of freedom render these few-body setups analytically and numerically tractable for weak and strong interactions [69–75]. This is especially the case for two and three harmonically confined atoms, where the complete energy structure as well as the corresponding eigenstates are known [69, 70, 72, 76]. The energy landscape of two cold atoms was in fact explored experimentally by confining two fermions with opposite spin in a single site of an optical lattice [62, 77]. The results displayed excellent

agreement with the theoretical predictions. This was also the case for two trapped atoms stemming from two different atomic species [78].

Few-body settings provide a very useful theoretical interpretation toolbox for the behavior of quantum gases, given their analytical or semi-analytical treatment. For instance, insights from the three boson problem helped identifying three-body bound states as the culprit for particle losses in a strongly interacting Bose gas [79]. Moreover, two interacting bosons in a one dimensional trap provided the necessary framework for further investigating the breathing mode spectrum in a few-to-many atom crossover [80]. In a similar vein, the energy levels of two atoms in a two dimensional trap provided a reference point for the breathing frequency of a strongly interacting two component Fermi gas [81]. Moreover, the analytical solutions of two confined particles with an effective mass were utilized to model the dynamical properties of two impurities embedded in a mesoscopic bosonic gas in one dimension [82].

Two dimensional few-body models however, have not been widely used so far. Their behavior is not so much explored as compared to other dimensionalities [244, 245], especially their dynamical aspects. Two dimensional few atom systems however possess unique traits such as the existence of a two-body bound state for all interactions [83, 84]. Moreover, the study of three-body bound states is of particular importance since they are more stable to three-body losses compared to three dimensions [85, 86]. In [B1–B3] we aim to provide further insights on the stationary and dynamical properties of two and three atoms confined in two dimensional harmonic traps. Their correlation properties are investigated for a wide range of interaction strengths. Furthermore, it is shown that the two-body bound state has an enhanced contribution in the dynamical response of the system following an interaction strength.

Bound state formation is a representative example where few-body setups are especially appealing for modeling such processes due to their tractability. On the two-body level, sweeps of external magnetic fields have been employed to associate weakly bound molecules (Feshbach dimers) out of atoms, a process called magnetoassociation [87–92]. More general time-dependent protocols have been utilized, such as modulated magnetic fields [93–95], achieving atom-molecule coherence [96, 97] and enhanced molecular fractions [98]. The dynamics of two cold atoms led to the identification of regimes where efficient molecular association is achieved with respect to the parameters of these protocols, such as the amplitude of the magnetic fields or the modulation duration [99–102]. Further dynamical protocols were proposed, where the interaction strengths are quenched to strong interactions, subsequently swept to smaller values [103] after a delay time. The two-body analysis revealed substantial molecular conversion for larger delay times.

The preparation and out-of-equilibrium dynamics [18, 21, 79, 104] of strongly interacting Bose ultracold gases sparked a lot of interest in treating the dynamics from a few-body perspective. It was shown that the short-time quench dynamics of two atoms yielded identical signatures for bound state formation with the respective short-time many-body description of a Bose-Einstein condensate [105, 106]. On the three particle level, the respective models have been proven especially fruitful for unraveling three-body bound state formation in strongly interacting Bose gases. These states are usually detected from resonant features in loss signals [107–112], and they are metastable. In the experimental work [79] however, a substantial population of trimers was observed by quenching the interactions to very strong values. Following this breakthrough, three-atom models shed light onto the dynamical buildup of three-body correlations occurring at strong interactions [113–117]. One of the key results is that trimer formation is enhanced when the length scale stemming from the density of the gas is comparable to the size of the associated trimer. Inspired by this observation, we

have conceived a dynamical protocol for selectively populating particular eigenstates in a three-body mixture confined in two dimensions [B4]. The protocol relies on the separation of spatial extent between three-body, two-body bound states, as well as atom-atom-atom eigenstates.

Employing modulated magnetic fields, it was shown that trimers in thermal gases not only could be associated, but also manipulated by forming coherent superpositions with atom-dimers [118, 119]. This dynamical protocol allowed for the high precision measurement of the binding energy of the first excited trimer state at repulsive interactions. The energy was extracted from the interference fringes manifested in the particle loss signal. The latter displayed a damping time, which was very long compared to typical lifetimes of such trimer states. In [B5] we set out to understand the association and decay mechanisms of this protocol, by solving the three particle problem with modulated interactions. We discovered that the superpositions of trimers with atom-dimers and atom-atom-atom eigenstates lead to a decay time, which is twice as long as the lifetime of trimers. In this way a plausible explanation is provided for the long coherence times observed in the experiment.

The ability to model bound state formation in cold gases by utilizing few-body setups is certainly a remarkable feature. There is however a more fundamental connection between few- and many-body systems. This is granted by the so-called two- and three-body contacts [67, 120–126]. The latter stem from the behavior of a system when two or three particles approach at very short distances. The contacts are defined through a multitude of relations, involving macroscopic observables such as the asymptotic expansion of the one-body density in momentum space [13, 120, 127], the rate of change of the energy with respect to interactions [123], and the decay width due to few-body losses [128, 129] to name only a few. These relations are universal, meaning that they equally apply to arbitrary particle number, quantum statistics or interaction strengths [13, 67].

The fact that the contacts are defined through a plethora of relations with seemingly unrelated observables is of course a unique trait. Utilizing the relations regarding the rate of change of the energy, the asymptotic tail of the transition rate in radiofrequency spectra, and a generalized virial theorem, the two-body contact for a two component Fermi gas was extracted from three independent measurements [130]. Its value was consistent for all three applied methods. Further experimental efforts focused on measuring the two-body contact through these relations, primarily in two component Fermi gases [130–132]. The three-body contact satisfies a smaller number of universal relations compared to the two-body one and it is more challenging to measure [131]. However, employing a universal relation regarding the asymptotic expansion of the transition rate in radiofrequency spectra, the three-body contact has been measured in a strongly interacting Bose gas [104].

The knowledge of the contacts therefore is sufficient for specifying certain macroscopic properties of a general ultracold system. These involve the energy [121], pressure [122, 124, 125], virial theorems [122, 133], static structure factor [134–137] and asymptotic expansions of radiofrequency spectra [138, 139]. The contacts themselves stem from the behavior of a setup when two or three particles approach at very short distances, and thus quantify short-range few-body correlations. In that regard, the contacts are microscopic quantities linked to macroscopic observables [67]. The contacts may assume different values in different settings, the relations that they satisfy however hold for any system, hence their universality.

The fact that the contacts quantify short-range few-body correlations makes them ideal diagnostics tools for the formation of bound states. As mentioned above, the three-body models used in [113, 115] employed the three-body contact to identify

regimes where enhanced trimer population has been achieved. Moreover, the oscillatory behavior of the two-body contact in strongly interacting quenched Bose gases [105] has been attributed to the presence of the Feshbach dimer in the dynamics. In [B1] we took advantage of this diagnostics tool to assess the contribution of the two-body bound state in the quench dynamics of two particles confined in two dimensions. Moreover, we identified a population of atom-dimers from the peaked structure of the two-body contact following an interaction quench in two dimensional three atom binary mixtures [B4].

Apart from providing a signature for bound state formation, the contacts were applied to other scenaria as well. For instance the two-body contact of strongly interacting two component fermions has been linked [140] to the deviation of their breathing frequency from twice the trapping frequency. This feature is known as the breathing frequency anomaly present in two dimensions [141–144]. Moreover the photoassociation rate for populating tightly bound molecules in strongly interacting two component Fermi gases [145] was related to the value of the two-body contact [146–148].

Despite the determination of certain macroscopic observables for arbitrary ultracold systems, the contacts fail to describe collective excitations. The reason is that the contacts are microscopic quantities stemming from the short-distance behavior of two and three particles, whereas collective phenomena arise from the many-particle character of a system. In order to address such processes a many-body description is required. A characteristic and well studied example is the dressing of impurity particles by collective modes of the environment in which they are embedded. Their bare properties such as their mass are modified, introducing the concept of the quasiparticle [149–152]. Ultracold atoms turned out to be ideal platforms for studying these setups [153–157], due to the controllability of the interactions by means of Feshbach resonances, in contrast to condensed matter settings. The stationary properties of such quasiparticles, such as energy [156, 157], effective mass [158–160], and lifetime [154, 157] have been investigated both in bosonic and fermionic media.

Embedding few interacting impurities in a many-body environment opens up the possibility of investigating induced interactions between them [82, 161, 162] and in-medium bound state formation. A prominent case consists of two impurities immersed in a many-body environment forming bipolarons [163–171], two-body bound states whose properties are altered compared to those formed just by two atoms. One illustrative scenario is that of two heavy atoms interacting with a light impurity. Within the Born-Oppenheimer approximation [75, 172, 173] an effective interaction can be induced between the two heavy particles, where the third atom acts as a mediator. Depending on the interspecies interaction strength, the effective interaction takes the form of a Yukawa potential or that of an Efimov attraction [172, 174]. Substituting the light particle with a degenerate Fermi sea results in interaction potentials with a sinusoidal dependence on the relative distance between the two heavy atoms [175, 176], a well studied potential form in the context of magnetic interactions [177, 178].

Similarly to the formation and coherent manipulation of few-body bound states, time-dependent protocols result in a controllable behavior of impurities in an ultracold medium. These protocols include for instance interspecies interaction quenches [179, 180], dragging the impurities in a many-body environment [181, 182] and modifying their external potential [183, 184]. All of these protocols led to interesting dynamical response, such as the dynamical breakdown of the quasiparticle picture [179, 185, 186], dissipative motion [181, 183] and slow relaxation dynamics [182, 187]. Along these lines we investigate in [B6] the dynamical behavior of few impurities interacting with a mesoscopic Bose gas in one dimension by modulating the interspecies interaction

strength. Depending on the interplay between intra- and interspecies interactions, phase separation regimes can be dynamically accessed [38, 39]. The impurities can become localized at the edges of the bosonic cloud or perform a breathing motion depending on the driving frequency as well.

### Objectives of this thesis

In this cumulative thesis, our main goal is to theoretically study the dynamical response of few ultracold atoms by considering time-dependent protocols, such as quenches or modulation of the interaction strengths. This is examined in two setups. First, the dynamics of two and three atoms confined in a harmonic oscillator is investigated, focusing on the few-body bound state formation. Short-range few-body correlations are utilized as probes for characterizing the participation of such bound states. Moreover, a three-body model is employed in order to provide a theoretical framework for the recently achieved coherent manipulation of trimer states, by means of modulated magnetic fields. Second, the dynamics of few interacting particles (impurities) is investigated when they are immersed in a many-body bosonic environment. By modulating the interspecies interaction strength different dynamical regimes can be accessed, where the behavior of the impurities can be controlled. In particular, we aim to

- ◇ understand the interplay of short-range few-body correlations between different classes of eigenstates in two and three atom setups confined in two dimensions;
- ◇ yield analytical insights for time-dependent observables such as the correlation properties of two and three particle settings, by quenching their interaction strength;
- ◇ investigate the microscopic excitation mechanisms induced by an interaction quench in few-body setups;
- ◇ take advantage of these mechanisms and devise interaction quench protocols for selectively populating few-body bound states in three-body binary mixtures;
- ◇ solve the three-body problem with modulated interactions to shed light on association and decay mechanisms of trimers in thermal gases;
- ◇ control the dynamical response of impurity atoms immersed in a many-body environment upon modulating their interspecies interaction strength.

The first four of these goals are achieved by utilizing the analytic solutions of few atoms confined in harmonic traps [Sec. 2.3]. For three-body systems in particular, we employ the adiabatic hyperspherical toolbox [Sec. 2.3.2], suited for determining the stationary properties of arbitrary three particle systems in two and three dimensions. Moreover, the split-operator method is included in our techniques arsenal to treat the dynamical behavior of three bosonic particles with modulated interactions. For the case of impurities in a bosonic medium, insights are provided within the scope of the Multi-Layer Multi-Configuration Time-Dependent Hartree method for mixtures, an ab-initio variational method for tackling the out-of-equilibrium dynamics of multicomponent systems [Sec. 2.5.2].



## Chapter 2

# Theoretical Framework

### 2.1 Quantum gases

Let us consider a macroscopic number of neutral atoms with mass  $m$ , density  $n$  at temperature  $T$ , trapped in an external potential. The interatomic interactions are described by isotropic short-range potentials of range  $r_0$  with a van der Waals tail [12], meaning that the potential decays with the sixth power of the interatomic distance for sufficiently large distances. At low enough densities, the system is dilute and only binary collisions can be taken into consideration [188].

The properties of these atoms crucially depend on the competition between the length scales set by the density, temperature and interactions. In particular, we may distinguish between the following cases:

- For high temperatures, the thermal de Broglie wavelength  $\Lambda_{th} = \left(\frac{2\pi\hbar^2}{mk_B T}\right)^{1/2}$  is much smaller than the mean interparticle spacing,  $n\Lambda_{th}^3 \ll 1$ . In this regime, we can treat the system on classical terms [12, 188]. The interactions however have an important effect on its properties.
  - If the average interparticle spacing is larger than the collisional length,  $n|a|^3 \ll 1$ , the system can be modeled as an ideal classical gas. The collisional length  $a$  determines the extent of the cross section,  $\sigma \propto a^2$ , and is roughly given by the range of the interatomic potential,  $r_0$  [12, 188]. However, this is not true in general as we will see later on [Sec. 2.2.4]. In this regime, the macroscopic properties of the atoms can be determined from a statistical description [189].
  - In the case where  $n|a|^3 \gtrsim 1$ , we are dealing with an interacting classical gas. An adequate description for its thermodynamic attributes, like pressure and chemical potential, is given by the van der Waals and Onnes equations of states [190].
- At low temperatures, the thermal de Broglie wavelength is comparable to or larger than the mean interparticle distance,  $n\Lambda_{th}^3 \gtrsim 1$ . In this limit the system of  $N$  atoms reaches the quantum degeneracy regime, and a quantum mechanical description is appropriate for treating their behavior. Depending on the strength of interactions we distinguish between two cases.
  - For nearly ideal quantum gases, the macroscopic properties of the system are evaluated from the bosonic or fermionic statistics [191]. Despite the absence of interactions, collective phenomena can emerge due to the quantum statistical correlations, such as the Bose-Einstein condensation [12,

13]. For weakly interacting quantum gases,  $n|a|^3 \ll 1$ , a mean-field treatment is adequate in treating the collective motion of the gas as well as elementary excitations [12, 192–194].

- For interacting gases,  $n|a|^3 \gtrsim 1$ , the description is certainly challenging and highly depends on the characteristics of the particular system in question and its dimensionality [27, 74].

Apart from the above mentioned length scales, there is an additional crucial one, the length of the external trapping potential. Utilizing the internal hyperfine structure of atomic species, it is possible to confine quantum gases in space by means of optical and magnetic fields [2, 3, 6, 12, 13, 55], realizing harmonic confinement for the gas in all three spatial directions. Importantly, the frequency aspect ratio of these harmonic traps can be tuned to large or small values, confining kinematically the cold atoms in low dimensions [27, 28].

## 2.2 Scattering of two interacting cold atoms

### 2.2.1 s-wave regime

The first step in understanding the stationary and dynamical properties of quantum gases is to consider the motion of two interacting neutral atoms in free space at low temperatures with relative energy  $E = \frac{\hbar^2 k^2}{2\mu_{2b}} > 0$ , where  $\mu_{2b}$  is the two-body reduced mass. Their relative wavefunction is expanded in spherical harmonics with definite angular momentum  $l$  due to the isotropic nature of the interaction potential. Depending on the statistics of the particles, the expansion can be restricted to a subspace of angular momenta. For instance, identical bosons (fermions) allow only even (odd)  $l$  in the expansion. The radial wavefunctions associated to the different angular momenta,  $\Psi_{k,l}(r)$ , satisfy the following relative radial Schrödinger equation [195],

$$\left\{ -\frac{d^2}{dr^2} - \frac{2}{r} \frac{d}{dr} + V_{int}(r) + \frac{l(l+1)}{r^2} \right\} \Psi_{k,l}(r) = k^2 \Psi_{k,l}(r), \quad (2.1)$$

where  $V_{int}(r)$  is the interatomic potential and the fourth term is the centrifugal barrier for finite  $l$ . Low temperatures translate to low collisional energy, meaning that the relative energy of the atoms is much smaller than the characteristic energy scale of the interaction potential,  $\frac{\hbar^2}{2\mu_{2b}r_0^2}$ . The latter condition is simply written as  $kr_0 \ll 1$ . The atoms scattering with  $l \neq 0$  experience a barrier with height of the order  $\frac{\hbar^2[l(l+1)]^{3/2}}{\mu_{2b}r_0^2}$ , which is way larger than their collisional energy, since  $kr_0 \ll 1$ . The probability to tunnel past the barrier and experience the van der Waals potential  $V_{int}(r)$  is therefore very low. In this sense, scattering processes with finite angular momentum ( $l \neq 0$ ) are suppressed at low energies. The only relevant process is for  $l = 0$ , the *s*-wave regime. Note that this regime does not apply to identical (spin-polarized) fermions.

For *s*-wave scattering, the relative wavefunction describing the scattered atoms at large interparticle distances is isotropic [12],

$$\Psi_{k,0}(r) \xrightarrow{r \gg r_0} \frac{1}{r} \sin[kr + \delta_0(k)]. \quad (2.2)$$

At such large distances the  $V_{int}(r)$  potential decays fast ( $r^{-6}$ ), and affects only the phase of the wavefunction. It is essentially that of free atoms shifted by  $\delta_0(k)$ , which is the phase that the wavefunction accumulated when the atoms were interacting at short interatomic distances. For the van der Waals potential the phase shifts depend on



the relative wavevector according to the following scaling law  $\delta_l(k) \sim k^{2l+1}$  for  $l = 0, 1$ , and  $k^4$  for  $l \geq 2$  [195–197]. In particular, in the limit of vanishing relative energy,  $\lim_{k \rightarrow 0} \tan \delta_0(k)/k = -a$  [188, 198, 199]. From this expression the  $s$ -wave scattering length  $a$  is defined. Revisiting Eq. (2.2), we see that  $\Psi_{k,0}(r) \xrightarrow{r \gg r_0} \sin[k(r-a)]/(r)$ .

In the  $s$ -wave regime scattering properties like the cross section depend only on the scattering length  $a$  instead of the short-range details of the interaction potential [12, 13]. Even more importantly, different interaction potentials yielding the same scattering length, will capture the same collisional properties in this regime.

### 2.2.2 Contact Pseudopotential

Instead of treating the motion of interacting particles with the van der Waals potential, which poses challenges when describing many-body systems, one can replace it with a contact pseudopotential [12], resulting in the same scattering length. This is achieved by extending the wavefunction (2.2) to zero interparticle separations, subject to an appropriate boundary condition at  $r \rightarrow 0$ ,  $\left. \frac{[r\Psi_{k,0}(r)]'}{r\Psi_{k,0}(r)} \right|_{r \rightarrow 0} = -\frac{1}{a}$ , the Bethe-Peierls condition [200]. The prime here denotes a derivative with respect to the interatomic separation. A pseudopotential that satisfies these properties is the Fermi-Huang pseudopotential [201, 202],

$$V_{int}(\mathbf{r}) = \frac{2\pi\hbar^2 a}{\mu_{2b}} \delta^{(3)}(\mathbf{r}) \frac{\partial}{\partial r}(r \cdot). \quad (2.3)$$

The scattering length  $a$  essentially determines the effective interaction strength between the atoms. Note that the regularization operator  $\frac{\partial}{\partial r}(r \cdot)$  lifts the  $1/r$  divergence of the two-body wavefunction at small distances.

Even though this pseudopotential yields the same  $s$ -wave scattering length with the actual van der Waals potential, the number of bound states is different. In principle van der Waals potentials can support many two-body bound states, whereas the pseudopotential (2.3) supports a single one for positive scattering length with energy  $-\hbar^2/(2\mu_{2b}a^2)$  [15]. It refers to the least bound state in the van der Waals interaction potential.

### 2.2.3 Scattering of neutral cold atoms in low dimensions

Scattering of neutral ultracold atoms in lower dimensions is completely different compared to the three dimensional case. Here we briefly review the main aspects of scattering in two and one dimension.

#### Two dimensions

Focusing on the  $s$ -wave regime, it is shown that the asymptotic expansion of the relative two-body wavefunction for interparticle distances larger than the range of the interaction potential  $r_0^{2D}$  takes the form [83, 203–205],

$$\Psi_{k,0}(r) \xrightarrow{r \gg r_0^{2D}} \ln\left(\frac{r}{a_{2D}}\right), \quad (2.4)$$

where  $a_{2D}$  is the two dimensional  $s$ -wave scattering length. Note that the  $s$ -wave limit refers to zero azimuthal quantum number [83], hence the zero subscript in the wavefunction. Here we have assumed the low energy limit of the  $s$ -wave scattering phase shift employed in [206]. Similarly to the three dimensional case a pseudopotential yielding the same scattering length extends the wavefunction (2.4) to

small interatomic distances with the appropriate Bethe-Peierls condition  $[r\Psi_{k,0}(r)' - \Psi_{k,0}(r)/\ln(r/a_{2D})]|_{r \rightarrow 0} = 0$  [207–209]. The derivation of such a pseudopotential however is not so straightforward as in three dimensions. In fact, there are multiple contact potentials in the literature [203, 210–213], and below we list a few of them,

$$V_{int}(\mathbf{r}) = \frac{\pi\hbar^2}{\mu_{2b}}\delta^{(2)}(\mathbf{r})r\frac{\partial}{\partial r}, \quad (2.5a)$$

$$V_{int}(\mathbf{r}) = \frac{\pi\hbar^2}{\mu_{2b}}\delta^{(2)}(\mathbf{r})\frac{1}{1 + \ln(r/a_{2D})}\frac{\partial}{\partial r}(r\cdot), \quad (2.5b)$$

$$V_{int}(\mathbf{r}) = -\frac{\pi\hbar^2}{\mu_{2b}}\delta^{(2)}(\mathbf{r})\frac{1}{\ln(a_{2D}\lambda e^\gamma/2)}\left[1 - \ln(\lambda r e^\gamma/2)r\frac{\partial}{\partial r}\right]. \quad (2.5c)$$

In Eq. (2.5c),  $\gamma = 0.577\dots$  is the Euler-Mascheroni constant [214] and  $\lambda$  is an arbitrary wavevector, which however does not impact the properties of the system [215]. Despite the apparent differences in all pseudopotentials, their action on a two-body relative wavefunction satisfying the Bethe-Peierls condition for short interparticle distances in two dimensions,  $\Psi(r) = B\ln(r/a_{2D})$ , is identical [215]. Namely,  $V_{int}(\mathbf{r})\Psi(r) = \frac{\pi\hbar^2}{\mu_{2b}}\delta^{(2)}(\mathbf{r})B$ .

In stark contrast to three dimensions, the two dimensional scattering length is always positive. A two-body bound state with energy  $E = -\frac{2\hbar^2 e^{-2\gamma}}{\mu_{2b}a_{2D}^2}$  is thus supported by the contact potential, regardless of the magnitude of the scattering length [207, 216]. Note that from the form of the pseudopotentials it is not clear which are the non-interacting and strongly interacting limits, in contrast to the three dimensional case. This is going to be clarified later on [Sec. 2.3], when the energy spectrum of two interacting atoms in a two dimensional harmonic oscillator will be discussed.

### One dimension

In one dimension, the asymptotic expansion of the relative wavefunction for distances much larger than the range of the interaction potential  $r_0^{1D}$  assumes the form [203, 217],

$$\Psi_k(x) \xrightarrow{|x| \gg r_0^{1D}} \sin[k(|x| - a_{1D})], \quad (2.6)$$

where  $a_{1D}$  is the one dimensional scattering length. A pseudopotential extending this wavefunction to zero interparticle spacings, with the appropriate Bethe-Peierls boundary condition [218],  $\frac{\Psi'_k(x)}{\Psi_k(x)}\Big|_{x \rightarrow 0^\pm} = \mp \frac{1}{a_{1D}}$  is the following [203, 213],

$$V_{int}(x) = -\frac{\hbar^2}{\mu_{2b}a_{1D}}\delta(x). \quad (2.7)$$

This contact potential supports a two-body bound state for positive one dimensional scattering lengths with energy  $E = -\frac{\hbar^2}{2\mu_{2b}a_{1D}^2}$  [69]. The form of the pseudopotential suggests counterintuitively that the non-interacting limit is reached for  $a_{1D} = \pm\infty$ , and that repulsive and attractive interactions occur when the one dimensional scattering length is negative and positive respectively. These limits will be more apparent when inspecting the energy spectrum of two atoms trapped in a one dimensional harmonic oscillator [Sec. 2.3].

### Quasi-low dimensional systems

As mentioned in Sec. 2.1, the way to realize low dimensional gases in the laboratory is by strongly confining them kinematically along one or multiple dimensions, utilizing harmonic traps with high frequency in these dimensions. Confinement introduces another length scale in the system, the oscillator length along the tightly confined direction(s), and modifies the three dimensional scattering properties of atoms. For very large trapping frequency(ies) in the confined direction(s), signatures of the low dimensional scattering properties emerge at length scales larger than the oscillator length associated to these frequencies [28, 29, 205, 219–223]. In this way, relations can be established between the three and lower dimensional scattering lengths.

For a quasi-one dimensional setup, this relation reads explicitly [224, 225],

$$a_{1D} = -\frac{a_{\perp}^2}{2a} \left[ 1 - \zeta(1/2) \frac{a}{a_{\perp}} \right], \quad (2.8)$$

where  $a_{\perp} = \sqrt{\frac{\hbar}{\mu_{2b}\omega_{\perp}}}$  is the oscillator length along the two strongly confined directions, and  $\omega_{\perp}$  is the trapping frequency.  $\zeta(\cdot)$  is the Riemann zeta function [226]. In a quasi-two dimensional setting, atoms are strongly confined along a single direction. The two dimensional scattering length is related to  $a$  according to [205]

$$a_{2D} = 2e^{-\gamma} \sqrt{\frac{\pi}{0.915}} a_{\perp} \exp \left\{ -\sqrt{\frac{\pi}{2}} \frac{a_{\perp}}{a} \right\}, \quad (2.9)$$

where  $a_{\perp}$  is now the oscillator length along the tightly confined dimension.

Both of these relations suggest that the lower dimensional scattering lengths can be tuned by changing the harmonic frequency(ies) in the tightly trapped dimension(s). In this way, the corresponding lower dimensional effective interaction strengths are altered [227–230], realizing in principle strongly interacting low dimensional gases [31, 141].

#### 2.2.4 Fano-Feshbach resonances

A powerful technique for realizing strong effective interactions is that of Fano-Feshbach resonances. In our previous discussion regarding the quantum scattering of neutral atoms [Sec. 2.2.1], we have assumed that particles scatter off a single van der Waals potential. However, due to the internal structure of the atoms, there are multiple potentials associated to different total spins of the particles (e.g. singlet and triplet potentials), exhibiting a van der Waals tail at large separation distances [188]. At even larger distances, the potentials saturate to finite energies  $E_{\alpha}$ , stemming solely from the Hamiltonian describing the total spin of the atoms [27, 199]. In this asymptotic region, the potentials are called channels. Depending on the colliding energy of the particles  $E$ , they are classified as open or closed. Open channels are those that possess an asymptotic energy smaller than the colliding energy,  $E_{\alpha} < E$ , and are thus classically energetically accessible. On the other hand, closed channels are those that have an asymptotic energy larger than  $E$ ,  $E_{\alpha} > E$ , and they are classically energetically inaccessible. Moreover, due to the hyperfine interactions in atoms and the coupling of total spin with nuclear spin, different total spin degrees of freedom are coupled to each other. This results in a coupling between the aforementioned potentials [188, 231].

Due to the different total spin character of the potentials, their relative spacing can be tuned by applying external magnetic fields. The thresholds of these potentials

are thus shifted according to the Zeeman effect. At a particular magnetic field  $B_{res}$ , the potentials are shifted in such a way that the colliding energy almost coincides with the energy of a bound state supported by a closed channel. When the particles approach at short distances, couplings between the open and closed channels become substantial and the atoms couple resonantly to the two-body bound state of the closed channel. This resonance modifies the (three dimensional) scattering length according to the following expression [15, 87],

$$a(B) \simeq a_{bg} \left( 1 - \frac{\Delta B}{B - B_{res}} \right). \quad (2.10)$$

$a_{bg}$  is the off-resonant scattering length and  $\Delta B$  is the width of the resonance. When the magnetic field is parked around  $B = \Delta B + B_{res}$ , a zero crossing occurs and a non-interacting gas can be realized. In contrast, in the vicinity of  $B \simeq B_{res}$ , strongly interacting quantum gases can be realized with  $n|a|^3 \gtrsim 1$ . This mechanism is called Fano-Feshbach resonance [232–235], conceived both in atomic and nuclear physics. A multitude of Feshbach resonances has been identified so far for many atomic species [15]. Given the excellent controllability of external magnetic fields [16, 236], Fano-Feshbach resonances are massively exploited for molecule production [79, 87], realizing strongly interacting gases [18, 237], crossing phase boundaries [14, 67, 238], or triggering dynamics by employing dynamical protocols of the scattering length [239] to name but a few. Note that Feshbach resonances have been achieved also with external optical fields [240].

## 2.3 Few cold atoms in a harmonic oscillator trap

In this section we investigate the experimentally relevant scenario of two and three interacting ultracold atoms confined in a harmonic trap [51, 55, 59–62, 241, 242]. These systems can be treated semi-analytically and they provide important insights on the dynamical formation of few-body bound states in quantum gases [73, 103, 106, 113, 114, 243].

### 2.3.1 Two interacting confined atoms

The problem of two interacting atoms confined in a harmonic oscillator can be simplified by separating the center-of-mass from the relative degrees of freedom. The Hamiltonian describing the latter is effectively that of a single-particle. In [69], analytical solutions were found for the eigenstates and eigenenergies of this Hamiltonian. The relative wavefunction was expanded in terms of the non-interacting eigenstates of the harmonic oscillator and subsequently the Bethe-Peierls condition was applied. With such an ansatz, an expression for the relative wavefunction is derived, whose corresponding eigenenergy is determined by a transcendental equation. This procedure was then generalized to lower dimensional settings. The wavefunctions describing the relative degrees of freedom assume an analytical form, which can be written in a compact way [69, 243],

$$\Psi_{i,d}(r) = \mathcal{N}_{i,d} \Gamma \left( \frac{d}{4} - \frac{E_i}{2} \right) e^{-r^2/(2a_{ho}^2)} U \left( \frac{d}{4} - \frac{E_i}{2}, \frac{d}{2}, \frac{r^2}{a_{ho}^2} \right), \quad d = 1, 2, 3. \quad (2.11)$$

The parameter  $d$  is related to the dimensionality of the system ( $d = 1$  stands for one dimension, and so on and so forth),  $r$  is the norm of the relative interatomic distance,

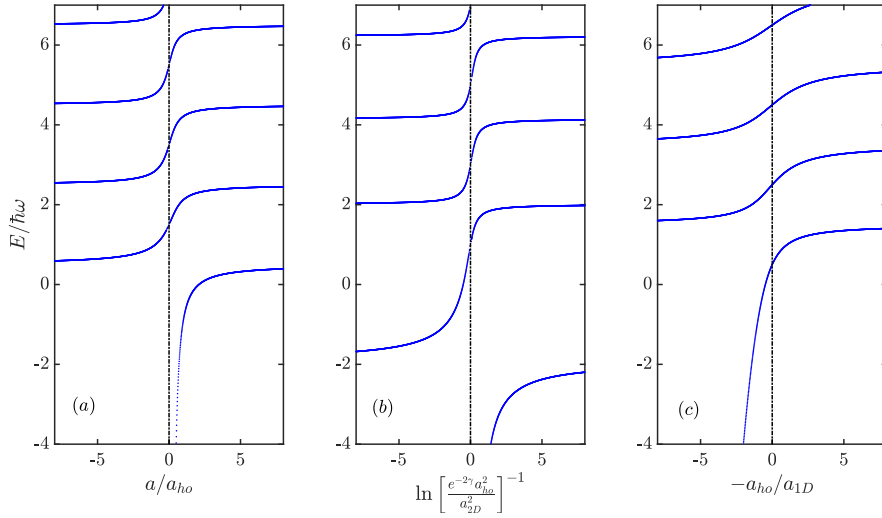


FIGURE 2.1: Energy spectrum of two interacting particles confined in a harmonic oscillator in (a) three, (b) two and (c) one dimension. The vertical dash-dotted lines in all three panels signify the non-interacting limit.

$\Gamma(\cdot)$  is the gamma function, and  $U(a, b, \cdot)$  is the confluent hypergeometric function of the second kind (Kummer, Tricomi) [214].  $a_{ho}$  is the harmonic oscillator length with the two-body reduced mass in the respective dimension. Note that these relative wavefunctions correspond to zero total angular momentum between the particles in three ( $l = 0$ ) and two ( $m = 0$ ) dimensions, and even-parity states upon exchange of the particle positions in one dimension. The normalization constants  $\mathcal{N}_{i,d}$  take the following expressions [B1, 244–246],

$$\mathcal{N}_{i,d} = \begin{cases} \frac{1}{\sqrt{2\pi^2 a_{ho}^3}} \sqrt{\frac{\Gamma\left(\frac{E_i}{2\hbar\omega} + \frac{1}{4}\right) \left(\frac{E_i}{2\hbar\omega} - \frac{3}{4}\right)}{\Gamma\left(-\frac{E_i}{2\hbar\omega} + \frac{7}{4}\right) \left[\psi\left(-\frac{E_i}{2\hbar\omega} + \frac{1}{4}\right) - \psi\left(-\frac{E_i}{2\hbar\omega} + \frac{3}{4}\right)\right]}}, & d = 3 \\ \frac{1}{a_{ho} \sqrt{\pi \psi^{(1)}\left(-\frac{E_i}{2\hbar\omega} + 1\right)}}, & d = 2 \\ \frac{1}{\sqrt{\pi a_{ho}}} \sqrt{\frac{\Gamma\left(-\frac{E_i}{2\hbar\omega} + \frac{3}{4}\right)}{\Gamma\left(-\frac{E_i}{2\hbar\omega} + \frac{1}{4}\right) \left[\psi\left(-\frac{E_i}{2\hbar\omega} + \frac{3}{4}\right) - \psi\left(-\frac{E_i}{2\hbar\omega} + \frac{1}{4}\right)\right]}}, & d = 1. \end{cases} \quad (2.12)$$

$\psi(\cdot)$  and  $\psi^{(1)}(\cdot)$  are the digamma and trigamma functions respectively [214].

The solutions (2.11) hold for any pair of particles, distinguishable or indistinguishable, and with any masses, as long as they interact through an  $s$ -wave pseudopotential. Moreover, they were also generalized for anisotropic harmonic traps in three dimensions [70, 76, 247]. In this context, the stationary properties of two atoms were investigated at the crossover to quasi low dimensional geometries.

The associated energy levels  $E_i$  are determined from the following transcendental equations [69, 71, 73, 203, 248],

$$\frac{\Gamma\left(-\frac{E_i}{2\hbar\omega} + \frac{3}{4}\right)}{\Gamma\left(-\frac{E_i}{2\hbar\omega} + \frac{1}{4}\right)} = \frac{a_{ho}}{2a} \quad d = 3, \quad (2.13a)$$

$$\psi\left(-\frac{E_i}{2\hbar\omega} + \frac{1}{2}\right) = \ln\left(\frac{a_{ho}^2 e^{-2\gamma}}{a_{2D}^2}\right) \quad d = 2, \quad (2.13b)$$

$$\frac{\Gamma\left(-\frac{E_i}{2\hbar\omega} + \frac{3}{4}\right)}{\Gamma\left(-\frac{E_i}{2\hbar\omega} + \frac{1}{4}\right)} = \frac{a_{ho}}{2a_{1D}} \quad d = 1, \quad (2.13c)$$

where  $\omega$  is the trapping frequency in the corresponding dimension. The functions on the left hand side are multi-valued from which one can determine the energies of the ground and excited states for all scattering lengths. The non-interacting limits  $E = 2n + d/2$ ,  $d = 1, 2, 3$ , are reached when  $a = 0$ ,  $1/a_{1D} = 0$  and  $\ln^{-1}(a_{ho}^2 e^{-2\gamma}/a_{2D}^2) = 0$ . These limits determine the appropriate interaction strengths in low dimensions that were elusive from the form of the pseudopotentials, especially in two dimensions [Sec. 2.2.3].

Figure 2.1 depicts the energy spectra for (a) three, (b) two, and (c) one dimension with respect to the corresponding interaction strengths in dimensionless units, as identified from the transcendental equations [Eqs. (2.13a)-(2.13c)]. Zero interactions are depicted with the dash-dotted lines. The energy levels that cross this dash-dotted line correspond to the spectrum of a particle in a harmonic oscillator in the respective dimension, taking into account only  $l = 0$ ,  $m = 0$  (zero total angular momentum) in three and two dimensions, and even-parity states in one dimension. For repulsive (attractive) interactions all energy levels are shifted upwards (downwards) with respect to their non-interacting values, regardless of the dimensionality of the system.

As discussed in Sections 2.2.2 and 2.2.3, the dependence of the energy of the two-body bound states on the scattering lengths is now clearly showcased in Fig. 2.1. In three dimensions [Fig. 2.1 (a)] a single bound state exists for repulsive interactions. As the scattering length becomes comparable or larger than the oscillator length, the energy of the bound state is shifted upwards to positive values. In two dimensions [Fig. 2.1 (b)] there is always a two-body bound state, regardless of the sign or magnitude of interactions, in contrast to the other dimensions. In one dimension [Fig. 2.1 (c)], a two-body bound state is supported only for attractive interactions (positive one dimensional scattering length). Note that strictly speaking all eigenstates are bound, since the atoms are confined in a harmonic trap. By two-body bound states we refer here to the genuine bound states, which are supported by the pseudopotentials even in the absence of a trap.

## 2.3.2 Three interacting atoms in a trap

### Jacobi and Hyperspherical coordinates

Three interacting atoms confined in a trap are also treated in the center-of-mass frame. In contrast however to two-particle systems, there are two relative coordinates, called Jacobi coordinates [75]. As sketched in Fig. 2.2 for an arbitrary three-body system, the first relative coordinate ( $\rho_1$ ) is proportional to the interparticle distance between two atoms. The second Jacobi vector  $\rho_2$  is proportional to the difference of the third particle with the center-of-mass of the two remaining atoms. The proportionality factors are usually related to the masses of the particles [249]. Note also that there

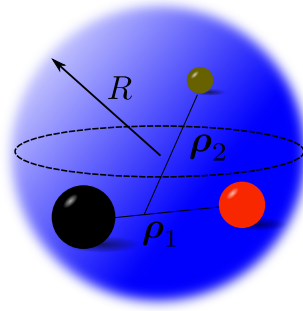


FIGURE 2.2: Sketch of the Jacobi coordinates for an arbitrary three-body system.  $\rho_1$  and  $\rho_2$  are the two Jacobi vectors and  $R$  is the hyperradius, describing the size of the system.

are three sets of Jacobi coordinates, in which a different particle is connected each time to the center-of-mass of the remaining two. All of the sets are related to each other through a transformation matrix depending on the masses, the kinematic rotation [250].

In the next step, one can transform the two Jacobi vectors to a generalization of the spherical coordinates in higher dimensional spaces, the so-called hyperspherical coordinates [66, 251]. These involve the hyperradius  $R$ , characterizing the spatial extent of the system, and hyperangles, collectively denoted as  $\Omega$ . These are related to the relative positions of the particles, as well as the angles associated to the configuration of the Jacobi vectors in space. In three dimensions there are five hyperangles, whereas in two and one dimension there are three and one respectively [252]. Note that there are multiple choices for the representation of the hyperangles [249, 253–255]. Moreover, in one dimension the term hyperspherical coordinates is abusive since there is only a single angle [256].

Upon this choice of coordinate system, the relative three-body Schrödinger equation is written as

$$\left[ -\frac{\hbar^2}{2\mu_{3b}} \frac{\partial^2}{\partial R^2} + \frac{1}{2}\mu_{3b}\omega^2 R^2 + \underbrace{\frac{\hbar^2[\Lambda^2 + (2d-3)(2d-1)/4]}{2\mu_{3b}R^2}}_{\mathcal{H}_{ad}(R;\Omega)} + V_{int}(R, \Omega) - E \right] \Psi(R, \Omega) = 0, \quad (2.14)$$

where  $\mu_{3b}^2 = m_1 m_2 m_3 / (m_1 + m_2 + m_3)$  is the three-body reduced mass, and  $\Lambda^2$  is the grand angular momentum operator describing the total angular momentum of the three particles [257, 258] expressed in  $d = 1, 2, 3$  dimensions.  $V_{int}(R, \Omega)$  is the sum of three pairwise contact interatomic potentials expressed in hyperspherical coordinates. The first term in Eq. (2.14) is the kinetic term, the second is the potential energy term due to the harmonic confinement, the third is a centrifugal barrier due to the angular momentum of the particles in the respective dimension, and the fourth one is the interaction potential.

### Potential curves

The Schrödinger equation (2.14) is solved by employing the adiabatic hyperspherical method [259–261]. The first step consists of diagonalizing the adiabatic Hamiltonian

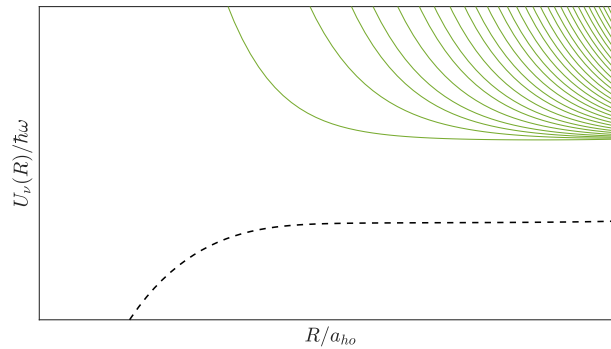


FIGURE 2.3: Schematic of potential curves  $U_\nu(R)$  with respect to the hyperradius  $R$ .

$\mathcal{H}_{ad}(R; \mathbf{\Omega})$  at every fixed  $R$ , obtaining an orthonormal basis set of hyperangular wavefunctions  $\Phi_\nu(R; \mathbf{\Omega})$  and a set of potential curves  $U_\nu(R)$  depending on the hyperradius,

$$\mathcal{H}_{ad}(R; \mathbf{\Omega})\Phi_\nu(R; \mathbf{\Omega}) = U_\nu(R)\Phi_\nu(R; \mathbf{\Omega}). \quad (2.15)$$

When zero-range pseudopotentials are considered for the interatomic interactions, it is very convenient to solve the above equation by employing the Green's function [262–264] of the grand angular momentum operator  $\Lambda^2$  [258]. One arrives at a semi-analytical expression for the hyperangular wavefunctions. Subsequently, the Bethe-Peierls conditions are applied, which take the form of a three dimensional matrix eigenvalue equation with zero eigenvalue. The eigenvectors depend solely on  $R$  and they serve a twofold purpose.

First, they are normalization coefficients for the hyperangular wavefunctions. Moreover, the  $\Phi_\nu(R; \mathbf{\Omega})$  eigenfunctions are expanded in terms of the three different sets of Jacobi coordinates with these eigenvectors as coefficients, from where the appropriate symmetry of the wavefunction can be easily implemented upon exchange of any particle pair. The potential curves  $U_\nu(R)$  are then specified from a transcendental equation stemming from the zero determinant of the matrix in the eigenvalue problem [262, 265]. The transcendental equation is general, since it depends on the masses, the statistics of the particles and the scattering length(s).

A sketch of potential curves is depicted in Fig. 2.3 corresponding to three bosonic particles. A first remark is that there is no upper bound on the number of potential curves. The number is truncated so that observables such as the energies are converged in the particular energy slice one is interested in. For every two-body bound state supported by the pairwise interatomic potential, there is a corresponding potential curve which at very large hyperradii  $R$  saturates at the energy of the corresponding dimer, the atom-dimer threshold [dashed curve in Fig. 2.3]. At such large sizes, these are channels describing a dimer and a third atom very far away. Since we are considering zero-range pseudopotentials for the pairwise interactions, there is at most a single two-body bound state, and this translates to a single potential curve  $U_1(R)$ . However, if we consider distinguishable particles or mixtures, there can be two or three two-body bound states, yielding the same number of potential curves with the appropriate atom-dimer thresholds [266].

For these atom-dimer potential curves, at shorter hyperradii the atoms experience a potential well whose depth depends on the masses and the scattering length(s). In this well, the atoms can form in principle three-body bound states, i.e. eigenstates



with energy lower than the atom-dimer threshold. The shape of the well greatly depends on the dimensionality of the system. In two dimensions there is a barrier at small hyperradii [85, 267], which depends on the parameters of the three-body setup, such as the scattering length(s) and the masses. Remarkably, in three dimensions there is no repulsive barrier and some of the potential curves with the atom-dimer threshold tend to  $-\infty$  [268]. One has to supplement the zero-range theory with a hard wall [269] that fixes the number of three-body bound states as well as the position of the ground trimer. Apart from trimers, these potential curves can also support atom-dimers with energy above the atom-dimer threshold. These are dimers interacting with the third atom.

The higher potential curves [solid lines in Fig. 2.3] saturate at large distances to zero. Every one of these corresponds to a different total angular momentum quantum number [251], and they describe three interacting atoms. In these potential curves, the particles cannot approach very close since they experience a centrifugal barrier.

### Hyperradial equations and eigenspectra

To obtain the eigenenergies and eigenstates of three atoms confined in a harmonic trap, we expand the three-body relative wavefunction in the hyperangular basis with  $R$ -dependent coefficients, the hyperradial channels  $F_\nu(R)$ ,  $\Psi(R, \mathbf{\Omega}) = \sum_\nu F_\nu(R) \Phi_\nu(R; \mathbf{\Omega})$  [66, 262]. Substituting this expansion in the three-body Schrödinger equation [Eq. (2.14)] and projecting with  $\Phi_{\nu'}^*(R; \mathbf{\Omega})$  integrating over the hyperangles, we obtain coupled first order differential equations depending on a single parameter, the hyper-radius  $R$ ,

$$-\frac{\hbar^2}{2\mu_{3b}} \frac{d^2}{dR^2} F_{\nu'}(R) + \frac{1}{2} \mu_{3b} \omega^2 R^2 F_{\nu'}(R) + U_{\nu'}(R) F_{\nu'}(R) - \frac{\hbar^2}{2\mu_{3b}} \sum_\nu \left[ 2P_{\nu'\nu}(R) \frac{d}{dR} + Q_{\nu'\nu}(R) \right] F_\nu(R) = E F_{\nu'}(R). \quad (2.16)$$

The matrix elements  $P_{\nu'\nu}(R)$  and  $Q_{\nu'\nu}(R)$  provide the couplings between different potential curves and they stem from the dependence of the hyperangular eigenfunctions on the size of the system  $R$ . The coupling elements are defined according to,

$$P_{\nu'\nu}(R) = \langle \Phi_{\nu'}(R; \mathbf{\Omega}) | \frac{\partial \Phi_\nu(R; \mathbf{\Omega})}{\partial R} \rangle_{\mathbf{\Omega}} \quad (2.17)$$

$$Q_{\nu'\nu}(R) = \langle \Phi_{\nu'}(R; \mathbf{\Omega}) | \frac{\partial^2 \Phi_\nu(R; \mathbf{\Omega})}{\partial R^2} \rangle_{\mathbf{\Omega}}, \quad (2.18)$$

where the  $\langle \dots \rangle_{\mathbf{\Omega}}$  symbol denotes integration only over the hyperangular degrees of freedom. In the case of contact pseudopotentials the coupling elements assume semi-analytical expressions [270, 271].

A convenient way to solve the coupled equations in (2.16) is by expressing the hyperradial channels in the B-spline basis [272, 273]. These are piece-wise polynomials constructed recursively, whose derivatives are known analytically. Moreover, the appropriate boundary conditions can be easily implemented.

A schematic of the energy spectrum of three interacting atoms in a trap is shown in Fig. 2.4 with respect to a single positive scattering length in three, two, and one dimension. Only three eigenstates are shown exemplarily, but of course the spectrum is far more dense [207, 274–282]. Overall, we can classify the eigenstates in

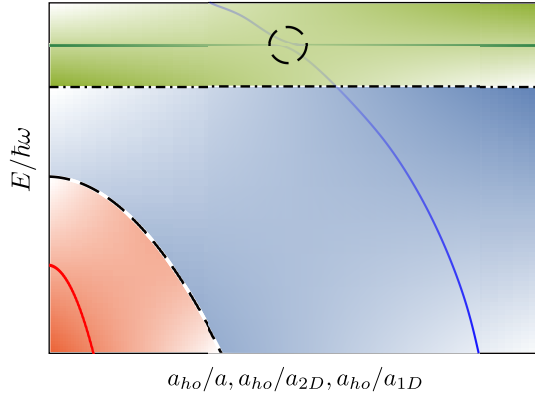


FIGURE 2.4: Cartoon of the energy spectrum of three atoms confined in a harmonic trap with respect to the scattering lengths in three, two and one dimension. Trimer states occur below the atom-dimer threshold [dashed line], and avoided crossings [dashed circle] occur between the atom-dimers and atom-atom-atom states.

three classes: Trimers [red region], atom-dimers [blue region], and atom-atom-atom eigenstates [green region].

Trimers [red eigenstate] have energy below the atom-dimer threshold [black dashed line] and their number greatly depends on the statistics of the particles [271], the masses [283], the scattering lengths [75], and the dimensionality of the setting [284, 285].

Above the zero-point threshold,  $d\hbar\omega$ ,  $d = 1, 2, 3$  [dash-dotted line in Fig. 2.4], atom-atom-atom states [green eigenstate] can be supported, describing three interacting atoms confined in a trap. Their existence can be traced to the potential curves with the repulsive barriers at short hyperradii [solid green potential curves in Fig. 2.3]. At particular values of the scattering length there are avoided crossings [dashed circle in Fig. 2.4] between the atom-atom-atom states and atom-dimers [blue eigenstate]. These crossings occur due to the couplings between the potential curves with the atom-dimer threshold [dashed curve in Fig. 2.3] and the potential curves supporting three interacting atoms [green solid curves in Fig. 2.3] through the  $P$  and  $Q$  matrix elements [Eqs. (2.17), (2.18)]. For energies way lower than the zero-point threshold [blue region], atom-dimers describe a strongly bound dimer interacting with a third atom. At this regime the energy is given approximately by the energy of the dimer plus the energy of a third atom in a harmonic trap. Close to the avoided crossings though [dashed circle in Fig. 2.4], these states resemble atom-atom-atom states. The same applies also for the latter eigenstates. The faded colors in the vicinity of the avoided crossing in Fig. 2.4 imply that these eigenstates do not have a definite character. The number of avoided crossings greatly increases for higher  $E/\hbar\omega$  due to the larger density of atom-atom-atom eigenstates. This occurs due to the large number of potential curves with a repulsive barrier at small hyperradii [green curves in Fig. 2.3].

## 2.4 Short-range correlations

In the previous section we have investigated the stationary properties of few interacting trapped atoms in terms of a single parameter, the scattering length. It turns out that the Bethe-Peierls boundary conditions give rise to other central quantities satisfying a plethora of relations. These are universal relations describing the stationary properties of arbitrary systems in three dimensions. Here, the universality means that they

are valid for few trapped atoms as well as strongly interacting many-body systems of bosons, fermions or mixtures thereof. The relations were generalized to lower dimensions as well.

### 2.4.1 Two-body contact and universal relations

As already discussed in Secs. 2.2.2 2.2.3, the  $s$ -wave scattering aspects of two atoms are properly captured by substituting the respective interaction potentials with contact pseudopotentials. The latter impose the appropriate Bethe-Peierls conditions for the two-body relative wavefunction at vanishing interparticle distances  $r$ , namely  $\Psi(r) \xrightarrow{r \rightarrow 0} B_3(1 - a/r), B_2 \ln(r/a_{2D}), B_1(r - a_{1D})$  in three ( $d = 3$ ), two ( $d = 2$ ) and one ( $d = 1$ ) dimension respectively. In these expressions,  $B_d$  is a normalization constant that depends on the eigenenergy associated with the relative wavefunction as well as the dimensionality [e.g. Eq. (2.11) for two trapped atoms]. The boundary conditions lead to a specific form for the asymptotic expansion of the relative two-body wavefunction in momentum space. It reads explicitly [13],

$$\tilde{\Psi}(k) \longrightarrow \begin{cases} -\frac{4\pi a B_3}{k^2} & d = 3, \\ -\frac{2\pi B_2}{k^2} & d = 2, \\ \frac{2B_1}{a_{1D} k^2} & d = 1, \end{cases} \quad (2.19)$$

where  $\tilde{\Psi}(k)$  is the Fourier transform of the relative two-body wavefunction.

These relations hold when the wavevector  $k$  is much larger than the inverse of the respective scattering length,  $k \gg |a|^{-1}, a_{2D}^{-1}, |a_{1D}|^{-1}$  [67]. It follows that the relative two-body momentum distribution  $|\tilde{\Psi}(k)|^2$  displays a  $1/k^4$  tail at large  $k$  in all dimensions,  $|\tilde{\Psi}(k)|^2 \xrightarrow{k \gg 1} C_d^{(2b)}/k^4$ ,  $d = 1, 2, 3$  [120–122, 286]. The proportionality factor  $C_d^{(2b)}$  is called the two-body contact. It is related to the probability of detecting two particles with very large relative wavevectors (larger than the inverse scattering length), i.e. at small interatomic distances (smaller than the scattering length). In this sense, the contact captures two-body short-range interparticle correlations. This innocuous asymptotic expansion, however, is the first in a series of relations that will appear later on, where the two-body contact plays a central role.

Consider for example two harmonically trapped atoms in three dimensions in an arbitrary eigenstate characterized by energy  $E_i$ . From the transcendental equation determining the energy levels (2.13a), we deduce that the rate of change of the  $i$ -th energy level with respect to the scattering length assumes the form [69]

$$-a \frac{dE_i}{da} = \frac{2}{\psi\left(-\frac{E_i}{2\hbar\omega} + \frac{1}{4}\right) - \psi\left(-\frac{E_i}{2\hbar\omega} + \frac{3}{4}\right)}. \quad (2.20)$$

From the expansion of the corresponding relative two-body wavefunction (2.11) at short interparticle distances, we get the appropriate  $1 - a/r$  behavior satisfying the Bethe-Peierls conditions,

$$\Psi_{i,3}(r) \xrightarrow{r \ll |a|} -\frac{1}{a\sqrt{2\pi a_{ho}}} \sqrt{\frac{\Gamma\left(-\frac{E_i}{2\hbar\omega} + \frac{1}{4}\right)\left(-\frac{E_i}{2\hbar\omega} + \frac{3}{4}\right)}{\Gamma\left(-\frac{E_i}{2\hbar\omega} + \frac{7}{4}\right)\left[\psi\left(-\frac{E_i}{2\hbar\omega} + \frac{1}{4}\right) - \psi\left(-\frac{E_i}{2\hbar\omega} + \frac{3}{4}\right)\right]}} \left(1 - \frac{a}{r}\right). \quad (2.21)$$

The two-body contact for the two atoms in that eigenstate then follows easily from the asymptotic expansion given by Eq. (2.19),

$$C_{i,3}^{(2b)} = -\frac{16\pi a}{a_{ho}^2} \frac{1}{\psi\left(-\frac{E_i}{2\hbar\omega} + \frac{1}{4}\right) - \psi\left(-\frac{E_i}{2\hbar\omega} + \frac{3}{4}\right)}. \quad (2.22)$$

Combining Eqs. (2.20) and (2.22), we arrive at the following expression for the rate of change of the  $i$ -th eigenenergy with respect to the scattering length,

$$\frac{dE_i}{d(-1/a)} = \frac{\hbar^2}{8\pi\mu_{2b}} C_{i,3}^{(2b)}. \quad (2.23)$$

Eq. (2.23) is completely general in the sense that it holds for any two-body eigenstate independently of the value of the scattering length. Applying the same reasoning to lower dimensions, similar rates of change are derived for the eigenenergy  $E_i$  associated with an arbitrary eigenstate, namely

$$\frac{dE_i}{d(\ln a_{2D})} = \frac{\hbar^2}{4\pi\mu_{2b}} C_{i,2}^{(2b)}, \quad (2.24)$$

$$\frac{dE_i}{da_{1D}} = \frac{\hbar^2}{4\mu_{2b}} C_{i,1}^{(2b)}. \quad (2.25)$$

All these relations imply that knowledge of the two-body contact for all eigenstates and scattering lengths is sufficient for reconstructing the energy spectrum presented in Fig. 2.1. Apart from two-body short-range correlations, the two-body contact determines also variations of the energy upon tuning the scattering length.

Remarkably, by employing the asymptotic expansion of the one-body density in momentum space for an arbitrary number of bosonic or fermionic particles, the same behavior of the momentum tail ( $k^{-4}$ ) is observed, see for instance Refs. [120–123, 126, 128, 287]. Moreover, the equations regarding the rate of change of the energy with respect to the scattering length can also be generalized, dubbed the adiabatic sweep theorems [13]. These relations hold both for weakly and strongly interacting systems, confined either in harmonic traps or in free space. In this sense they are called universal. Note, however, that the two-body contact in all of these setups is in principle different, since it is derived from the wavefunction describing the system in question [see asymptotic expansion in Eq. (2.19)].

Moreover, the sweep theorems are further generalized [120] for finite temperature systems. In this case, the two-body contact of a system is related to the rate of change of the Helmholtz free energy  $F = E - TS$  as a function of the scattering length at fixed temperature  $T$ ,

$$\left. \frac{dF}{d(-1/a)} \right|_T = \frac{\hbar^2}{8\pi\mu_{2b}} C_3^{(2b)}. \quad (2.26)$$

In this context, the two-body contact determines the thermodynamic properties of a system in thermal equilibrium, and can be thought of as the conjugate thermodynamic variable to the inverse scattering length. From the free energy, additional thermodynamic quantities can be estimated as well. In particular, the pressure of a homogeneous system is related to the energy density  $\mathcal{E}$  of a system and the contact density  $\mathcal{C}_3^{(2b)} = C_3^{(2b)}/V$  [122, 124, 125, 288],

$$P = \frac{2}{3}\mathcal{E} + \frac{\hbar^2}{12\pi ma} \mathcal{C}_3^{(2b)}, \quad (2.27)$$

which has been extended to lower dimensions as well, see e.g. Refs. [124, 125]. For externally trapped systems, a generalized virial theorem can be derived involving the two-body contact [122, 133],

$$E_{kin} + E_{int} - E_{pot} = -\frac{\hbar^2}{8\pi ma} C_3^{(2b)}. \quad (2.28)$$

In the latter expression,  $E_{kin}$ ,  $E_{int}$  and  $E_{pot}$  are the kinetic, interaction and potential energies of the system respectively. All of these relations hold for any system. Note that interestingly many more relations were derived, connecting the two-body contact with other observables such as the static structure factor [134–137].

Apart from the thermodynamic relations describing arbitrary systems in equilibrium, the two-body contact is also important in determining their dynamical aspects. A characteristic example arises when considering population transfer of atoms from one hyperfine state to another by applying radiofrequency (rf) pulses. The underlying transition rate  $\Gamma(\omega_{rf})$  has the following asymptotic tail at large frequency domains of the rf signal,  $\omega_{rf}$  [138, 139],

$$\Gamma(\omega_{rf}) \xrightarrow{\omega_{rf} \rightarrow \infty} \frac{\hbar^{1/2} \Omega^2}{4\pi m^{1/2} \omega_{rf}^{3/2}} C_3^{(2b)}, \quad (2.29)$$

where  $\Omega$  is the Rabi coupling between the two different hyperfine states. This relation was employed to measure the two-body contact in two-component Fermi gases [130–132]. Moreover, collisions between spinful atoms can lead to two-body losses through inelastic channels (e.g. spin flips). Then, the decay width for the depletion of atoms in one spin component takes the form [128],

$$\Gamma \simeq \frac{\hbar^2 [-\Im(a)]}{2\pi m |a|^2} C_3^{(2b)}. \quad (2.30)$$

Note that in the case of inelastic collisions the scattering length is complex [289].

From the above description, the importance of the two-body contact becomes evident. It is a microscopic quantity directly related to the macroscopic state of a system through a series of relations [Eqs. (2.23), (2.27), (2.28), (2.29), (2.30)] [13]. This is a general statement holding for a plethora of different systems, being weakly or strongly interacting, fermions or bosons, having few or many particles. In this sense, all of the above relations are universal. Furthermore, they were even extended to mixtures [123, 290].

### 2.4.2 Three-body contact

The asymptotic expansion of the single-particle momentum distribution of an arbitrary system displayed a  $1/k^4$  tail at large momenta, introducing the two-body contact. This occurs irrespective of the dimensionality. When considering however bosonic particles, a next-to-leading order term appears, stemming from the behavior of three identical particles at short distances [i.e. at small hyperradius  $R$ ]. This term strongly depends on the dimension of the setup. In three dimensions, the asymptotic expansion of the one-body density in momentum space of such a system assumes the following form [129, 291],

$$n(k) \xrightarrow{k \gg |a|^{-1}} \frac{C_3^{(2b)}}{k^4} + \frac{89.26 \sin[2s_0 \ln(k/k_*) - 1.338]}{k^5} C_3^{(3b)}, \quad (2.31)$$

where  $s_0 = 1.00624$ . In analogy to the two-body contact, the coefficient of the next-to-leading order term ( $k^{-5}$ ) is identified as the three-body contact  $C_3^{(3b)}$ . It is related to the probability of finding three bosons at distances much smaller than  $|a|$  [123].

In that regard the three-body contact quantifies short-range three-body correlations. In Eq. (2.31),  $k_*$  is the wavevector associated with the energy of the ground three-body bound state,  $-\hbar^2 k_*^2/m$ , at strong interactions,  $|a| \rightarrow \infty$  [75]. For a contact pseudopotential, the  $k_*$  parameter is related to the hard wall  $R_t$  (otherwise called the three-body parameter) that regularizes the potential curves at small hyperradii, fixes the number of three-body bound states and determines the position of the energy of the ground trimer,  $R_t = \sqrt{2} k_*^{-1} \exp\{\Im[\ln(\Gamma(1 + is_0))]/s_0\}$  [292], see also the relevant discussion for the potential curves in Sec. 2.3.2.

The fact that this momentum scale comes into play in the next-to-leading order term of the one-body momentum density is related to the Efimov effect [107, 172, 269, 293–298]. Namely, for three particles in free space interacting via pairwise interactions with a very large scattering length, an infinity of three-body bound states occurs, whose energies display a geometric progression. Due to the latter, the energies of the three-body bound states accumulate at the zero-energy threshold. For a zero-range model, the energy spectrum is unbounded from below, and one has to supplement the theory with the three-body parameter  $R_t$  to fix the energy of the ground trimer [75].

Similarly to the two-body contact,  $C_3^{(3b)}$  defined through the asymptotic expansion (2.31) satisfies also a few universal relations. First of all, an equivalent adiabatic sweep theorem states that the rate of change of the energy with respect to variations of the three-body parameter at fixed scattering length is proportional to  $C_3^{(3b)}$  [123, 129, 291],

$$\left. \frac{dE}{d \ln(R_t)} \right|_a = \frac{2\hbar^2}{m} C_3^{(3b)} \quad \text{or} \quad k_* \left. \frac{dE}{dk_*} \right|_a = -\frac{2\hbar^2}{m} C_3^{(3b)}. \quad (2.32)$$

Moreover, the virial theorem presented in Eq. (2.28) for the two-body contact is generalized when considering bosonic particles, incorporating the three-body contact as well [133, 291],

$$E_{kin} + E_{int} - E_{pot} = -\frac{\hbar^2}{16\pi m a} C_3^{(2b)} - \frac{\hbar^2}{m} C_3^{(3b)}. \quad (2.33)$$

Within the context of the virial theorem, effects stemming from three-body physics become dominant at strong interactions in comparison to two-body effects.

Furthermore, the universal relation associated to the frequency tail of the rf transition rate is also modified when considering identical bosons. In particular, the asymptotic behavior of the transition rate  $\Gamma(\omega_{rf})$  to transfer population from one hyperfine state to another acquires an additional next-to-leading order term related to the three-body contact [291],

$$\Gamma(\omega_{rf}) \xrightarrow{\omega_{rf} \rightarrow \infty} \Omega^2 \left[ \frac{\hbar^{1/2}}{4\pi m^{1/2} \omega_{rf}^{3/2}} C_3^{(2b)} + \frac{\hbar^2 C_3^{(3b)}}{2m \omega_{rf}^2} \left( 9.23 - 13.6 \sin[s_0 \ln\left(\frac{m \omega_{rf}}{\hbar k_*^2}\right) + 2.66] \right) \right], \quad (2.34)$$

decaying as  $\omega_{rf}^{-2}$ . Note again the appearance of the wavevector  $k_*$  due to the Efimov effect. This relation was in fact utilized to measure the three-body contact of a strongly interacting  $^{39}\text{K}$  gas [104], by employing Ramsey interferometry and creating a superposition of two hyperfine states.

A universal formula is also derived, relating the three-body contact with the decay width due to three-body losses, generalizing in that sense Eq. (2.30). Low-energy three-body collisions can be inelastic when a deeply bound dimer plus another atom

are formed afterwards. These deep dimers are, of course, not accounted for by the zero-range model, but rather by van der Waals potentials [299]. Due to energy conservation, the large negative potential energy of the deep dimer is converted to large kinetic energy of the latter and the remaining atom. The sum of these two energy terms matches the low initial colliding energy of three atoms. As a result all three particles escape from the gas, a process called three-body recombination [66]. Three-body bound states are thus metastable due to these processes, with the exception of  $^4\text{He}$  trimers [300]. Within the zero-range model, inelastic three-body collisions are treated by letting the three-body parameter to be complex, namely  $\ln(R_t) \rightarrow \ln(R_t) - \frac{i\eta}{s_0}$ , where  $\eta$  is called the inelasticity parameter [123]. This is in direct analogy with the complex scattering length in the presence of two-body losses. In the limit  $\eta \rightarrow 0$ , a simple equation is derived connecting the decay width of a bosonic gas due to three-body losses  $\Gamma$  with the three-body contact [113, 123, 129],

$$\Gamma \xrightarrow{\eta \rightarrow 0} \frac{4\hbar\eta}{ms_0} C_3^{(3b)}. \quad (2.35)$$

All of the above relations for the three-body contact are universal in the sense that they apply independently of the bosonic species, the value of the interaction strength or the particle number. They are expected to be modified when considering bosonic mixtures [123]. In the case of two-component fermions however, three-body short-range correlations, and hence the three-body contact are predominantly suppressed due to the Pauli exclusion principle.

In two dimensions, the equivalent asymptotic expansion of the one-body density in momentum space  $n(k)$  is completely different due to the absence of the Efimov effect [209, 301], even though trimer states do exist [284]. The expansion of  $n(k)$  therefore reads [302, 303],

$$n(k) \xrightarrow{k \gg a_{2D}^{-1}} \frac{C_2^{(2b)}}{k^4} + \frac{\ln^3(ka_{2D})}{k^6} C_2^{(3b)}, \quad (2.36)$$

defining the two dimensional three-body contact  $C_2^{(3b)}$ . Note that in the next-to-leading order term ( $k^{-6}$ ) no additional length scale is introduced, only the two dimensional scattering length. To the best of my knowledge there are no universal relations that the two dimensional three-body contact satisfies, in contrast to the three dimensional one. This behavior may be related to the fact that three-body physics in two dimensions is determined from a single length scale, the two dimensional scattering length. Namely, the behavior of the potential curves [see Sec. 2.3.2], as well as the three-body binding energies are solely determined by  $a_{2D}$  [270].

## 2.5 Interacting ultracold quantum gases

The universal relations that the two- and three-body contacts enjoy are powerful since they link macroscopic properties, such as the energy, pressure and loss rates with microscopic quantities for arbitrary systems. The contacts stem from the behavior of atoms when approaching at very short distances, smaller than the absolute value of the scattering length. In this sense, these relations describe the buildup of short range correlations. Despite their universality, they fail to characterize the behavior of arbitrary systems at larger length scales, e.g. at which collective excitations occur. In order to deal with such phenomena there exist multiple approaches. For weakly interacting quantum gases with a large macroscopic particle number, a mean-field treatment is adequate, where the motion of every atom is dictated by the density of

the entire gas [304]. For smaller number of atoms and/or stronger interactions such a picture breaks down and a many-body description is required [27].

### 2.5.1 Weakly interacting gases

Here, we are interested in the description of collective phenomena within a mean-field treatment. Consider a single component weakly interacting bosonic gas with  $N$  atoms in three dimensions given by the following effective Hamiltonian [12],

$$\mathcal{H} = \sum_{i=1}^N \left[ -\frac{\hbar^2}{2m} \nabla_i^2 + V_{pot}(\mathbf{r}_i) \right] + \frac{4\pi\hbar^2 a}{m} \sum_{i<j} \delta^{(3)}(\mathbf{r}_i - \mathbf{r}_j), \quad (2.37)$$

where  $\mathbf{r}_i$  are the positions of the particles in the lab frame and  $V_{pot}(\mathbf{r})$  is the external harmonic trap potential. The three dimensional scattering length  $a$  is smaller than any other length scale of the system and the particle number  $N$  is very large. The effective interaction contact potential is different from the one in Eq. (2.3) [Sec. 2.2.2]. The reason is that the wavefunction describing the quantum gas,  $\Psi(\mathbf{r}_1, \dots, \mathbf{r}_N)$  is regular when  $|\mathbf{r}_i - \mathbf{r}_j| \simeq 0 \ \forall i \neq j$ . Namely, it does not exhibit the divergent  $1 - a/|\mathbf{r}_i - \mathbf{r}_j|$  behavior due to the Bethe-Peierls boundary condition. Essentially the wavefunction treats particles at a length scale larger than the scattering length [12] and captures the collective behavior of the gas. The regularization operator therefore acts as an identity operator on such regular wavefunctions.

For bosonic gases in the limit of zero temperature,  $n\Lambda_{th}^3 \gg 1$  [Sec. 2.1] and weak interactions  $n|a|^3 \ll 1$ , an appropriate ansatz for the wavefunction is given by a product of single particle wavefunctions [Hartree product for bosons],

$$\Psi(\mathbf{r}_1, \dots, \mathbf{r}_N) = \prod_{i=1}^N \varphi(\mathbf{r}_i), \quad (2.38)$$

normalized to unity  $\int d\mathbf{r} |\varphi(\mathbf{r})|^2 = 1$ . This ansatz implies that all particles occupy a single quantum state. In the ideal quantum gas limit ( $a = 0$ ), this describes the well-known phenomenon of Bose-Einstein condensation [305, 306]. However, we are interested in the behavior of that quantum state in the weakly interacting regime,  $n|a|^3 \ll 1$ . The energy of the bosonic gas is given by the expectation value [12]

$$\begin{aligned} E &= \int \prod_{p=1}^N d\mathbf{r}_p \Psi^*(\mathbf{r}_1, \dots, \mathbf{r}_N) \mathcal{H} \Psi(\mathbf{r}_1, \dots, \mathbf{r}_N) \\ &= N \int d\mathbf{r} \left[ \frac{\hbar^2}{2m} |\nabla\varphi(\mathbf{r})|^2 + V_{pot}(\mathbf{r}) |\varphi(\mathbf{r})|^2 + \frac{(N-1)}{2} \frac{4\pi\hbar^2 a}{m} |\varphi(\mathbf{r})|^4 \right]. \end{aligned} \quad (2.39)$$

The subscripts denoting the different particles have been dropped, since all of the expectation values are the same, hence the  $N$  factor in front. For the kinetic energy term, Gauss theorem was utilized and the surface terms on a sphere with large radius vanish, since the wavefunction  $\varphi(\mathbf{r})$  vanishes (exponentially) at large distances due to the harmonic trap potential.

Eq. (2.39) is an energy functional with respect to the unknown wavefunction  $\varphi(\mathbf{r})$ . It is convenient to express it instead in terms of  $\Phi(\mathbf{r}) = \sqrt{N}\varphi(\mathbf{r})$ ,

$$E[\Phi(\mathbf{r})] = \int d\mathbf{r} \left[ \frac{\hbar^2}{2m} |\nabla\Phi(\mathbf{r})|^2 + V_{pot}(\mathbf{r}) |\Phi(\mathbf{r})|^2 + \frac{1}{2} \frac{4\pi\hbar^2 a}{m} |\Phi(\mathbf{r})|^4 \right]. \quad (2.40)$$



Since we are dealing with a macroscopic number of bosons, we have employed that  $N(N-1) \simeq N^2$ . To determine the macroscopic wavefunction  $\Phi(\mathbf{r})$ , we seek solutions that render the energy functional stationary with respect to variations of  $\Phi^*(\mathbf{r})$ ,  $\frac{\delta E[\Phi(\mathbf{r})]}{\delta \Phi^*(\mathbf{r}')} = 0$ . Moreover, the stationarity should be achieved at fixed particle number  $N = \int d\mathbf{r} |\Phi(\mathbf{r})|^2$ . This is guaranteed by minimizing the energy functional with a Lagrange multiplier, known as the chemical potential  $\mu$ ,

$$\frac{\delta E[\Phi(\mathbf{r})]}{\delta \Phi^*(\mathbf{r}')} - \mu \Phi(\mathbf{r}') = 0 \implies \left[ -\frac{\hbar^2}{2m} \nabla'^2 + V_{pot}(\mathbf{r}') + \frac{4\pi\hbar^2 a}{m} |\Phi(\mathbf{r}')|^2 \right] \Phi(\mathbf{r}') = \mu \Phi(\mathbf{r}'). \quad (2.41)$$

This is the widely used Gross-Pitaevskii equation [193, 304, 307–309] characterizing the ground state properties of weakly interacting bosonic gases. It determines the macroscopic mean-field wavefunction  $\Phi(\mathbf{r})$ .

To assess the time-dependent behavior of the macroscopic mean-field wavefunction, we seek solutions  $\Phi(\mathbf{r}, t)$  that render the functional

$$S[\Phi(\mathbf{r}, t)] = \int d\mathbf{r} dt \left[ i\hbar \Phi^*(\mathbf{r}, t) \frac{\partial \Phi(\mathbf{r}, t)}{\partial t} - \Phi^*(\mathbf{r}, t) \mathcal{H} \Phi(\mathbf{r}, t) \right] \quad (2.42)$$

stationary. Varying the above functional with respect to  $\Phi^*(\mathbf{r}', t')$ , one arrives at the time-dependent Gross-Pitaevskii equation,

$$i\hbar \frac{\partial \Phi(\mathbf{r}', t')}{\partial t'} = \left[ -\frac{\hbar^2}{2m} \nabla'^2 + V_{pot}(\mathbf{r}') + \frac{4\pi\hbar^2 a}{m} |\Phi(\mathbf{r}', t')|^2 \right] \Phi(\mathbf{r}', t'). \quad (2.43)$$

The above equation captures a plethora of dynamical phenomena in weakly interacting bosonic gases. Its predictions have been experimentally verified for a multitude of atomic species [193, 310–314].

As discussed at the beginning of this subsection, the Gross-Pitaevskii equation should capture phenomena related to collective excitations with length scales larger than the scattering length  $a$ . An estimate of the typical length scale for non-linear collective excitations can be given by the stationary Gross-Pitaevskii equation [Eq. (2.41)] when considering perturbations induced by a hard wall at  $r = 0$  [12]. The  $|\Phi(\mathbf{r})|^2$  density then transitions from a vanishing value at  $r = 0$  to its background value in the absence of that obstacle  $n_{bg}$ . It is assumed that this transition occurs on a length scale smaller than the oscillator length, which is the case for very weak trapping frequencies. The variation of the density takes place on a characteristic length scale  $\xi$ . The kinetic energy associated to this variation is of the order  $\hbar^2/(2m\xi^2)$ . At the transition between the vanishing value of  $|\Phi(\mathbf{r})|^2$  and its background value it is approximately comparable to the interaction energy  $4\pi\hbar^2 a n_{bg}/m$ . Equating these energies, we get  $\xi = 1/\sqrt{8\pi n_{bg} a}$ , called the healing length. As the name suggests it is the length scale where the density of the condensate "recovers" from a local disturbance, tending to its background value in the absence of that obstacle. The healing length is the length scale associated to non-linear structures such as solitons and vortices [304, 310, 311, 315–318].

Assuming tight trapping along a single or multiple dimensions, one can derive low dimensional Gross-Pitaevskii equations featuring an effective interparticle interaction strength. The equations can capture the macroscopic behavior of bosonic systems in two ( $d = 2$ ) and one ( $d = 1$ ) dimension, whenever the energy gap between two subsequent levels of the trap in the strongly confined dimension(s) is way larger than

all other relevant energy scales in the system. The bosons are thus kinematically confined along the weakly confined dimension(s). In that regard the wavefunction,  $\Phi(\mathbf{r})$ , can be separated as [319–322],

$$\Phi(\mathbf{r}) = \tilde{\Phi}(\mathbf{r}_{\parallel})\phi_0(\mathbf{r}_{\perp}), \quad (2.44)$$

where  $\mathbf{r}_{\parallel}$  ( $\mathbf{r}_{\perp}$ ) are the coordinates of the weakly (strongly) confined dimension(s).  $\phi_0(\mathbf{r}_{\perp})$  is the harmonic oscillator ground state along the tightly confined dimension(s) and it is normalized to unity. Multiplying Eq. (2.43) on the left with  $\phi_0^*(\mathbf{r}_{\perp})$  and integrating over the  $\mathbf{r}_{\perp}$  degrees of freedom, one arrives at the following effective low-dimensional time-dependent Gross-Pitaevskii equations [304],

$$i\hbar \frac{\partial \tilde{\Phi}(\mathbf{r}_{\parallel})}{\partial t} = \left[ -\frac{\hbar^2}{2m} \nabla_{\parallel}^2 + V_{pot}(\mathbf{r}_{\parallel}) + \frac{\sqrt{8\pi}\hbar^2 a}{ma_{\perp}} |\tilde{\Phi}(\mathbf{r}_{\parallel})|^2 \right] \tilde{\Phi}(\mathbf{r}_{\parallel}), \quad d = 2 \quad (2.45a)$$

$$i\hbar \frac{\partial \tilde{\Phi}(r_{\parallel})}{\partial t} = \left[ -\frac{\hbar^2}{2m} \frac{\partial^2}{\partial r_{\parallel}^2} + V_{pot}(r_{\parallel}) + \frac{2\hbar^2 a}{ma_{\perp}^2} |\tilde{\Phi}(r_{\parallel})|^2 \right] \tilde{\Phi}(r_{\parallel}), \quad d = 1, \quad (2.45b)$$

where  $a_{\perp}$  is the oscillator length in the tightly confined dimension(s).

In the case of weakly interacting two-component (total spin 1/2) ultracold fermionic gases, their mean-field description is given in terms of a single Slater determinant. This is a generalization of the Hartree product [Eq. (2.38)], taking into account the anti-symmetry of the wavefunction upon exchange of two fermions. The  $N$  single-particle functions comprising the Slater determinant are determined in a self consistent way from the Hartree-Fock equations [323, 324], which is the equivalent formal mean-field description for fermions.

## 2.5.2 Mesoscopic systems

The problem of strongly interacting ultracold mesoscopic systems, i.e. containing an intermediate particle number, is very intricate due to the treatment of many degrees of freedom and the potential development of strong correlations. Many methods have been developed aiming to tackle these systems, as for example variational methods [325–329], density matrix renormalization group methods [330–333] and quantum Monte Carlo [159, 334–336]. The above list is of course by no means exhaustive.

One among the variational methods is the Multi-Layer Multi-Configuration Time-Dependent Hartree method for atomic mixtures (ML-MCTDHX) [337–340]. The above method describes the stationary and dynamical properties of mesoscopic systems, consisting of bosons, fermions or mixtures of any quantum statistics at zero temperature. It is employed mostly for one dimensional systems, however extensions exist for treating higher dimensional systems as well [339, 341, 342]. The method has been utilized for a variety of trapping potentials, such as harmonic traps [179, 181, 343–348], double wells [349–356] and optical lattices [357–362] to name a few.

### ML-MCTDHX

Here we briefly outline the general structure of the ML-MCTDHX method and restrict our discussion for simplicity in a one dimensional binary mixture. More thorough reviews focusing on a detailed description of the properties of this approach can be found in [337–340, 363–367]. The variational method has been successfully applied to assess the dynamical response of strongly driven bosons. Its predictions were on par with the experimental findings [368, 369].

Consider a binary mixture consisting of species  $A$  and  $B$  which can be of arbitrary statistics, confined in a one dimensional harmonic oscillator trap. The positions of the  $N_\sigma$  particles of species  $\sigma$  are collectively denoted as  $\mathbf{x}^\sigma = (x_1^\sigma, \dots, x_{N_\sigma}^\sigma)$ . As part of the name suggests, the ML-MCTDHX method relies on a multi-layered structure of the many-body wavefunction. The top layer consists of expanding the wavefunction describing the dynamic properties of the mixture in a truncated Schmidt decomposition for the wavefunctions of both species,

$$\Psi(\mathbf{x}^A, \mathbf{x}^B, t) = \sum_{k=1}^D \sqrt{\lambda_k(t)} \Phi_k^A(\mathbf{x}^A, t) \Phi_k^B(\mathbf{x}^B, t), \quad (2.46)$$

where  $\lambda_k(t)$  are called the Schmidt coefficients and  $D \leq \min\{\dim(\mathcal{H}_A), \dim(\mathcal{H}_B)\}$  [370] denotes the truncation rank. The  $\Phi_k^\sigma(\mathbf{x}^\sigma, t)$  are called the species functions. The Schmidt coefficients capture (interspecies) correlations between the two species. The Schmidt decomposition guarantees that when at least two coefficients have significant contribution, the  $\Psi(\mathbf{x}^A, \mathbf{x}^B, t)$  wavefunction cannot be written as a product of two independent wavefunctions, pertaining to species  $A$  and  $B$ . This implies that interspecies correlations develop and the species become entangled. On the other hand, when only a single coefficient is non-zero,  $\lambda_1(t) \simeq 1$ , such a product state is possible and the species are not entangled. Let us note that out of computational simplicity, the top layer is implemented as follows,

$$\Psi(\mathbf{x}^A, \mathbf{x}^B, t) = \sum_{k,l=1}^D A_{k,l}(t) \Phi_k^A(\mathbf{x}^A, t) \Phi_l^B(\mathbf{x}^B, t), \quad (2.47)$$

which is equivalent to Eq. (2.46) via a unitary transformation of the species functions [363].

The next layer consists of expanding each of the species function  $\Phi_k^\sigma(\mathbf{x}^\sigma, t)$  in  $d_\sigma$  time-dependent single-particle basis functions, namely

$$\begin{aligned} \Phi_k^\sigma(\mathbf{x}^\sigma, t) = & \sum_{\substack{(n_1, \dots, n_{d_\sigma}) \\ \sum_i n_i = N_\sigma}} C_k^{(n_1, \dots, n_{d_\sigma})}(t) \sum_{i=1}^{N_\sigma!} \text{sign}(\mathcal{P}_i)^\zeta \\ & \times \left[ \prod_{j_1=1}^{n_1} \varphi_1(x_{\mathcal{P}_i(j_1)}^\sigma, t) \dots \prod_{j_{d_\sigma}=1}^{n_{d_\sigma}} \varphi_{d_\sigma}(x_{\mathcal{P}_i(n_1+\dots+n_{d_\sigma-1}+j_{d_\sigma})}^\sigma, t) \right]. \end{aligned} \quad (2.48)$$

The  $N_\sigma$  particles are accommodated in the  $d_\sigma$  single-particle functions and this can be done in many distinct ways, called configurations. A configuration is denoted as  $(n_1, \dots, n_{d_\sigma})$  where  $n_i$  signifies the number of particles occupying the  $i$ -th single-particle function (orbital). All of the distinct configurations are subject to the constraint  $\sum_i n_i = N_\sigma$ , i.e. particle number conservation. Depending on the species statistics, the number of all possible configurations can differ. Bosonic particles tend to cluster together and many of them can occupy a single orbital. Taking that into account there are  $\mathcal{N}_\sigma = \binom{N_\sigma+d_\sigma-1}{d_\sigma-1}$  ways of distributing them into  $d_\sigma$  orbitals. For fermions, this number is  $\mathcal{N}_\sigma = \binom{d_\sigma}{N_\sigma}$ , since the Pauli exclusion principle dictates the distribution of the atoms. In that regard, the number of orbitals is always larger or equal than the number of fermionic particles. Given the indistinguishability of the particles, we have to (anti)symmetrize the wavefunction when considering all possible permutations of (fermions) bosons denoted by  $\mathcal{P}_i$ ,  $i = 1, \dots, N_\sigma!$ . This operation represents the  $i$ -th element of the  $\mathcal{S}_{N_\sigma}$  permutation group. The symmetry/antisymmetry

is properly taken into account with the exponent  $\zeta$ , assuming the value 0 for bosons and 1 for fermions.

The advantage of ML-MCTDHX over other variational methods is that the many-body wavefunction describing the stationary state and dynamics of the mixture is expanded over time-dependent single-particle functions with time-dependent expansion coefficients. This greatly reduces the number of required basis states, as compared to the case where only the expansion coefficients are time-dependent. The single-particle functions  $\varphi$  as well as the expansion coefficients  $A$  and  $C$  are determined variationally. Given the many-body ansatz [Eqs. (2.47), (2.48)], one needs to find solutions yielding a stationary action [371],

$$S[A, C, \varphi] = \int dt \langle \Psi | \mathcal{H} - i\hbar \frac{d}{dt} | \Psi \rangle. \quad (2.49)$$

This is subject to the constraint that the species functions and single-particle functions remain orthonormalized during the entire time evolution of the two component setting.

The stationarity of the action (2.49) results in many integro-differential equations for the  $A_{k,l}(t)$ ,  $C_k^{(n_1, \dots, n_{d_\sigma})}(t)$  and  $\varphi$  variational parameters. In a nutshell, there are  $D^2$  first-order differential equations for the  $A_{k,l}(t)$  coefficients. Regarding the expansion in species functions and the  $C_k^{(n_1, \dots, n_{d_\sigma})}(t)$  parameters, there are  $D \sum_\sigma \mathcal{N}_\sigma$  non-linear integro-differential equations. Finally, the single-particle functions satisfy a set of  $d_A + d_B$  non-linear integro-differential equations. These equations of motion can be generalized to any number of species of arbitrary statistics [337–340].

The parameters  $d_\sigma$  and  $D$  are chosen such that observables of interest are converged within a specified tolerance, see also [74] for more details. In the limiting case where  $d_A = d_B = D = 1$ , one retrieves the Hartree product [Eq. (2.38)] for a binary mixture,

$$\Psi(\mathbf{x}^A, \mathbf{x}^B, t) = \prod_{i=1}^{N_A} \varphi_A(x_i^A, t) \prod_{j=1}^{N_B} \varphi_B(x_j^B, t). \quad (2.50)$$

The variational principle then leads to two coupled Gross-Pitaevskii equations for the single-particle functions  $\varphi_A$  and  $\varphi_B$  [372, 373]. This is the mean-field limit where both intra- and interspecies correlations are neglected. Moreover, by considering just a single Schmidt coefficient ( $D = 1$ ), interspecies correlations are discarded, highlighting in this way the impact of intraspecies ones. This is the so-called species mean-field approach [343, 354, 355].

## Chapter 3

# Outline of Scientific contributions

### 3.1 Correlations and dynamical response of few-body trapped systems

**S**cattering of two and three atoms at low energies is important for understanding the collisional properties of ultracold quantum gases, especially loss processes [66] and Feshbach resonances [15] [Sec. 2.2.4]. The latter are fundamental in controlling the interatomic interactions and exploring strongly interacting quantum gases. In order to monitor the dynamics of atomic systems, external electromagnetic fields are being utilized, acting as harmonic oscillator traps and confining the atoms in space.

In that regard, investigating the dynamics of two and three atoms in harmonic traps is crucial, being the most elementary non-trivial trapped systems. Their stationary properties have been extensively studied [see Sec. 2.3], and analytic solutions are found for the energy levels and relative wavefunctions [69, 71, 72, 203, 243, 262, 374]. Few-body trapped setups are analytically tractable even in the case of strong interactions [72]. Therefore, their analytical properties can be utilized to study their dynamical response [61, 375], yielding insights into efficient protocols for populating few-body bound states [244, 245, 87, 97, 103, 376]. Moreover, few-body trapped setups have been employed to probe the dynamics of many-body systems at short timescales and large momenta [105, 106, 114]. The contacts lie at the heart of this connection [Sec. 2.4].

In the following outlined works, we aim to provide further insights on the correlation properties of two- and three-body trapped systems. Analytical expressions are provided for the two-body contact for atoms in the dimensional crossover from two to one dimension. Beyond two particles, we map out the three-body contact over a wide range of scattering lengths for two-dimensional three-body binary mixtures. The latter consist of two identical bosons or spin-polarized fermions interacting with a third distinguishable particle. In this context, the interplay of two- and three-body correlations between distinct eigenstates is analyzed.

The correlation properties are utilized to probe the dynamics of these systems upon abrupt variations of the scattering lengths (interaction quench). Substantial enhancement of correlation measures signals the dynamical contribution of few-body bound states. In order to enhance their participation in the quench dynamics, a protocol is proposed to selectively excite distinct eigenstates. A good grasp on three-particle models allows us also to tackle the dynamical generation of a coherent superposition of Efimov trimer with atom-dimer states in thermal gases. Such a superposition is achieved upon modulating the scattering length in a fashion similar to Ramsey spectroscopy.

### 3.1.1 Dynamical response of two particles in two dimensions [B1]

Our starting point for exploring correlation measures of few atoms are two-dimensional systems. They are inherently different from their three- or one-dimensional counterparts, due to the existence of a two-body bound state irrespective of the sign of the interaction strength [Sec. 2.2.3]. In [B1], the role of this bound state is revealed in the interaction quench dynamics of two atoms over a wide range of interaction strengths. For that purpose several observables are investigated, such as the fidelity [377] and the two-body contact, quantifying short-range two-body correlations.

As a first step, the energy level structure is identified for all interaction strengths, and an asymptotic expansion is given for the energy levels at strong interactions, hinting at the absence of the Bose-Fermi mapping in two dimensions [378–380]. The short-range correlation properties are subsequently explored, and analytic expressions for the two-body contact are derived, independently of the interaction strength or the eigenstate. The time-evolved relative wavefunction is expanded in terms of the stationary eigenstates at the final interaction strengths, and analytical expressions are derived for the expansion coefficients. This allows us to express the time evolution of any observable, such as the fidelity, measuring the deviation of the time-evolved state from the initial one, the radial probability density in real and momentum space, and the two-body contact in a closed analytical form.

Subsequently, three different dynamical protocols are considered : Quenches from attractive to repulsive interactions (i), the reverse scenarios (ii), and quenches from the non-interacting case to infinitely strong interactions (iii). The system is initialized in the ground atom-atom state, describing two interacting particles in a harmonic trap. In both quench protocols (i) and (ii), it is found that the particles significantly deviate from their initial state, when the interaction strength is quenched from attractive or repulsive interactions in the vicinity of the non-interacting region.

From the Fourier spectra of the fidelity [381–383] in conjunction with the expansion coefficients, we identify the contributing eigenstates in the dynamics at the final interaction strength. In the vicinity of vanishing interaction strengths, many non-interacting eigenstates are populated. Quenching the interactions from repulsive to attractive values and vice versa, it is found that the ground atom-atom eigenstate is mainly contributing, along with the two-body bound state. Signatures of the latter are observed in the evolution of the radial probability density in real and momentum space. In real space we observe peaks at short distances, matching the structure of the bound state radial density. In reciprocal space large tails are present in the evolution of the radial density, due to the extended structure of the two-body bound state density in momentum space. Moreover, beatings are present in the evolution of the two-body contact, associated to energy differences between the two-body bound state and the ground atom-atom state. These interferences are encountered for quench scenarios (i) and (ii).

The role of the initial states in the quench dynamics is also investigated. It is shown that the system is substantially perturbed from its starting configuration, when initialized in the two-body bound state. This behavior persists for both protocols (i) and (ii). In contrast, smaller deviations occur when higher-lying excited states are considered for the initialization.

Another efficient way of perturbing the two-body setup is explored by quenching the interaction strength from zero to strong values [protocol (iii)]. A significant growth of short-range two-body correlations is manifested by inspecting the two-body contact. This behavior is attributed to the population of the bound state as well as higher excited eigenstates, displaying enhanced short-range correlations.

### 3.1.2 Correlation and dynamical properties of two atoms in the dimensional crossover from two dimensions to one [B2]

Having at hand the stationary and dynamical properties of two interacting atoms in two dimensions, we set out to study the impact of the dimensional crossover from two dimensions to one. The dimensional crossover for cold gases is usually achieved by changing the ratio between the trapping frequencies along certain direction(s), thus confining kinematically cold atoms along the desired dimension(s). Apart from being able to control the dimensionality of the system, such a crossover leads also to the effective tunability of the interaction strength [Sec. 2.2.3]. In [B2] the dimensional crossover of two interacting particles is investigated from two dimensions to one. This is an interesting regime, given the completely different energy structure of confined atoms in one and two dimensions, such as the existence of a two-body bound state. We focus in establishing relations between quantities in these two dimensions, such as the scattering lengths and short-range two-body correlations. Moreover, the stationary and dynamical properties of two atoms are examined in the intermediate regime, where different ratios of the trapping frequencies are considered.

Initially, we express the relative Hamiltonian in cartesian coordinates and establish a transcendental equation for the energy levels, valid for arbitrary ratio  $\alpha$  between the trapping frequencies along the  $y$  and  $x$  spatial directions. By setting  $\alpha = 1$ , the energy spectrum of two particles in two dimensions is retrieved. At large values of the anisotropy parameter, we recover the transcendental equation determining the energy levels of two interacting atoms in one dimension. This equation is expressed in terms of the two dimensional scattering length. From there a mapping is established between the two- and one-dimensional scattering lengths. It is shown that already from  $\alpha = 10$ , the energy levels have a very good agreement with those obtained from the pure one-dimensional case. For smaller anisotropies, the energy levels are not equidistant, displaying larger gaps every  $\alpha$ -th state, for integer  $\alpha$ . This behavior is traced to the energy gaps present in the non-interacting spectrum. Interestingly, the energy difference between the ground atom-atom and the two-body bound state increases as the trapping frequency ratio becomes larger, for all interaction strengths except from the vicinity of zero two-dimensional interactions.

Subsequently, analytic expressions are derived for the relative two-body wavefunction, granting access to the density distributions of eigenstates in real and momentum space. As the anisotropy parameter  $\alpha$  gets larger, the densities in real space become more elongated along the weakly confined dimension. For higher excited states, a two-hump structure is discernible. On the contrary, in momentum space the elongation of the density patterns occurs in the strongly confined dimension, as  $\alpha$  increases.

At interparticle distances smaller than the harmonic oscillator length along the weakly confined direction, the two-body wavefunction develops a logarithmic singularity, invoked by the character of two-dimensional interactions. This divergence is related to the two-body contact, for which we have derived analytic expressions for any trapping frequency ratio, thereby extending our previous results [B1]. At large anisotropies  $\alpha$ , a simple linear relation is found between the two- and one-dimensional two-body contacts. The proportionality factor depends on the oscillator length in the strongly confined dimension, similarly to the relations established in the literature between the three- and lower-dimensional two-body contacts [125, 384, 385]. Subsequently, an analysis is carried out for the two-body contact of the bound and ground atom-atom state for intermediate anisotropy. Short-range two-body correlations of the bound state display a monotonic increase with respect to the anisotropy  $\alpha$ , regardless of the interaction strength. In contrast, the two-body contact of the ground

atom-atom state saturates for large ratio of the trapping frequency, regardless of the interaction strength.

The knowledge of the stationary properties of the two particles for arbitrary frequency ratio, allows us to treat the system from a dynamical perspective across the dimensional crossover. Similar to [B1], interaction quenches are employed from attractive to repulsive interactions (i) and vice versa (ii). The time-evolved wavefunction is expanded in terms of the stationary eigenstates at final interaction strengths, and analytical expressions are derived for the expansion coefficients. In order to quantify the degree of perturbation of the system from its initial arrangement, the fidelity is utilized. It is shown that regardless of the interaction strength, the setup is more efficiently perturbed when small ratios of the trapping frequency are considered. This behavior is observed for both quench protocols (i) and (ii). Moreover, strong deviations from the initial configuration are reported for quenches to the weakly interacting regime. This phenomenon is consistent with the results obtained in [B1], for the pure two-dimensional case, and takes place for arbitrary anisotropy values.

From the Fourier spectra of the position variance along the two spatial directions, the contributing stationary eigenstates are identified, revealing the microscopic mechanisms of the quench dynamics. Close to zero interactions, a plethora of non-interacting states appear in the variance spectra in both dimensions, reflecting the fact that the system is efficiently driven out-of-equilibrium. Further away from that regime, mostly the ground atom-atom and bound states are populated. The number of excitations in the strongly confined dimension is larger than the respective one in the weakly confined one, but with a smaller amplitude. This occurs irrespective of the ratio between the trapping frequencies. The difference in the number is explained in terms of the amplitudes of the Fourier spectra, for which we derive analytical formulas related to the expansion coefficients. The smaller amplitude of excitations in the spectrum along the strongly confined dimension is readily explained by inspecting the profiles of one-body densities at distinct time intervals. The two atoms undergo a breathing motion, which is more prominent along the weakly confined direction. As the anisotropy increases, the dynamics along the strongly confined dimension is essentially frozen, leading to small amplitude excitations.

This work concludes our investigations for the stationary and dynamical aspects of two-body setups in two dimensions, setting the stage for exploring three-body systems.

### 3.1.3 Stationary properties of two-dimensional three-body mixtures [B3]

The stationary properties of three-body systems are far more intricate compared to the attributes of two atom setups. This is not only due to the presence of three-body bound states, but also because three-body setups can consist of elementary mass balanced or imbalanced binary mixtures, possessing different quantum statistics. In [B3] such binary mixtures are considered consisting of two identical bosonic particles (BBX) or two spin polarized fermions (FFX) interacting with a third distinguishable particle (X), all of them confined in a two dimensional harmonic trap. Their two- and three-body short-range correlation properties are extensively studied for different mass ratios and interspecies scattering lengths. These two dimensional systems are more stable from losses stemming from three-body recombination compared to their counterparts in three dimensions [85, 86, 386].

The three-body mixtures are treated within the adiabatic hyperspherical approach [Sec. 2.3.2]. Solving the hyperangular equation, we obtain a set of potential curves corresponding to a light-light-heavy (LLH), equal mass (EM), and heavy-heavy-light



(HHL) setup. The considered values for the mass ratios are chosen so that they correspond to mixtures of  ${}^6\text{Li}$  and  ${}^{133}\text{Cs}$  (BBX HHL, FFX LLH),  ${}^6\text{Li}$  and  ${}^7\text{Li}$  (BBX EM, FFX EM),  ${}^7\text{Li}$  and  ${}^{173}\text{Yb}$  (BBX LLH, FFX HHL). From the solution of the coupled hyperradial equations [Sec. 2.3.2], the resulting eigenenergies are categorized in three classes: trimers, i.e. three-body bound states, atom-dimers, which are two-body bound states interacting with a third particle, and atom-atom-atom states, describing three interacting particles in a harmonic oscillator. For BBX and FFX systems alike, the number of trimers increases as the identical particles become heavier [285, 387]. For fermions however, LLH and EM setups do not support any trimer state in contrast to BBX systems. It is found that the mass ratio threshold for forming trimer states in FFX HHL systems is shifted to higher values compared to free space [283]. This occurs since the trimer states with energy close to the atom-dimer threshold are highly affected by the trap, and their energy is shifted upwards. Moreover, the energy spectra reveal an abundance of avoided crossings between atom-dimers and atom-atom-atom states with respect to the interspecies scattering length, regardless of the particle statistics or mass ratio.

Subsequently, a formalism is developed for describing few-body short-range correlations for two dimensional three-body systems in the presence of an external potential. Our approach extends the usual treatment of few-body correlations for such systems in free space [302, 303]. In particular, this formalism applies to all eigenstates, and employs the adiabatic hyperspherical formalism in the asymptotic expansion of the one-body densities in momentum space. Regarding two-body correlations, a clear separation of scales is found for the three classes of eigenstates. Namely, trimer states exhibit a more enhanced two-body contact compared to the contact of atom-dimers. The latter in turn display magnified two-body correlations with respect to atom-atom-atom eigenstates.

The two-body contact of atom-dimers and atom-atom-atom states features an oscillatory behavior with respect to the interspecies scattering length and displays an upper and a lower bound. The oscillations occur due to the avoided crossings between these two types of states as one tunes the interspecies scattering length. Starting for example from an atom-atom-atom state, the two-body contact subsequently jumps to a higher value when the interspecies scattering length approaches a crossing with an atom-dimer. Eventually the contact will jump to a lower value when another crossing is encountered at a different interspecies scattering length, and now the atom-dimer converts to another atom-atom-atom eigenstate. The lower bound tends to zero as one considers highly excited atom-atom-atom states. The particles in these states are further apart from each other, and thus their short-range two-body correlations encapsulated by the two-body contact are suppressed. The upper bound is associated to atom-dimer states close to the atom-dimer threshold. For small interspecies scattering lengths the bound is given by the two-body contact stemming from a deeply bound dimer and a third particle being further away. This picture breaks down for large interspecies scattering lengths, where the dimer is loosely bound. The oscillatory pattern of the two-body contact as well as the existence of the bounds are manifested both for BBX and FFX systems for all considered mass ratios.

Focusing on the three-body contact, the same hierarchy of three-body correlations is observed as for the two-body contact. Trimer states display a much more enhanced Tan contact compared to atom-dimers, which in turn display significant three-body correlations compared to the atom-atom-atom eigenstates. An oscillatory pattern, similar to the one identified for the two-body contact, is encountered between the atom-dimer and atom-atom-atom eigenstates for varying interspecies scattering lengths. This behavior is again attributed to the multiple avoided crossings between

these two types of states. A lower bound is also identified, associated to highly excited atom-atom-atom states. However, an upper bound in the three-body contact is absent. Atom-dimers close to the atom-dimer threshold display more enhanced three-body correlations, compared to other atom-dimers being energetically further away from that threshold. The above mentioned properties of the three-body contact are investigated only for BBX systems and different mass ratios. For FFX settings, three-body short-range correlations are suppressed due to the Pauli exclusion principle [303].

Given the prominent oscillatory behavior of the two- and three-body contact for atom-dimers and atom-atom-atom states with respect to the interspecies scattering length, we subsequently examine whether these features persist in the presence of temperature effects [388–391]. Thermal effects are taken into account by weighting observables according to the Maxwell-Boltzmann distribution. Trimer states and deep atom-dimers are typically not populated in thermal gases in equilibrium, and hence they are excluded from the thermal average. For increasing temperature it is found that the magnitude of Tan contacts decreases. Thermal energy prevents the particles from approaching to small distances and become correlated. Moreover, the amplitude of oscillations with respect to the interspecies scattering length decreases and the two- and three-body contacts become eventually smooth.

Furthermore, we provide insights regarding the spatial configuration of three-particle systems for the binary mixtures of different statistics, by employing the one-body densities. For BBX systems, the structures are all isotropic due to the zero total angular momentum. For FFX systems however, interesting patterns emerge in the density of atom-atom-atom states. In particular, a phase separation occurs and the fermions are repelled from the trap center, where the X particle resides. For atom-dimers however, fermions are attracted to the third distinguishable particle, forming a more localized structure at the trap center.

#### 3.1.4 Dynamical excitation of distinct eigenstates in three-body two-dimensional mixtures [B4]

Having at hand the correlation properties of three-body mass-imbalanced mixtures, we now aim to investigate dynamical protocols for populating particular types of eigenstates in two dimensions [B4]. Our studies are motivated by joint experimental and theoretical works in three dimensions, where an enhanced population of Efimov trimers was detected following quenches from zero to strong interactions [79, 113].

The three-body binary mixtures are initialized in a non-interacting state with variable spatial extent. The latter can be achieved by confining the system in harmonic traps of adjustable trap frequency, whereas Fano-Feshbach resonances can be employed to achieve a non-interacting state. Subsequently, all interactions are turned on abruptly (interaction quench). The dynamical response of the three-body systems is evaluated over a wide range of final interspecies scattering lengths by inspecting the time-averaged fidelity.

First, we focus on LLH settings. Two regimes are identified depending on the ratio between the harmonic oscillator length with the three-body reduced mass and the initial spatial extent of the system. When the initial spatial extent is larger than the harmonic oscillator length, the BBX and FFX systems are more efficiently perturbed from their initial state compared to the reverse case. From the Fourier spectra of the fidelity we infer that mostly atom-atom-atom eigenstates are contributing to the dynamics. In contrast, when the spatial extent is smaller than the oscillator length, a superposition of few trimers and atom-dimer states is dynamically generated. In

essence, selective classes of eigenstates are excited depending on the initial spatial configuration. This mechanism allows for efficiently creating superpositions of few-body bound states. It relies on the separation of length scales between the latter and states which are supported solely by the trap (atom-atom-atom). The length scale of few-body bound states is typically smaller than the oscillator length. Hence the three-body setup prepared in an initial configuration with small size has a large overlap with these bound states.

The dynamical formation of bound states is imprinted on the time-averaged short-range few-body correlations. For any final interspecies scattering length, these observables are greatly enhanced when the width of the initial state is smaller than the harmonic oscillator length, as compared to the opposite scenario. When the width increases, the magnitude of short-range correlations not only decreases, but also develops a prominent oscillatory pattern with respect to the interspecies scattering length. From our results in [B3] we know that such a feature occurs due to the presence of avoided crossings between atom-dimers and atom-atom-atom eigenstates as the interspecies interaction is varied. This pattern is therefore a signature of the dynamical participation of atom-dimers at certain interspecies scattering lengths.

Turning to HHL settings, the BBX and FFX mixtures are efficiently perturbed from their initial configuration regardless of the starting spatial extent. Subsequent analysis of the microscopic mechanisms through the Fourier spectra of the fidelity reveals that similarly to LLH setups, a superposition of trimers and atom-dimers is populated when the initial spatial extent is smaller than the harmonic oscillator length. The difference from LLH settings is that atom-atom-atom eigenstates are excited as well, driving the binary mixtures further out of equilibrium. For widths larger than the oscillator length, a large number of atom-atom-atom eigenstates is predominantly populated.

The distinct excitation processes are also imprinted on the time-evolution of the two- and three-body correlation measures for HHL setups. As the width increases, the magnitude of the contacts decreases, signaling the presence of eigenstates with suppressed short-range correlations, namely atom-atom-atom ones. Moreover, an enhanced oscillatory structure appears with respect to the interspecies scattering lengths, stemming from the large number of avoided crossings between atom-dimers and atom-atom-atom eigenstates. Due to the sharper avoided crossings present in the energy spectra of HHL setups [B3] compared to their LLH counterparts, the oscillatory pattern is manifested mostly as a sharp peak sequence.

We conclude this work by providing parameters such as magnetic field strengths and trapping frequencies that could lead to a potential experimental realization of our setup. The key aspect of this project is that we have proposed a dynamical scheme for selectively generating superpositions of few-body bound states in two dimensional three-body mixtures.

### 3.1.5 Interferometry of Efimov trimers in thermal gases with modulated magnetic fields [B5]

A dynamical protocol was recently devised experimentally [118, 119], creating coherent superpositions of Efimov trimers with atom-dimers in three dimensional  $^7\text{Li}$  thermal gases. The dynamical scheme capitalized on a sequence of modulated magnetic fields (pulses) around a background value, separated by a varying free evolution time (dark time). The length of the pulses is such that when converted to an energy scale, it matches the energy difference between the first excited Efimov trimer and the first atom-dimer. Therefore these states are not energetically resolved, and they are both

addressed by the pulses. This scenario mimics Ramsey interferometry with magnetic fields, and was employed to extract the binding energy of the first excited Efimov trimer from the manifested interference fringes of the measured atom number. The latter displayed a large damping time, the origin of which remained unclear. Possible suspects were the lifetime of the trimer state or the elastic collisions between trimers, dimers and free atoms. In [B5] we shed light on the association and decay mechanisms of this protocol, from a theoretical perspective.

We start our analysis by considering three  $^{85}\text{Rb}$  atoms confined in a three dimensional harmonic trap. The oscillator length is chosen such that it corresponds to the mean interparticle distance stemming from the peak density of  $^{85}\text{Rb}$  gases in typical experiments. The reason behind the choice of this species is that we know from recent experiments [79] the lifetime of trimers and dimers, which can be reproduced within the scope of a zero-range model for large background interactions. Thermal effects are taken into account by initializing the system in an ensemble of atom-atom-atom states and weighting the observables according to a Maxwell-Boltzmann distribution. The observable we are interested in is the rescaled Efimov trimer probability after the second magnetic field pulse relative to the first one.

Initially, we exclude any trimer decay width from our calculations, focusing on the impact of thermal effects on the interference fringes in the trimer probability. The latter displays a rich multifrequency pattern, which can be divided in two regions. At short dark times, large amplitude oscillations are manifested, persisting for large temperature variations. The frequency spectrum in that region reveals a single prevailing frequency, matching the energy difference between the first excited Efimov and the first atom-atom-atom state. At longer dark times, the amplitude of oscillations drastically drops due to temperature effects, and three dominant frequencies appear in the Fourier spectra, being robust against thermal effects. The highest matches the frequency identified in the short dark time region. The second is associated to the energy difference between the first atom-dimer and atom-atom-atom eigenstate. The lowest one stems from the superposition of the first excited Efimov trimer with the first atom-dimer, consistent with the experimental detection [118]. Note that the two other high frequencies were not observed in [118].

To better understand the appearance of three dominant frequencies in the Efimov trimer probability, we construct a three-level model. It is based on the first excited Efimov state, the first atom-dimer and a single atom-atom-atom state. The results obtained from different atom-atom-atom eigenstates are eventually weighted according to the Maxwell-Boltzmann distribution, taking thus into account thermal effects. From this three-level model in conjunction with time-dependent first order perturbation theory, analytical approximate formulas are derived for the Efimov trimer probability. The predictions of that model for the frequencies agree very well with our numerical computations. Moreover, the amplitude of oscillations at early dark times is shown to decay according to a power law formula, depending strongly on the temperature.

Now that the impact of thermal effects on the interference fringes has been appreciated, we proceed to include the decay width of the Efimov trimer in our calculations. The background scattering length is parked at a large value ( $2030 a_0$ ), where the zero-range model yields reliable predictions for the decay width. The duration of the pulses is shorter than the lifetime of Efimov states, and the latter is included only during the dark time between the magnetic field pulses. In order to distinguish the amplitude damping due to thermal effects from the damping due to the lifetime, we fit the envelope of oscillations at later dark times with an exponential decay. Two characteristic decay times are identified. The first one, emerging at intermediate dark times, matches

the lifetime of the first excited Efimov trimer. The decay occurs as if no interference would be present, and the trimer probability signal would decay solely according to the lifetime of the Efimov state. The second decay time is extracted at later dark times, and is found to be twice as long as the lifetime of the trimer. This doubling is attributed to the manifested interferences between this state and the first atom-dimer and first atom-atom-atom state. To corroborate our findings, the three-level model is again employed incorporating now the decay width of the trimer. Within this framework, we clearly see that the signal stemming from interference terms of the Efimov trimer with the first atom-dimer and the first atom-atom-atom state possesses a decay width, being half of the width of the trimer state. This behavior explains the unusually long damping timescales observed in the interference fringes of the  $^7\text{Li}$  experiment [118].

The fact that interference terms exist also between the first atom-atom-atom and Efimov state, allows us to extend the dynamical protocol to attractive interactions, where atom-dimers are absent [Sec. 2.3.1]. Indeed, by considering large negative background scattering lengths, a single frequency is present in the probability to occupy Efimov trimers, matching the energy difference between the two aforementioned eigenstates. The damping time of the oscillations is again found to be twice as long as the lifetime of the Efimov state.

Our work [B5] provides a sound theoretical interpretation of the results reported in [118], and demonstrates that the interferometer can be employed to accurately assess the intrinsic properties of Efimov states for all interaction strengths. It also paves the way for understanding possible modifications inflicted upon the properties of Efimov states by many-body environments [392].

## 3.2 Dynamics of few particles in a many-body environment

So far, we have studied the static and dynamic properties of few-body trapped systems. Apart from being elementary settings where analytical insights are obtained regarding their dynamics, it has been shown [97, 105, 106] that they are also adequate in describing the behavior of many-body setups at short timescales and large momenta. This connection is illustrated by the two-body contact, derived from the asymptotic expansion of the one-body density in momentum space. For example, the evolution of the two-body contact showed very good agreement between two- and many-body models describing quenched Bose-Einstein condensates at early evolution times [105, 106].

However, few-body models in principle fail to describe the dynamics of quantum gases, since many-body effects kick in and collective phenomena emerge. In order to study such processes, an appropriate description of many-body systems is needed. Such a formalism allows the study of modified properties of few particles (impurities), immersed in a many-body environment. A few characteristic examples are one or two impurities dressed with excitations in a Fermi sea or a Bose-Einstein condensate, forming polarons [153–158, 160, 393–395], bipolarons [164–171, 175], or even in-medium Efimov states [163, 174]. In this section, we address the dynamics of few bosonic impurities in a mesoscopic Bose gas, and explore collective phenomena such as phase separation and dark-bright soliton formation.

### 3.2.1 Pattern formation of impurities subjected to driving of the impurity-medium interactions [B6]

Particle imbalanced two-component mixtures are particularly intriguing, since the dressing mechanisms of impurities in a many-body medium can be assessed. These mechanisms can be subsequently altered or controlled by devising dynamical protocols such as quenches of the impurity-medium (interspecies) interaction strength [179, 180]. Moreover, driving of the interspecies interactions has proven especially fruitful in generating and stabilizing non-linear excitations in two-component setups [396–398], and pattern formation in Bose-Einstein condensates, such as Faraday waves [239, 368, 399–403]. In [B6] we study the dynamical response of few interacting impurities in a bosonic many-body medium, upon driving the impurity-medium interaction strength. For that end we employ a variational many-body method, ML-MCTDHX (Sec. 2.5.2). In particular, the latter is driven across the phase separation boundary between the two species [38, 39]. Our aim is to identify dynamical regimes where localization of the impurities can occur, or patterns are imprinted in the bosonic medium. A mixture of two hyperfine states of  $^{87}\text{Rb}$  is considered, confined in a one dimensional harmonic trap, with an imbalance of 10 and 100 particles in these two states. The intraspecies interaction strengths are kept fixed, while the interspecies interaction is modulated by means of Feshbach resonances.

First, the response of the system is investigated for drivings from the miscible to the immiscible phase. For modulation frequencies smaller than the trapping one, it is found that the mixture alternates between the miscible and immiscible regime, in phase with the modulation of the interspecies interaction strength. Within a mean-field description, dark-bright soliton pairs are identified when the mixture resides in its immiscible phase. For driving frequencies larger than the trapping one, these pairs of non-linear excitations perform a breathing motion during a quarter of their oscillation period, and subsequently merge in a single bound state at the trap center. However, taking correlations into account, this picture breaks down and some of the impurities are expelled towards the edges of the trap, where they tend to equilibrate, while a significant fraction of them is localized at the trap center. At the positions of the impurities, the many-body medium develops density dips, the biggest one being at the trap center. This central dip splits the bosonic medium into two main parts, which by inspecting second-order noise correlations [404–406] are found to be two-body anti-correlated. Namely, it is more likely to locate two bosons in the two separated regions, than in the same one. Anticorrelations occur mostly for the impurities as well.

In order to intuitively understand the dynamics of impurities, we rely on a time-dependent effective potential [179, 351, 407], taking into account the harmonic trap and the instantaneous density profile of the medium, weighted by the interspecies interaction strength. In this picture, the impurity excitations stem essentially from an effective trap provided by the bosonic medium. For modulation frequencies larger than the trapping one, the one-body density of the impurities can be assigned mainly in the three lowest eigenstates of that effective potential.

Now, let us investigate the opposite driving scenario, from the immiscible to the miscible region. Again, for modulation frequency smaller than the trapping one, the system is consecutively dragged from the immiscible to the miscible phase, in accordance with the impurity-medium driving protocol. For modulation frequency larger than the trapping frequency however, the picture is completely different from the reverse scenario. Tracking the dynamical response of the system within the mean-field perspective, pairs of dark-bright solitons emerge, with a smaller oscillation period compared to the one identified in the opposite driving scheme. These non-linear

structures become distorted by excitations of the bosonic medium at later evolution times, showing no sign of merging. Within the correlated framework however, almost stationary density dips and humps appear close to the trap center in the density profile of the bath and the impurities respectively. The two opposite regions enclosed by the dips and the edges of the cloud of the bath display loss of one-body coherence, meaning that particles are localized in either of those regions. Furthermore, two particles of the medium tend to cluster together at the same density dip, as indicated by the second-order noise correlations. The same applies also to impurities, which show a bunching behavior at the same density hump. Moreover, a breathing motion is observed in the density profile of the impurities, and the breathing frequency extracted from the effective potential shows good agreement with the measured one.

Next, we comment on the role of the impurity number and intraspecies interactions, for the interesting regime where the modulation frequency is larger than the trapping one. Upon considering only two non-interacting impurities, we find that they remain localized at the trap center, irrespective of the driving protocol from the miscible or immiscible phase. The same applies also to 10 non-interacting impurities. Only by increasing the impurity intraspecies repulsion, do the characteristic density patterns of the two driving protocols start appearing. Namely, a fraction of impurities is expelled towards the edges of the medium cloud, when driving the impurity-medium interactions from the miscible to the immiscible phase. In the opposite driving scheme, the breathing motion in the one-body density of the impurities becomes more visible, along with the stationary density humps.





## Chapter 4

# Scientific contributions

### 4.1 Correlations and dynamical response of few-body trapped systems

#### 4.1.1 Analytical treatment of the interaction quench dynamics of two bosons in a two-dimensional harmonic trap

## Analytical treatment of the interaction quench dynamics of two bosons in a two-dimensional harmonic trap

G. Bougas,<sup>1</sup> S. I. Mistakidis,<sup>1</sup> and P. Schmelcher<sup>1,2</sup>

<sup>1</sup>*Center for Optical Quantum Technologies, Department of Physics, University of Hamburg, Luruper Chaussee 149, 22761 Hamburg, Germany*

<sup>2</sup>*The Hamburg Center for Ultrafast Imaging, Universität Hamburg, Luruper Chaussee 149, 22761 Hamburg, Germany*



(Received 28 May 2019; revised manuscript received 5 September 2019; published 4 November 2019)

We investigate the quantum dynamics of two bosons, trapped in a two-dimensional harmonic trap, upon quenching arbitrarily their interaction strength and thereby covering the entire energy spectrum. Utilizing the exact analytical solution of the stationary system, we derive a closed analytical form of the expansion coefficients of the time-evolved two-body wave function, whose dynamics is determined by an expansion over the postquench eigenstates. The emergent dynamical response of the system is analyzed in detail by inspecting several observables such as the fidelity, the reduced one-body densities, the radial probability density of the relative wave function in both real and momentum space, and the Tan contact, which unveils the existence of short range two-body correlations. When the system is initialized in its bound state, it is perturbed in the most efficient manner as compared to any other initial configuration. Moreover, starting from an interacting ground state, the two-boson response is enhanced for quenches toward the noninteracting limit.

DOI: [10.1103/PhysRevA.100.053602](https://doi.org/10.1103/PhysRevA.100.053602)

### I. INTRODUCTION

Ultracold quantum gases provide an excellent and highly controllable test bed for realizing a multitude of systems without the inherent complexity of their condensed matter counterparts [1]. Key features of ultracold atoms include the ability to manipulate their interparticle interactions by employing Feshbach resonances [2,3], tune the dimensionality of the system [4,5], and trap few-body ensembles possessing unique properties [6–10]. Two-dimensional (2D) systems are of particular interest because of their peculiar scattering properties, the emergent phase transitions such as the Berezinskii-Kosterlitz-Thouless transition [11–16], and the existence of long-range thermal fluctuations in the homogeneous case. These thermal fluctuations in turn prohibit the development of a condensed phase but can allow a residual quasicrystalline state [17].

Among the few solvable quantum problems, one is the system of two ultracold atoms confined in an isotropic harmonic oscillator. Here the two atoms interact via a contact pseudopotential where only *s*-wave scattering is taken into account [18], an approximation which is valid at ultralow temperatures where two-body interactions dominate [19]. The stationary properties of this system have been extensively studied for various dimensionalities and for arbitrary values of the coupling strength [20–23]. Generalizations have also been reported including, for instance, the involvement of anisotropic traps [24], higher partial waves [25,26], and (very recently) long-range interactions [27] and hard-core interaction potentials [28]. Remarkably enough, exact solutions of few-body setups have also been obtained regarding the stationary properties of three harmonically trapped identical atoms in all dimensions [29–34].

A quench of one of the intrinsic system's parameters is the most simple way to drive it out of equilibrium [35]. Quenches of <sup>87</sup>Rb condensates confined in a 2D pancake geometry have been employed, for instance, by changing abruptly the trapping frequency to excite collective breathing modes [36,37], in line with the theoretical predictions [38,39]. On the contrary, the breathing frequency of two-dimensional Fermi gases has been recently measured experimentally [40,41] and found to deviate from theoretical predictions at strong interactions, a behavior called quantum anomaly. Also, oscillations of the density fluctuations reminiscent of the Sakharov oscillations [42] have been observed by quenching the interparticle repulsion. Furthermore, it has been shown that the dynamics of an expanding Bose gas when switching off the external trap leads to the fast and slow equilibration of the atomic sample in one and two spatial dimensions, respectively [43]. Moreover, the collisional dynamics of two <sup>6</sup>Li atoms has been experimentally monitored after quenching the frequencies of a three-dimensional harmonic trap [44]. Turning to two harmonically trapped bosons, the existing analytical solutions have been employed in order to track the interaction quench dynamics in one- [45–48] and three-dimensional systems [49]. Focusing on a single dimension, an analytical expression regarding the eigenstate transition amplitudes after the quench has been derived [45]. Moreover, by utilizing the Bose-Fermi mapping theorem [50,51], a closed form of the time-evolved two-body wave function for quenches toward the infinite interaction strength has been obtained [47], with a dynamical crossover from bosonic to fermionic properties.

Besides these investigations, the interaction quench dynamics of the two-boson system in two spatial dimensions employing an analytical treatment has not been addressed. Here, the existence of a bound state for all interaction strengths

might be crucial, giving rise to a very different dynamics compared to its one-dimensional analog. Also, regarding the strongly interacting regime, the Bose-Fermi theorem does not hold. Therefore, it is not clear whether signatures of fermionic properties can be unveiled, although there are some suggestions for their existence [52–54]. Another interesting feature is the inherent analogy between three bosons interacting via a three-body force in one dimension and two bosons interacting via a two-body force in two spatial dimensions [55–59]. Therefore, our work can provide additional hints on the largely unexplored three-body dynamics of three bosons in one spatial dimension [60]. The present investigation will enable us to unravel the role of the different eigenstates for the dynamical response of the system and might inspire future studies examining state transfer processes [61,62], which are currently mainly restricted to one-dimensional setups.

In this work, we study the interaction quench dynamics of two harmonically confined bosons in two spatial dimensions for arbitrary interaction strengths. To set the stage, we briefly review the analytical solution of the system for an arbitrary stationary eigenstate and discuss the corresponding two-body energy eigenspectrum [20]. Subsequently, the time-evolving two-body wave function is derived as an expansion over the postquench eigenstates of the system with the expansion coefficients acquiring a closed form. The quench-induced dynamical response of the system is showcased via inspecting the fidelity evolution. The underlying eigenstate transitions that predominantly participate in the dynamics are identified in the fidelity spectrum [63–65]. It is found that after initializing the system in its ground state, characterized by finite interactions of either sign, it is driven more efficiently out of equilibrium when employing an interaction quench in the vicinity of the noninteracting limit. Because of the interaction quench, the two bosons perform a breathing motion, visualized in the temporal evolution of the single-particle density and the radial probability density in both real and momentum space. These observables develop characteristic structures which signal the participation of the bound and energetically higher lying excited states of the postquench system. The dynamics of the short-range correlations is captured by the two-body contact, which is found to perform an oscillatory motion possessing a multitude of frequencies. In all cases, the predominantly involved frequency corresponds to the energy difference between the bound and ground states. Additionally, the amplitude of these oscillations is enhanced when quenching the system from weak to infinite interactions. Moreover, it is shown that the system's dynamical response crucially depends on the initial state and in particular that, starting from an energetically higher excited state, the system is perturbed to a lesser extent and fewer postquench eigenstates contribute in the dynamics [66–70]. However, if the quench is performed from the bound state, the system is perturbed in the most efficient manner compared to any other initial-state configuration. Finally, we observe that after quenching the system from its ground state at zero interactions toward the infinitely strong ones the time-evolved wave function becomes almost orthogonal to the initial one at certain time intervals.

This work is structured as follows. In Sec. II, we introduce our setup, provide a brief summary of its energy spectrum, and most importantly derive a closed form of the time-evolved

wave function while discussing also basic observables. Subsequently, we investigate the interaction quench dynamics from attractive to repulsive interactions in Sec. III and vice versa in Sec. IV, as well as from zero to infinitely large coupling strengths in Sec. V. We summarize our results and provide an outlook in Sec. VI.

## II. THEORETICAL FRAMEWORK

### A. Setup and its stationary solutions

We consider two ultracold bosons trapped in a 2D isotropic harmonic trap. The interparticle interaction is modeled by a contact  $s$ -wave pseudopotential, which is an adequate approximation within the ultracold regime. The Hamiltonian of the system, employing harmonic oscillator units ( $\hbar = m = \omega = 1$ ), reads

$$\mathcal{H} = \frac{1}{2} \sum_{i=1}^2 [-\nabla_i^2 + r_i^2] + 2V_{pp}(\mathbf{r}_1 - \mathbf{r}_2), \quad (1)$$

where  $\mathbf{r}_1$  and  $\mathbf{r}_2$  denote the spatial coordinates of each boson. Note that the prefactor 2 is used for later convenience in the calculations. The contact regularized pseudopotential can be expressed as [71]

$$V_{pp}(\mathbf{r}) = -\frac{\pi \delta(\mathbf{r})}{\ln(Aa\Lambda)} \left[ 1 - \ln(A\Lambda r) r \frac{\partial}{\partial r} \right], \quad (2)$$

with  $\Lambda$  being an arbitrary dimensionful parameter possessing the dimension of a wave vector and  $A = e^\gamma/2$  where  $\gamma = 0.577\dots$  is the Euler-Mascheroni constant. We remark that the parameter  $\Lambda$  does not affect the value of any observable or the energies and eigenstates of the system, as has been shown in Refs. [16,71]. Furthermore, the 2D  $s$ -wave scattering length is given by  $a$ .

To proceed, we perform a separation of variables in terms of the center of mass,  $\mathbf{R} = \frac{1}{\sqrt{2}}(\mathbf{r}_1 + \mathbf{r}_2)$ , and the relative coordinates  $\boldsymbol{\rho} = \frac{1}{\sqrt{2}}(\mathbf{r}_1 - \mathbf{r}_2)$ . Employing this separation, the Hamiltonian (1) acquires the form  $\mathcal{H} = \mathcal{H}_{c.m.} + \mathcal{H}_{rel}$  with

$$\mathcal{H}_{c.m.} = -\frac{1}{2}\nabla_{\mathbf{R}}^2 + \frac{1}{2}R^2, \quad (3)$$

being the Hamiltonian of the center of mass and

$$\mathcal{H}_{rel} = -\frac{1}{2}\nabla_{\boldsymbol{\rho}}^2 + \frac{1}{2}\rho^2 + V_{pp}(\boldsymbol{\rho}) \quad (4)$$

is the Hamiltonian corresponding to the motion in the relative coordinate frame.

As a result, the Schrödinger equation can be cast into the form  $\mathcal{H}\Psi(\mathbf{r}_1, \mathbf{r}_2) = E\Psi(\mathbf{r}_1, \mathbf{r}_2)$ . Here the total energy of the system has two contributions, namely  $E = E_{c.m.} + E_{rel}$ , and the system's wave function is a product of a center-of-mass part and a relative coordinate part, i.e.,  $\Psi(\mathbf{r}_1, \mathbf{r}_2) = \Psi_{c.m.}(\mathbf{R})\Psi_{rel}(\boldsymbol{\rho})$ . Since the center-of-mass Hamiltonian  $\mathcal{H}_{c.m.}$  is interaction independent [see Eq. (3)], its eigenstates correspond to the well-known noninteracting 2D harmonic oscillator states [72]. We assume that the center-of-mass wave function takes the form  $\Psi_{c.m.}(\mathbf{R}) = \frac{e^{-R^2/2}}{\sqrt{\pi}}$ , namely the noninteracting ground state of the 2D harmonic oscillator. Since we are interested in the interaction quench dynamics of the two interacting bosons, we omit the center-of-mass wave function in what follows for simplicity. Following the above-mentioned

separation of coordinates, the problem boils down to solving the relative part of the Hamiltonian,  $\mathcal{H}_{\text{rel}}$ , which is interaction dependent. For this purpose, we assume an ansatz for the relative wave function, which involves an expansion over the noninteracting energy eigenstates of the 2D harmonic oscillator

$$\varphi_{n,m}(\rho, \theta) = \sqrt{\frac{n!}{\pi \Gamma(n + |m| + 1)}} e^{-\rho^2/2} \rho^{|m|} L_n^{(m)}(\rho^2) e^{im\theta}. \quad (5)$$

In this expression,  $\Gamma(n)$  is the gamma function while  $L_n^{(m)}$  refer to the generalized Laguerre polynomials of degree  $n$  and value of angular momentum  $m$ . Also,  $\rho = (\rho, \theta)$ , where  $\rho$  is the relative polar coordinate and  $\theta$  is the relative angle. The energy of the noninteracting 2D harmonic oscillator eigenstates in harmonic oscillator units is  $E_{\text{rel},n,m} = 2n + |m| + 1$  [72]. Within our relative coordinate wave function ansatz [see Eq. (6) below], we will employ, however, only those states that are affected by the pseudopotential and thus have a nonvanishing value at  $\rho = 0$ . These are the states with bosonic symmetry  $m = 0$ , i.e., zero angular momentum. The states with odd  $m$  are fermionic, since under the exchange  $\theta \rightarrow \theta - \pi$ , they acquire an extra minus sign due to the term  $e^{im\theta}$ . Therefore, the ansatz for the relative wave function reads

$$\Psi_{\text{rel}}(\rho) = \sum_{n=0}^{\infty} c_n \varphi_n(\rho), \quad (6)$$

where the summation is performed over the principal quantum number  $n$  and we omit the angle  $\theta$  since only the states with  $m = 0$  are taken into account. Note that this ansatz has already been reported previously, e.g., in Refs. [20,45]. In order to determine the expansion coefficients  $c_n$ , we plug Eq. (6) into the Schrödinger equation that  $\mathcal{H}_{\text{rel}}$  satisfies and project the resulting equation onto the state  $\varphi_n^*(\rho)$ . Following this procedure, we arrive at

$$c_n'(E_{\text{rel},n'} - E_{\text{rel}}) = \frac{\pi \varphi_n^*(0)}{\ln(Aa\Lambda)} \left\{ \left[ 1 - \ln(\sqrt{2}A\Lambda\rho) \rho \frac{\partial}{\partial \rho} \right] \sum_{n=0}^{\infty} c_n \varphi_n(\rho) \right\}_{\rho \rightarrow 0}. \quad (7)$$

The right-hand side of Eq. (7) is related to a normalization factor of the relative wave function  $|\Psi_{\text{rel}}\rangle$ . Indeed, it has been shown [20,45] that the coefficients take the form

$$c_n = A_1 \frac{\varphi_n^*(0)}{E_{\text{rel},n} - E_{\text{rel}}}, \quad (8)$$

with  $A_1 = \frac{2\sqrt{\pi}}{\sqrt{\psi^{(1)}(\frac{1-E_{\text{rel}}}{2})}}$  being a normalization constant and  $\psi^{(1)}(z)$  being the trigamma function.

By inserting this expression of  $c_n$  into Eq. (6), we can determine the relative wave function. This can be achieved by making use of the generating function of the Laguerre polynomials, i.e.,  $\sum_{n=0}^{\infty} t^n L_n(x) = \frac{1}{1-t} e^{-\frac{tx}{1-t}}$ . Thus, the relative wave function takes the form [33]

$$\Psi_{\text{rel},\nu_i}(\rho) = \frac{\Gamma(-\nu_i)}{\sqrt{\pi} \psi^{(1)}(-\nu_i)} e^{-\rho^2/2} U(-\nu_i, 1, \rho^2), \quad (9)$$

where  $U(a, b, z)$  refers to the confluent hypergeometric function of the second type (also known as Tricomi's function) and  $2\nu_i + 1$  is the energy of the  $i = 0, 1, \dots$  interacting eigenstate [73]. In what follows, we will drop the subscript rel and denote these relative coordinate states by  $|\Psi_{\nu_i}\rangle$ . It is important to note at this point that this relative wave-function ansatz solves also the problem of three one-dimensional harmonically trapped bosons interacting via three-body forces; see, e.g., Ref. [60] for more details.

To find the energy spectrum of  $\mathcal{H}_{\text{rel}}$ , we employ Eq. (7) along with the form of  $c_{n,i} = \frac{\sqrt{\pi} \varphi_n^*(0)}{(n-\nu_i) \sqrt{\psi^{(1)}(-\nu_i)}}$ . Note that in order to determine the right-hand side of Eq. (7), we make use of the behavior of the relative wave function (9) close to  $\rho = 0$ . In this way, we obtain the following algebraic equation regarding the energy of the relative coordinates [20,21],  $2\nu_i + 1$ ,

$$\psi(-\nu_i) = \ln\left(\frac{1}{2a^2}\right) + 2 \ln 2 - 2\gamma, \quad (10)$$

where  $\psi(x)$  is the digamma function. Note here that a different form of the algebraic Eq. (10) can be found in Ref. [20] and stems from a different definition of the scattering length  $a$  [21]. It is also important to emphasize that the energy spectrum given by Eq. (10) is independent of the form of the pseudopotential,  $V_{\text{pp}}(\mathbf{r})$ , i.e., independent of  $\Lambda$ ,  $A$ , or any short-range potential, as long as its range is much smaller than the harmonic oscillator length [21]. Denoting  $a_0 \equiv \frac{a}{2} e^{\gamma}$ , the algebraic Eq. (10) can be casted into the simpler form  $\psi(-\nu_i) = \ln\left(\frac{1}{2a_0^2}\right)$ . Also, we define the interparticle interaction strength [5,15,20,21,74,75] to be

$$g = \frac{1}{\ln\left(\frac{1}{2a_0^2}\right)}. \quad (11)$$

The energy  $E_{\text{rel}}$  of the two bosons as a function of the interparticle interaction strength is presented in Fig. 1. As can be seen, for  $g = 0$   $E_{\text{rel}}$  has the simple form  $E_{\text{rel},n} = 2n + 1$ , and thus we recover the noninteracting energy spectrum of a 2D harmonic oscillator with zero angular momentum [19,72]. In this case, the energy spacing between two consecutive eigenenergies is independent of  $n$ , i.e.,  $\Delta E = E_{\text{rel},n+1} - E_{\text{rel},n} = 2$ . For repulsive (attractive) interactions, the energy is increased (lowered) with respect to its value at  $g = 0$ . Also, and in contrast to the one-dimensional case, there are bound states  $|\Psi_{\nu_0}\rangle$ , namely eigenstates characterized by negative energy, in both interaction regimes. Note that herein we shall refer to these eigenstates with negative energy as bound states ( $\nu_0$ ) while the corresponding eigenstates with positive energy in increasing energetic order will be denoted, e.g., as the first ( $\nu_1$ ), second ( $\nu_2$ ), etc., eigenstates and called ground state, first excited state, etc. The presence of these bound states can be attributed to the existence of the centripetal term  $-\frac{1}{4r^2}$ , in the 2D radial Schrödinger equation [72], which supports a bound state even for weakly attractive potentials, in contrast to the 3D case [14,76]. These energy states,  $\nu_0$ , correspond to the molecular branch of two cold atoms in two dimensions. This is clearly captured by the lowest energy branch of Fig. 1, as has been demonstrated in Ref. [33]. Note that due to a different definition of the

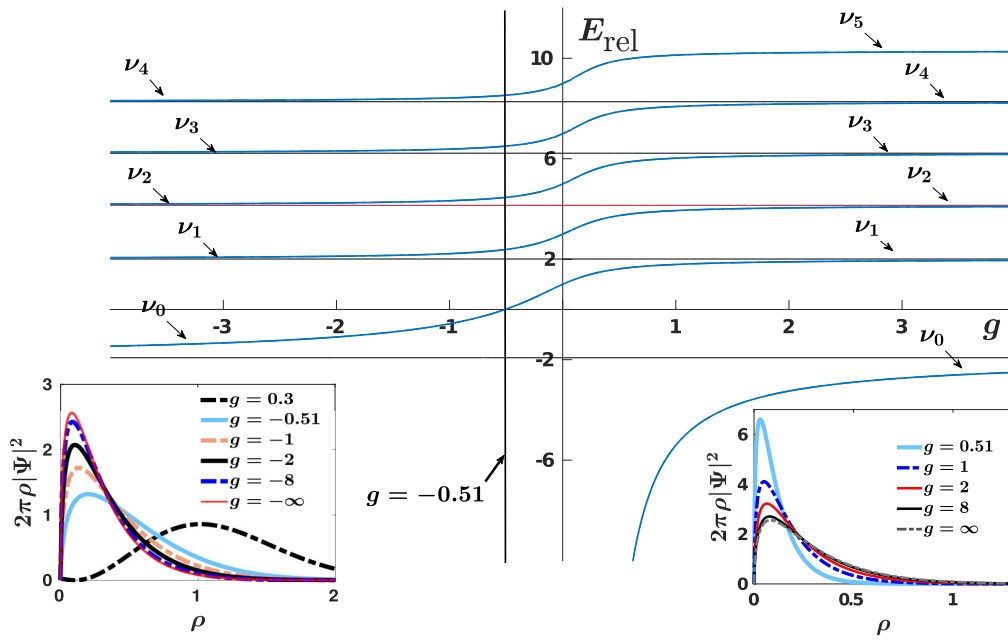


FIG. 1. Energy spectrum of two bosons trapped in a 2D harmonic trap for varying interaction strengths  $g$ . In the spectrum for  $g > -0.51$ , we display the bound state,  $\nu_0$ , and higher lying eigenstates up to the fourth excited state,  $\nu_5$ . On the other hand, for  $g < -0.51$  the spectrum contains the bound state,  $\nu_0$ , as well as higher excited states up to the third excited state,  $\nu_4$ . The black solid horizontal lines indicate the asymptotic values of the energy determined by  $\psi(-\nu_i) = 0$ , in the limit of strong interactions. The black solid vertical line at  $g = -0.51$  marks the boundary at which the bound state for negative interaction strengths becomes the ground state for  $g > -0.51$ . The insets show the radial probability density of the bound states  $\nu_0$  for different attractive (left panel) and repulsive (right panel) interactions, as well as the radial probability density of the ground state,  $\nu_1$ , at  $g = 0.3$  (left panel).

coupling constant compared to Ref. [33], which possesses a bijective mapping to our definition of the coupling strength [75], the molecular branch maps to the bound states ( $\nu_0$ ) herein in both the repulsive and the attractive interaction regimes. To further appreciate the influence of these bound states, we also provide in the insets of Fig. 1 their radial probability densities  $2\pi\rho|\Psi|^2$  [14] for various interaction strengths as well as the radial probability density of the ground state  $|\Psi_{\nu_1}\rangle$  at  $g = 0.3$ . In the repulsive regime of interactions (right panel of Fig. 1), the full width at half maximum of  $2\pi\rho|\Psi|^2$  is smaller than the one of the attractive regime (left panel of Fig. 1). This behavior is caused by the much stronger energy of the bound state at  $g > 0$  compared to the  $g < 0$  case. For large interaction strengths,  $|g| > 8$ , the widths of  $2\pi\rho|\Psi|^2$  tend to be the same. Another interesting feature of the 2D energy spectrum is the occurrence of a boundary signifying a crossover from the bound to the ground state ( $\nu_0 \rightarrow \nu_1$ ) at  $g = -0.51$ ; see the corresponding vertical line in Fig. 1. This means that the negative eigenenergy of  $|\Psi_{\nu_0}\rangle$  crosses the zero-energy axis and becomes the positive eigenenergy of  $|\Psi_{\nu_1}\rangle$  at  $g = -0.51$ . This crossover is captured, for instance, by  $2\pi\rho|\Psi|^2$  which changes from a delocalized (e.g., at  $g = 0.3$ ) to a localized (e.g., at  $g = -1$ ) distribution. The existence of this boundary affects the labeling of all the states and therefore  $\nu_i$  becomes  $\nu_{i+1}$  as it crosses from the repulsive side of interactions. We note here that with  $|\Psi_{\nu_i}\rangle$  ( $|\Psi_{\nu_0}\rangle$ ) we label the ground (bound) state and with  $|\Psi_{\nu_i}\rangle$ ,  $i > 1$ , the corresponding excited states. For repulsive interactions, the energy of the bound state diverges at  $g = 0$  as  $-1/a_0^2$  [26,76] or as  $-2e^{1/g}$  in terms of the interparticle strength,

while it approaches its asymptotic value for very strong interactions (see Fig. 1). The two bound states share the same asymptotic value  $E_{\text{rel}} = -1.923264$  at  $g \rightarrow \pm\infty$ . We remark that this behavior of the bound state in the vicinity of  $g = 0$  is the same as the one of the so-called universal bound state of two cold atoms in two dimensions in the absence of a trap [26]. We also note that the states  $|\Psi_{\nu_i}\rangle$  with  $i \neq 0$  approach their asymptotic values faster (being close to their asymptotic value already for  $g = 2$ ) than the bound states. The asymptotic values are determined via the algebraic equation  $\psi(-\nu_i) = 0$ . Moreover, it can be shown that approximately the positive energy in the infinite interaction limit is given by the formula  $E_{\text{rel}} \approx 2n + 1 - \frac{2}{\ln(n)} + \mathcal{O}((\ln n)^{-2})$  when  $n \gg 1$  [73].

## B. Time evolution of basic observables

To study the dynamics of the two harmonically trapped bosons, we perform an interaction quench starting from a stationary state of the system,  $|\Psi_{\nu_i}^{\text{in}}(0)\rangle$ , at  $g^{\text{in}}$  to the value  $g^f$ . Let us also remark in passing that the dynamics of two bosons in a 2D harmonic trap employing an analytical treatment has not yet been reported. The time evolution of the system's initial wave function reads

$$\begin{aligned} |\Psi_{\nu_i}(t)\rangle &= e^{-i\hat{H}t} |\Psi_{\nu_i}^{\text{in}}(0)\rangle \\ &= \sum_j e^{-i(2\nu_j^f+1)t} |\Psi_{\nu_j}^f\rangle \langle \Psi_{\nu_j}^f | \Psi_{\nu_i}^{\text{in}}(0)\rangle, \end{aligned} \quad (12)$$

where  $|\Psi_{\nu_j}^f\rangle$  denotes the  $j$ th eigenstate of the postquench Hamiltonian  $\hat{H}$  with energy  $(2\nu_j^f + 1)$ . Note that the indices “in” and  $f$  indicate that the corresponding quantities of

interest refer to the initial (prequench) and final (postquench) state of the system, respectively. Moreover, the overlap coefficients,  $\langle \Psi_{v_j}^f | \Psi_{v_i}^{\text{in}}(0) \rangle$ , between the initial wave function and a final eigenstate  $|\Psi_{v_j}^f\rangle$  determine the degree of participation of this postquench eigenstate in the dynamics. Recall also here that  $\Psi_{\text{c.m.}}(\mathbf{R})$ , is not included in Eq. (12) since the latter is not

affected by the quench [see also Sec. II A] and therefore does not play any role in the description of the dynamics.

It can be shown that initializing the system in the eigenstate  $|\Psi_{v_i}^{\text{in}}\rangle$  at  $g^{\text{in}}$ , the probability to occupy the eigenstate  $|\Psi_{v_j}^f\rangle$  after the quench is given by

$$\begin{aligned} d_{v_j^f, v_i^{\text{in}}} &\equiv \langle \Psi_{v_j}^f | \Psi_{v_i}^{\text{in}} \rangle = \frac{\Gamma(-v_i^{\text{in}})\Gamma(-v_j^f)}{\sqrt{\psi^{(1)}(-v_i^{\text{in}})\psi^{(1)}(-v_j^f)}} \int_0^\infty dr e^{-r} U(-v_i^{\text{in}}, 1, r) U(-v_j^f, 1, r) \\ &= \frac{\Gamma(-v_j^f) G_{33}^{32} \left( \begin{matrix} 1 & 0 & 0 \\ 0 & 0 & -v_j^f \\ & & -1 - v_i^{\text{in}} \end{matrix} \right)}{\Gamma(-v_i^{\text{in}}) \sqrt{\psi^{(1)}(-v_i^{\text{in}})\psi^{(1)}(-v_j^f)}}, \end{aligned} \quad (13)$$

with  $G_{m,n}^{p,q} \left( \begin{matrix} z & a_1, \dots, a_p \\ b_1, \dots, b_q \end{matrix} \right)$  being the Meijer  $G$  function [77]. Remarkably enough, the coefficients  $d_{v_j^f, v_i^{\text{in}}}$  can also be expressed in a much simpler form if we make use of the ansatz of Eq. (6). Indeed, by employing the orthonormality properties of the noninteracting eigenstates  $\varphi_n(\rho)$  and the explicit expression of the expansion coefficients appearing in the ansatz (6), the overlap coefficients between the final and initial eigenstates reads

$$d_{v_j^f, v_i^{\text{in}}} = \frac{\left[ \frac{1}{g^f} - \frac{1}{g^{\text{in}}} \right]}{(v_i^{\text{in}} - v_j^f) \sqrt{\psi^{(1)}(-v_i^{\text{in}})\psi^{(1)}(-v_j^f)}}. \quad (14)$$

It should be emphasized here that this is a closed form of the overlap coefficients and the only parameters that need to be determined are the energies, which are determined from the algebraic equation (10). As a result, in order to obtain the time evolution of  $|\Psi_{v_i}^{\text{in}}(0)\rangle$ , we need to numerically evaluate Eq. (12), which is an infinite summation over the postquench eigenstates denoted by  $|\Psi_{v_j}^f\rangle$ . In practice, this infinite summation is truncated to a finite one with an upper limit which ensures that the values of all observables have been converged with respect to a further adding of eigenstates.

Having determined the time evolution of the system's wave function [Eq. (12)] enables us to determine any observable of interest in the course of the dynamics. To inspect the dynamics of the system from a single-particle perspective, we monitor its one-body density

$$\begin{aligned} \rho^{(1)}(\mathbf{r}_1, t) &= \int d\mathbf{r}_2 \tilde{\Psi}(\mathbf{r}_1, \mathbf{r}_2; t) \tilde{\Psi}^*(\mathbf{r}_1, \mathbf{r}_2; t) \\ &= \frac{e^{-(x^2+y^2)}}{\pi^2} \sum_{j,k} \frac{e^{2i(v_j^f - v_k^f)t} \Gamma(-v_k^f) \Gamma^*(-v_j^f) d_{v_k^f, v_i^{\text{in}}} d_{v_j^f, v_i^{\text{in}}}^*}{\sqrt{\psi^{(1)}(-v_k^f)\psi^{(1)*}(-v_j^f)}} \\ &\quad \times \int_{-\infty}^\infty dz dw e^{-z^2 - w^2} U^*(-v_j^f, 1, (x-z)^2/2 + (y-w)^2/2) U(-v_k^f, 1, (x-z)^2/2 + (y-w)^2/2). \end{aligned} \quad (15)$$

In this expression, the total wave function of the system is denoted by  $\tilde{\Psi}(\mathbf{r}_1, \mathbf{r}_2) = \Psi_{\text{c.m.}}(\mathbf{R}(\mathbf{r}_1, \mathbf{r}_2), t) \Psi_{\text{rel}, v_i}(\rho(\mathbf{r}_1, \mathbf{r}_2), t)$  [78]. To arrive at the second line of Eq. (15), we have expressed the relative,  $\rho^2 = \frac{1}{2}(r_1^2 + r_2^2 - 2\mathbf{r}_1 \cdot \mathbf{r}_2)$ , and the center-of-mass coordinates,  $R^2 = \frac{1}{2}(r_1^2 + r_2^2 + 2\mathbf{r}_1 \cdot \mathbf{r}_2)$ , in terms of the Cartesian coordinates  $(\mathbf{r}_1, \mathbf{r}_2)$  and integrated out the ones pertaining to the other particle. In particular, we adopted the notation  $\mathbf{r}_1 = (x, y)$  and  $\mathbf{r}_2 = (z, w)$  for the coordinates that are being integrated out. Moreover, the integral  $I_{v_j^f, v_k^f}$  appearing in the last line of Eq. (15) can be further simplified by employing the replacements  $z' = x - z$ ,  $w' = y - w$  and then the new variables can be expressed in terms of polar coordinates. The emergent angle integration can be readily performed and the integral with respect to the radial

coordinate becomes

$$\begin{aligned} I_{v_j^f, v_k^f} &= 2\pi e^{-(x^2+y^2)} \int_0^\infty dr r e^{-r^2} I_0(2r\sqrt{x^2+y^2}) \\ &\quad \times U^*\left(-v_j^f, 1, \frac{r^2}{2}\right) U\left(-v_k^f, 1, \frac{r^2}{2}\right). \end{aligned} \quad (16)$$

Here,  $I_0(x)$  is the zeroth-order modified Bessel function of the first kind [73,77].

Another interesting quantity which provides information about the state of the system on the two-body level is the radial probability density of the relative wave function

$$\mathcal{B}(\rho, t) = 2\pi \rho |\Psi(\rho, t)|^2. \quad (17)$$

It provides the probability density to detect two bosons for a fixed time instant  $t$  at a relative distance  $\rho$ . It can be directly determined by employing the overlap coefficients of Eq. (14). Moreover, the corresponding radial probability density in momentum space reads

$$\mathcal{C}(k, t) = 2\pi k |\tilde{\Psi}(k, t)|^2. \quad (18)$$

Here, the relative wave function in momentum space is obtained from the two-dimensional Fourier transform

$$\tilde{\Psi}(k, t) = 2\pi \int_0^\infty d\rho \rho \Psi(\rho, t) J_0(2\pi \rho k), \quad (19)$$

where  $J_0(x)$  is the zeroth-order Bessel function.

To estimate the system's dynamical response after the quench, we resort to the fidelity evolution  $F(t)$ . It is defined as the overlap between the time-evolved wave function at time  $t$  and the initial one [79], namely

$$F(t) = \langle \Psi(0) | e^{-i\hat{H}t} | \Psi(0) \rangle = \sum_j e^{-i(2\nu_j^f + 1)t} |d_{\nu_j^f, \nu_j^{\text{in}}}|^2. \quad (20)$$

Evidently,  $F(t)$  is a measure of the deviation of the system from its initial state [45]. In what follows, we will make use of the modulus of the fidelity,  $|F(t)|$ . Most importantly, the frequency spectrum of the modulus of the fidelity  $F(\omega) = \frac{1}{\sqrt{2\pi}} \int_{-\infty}^\infty dt |F(t)| e^{i\omega t}$  grants access to the quench-induced dynamical modes [63,64,80–82]. Indeed, the emergent frequencies appearing in the spectrum correspond to the energy differences of particular postquench eigenstates of the system and therefore enable us to identify the states that participate in the dynamics (see also the discussion below).

Another observable of interest is the two-body contact  $\mathcal{D}$ . The latter is defined from the momentum distribution in the limit of very large momenta, i.e.,  $\mathcal{C}(k, t) \xrightarrow{k \rightarrow \infty} \frac{2\pi \mathcal{D}(t)}{k^3}$  and captures the occurrence of short-range two-body correlations [83–85]. Moreover, this quantity can be experimentally monitored [86,87] and satisfies a variety of universal relations independently of the quantum statistics, the number of particles, or the system's dimensionality [85,88–90]. Having at hand the eigenstates of the system, we can expand the time evolved contact after a quench from  $|\Psi_{\nu_j^{\text{in}}}\rangle$  at  $g^{\text{in}}$  to an arbitrary  $g^f$  in terms of the contacts of the postquench eigenstates [91]. Namely,

$$\mathcal{D}(t) = \left| \sum_j e^{-i(2\nu_j^f + 1)t} d_{\nu_j^f, \nu_j^{\text{in}}} \sqrt{|\mathcal{D}_j|} \right|^2. \quad (21)$$

The contacts  $\mathcal{D}_j$  of the postquench eigenstates  $|\Psi_{\nu_j^f}\rangle$  can be inferred by employing the behavior of the eigenstates [Eq. (9)] close to zero distance,  $\rho \rightarrow 0$ , between the atoms

$$\Psi_{\nu_j}(\rho) \xrightarrow{\rho \rightarrow 0} -\frac{2 \ln \rho}{\sqrt{\pi} \psi^{(1)}(-\nu_j)}. \quad (22)$$

By plugging Eq. (22) into Eq. (19) and restricting ourselves to small  $\rho$  values, we obtain the contact from the leading-order term ( $\approx 1/k^2$ ) of the resulting expression. The contact for the postquench eigenstates  $|\Psi_{\nu_j^f}\rangle$  reads

$$\mathcal{D}_j = \frac{1}{\pi^3 \psi^{(1)}(-\nu_j)}. \quad (23)$$

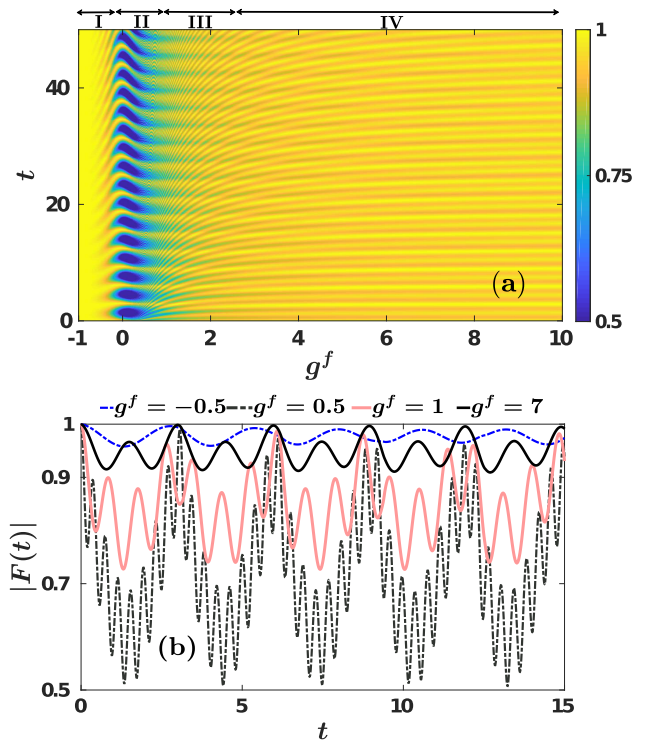


FIG. 2. (a) Fidelity evolution of the two bosons following an interaction quench from  $g^{\text{in}} = -1$  and  $|\Psi_{\nu_1}^{\text{in}}\rangle$  to various postquench interaction strengths. (b) Fidelity evolution at representative postquench interaction strengths (see legend).

Note that in order to capture the quench-induced dynamical modes that participate in the dynamics of the contact, we employ its corresponding frequency spectrum, i.e.,  $\mathcal{D}(\omega) = \int_{-\infty}^\infty dt \mathcal{D}(t) e^{i\omega t}$ .

Having analyzed the exact solution of the two bosons trapped in a 2D harmonic trap both for the stationary and the time-dependent cases, we subsequently explore the corresponding interaction quench dynamics. In particular, we initialize the system into its ground state  $|\Psi_{\nu_1}^{\text{in}}\rangle$  for attractive interactions and perform interaction quenches toward the repulsive regime (Sec. III) and vice versa (Sec. IV).

### III. QUENCH DYNAMICS OF TWO ATTRACTIVE BOSONS TO REPULSIVE INTERACTIONS

We first study the interaction quench dynamics of two attractively interacting bosons confined in a 2D isotropic harmonic trap. More specifically, the system is initially prepared in its corresponding ground state  $|\Psi_{\nu_1}^{\text{in}}\rangle$  at  $g^{\text{in}} = -1$ . At  $t = 0$ , we perform an interaction quench toward the repulsive interactions, letting the system evolve. Our main objective is to analyze the dynamical response of the system and identify the underlying dominant microscopic mechanisms.

#### A. Dynamical response

To examine the dynamical response of the system after the quench, we employ the corresponding fidelity evolution  $|F(t)|$  [see Eq. (20)] [92]. Figure 2(a) shows  $|F(t)|$  for various postquench interaction strengths  $g^f$ . We observe the

emergence of four distinct dynamical regions where the fidelity exhibits a different behavior. In region I,  $-1 < g^f < -0.27$ ,  $|F(t)|$  performs small amplitude oscillations in time [see also  $|F(t)|$  for  $g^f = -0.5$  in Fig. 2(b)] and therefore the system remains essentially unperturbed. Note that the oscillation period is slightly smaller than  $\pi$  [see also the discussion below]; e.g., see Fig. 2(b) for  $g^f = -0.5$ . Entering region II,  $-0.27 < g^f < 0.8$ , the system departs significantly from its initial state since  $|F(t)|$  exhibits large amplitude oscillations in time [see the blue lobes in Fig. 2(a) within region II] deviating appreciably from unity [see also Fig. 2(b) at  $g^f = 0.5$ ]. A more careful inspection of  $|F(t)|$  reveals that it oscillates with at least two frequencies, namely a faster one and a slower one. Indeed,  $|F(t)|$  oscillates rapidly (fast frequency) within a large amplitude envelope of period  $\simeq \pi$  (slow frequency). Within region III,  $0.8 < g^f < 2.7$ , the oscillation amplitude of  $|F(t)|$  becomes smaller when compared to region II. Most importantly, we observe the appearance of irregular minima and maxima in  $|F(t)|$  being shifted with time [Fig. 2(b) at  $g^f = 1$ ]. For strong interactions,  $2.7 < g^f < 10$ , we encounter region IV in which  $|F(t)| > 0.9$  performs small-amplitude oscillations that resemble the ones already observed within region I [Fig. 2(b) at  $g^f = 7$ ]. An important difference with respect to region I is that the oscillations of  $|F(t)|$  are faster and there is more than one frequency involved; compare  $|F(t)|$  at  $g^f = -0.5$  and  $g^f = 7$  in Fig. 2(b).

To gain more insights onto the dynamics, we next resort to the frequency spectrum of the fidelity  $F(\omega)$ , shown in Fig. 3(a) for varying postquench interaction strengths. This spectrum provides information about the contribution of the different postquench states that participate in the dynamics. Indeed, the square of the fidelity [see Eq. (20)] can be expressed as

$$|F(t)|^2 = \sum_j |d_{v_j^f, v_1^{\text{in}}}|^4 + 2 \sum_{j \neq k} |d_{v_j^f, v_1^{\text{in}}}|^2 |d_{v_k^f, v_1^{\text{in}}}|^2 \cos(\omega_{v_j^f, v_k^f} t), \quad (24)$$

where  $d_{v_j^f, v_1^{\text{in}}}$  are the overlap coefficients between the initial (prequench)  $|\Psi_{v_1^{\text{in}}}\rangle$  and the final (postquench)  $|\Psi_{v_j^f}\rangle$  eigenstates. The corresponding overlap coefficients  $|d_{v_j^f, v_1^{\text{in}}}|^2$  for an increasing postquench interaction strength are presented in Fig. 3(b). Moreover, the frequencies  $\omega_{v_j^f, v_k^f}$  are determined by the energy differences between two distinct eigenstates of the postquench Hamiltonian, namely  $\omega_{v_j^f, v_k^f} = 2(v_j^f - v_k^f) \equiv \omega_{v_j, v_k}$  with  $j \neq k$ . Note also that the amplitudes of the frequencies [encoded in the color bar of Fig. 3(a)] mainly depend on the product of their respective overlap coefficients, i.e.,  $|d_{v_j^f, v_1^{\text{in}}}|^2 |d_{v_k^f, v_1^{\text{in}}}|^2$ . Finally, the values of the frequencies  $\omega_{v_j, v_k}$  along with the coefficients  $|d_{v_j^f, v_1^{\text{in}}}|^2$  [Fig. 3(b)] determine the dominantly participating postquench eigenstates [45,63,64,80].

Focusing on region I, we observe that in  $F(\omega)$  there are two frequencies, hardly visible in Fig. 3(a). The most dominant one corresponds to  $\omega_{v_1, v_0}$  for  $-1 < g^f < -0.51$  and to  $\omega_{v_2, v_1}$  for  $-0.51 < g^f < -0.27$ . It is larger than 2, thus giving rise to a period of  $|F(t)|$  smaller than  $\pi$ . The fainter one

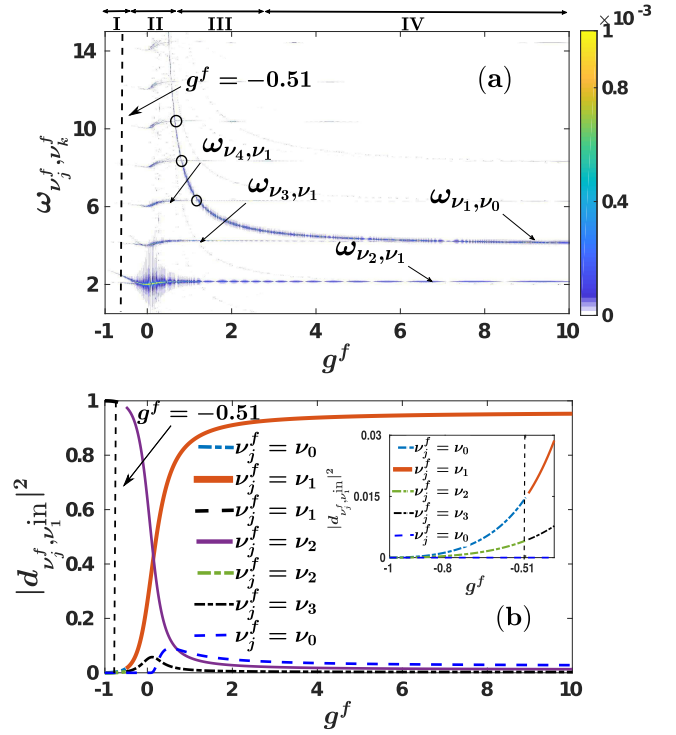


FIG. 3. (a) The fidelity spectrum  $F(\omega)$  after an interaction quench from  $g^{\text{in}} = -1$  to different final interaction strengths  $g^f$ . (b) The corresponding largest overlap coefficients  $|d_{v_j^f, v_1^{\text{in}}}|^2$  (see legend). The black dashed vertical line at  $g^f = -0.51$  marks the boundary at which the bound state for negative interaction strengths becomes the ground state for  $g^f > -0.51$ ; see also Fig. 1. The inset presents a magnification of  $|d_{v_j^f, v_1^{\text{in}}}|^2$  for  $-1 \leq g^f \leq -0.4$ .

corresponds to  $\omega_{v_2, v_1}$  for  $-1 < g^f < -0.51$  and to  $\omega_{v_3, v_2}$  for  $-0.51 < g^f < -0.27$ . For reasons of clarity, let us mention that each of these frequencies, of course, coincides with the corresponding energy difference between the respective eigenstates of the system's eigenspectrum (Fig. 1). Recall that at  $g^f = -0.51$  indicated by the vertical line in Fig. 3 (see also Fig. 1), the labeling of the eigenstates changes and, e.g., the frequency  $\omega_{v_1, v_0}$  becomes  $\omega_{v_2, v_1}$ . As can be seen from Fig. 3(a),  $\omega_{v_1, v_0}$  decreases for increasing  $g^f$ , which is in accordance with the behavior of the energy gap  $\omega_{v_1, v_0} = 2(v_1^f - v_0^f)$  in the system's eigenspectrum (Fig. 1). Turning to region II, a multitude of almost equidistant frequencies appears. This behavior is clearly captured in the vicinity of  $g^f = 0$ , where the energy difference between consecutive eigenenergies exhibits an almost equal spacing of the order of  $\Delta E \simeq 2$  (see also Fig. 1). To characterize the observed frequency branches in terms of transitions between the system's eigenstates, we determine the corresponding overlap coefficients  $d_{v_j^f, v_1^{\text{in}}}$  shown in Fig. 3(b) and also the respective eigenstate energy differences known from the eigenspectrum of the system (Fig. 1). In this way, we identify the most prominent frequency  $\omega_{v_2, v_1}$  appearing in  $F(\omega)$  which is near  $\omega \approx 2$ . Additionally, a careful inspection of Fig. 3(b) reveals that there is a significant decrease of  $|d_{v_2^f, v_1^{\text{in}}}|^2$  for a larger  $g^f$  and subsequently energetically higher excited states come into



play, e.g.,  $|\Psi_{\nu_3}^f\rangle$ . These latter contributions give rise to the appearance of energetically higher frequencies in  $F(\omega)$ . Indeed, the bound state,  $|\Psi_{\nu_0}^f\rangle$ , possesses a non-negligible population already for  $g^f > 0.27$  [Fig. 3(b)], giving rise to the frequency branch  $\omega_{\nu_1, \nu_0}$  that at  $g^f \approx 0.54$  has a quite large value of approximately 14.9 and decreases rapidly as  $g^f$  increases. Of course, this behavior stems directly from the energy gap between the bound,  $|\Psi_{\nu_0}^f\rangle$ , and the ground,  $|\Psi_{\nu_1}^f\rangle$ , states as it can be easily confirmed by inspecting the eigenspectrum (Fig. 1). In the intersection between regions II and III,  $\omega_{\nu_1, \nu_0}$  becomes degenerate with the other frequency branches [see the black circles in Fig. 3(a)], e.g.,  $\omega_{\nu_4, \nu_1}$  in the vicinity of  $g^f = 1$  and  $\omega_{\nu_3, \nu_1}$  close to  $g^f = 3$  [Fig. 3(a)]. The aforementioned frequency branches are much fainter when compared to  $\omega_{\nu_1, \nu_0}$ , since the overlap coefficients between the relevant eigenstates are small, e.g.,  $|d_{\nu_3, \nu_1}^f|^2 < |d_{\nu_0, \nu_1}^f|^2$  [Fig. 3(b)]. Finally, in region IV, there are mainly two dominant frequencies, namely  $\omega_{\nu_1, \nu_0}$  and  $\omega_{\nu_2, \nu_1}$ , that acquire constant values as  $g^f$  increases. Indeed, in this region  $|d_{\nu_1, \nu_0}^f|^2$ ,  $|d_{\nu_0, \nu_1}^f|^2$ , and  $|d_{\nu_2, \nu_1}^f|^2$  are the most significantly populated coefficients [Fig. 3(b)], which in turn yield these two frequencies.

### B. Role of the initial state

To investigate the role of the initial eigenstate in the dynamical response of the two bosons, we consider an interaction quench from  $g^{\text{in}} = -1$  to  $g^f = 1$  but initializing the system at energetically different excited states, i.e.,  $|\Psi_{\nu_k}^{\text{in}}\rangle$ ,  $k > 1$ , and the bound state  $|\Psi_{\nu_0}^{\text{in}}\rangle$ . In particular, Fig. 4(a) illustrates  $|F(t)|$  with a prequench eigenstate being the bound state and the first, third, fifth, and seventh excited states. In all cases,  $|F(t)|$  exhibits an irregular oscillatory motion as in the case of  $|\Psi_{\nu_1}^{\text{in}}\rangle$ ; see also Fig. 2(b). Evidently, for an energetically higher initial eigenstate (but not the bound state),  $|F(t)|$  takes larger values and therefore the system is less perturbed. However, when the two bosons are prepared in the bound state,  $|\Psi_{\nu_0}^{\text{in}}\rangle$ , of the system, then  $|F(t)|$  drops to smaller values as compared to the case of energetically higher initial states and the system becomes more perturbed.

The impact of the initial state on the oscillation amplitude of  $|F(t)|$  is reflected on the values of the corresponding overlap coefficients that appear in the expansion of the fidelity in Eq. (24). More precisely, when an overlap coefficient possesses a dominant population with respect to the others then  $|F(t)|$  exhibits a smaller oscillation amplitude than in the case where at least two overlap coefficients possess a non-negligible population. For convenience and in order to identify the states that take part in the dynamics, we provide the relevant overlap coefficients,  $|d_{\nu_j, \nu_k}^f|^2$ , for the quench  $g^{\text{in}} = -1 \rightarrow g^f = 1$  in Table I for various initial eigenstates  $|\Psi_{\nu_k}^{\text{in}}\rangle$ . Indeed, an initial energetically higher lying excited state results in the dominant population of one postquench state while the other states exhibit a very small contribution, e.g., see the last column of Table I. For this reason, an initially energetically higher excited state leads to a smaller oscillation amplitude of  $|F(t)|$ . Moreover, the large frequency oscillations appearing in  $|F(t)|$  are caused by the presence of several higher than first-order eigenstate transitions, e.g.,  $\omega_{\nu_6, \nu_4}$ ,  $\omega_{\nu_7, \nu_4}$ ,  $\omega_{\nu_4, \nu_0}$  in the case of starting from  $|\Psi_{\nu_4}^{\text{in}}\rangle$  [Fig. 4(b)].

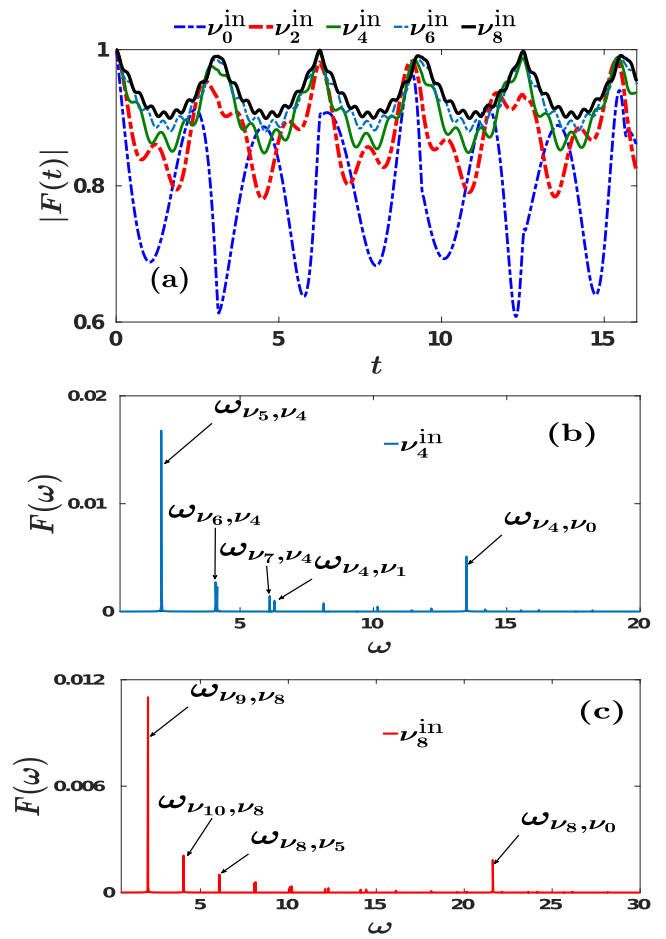


FIG. 4. (a) Fidelity evolution when performing a quench from  $g^{\text{in}} = -1$  to  $g^f = 1$  starting from energetically higher excited states  $|\Psi_{\nu_k}^{\text{in}}\rangle$ ,  $k > 1$ , as well as the bound state  $|\Psi_{\nu_0}^{\text{in}}\rangle$  (see legend). The corresponding fidelity spectrum when initializing the system in (b)  $|\Psi_{\nu_4}^{\text{in}}\rangle$  and (c)  $|\Psi_{\nu_8}^{\text{in}}\rangle$ .

The transition mainly responsible for these large frequency oscillations of  $|F(t)|$  involves the bound state  $|\Psi_{\nu_0}^f\rangle$ . Indeed, by inspecting  $|F(t)|$  of different initial configurations shown in Fig. 4(a), we observe that starting from energetically higher excited states such that  $\nu_j > \nu_4$  the respective contribution of  $|\Psi_{\nu_0}^f\rangle$  diminishes (see also Table I), leading to a decay of the amplitude of these large frequency oscillations of  $|F(t)|$ . The aforementioned behavior becomes evident, e.g., by comparing  $|F(t)|$  for  $\nu_2^{\text{in}}$  and  $\nu_8^{\text{in}}$  in Fig. 4(a).

On the other hand, in order to unveil the participating frequencies in the dynamics of  $|F(t)|$ , we calculate its spectrum  $|F(\omega)|$ , shown in Figs. 4(b) and 4(c). We observe that starting from an energetically higher excited state several frequencies, referring to different eigenstate transitions, are triggered. Most of these frequencies which refer to different initial states almost coincide, e.g.,  $\omega_{\nu_5, \nu_4}$  with  $\omega_{\nu_9, \nu_8}$ , since the energy gap of the underlying eigenstates is approximately the same (see also Fig. 1). They possess, however, a distinct amplitude. Additionally, there are also distinct contributing frequencies, e.g., compare  $\omega_{\nu_4, \nu_0}$  with  $\omega_{\nu_8, \nu_0}$ . The latter are in turn responsible for the dependence of the oscillation period

TABLE I. Overlap coefficients  $|d_{v_j^f, v_i^{\text{in}}}|^2$  for the quench from  $g^{\text{in}} = -1$  to  $g^f = 1$  starting from various excited states, namely  $|\Psi_{v_0}^{\text{in}}\rangle$ ,  $|\Psi_{v_2}^{\text{in}}\rangle$ ,  $|\Psi_{v_4}^{\text{in}}\rangle$ ,  $|\Psi_{v_6}^{\text{in}}\rangle$ , and  $|\Psi_{v_8}^{\text{in}}\rangle$ . Only the coefficients with a value larger than 0.9% are presented.

	$ d_{v_j^f, v_0^{\text{in}}} ^2$	$ d_{v_j^f, v_2^{\text{in}}} ^2$	$ d_{v_j^f, v_4^{\text{in}}} ^2$	$ d_{v_j^f, v_6^{\text{in}}} ^2$	$ d_{v_j^f, v_8^{\text{in}}} ^2$
$v_j^f = v_0$	0.7896	0.0367	0.0147		
$v_j^f = v_1$	0.1214	0.0198			
$v_j^f = v_2$	0.0351	0.8765			
$v_j^f = v_3$	0.0163	0.0464	0.0187		
$v_j^f = v_4$	0.0092	0.0092	0.9078		
$v_j^f = v_5$			0.0351	0.0164	
$v_j^f = v_6$				0.9249	
$v_j^f = v_7$				0.0286	0.0145
$v_j^f = v_8$					0.9358
$v_j^f = v_9$					0.0243

of  $|F(t)|$  on the initial eigenstate of the system. Finally, let us note that if the system is quenched to other final interaction strengths (not shown here for brevity reasons), across the four dynamical regions identified in Fig. 2(a), then  $|F(t)|$  follows a similar pattern as discussed in Fig. 4(a).

### C. One-body density evolution

To monitor the dynamical spatial redistribution of the two atoms after the quench at the single-particle level, we next examine the evolution of the one-body density  $\rho^{(1)}(x, y, t)$  [Eq. (15)]. Figures 5(a)–5(f) depict  $\rho^{(1)}(x, y, t)$  following an interaction quench from  $g^{\text{in}} = -1$  to  $g^f = 1$  when the system is initialized in its ground-state configuration  $|\Psi_{v_1}^{\text{in}}\rangle$ . Note that the shown time instants of the evolution are in the vicinity of the local minima and maxima of the fidelity [see also Fig. 2(b)], where the system deviates strongly and weakly from its initial state respectively. Overall, we observe that the atoms undergo a breathing motion manifested as a contraction and expansion dynamics of  $\rho^{(1)}(x, y, t)$ ; see, for instance, the increase of the density close to  $x = y = 0$  [Figs. 5(b) and 5(c)]

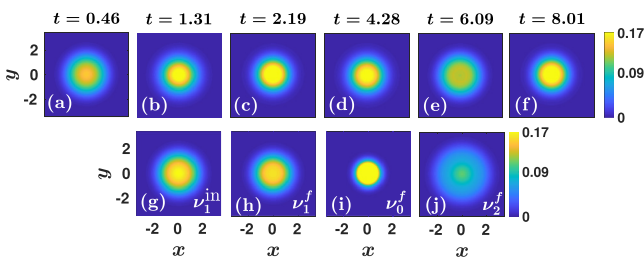


FIG. 5. [(a)–(f)] Time evolution of the one-body density following an interaction quench from  $g^{\text{in}} = -1$  to  $g^f = 1$ . The system of two bosons is initialized in its ground state,  $|\Psi_{v_1}^{\text{in}}\rangle$ , trapped in a 2D harmonic oscillator. [(g)–(j)] The corresponding one-body densities for the pre- and postquench eigenstates (see legends) whose overlap coefficients are the dominant ones for the specific quench.

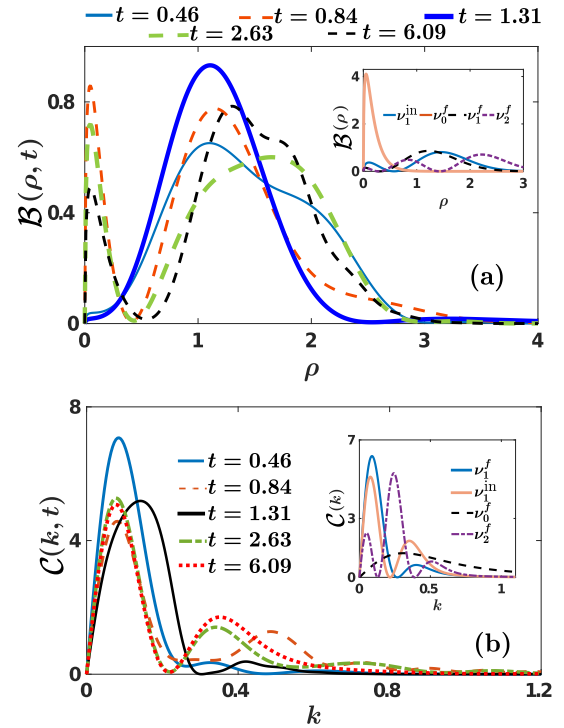


FIG. 6. (a) Time evolution of the radial probability density,  $\mathcal{B}(\rho, t)$ , of the two atoms at selected time instants (see legend) for an interaction quench from  $g^{\text{in}} = -1$  to  $g^f = 1$  starting from the ground state  $|\Psi_{v_1}^{\text{in}}\rangle$ . The inset illustrates  $\mathcal{B}(\rho)$  of the initial state and different postquench eigenstates (see legend). (b) Temporal evolution of the corresponding radial probability density in momentum space,  $\mathcal{C}(k, t)$  at specific time instants (see legend). The inset depicts  $\mathcal{C}(k)$  of the initial state and various postquench eigenstates (see legend).

and its subsequent spread [Figs. 5(d) and 5(e)]. To provide further hints on the dynamical superposition [66,67,70] of states, we show in Figs. 5(g)–5(j) the corresponding  $\rho^{(1)}(x, y, t = 0)$  of the initial state, i.e.,  $|\Psi_{v_1}^{\text{in}}\rangle$ , and the densities of the three most significant, in terms of the overlap coefficients, final states, namely  $|\Psi_{v_1}^f\rangle$ ,  $|\Psi_{v_0}^f\rangle$ , and  $|\Psi_{v_2}^f\rangle$ . Comparing these  $\rho^{(1)}(x, y, t = 0)$  with the  $\rho^{(1)}(x, y, t)$ , we can deduce that during evolution the one-body density of the system is mainly in a superposition of the  $|\Psi_{v_1}^f\rangle$  and the  $|\Psi_{v_0}^f\rangle$ . The excited state  $|\Psi_{v_2}^f\rangle$  has a smaller contribution to the dynamics of  $\rho^{(1)}(x, y, t)$  [e.g., see Fig. 5(e)] compared to the other states.

### D. Evolution of the radial probability density

In order to gain a better understanding of the nonequilibrium dynamics of the two bosons, we also employ the time evolution of the radial probability density of the relative wave function  $\mathcal{B}(\rho, t)$  [Eq. (17)]. Recall that this quantity provides the probability density of finding the two bosons at a distance  $\rho$  apart for a fixed time instant. The dynamics of  $\mathcal{B}(\rho, t)$  after a quench from  $g^{\text{in}} = -1$  to  $g^f = 1$ , starting from  $|\Psi_{v_1}^{\text{in}}\rangle$ , is illustrated at selected time instants in Fig. 6(a). We can

infer that the emergent breathing motion of the two bosons is identified via the succession in time of a single-peak [e.g., at  $t = 0.46, 1.31$ ] and a double-peak [e.g., at  $t = 0.84, 2.63$ ] structure in the dynamics of  $\mathcal{B}(\rho, t)$ . Here, the one peak is located close to  $\rho = 0$  and the other close to the harmonic oscillator length (unity in our choice of units). Moreover, by comparing  $\mathcal{B}(\rho, t)$  [Fig. 6(a)] with  $\rho^{(1)}(x, y, t)$  (Fig. 5) suggests that a double-peak structure in  $\mathcal{B}(\rho, t)$  refers to an expansion of  $\rho^{(1)}(x, y, t)$  (e.g., at  $t = 6.09$ ), while a single-peaked  $\mathcal{B}(\rho, t)$  corresponds to a contraction of  $\rho^{(1)}(x, y, t)$  (e.g., at  $t = 1.31$ ). Indeed, for a double-peak structure of  $\mathcal{B}(\rho, t)$ , its secondary maximum always occurs at slightly larger radii than the maximum of a single-peak distribution of  $\mathcal{B}(\rho, t)$ , possessing also a more extended tail. This further testifies the expanding (contracting) tendency of the cloud in the former (latter) case. To reveal the microscopic origin of the structures building upon  $\mathcal{B}(\rho, t)$ , we also calculate this quantity [see the inset of Fig. 6(a)] for the states  $|\Psi_{\nu_1}^{\text{in}}\rangle$ ,  $|\Psi_{\nu_1}^f\rangle$ ,  $|\Psi_{\nu_0}^f\rangle$ , and  $|\Psi_{\nu_2}^f\rangle$  that primarily contribute to the dynamics in terms of the overlap coefficients [see also Fig. 3(b)]. Indeed, comparing  $\mathcal{B}(\rho, t)$  [Fig. 6(a)] with  $\mathcal{B}(\rho)$  of the stationary eigenstates [inset of Fig. 6(a)] enables us to deduce that  $\mathcal{B}(\rho, t)$  resides mainly in a superposition of the ground ( $|\Psi_{\nu_1}^f\rangle$ ), the bound ( $|\Psi_{\nu_0}^f\rangle$ ), and the first excited ( $|\Psi_{\nu_2}^f\rangle$ ) eigenstates. Also, it can be clearly seen that the main contribution stems from the ground state, while the other two states possess smaller contributions. In particular, the participation of the bound state can be inferred due to the existence of the peak close to  $\rho = 0$ , which, e.g., for  $t = 0.84$  becomes prominent, whereas the presence of the excited state  $|\Psi_{\nu_2}^f\rangle$  is discernible from the spatial extent of the  $\mathcal{B}(\rho, t)$ , e.g., at  $t = 2.63$  [Fig. 6(a)].

To showcase the motion of the two atoms in momentum space, we invoke the evolution of the radial probability density in momentum space  $\mathcal{C}(k, t)$  [93] illustrated in Fig. 6(b) for the quench  $g^{\text{in}} = -1 \rightarrow g^f = 1$  starting from  $|\Psi_{\nu_1}^{\text{in}}\rangle$ . We observe that in the course of the dynamics a pronounced peak close to  $k = 0$  and a secondary one located at values of larger  $k$  appear in  $\mathcal{C}(k, t)$ . Moreover, the breathing motion in momentum space is manifested by the lowering and raising of the zero momentum peak accompanied by a subsequent enhancement or reduction of the tail of  $\mathcal{C}(k, t)$ , as shown, e.g., at  $t = 0.84, 6.09$ . Note also that the tail of  $\mathcal{C}(k, t)$  decays in a much slower manner compared to the tail of  $\mathcal{B}(\rho, t)$ . Indeed, the latter decays asymptotically as  $\sim e^{-\rho^2}$  [see also Eq. (9)] while by fitting the tail of  $\mathcal{C}(k, t)$  we observe a decay law  $\sim 1/k^3$  (not shown here for brevity) [83–85,94]. Additionally, in order to unveil the corresponding superposition of states that contribute to the momentum distribution, the inset of Fig. 6(b) presents  $\mathcal{C}(k)$  of the postquench eigenstates that possess the most significantly populated overlap coefficients [see also Fig. 3(b)]. As can be seen, the bound state ( $|\Psi_{\nu_0}^f\rangle$ ) exhibits a broad momentum distribution with a tail that extends to large values of  $k$ , while  $\mathcal{C}(k)$  of the ground state ( $|\Psi_{\nu_1}^f\rangle$ ) contributes the most and has a main peak around  $k = 0$ . On the other hand, the excited state ( $|\Psi_{\nu_2}^f\rangle$ ) contributes to a lesser extent, and its presence is mainly identified when the momentum distribution exhibits two nodes, e.g., at  $t = 2.63$ .

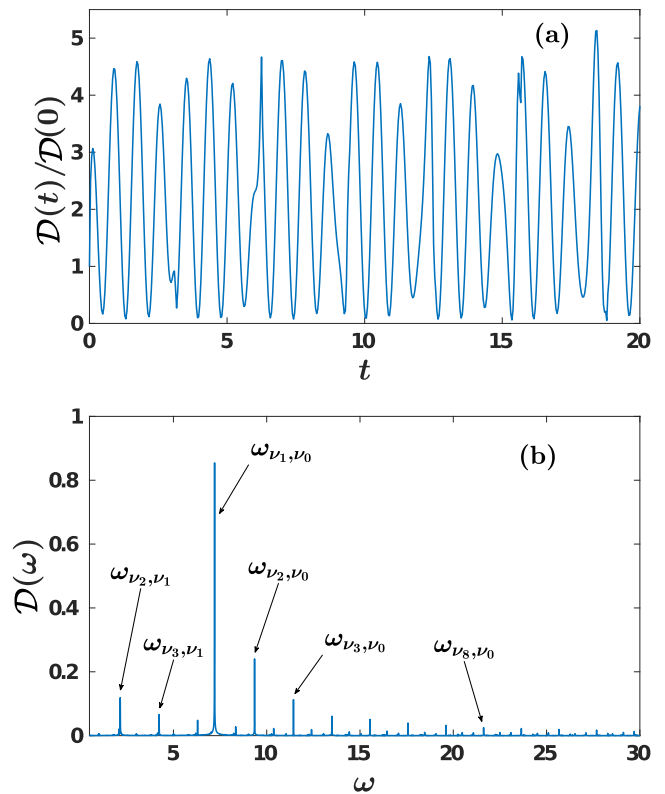


FIG. 7. (a) Temporal evolution of the normalized contact  $D(t)/D(0)$  upon considering an interaction quench from  $g^{\text{in}} = -1$  to  $g^f = 1$ . (b) The corresponding frequency spectrum.

### E. Evolution of the contact

Subsequently, we examine the contact  $D(t)/D(0)$  in the course of the evolution after a quench from  $g^{\text{in}} = -1$  to  $g^f = 1$ ; see Fig. 7(a). Recall that the contact reveals the existence of short-range two-body correlations. Evidently  $D(t)/D(0)$  exhibits an irregular oscillatory behavior containing a variety of different frequencies. Indeed, by inspecting the corresponding frequency spectrum depicted in Fig. 7(b), a multitude of frequencies appear. The most predominant frequencies possessing the largest amplitude originate from the energy difference between the bound state,  $|\Psi_{\nu_0}\rangle$ , and energetically higher lying states, such as  $\omega_{\nu_1, \nu_0}$ ,  $\omega_{\nu_2, \nu_0}$  and  $\omega_{\nu_3, \nu_0}$ . Also here  $\omega_{\nu_2, \nu_1}$  has a comparable value to  $\omega_{\nu_3, \nu_0}$  and thus contributes non-negligibly to the dynamics of  $D(t)/D(0)$ . Moreover, there is a multitude of other contributing frequencies, e.g.,  $\omega_{\nu_8, \nu_0}$  having an amplitude smaller than  $\omega_{\nu_3, \nu_0}$ . These frequencies indicate the presence of higher lying states in the dynamics of the contact. The above-described behavior of  $D(t)/D(0)$  is expected to occur since the contact is related to short-range two-body correlations, and as such its dynamics involves a large number of postquench eigenstates, giving rise to the frequencies observed in Fig. 7(b).

## IV. QUENCH DYNAMICS OF TWO REPULSIVE BOSONS TO ATTRACTIVE INTERACTIONS

As a next step, we shall investigate the interaction quench dynamics of two initially repulsive bosons toward the

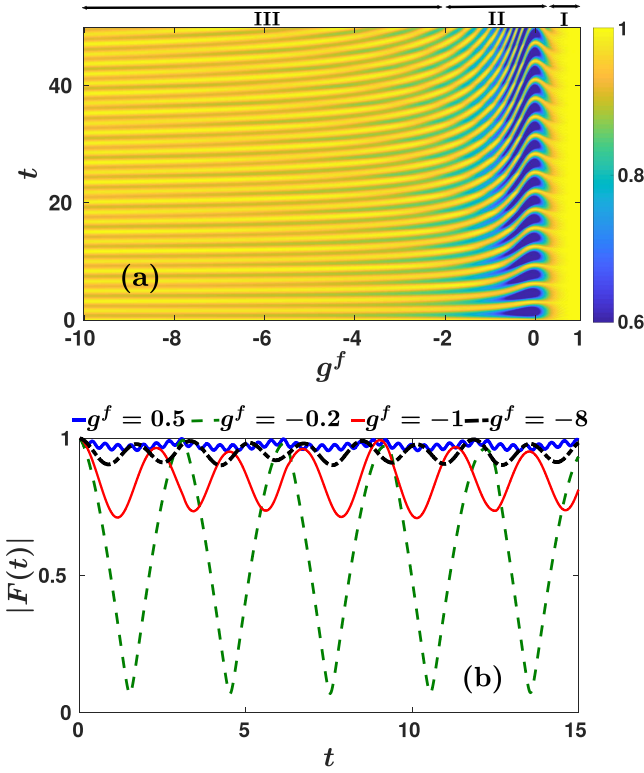


FIG. 8. (a) Fidelity evolution of two bosons after an interaction quench from  $|\Psi_{\nu_1}^{\text{in}}\rangle$  at  $g^{\text{in}} = 1$  to different final interaction strengths  $g^f$ . (b) Time evolution of the fidelity for selected postquench interaction strengths (see legend).

attractive side of interactions. In particular, throughout this section we initialize the system in its ground-state configuration  $|\Psi_{\nu_1}^{\text{in}}\rangle$  at  $g^{\text{in}} = 1$  (unless it is stated otherwise) and perform an interaction quench to the attractive side of the spectrum.

### A. Dynamical response

In order to study the dynamical response of the system, we invoke the fidelity evolution [Eq. (20)] [92] shown in Fig. 8(a) with respect to  $g^f$ . We observe the appearance of three different dynamical regions, in a similar fashion to the response of the reverse-quench scenario discussed in Sec. III A. Within region I,  $0.35 < g^f < 1$ ,  $|F(t)|$  undergoes small-amplitude oscillations [see also Fig. 8(b)] and the system remains close to its initial state. However, in region II, characterized by  $-2.36 < g^f < 0.35$ , the system becomes significantly perturbed since overall  $|F(t)|$  oscillates between unity and zero. For instance, see  $|F(t)|$  in Fig. 8(b) at  $g^f = -0.2$  where, e.g., at  $t \simeq \pi/2, 3\pi/2$   $|F(t)| \simeq 0.07$ . Region III where  $-10 < g^f < -2.36$  incorporates the intermediate and strongly attractive regime of interactions. Here,  $|F(t)|$  oscillates with a small amplitude, while its main difference compared to region I is that the oscillation period is larger. Another interesting feature of  $|F(t)|$  is that as we enter deeper into region III the oscillation amplitude decreases and the corresponding period becomes smaller (see also the discussion below).

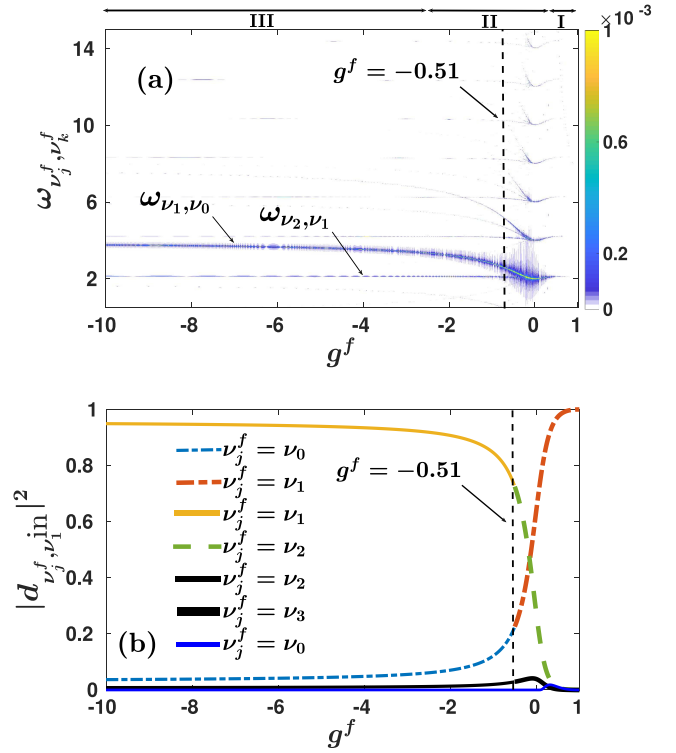


FIG. 9. (a) Frequency spectrum of the fidelity,  $F(\omega)$ , when performing an interaction quench from  $g^{\text{in}} = 1$  to various final interaction strengths. (b) The corresponding most significantly contributing overlap coefficients  $|d_{\nu_j^f, \nu_1^{\text{in}}}^2|$ . The black dashed vertical line at  $g^f = -0.51$  indicates the boundary at which the bound state for negative interactions becomes the ground state for  $g^f > -0.51$ ; see also Fig. 1.

To identify the postquench eigenstates that participate in the nonequilibrium dynamics of the two bosons, we next calculate the fidelity spectrum  $F(\omega)$  [Fig. 9(a)] as well as the most notably populated overlap coefficients  $|d_{\nu_j^f, \nu_1^{\text{in}}}^2|$  [Fig. 9(b)] for a varying postquench interaction strength. In region I, we observe the occurrence of a predominant frequency, namely  $\omega_{\nu_2, \nu_1}$ , in  $F(\omega)$ . This frequency is associated with the notable population of the coefficients  $|d_{\nu_1^f, \nu_1^{\text{in}}}^2|$  and  $|d_{\nu_2^f, \nu_1^{\text{in}}}^2|$  [Fig. 9(b)]. Recall that the amplitude of the frequency peaks appearing in  $F(\omega)$  depends on the participating overlap coefficients, as explicitly displayed in Eq. (24). Entering region II, there is a multitude of contributing frequencies, the most prominent of them being  $\omega_{\nu_2, \nu_1}$ . The appearance of the different frequencies is related to the fact that in this regime  $|d_{\nu_1^f, \nu_1^{\text{in}}}^2|$  drops significantly for more attractive interactions accompanied by the population of other states such as  $|\Psi_{\nu_2}^f\rangle$  and  $|\Psi_{\nu_3}^f\rangle$  [see Fig. 9(b)]. It is important to remember here that at the vertical line  $g^f = -0.51$  [see also Fig. 1] there is a change in the labeling of the eigenstates, resulting in the alteration of the frequencies from  $\omega_{\nu_j, \nu_k}$  to  $\omega_{\nu_{j-1}, \nu_{k-1}}$  when crossing this line toward the attractive regime. In region III, there are essentially two excited frequencies, namely  $\omega_{\nu_1, \nu_0}$  and  $\omega_{\nu_2, \nu_1}$ . The former is the most dominant since here the mainly contributing states are  $|\Psi_{\nu_1}^f\rangle, |\Psi_{\nu_0}^f\rangle$ , as can be seen from

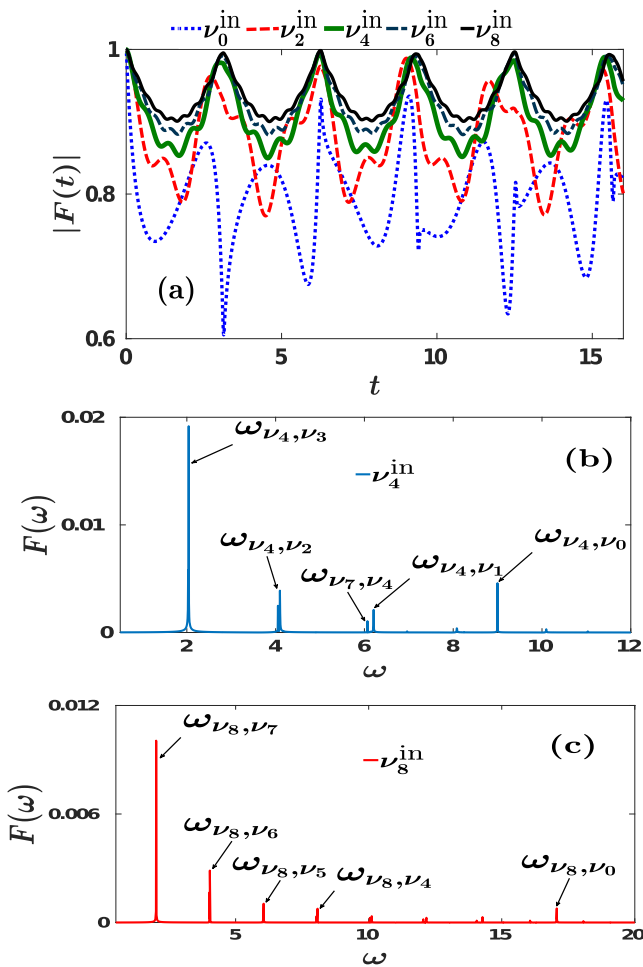


FIG. 10. (a) Fidelity evolution of the two bosons when performing a quench from  $g^{\text{in}} = 1$  to  $g^f = -1$  starting from various excited states (see legend). The fidelity spectrum when the system is initially prepared in (b)  $|\Psi_{\nu_4}^{\text{in}}\rangle$  and (c)  $|\Psi_{\nu_8}^{\text{in}}\rangle$ .

Fig. 9(b). Note also that  $\omega_{\nu_1, \nu_0}$  increases for decreasing  $g^f$ , a behavior that reflects the increasing energy gap in the system's energy spectrum (Fig. 1). On the other hand, the amplitude of  $\omega_{\nu_2, \nu_1}$  is weaker and essentially fades away for strong attractive interactions. This latter behavior can be attributed to the fact that the contribution of the  $|\Psi_{\nu_2}^f\rangle$  state in this region decreases substantially.

### B. Role of the initial state

In order to expose the role of the initial state for the two-boson dynamics, we explore interaction quenches from  $g^{\text{in}} = 1$  toward  $g^f = -1$  but initializing the system in various excited states  $|\Psi_{\nu_k}^{\text{in}}\rangle$ ,  $k > 1$ , or the bound state  $|\Psi_{\nu_0}^{\text{in}}\rangle$ . The emergent dynamical response of the system as captured via  $|F(t)|$  is depicted in Fig. 10(a) starting from the bound state and the first, third, fifth, and seventh excited states. Inspecting the behavior of  $|F(t)|$ , we can infer that the system becomes more perturbed when it is prepared in an energetically lower excited state since the oscillation amplitude of  $|F(t)|$  increases accordingly; compare, for instance,  $|F(t)|$  for  $\nu_2^{\text{in}}$  and  $\nu_6^{\text{in}}$ . Moreover, starting from the bound state, the system is

TABLE II. The most significantly populated overlap coefficients,  $|d_{\nu_j^f, \nu_k^{\text{in}}}^2|$ , for the quench from  $g^{\text{in}} = 1$  to  $g^f = -1$  initializing the system at various initial states. Only the coefficients with a value larger than 0.9% are shown.

	$ d_{\nu_j^f, \nu_0^{\text{in}}}^2 $	$ d_{\nu_j^f, \nu_2^{\text{in}}}^2 $	$ d_{\nu_j^f, \nu_4^{\text{in}}}^2 $	$ d_{\nu_j^f, \nu_6^{\text{in}}}^2 $	$ d_{\nu_j^f, \nu_8^{\text{in}}}^2 $
$\nu_j^f = \nu_0$	0.7896	0.0351	0.0092		
$\nu_j^f = \nu_1$	0.0729	0.0556			
$\nu_j^f = \nu_2$	0.0367	0.8765	0.0092		
$\nu_j^f = \nu_3$	0.0221	0.0198	0.0399		
$\nu_j^f = \nu_4$	0.0147		0.9078		
$\nu_j^f = \nu_5$			0.0175	0.0315	
$\nu_j^f = \nu_6$				0.9248	
$\nu_j^f = \nu_7$				0.0154	0.0262
$\nu_j^f = \nu_8$					0.9357
$\nu_j^f = \nu_9$					0.0138

significantly perturbed compared to the previous cases and  $|F(t)|$  showcases an irregular oscillatory behavior. This pattern is maintained if the quench is performed to other values of  $g^f$  which belong to the attractive regime (not shown here for brevity). Recall that a similar behavior of  $|F(t)|$  occurs for the reverse quench process; see Sec. III B and Fig. 4(a).

The above-mentioned behavior of the fidelity evolution can be understood by employing the corresponding overlap coefficients  $|d_{\nu_j^f, \nu_k^{\text{in}}}^2|$ ; see also Eq. (24). As already discussed in Sec. III B, the fidelity remains close to its initial value in the case where one overlap coefficient dominates the others and deviates significantly from unity when at least two overlap coefficients possess a notable population. The predominantly populated overlap coefficients,  $|d_{\nu_j^f, \nu_k^{\text{in}}}^2|$ , are listed in Table II when starting from different initial eigenstates  $|\Psi_{\nu_k}^{\text{in}}\rangle$ . A close inspection of this table reveals that starting from an energetically higher excited state leads to a lesser amount of contributing overlap coefficients with one among them becoming the dominant one. This behavior explains the decreasing tendency of the oscillation amplitude of  $|F(t)|$  for an initially energetically higher excited state; e.g., compare  $|F(t)|$  of  $|\Psi_{\nu_2}^{\text{in}}\rangle$  and  $|\Psi_{\nu_6}^{\text{in}}\rangle$  in Fig. 10(a). Accordingly, an initially lower (higher) lying excited state results in a larger (smaller) amount of excitations and thus to more (less) contributing frequencies. The latter can be readily seen by resorting to the fidelity spectrum  $F(\omega)$  shown in Figs. 10(b) and 10(c) when starting from  $|\Psi_{\nu_4}^{\text{in}}\rangle$  and  $|\Psi_{\nu_8}^{\text{in}}\rangle$ , respectively.

### C. One-body density evolution

To visualize the nonequilibrium dynamics of the two bosons, we next monitor the time evolution of the one-body density [Eq. (15)] depicted in Figs. 11(a)–11(f) for a quench from  $|\Psi_{\nu_1}^{\text{in}}\rangle$  at  $g^{\text{in}} = 1$  to  $g^f = -0.2$ . Note that the time instants portrayed in Fig. 11 refer to roughly the minima and maxima of the respective fidelity evolution [see Fig. 8(b)]. Overall, the atomic cloud performs a breathing motion during evolution; namely, it expands and contracts in a periodic manner.

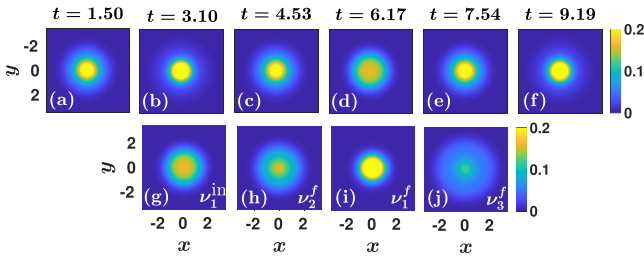


FIG. 11. [(a)–(f)] Snapshots of the one-body density evolution following an interaction quench from  $|\Psi_{v_1}^{\text{in}}\rangle$  at  $g^{\text{in}} = 1$  to  $g^{\text{f}} = -0.2$ . [(g)–(j)] The corresponding one-body densities for different stationary eigenstates (see legend) that possess the largest overlap coefficients.

Moreover, we deduce that when the fidelity is minimized (e.g., at  $t = 1.5, 4.53, 7.54$ ), the one-body density expands [Figs. 11(a), 11(c) and 11(e)], while for the case of a maximum fidelity  $\rho^{(1)}(x, y, t)$  contracts [Figs. 11(b) and 11(f)]. To understand which states are imprinted in  $\rho^{(1)}(x, y, t)$ , we further show in Figs. 11(g)–11(j)  $\rho^{(1)}(x, y, t = 0)$  of the initial state  $|\Psi_{v_1}^{\text{in}}\rangle$  and the three most significantly populated, according to the overlap coefficients  $|d_{v_j^{\text{f}}, v_1^{\text{in}}}|^2$ , final states, i.e.,  $|\Psi_{v_1}^{\text{f}}\rangle$ ,  $|\Psi_{v_2}^{\text{f}}\rangle$ , and  $|\Psi_{v_3}^{\text{f}}\rangle$  [69,70]. Comparing the  $\rho^{(1)}(x, y, t = 0)$  of these stationary states with  $\rho^{(1)}(x, y, t)$ , it becomes evident that during evolution  $\rho^{(1)}(x, y; t)$  is mainly in a superposition of the ground state [Fig. 11(i)] and the first excited state [Fig. 11(h)].

#### D. Evolution of the radial probability density

As a next step, we examine the evolution of the radial probability density  $\mathcal{B}(\rho, t)$  [Eq. (17)] presented in Fig. 12(a) for a quench from  $|\Psi_{v_1}^{\text{in}}\rangle$  and  $g^{\text{in}} = 1$  to  $g^{\text{f}} = -0.2$ . Note that the snapshots of  $\mathcal{B}(\rho, t)$  depicted in Fig. 12(a) correspond again to time instants at which the fidelity evolution exhibits local minima and maxima [see also Fig. 8(b)]. We observe that when  $|F(t)|$  is minimized, e.g., at  $t = 1.50, 4.00, 7.74$ ,  $\mathcal{B}(\rho, t)$  shows a double-peak structure around  $\rho \approx 0.5$  and  $\rho \approx 2$  respectively. However, for times that correspond to a maximum of the fidelity, e.g., at  $t = 3.1, 6.17, \mathcal{B}(\rho, t)$  deforms to a single-peak distribution around  $\rho \approx 1.2$ . To relate this alternating behavior of  $\mathcal{B}(\rho, t)$  with the breathing motion of the two bosons, we can infer that when  $\mathcal{B}(\rho, t)$  possesses a double-peak distribution the cloud expands while in the case of a single-peak structure it contracts; see also Fig. 11. It is also worth mentioning here that for the times at which  $\mathcal{B}(\rho, t)$  exhibits a double-peak structure there is a quite significant probability density tail for  $\rho > 1.5$ . This latter behavior is a signature of the participation of energetically higher lying excited states, as we shall discuss below.

Indeed, the inset of Fig. 12(a) depicts  $\mathcal{B}(\rho)$  of the initial ( $|\Psi_{v_1}^{\text{in}}\rangle$ ) and the postquench ( $|\Psi_{v_1}^{\text{f}}\rangle$  and  $|\Psi_{v_2}^{\text{f}}\rangle$ ) states that have the major contribution for this specific quench in terms of the overlap coefficients [see also Fig. 9(b)]. Comparing  $\mathcal{B}(\rho, t)$  with  $\mathcal{B}(\rho)$ , we can deduce that mainly the ground,  $|\Psi_{v_1}^{\text{f}}\rangle$ , and the first excited,  $|\Psi_{v_2}^{\text{f}}\rangle$ , states of the postquench system are imprinted in the dynamics of the relative density. More specifically,  $|\Psi_{v_2}^{\text{f}}\rangle$  gives rise to the enhanced tail of  $\mathcal{B}(\rho, t)$

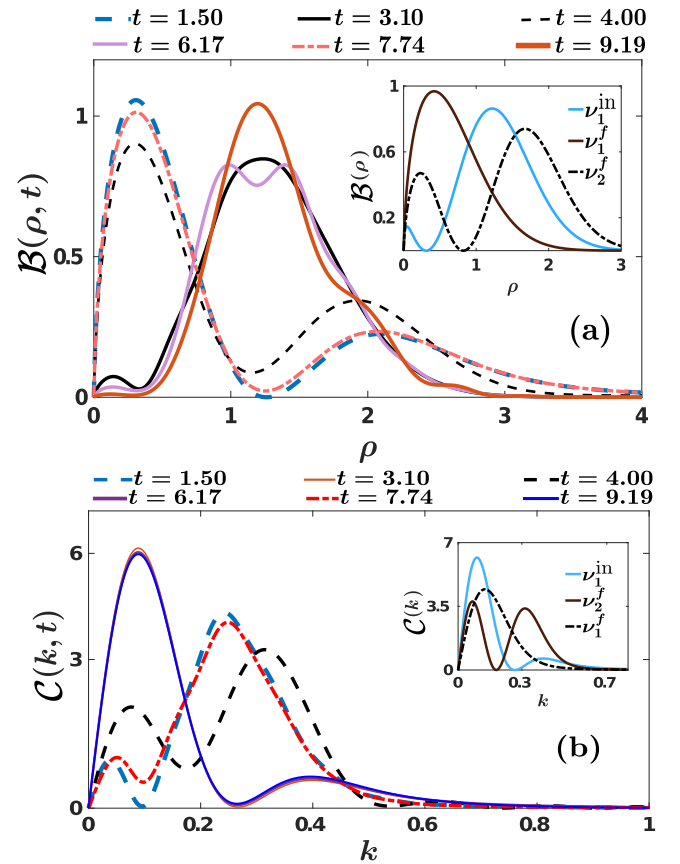


FIG. 12. (a) Temporal evolution of the radial probability density,  $\mathcal{B}(\rho, t)$ , upon considering a quench from  $g^{\text{in}} = 1$  to  $g^{\text{f}} = -0.2$  starting from the ground state,  $|\Psi_{v_1}^{\text{in}}\rangle$ . The inset shows  $\mathcal{B}(\rho)$  of the prequench state  $|\Psi_{v_1}^{\text{in}}\rangle$  and of the postquench eigenstates  $|\Psi_{v_1}^{\text{f}}\rangle$ ,  $|\Psi_{v_2}^{\text{f}}\rangle$  with the most relevant overlap coefficients. (b) The corresponding  $\mathcal{C}(k, t)$  of panel (a). The inset presents  $\mathcal{C}(k)$  of the  $|\Psi_{v_1}^{\text{in}}\rangle$  and of the  $|\Psi_{v_1}^{\text{f}}\rangle$ ,  $|\Psi_{v_2}^{\text{f}}\rangle$ .

[Fig. 12(a)], while the participation of  $|\Psi_{v_1}^{\text{f}}\rangle$  (possessing also the major contribution) leads to the central peak of  $\mathcal{B}(\rho, t)$  close to  $\rho = 0$ .

The radial probability density in momentum space [93],  $\mathcal{C}(k, t)$ , is shown in Fig. 12(b) for selected time instants of the evolution following the quench  $g^{\text{in}} = 1 \rightarrow g^{\text{f}} = -0.2$ . We observe that  $\mathcal{C}(k, t)$  exhibits always a two-peak structure with the location and amplitude of the emergent peaks being changed in the course of the evolution. In particular, when the atomic cloud contracts, e.g., at  $t = 3.10, 9.19$  [see also Figs. 11(b) and 11(f)],  $\mathcal{C}(k, t)$  has a large amplitude peak around  $k \approx 0.1$  and a secondary one of small amplitude close to  $k \approx 0.4$ . However, for an expansion of the two bosons, e.g., at  $t = 1.50$  [Figs. 11(a)], the radial probability density in momentum space shows small- and large-amplitude peaks around  $k \approx 0.05$  and  $k \approx 0.3$ , respectively. Moreover, the momentum distribution during evolution is mainly in a superposition of the ground state  $|\Psi_{v_1}^{\text{f}}\rangle$  and the first excited state  $|\Psi_{v_2}^{\text{f}}\rangle$ ; see, in particular, the inset of Fig. 12(b), which illustrates  $\mathcal{C}(k)$  of these stationary states. As can be readily seen,  $|\Psi_{v_2}^{\text{f}}\rangle$  is responsible for the secondary peak of  $\mathcal{C}(k, t)$  at

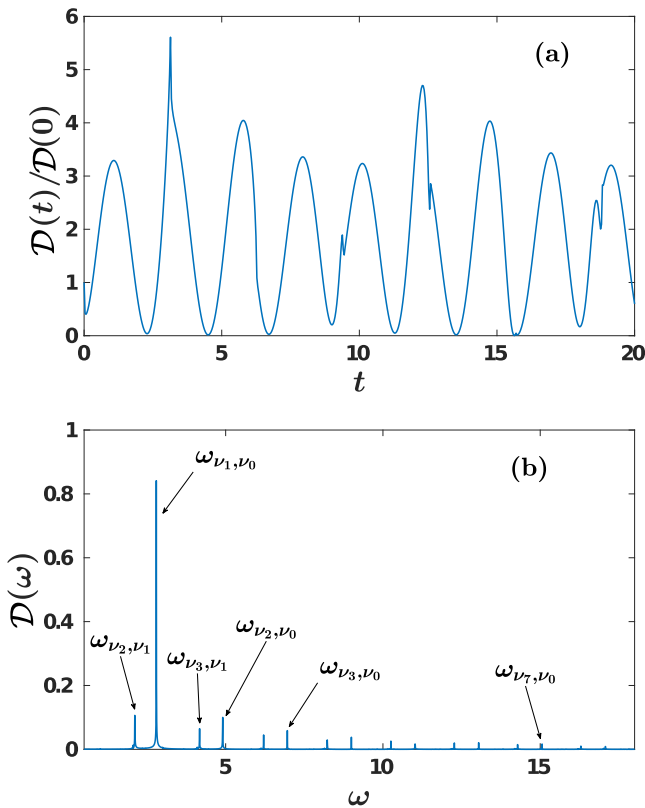


FIG. 13. (a) Time evolution of the rescaled contact  $\mathcal{D}(t)/\mathcal{D}(0)$  following a quench from  $g^{\text{in}} = 1$  to  $g^f = -1$ . (b) The corresponding frequency spectrum.

higher momenta, while the ground-state contributes mainly to the peak close to  $k = 0$ .

### E. Dynamics of the contact

To unravel the emergence of short-range two-body correlations, we next track the time evolution of the rescaled contact  $\mathcal{D}(t)/\mathcal{D}(0)$  after an interaction quench from  $g^{\text{in}} = 1$  to  $g^f = -1$ ; see Fig. 13(a). As can be seen, the rescaled contact exhibits an irregular multifrequency oscillatory pattern in time. It is also worth mentioning that here the involved frequencies in the dynamics of  $\mathcal{D}(t)/\mathcal{D}(0)$  are smaller when compared to the ones excited in the reverse quench scenario; see, in particular, Figs. 13(b) and 7(b). By inspecting the corresponding frequency spectrum presented in Fig. 13(b), we can deduce that the most prominent frequency  $\omega_{\nu_1, \nu_0} \approx 2.5$  corresponds to the energy difference between the bound and ground states. Moreover, this predominant frequency is smaller than the corresponding dominant frequency  $\omega_{\nu_1, \nu_0} \approx 7.5$  occurring at the reverse quench process [Fig. 7(b)]. There is also a variety of other contributing frequencies which signal the participation of higher lying states in the evolution of the contact, such as  $\omega_{\nu_7, \nu_0}$ ,  $\omega_{\nu_2, \nu_1}$ ,  $\omega_{\nu_3, \nu_1}$ , and  $\omega_{\nu_2, \nu_0}$ , exhibiting, however, a much smaller amplitude as compared to  $\omega_{\nu_1, \nu_0}$ . These frequencies are essentially responsible for the observed irregular motion of  $\mathcal{D}(t)/\mathcal{D}(0)$ .

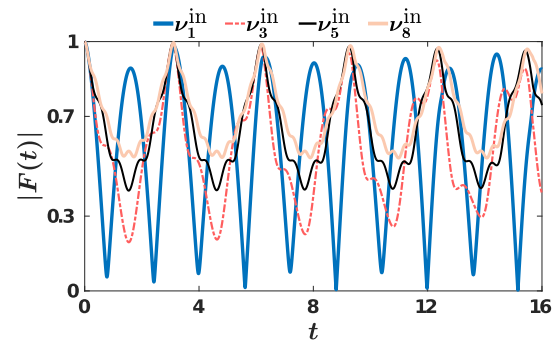


FIG. 14. Fidelity evolution when applying an interaction quench  $g^{\text{in}} = 0 \rightarrow g^f = \infty$ . The system is initialized in different eigenstates (see legend).

### V. QUENCH FROM ZERO TO INFINITE INTERACTIONS

Up to now, we have discussed in detail the interaction quench dynamics of two bosons trapped in a 2D harmonic trap for weak, intermediate, and strong couplings in both the attractive and the repulsive regime. Next, we aim at briefly analyzing the corresponding interaction quench dynamics from  $g^{\text{in}} = 0$  to  $g^f = \infty$ . We remark here that when the system is initialized at  $g^{\text{in}} = 0$  the formula of Eq. (14) is no longer valid and the overlap coefficients between the eigenstates  $|\Psi_{\nu_i}^{\text{in}}\rangle$  and  $|\Psi_{\nu_j}^f\rangle$  are given by

$$\begin{aligned} d_{\nu_j^f, \nu_i^{\text{in}}} &= \frac{2\Gamma(-\nu_j^f)}{\sqrt{\psi^{(1)}(-\nu_j^f)}} \int_0^\infty dr r e^{-r^2} U(-\nu_j^f, 1, r^2) L_{\nu_i^{\text{in}}}(r^2) \\ &= \frac{1}{(\nu_i^{\text{in}} - \nu_j^f) \sqrt{\psi^{(1)}(-\nu_j^f)}}. \end{aligned} \quad (25)$$

The dynamical response of the system after such a quench [ $g^{\text{in}} = 0 \rightarrow g^f = \infty$ ] as captured by the fidelity evolution [Eq. (20)] is illustrated in Fig. 14 when considering different initial states  $|\Psi_{\nu_k}^{\text{in}}\rangle$ . Evidently, when the system is initialized in its ground state  $|\Psi_{\nu_1}^{\text{in}}\rangle$ ,  $|F(t)|$  performs large amplitude oscillations. The latter implies that the time-evolved wave function becomes almost orthogonal to the initial one at certain time intervals and as a consequence the system is significantly perturbed. Also, it can directly be deduced by the fidelity evolution that when the system is prepared in an energetically higher excited state it is less perturbed since the oscillation amplitude of  $|F(t)|$  is smaller; e.g., compare  $|F(t)|$  for  $|\Psi_{\nu_1}^{\text{in}}\rangle$  and  $|\Psi_{\nu_5}^{\text{in}}\rangle$ . This tendency, which has already been discussed in Secs. III B and IV B, can be explained in terms of the distribution of the amplitude of the overlap coefficients; see also Eq. (24). Indeed, if there is a single dominant overlap coefficient, then  $|F(t)| \approx 1$ , while if more than one overlap coefficients possess large values  $|F(t)|$  deviates appreciably from unity. Here, for instance, the first two most dominant overlap coefficients when starting from  $|\Psi_{\nu_1}^{\text{in}}\rangle$  and  $|\Psi_{\nu_5}^{\text{in}}\rangle$  are  $|d_{\nu_0^f, \nu_1^{\text{in}}}^2| = 0.4837$ ,  $|d_{\nu_1^f, \nu_1^{\text{in}}}^2| = 0.4402$  and  $|d_{\nu_4^f, \nu_5^{\text{in}}}^2| = 0.6453$ ,  $|d_{\nu_5^f, \nu_5^{\text{in}}}^2| = 0.1894$ , respectively.

To further unravel the motion of the two bosons, we next employ the time evolution of their radial probability

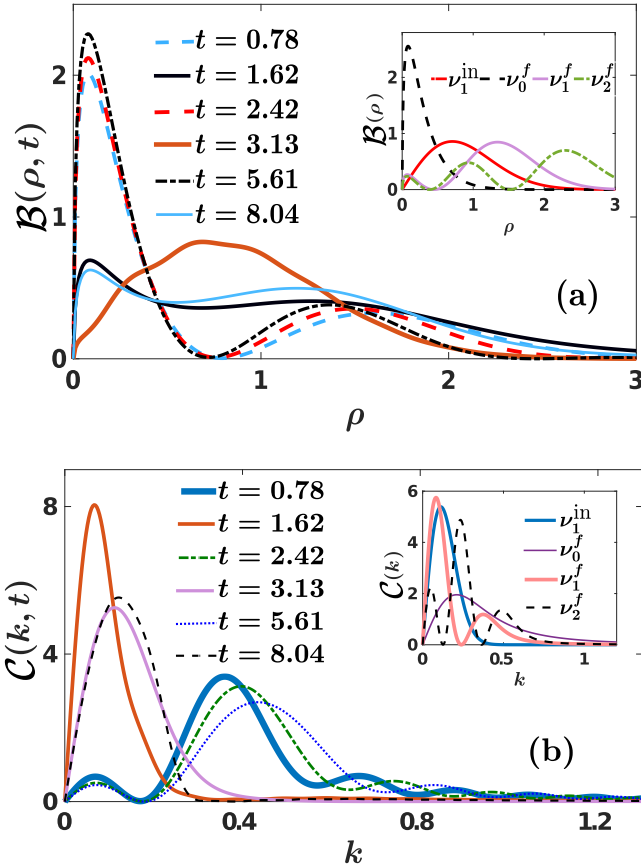


FIG. 15. (a) Radial probability,  $\mathcal{B}(\rho, t)$ , at specific time instants of the evolution following an interaction quench  $g^{\text{in}} = 0 \rightarrow g^f = \infty$ . The system is prepared in its ground state  $|\Psi_{\nu_1}^{\text{in}}\rangle$ . The inset illustrates  $\mathcal{B}(\rho)$  of the initial state  $|\Psi_{\nu_1}^{\text{in}}\rangle$  and some of the postquench eigenstates  $|\Psi_{\nu_0}^f\rangle$ ,  $|\Psi_{\nu_1}^f\rangle$ , and  $|\Psi_{\nu_2}^f\rangle$ . (b) Time evolution of the corresponding radial probability density in momentum space,  $\mathcal{C}(k, t)$ . The inset shows  $\mathcal{C}(k)$  of the initial state  $|\Psi_{\nu_1}^{\text{in}}\rangle$  and of certain postquench eigenstates, namely  $|\Psi_{\nu_0}^f\rangle$ ,  $|\Psi_{\nu_1}^f\rangle$ , and  $|\Psi_{\nu_2}^f\rangle$ .

density,  $\mathcal{B}(\rho, t)$ , in real space [see also Eq. (17)]. Figure 15(a) shows snapshots of  $\mathcal{B}(\rho, t)$  after an interaction quench from  $|\Psi_{\nu_1}^{\text{in}}\rangle$  at  $g^{\text{in}} = 0$  to  $g^f = \infty$ . As can be seen for the time intervals where  $|F(t)|$  is minimized (Fig. 14), e.g., at  $t = 0.78, 2.42, 5.61$ ,  $\mathcal{B}(\rho, t)$  exhibits a pronounced peak close to  $\rho = 0$  and a secondary one at a larger radii,  $\rho \approx 1.5$ . However, when  $|F(t)| \approx 1$  ( $t = 1.62, 3.13, 8.04$ ),  $\mathcal{B}(\rho, t)$  shows a more delocalized distribution. To explain this behavior of  $\mathcal{B}(\rho, t)$ , we next calculate  $\mathcal{B}(\rho)$  of the initial state (i.e.,  $|\Psi_{\nu_1}^{\text{in}}\rangle$ ) and of the postquench eigenstates that possess the most dominant overlap coefficients, namely  $|\Psi_{\nu_0}^f\rangle$ ,  $|\Psi_{\nu_1}^f\rangle$ , and  $|\Psi_{\nu_2}^f\rangle$ , following the above-described quench scenario [see the inset of Fig. 15(a)]. Comparing  $\mathcal{B}(\rho, t)$  with  $\mathcal{B}(\rho)$ , we observe that the bound state,  $|\Psi_{\nu_0}^f\rangle$ , gives rise to the prominent peak close to  $\rho = 0$  [see Fig. 15(a)]. Moreover, the states  $|\Psi_{\nu_1}^f\rangle$  and  $|\Psi_{\nu_2}^f\rangle$  are responsible for the emergent spatial delocalization of  $\mathcal{B}(\rho, t)$ . Of course, the ground state ( $|\Psi_{\nu_1}^{\text{in}}\rangle$ ) plays a more important role here than the first excited state ( $|\Psi_{\nu_2}^f\rangle$ ), since  $|d_{\nu_1^f, \nu_1^{\text{in}}}^f|^2 = 0.4402$  and  $|d_{\nu_2^f, \nu_1^{\text{in}}}^f|^2 = 0.0406$ , respectively [see the inset of Fig. 15(a)].

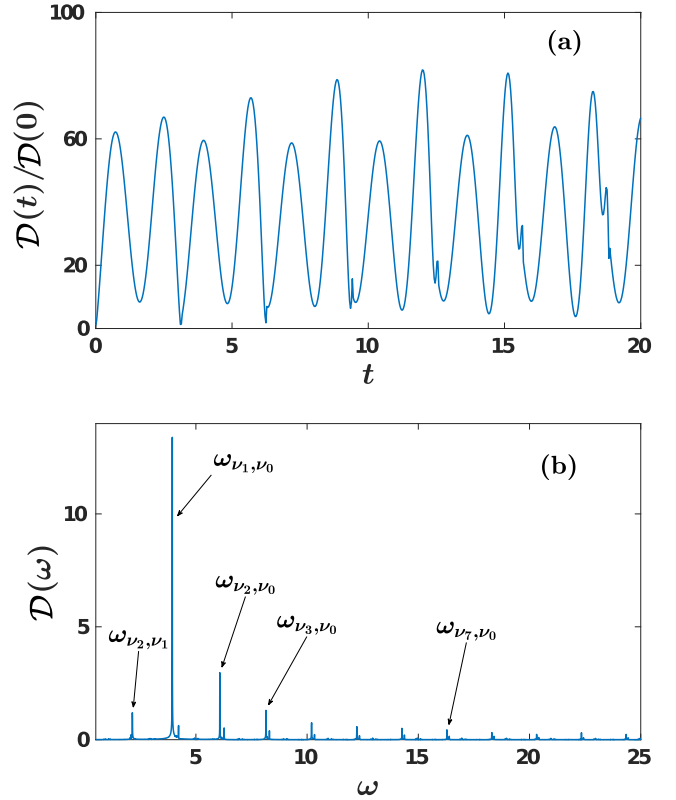


FIG. 16. (a) Time evolution of the rescaled contact  $\mathcal{D}(t)/\mathcal{D}(0)$  for the interaction quench from  $g^{\text{in}} = 0.2$  to  $g^f = \infty$ . (b) The respective frequency spectrum  $\mathcal{D}(\omega)$ .

Turning to the dynamics in momentum space, Fig. 15(b) presents  $\mathcal{C}(k, t)$  at specific time instants for the quench  $g^{\text{in}} = 0 \rightarrow g^f = \infty$  starting from the ground state  $|\Psi_{\nu_1}^{\text{in}}\rangle$ . We observe that when the system deviates notably from its initial state (i.e.,  $t = 0.78, 2.42, 5.61$ ), meaning also that  $|F(t)| \ll 1$ , then  $\mathcal{C}(k, t)$  shows a two-peak structure with the first peak located close to  $k = 0$  and the second one at  $k \approx 0.4$ . Notice also here that the tail of  $\mathcal{C}(k, t)$  has an oscillatory behavior. On the other hand, if  $|F(t)|$  is close to unity (e.g., at  $t = 1.62, 3.13, 8.04$ ) where also  $\mathcal{B}(\rho, t)$  is spread out [Fig. 15(a)], the corresponding  $\mathcal{C}(k, t)$  has a narrow momentum peak close to zero and a quickly decaying tail at large  $k$ .

The inset of Fig. 15(b) illustrates  $\mathcal{C}(k)$  of the initial eigenstate and some specific postquench ones which possess the largest contributions for the considered quench according to the overlap coefficients. It becomes evident that both the bound state,  $|\Psi_{\nu_0}^f\rangle$ , and the ground state,  $|\Psi_{\nu_1}^f\rangle$ , of the postquench system are mainly imprinted in  $\mathcal{C}(k, t)$ . Indeed, the bound state has a broad momentum distribution, whereas the ground state possesses a main peak close to  $k = 0$ . On the other hand, the first excited state ( $|\Psi_{\nu_2}^f\rangle$ ) has a smaller contribution compared to the previous ones and its presence can be discerned in Fig. 15(b) from the oscillatory tails of  $\mathcal{C}(k, t)$  at large momenta.

Finally, we examine the dynamics of the rescaled contact  $\mathcal{D}(t)/\mathcal{D}(0)$  illustrated in Fig. 16(a) following a quench from  $g^{\text{in}} = 0.2$  to  $g^f = \infty$ . Note here that we choose  $g^{\text{in}} = 0.2$  and not exactly  $g^{\text{in}} = 0$ , since the contact is well defined only for



interacting eigenstates [88]. Evidently,  $\mathcal{D}(t)/\mathcal{D}(0)$  undergoes a large amplitude multifrequency oscillatory motion. The large amplitude of these oscillations stems from the fact that the system is quenched to unitarity and therefore the buildup of short-range two-body correlations is substantial, especially when compared to the correlations occurring for finite interactions as, e.g., the ones displayed in Figs. 7(a) and 13(a). We remark that similar large-amplitude oscillations of the contact, at the frequency of the two-body bound state, have already been observed in Ref. [95] during the interaction quench dynamics of a three-dimensional homogeneous BEC from zero to very large interactions. Regarding the participating frequencies identified in the spectrum of the contact shown in Fig. 16(b), we can clearly infer that the dominant frequencies refer to the energy differences between the bound state,  $|\Psi_{v_0}\rangle$ , and higher lying states, e.g.,  $\omega_{v_1, v_0}$ ,  $\omega_{v_2, v_0}$ . The existence of other contributing frequencies in the spectrum, such as  $\omega_{v_2, v_1}$  and  $\omega_{v_3, v_0}$ , has also an impact on the dynamics of the contact and signals the involvement of higher lying states.

## VI. CONCLUSIONS

We have explored the quantum dynamics of two bosons trapped in an isotropic two-dimensional harmonic trap and interacting via a contact  $s$ -wave pseudopotential. As a first step, we have presented the analytical solution of the interacting two-body wave function for an arbitrary stationary eigenstate. We also briefly discuss the corresponding two-body energy eigenspectrum covering both the attractive and repulsive interaction regimes, showcasing the importance of the existing bound state.

To trigger the dynamics, we consider an interaction quench from repulsive to attractive interactions and vice versa as well as a quench from zero to infinite interactions. With knowledge of the stationary properties of the system, the form of the time-evolving two-body wave function is provided. Most importantly, we showcase that the expansion coefficients can be derived in a closed form and therefore the dynamics of the two-body wave function can be obtained by numerically determining its expansion with respect to the eigenstates of the postquench system. In all cases, the dynamical response of the system has been analyzed in detail and the underlying eigenstate transitions that mainly contribute to the dynamics have been identified in the fidelity spectrum together with the system's eigenspectrum.

We have shown that after initializing the system in its ground state, characterized by either repulsive or attractive interactions, it is driven more efficiently out of equilibrium, as captured by the fidelity evolution, when performing an interaction quench toward the vicinity of zero interactions. However, if we follow a quench toward the intermediate or strong coupling regimes of either sign, then the system remains close to its initial state. As a consequence of the interaction quench, the two bosons undergo a breathing motion which has been visualized by monitoring the temporal evolution of the single-particle density and the radial probability density, in both real and momentum space. The characteristic structures building upon the above-mentioned quantities enable us also to infer the participation of energetically higher lying excited states of the postquench system.

To inspect the dependence of the system's dynamical response, we have examined also quenches for a variety of different initial states such as the bound state or an energetically higher excited state in both the repulsive and attractive interaction regimes. It has been found that when starting from energetically higher excited states, the system is perturbed to a lesser extent and fewer postquench eigenstates contribute in the emergent dynamics. A crucial role here is played by the bound state of the postquench system, both in the attractive and repulsive regimes, whose contribution is essentially diminished as we initialize the two bosons at higher excited states. On the other hand, when the quench is performed from the bound state, independent of the interaction strength, the system is driven out of equilibrium in the most efficient manner of any initial state configuration.

Additionally, upon quenching the system from zero to infinite interactions starting from its ground state, the time-evolved wave function becomes even orthogonal to the initial one at certain time intervals. Again here, if the two bosons are prepared in an energetically higher excited state then the system becomes more unperturbed. Inspecting the evolution of the radial probability density, we have identified that it mainly resides in a superposition of the bound and ground states alternating from a two peaked structure to a more spread distribution.

To unveil the emergence of short-range two-body correlations, we have examined the dynamics of the Tan's contact in all of the above-mentioned quench scenarios. In particular, we have found that the contact performs a multifrequency oscillatory motion in time. The predominant frequency of these oscillations refers to the energy difference between the bound and ground states. The participation of other frequencies possessing a comparable smaller amplitude signals the contribution of higher lying states in the dynamics of the contact. Moreover, upon quenching the system from weak to infinite interactions, the oscillation amplitude of the contact is substantially enhanced, indicating the significant development of short-range two-body correlations as compared to the correlations occurring at finite postquench interactions.

There is a variety of fruitful directions to follow in future works. An interesting one would be to consider two bosons confined in an anisotropic two-dimensional harmonic trap and examine the stationary properties of this system in the dimensional crossover from two to one dimensions. Having at hand such an analytical solution would allow us to study the corresponding dynamics of the system upon changing its dimensionality, e.g., by considering a quench of the trap frequency in one of the spatial directions which enable us to excite higher than the monopole mode. Also one could utilize the spectra with respect to the different anisotropy in order to achieve controllable state transfer processes [61,62]. Besides the dimensionality crossover, it would be interesting to study the effect of the presence of the temperature in the interaction quench dynamics examined herein. Finally, the dynamics of three two-dimensional trapped bosons requires further investigation. Even though the Efimov effect is absent in that case [96], the energy spectrum is rich, possessing dimer and trimer states [33], and the corresponding dynamics might reveal intriguing dynamical features when quenching from one to another configuration.

## ACKNOWLEDGMENTS

G.B. kindly acknowledges financial support by the State Graduate Funding Program Scholarships (HmbNFG). S.I.M. and P.S. gratefully acknowledge financial support by the

Deutsche Forschungsgemeinschaft (DFG 170620586) in the framework of the SFB 925 “Light-induced dynamics and control of correlated quantum systems.” The authors thank G. M. Koutentakis for fruitful discussions.

- [1] M. Lewenstein, A. Sanpera, V. Ahunfiger, B. Damski, A. Sen, and U. Sen, *Adv. Phys.* **56**, 243 (2007).
- [2] S. Inouye, M. R. Andrews, J. Stenger, H. J. Miesner, D. M. Stamper-Kurn, and W. Ketterle, *Nature (London)* **392**, 151 (1998).
- [3] C. Chin, R. Grimm, P. Julienne, and E. Tiesinga, *Rev. Mod. Phys.* **82**, 1225 (2010).
- [4] A. Görlitz, J. M. Vogels, A. E. Leanhardt, C. Raman, T. L. Gustavson, J. R. Abo-Shaer, A. P. Chikkatur, S. Gupta, S. Inouye, T. Rosenband, and W. Ketterle, *Phys. Rev. Lett.* **87**, 130402 (2001).
- [5] D. S. Petrov, D. M. Gangardt, and G. V. Shlyapnikov, *J. Phys. IV (France)* **116**, 5 (2004).
- [6] A. N. Wenz, G. Zürn, S. Murmann, I. Brouzos, T. Lompe, and S. Jochim, *Science* **342**, 457 (2013).
- [7] F. Serwane, G. Zürn, T. Lompe, T. B. Ottenstein, A. N. Wenz, and S. Jochim, *Science* **332**, 336 (2011).
- [8] D. Blume, *Rep. Prog. Phys.* **75**, 046401 (2012).
- [9] T. Sowiński and M. Á. García-March, *Rep. Prog. Phys.* **82**, 104401 (2019).
- [10] C. H. Greene, P. Giannakeas, and J. Pérez-Ríos, *Rev. Mod. Phys.* **89**, 035006 (2017).
- [11] Z. Hadzibabic and J. Dalibard, *Rivista del Nuovo Cimento* **34**, 389 (2011).
- [12] I. Bloch, J. Dalibard, and W. Zwerger, *Rev. Mod. Phys.* **80**, 885 (2008).
- [13] Z. Hadzibabic, P. Krüger, M. Cheneau, B. Battelier, and J. Dalibard, *Nature (London)* **441**, 1118 (2006).
- [14] M. A. Cirone, K. Rzażewski, W. P. Schleich, F. Straub, and J. A. Wheeler, *Phys. Rev. A* **65**, 022101 (2001).
- [15] D. S. Petrov and G. V. Shlyapnikov, *Phys. Rev. A* **64**, 012706 (2001).
- [16] L. Pricoupenko and M. Olshani, *J. Phys. B: At. Mol. Opt. Phys.* **40**, 2065 (2007).
- [17] J. M. Kosterlitz and D. J. Thouless, *J. Phys. C: Solid State Phys.* **6**, 1181 (1973).
- [18] K. Huang and C. N. Yang, *Phys. Rev.* **105**, 767 (1957).
- [19] C. Cohen-Tannoudji, *Advances in Atomic Physics: An Overview* (World Scientific, Singapore, 2011).
- [20] T. Busch, B. G. Englert, K. Rzażewski, and M. Wilkens, *Found. Phys.* **28**, 549 (1997).
- [21] A. Farrell and B. Zyl, *J. Phys. A: Math. Theor.* **43**, 015302 (2009).
- [22] P. Shea, B. Zyl, and R. Bhaduri, *Am. J. Phys.* **77**, 511 (2009).
- [23] M. Combescure, C. Fayard, A. Khare, and J.-M. Richard, *J. Phys. A: Math. Theor.* **44**, 275302 (2011).
- [24] Z. Idziaszek and T. Calarco, *Phys. Rev. A* **74**, 022712 (2006).
- [25] R. Stock, A. Silberfarb, E. L. Bolda, and I. H. Deutsch, *Phys. Rev. Lett.* **94**, 023202 (2005).
- [26] N. T. Zinner, *J. Phys. A: Math. Theor.* **45**, 205302 (2012).
- [27] P. Kościuk and T. Sowiński, *Sci. Rep.* **9**, 12018 (2019).
- [28] D. Saraidaris, I. Mitrakos, I. Brouzos, and F. Diakonou, [arXiv:1903.08499](https://arxiv.org/abs/1903.08499).
- [29] N. L. Harshman, *Phys. Rev. A* **86**, 052122 (2012).
- [30] M. A. García-March, B. Juliá-Díaz, G. E. Astrakharchik, J. Boronat, and A. Polls, *Phys. Rev. A* **90**, 063605 (2014).
- [31] A. S. Dehkharghani, [arXiv:1801.04993](https://arxiv.org/abs/1801.04993).
- [32] S. Jonsell, H. Heiselberg, and C. J. Pethick, *Phys. Rev. Lett.* **89**, 250401 (2002).
- [33] X.-J. Liu, H. Hu, and P. D. Drummond, *Phys. Rev. B* **82**, 054524 (2010).
- [34] J. Portegies and S. Kokkelmans, *Few-Body Systems* **51**, 219 (2011).
- [35] T. Langen, R. Geiger, and J. Schmiedmayer, *Annu. Rev. Condens. Matter Phys.* **6**, 201 (2015).
- [36] F. Chevy, V. Bretin, P. Rosenbusch, K. W. Madison, and J. Dalibard, *Phys. Rev. Lett.* **88**, 250402 (2002).
- [37] K. Merloti, R. Dubessy, L. Longchambon, A. Perrin, P.-E. Pottie, V. Lorent, and H. Perrin, *New J. Phys.* **15**, 033007 (2013).
- [38] L. P. Pitaevskii, *Phys. Lett. A* **221**, 14 (1996).
- [39] L. P. Pitaevskii and A. Rosch, *Phys. Rev. A* **55**, R853(R) (1997).
- [40] M. Holten, L. Bayha, A. C. Klein, P. A. Murthy, P. M. Preiss, and S. Jochim, *Phys. Rev. Lett.* **121**, 120401 (2018).
- [41] T. Pepler, P. Dyke, M. Zamorano, I. Herrera, S. Hoinka, and C. J. Vale, *Phys. Rev. Lett.* **121**, 120402 (2018).
- [42] C. Hung, V. Gurarie, and C. Chin, *Science* **341**, 1213 (2013).
- [43] V. Gritsev, P. Barmettler, and E. Demler, *New J. Phys.* **12**, 113005 (2010).
- [44] Q. Guan, V. Klinkhamer, R. Klemt, J. H. Becher, A. Bergschneider, P. M. Preiss, S. Jochim, and D. Blume, *Phys. Rev. Lett.* **122**, 083401 (2019).
- [45] L. Budewig, S. I. Mistakidis, and P. Schmelcher, *Mol. Phys.* **117**, 2043 (2019).
- [46] M. Á. García March, T. Fogarty, S. Campbell, T. Busch, and M. Paternostro, *New J. Phys.* **18**, 103035 (2016).
- [47] L. M. A. Kehrberger, V. J. Bolsinger, and P. Schmelcher, *Phys. Rev. A* **97**, 013606 (2018).
- [48] J. P. Corson and J. L. Bohn, *Phys. Rev. A* **94**, 023604 (2016).
- [49] A. G. Sykes, J. P. Corson, J. P. D’Incao, A. P. Koller, C. H. Greene, A. M. Rey, K. R. A. Hazzard, and J. L. Bohn, *Phys. Rev. A* **89**, 021601(R) (2014).
- [50] L. Tonks, *Phys. Rev.* **50**, 955 (1936).
- [51] M. Girardeau, *J. Math. Phys.* **1**, 516 (1960).
- [52] I. Romanovsky, C. Yannouleas, and U. Landman, *Phys. Rev. Lett.* **93**, 230405 (2004).
- [53] P. Mujal, A. Polls, and B. Juliá-Díaz, *Condens. Matter* **3**, 9 (2018).
- [54] P. Mujal, E. Sarlé, A. Polls, and B. Juliá-Díaz, *Phys. Rev. A* **96**, 043614 (2017).
- [55] M. Valiente, *Phys. Rev. A* **100**, 013614 (2019).
- [56] Y. Nishida, *Phys. Rev. A* **97**, 061603(R) (2018).
- [57] L. Pricoupenko, *Phys. Rev. A* **97**, 061604(R) (2018).

- [58] G. Guijarro, A. Pricoupenko, G. E. Astrakharchik, J. Boronat, and D. S. Petrov, *Phys. Rev. A* **97**, 061605(R) (2018).
- [59] Y. Sekino and Y. Nishida, *Phys. Rev. A* **97**, 011602(R) (2018).
- [60] M. Valiente and V. Pastukhov, *Phys. Rev. A* **99**, 053607 (2019).
- [61] T. Fogarty, L. Ruks, J. Li, and T. Busch, *SciPost Phys.* **6**, 021 (2019).
- [62] I. Reshodko, A. Benseny, and T. Busch, *Phys. Rev. A* **96**, 023606 (2017).
- [63] S. I. Mistakidis and P. Schmelcher, *Phys. Rev. A* **95**, 013625 (2017).
- [64] S. I. Mistakidis, L. Cao, and P. Schmelcher, *J. Phys. B: At. Mol. Opt. Phys.* **47**, 225303 (2014).
- [65] T. Plaßmann, S. I. Mistakidis, and P. Schmelcher, *J. Phys. B: At. Mol. Opt. Phys.* **51**, 225001 (2018).
- [66] T. Sowiński, M. Brewczyk, M. Gajda, and K. Rzażewski, *Phys. Rev. A* **82**, 053631 (2010).
- [67] G. C. Katsimiga, S. I. Mistakidis, G. M. Koutentakis, P. G. Kevrekidis, and P. Schmelcher, *Phys. Rev. A* **98**, 013632 (2018).
- [68] P. Siegl, S. I. Mistakidis, and P. Schmelcher, *Phys. Rev. A* **97**, 053626 (2018).
- [69] G. C. Katsimiga, G. M. Koutentakis, S. I. Mistakidis, P. G. Kevrekidis, and P. Schmelcher, *New J. Phys.* **19**, 073004 (2017).
- [70] G. C. Katsimiga, S. I. Mistakidis, G. M. Koutentakis, P. G. Kevrekidis, and P. Schmelcher, *New J. Phys.* **19**, 123012 (2017).
- [71] M. Olshanii and L. Pricoupenko, *Phys. Rev. Lett.* **88**, 010402 (2001).
- [72] J. J. Sakurai, *Advanced Quantum Mechanics* (Pearson Education, New Delhi, 2013).
- [73] M. Abramowitz, and I. A. Stegun, *Handbook of Mathematical Functions with Formulas, Graphs, and Mathematical Tables*, Applied Mathematics Series Vol. 55 (National Bureau of Standards, Washington, DC, 1964).
- [74] R. A. Doganov, S. Klaiman, O. E. Alon, A. I. Streltsov, and L. S. Cederbaum, *Phys. Rev. A* **87**, 033631 (2013).
- [75] We remark that a different definition of the 2D interparticle interaction strength has been used, e.g., in Ref. [33], having the form  $g \sim 1/a$ . The latter possesses a bijective mapping to our choice of  $g$ .
- [76] A. Galea, T. Zielinski, S. Gandolfi, and A. Gezerlis, *J. Low Temp. Phys.* **189**, 451 (2017).
- [77] I. S. Gradshteyn and I. M. Ryzhik, *Table of Integrals, Series, and Products* (Academic Press, New York, 2014).
- [78] K. Sakmann, A. I. Streltsov, O. E. Alon, and L. S. Cederbaum, *Phys. Rev. A* **78**, 023615 (2008).
- [79] T. Gorin, T. Prosen, T. H. Seligman, and M. Žnidarič, *Phys. Rep.* **435**, 33 (2006).
- [80] S. I. Mistakidis, L. Cao, and P. Schmelcher, *Phys. Rev. A* **91**, 033611 (2015).
- [81] J. Neuhaus-Steinmetz, S. I. Mistakidis, and P. Schmelcher, *Phys. Rev. A* **95**, 053610 (2017).
- [82] S. I. Mistakidis, G. M. Koutentakis, and P. Schmelcher, *Chem. Phys.* **509**, 106 (2018).
- [83] F. F. Bellotti, T. Frederico, M. T. Yamashita, D. V. Fedorov, A. S. Jensen, and N. T. Zinner, *Phys. Rev. A* **87**, 013610 (2013).
- [84] M. Valiente, N. T. Zinner, and K. Mølmer, *Phys. Rev. A* **84**, 063626 (2011).
- [85] F. Werner and Y. Castin, *Phys. Rev. A* **86**, 053633 (2012).
- [86] J. T. Stewart, J. P. Gaebler, T. E. Drake, and D. S. Jin, *Phys. Rev. Lett.* **104**, 235301 (2010).
- [87] R. J. Wild, P. Makotyn, J. M. Pino, E. A. Cornell, and D. S. Jin, *Phys. Rev. Lett.* **108**, 145305 (2012).
- [88] S. Tan, *Ann. Phys.* **323**, 2952 (2008).
- [89] S. Tan, *Ann. Phys.* **323**, 2971 (2008).
- [90] S. Tan, *Ann. Phys.* **323**, 2987 (2008).
- [91] V. E. Colussi, J. P. Corson, and J. P. D’Incao, *Phys. Rev. Lett.* **120**, 100401 (2018).
- [92] T. Keller and T. Fogarty, *Phys. Rev. A* **94**, 063620 (2016).
- [93] P. A. Murthy, N. Defenu, L. Bayha, M. Holten, P. M. Preiss, T. Enss, and S. Jochim, *Science* **365**, 268 (2019).
- [94] F. Werner and Y. Castin, *Phys. Rev. A* **86**, 013626 (2012).
- [95] J. P. Corson and J. L. Bohn, *Phys. Rev. A* **91**, 013616 (2015).
- [96] E. Nielsen, D. V. Fedorov, A. S. Jensen, and E. Garrido, *Phys. Rep.* **347**, 373 (2001).

### **4.1.2 Stationary and dynamical properties of two harmonically trapped bosons in the crossover from two dimensions to one**

## Stationary and dynamical properties of two harmonically trapped bosons in the crossover from two dimensions to one

G. Bougas,<sup>1</sup> S. I. Mistakidis<sup>1</sup>, G. M. Alshalan,<sup>2</sup> and P. Schmelcher<sup>1,3</sup>

<sup>1</sup>*Center for Optical Quantum Technologies, Department of Physics, University of Hamburg, Luruper Chaussee 149, 22761 Hamburg, Germany*

<sup>2</sup>*Department of Physics and Research Laboratory of Electronics, Massachusetts Institute of Technology, Cambridge, Massachusetts 02139, USA*

<sup>3</sup>*The Hamburg Centre for Ultrafast Imaging, Universität Hamburg Luruper Chaussee 149, 22761 Hamburg, Germany*



(Received 29 January 2020; revised 6 June 2020; accepted 8 June 2020; published 15 July 2020)

We unravel the stationary properties and the interaction quench dynamics of two bosons, confined in a two-dimensional anisotropic harmonic trap. A transcendental equation is derived giving access to the energy spectrum and revealing the dependence of the energy gaps on the anisotropy parameter. The relation between the two- and one-dimensional scattering lengths as well as the Tan contacts is established. The contact, capturing the two-body short-range correlations, shows an increasing tendency for a larger anisotropy. Subsequently, the interaction quench dynamics from attractive to repulsive values and vice versa is investigated for various anisotropies. A closed analytical form of the expansion coefficients of the two-body wave function, during the time evolution is constructed. The response of the system is studied by means of the time-averaged fidelity, the spectra of the spatial extent of the cloud in each direction, and the one-body density. It is found that as the anisotropy increases, the system becomes less perturbed independently of the interactions, while for fixed anisotropy quenches toward the noninteracting regime perturb the system in the most efficient manner. Furthermore, we identify that in the tightly confined direction more frequencies are involved in the dynamics stemming from higher lying excited states.

DOI: [10.1103/PhysRevA.102.013314](https://doi.org/10.1103/PhysRevA.102.013314)

### I. INTRODUCTION

Ultracold gases offer a highly controllable platform for studying quantum few- and many-body systems due to their extraordinary tunability [1,2]. Feshbach resonances play a pivotal role, since the interparticle interaction strength can be arbitrarily adjusted by means of magnetic and optical fields [3,4]. Moreover, advances in atom trapping enable us to realize systems of different dimensionality [5–8] and particle number, thus rendering few-body ensembles which exhibit remarkable properties, such as the Efimov effect, experimentally tractable [2,9–13].

Utilizing anisotropic harmonic traps allows us to reach the quasi-two-dimensional (quasi-2D) and quasi-one-dimensional (quasi-1D) regimes by manipulating the axial ( $\omega_z$ ) or the radial frequency ( $\omega_r$ ), such that  $\hbar\omega_z$  ( $\hbar\omega_r$ ) becomes much larger than all the intrinsic energy scales of the system [8,14,15]. The crossover to different dimensions has been investigated in various setups and several relations have been established for the scattering properties in different dimensions, e.g., between the scattering lengths [16–22]. These relations give rise to confinement-induced resonances [16,23–26], which provide further means to tune the interparticle interaction in lower dimensional settings. Moreover, it has been showcased that the two-body Tan contact in three dimensions (3D), 2D, and 1D are proportional by factors depending on the dimension

[15,27,28]. Interestingly, next-to-leading-order terms in the asymptotic expansion of the two-body momentum distribution reveal the contribution of the three-body contact and the role of dimensionality [29]. Recently, on the two-body level, a correspondence between a dimension-dependent centrifugal barrier and a confining potential has been established [30]. Importantly, apart from the stationary properties, the nonequilibrium dynamics of Bose and Fermi gases at the dimensional crossover has attracted considerable interest [31–34]. This is corroborated by the advent of new trapping techniques, e.g., utilizing optical tweezers [35,36], which paves the way for monitoring the time-evolution of few-body systems. For instance, the collisional dynamics of two  ${}^6\text{Li}$  atoms [13] has been experimentally probed, by quenching the frequencies of an anisotropic 3D harmonic oscillator.

The stationary properties of two ultracold atoms confined in an isotropic harmonic oscillator trap have been thoroughly explored across all dimensions [37–39]. Generalizations of these studies include, for instance, the involvement of anisotropic traps in three dimensions [40–43], higher partial waves [44,45], long-range interactions [46], and hard-core interaction potentials [47]. Moreover, a correspondence between three bosons interacting via three-body forces in 1D and two bosons interacting via pairwise interactions in 2D has been established [48–53]. The stationary solutions have been utilized in order to probe the nonequilibrium dynamics of two atoms, by quenching the interaction strength in all

dimensions [54–57]. The solutions also serve as a simple model for the dynamics of quenched Bose gases, at short times and larger momenta than those set by the density of the gas [58,59]. Analytical expressions for several observables are known, including, for instance, momentum distributions [60] and thermodynamical quantities [61,62].

Even though the dimensional crossover at the two-body level has been extensively studied from three to lower dimensions, the crossover from two to one dimensions is yet an unexplored problem, in terms of both the stationary and the dynamical properties. In this work, we shed light into the stationary properties and interaction quench dynamics of two ultracold bosons trapped in an anisotropic 2D harmonic trap. However, our results have a more general character and can be equally applied to two distinguishable  $s$ -wave interacting ultracold atoms in even-parity states of their relative coordinate. A transcendental equation for the anisotropic system is derived, allowing us to probe the underlying energy spectrum for arbitrary interactions and anisotropies. For instance, it is shown that the energy gaps between the involved eigenstates for a fixed interaction strength strongly depend on the anisotropy. An analytical expression for the two-boson wave function both in real and momentum space is constructed and the relation between the 2D and the 1D scattering lengths is established. We find that the momentum distribution exhibits a multihump structure along the weaker confined direction while the corresponding one-body densities feature two-hump patterns. Remarkably, the 2D and the 1D Tan contacts, capturing the occurrence of short-range two-body correlations, are found to be proportional to each other by a simple relation. The Tan contact of the bound and the ground state shows an increasing tendency for larger anisotropies independently of the sign of the interaction, and in particular for the ground state it tends to saturate when approaching the 1D regime.

Subsequently, we focus on the interaction quench dynamics of the two particles from attractive to repulsive interactions and vice versa. The response of the system is analyzed in terms of the time-averaged fidelity, and the frequency spectra of the spatial extent of the bosonic cloud in both confined directions. We showcase that the time-evolved state deviates significantly from the initial one in the vicinity of zero postquench interactions, when the latter is initialized at finite attractive or repulsive interactions. For increasing anisotropy, the system becomes less perturbed following an interaction quench, independent of the interactions. The quench excites a breathing motion, visualized in the time evolution of the reduced one-body density, in both the  $x$  and  $y$  directions with a distinct number of participating frequencies in each spatial direction.

This work is structured as follows. In Sec. II, we introduce our setup of the two trapped bosons in a 2D anisotropic harmonic trap. Subsequently, in Sec. III the energy spectra are presented for various anisotropies, while Sec. IV contains the expression of the two-body wave function in real and momentum space. Section V is dedicated to the behavior of the reduced one-body density for several anisotropy parameters and Sec. VI showcases the Tan contact of the bound and the ground states with respect to the anisotropy. In Sec. VII, the interaction quench dynamics of two bosons is explored for different anisotropies. We lay out our concluding remarks

and provide an outlook in Sec. VIII. Appendix A provides details on the derivation of the transcendental equation which determines the relative energy of the two bosons. Appendix B provides the 1D energy spectrum of two bosons by inspecting the quasi-1D limit of the transcendental equation. Details on the calculation of the 2D Tan contact and its quasi-1D limit are presented in Appendix C. Appendix D includes an analytical derivation of the spatial extent of the bosonic cloud in both directions and the corresponding frequency amplitudes.

## II. HAMILTONIAN AND EIGENVALUE PROBLEM

We consider two ultracold bosons trapped in a 2D anisotropic harmonic trap interacting via an  $s$ -wave pseudopotential. Note that the following analysis applies to the general case of ultracold atoms except for two spin-polarized fermions [39]; see in particular the discussion following Eq. (7). The latter constitutes an adequate approximation within the ultracold regime [3,4]. The Hamiltonian of the system reads

$$\mathcal{H} = \sum_{i=1}^2 \left[ -\frac{\hbar^2}{2m} \nabla_i^2 + m\omega_x^2 \frac{(x_i^2 + \alpha^2 y_i^2)}{2} \right] + 2V_{\text{pp}}(\boldsymbol{\rho}_1 - \boldsymbol{\rho}_2). \quad (1)$$

For simplicity, below, we shall adopt harmonic oscillator units namely  $\hbar = m = \omega_x = 1$  unless it is stated otherwise. Additionally, the anisotropy parameter  $\alpha = \frac{\omega_y}{\omega_x}$  is the ratio of the harmonic trap frequencies along the  $y$  and  $x$  spatial directions. Evidently,  $\alpha$  takes values from unity (2D case) up to infinity (1D case). Also,  $\boldsymbol{\rho}_i = (x_i, y_i)$  denotes the position of the  $i$ th boson in the 2D plane while the prefactor 2 in Eq. (1) is used for later convenience. The zero-range regularized  $s$ -wave pseudopotential assumes the following form [63]:

$$V_{\text{pp}}(\boldsymbol{\rho}) = -\frac{\pi \delta(\boldsymbol{\rho})}{\ln(Aa_{2D}\Lambda)} \left[ 1 - \ln(A\Lambda\rho) \rho \frac{\partial}{\partial \rho} \right], \quad (2)$$

where  $\Lambda$  is an arbitrary dimensionful parameter possessing the units of momentum and  $A = e^\gamma/2$  with  $\gamma = 0.577\dots$  being the Euler-Mascheroni constant. Note that the arbitrary parameter  $\Lambda$  does not affect any observable of the system and eventually drops out of the calculations when the pseudopotential is applied to wave functions exhibiting a logarithmic behavior at the origin  $\rho = 0$  [63,64]. The 2D  $s$ -wave scattering length is  $a_{2D}$ .

To separate the center-of-mass ( $X, Y$ ) and relative ( $x, y$ ) coordinates, we employ the following transformations in terms of the Cartesian coordinates  $(x_i, y_i)$   $X = \frac{x_1 + x_2}{\sqrt{2}}$ ,  $Y = \frac{y_1 + y_2}{\sqrt{2}}$ , and  $x = \frac{x_1 - x_2}{\sqrt{2}}$ ,  $y = \frac{y_1 - y_2}{\sqrt{2}}$ . Therefore, the Hamiltonian of Eq. (1) separates into the center of mass  $\mathcal{H}_{\text{c.m.}}$  and the relative  $\mathcal{H}_{\text{rel}}$  Hamiltonian, namely  $\mathcal{H} = \mathcal{H}_{\text{c.m.}} + \mathcal{H}_{\text{rel}}$  with

$$\begin{aligned} \mathcal{H}_{\text{c.m.}} &= -\frac{1}{2}(\partial_X^2 + \partial_Y^2) + \frac{1}{2}(X^2 + \alpha^2 Y^2) \\ \mathcal{H}_{\text{rel}} &= -\frac{1}{2}(\partial_x^2 + \partial_y^2) + \frac{1}{2}(x^2 + \alpha^2 y^2) \\ &\quad - \frac{\pi \delta(x)\delta(y)}{\ln(\sqrt{2}Aa_{2D}\Lambda)} \left[ 1 - \ln(\sqrt{2}A\Lambda\rho) \rho \frac{\partial}{\partial \rho} \right], \end{aligned} \quad (3)$$

where  $\rho = \sqrt{x^2 + y^2}$ . Because of the above-described separation of the Hamiltonian, the corresponding wave function of

the system can subsequently be written as a product state, i.e.,  $\Psi(\boldsymbol{\rho}_1, \boldsymbol{\rho}_2) = \Psi_{\text{c.m.}}(X, Y)\Psi_{\text{rel}}(x, y)$ .

The eigenvalue problem of the center of mass (c.m.) is easy to solve since it consists of two decoupled noninteracting 1D harmonic oscillators in the  $x$  and  $y$  directions; see Eq. (3). Indeed, the corresponding wave function reads

$$\Psi_{\text{c.m.}}(X, Y) = \phi_n(X)\phi_m(Y), \quad (4)$$

where  $\phi_n(z) = \frac{e^{-\omega z^2/2}}{\sqrt{2^n n!}} \left(\frac{\omega}{\pi}\right)^{1/4} H_n(\sqrt{\omega}z)$  with  $n = 0, 1, 2, \dots$  are the eigenfunctions of a 1D harmonic oscillator of frequency  $\omega = 1, \alpha$  and energy  $E_n = (n + 1/2)\omega$  in harmonic oscillator units [65].  $H_n$  are the Hermite polynomials of degree  $n$ . Thus, the energy of the center of mass reads  $E_{\text{c.m.}}^{\tilde{n}, \tilde{m}} = \tilde{n} + \alpha\tilde{m} + \frac{\alpha+1}{2}$ . Throughout this work, we assume that the center-of-mass wave function is in its ground state  $\Psi_{\text{c.m.}}(X, Y) = \phi_0(X)\phi_0(Y)$ .

To tackle the eigenvalue problem of the relative Hamiltonian,  $\mathcal{H}_{\text{rel}}$ , we utilize as a wave-function ansatz an expansion over the noninteracting eigenstates  $\phi_n(z)$  [37,54] in both spatial directions, i.e.,

$$\Psi_{\text{rel}}(x, y) = \sum_{n,m} c_{n,m} \phi_n(x)\phi_m(y). \quad (5)$$

Here,  $c_{n,m}$  denote the corresponding expansion coefficients (see also below). By plugging Eq. (5) into the Schrödinger equation for the relative Hamiltonian  $\mathcal{H}_{\text{rel}}\Psi_{\text{rel}} = E_{\text{rel}}\Psi_{\text{rel}}$ , see also Eq. (3), and projecting onto the noninteracting eigenstates  $\phi_n^*(x)\phi_m^*(y)$ , one arrives at the following equation:

$$0 = c_{n',m'}(E_{\text{rel}}^{n',m'} - E_{\text{rel}}) - \frac{\pi \phi_{n'}^*(0)\phi_{m'}^*(0)}{\ln(a_{2D}A\Lambda)} \times \left\{ \left[ 1 - \ln(\sqrt{2}A\Lambda\rho) \rho \frac{\partial}{\partial \rho} \right] \Psi_{\text{rel}}(x, y) \right\}_{\rho \rightarrow 0}, \quad (6)$$

where  $\rho = \sqrt{x^2 + y^2}$  and  $E_{\text{rel}}^{n,m} = n + \alpha m + \frac{\alpha+1}{2}$ . The regularization operator enclosed in the parentheses (...) of Eq. (6) acts on the relative wave function and subtracts the logarithmic divergence close to the origin,  $\rho = 0$  [64,66]. As a consequence, the expression in the right-hand side of Eq. (6) is related to a normalization factor denoted below by  $B$  of the wave function, as it has been argued in Refs. [37,54], that will be determined later. The expansion coefficients,  $c_{n,m}$ , thus take the following form:

$$c_{n,m} = B \frac{\phi_n^*(0)\phi_m^*(0)}{E_{\text{rel}}^{n,m} - E_{\text{rel}}}. \quad (7)$$

Note that the expansion coefficients vanish for odd  $n, m$ . Indeed, the 2D pseudopotential of Eq. (2) affects only states with a nonvanishing value at  $x = y = 0$  which in turn involve only even Hermite polynomials, i.e., even-parity states of the relative coordinate, in the ansatz (5) [40,41]. Therefore, our analysis is also valid for two distinguishable ultracold atoms in even-parity states, i.e., the ones that are affected by the  $s$ -wave interaction. The odd-parity states are not impacted by the contact potential. Having at hand the expansion coefficients [see Eq. (7)], one can directly perform the double summation appearing in Eq. (5). For that end, we express the denominator of the expansion coefficients [Eq. (7)] in an

integral representation [37,40,41]

$$\frac{1}{E_{\text{rel}}^{n,m} - E_{\text{rel}}} = \int_0^\infty dt e^{-t(E_{\text{rel}}^{n,m} - E_{\text{rel}})}, \quad (8)$$

and then perform the double summation by using the Mehler identity for the Hermite polynomials [67]. Therefore, the relative wave function reads

$$\Psi_{\text{rel}}(x, y) = B \frac{\sqrt{\alpha}}{2\pi} e^{-(x^2 + \alpha y^2)/2} \times \int_0^{+\infty} dt \exp\left(\frac{e^{-t}x^2}{e^{-t}-1} + \frac{\alpha e^{-\alpha t}y^2}{e^{-\alpha t}-1}\right) \times \frac{e^{-tf(E)/2}}{\sqrt{1-e^{-t}}\sqrt{1-e^{-\alpha t}}}, \quad (9)$$

where  $f(E) = \frac{\alpha+1}{2} - E$ . The above integral converges provided that  $f(E) > 0$ . Later on, and in particular in Appendix A, we shall consider values of  $f(E) < 0$  by means of analytic continuation [40,41]. Note also that in Eq. (9) we have dropped the subscript rel from the energy for simplicity.

Furthermore, by employing the form of the expansion coefficients [Eq. (7)], the relative energy is determined via Eq. (6), namely

$$\left\{ \left( 1 - \ln(\sqrt{2}A\Lambda\rho) \rho \frac{\partial}{\partial \rho} \right) \frac{\Psi_{\text{rel}}(x, y)}{B} \right\}_{\rho \rightarrow 0} = \frac{\ln(a_{2D}A\Lambda)}{\pi}, \quad (10)$$

where  $\Psi_{\text{rel}}(x, y)$  is determined by Eq. (9). The aim of the following section is to solve Eq. (10) for an arbitrary anisotropy parameter  $\alpha$ , in order to determine the stationary properties of the two bosons by calculating their energy spectra and eigenstates.

### III. ENERGY SPECTRA

#### A. Transcendental equation

To find the relative energy  $E$ , we need to solve Eq. (10) and therefore establish a formula that captures the behavior of the wave function close to  $x = y = 0$ . For  $x, y \rightarrow 0$ , the main contribution to the integral (9) stems from very small values of the integration variable  $t$  [40,41]. Indeed, the integral appearing in Eq. (9) can be split into two parts,

$$\Psi_{\text{rel}}(x, y)|_{x,y \ll 1} = \frac{B}{2\pi} \int_0^L dt \frac{e^{-(x^2+y^2)/t}}{t} + B \frac{\sqrt{\alpha}}{2\pi} \int_L^{+\infty} dt \frac{e^{-tf(E)/2}}{\sqrt{1-e^{-t}}\sqrt{1-e^{-\alpha t}}}. \quad (11)$$

In the first part, we have linearized all the exponentials around  $t = 0$ , while in the second part, we have set  $x = y = 0$  directly. The parameter  $L$  is very small, being of the order of  $x, y$ . The first integral corresponds to  $\Gamma(0, \frac{x^2+y^2}{L})$ , where  $\Gamma(x, y)$  is the incomplete gamma function [68]. For small  $r^2 = x^2 + y^2$ , this gamma function can be expanded as follows:

$$\Gamma\left(0, \frac{r^2}{L}\right) \xrightarrow{r \rightarrow 0} -\gamma - \ln\left(\frac{r^2}{L}\right) + \frac{r^2}{L} + O(r^4). \quad (12)$$

Note that this result is independent of  $\alpha$ , since at very small interparticle distances  $r \rightarrow 0$  the confining potential does

not play any crucial role and the wave function develops a logarithmic behavior, as a consequence of the 2D interaction pseudopotential [15,69]. At this point, it is better to restore the units, i.e.,  $x^2 + y^2 \rightarrow \frac{x^2 + y^2}{l_x^2}$ , where  $l_x = \sqrt{\frac{\hbar}{m\omega_x}}$  is the harmonic oscillator length in the  $x$  direction. Thus, we can deduce that the pure 2D regime is accessed when the interparticle distance  $r$  is much smaller than  $l_x$ .

Since the behavior of the relative wave function  $\Psi_{\text{rel}}(x, y)$  is now available [see Eq. (11)] close to  $x = y = 0$ , one can insert Eq. (11) into Eq. (10) and in turn derive a transcendental equation that will allow us to determine the relative energy of the two bosons (see Appendix A for more details). The resulting transcendental equation reads

$$-\gamma + 2 \ln 2 + \underbrace{\sqrt{\alpha} \int_0^1 dz \ln(1-z) \varphi' \left( z, \frac{f(E)}{2} \right)}_{P(f(E)/2)} = -\frac{1}{g}, \quad (13)$$

where  $g = [\ln(\frac{1}{2\alpha_{2D}})]^{-1}$  is the 2D coupling constant [37,38,70],  $\varphi(z, f(E)/2) = z^{f(E)/2-1} \frac{\sqrt{1-z}}{\sqrt{1-z^\alpha}}$ , and the differentiation is performed with respect to the variable  $z$ . Equation (13) provides the energy spectrum of the two bosons for an arbitrary anisotropy parameter  $\alpha$ . As has been mentioned earlier, this equation is valid only for  $f(E) > 0$ . Its extension to negative values is granted by the recurrence formula (see also Appendix A)

$$P\left(\frac{f(E)}{2}\right) = P\left(\alpha + \frac{f(E)}{2}\right) + \sum_{n=0}^{\infty} \binom{1/2}{n} \frac{\sqrt{\pi}(-1)^n \Gamma\left(\frac{f(E)}{2} + \alpha n\right)}{\Gamma\left(\frac{1}{2} + \frac{f(E)}{2} + \alpha n\right)}. \quad (14)$$

### B. Quasi-1D limit

Before calculating the energies for various values of  $\alpha$ , let us first retrieve the 1D energy spectrum, by assuming that  $\alpha \gg 1$ . In this case, the harmonic confinement along the  $y$  direction is tight and therefore we enter the quasi-1D regime, at least when the interparticle distance is comparable or larger than the harmonic oscillator length in the  $x$  direction, i.e.,  $r \geq l_x$  (see also the previous discussion). For  $\alpha \gg 1$ , the transcendental equation (13) becomes (see also Appendix B)

$$\sqrt{\pi\alpha} \frac{\Gamma\left(\frac{f(E)}{2}\right)}{\Gamma\left(\frac{1}{2} + \frac{f(E)}{2}\right)} - \ln(\alpha) + D = \ln(a_{2D}^2), \quad (15)$$

where  $D = -\gamma - 2\sqrt{k} + \ln(2k) + \frac{k}{4} - \frac{k^2}{192} - \frac{k^3}{1152}$  and  $k \approx 6$ ; see for details Appendix B. The above formula is reminiscent of the transcendental equation of two bosons confined in a 1D harmonic trap, which determines the energy spectrum of this system and reads [37]

$$\sqrt{2}a_{1D} = \frac{\Gamma\left(\frac{1}{4} - \frac{E}{2}\right)}{\Gamma\left(\frac{3}{4} - \frac{E}{2}\right)} = -\frac{2\sqrt{2}}{g_{1D}}. \quad (16)$$

This expression is derived by following the same steps as in Sec. II but in 1D and with the pseudopotential  $V_{pp}(x) = -\frac{2}{a_{1D}}\delta(x)$  [23]. Most importantly, by employing a proper rescaling of the energies in Eq. (15), namely  $E' = -f(E) +$

$1/2$  and comparing Eqs. (15) and (16), we obtain a relation between the 2D,  $a_{2D}$ , and the 1D,  $a_{1D}$ , scattering lengths

$$a_{2D} = \frac{D_0}{\sqrt{\alpha}} e^{\sqrt{\pi\alpha}a_{1D}/\sqrt{2}}, \quad (17)$$

with  $D_0 = e^{D/2}$ . We remark that when restoring the units of the system, this expression acquires the form  $a_{2D} = l_y D_0 e^{\sqrt{\pi}a_{1D}/(\sqrt{2}l_y)}$ , where  $l_y$  is the harmonic oscillator length in the  $y$  direction. Recently, a similar relation between these two scattering lengths has been established in Ref. [22], by means of nonrelativistic effective field theory. The connection between the scattering lengths is achieved by imposing periodic boundary conditions along one direction and comparing the effective range expansion with the purely 1D one. Apart from the scattering lengths, we are able to establish also a relation among the coupling constants in one and two dimensions,

$$\frac{1}{g} = \ln(\alpha) - \ln 2 + \frac{2\sqrt{2\pi\alpha}}{g_{1D}} - D, \quad (18)$$

where  $g$  denotes the 2D effective coupling constant and  $g_{1D}$  denotes the corresponding 1D effective interaction strength; see also Eq. (16).

Let us also note in passing that the 2D energy spectrum can also be easily retrieved. Indeed, by substituting  $\alpha = 1$  in Eq. (9), one gets

$$\Psi_{\text{rel}}(x, y) = \frac{B}{2\pi} e^{-(x^2+y^2)/2} \Gamma\left(\frac{f(E)}{2}\right) U\left(\frac{f(E)}{2}, 1, x^2 + y^2\right), \quad (19)$$

which is the 2D wave function of two interacting bosons confined in a radial trap [55]. Here,  $U(a, b, z)$  is the confluent hypergeometric function of the second kind [68]. Then, by plugging Eq. (19) into Eq. (10), we retrieve the known 2D energy spectrum [55]

$$\psi\left(\frac{f(E)}{2}\right) = \ln\left(\frac{1}{2a_{2D}^2}\right) + 2 \ln 2 - 2\gamma, \quad (20)$$

with  $\psi(z)$  being the digamma function [68].

For convenience, in the following, we will refer to the states with energy less than the zero-point energy,  $E_0 \equiv \frac{\alpha+1}{2}$ , as bound states [40,41]. The energetically higher lying states will be subsequently labeled the ground state, first excited state, and so forth. Additionally, the energetic order of the eigenstates will be denoted by the subscripts 0 for the bound state, 1 for the ground state, and in general  $i$  denoting the  $(i-1)$ -th excited state. This labeling of the energies is explicitly showcased in Fig. 1(a), and then it is omitted for brevity. Furthermore, a black dashed line is included to indicate the zero-point energy.

Figure 1 illustrates the two extreme regimes, namely the 2D case, for  $\alpha = 1$  [Fig. 1(a)], and the quasi-1D case, for  $\alpha \gg 1$  [Fig. 1(b)]. In the quasi-1D regime, the spectrum of Eqs. (13) and (14) is shown for  $\alpha = 10$  and compared with the energy spectrum directly derived from Eq. (16) for the 1D case. The two resulting energy spectra are presented together for a varying  $g_{1D}$  in Fig. 1(b). The zero-point energy is put to  $\frac{\alpha+1}{2}$ . As can be seen, regarding the excited states there is a perfect match for all values of  $g_{1D}$ . We should note, however, that for  $|g| > 5$  there is a slight deviation between



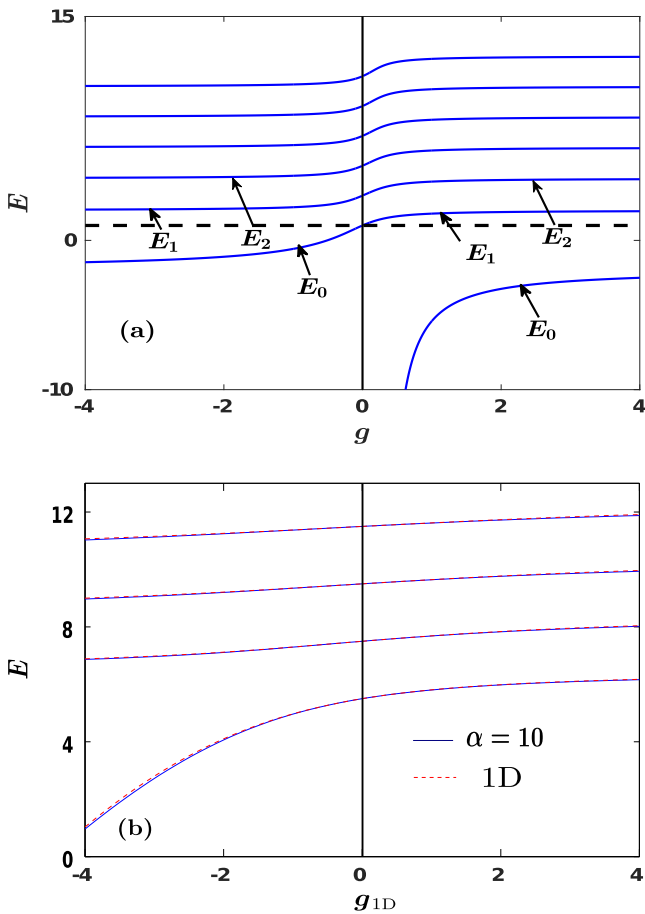


FIG. 1. (a) Energy spectrum with anisotropy  $\alpha = 1$ , thus recovering the 2D limit, for various 2D interaction strengths. The black dashed line indicates the zero-point energy. (b) Comparison of the energy spectra for  $\alpha = 10$  (blue line) and for a pure 1D system (red dashed line), with respect to the 1D interaction strength  $g_{1D}$ . In both cases the system consists of two ultracold bosons confined in an anisotropic 2D harmonic trap. All quantities shown are in dimensionless units.

the two energies, which is of the order of 2% at infinite  $g_{1D}$ . For a larger anisotropy, this discrepancy becomes smaller; for instance, it is of the order of 0.5% at  $\alpha = 100$ . Deviations between the two spectra arise also for the bound state in the attractive interaction regime, and in particular for large negative interactions  $g_{1D} < -10$  they become of the order of 15%. The aforementioned discrepancy is due to the fact that the bound state in the pure 1D system exhibits a lower energy compared to the corresponding 2D setup. Indeed, the 2D system possesses bound states both in the attractive and the repulsive interaction regimes [55,71] and for attractive couplings the energy of the bound state remains finite independently of the negative value of the interaction strength; see Fig. 1(a). For positive values, though, the energy of the bound state is not bounded from below. This is in sharp contrast to the pure 1D system where the energy of the bound state in the attractive regime diverges at very strong interactions [54]. As we shall discuss in the following, the energy gap between the bound and the ground states increases as the

anisotropy parameter acquires larger values. However, for a larger value of  $\alpha$  the above-mentioned discrepancy between the energies of the bound states in strictly 1D as compared to 2D [see Fig. 1(b)] becomes smaller and occurs for stronger attractions. Note also that in Fig. 1(b) there is a bound state in the repulsive interaction regime, having an energy much lower than the energy of the other states of the spectrum and is way below the shown energy scales.

### C. Energy dependence on the anisotropy parameter

To expose the dependence of the eigenenergies on the anisotropy parameter  $\alpha$ , corresponding energy spectra are shown in Fig. 2 for different values of  $\alpha$ , thus accessing the dimensional crossover from the quasi-1D to the 2D regime. Evidently, in all cases the energy spacing among the different eigenstates is not equal, in contrast to the 2D case [Fig. 1(a)], and greatly depends on  $\alpha$ . This behavior is anticipated by the expression of the energy for zero interactions, namely  $E = 2(n + am) + \frac{\alpha+1}{2}$ ,  $n, m \in N$ . For integer values of  $\alpha$ , the energy spacing between consecutive energy states becomes larger every  $\alpha$ th state in both the attractive and the repulsive interaction regimes starting from the ground state; see, for instance, Figs. 2(b) and 2(d). However, for noninteger  $\alpha$  values, the energy spacings become more irregular, as depicted in Figs. 2(a), 2(c) and 2(e). For instance, at  $\alpha = 1.1$  and  $g = 0$  [Fig. 2(a)], the energetic difference between the third and the fourth excited states is  $2\alpha = 0.2$ . We should mention here that qualitatively similar results have been reported also for two bosons confined in a 3D anisotropic trap [40,41]. Moreover, the energy gap between the bound and ground states increases for a larger anisotropy parameter independently of the sign of the interaction strength; see Figs. 2(a)–2(f).

The energy of the bound states is shifted upward for an increasing value of  $\alpha$  due to the increase of the zero-point energy,  $\frac{\alpha+1}{2}$ . To elaborate on the impact of the anisotropy parameter on the energy gaps, we depict in Fig. 3 the energy difference between the bound and ground states, i.e.,  $E_1 - E_0$ , as a function of  $\alpha$  for various repulsive [Fig. 3(a)] and attractive [Fig. 3(b)] interactions. We observe that the aforementioned energy difference increases for large  $\alpha$  independently of the interactions and it does not saturate, e.g., at  $\alpha = 200$  and for  $g = 3$   $E_1 - E_0 = 38.97$ . Moreover, on the repulsive interaction regime [Fig. 3(a)], when  $\alpha$  is kept constant,  $E_1 - E_0$  takes larger values at weak interactions. This is due to the divergence of the energy of the bound state close to the noninteracting limit of the repulsive interaction regime [45,71]. Also deep into the quasi-1D regime, i.e.,  $\alpha \gg 1$ , the bound state is largely separated from the other states of the energy spectrum for all interaction strengths. On the attractive side [Fig. 3(b)], at fixed  $\alpha$ , the energy gap  $E_1 - E_0$  is larger at stronger attractions. For fixed attractive interaction  $g$ ,  $E_1 - E_0$  becomes larger as the anisotropy parameter increases. Recall that for  $g = 0$  the energy of the bound state is always  $\frac{\alpha+1}{2}$ , i.e., it crosses the bound-state threshold [see Fig. 1(a)], and hence it is connected with  $E_1$  at the repulsive side of the spectrum [Figs. 2(a)–2(f)].

Figure 4 displays the energy difference between the second excited and ground states,  $E_3 - E_1$ , as well as between the fourth excited and ground states  $E_5 - E_1$  in the corresponding

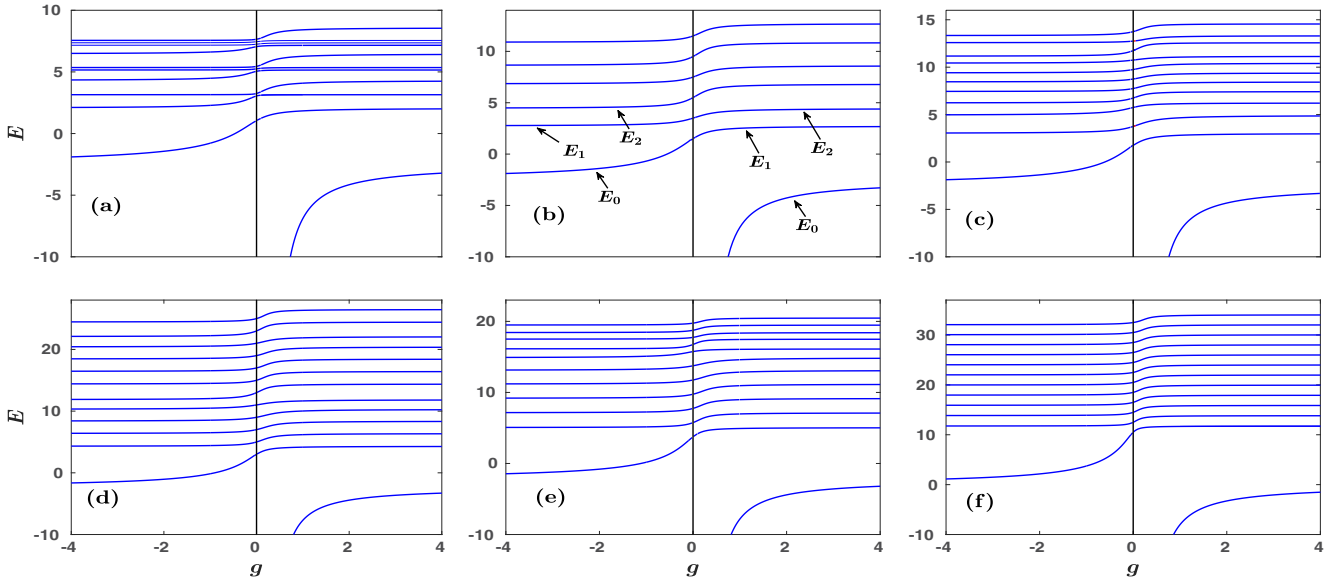


FIG. 2. Energy spectra for anisotropy parameter (a)  $\alpha = 1.1$ , (b)  $\alpha = 2$ , (c)  $\alpha = 2.5$ , (d)  $\alpha = 5$ , (e)  $\alpha = 6.5$ , and (f)  $\alpha = 20$  for varying 2D coupling strength  $g$ . The labeling of the energy states is showcased only in panel (b) for convenience. In all cases, the quantities displayed are in dimensionless units.

inset, for example, for  $g = 3$ . In both cases, for small  $0 < \alpha < 5$  the energy spacings feature jumps and subsequently saturate for adequately large  $\alpha > 9$ . These energy jumps occur for integer values of  $\alpha$  and depend on the level of the excited state; for instance, there are two jumps in the main Fig. 4 and four jumps in the inset. For values of  $\alpha$ , a little bit smaller or larger than these integer values, the energy gaps between the states decrease; see, e.g., Fig. 2(a), and hence the aforementioned jumps are manifested in the energy difference between excited states and the ground state. However, for anisotropies higher than the level of the examined excited state, the energy gap with the ground state saturates, because the change in the energy spacing occurs at even higher excited states. This is the case for the fourth excited state in Figs. 2(d)–2(f). We finally remark that for other interaction strengths of either sign,  $E_3 - E_1$  and  $E_5 - E_1$ , exhibit a similar to the above-described behavior.

#### IV. EIGENSTATE ANALYSIS

##### A. Two-body wave function

To acquire complete knowledge on the stationary properties of the system, we next determine the two-boson wave function. The starting point is Eq. (9), where the integral is convergent for  $f(E) > 0$ . However, it is advantageous to establish a more convenient form of  $\Psi_{\text{rel}}(x, y)$  in order to span the entire energy spectrum. To this end, one can utilize the wave-function ansatz introduced in Eq. (5) along with the underlying expansion coefficients [Eq. (7)]. Indeed, by expressing the denominator of Eq. (7) in an integral representation, see Eq. (8), and performing a single out of the two summations with the aid of the Mehler identity [67], the two-boson wave function of the relative coordinate takes

the simplified form

$$\begin{aligned} \Psi_{\text{rel}}(x, y) &= \frac{B\sqrt{\alpha}}{\pi} e^{-(x^2+\alpha y^2)/2} \sum_{m=0}^{\infty} \frac{H_m(0)H_m(\sqrt{\alpha}y)\Gamma\left(\frac{\alpha m - \mathcal{E}}{2}\right)}{2^{m+1}m!} \\ &\times U\left(\frac{\alpha m - \mathcal{E}}{2}, \frac{1}{2}, x^2\right), \end{aligned} \quad (21)$$

where  $\mathcal{E} = E - (\alpha + 1)/2$ . In practice, this summation is truncated when numerically calculating the wave function, with an upper bound which is chosen such that convergence is achieved [54]. Note that the wave function in real space exhibits a logarithmic divergence close to the origin  $x = y = 0$ , as already argued in Eq. (12). However, the wave function of Eq. (21) cannot capture this behavior when truncating the infinite summation. Indeed, inserting  $x = y = 0$  in Eq. (21), the wave function does not converge as we increase the cutoff in the summation. Moreover, the normalization constant  $B$  can be easily determined analytically if we express the confluent hypergeometric function  $U(a, b, x)$  in terms of parabolic cylinder functions  $D_z(x)$  [68]. For this choice, the integration can be performed analytically [72], resulting in

$$\begin{aligned} B^{-2} &= \frac{\sqrt{\alpha}}{\sqrt{\pi}} \sum_{m=0}^{\infty} \frac{H_m(0)^2 \Gamma\left(\frac{\alpha m - \mathcal{E}}{2}\right)}{2^{m+2}m! \Gamma\left(\frac{\alpha m - \mathcal{E}}{2} + \frac{1}{2}\right)} \\ &\times \left[ \psi\left(\frac{1}{2} - \frac{\mathcal{E} - \alpha m}{2}\right) - \psi\left(-\frac{\mathcal{E} - \alpha m}{2}\right) \right], \end{aligned} \quad (22)$$

which corresponds to the analytical expression of the normalization coefficients.

As pointed out in Sec. III, the 2D wave function can be easily retrieved when  $\alpha = 1$ ; see Eq. (19). In the following, the wave function will be evaluated and further investigated deep into the quasi-1D regime, i.e., in the case of  $\alpha \gg 1$ .

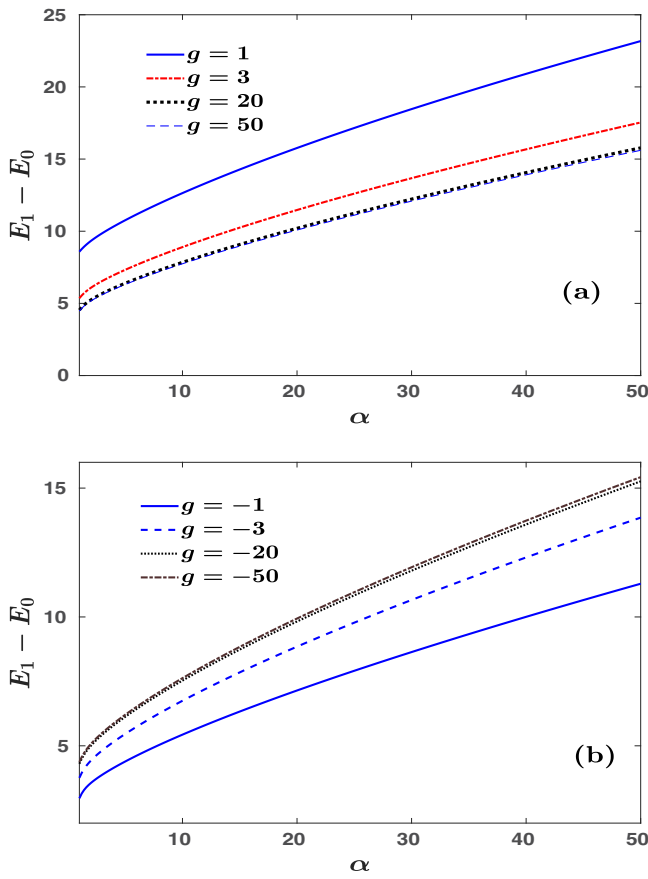


FIG. 3. Energy difference between the bound and the ground states,  $E_1 - E_0$ , at different (a) repulsive and (b) attractive 2D interaction strengths (see legends) for varying anisotropy parameter  $\alpha$ . For all observables, dimensionless units are adopted.

Starting from Eq. (9), we note that in this case the wave function is elongated in the  $x$  direction. Thus, in order to avoid the logarithmic divergence appearing at  $x = y = 0$ , we shall restrict ourselves to  $y = 0$  and  $x \gtrsim l_x$ . With these

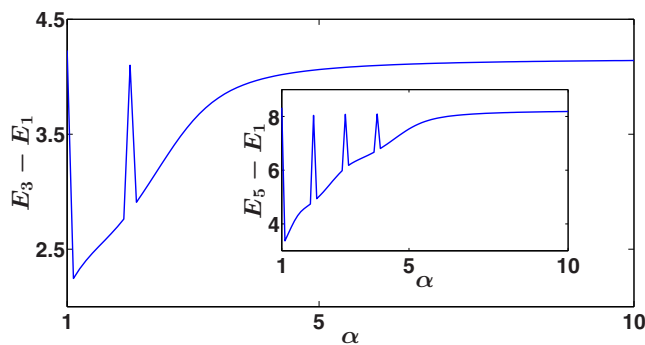


FIG. 4. Energy difference between the second excited and ground states, namely  $E_3 - E_1$ , for increasing anisotropy parameter  $\alpha$ . The inset presents the energy difference between the fourth excited and ground states, i.e.,  $E_5 - E_1$ , with respect to  $\alpha$ . In both cases, the 2D interaction strength of the two bosons is  $g = 3$ . In all cases, the quantities displayed are in dimensionless units.

simplifications, Eq. (9) is rewritten as

$$\Psi_{\text{rel}}(x, 0) \approx \frac{B\sqrt{\alpha}}{2\pi} e^{-x^2/2} \times \int_0^\infty dw \exp\left\{-\frac{x^2 e^{-w}}{1 - e^{-w}}\right\} \frac{e^{-wf(E)/2}}{\sqrt{1 - e^{-w}}}. \quad (23)$$

Note that the square root involving the anisotropy parameter  $\alpha$  in Eq. (9) can be neglected, since for  $w \gg \frac{1}{\alpha}$  the exponent  $e^{-\alpha w}$  tends to zero. Also, for  $w \ll \frac{1}{\alpha}$ , the  $\frac{1}{w}$  divergence in Eq. (11) is counterbalanced by the factor  $e^{-x^2/w}$ , and the entire integrand vanishes. Employing a change of variables,  $z = \frac{e^{-w}}{1 - e^{-w}}$ , it is easy to show that the wave function of two interacting bosons in a quasi-1D trap [54] takes the approximate form

$$\Psi_{\text{rel}}(x, 0) \approx \frac{B\sqrt{\alpha}}{2\pi} e^{-x^2/2} \Gamma\left(\frac{f(E)}{2}\right) U\left(\frac{f(E)}{2}, \frac{1}{2}, x^2\right). \quad (24)$$

The approximate nature of this expression stems from the fact that we have restricted ourselves to the spatial region  $x \gtrsim l_x$ .

### B. Momentum distribution

Consequently, it is straightforward to calculate the wave function in momentum space. To this end, we utilize its expansion in terms of the Hermite polynomials introduced in Eq. (5) as well as an identity regarding their Fourier transform.<sup>1</sup> Therefore, the wave function  $\Psi_{\text{rel}}(k_x, k_y)$  in momentum space reads

$$\Psi_{\text{rel}}(k_x, k_y) = \frac{B}{\pi} e^{-(k_x^2 + k_y^2/\alpha)/2} \times \sum_{n,m} (-i)^{n+m} \frac{H_n(0)H_m(0)H_n(k_x)H_m\left(\frac{k_y}{\sqrt{\alpha}}\right)}{2^{n+m} n! m! (n + \alpha m - \mathcal{E})}. \quad (25)$$

Since the wave function in real space exhibits a logarithmic divergence at the origin ( $x = y = 0$ ), it is better to analyze the structure of the two-boson wave function in momentum space. Figure 5 illustrates the momentum distribution  $|\Psi_{\text{rel},j}(k_x, k_y)|^2$  for different anisotropy parameters  $\alpha = 1.1$  [Figs. 5(a)],  $\alpha = 2.5$  [Figs. 5(b)], and  $\alpha = 5$  [Figs. 5(c)], regarding the ground ( $j = 1$ ) and higher excited states ( $j = 2, 3$ ) at  $g = 1$ . Independently of the energetic order of the state, we observe that as the anisotropy parameter increases the momentum distribution is elongated along the  $k_y$  direction; see, e.g., Figs. 5(a1), 5(b1), and 5(c1). This elongation occurs since the momentum distribution is more long-ranged for  $k_y$  than  $k_x$ , according to the exponential decay given by Eq. (25). Additionally, the momentum distribution for large anisotropies [see, e.g., Figs. 5(c1)–5(c3)] exhibits a multihump structure along the  $k_x$  direction. This multihump structure becomes more pronounced for energetically higher excited states; compare, for instance, Figs. 5(c2) and 5(c3). The latter behavior is attributed to the fact that the major contribution in the double

<sup>1</sup> $\mathcal{F}\{e^{-\alpha x^2/2} H_n(x\sqrt{\alpha})\} = \frac{(-i)^n}{\sqrt{\alpha}} e^{-k^2/(2\alpha)} H_n\left(\frac{k}{\sqrt{\alpha}}\right)$ , where  $\mathcal{F}\{g(x)\}$  denotes the Fourier transform of a function  $g(x)$ .

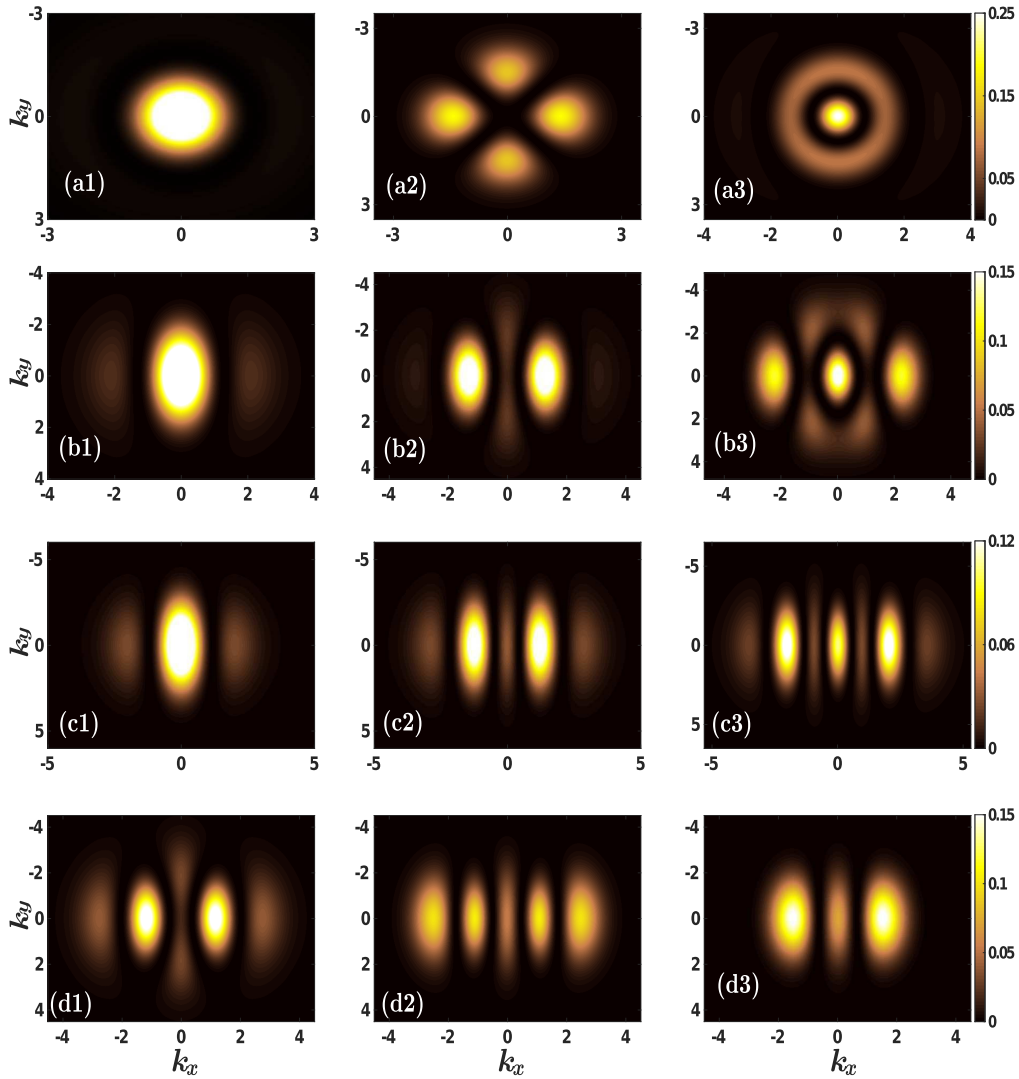


FIG. 5. Momentum distributions  $|\Psi_{\text{rel},j}(k_x, k_y)|^2$  for  $\alpha = 1.1$  [(a) series],  $\alpha = 2.5$  [(b) series], and  $\alpha = 5$  [(c) series]. The subindices (1, 2, 3) stand for the ground, first, and second excited states, respectively. All cases refer to interaction strength  $g = 1$ .  $|\Psi_{\text{rel},2}(k_x, k_y)|^2$  of the first excited state ( $j = 2$ ) for  $\alpha = 2.5$  at (d1)  $g = -1$ , (d2)  $g = -0.1$ , and (d3)  $g = 0.1$ . For all observables, dimensionless units are adopted.

summation of Eq. (25) for high energies  $\mathcal{E}$  (i.e., higher excited states) stems from higher order Hermite polynomials which are responsible for the observed multihump structure of the momentum distribution. Note also that for larger values of  $\alpha$ , a similar structure of the momentum distribution occurs as described in Figs. 5(c1)–5(c3) (not shown here for brevity). The momentum distribution of the first excited state ( $j = 2$ )  $|\Psi_{\text{rel},2}(k_x, k_y)|^2$  for  $\alpha = 2.5$  is also presented at  $g = -1$ ,  $g = -0.1$ , and  $g = 0.1$  in Figs. 5(d1)–5(d3). We deduce that as the attraction increases,  $|\Psi_{\text{rel},2}(k_x, k_y)|^2$  becomes more localized toward smaller values of  $k_x$  while its outer humps are depleted; compare Figs. 5(d1) and 5(d2). Also, in the vicinity of  $g = 0$  but on the attractive side,  $|\Psi_{\text{rel},2}(k_x, k_y)|^2$  develops an additional outer hump [Fig. 5(d2)] compared to the momentum distribution for weak repulsions [Fig. 5(d3)]. This is exactly due to the mismatch in the energy  $\mathcal{E}_2$  in the vicinity of zero interactions; see Fig. 2(c).

A more complicated momentum structure of the first excited state ( $j = 2$ ) occurs for  $\alpha = 1.1$ , where  $|\Psi_{\text{rel},2}(k_x, k_y)|^2$  displays a pedal-like structure [Fig. 5(a2)]. We remark that for increasing anisotropy within the interval  $\alpha \in [1.1, 1.9]$ , it is found that this pedal-like distribution becomes fainter along  $k_y$  and more squeezed in the  $k_x$  direction (not shown here). Moreover, these pedal patterns approach the origin, i.e.,  $k_x = k_y = 0$  for  $\alpha \rightarrow 1.9$ . Let us also note that the energy of the first excited state at  $\alpha = 1.1$  and  $g = 1$  ( $E = 3.14633$ ) is close to the energy of a fermionic state with odd  $n, m$  in the expression  $E = n + \alpha m + \frac{\alpha+1}{2}$  ( $E = 3.15$ ). As  $\alpha$  increases in the interval  $\alpha \in [1.1, 1.9]$ , the energy of the first excited state at  $g = 1$  deviates significantly from the energy of the energetically closest fermionic state. The momentum distribution of the fermionic state exhibits also a pedal structure similar to the one presented in Fig. 5(a2) but with a nodal line at  $k_x = 0$  and  $k_y = 0$ . For  $\alpha = 1.9$ ,  $|\Psi_{\text{rel},2}(k_x, k_y)|^2$  shows a behavior

similar to the one displayed in Fig. 5(b2) for  $\alpha = 2.5$ . At this value of  $\alpha = 2.5$ ,  $|\Psi_{\text{rel},3}(k_x, k_y)|^2$  of the second excited state ( $j = 3$ ) [Fig. 5(b3)] exhibits populated tails for large  $k_y$  values. As  $\alpha$  increases, these tails of the momentum distribution, in the  $k_y$  direction, are suppressed and become apparent only for higher lying excited states (not shown here for brevity).

## V. ONE-BODY DENSITIES

Having at hand the two-boson wave function for an arbitrary anisotropy parameter enables us to access all the properties of the system. As a case example, we shall investigate the corresponding one-body densities  $\rho^{(1)}(x_1, y_1)$  for several states and anisotropies. The one-body density of two bosons reads [73]

$$\rho^{(1)}(x_1, y_1) = \int dx_2 dy_2 |\Psi_{\text{c.m.}}[X(x_1, x_2), Y(y_1, y_2)] \Psi_{\text{rel}}[x(x_1, x_2), y(y_1, y_2)]|^2. \quad (26)$$

For the relative coordinate wave function, we employ the expansion of Eq. (21). The center-of-mass wave function resides in its ground state, as was discussed in Sec. II. To perform the integral appearing in Eq. (26), we utilize the coordinate transformations of the center-of-mass and relative coordinates, and therefore express all variables in terms of the positions of the two bosons. In this way, the one-body density reads

$$\begin{aligned} \rho^{(1)}(x_1, y_1) &= \frac{B^2 \alpha^{3/2}}{\pi^3} e^{-(x_1^2 + \alpha y_1^2)} \sum_{n,m} f(n) f(m) \overbrace{\int_{-\infty}^{+\infty} dy_2 e^{-\alpha y_2^2} H_n\left(\sqrt{\alpha} \frac{y_1 - y_2}{\sqrt{2}}\right) H_m\left(\sqrt{\alpha} \frac{y_1 - y_2}{\sqrt{2}}\right)}^J \\ &\quad \times \int_{-\infty}^{+\infty} dx_2 e^{-x_2^2} U\left(\frac{\alpha m - \mathcal{E}}{2}, \frac{1}{2}, \frac{(x_1 - x_2)^2}{2}\right) U\left(\frac{\alpha n - \mathcal{E}}{2}, \frac{1}{2}, \frac{(x_1 - x_2)^2}{2}\right), \end{aligned} \quad (27)$$

with  $f(n) = \frac{H_n(0) \Gamma(\frac{\alpha n - \mathcal{E}}{2})}{2^{n+1} \Gamma(n+1)}$ . The first integral denoted by  $J$  can be calculated analytically by using the transformation  $y_2 \rightarrow \sqrt{\alpha} y_2$ , and subsequently the substitution  $y_2 = y_1 \sqrt{\alpha} - y_2$  [72]. Then, the integral is

$$J = \frac{\sqrt{\pi}}{\sqrt{\alpha}} \sum_{k=0}^{\min(n,m)} 2^k k! \binom{m}{k} \binom{n}{k} \frac{1}{2} \frac{m+n-k}{2} H_{m+n-2k}(y_1 \sqrt{\alpha}). \quad (28)$$

Figure 6 illustrates the one-body densities of the bound, ground, first excited, and second excited states at  $g = 1$  when  $\alpha = 1.1$  [Figs. 6(a1)–6(a4)],  $\alpha = 2.5$  [Figs. 6(b1)–6(b4)], and  $\alpha = 5$  [Figs. 6(c1)–6(c4)]. If  $\alpha \approx 1$ ,  $\rho^{(1)}(x, y)$  of the higher lying excited states [Figs. 6(a2)–6(a4)] tends to show an almost isotropic distribution along the  $x$  and  $y$  directions. On the other hand, for a large anisotropy parameter  $\alpha$ , the 1D limit is approached and therefore  $\rho^{(1)}(x, y)$  becomes more elongated in the  $x$  direction [Figs. 6(c1)–6(c4)]. Indeed, as the anisotropy  $\alpha$  increases, the one-body densities of the ground and higher excited states develop a prominent two-hump structure in the elongated  $x$  direction; see, for instance, Figs. 6(c2)–6(c4), where  $\alpha = 5$ . This is reminiscent of the behavior of the one-body densities of two bosons confined in a 1D harmonic trap [54,56]. Entering the intermediate anisotropy regime, e.g.,  $\alpha = 2.5$  [Figs. 6(b1)–6(b4)],  $\rho^{(1)}(x, y)$  exhibits population tails along the  $y$  direction as well. The two-hump structure of  $\rho^{(1)}(x, y)$  is present in the ground [Fig. 6(b2)] and the first excited [Fig. 6(b3)] states, but disappears in the second excited state [Fig. 6(b4)] and in higher excited states as well (not shown). However, for small anisotropies [Figs. 6(a1)–6(a4)],  $\alpha = 1.1$ , the one-body density resembles the structure of the corresponding pure 2D case [55]. The only exception is the first excited state [Fig. 6(a3)], which features a small density dip at the center  $x = y = 0$ . Recall that this latter state corresponds to the pedal-like structure of the momentum distribution depicted in Fig. 5(a2). Finally, the one-body density of the bound states [Figs. 6(a1), 6(b1), and 6(c1)] is

more elongated in the  $x$  direction and somewhat localized near the origin,  $x = y = 0$ . The latter is due to the fact that the bound state is strong in the repulsive interaction regime, as was discussed in Sec. III (see Fig. 2).

## VI. TAN CONTACTS

In Sec. III, it was argued that at interparticle distances much smaller than  $l_x$ , the two-boson wave function develops a logarithmic divergence. This behavior is caused by the contact interaction in 2D, see also Eq. (2), which can also be expressed as a boundary condition for the wave function at zero interparticle distances [74,75], where the Tan contact is defined [76–82]. In this section, we measure the Tan contact as a function of the anisotropy parameter  $\alpha$  for various eigenstates and several interaction strengths.

The Tan contact,  $\mathcal{D}$ , is defined from the momentum distribution in the limit of very large momenta, namely  $|\Psi(k)|^2 \xrightarrow{k \rightarrow \infty} \frac{\mathcal{D}}{k^4}$ , in all dimensions [79,83,84]. Since the wave function at small interparticle distances depends only on the radius  $r^2 = x^2 + y^2$  [see also Eq. (12)], and the Tan contact is determined by the behavior of the wave function at  $r \rightarrow 0$  [60],  $\mathcal{D}$  is isotropic; i.e., it does not depend on the  $x$  or  $y$  direction. The contact reads (for details, see Appendix C)

$$\mathcal{D}(\alpha, \mathcal{E}) = \frac{B^2(\alpha, \mathcal{E})}{4\pi^4}. \quad (29)$$

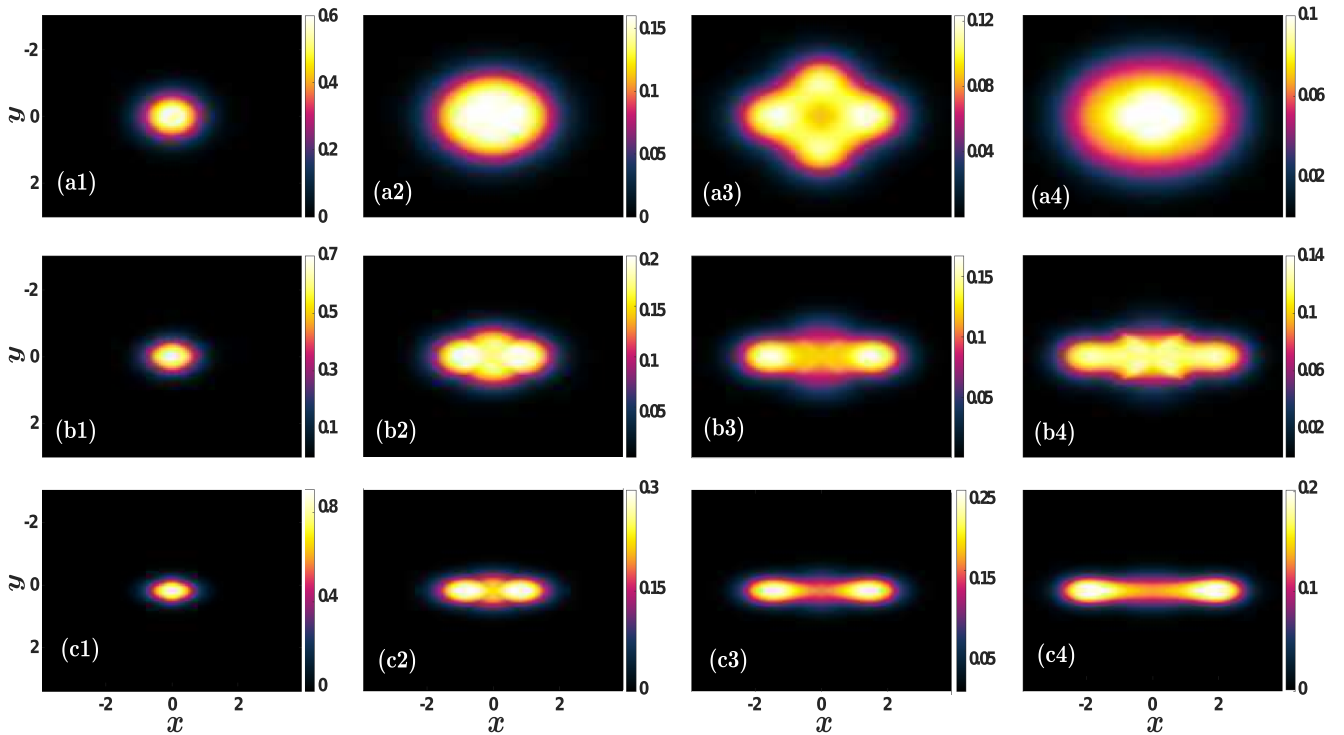


FIG. 6. One-body densities,  $\rho^{(1)}(x_1, y_1)$  for  $\alpha = 1.1$  [(a) series],  $\alpha = 2.5$  [(b) series], and  $\alpha = 5$  [(c) series]. The subscripts (1, 2, 3, 4) refer to the bound, ground, first excited, and second excited states respectively. In all cases, the interparticle interaction strength is  $g = 1$ . All quantities shown are in dimensionless units.

Therefore, this Tan contact is essentially defined by the normalization constant  $B(\alpha, \mathcal{E})$  of the wave function [Eq. (22)] and refers to the two-body state, which is in turn characterized by the anisotropy parameter  $\alpha$  and the energy  $\mathcal{E}$ . In the quasi-1D limit, i.e.,  $\alpha \gg 1$ , we obtain the following relation (for details, see Appendix C):

$$\mathcal{D}_{2D} = l_y \sqrt{\pi} \mathcal{D}_{1D}. \quad (30)$$

As a consequence, the 2D and the 1D contacts are linked via a geometric factor  $\sqrt{\pi}$  and the harmonic oscillator length of the strongly confined direction. Note that the three-dimensional contact is also related to the lower dimensional ones through specific geometric factors and the oscillator lengths in the tightly confined directions [15,27,28]. In what follows, we shall explore  $\mathcal{D}(\alpha, \mathcal{E})$  rescaled by the factor  $1/l_y$  (or  $\sqrt{\alpha}$  in harmonic oscillator units) in order to expose the connection between the contacts in 1D and 2D, and subsequently showcase the saturation of the  $\mathcal{D}_{2D}$  for large values of  $\alpha$  toward the value of the 1D contact.

Figure 7 depicts  $\sqrt{\alpha} \mathcal{D}(\alpha, \mathcal{E}_0)$  of the bound states with respect to  $\alpha$ , for both repulsive [Fig. 7(a)] and attractive [Fig. 7(b)] interaction strengths. We observe that for increasing  $\alpha$ , and independent of the interaction strength, the contact takes larger values and does not saturate. This enhancement of two-body short-range correlations is attributed to the fact that the bound states in the repulsive and attractive regimes become more deeply bound as the anisotropy increases; see also Fig. 2. Furthermore, at fixed anisotropy  $\alpha$  and weak interparticle interactions [Fig. 7(a)], the contact is enhanced compared to the one for larger interaction strengths. This can be explained from the fact that the bound state diverges for

weak repulsive interactions [see Figs. 2(a)–2(f)] and therefore the degree of short-range correlations is enhanced. On the contrary, for attractive interactions [Fig. 7(b)], the contact increases as the interactions become more attractive, while  $\alpha$  is kept fixed. Indeed, inspecting Figs. 2(a)–2(f) reveals that for a stronger attraction the contribution of the bound state becomes substantial.

The rescaled contact  $\sqrt{\alpha} \mathcal{D}(\alpha, \mathcal{E}_1)$  of the ground state as a function of the anisotropy parameter  $\alpha$  is illustrated in Fig. 8 for various repulsive [Fig. 8(a)] and attractive [Fig. 8(b)] interactions. As can be seen, in contrast to Fig. 7,  $\sqrt{\alpha} \mathcal{D}(\alpha, \mathcal{E}_1)$  features an initial growth and then it saturates to a value that is proportional to the 1D contact [Eq. (30)] for all coupling strengths. Initially at  $\alpha = 1$ , the contact possesses a higher value for strong repulsions [82]; see Fig. 8(a). However, this behavior is reversed as the anisotropy increases, and  $\sqrt{\alpha} \mathcal{D}(\alpha, \mathcal{E}_1)$  acquires larger values for weaker repulsive interactions; compare, for instance,  $g = 1$  and  $g = 3$  in Fig. 8(a) for  $\alpha \geq 5$ . This latter feature is better visualized in the inset of Fig. 8(a), where  $\sqrt{\alpha} \mathcal{D}(\alpha, \mathcal{E}_1)$  is showcased within the anisotropy interval  $\alpha \in [1, 3]$  and the aforementioned inverted behavior occurs at  $\alpha \simeq 2$ . Indeed, for increasing  $\alpha$ , we enter deep into the quasi-1D regime and therefore one should use the corresponding 1D interaction strength related to its 2D counterpart via Eq. (18). This relation maps the repulsive 2D interactions to attractive 1D interactions for large values of the anisotropy  $\alpha$ . For instance, Eq. (18) provides the mapping  $g_{2D} = (1, 3, 20, 50) \mapsto g_{1D} = (-6.403, -5.045, -4.628, -4.588)$  for  $\alpha = 10$ . Similarly, for attractive interactions, an increasing behavior of the short-range two-body correlations as captured by  $\sqrt{\alpha} \mathcal{D}(\alpha, \mathcal{E}_1)$

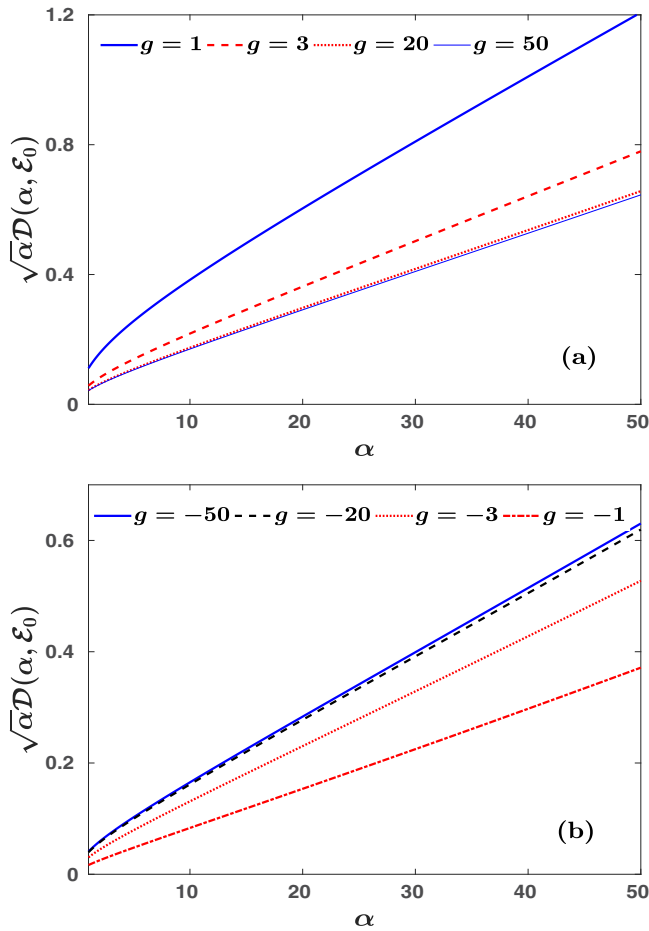


FIG. 7. Rescaled Tan contact  $\sqrt{\alpha}\mathcal{D}(\alpha, \mathcal{E}_0)$  of the bound state at various (a) repulsive and (b) attractive interaction strengths (see legends) for increasing anisotropy parameter  $\alpha$ . In all cases, the quantities displayed are in dimensionless units.

occurs and then a tendency of saturation is observed independently of the coupling strength [Fig. 8(b)]. When  $\alpha$  is fixed,  $\sqrt{\alpha}\mathcal{D}(\alpha, \mathcal{E}_1)$  acquires larger values for a stronger attraction. Here, Eq. (18) maps the strong 2D attraction to the strong 1D attraction for large anisotropies. Explicitly, this mapping reads  $g_{2D} = (-50, -20, -3, -1) \mapsto g_{1D} = (-4.535, -4.496, -4.162, -3.542)$  for  $\alpha = 10$ .

Another interesting observation is that  $\sqrt{\alpha}\mathcal{D}(\alpha, \mathcal{E}_1)$  shows a peak within  $\alpha \in [2, 4]$ ; see Figs. 8(a) and 8(b). Indeed, for a small anisotropy parameter the energy of the ground state,  $\mathcal{E}_1$ , increases in both the repulsive and attractive interaction regimes for larger  $\alpha$  satisfying  $\alpha \in [2, 4]$ . Hence, the Tan contact is also enhanced in this  $\alpha$  interval. Note also that  $\sqrt{\alpha}\mathcal{D}(\alpha, \mathcal{E}_1)$  for fixed  $\alpha$  becomes smaller [larger] for increasing repulsive [attractive] 2D coupling strength; see Figs. 8(a) and 8(b). However, if  $\alpha$  exceeds a critical value depending on  $g$ , we approach the quasi-1D region and Eq. (18) maps the 2D to the 1D coupling strength. In particular, for  $\alpha \in [2, 6]$ , the 1D coupling becomes less attractive, acquiring larger negative values for increasing  $\alpha$ . Hence, qualitatively  $\sqrt{\alpha}\mathcal{D}(\alpha, \mathcal{E}_1)$  initially increases up to a point where the crossover to 1D starts to become important and then it decreases similarly to the absolute value of  $g_{1D}$  [83]. Subsequently, the 1D attraction

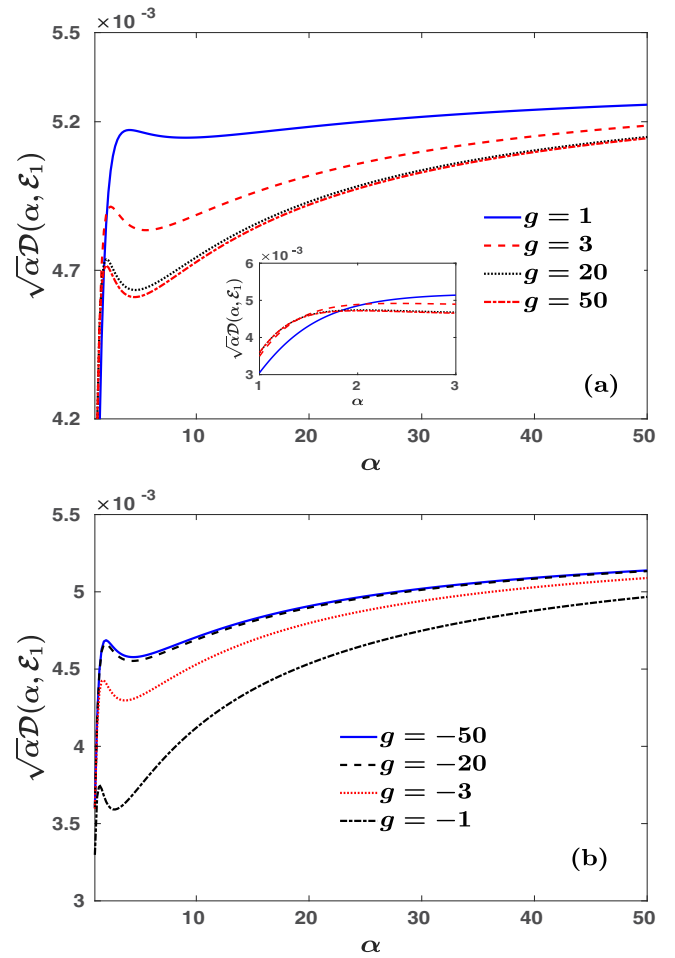


FIG. 8. Rescaled Tan contact  $\sqrt{\alpha}\mathcal{D}(\alpha, \mathcal{E}_1)$  of the ground states at different (a) repulsive and (b) attractive interactions (see legends) for varying anisotropy  $\alpha$ . The inset in panel (a) presents a magnification of  $\sqrt{\alpha}\mathcal{D}(\alpha, \mathcal{E}_1)$  within the anisotropy interval  $\alpha \in [1, 3]$ . For all observables, dimensionless units are adopted.

is enhanced and the contact increases up to its saturation value.

## VII. INTERACTION QUENCH DYNAMICS

### A. Time evolution of the wave function

Having analyzed the stationary properties of the two-boson system in the dimensional crossover from 2D to 1D, we next proceed by investigating the resulting interaction quench dynamics of this setup for a fixed anisotropy parameter  $\alpha$  and different postquench 2D interaction strengths  $g$ . As already discussed in Sec. II, the center-of-mass wave function  $\Psi_{\text{c.m.}}(X, Y)$  [Eq. (4)] lies in the ground state and thus it is not affected by the interaction quench. Therefore, the center-of-mass wave function does not play any role in the description of the interaction quench dynamics and it will not be considered in the following analysis.

To be more precise, in order to study the dynamics, the system is initially prepared in an eigenstate  $|\Psi_{\text{rel},i}^{\text{in}}(x, y; 0)\rangle$  at an initial interaction strength  $g_i^{\text{in}}$  with energy  $\mathcal{E}_i^{\text{in}}$  and at  $t = 0$  this coupling strength is suddenly changed (quenched)

to a final (postquench) value  $g$ . Then, the time evolution of the initial wave function reads

$$\begin{aligned} |\Psi_{\text{rel},i}^{\text{in}}(x, y; t)\rangle &= e^{-i\hat{H}t} |\Psi_{\text{rel},i}^{\text{in}}(x, y; 0)\rangle \\ &= \sum_j e^{-i\mathcal{E}_j t} |\Psi_{\text{rel},j}^f(x, y)\rangle \underbrace{\langle \Psi_{\text{rel},j}^f(x, y) | \Psi_{\text{rel},i}^{\text{in}}(x, y; 0)\rangle}_{d_{i,j}}, \end{aligned} \quad (31)$$

where the summation is performed over the eigenstates of the postquench Hamiltonian  $|\Psi_{\text{rel},j}^f(x, y)\rangle$  with energy  $\mathcal{E}_j$ . The underlying overlap coefficients,  $d_{i,j}$ , are determined by employing the ansatz introduced in Eq. (5) as well as the orthonormality of the noninteracting wave functions  $\phi_n(x)$  and have the form

$$\begin{aligned} d_{i,j} &= \frac{B_i B_j}{\mathcal{E}_i^{\text{in}} - \mathcal{E}_j} \sqrt{\frac{\alpha}{\pi}} \sum_{m \geq 0} \frac{H_m^2(0)}{2^{m+1} m!} \\ &\times \left[ \frac{\Gamma\left(\frac{\alpha m - \mathcal{E}_i^{\text{in}}}{2}\right)}{\Gamma\left(\frac{1 + \alpha m - \mathcal{E}_i^{\text{in}}}{2}\right)} - \frac{\Gamma\left(\frac{\alpha m - \mathcal{E}_j}{2}\right)}{\Gamma\left(\frac{1 + \alpha m - \mathcal{E}_j}{2}\right)} \right]. \end{aligned} \quad (32)$$

These overlap coefficients between the initial wave function,  $\Psi_{\text{rel},i}^{\text{in}}(x, y; 0)$ , and a final eigenstate,  $\Psi_{\text{rel},j}^f(x, y)$ , determine the degree of participation of this postquench eigenstate in the dynamics.

### B. Dynamical response of the system

A well-known observable of interest that enables us to identify the dynamical response of the system to its external perturbation, herein an interaction quench, is the fidelity. The latter is defined by the overlap between the time-evolved and the initial wave functions [57,85–88], namely

$$F(t) = \langle \Psi_{\text{rel},i}^{\text{in}} | e^{-i\hat{H}t} | \Psi_{\text{rel},i}^{\text{in}} \rangle = \sum_j e^{-i\mathcal{E}_j t} |d_{i,j}|^2. \quad (33)$$

Evidently,  $F(t)$  is tailored to estimate the instantaneous deviation of the system from its initial state. Below, in order to capture the mean dynamical response of the system after a quench, we invoke the time-averaged fidelity i.e.,  $|\bar{F}| = \lim_{T \rightarrow \infty} \frac{1}{T} \int_0^T dt |F(t)|$ .

The resulting  $|\bar{F}|$  following an interaction quench from the ground state either at  $g^{\text{in}} = -1$  to repulsive postquench interactions is shown in Fig. 9(a) or at  $g^{\text{in}} = 1$  toward the attractive regime is depicted in Fig. 9(b) for various anisotropies, namely  $\alpha = 2, 6.5$  and  $50$ . In both quench scenarios and for all displayed anisotropies,  $|\bar{F}|$  drops from unity by developing a characteristic dip in the vicinity of zero postquench interactions, indicating that the system is significantly perturbed for these values of  $g$ . However,  $|\bar{F}|$  tends to approach values close to unity for large attractive or repulsive postquench interaction strengths  $g$ , evincing that the system remains close to its initial state. The above-described behavior of  $|\bar{F}|$  indicates the fact that the time-evolved two-body state in the vicinity of zero interactions is a nontrivial superposition containing many postquench eigenstates. However, for quenches to strong attractive or repulsive interactions, the system populates a much

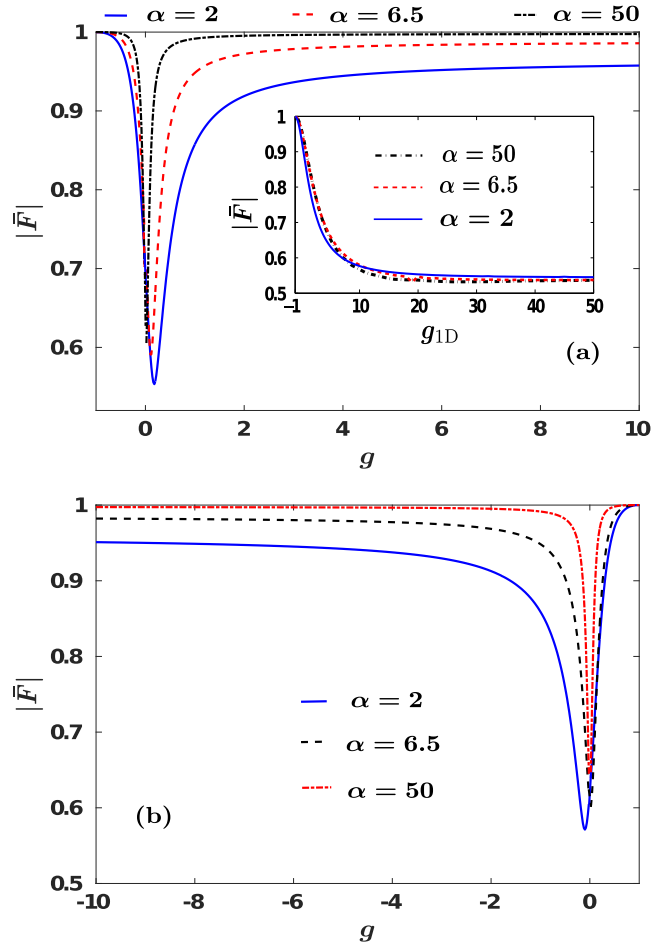


FIG. 9. Time-averaged fidelity  $|\bar{F}|$  as a function of the 2D interaction strength  $g$  for various anisotropies (see legends). (a) The dynamics is triggered by following an interaction quench from the ground state of the system with  $g^{\text{in}} = -1$  to larger interactions. (Inset)  $|\bar{F}|$  following a quench from  $g_{\text{1D}}^{\text{in}} = -1$  to larger 1D interactions for different anisotropies (see legend). (b) The quench is applied from the ground state of the two bosons with  $g^{\text{in}} = 1$  to smaller values of the interaction strengths. All quantities shown are in dimensionless units.

smaller amount of postquench eigenstates and thus deviates from the initial state to a lesser extent compared to the  $g = 0$  case. For instance, the initial state  $E_1$  at  $g^{\text{in}} = -1$  is energetically close to the postquench  $E_1$  at  $g > 1$  and therefore this eigenstate predominantly contributes to the time-evolved wave function. This is in contrast to, e.g., the case of a quench to  $g = 0$  where both the  $E_0$  and  $E_1$  postquench eigenstates are energetically close to the initial  $E_1$ . The explicit contribution of the postquench eigenstates will be discussed below in detail.

The width of the aforementioned dip of  $|\bar{F}|$  becomes more narrow as  $\alpha$  increases and its location is displaced toward zero postquench interactions. Also, the minimum value of  $|\bar{F}|$  in the region of the dip increases for a larger anisotropy. Interestingly, for large postquench attractive or repulsive interactions, e.g.,  $|g| = 8$  in Figs. 9(a) and 9(b), the system deviates more from its initial configuration as the anisotropy  $\alpha$



becomes smaller. Furthermore, in both quench scenarios, as  $\alpha$  increases,  $|\bar{F}|$  tends to saturate close to unity for smaller interaction strengths  $g$ ; see Figs. 9(a) and 9(b). This latter behavior stems from the underlying energy spectrum presented in Fig. 2 and the associated energy gaps. Indeed, as the anisotropy increases, the saturation of the energies to their values at  $g = 0$  occurs at smaller attractive or repulsive interactions. Therefore, by decreasing the anisotropy of the 2D system, we can drive it out of equilibrium in a more efficient manner.

To further expose the interplay between the 2D and the 1D effective coupling constants, we showcase in the inset of Fig. 9(a) the dependence of  $|\bar{F}|$  on  $g_{1D}$  for distinct values of  $\alpha$ . Here, the explicit relation between the  $g_{2D}$  and the  $g_{1D}$  [Eq. (18)] has been used. As before, initially,  $g_{1D}^{\text{in}} = -1$  and the interaction quench is performed toward the repulsive regime. In all cases, i.e., independently of  $\alpha$ ,  $|\bar{F}|$  exhibits a decreasing tendency for increasing  $g_{1D}$  until it approaches a fixed value for large  $g_{1D}$ . Recall that the energy spacings among the involved eigenstates in 1D [Fig. 1(b)] saturate only for very large attractive or repulsive interactions and thus  $|\bar{F}|$  tends to a constant value after  $g_{1D} > 20$ . For these values of  $g_{1D}$ , we approach the strongly interacting regime and the (time-averaged) overlap of the time-dependent two-body state with the initial one is very small [54]. It is also worth mentioning that the deviation of  $|\bar{F}|$  between  $\alpha = 6.5$  and  $\alpha = 50$  is very small. However, for  $\alpha = 2$ , where the quasi-1D limit is not well established,  $|\bar{F}|$  differs noticeably, e.g., from the case of  $\alpha = 6.5$ . Note again that the quasi-1D limit is adequately approached for  $\alpha > 10$ ; see also Fig. 1(b). Therefore, the involved energy spacings which are considerably different between  $\alpha = 2$  [Fig. 2(b)],  $\alpha = 6.5$  [Fig. 2(e)], and  $\alpha = 50$  result in the observed discrepancy of  $|\bar{F}|$  between the aforementioned values of  $\alpha$ .

### C. Dynamics of the position variance along each spatial direction

Because of the considered anisotropy of the 2D harmonic trap, different frequencies will be excited along the two spatial directions after the quench, thus yielding a much richer dynamics compared to the purely isotropic case, as has been reported in several experiments with anisotropic 3D traps [33]. To study the excitations in the different spatial directions of the trap, we resort to the frequency spectra of the spatial extent of the relative wave function along the  $x$  and  $y$  directions [86,89,90]. The instantaneous spatial extent of the two-boson cloud in each spatial direction is given by the respective variances

$$\langle x^2(t) \rangle = \int_{-\infty}^{\infty} dx dy x^2 |\Psi_{\text{rel},i}^{\text{in}}(x, y; t)|^2, \quad (34)$$

$$\langle y^2(t) \rangle = \int_{-\infty}^{\infty} dx dy y^2 |\Psi_{\text{rel},i}^{\text{in}}(x, y; t)|^2. \quad (35)$$

These observables allow us to monitor the expansion and contraction of the bosonic cloud in the course of the time evolution and also to identify the frequencies of the participating modes in the dynamics along each spatial direction. This can be achieved by utilizing the frequency spectra of

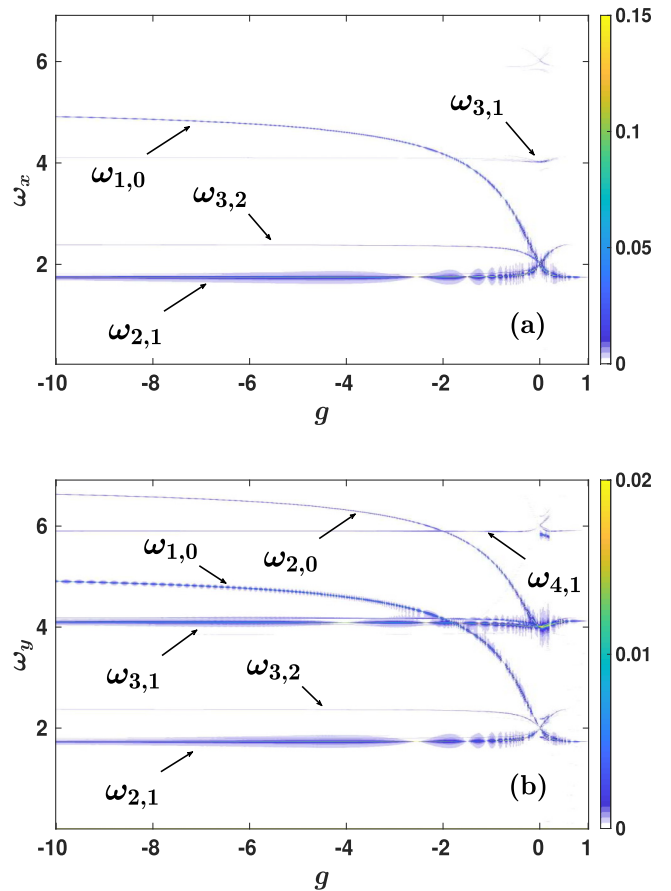


FIG. 10. Frequency spectrum (a)  $F(\omega_x)$  of  $\langle x^2(t) \rangle$  and (b)  $F(\omega_y)$  of  $\langle y^2(t) \rangle$ . The anisotropy of the system is  $\alpha = 2$  and the interaction quench is performed from the ground state at  $g^{\text{in}} = 1$  to various attractive final interactions. The identified energy differences,  $\omega_{ij}$ , corresponding to the observed frequency branches are also shown. In all cases, the quantities displayed are in dimensionless units.

$\langle x^2(t) \rangle$  and  $\langle y^2(t) \rangle$ , namely  $F(\omega_x) = \frac{1}{\sqrt{2\pi}} \int_{-\infty}^{\infty} dt e^{i\omega_x t} \langle x^2(t) \rangle$  and  $F(\omega_y) = \frac{1}{\sqrt{2\pi}} \int_{-\infty}^{\infty} dt e^{i\omega_y t} \langle y^2(t) \rangle$ , respectively.

Case examples of the above-mentioned frequency spectra are provided in Fig. 10 for  $\alpha = 2$  and in Fig. 11 for  $\alpha = 6.5$ , upon applying an interaction quench from the ground state at  $g^{\text{in}} = 1$  toward the attractive interaction regime. Note that the emergent frequencies stem from the energy difference between specific eigenstates of the postquench Hamiltonian and will be denoted in the following as  $\omega_{i,j} = \mathcal{E}_i - \mathcal{E}_j$  [54,55,89]. Moreover, the amplitude of these frequencies suggests their degree of participation in the time evolution, which can be explicitly measured via the respective overlap coefficients [Eq. (32)]. The latter essentially means that a relatively large [small] amplitude of  $\omega_{i,j}$  indicates a dominant [suppressed] contribution of the involved eigenstates. Regarding the motion of the bosons along the  $x$  direction, we calculate the frequency spectrum  $F(\omega_x)$ ; see Fig. 10(a). In the attractive interaction regime, there is a dominant frequency marked as  $\omega_{2,1}$ , which corresponds to the energy difference between the ground and first excited states. Indeed, by calculating the corresponding overlap coefficients [Eq. (32)] for attractive postquench interactions, it turns out that the final ground state ( $E_1$ ) possesses

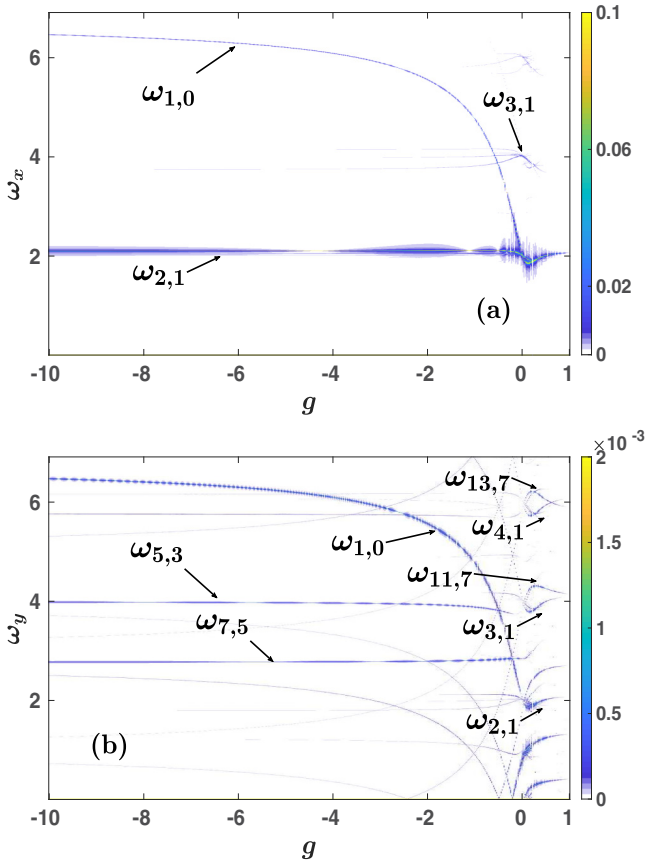


FIG. 11. Frequency spectrum (a)  $F(\omega_x)$  of  $\langle x^2(t) \rangle$  and (b)  $F(\omega_y)$  of  $\langle y^2(t) \rangle$ . The anisotropy of the system is  $\alpha = 6.5$  following an interaction quench from the ground state at  $g^{\text{in}} = 1$  to different attractive final interactions. Specific energy differences,  $\omega_{ij}$ , referring to the observed frequency branches are also depicted. All quantities shown are in dimensionless units.

the largest population, while the next-to-leading-order occupied one is the first excited state ( $E_2$ ). Additionally, there are two other frequencies denoted by  $\omega_{1,0}$  and  $\omega_{3,2}$  possessing a relatively much smaller amplitude than  $\omega_{2,1}$ . These frequencies refer to the energy differences between the bound and ground states and between the second excited and first excited states, respectively. Close to zero postquench interactions, all these frequencies approach  $\omega_x \simeq 2$ . The latter can be easily deduced by inspecting the corresponding energy spectrum at  $\alpha = 2$  [see Fig. 2(b)], where the energy spacing is uniform at zero interactions in contrast to the nonuniform energy gaps appearing in both the repulsive and the attractive interaction regimes. Furthermore, in the vicinity of  $g = 0$ , another frequency contributes to the spectrum of  $\langle x^2(t) \rangle$ , namely  $\omega_{3,1}$ , whose amplitude decreases substantially for attractive as well as repulsive interactions.

Entering the repulsive interaction regime, we observe that mainly two frequencies dominate, i.e.,  $\omega_{2,1}$  and  $\omega_{3,2}$ . Note that  $\omega_{2,1}$  has a larger amplitude since it corresponds to the energy difference between the ground and first excited states, which are the most significantly occupied states in this postquench interaction regime. Turning to the dynamical evolution in the  $y$  direction, the spectrum  $F(\omega_y)$  is presented in Fig. 10(b).

Evidently, a larger number of frequencies are involved in the dynamics, but with an amplitude being an order of magnitude smaller than the corresponding ones in the  $x$  direction. The latter is attributed to the fact that the variance in the  $y$  direction, which is tightly confined by the harmonic trap, is smaller compared to the one in the elongated  $x$  direction. To qualitatively explain the larger number of frequencies along the  $y$  direction, one can resort to an analytic expression for  $F(\omega_y)$  and  $F(\omega_x)$ , namely

$$F(\omega_x) = \frac{B^2 \sqrt{2\alpha}}{4\pi} \sum_{i,j} \delta[\omega_x - \omega_{i,j}] \mathcal{A}_x(i, j), \quad (36)$$

$$F(\omega_y) = \frac{B^2 \sqrt{2}}{4\alpha^{5/2} \pi} \sum_{i,j} \delta[\omega_y - \omega_{i,j}] \mathcal{A}_y(i, j). \quad (37)$$

For the detailed derivation of these spectra as well as the explicit expressions of the involved amplitudes  $\mathcal{A}_x(i, j)$  and  $\mathcal{A}_y(i, j)$ , see Appendix D. It is worth mentioning here that both  $\mathcal{A}_x(i, j)$  and  $\mathcal{A}_y(i, j)$  depend on  $\omega_{i,j}$ . Closely comparing  $\mathcal{A}_x(i, j)$  and  $\mathcal{A}_y(i, j)$  (see also Appendix D), we can deduce that for  $(i, j) = (1, 2)$   $\mathcal{A}_x(i, j) \gtrsim \mathcal{A}_y(i, j)$  is satisfied, while for all other pairs  $i \neq j > 2$  it holds that  $\mathcal{A}_y(i, j) > \mathcal{A}_x(i, j)$ . The latter means that a larger number of frequencies contributes to  $\mathcal{A}_y(i, j)$  than  $\mathcal{A}_x(i, j)$  and especially the higher order ones possess a vanishing contribution to  $\mathcal{A}_x(i, j)$ . In particular, for attractive interactions there are predominantly four contributing frequencies, namely  $\omega_{2,1}$  and  $\omega_{3,1}$ , which stem from the energy difference between the ground and the first and second excited states, respectively. Also, the frequencies  $\omega_{1,0}$  and  $\omega_{2,0}$  are imprinted in the spectrum and refer to the energy difference between the bound state and the ground and first excited states, respectively. Near the noninteracting regime,  $g = 0$ , two more frequencies appear, i.e.,  $\omega_{4,1}$  and  $\omega_{3,2}$  [hardly visible in Fig. 10(b)]. Note that at  $g = 0$  all three frequencies,  $\omega_{2,1}$ ,  $\omega_{3,2}$ , and  $\omega_{1,0}$  merge to  $\omega_y \simeq 2$ ; see also the previous discussion. However, on the repulsive regime, essentially two frequencies dominate, i.e.,  $\omega_{2,1}$  and  $\omega_{3,1}$ .

The frequency spectra of  $\langle x^2(t) \rangle$  and  $\langle y^2(t) \rangle$  for a larger anisotropy  $\alpha = 6.5$  and for the same interaction quench scenario as before are illustrated in Fig. 11. Along the  $x$  direction [Fig. 11(a)] and for interparticle attractions, the most prominent frequency corresponds to the energy difference between the ground and first excited states i.e.,  $\omega_{2,1}$ . In terms of the involved overlap coefficients, these two states have the dominant contribution during the dynamics. There is also another frequency, stemming from the energy difference of the bound and the ground states,  $\omega_{1,0}$ , which becomes more prominent close to zero postquench interactions. This frequency possesses a larger value compared to the corresponding one for  $\alpha = 2$  [see also Fig. 10(a)], since the energy difference between the two involved states grows with increasing anisotropy parameter, as shown explicitly in Fig. 3(b). For  $g \approx 0$ , there is an additional frequency present, namely  $\omega_{3,1}$ , which disappears for attractive as well as repulsive interactions. The frequencies regarding the dynamics along the  $y$  direction [Fig. 11(b)] are fainter than the respective ones in the  $x$  direction by almost two orders of magnitude.

Moreover for attractive interactions, more frequencies are involved in the dynamics in the strongly confined direction,

with the most prominent one stemming from the energy difference between the ground and bound states,  $\omega_{1,0}$ . In the vicinity of zero interactions, there is a multitude of frequencies referring to the energy difference between the ground and higher excited states such as  $\omega_{2,1}$  and  $\omega_{4,1}$ , as well as frequencies stemming from higher lying energy eigenstates, e.g.,  $\omega_{11,7}$  and  $\omega_{13,7}$ . The larger number of frequencies in the  $y$  direction and their smaller amplitude compared to the ones appearing along the  $x$  direction can be explained with the same reasoning applied to Fig. 10(b); see in particular the discussion in the context of Eq. (37). Note here that some of the frequencies depicted in Fig. 11(b) have a very small amplitude and are not identified by specific energy differences between the eigenstates of the system. A further increase of

the anisotropy parameter  $\alpha$  essentially freezes out the motion along the  $y$  direction and the frequencies involved in the dynamics become fainter (not shown for brevity). The most prominent frequency that remains is the energy difference between the bound and ground states in the attractive regime.

#### D. One-body density evolution

To unveil the dynamical spatial redistribution of the two bosons, subjected to an interaction quench, from a single-particle perspective we inspect their reduced one-body density, which can be experimentally probed [13,73]. In particular, the time evolution of the one-body reduced density starting from a state characterized by energy  $\mathcal{E}_i^{\text{in}}$  at  $g^{\text{in}}$  toward  $g$  reads

$$\begin{aligned} \rho^{(1)}(x_1, y_1; t) = & \left( \frac{\sqrt{\alpha}}{\pi} \right)^3 e^{-(x_1^2 + \alpha y_1^2)} \sum_{j,j'} e^{i(\mathcal{E}_j - \mathcal{E}_{j'})t} B_j B_{j'} d_{i,j} d_{i,j'}^* \sum_{n,m} \frac{H_n(0) H_m(0)}{2^{n+m+2} n! m!} \\ & \times \Gamma\left(\frac{\alpha n - \mathcal{E}_j}{2}\right) \Gamma\left(\frac{\alpha m - \mathcal{E}_{j'}}{2}\right) \int_{-\infty}^{\infty} dy_2 e^{-\alpha y_2^2} H_n\left(\sqrt{\alpha} \frac{y_1 - y_2}{\sqrt{2}}\right) H_m\left(\sqrt{\alpha} \frac{y_1 - y_2}{\sqrt{2}}\right) \\ & \times \int_{-\infty}^{\infty} dx_2 e^{-x_2^2} U\left(\frac{\alpha n - \mathcal{E}_j}{2}, \frac{1}{2}, \frac{(x_1 - x_2)^2}{2}\right) U\left(\frac{\alpha m - \mathcal{E}_{j'}}{2}, \frac{1}{2}, \frac{(x_1 - x_2)^2}{2}\right). \end{aligned} \quad (38)$$

Figures 12 and 13 display snapshots of the reduced one-body density for a quench from the ground state at  $g^{\text{in}} = 1$  to  $g = -0.2$  for  $\alpha = 2$  and 6.5 respectively. We remark that the postquench interaction is close to the noninteracting regime where the time-evolved state deviates significantly from the initial one; see also Fig. 9(b). Also, the depicted time instants correspond to the timescales set by the prevalent frequencies in the dynamics of the  $x$  and  $y$  direction variances identified in Figs. 10 and 11. These frequencies are the energy differences between the predominantly contributing postquench eigen-

states in the dynamics of the system as it can also be verified by calculating the respective overlap coefficients [Eq. (32)].

Referring to the case of  $\alpha = 2$  (Fig. 12), we observe the appearance of two-humped structures in both the  $x$  and  $y$  directions; see, for instance, Figs. 12(a), 12(b), 12(c), and 12(e). The appearance of these hump patterns is predominantly attributed to the participation of the postquench eigenstates,  $E_1$  [Fig. 10(j)] and  $E_2$  [Fig. 10(k)] during the dynamics. Notably the eigenstate with energy  $E_2$  has a relatively much smaller impact on the shape of  $\rho^{(1)}(x_1, y_1; t)$  compared to one with

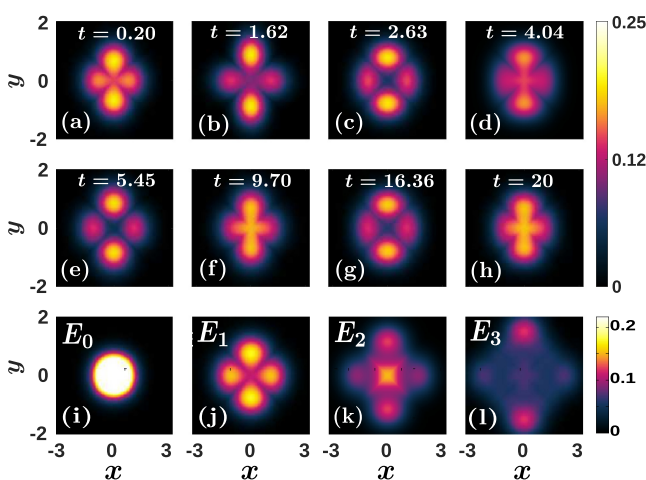


FIG. 12. [(a)–(h)] Instantaneous one-body density following an interaction quench from the ground state at  $g^{\text{in}} = 1$  to  $g = -0.2$ . [(i)–(l)] One-body density of the dominantly populated postquench eigenstates in the time evolution. The system consists of two bosons and the anisotropy of the 2D harmonic trap is  $\alpha = 2$ . For all observables, dimensionless units are adopted.

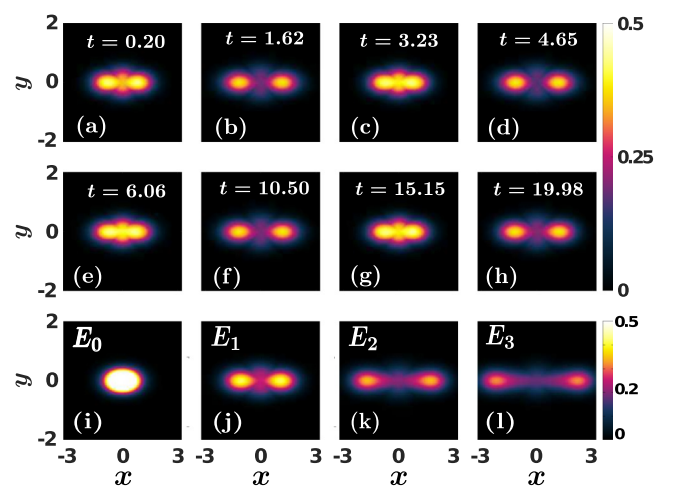


FIG. 13. [(a)–(h)] Snapshots of the one-body density after an interaction quench from the ground state at  $g^{\text{in}} = 1$  to  $g = -0.2$ . [(i)–(l)] One-body density of the dominantly contributing postquench eigenstates during the dynamics. The anisotropy of the 2D harmonic trap is  $\alpha = 6.5$ . All quantities shown are in dimensionless units.

energy  $E_1$ , a result that is also confirmed by inspecting the corresponding overlap coefficients since  $d_{1,1} \gg d_{1,2}$ . However, during the contraction of the bosonic cloud, the two-hump structure is destroyed by means of a smoothing of the density profile and the development of a crosslike pattern [Figs. 12(f) and 12(h)]. This structural change of  $\rho^{(1)}(x_1, y_1; t)$  is caused by the predominant contribution of the postquench bound state with energy  $E_0$  [Fig. 10(i)], whose presence is manifested in the contraction of the cloud. Note that the contraction of the bosons is identified by inspecting the time evolution of  $\langle x^2(t) \rangle$  and  $\langle y^2(t) \rangle$  (not shown for brevity). In particular, when  $\langle x^2(t) \rangle$  and  $\langle y^2(t) \rangle$  experience minima [maxima], the bosons feature a contraction [expansion]. Moreover, the two-hump structure shown in the one-body density [Figs. 12(b), 12(c) and 12(e)] is associated with the expansion of the cloud, a result that can again be confirmed from the dynamics of  $\langle x^2(t) \rangle$  and  $\langle y^2(t) \rangle$ .

For a larger anisotropy, e.g.,  $\alpha = 6.5$  shown in Fig. 13, the motion along the  $y$  direction is frozen out, as anticipated by the frequency spectra presented in Fig. 11(b). Thus, the single-particle density evolution takes place predominantly along the  $x$  direction and corresponds to a breathing dynamics. Indeed, when the density expands, there is a two-hump structure [see Figs. 13(b), 13(d) and 13(f)], while for a contraction in the  $x$  direction [see Figs. 13(c), 13(e) and 13(g)] the two-hump pattern disappears and the density dip around the trap center is filled. Again, the contraction and expansion of the two bosons is identified by inspecting the minima and maxima of  $\langle x^2(t) \rangle$  and  $\langle y^2(t) \rangle$  after the quench. We finally remark that the time-evolved state resides mainly in a superposition of the bound state,  $E_0$  [Fig. 13(i)], and the ground state,  $E_1$  [Fig. 13(j)]. This fact is verified by calculating the corresponding overlap coefficients [Eq. (32)] and it is also readily supported by comparing the instantaneous  $\rho^{(1)}(x_1, y_1; t)$  with the  $\rho^{(1)}(x_1, y_1; 0)$  of the corresponding postquench eigenstates. Other energetically higher lying excited states have a much smaller contribution in the time-evolved two-body state and thus their impact is less obvious in  $\rho^{(1)}(x_1, y_1; t)$ ; see, e.g., Figs. 13(k) and 13(l) for  $E_2$  and  $E_3$  respectively.

### VIII. SUMMARY AND OUTLOOK

We have investigated the stationary properties and the interaction quench dynamics of two bosons confined in an anisotropic 2D harmonic trap and interacting through an  $s$ -wave pseudopotential. A transcendental equation with respect to the anisotropy parameter is derived, giving access to the energy spectrum of the system. The spectrum is in turn explored for a wide range of attractive and repulsive 2D coupling strengths and arbitrary values of the anisotropy.

It is found that the energy spacing between the involved energy eigenstates for a fixed interaction strength strongly depends on the anisotropy. Deep in the quasi-1D regime, where the anisotropy is very large, the energy spectrum of the purely 1D setup is retrieved. Importantly, a relation is established between the 2D and 1D scattering lengths. Moreover, we have derived an analytical expression for the two-boson wave function both in real and momentum space. It is shown that for interparticle distances much smaller than the harmonic oscillator length in the less tightly confined direction, the wave function exhibits a logarithmic singularity, a feature which is

inherently related to two spatial dimensions. In momentum space, the wave function exhibits a multihump structure along the weaker confined direction with the humps being elongated along the other direction. This latter behavior becomes more prominent as the anisotropy increases. The corresponding one-body densities feature a two-hump structure along the spatial direction where the confinement is less tight, a behavior that is more pronounced for a larger anisotropy. For higher lying excited states, the interhump separation is enhanced.

Subsequently we have investigated the Tan contact, which captures short-range two-body correlations, for different anisotropies in both the repulsive and the attractive interaction regimes. Inspecting the contact of the bound state reveals an increasing tendency for larger anisotropies independently of the sign of the interaction and does not saturate as the quasi-1D region is approached. Furthermore, the short-range two-body correlations of the ground state increases for small anisotropies and subsequently saturates for larger ones. Within the quasi-1D regime, a relation is established among the 2D and 1D contacts, unveiling that they are proportional by a geometric factor and the harmonic oscillator length along the strongly confined direction.

Apart from the stationary properties, we have also examined the dynamical evolution of the system by applying an interaction quench for different anisotropies. Employing the time-averaged fidelity of the system, we have showcased that the time-evolved state deviates significantly from the initial one in the vicinity of zero postquench interactions while it is less perturbed for stronger postquench interactions. Moreover, for increasing anisotropy, the system becomes less perturbed after an interaction quench of fixed amplitude in both the attractive and the repulsive coupling regimes. The quench excites a breathing motion in both the  $x$  and  $y$  directions, with a distinct number of participating frequencies in each spatial direction. At large anisotropies, the motion along the  $y$  direction freezes out, and there are many eigenstates contributing in the dynamics, with the most prominent one being the bound state. The dynamical response is also visualized on the one-body level, by monitoring the evolution of the reduced one-body density after an interaction quench in the vicinity of zero interactions, where the time-evolved state deviates substantially from the initial one. For small anisotropies, the bosonic cloud undergoes a periodic expansion and contraction dynamics in both spatial directions, with the appearance of a two-hump structure building upon the one-body density in both the  $x$  and  $y$  spatial directions. An increasing anisotropy causes density oscillations and the development of two humps along the less tight direction, while the motion in the tightly confined direction is frozen out.

There are several research directions that one can pursue in future works. A straightforward extension is to perform a quench of the anisotropy parameter and investigate the resulting nonequilibrium dynamics of the two-bosons from the 2D plane to the quasi-1D regime and vice versa. Here, it is interesting to inspect how efficiently one can populate specific eigenstates since this quench changes the energy gaps between the various states. Another prospect is to consider a long-range interaction between the atoms, such as a dipolar coupling, in order to study how the long-range character affects the energy spectra and also the nonequilibrium

dynamics. Finally, the extension to three interacting bosons in an anisotropic 2D trap and exploring their stationary and dynamical properties is certainly of interest. The latter endeavor can shed light, e.g., into the dynamical formation of trimer bound states.

### ACKNOWLEDGMENTS

G.B. and S.I.M. would like to thank A. I. Karanikas for fruitful discussions regarding the integral formulas. G.B. kindly acknowledges financial support by the State Graduate Funding Program Scholarships (HmbNFG). S.I.M. gratefully acknowledges financial support in the framework of the Lenz-Ising Award of the Department of Physics of the University of Hamburg. This work was supported within the framework of the PIER Hamburg-MIT Germany program funded by the Ministry of Science, Research, and Equalities of the Free and Hanseatic City of Hamburg. P.S. gratefully acknowledges financial support by the Deutsche Forschungsgemeinschaft (DFG) in the framework of the SFB 925 ‘‘Light-induced dynamics and control of correlated quantum systems’’ (DFG No. 170620586).

### APPENDIX A: TRANSCENDENTAL EQUATION FOR THE RELATIVE ENERGIES

In this Appendix, the transcendental equation for determining the energy of two bosons confined in a 2D harmonic trap with anisotropy parameter  $\alpha$  is derived. When we plug Eq. (11) into Eq. (10) and perform the change of variables  $z = e^{-t}$  in  $I(f(E)/2)$ , the equation that determines the energy of the system reads

$$-\gamma + \ln L + \ln 2 + \sqrt{\alpha} \int_0^{e^{-L}} dz \frac{z^{f(E)/2-1}}{\sqrt{1-z}\sqrt{1-z^\alpha}} = \ln(a_{2D}^2). \quad (\text{A1})$$

As has already been remarked in Sec. II, the integral appearing in the general form of the wave function [Eq. (9)] converges for  $f(E) > 0$ , which corresponds to eigenstates with energy lower than  $\frac{\alpha+1}{2}$ . To extend Eq. (A1) to energies larger than the zero-point oscillation energy, we shall use the following relation that the integral  $I(f(E)/2)$  satisfies:

$$I(f(E)/2) = I(\alpha + f(E)/2) + \int_0^{e^{-L}} dz \frac{z^{f(E)/2-1}\sqrt{1-z^\alpha}}{\sqrt{1-z}}. \quad (\text{A2})$$

The latter integral can be performed analytically, if the term  $\sqrt{1-z^\alpha}$  is expanded as a Taylor series yielding

$$I\left(\frac{f(E)}{2}\right) = I\left(\alpha + \frac{f(E)}{2}\right) + \sum_{n=0}^{\infty} \binom{1/2}{n} \frac{\sqrt{\pi}(-1)^n \Gamma\left(\frac{f(E)}{2} + \alpha n\right)}{\Gamma\left(\frac{1}{2} + \frac{f(E)}{2} + \alpha n\right)}. \quad (\text{A3})$$

The last point that one needs to take care of is the divergence of the integral  $I(f(E)/2)$  as  $L \rightarrow 0$ . This divergence turns out to be logarithmic and it can be extracted from the following

integral

$$I\left(\frac{f(E)}{2}\right) = -\frac{\ln L}{\sqrt{\alpha}} + \int_0^1 dz \ln(1-z)\varphi'\left(z, \frac{f(E)}{2}\right), \quad (\text{A4})$$

where  $\varphi(z, \frac{f(E)}{2}) = z^{f(E)/2-1} \frac{\sqrt{1-z}}{\sqrt{1-z^\alpha}}$  and the differentiation is with respect to the variable  $z$ . Moreover, the first term cancels exactly the term  $\ln L$  present in the transcendental Eq. (A1). We can further express Eq. (A1) in the form

$$-\gamma + 2 \ln 2 + \sqrt{\alpha} \int_0^1 dz \ln(1-z)\varphi'\left(z, \frac{f(E)}{2}\right) = -\frac{1}{g}. \quad (\text{A5})$$

The latter is exactly the transcendental equation that we are seeking. We remark that Eq. (A3) extends the validity of Eq. (A5) to  $f(E) < 0$ , determining thus completely the relative energy of the two bosons.

### APPENDIX B: RETRIEVING THE 1D SPECTRUM

To recover the well-known 1D energy spectrum from the transcendental Eq. (A5), we assume that  $\alpha \gg 1$ . In this case, one can separate the integral  $I(\frac{f(E)}{2})$  into two parts, namely

$$I\left(\frac{f(E)}{2}\right) = \underbrace{\int_0^\theta dx \frac{x^{f(E)/2-1}}{\sqrt{1-x}}}_{I_1} + \underbrace{\int_\theta^{e^{-L}} dx \frac{1}{\sqrt{1-x}\sqrt{1-x^\alpha}}}_{I_2}, \quad (\text{B1})$$

where  $\theta$  is a parameter very close to unity, such that  $\frac{1}{\sqrt{1-x^\alpha}} \leq 1 + \epsilon$  on the interval  $[0, \theta]$ , with  $\epsilon \ll 1$ . In this case,  $\theta = 1 - \frac{k}{\alpha}$ , where  $k \approx 6$  for achieving an accuracy of  $\epsilon \approx 0.001$ . Therefore,  $I_1$  reads

$$I_1 = \sqrt{\pi} \frac{\Gamma\left(\frac{f(E)}{2}\right)}{\Gamma\left(\frac{1}{2} + \frac{f(E)}{2}\right)} - 2\sqrt{\frac{k}{\alpha}} + O(\alpha^{-3/2}), \quad (\text{B2})$$

assuming that  $\theta$  is very close to 1. In the second part,  $I_2$ , the dependence on the energy is dropped, since in this interval  $x$  is very close to unity. Furthermore, the term  $1/\sqrt{1-x^\alpha}$  can be expanded for  $x$  close to unity as follows:

$$\begin{aligned} \frac{1}{\sqrt{1-x^\alpha}} &= \frac{1}{\sqrt{\alpha}\sqrt{1-x}} + \frac{(\alpha-1)\sqrt{1-x}}{4\sqrt{\alpha}} \\ &+ \frac{(\alpha^2+6\alpha-7)(1-x)^{3/2}}{96\sqrt{\alpha}} \\ &+ \frac{(\alpha^3-3\alpha^2-13\alpha+15)(1-x)^{5/2}}{384\sqrt{\alpha}} \\ &+ O\left(\frac{(1-x)^{7/2}}{10240}\right). \end{aligned} \quad (\text{B3})$$

Keeping the first four terms, the integral  $I_2$  becomes

$$I_2 = -\frac{\ln L}{\sqrt{\alpha}} + \frac{\ln(k/\alpha)}{\sqrt{\alpha}} + \frac{k}{4\sqrt{\alpha}} - \frac{k^2}{192\sqrt{\alpha}} - \frac{k^3}{1152\sqrt{\alpha}} + O(\alpha^{-1}). \quad (\text{B4})$$

The other terms are of the order of  $O(\frac{1}{\alpha})$  and for sufficiently large  $\alpha$  become negligible. After we gather the two integrals  $I_1$  and  $I_2$  [Eqs. (B2) and (B4)] together, the transcendental Eq. (A1) becomes

$$-\gamma + \sqrt{\pi\alpha} \frac{\Gamma(\frac{f(E)}{2})}{\Gamma(\frac{1}{2} + \frac{f(E)}{2})} - 2\sqrt{k} + \ln(2k) - \ln(\alpha) + \frac{k}{4} - \frac{k^2}{192} - \frac{k^3}{1152} = \ln(a_{2D}^2). \quad (\text{B5})$$

This expression is the transcendental equation of two bosons deep into the quasi-1D regime.

#### APPENDIX C: THE TAN CONTACT AND ITS QUASI-1D LIMIT

To find the Tan contact, we start from the 2D Fourier transform of a radially symmetric wave function  $\Psi(\rho)$  [55], namely

$$\tilde{\Psi}(k, t) = 2\pi \int_0^\infty d\rho \rho \Psi(\rho, t) J_0(2\pi\rho k), \quad (\text{C1})$$

where  $J_0(x)$  denotes the zeroth-order Bessel function. In our setup, the wave function  $\Psi(x, y)$  is radially symmetric only for small  $x, y$ . Thus, if we restrict the integration at very small values of  $\rho$ , i.e., very large momenta, the contact is obtained from the leading-order term ( $\sim 1/k^2$ ) in the resulting expression [55] and reads

$$\mathcal{D}(\alpha, \mathcal{E}) = \frac{B^2(\alpha, \mathcal{E})}{4\pi^4}. \quad (\text{C2})$$

Moreover, if  $\alpha = 1$ , Eq. (C2) reduces to  $\mathcal{D}(1, \mathcal{E}) = \frac{1}{\pi^3 \psi^{(1)}(-\mathcal{E}/2)}$ , which is the contact of a stationary eigenstate in an isotropic 2D trap [55], and  $\psi^{(1)}(z)$  is the trigamma function [68].

For large  $\alpha$ , i.e., in the quasi-1D regime, only the term  $m = 0$  dominates in the summation of Eq. (22) for the normalization constant  $B$ . Hence, in this case the contact can be written as follows:

$$\frac{B^2(\alpha \gg 1, \mathcal{E})}{4\pi^4} = \frac{1}{\pi^{7/2}} \frac{\Gamma(-\frac{\mathcal{E}}{2} + \frac{1}{2})}{\Gamma(-\frac{\mathcal{E}}{2}) [\psi(\frac{1-\mathcal{E}}{2}) - \psi(-\frac{\mathcal{E}}{2})] \sqrt{\alpha}}. \quad (\text{C3})$$

This form is analogous to the Tan contact for two interacting bosons confined in a 1D harmonic trap [60,84], rescaled by the anisotropy parameter  $\alpha$ . To be more precise, the 1D Tan contact, when adopting the same convention for the Fourier transform as in Eq. (C1), namely  $\tilde{\Psi}(k) = \int_{-\infty}^\infty dx e^{-2\pi i k x} \Psi(x)$ , reads [84]

$$\mathcal{D}_{1D} = \frac{\Gamma(\frac{1}{2} - \epsilon)}{\pi^4 \Gamma(-\epsilon) [\psi(\frac{1}{2} - \epsilon) - \psi(-\epsilon)]}, \quad (\text{C4})$$

where  $\epsilon = \frac{E}{2} - \frac{1}{4}$ , and the energy  $E$  is determined by the transcendental Eq. (16). When restoring the units of the system, a relation is established among the 1D and the 2D contacts, namely

$$\mathcal{D}_{2D} = l_y \sqrt{\pi} \mathcal{D}_{1D}, \quad (\text{C5})$$

which holds in the quasi-1D regime.

#### APPENDIX D: ANALYTICAL EXPRESSION FOR THE FREQUENCY AMPLITUDES OF THE TWO-ATOM VARIANCE

The frequency amplitudes of the spatial extent of the two atoms during the dynamics can be analytically determined, by employing the following expansion of the time-evolved relative wave function in terms of the postquench eigenstates:

$$\Psi_{\text{rel},i}^{\text{in}}(x, y; t) = \sum_j e^{-i\mathcal{E}_j t} \Psi_{\text{rel},j}^f(x, y) d_{i,j}. \quad (\text{D1})$$

Here  $\Psi_{\text{rel},j}^f(x, y)$  are the postquench eigenstates [see also Eq. (21)] with energy  $\mathcal{E}_j = E_j - (\alpha + 1)/2$ . Also,  $d_{i,j}$  denote the overlap coefficients between the postquench and initial eigenstates [Eq. (32)]. By substituting the above relation into  $\langle x^2(t) \rangle = \int_{-\infty}^\infty dx dy x^2 |\Psi_{\text{rel},i}^{\text{in}}(x, y; t)|^2$  and performing the integration over the  $y$  direction, we obtain

$$\langle x^2(t) \rangle = \frac{B^2 \sqrt{\alpha}}{4\pi^{3/2}} \sum_{j,j'} d_{i,j} d_{i,j'} e^{-i(\mathcal{E}_j - \mathcal{E}_{j'})t} \sum_m \frac{H_m^2(0)}{2^m m!} \times \Gamma\left(\frac{\alpha m - \mathcal{E}_j}{2}\right) \Gamma\left(\frac{\alpha m - \mathcal{E}_{j'}}{2}\right) I_{j,j'}^m, \quad (\text{D2})$$

where the last integral reads

$$I_{j,j'}^m = \int_{-\infty}^\infty dx x^2 e^{-x^2} U\left(\frac{\alpha m - \mathcal{E}_j}{2}, \frac{1}{2}, x^2\right) \times U\left(\frac{\alpha m - \mathcal{E}_{j'}}{2}, \frac{1}{2}, x^2\right). \quad (\text{D3})$$

Along the same lines, we can calculate the explicit expression for  $\langle y^2(t) \rangle$ , namely

$$\langle y^2(t) \rangle = \frac{B^2}{4\alpha^{5/2} \pi^{3/2}} \sum_{j,j'} d_{i,j} d_{i,j'} e^{-i(\mathcal{E}_j - \mathcal{E}_{j'})t} \sum_n \frac{H_n^2(0)}{2^n n!} \times \Gamma\left(\frac{n - \mathcal{E}_j}{2\alpha}\right) \Gamma\left(\frac{n - \mathcal{E}_{j'}}{2\alpha}\right) I_{j,j'}^n, \quad (\text{D4})$$

with the latter integral having the form

$$I_{j,j'}^n = \int_{-\infty}^\infty dy y^2 e^{-y^2} U\left(\frac{n - \mathcal{E}_j}{2\alpha}, \frac{1}{2}, y^2\right) \times U\left(\frac{n - \mathcal{E}_{j'}}{2\alpha}, \frac{1}{2}, y^2\right). \quad (\text{D5})$$

Taking the Fourier transform of both  $\langle x^2(t) \rangle$  and  $\langle y^2(t) \rangle$ , we find

$$F(\omega_x) = \frac{B^2 \sqrt{2\alpha}}{4\pi} \sum_{j,j'} \delta[\omega_x - \omega_{j,j'}] \mathcal{A}_x(j, j'), \quad (\text{D6})$$

$$F(\omega_y) = \frac{B^2 \sqrt{2}}{4\alpha^{5/2} \pi} \sum_{j,j'} \delta[\omega_y - \omega_{j,j'}] \mathcal{A}_y(j, j'), \quad (\text{D7})$$

where the energy differences between the initial and the postquench eigenstates are  $\omega_{j,j'} = \mathcal{E}_j - \mathcal{E}_{j'}$ . Importantly, the corresponding amplitudes in the  $x$  and  $y$  spatial directions read

$$\mathcal{A}_x(j, j') = d_{i,j} d_{i,j'} \sum_m \frac{H_m^2(0)}{2^m m!} \Gamma\left(\frac{\alpha m - \mathcal{E}_j}{2}\right) \Gamma\left(\frac{\alpha m - \mathcal{E}_{j'}}{2}\right) I_{j,j'}^m \quad (\text{D8})$$

$$\mathcal{A}_y(j, j') = d_{i,j} d_{i,j'} \sum_n \frac{H_n^2(0)}{2^n n!} \Gamma\left(\frac{n - \mathcal{E}_j}{2\alpha}\right) \Gamma\left(\frac{n - \mathcal{E}_{j'}}{2\alpha}\right) I_{j,j'}^n \quad (\text{D9})$$

Inspecting these amplitudes for fixed  $j, j'$  we can conclude by a direct numerical evaluation that for  $j' = j + 1$  and  $j = 1, 2$ , i.e., the ground and the first excited states, it holds that  $\mathcal{A}_x(j, j') \gtrsim \mathcal{A}_y(j, j')$ . Otherwise, it is found that  $\mathcal{A}_y(j, j') > \mathcal{A}_x(j, j')$ . As a consequence, in this latter case, there is a larger number of participating frequencies in  $F(\omega_y)$  than  $F(\omega_x)$  and therefore in the dynamics of the  $y$  spatial direction. Indeed, by calculating numerically  $\mathcal{A}_y(j, j')$  [ $\mathcal{A}_x(j, j')$ ] it can be shown that higher lying energy states possess a non-negligible [suppressed] contribution.

- 
- [1] I. Bloch, J. Dalibard, and W. Zwerger, *Rev. Mod. Phys.* **80**, 885 (2008).
- [2] D. Blume, *Rep. Prog. Phys.* **75**, 046401 (2012).
- [3] S. Inouye, M. R. Andrews, J. Stenger, H. J. Miesner, D. M. Stamper-Kurn, and W. Ketterle, *Nature (London)* **392**, 151 (1998).
- [4] C. Chin, R. Grimm, P. Julienne, and E. Tiesinga, *Rev. Mod. Phys.* **82**, 1225 (2010).
- [5] A. Görlitz, J. M. Vogels, A. E. Leanhardt, C. Raman, T. L. Gustavson, J. R. Abo-Shaer, A. P. Chikkatur, S. Gupta, S. Inouye, T. Rosenband, and W. Ketterle, *Phys. Rev. Lett.* **87**, 130402 (2001).
- [6] D. S. Petrov, D. M. Gangardt, and G. V. Shlyapnikov, *J. Phys. IV (France)* **116**, 5 (2004).
- [7] K. Merloti, R. Dubessy, L. Longchambon, A. Perrin, P.-E. Pottie, V. Lorent, and H. Perrin, *New J. Phys.* **15**, 033007 (2013).
- [8] I. Boettcher, L. Bayha, D. Kedar, P. A. Murthy, M. Neidig, M. G. Ries, A. N. Wenz, G. Zürn, S. Jochim, and T. Enss, *Phys. Rev. Lett.* **116**, 045303 (2016).
- [9] A. N. Wenz, G. Zürn, S. Murmann, I. Brouzos, T. Lompe, and S. Jochim, *Science* **342**, 457 (2013).
- [10] F. Serwane, G. Zürn, T. Lompe, T. B. Ottenstein, A. N. Wenz, and S. Jochim, *Science* **332**, 336 (2011).
- [11] T. Sowiński and M. Á. García-March, *Rep. Prog. Phys.* **82**, 104401 (2019).
- [12] C. H. Greene, P. Giannakeas, and J. Pérez-Ríos, *Rev. Mod. Phys.* **89**, 035006 (2017).
- [13] Q. Guan, V. Klinkhamer, R. Klemt, J. H. Becher, A. Bergschneider, P. M. Preiss, S. Jochim, and D. Blume, *Phys. Rev. Lett.* **122**, 083401 (2019).
- [14] G. C. Katsimiga, S. I. Mistakidis, G. M. Koutentakis, P. G. Kevrekidis, and P. Schmelcher, *New J. Phys.* **19**, 123012 (2017).
- [15] M. He and Q. Zhou, *Phys. Rev. A* **100**, 012701 (2019).
- [16] M. Olshanii, *Phys. Rev. Lett.* **81**, 938 (1998).
- [17] D. S. Petrov and G. V. Shlyapnikov, *Phys. Rev. A* **64**, 012706 (2001).
- [18] D. S. Petrov, M. Holzmann, and G. V. Shlyapnikov, *Phys. Rev. Lett.* **84**, 2551 (2000).
- [19] L. Pricoupenko, *Phys. Rev. Lett.* **100**, 170404 (2008).
- [20] S. Lammers, I. Boettcher, and C. Wetterich, *Phys. Rev. A* **93**, 063631 (2016).
- [21] B. M. Faigle-Cedzich, J. M. Pawłowski, and C. Wetterich, *arXiv:1910.07365*.
- [22] S. R. Beane and M. Jafry, *J. Phys. B: At. Mol. Opt. Phys.* **52**, 035001 (2019).
- [23] T. Bergeman, M. G. Moore, and M. Olshanii, *Phys. Rev. Lett.* **91**, 163201 (2003).
- [24] E. Haller, M. J. Mark, Russell Hart, J. G. Danzl, L. Reichsöllner, V. Melezhik, P. Schmelcher, and H.-C. Nägerl, *Phys. Rev. Lett.* **104**, 153203 (2010).
- [25] V. S. Melezhik and P. Schmelcher, *Phys. Rev. A* **84**, 042712 (2011).
- [26] P. Giannakeas, F. K. Diakonou, and P. Schmelcher, *Phys. Rev. A* **86**, 042703 (2012).
- [27] M. Valiente, N. T. Zinner, and K. Mølmer, *Phys. Rev. A* **86**, 043616 (2012).
- [28] J. Decamp, M. Albert, and P. Vignolo, *Phys. Rev. A* **97**, 033611 (2018).
- [29] F. F. Bellotti, T. Frederico, M. T. Yamashita, D. V. Fedorov, A. S. Jensen, and N. T. Zinner, *Phys. Rev. A* **87**, 013610 (2013).
- [30] E. Garrido and A. S. Jensen, *Phys. Rev. Res.* **1**, 023009 (2019).
- [31] T. Peppler, P. Dyke, M. Zamorano, I. Herrera, S. Hoinka, and C. J. Vale, *Phys. Rev. Lett.* **121**, 120402 (2018).
- [32] M. Holten, L. Bayha, A. C. Klein, P. A. Murthy, P. M. Preiss, and S. Jochim, *Phys. Rev. Lett.* **121**, 120401 (2018).
- [33] M. Kottke, T. Schulte, L. Cacciapuoti, D. Hellweg, S. Drenkelforth, W. Ertmer, and J. J. Arlt, *Phys. Rev. A* **72**, 053631 (2005).
- [34] V. J. Bolsinger, S. Krönke, and P. Schmelcher, *Phys. Rev. A* **96**, 013618 (2017).
- [35] L. Anderegg, L. W. Cheuk, Y. Bao, S. Burchesky, W. Ketterle, K.-K. Ni, and J. M. Doyle, *Science* **365**, 1156 (2019).
- [36] L. R. Liu, J. D. Hood, Y. Yu, J. T. Zhang, N. R. Hutzler, T. Rosenband, and K.-K. Ni, *Science* **360**, 900 (2018).
- [37] T. Busch, B. G. Englert, K. Rzazewski, and M. Wilkens, *Found. Phys.* **28**, 549 (1997).
- [38] A. Farrell and B. Zyl, *J. Phys. A: Math. Theor.* **43**, 015302 (2009).
- [39] P. Shea, B. Zyl, and R. Bhaduri, *Am. J. Phys.* **77**, 511 (2009).

- [40] Z. Idziaszek and T. Calarco, *Phys. Rev. A* **74**, 022712 (2006).
- [41] Z. Idziaszek and T. Calarco, *Phys. Rev. A* **71**, 050701(R) (2005).
- [42] E. L. Bolda, E. Tiesinga, and P. S. Julienne, *Phys. Rev. A* **68**, 032702 (2003).
- [43] Y. Chen, D.-W. Xiao, R. Zhang, and P. Zhang, *Phys. Rev. A* **101**, 053624 (2020).
- [44] R. Stock, A. Silberfarb, E. L. Bolda, and I. H. Deutsch, *Phys. Rev. Lett.* **94**, 023202 (2005).
- [45] N. T. Zinner, *J. Phys. A: Math. Theor.* **45**, 205302 (2012).
- [46] P. Kościć and T. Sowiński, *Sci. Rep.* **9**, 12018 (2019).
- [47] D. Saraidaris, I. Mitrakos, I. Brouzos, and F. K. Diakonou, [arXiv:1903.08499](https://arxiv.org/abs/1903.08499).
- [48] M. Valiente, *Phys. Rev. A* **100**, 013614 (2019).
- [49] Y. Nishida, *Phys. Rev. A* **97**, 061603(R) (2018).
- [50] L. Pricoupenko, *Phys. Rev. A* **97**, 061604(R) (2018).
- [51] G. Guijarro, A. Pricoupenko, G. E. Astrakharchik, J. Boronat, and D. S. Petrov, *Phys. Rev. A* **97**, 061605(R) (2018).
- [52] Y. Sekino and Y. Nishida, *Phys. Rev. A* **97**, 011602(R) (2018).
- [53] M. Valiente and V. Pastukhov, *Phys. Rev. A* **99**, 053607 (2019).
- [54] L. Budewig, S. I. Mistakidis, and P. Schmelcher, *Mol. Phys.* **117**, 2043 (2019).
- [55] G. Bougas, S. I. Mistakidis, and P. Schmelcher, *Phys. Rev. A* **100**, 053602 (2019).
- [56] L. M. A. Kehrberger, V. J. Bolsinger, and P. Schmelcher, *Phys. Rev. A* **97**, 013606 (2018).
- [57] T. Keller and T. Fogarty, *Phys. Rev. A* **94**, 063620 (2016).
- [58] A. G. Sykes, J. P. Corson, J. P. D’Incao, A. P. Koller, C. H. Greene, A. M. Rey, K. R. A. Hazzard, and J. L. Bohn, *Phys. Rev. A* **89**, 021601(R) (2014).
- [59] J. P. Corson and J. L. Bohn, *Phys. Rev. A* **91**, 013616 (2015).
- [60] J. P. Corson and J. L. Bohn, *Phys. Rev. A* **94**, 023604 (2016).
- [61] M. Á. García March, T. Fogarty, S. Campbell, T. Busch, and M. Paternostro, *New J. Phys.* **18**, 103035 (2016).
- [62] T. N. Ikeda, T. Mori, E. Kaminishi, and M. Ueda, *Phys. Rev. E* **95**, 022129 (2017).
- [63] M. Olshanii and L. Pricoupenko, *Phys. Rev. Lett.* **88**, 010402 (2001).
- [64] L. Pricoupenko and M. Olshanii, *J. Phys. B: At. Mol. Opt. Phys.* **40**, 2065 (2007).
- [65] J. J. Sakurai, *Advanced Quantum Mechanics* (Pearson Education, New Delhi, 2013).
- [66] K. Wódkiewicz, *Phys. Rev. A* **43**, 68 (1991).
- [67] M. E. H. Ismail, *Classical and Quantum Orthogonal Polynomials in One Variable*, Encyclopedia of Mathematics and Its Applications Vol. 98 (Cambridge University Press, Cambridge, UK, 2005).
- [68] M. Abramowitz and I. A. Stegun, *Handbook of Mathematical Functions with Formulas, Graphs, and Mathematical Tables*, Applied Mathematics Series Vol. 55 (National Bureau of Standards, Washington, DC, 1964).
- [69] V. Makhalov, K. Martiyanov, and A. Turlapov, *Phys. Rev. Lett.* **112**, 045301 (2014).
- [70] R. A. Doganov, S. Klaiman, O. E. Alon, A. I. Streltsov, and L. S. Cederbaum, *Phys. Rev. A* **87**, 033631 (2013).
- [71] X.-J. Liu, H. Hu, and P. D. Drummond, *Phys. Rev. B* **82**, 054524 (2010).
- [72] I. S. Gradshteyn and I. M. Ryzhik, *Table of Integrals, Series, and Products* (Academic Press, New York, 2014).
- [73] K. Sakmann, A. I. Streltsov, O. E. Alon, and L. S. Cederbaum, *Phys. Rev. A* **78**, 023615 (2008).
- [74] L. Pricoupenko, *Phys. Rev. A* **83**, 062711 (2011).
- [75] R. Combescot, F. Alzetto, and X. Leyronas, *Phys. Rev. A* **79**, 053640 (2009).
- [76] S. Tan, *Ann. Phys.* **323**, 2952 (2008).
- [77] S. Tan, *Ann. Phys.* **323**, 2971 (2008).
- [78] S. Tan, *Ann. Phys.* **323**, 2987 (2008).
- [79] F. Werner and Y. Castin, *Phys. Rev. A* **86**, 053633 (2012).
- [80] M. Olshanii and V. Dunjko, *Phys. Rev. Lett.* **91**, 090401 (2003).
- [81] R. J. Wild, P. Makotyn, J. M. Pino, E. A. Cornell, and D. S. Jin, *Phys. Rev. Lett.* **108**, 145305 (2012).
- [82] J. T. Stewart, J. P. Gaebler, T. E. Drake, and D. S. Jin, *Phys. Rev. Lett.* **104**, 235301 (2010).
- [83] M. Barth and W. Zwerger, *Ann. Phys.* **326**, 2544 (2011).
- [84] F. T. Sant’Ana, F. Hébert, V. G. Rousseau, M. Albert, and P. Vignolo, *Phys. Rev. A* **100**, 063608 (2019).
- [85] T. Gorin, T. Prosen, T. H. Seligman, and M. Žnidarič, *Phys. Rep.* **435**, 33 (2006).
- [86] T. Plaßmann, S. I. Mistakidis, and P. Schmelcher, *J. Phys. B: At. Mol. Opt. Phys.* **51**, 225001 (2018).
- [87] J. Neuhaus-Steinmetz, S. I. Mistakidis, and P. Schmelcher, *Phys. Rev. A* **95**, 053610 (2017).
- [88] J. Goold, T. Fogarty, N. Lo Gullo, M. Paternostro, and T. Busch, *Phys. Rev. A* **84**, 063632 (2011).
- [89] S. I. Mistakidis, L. Cao, and P. Schmelcher, *J. Phys. B: At. Mol. Opt. Phys.* **47**, 225303 (2014).
- [90] S. I. Mistakidis, G. M. Koutentakis, and P. Schmelcher, *Chem. Phys.* **509**, 106 (2018).



**4.1.3 Few-body correlations in two-dimensional Bose and Fermi ultracold mixtures**

PAPER • OPEN ACCESS

## Few-body correlations in two-dimensional Bose and Fermi ultracold mixtures

To cite this article: G Bougas *et al* 2021 *New J. Phys.* **23** 093022

View the [article online](#) for updates and enhancements.

You may also like

- [Collisional dynamics of a few atom quantum system with tunable interaction](#)  
Neha Singh, Ruhanshi Barad, Shweta et al.
- [Efimov physics: a review](#)  
Pascal Naidon and Shimpei Endo
- [Contact parameters in two dimensions for general three-body systems](#)  
F F Bellotti, T Frederico, M T Yamashita et al.



## PAPER

## Few-body correlations in two-dimensional Bose and Fermi ultracold mixtures

## OPEN ACCESS

RECEIVED  
11 May 2021REVISED  
18 June 2021ACCEPTED FOR PUBLICATION  
24 June 2021PUBLISHED  
14 September 2021

Original content from  
this work may be used  
under the terms of the  
[Creative Commons  
Attribution 4.0 licence](#).

Any further distribution  
of this work must  
maintain attribution to  
the author(s) and the  
title of the work, journal  
citation and DOI.

G Bougas<sup>1,\*</sup>, S I Mistakidis<sup>1</sup> , P Giannakeas<sup>2</sup> and P Schmelcher<sup>1,3</sup> <sup>1</sup> Center for Optical Quantum Technologies, Department of Physics, University of Hamburg, Luruper Chaussee 149, 22761 Hamburg, Germany<sup>2</sup> Max-Planck-Institut für Physik komplexer Systeme, Nöthnitzer Str. 38, D-01187 Dresden, Germany<sup>3</sup> The Hamburg Centre for Ultrafast Imaging, University of Hamburg, Luruper Chaussee 149, 22761 Hamburg, Germany

\* Author to whom any correspondence should be addressed.

E-mail: [gbougas@physnet.uni-hamburg.de](mailto:gbougas@physnet.uni-hamburg.de)**Keywords:** two-dimensional systems, Tan contacts, thermal gases, hyperspherical formalism, Bose and Fermi mixtures, three-body bound states**Abstract**

Few-body correlations emerging in two-dimensional harmonically trapped mixtures, are comprehensively investigated. The presence of the trap leads to the formation of atom-dimer and trap states, in addition to trimers. The Tan's contacts of these eigenstates are studied for varying interspecies scattering lengths and mass ratio, while corresponding analytical insights are provided within the adiabatic hyperspherical formalism. The two- and three-body correlations of trimer states are substantially enhanced compared to the other eigenstates. The two-body contact of the atom-dimer and trap states features an upper bound regardless of the statistics, treated semi-classically and having an analytical prediction in the limit of large scattering lengths. Such an upper bound is absent in the three-body contact. Interestingly, by tuning the interspecies scattering length the contacts oscillate as the atom-dimer and trap states change character through the existent avoided-crossings in the energy spectra. For thermal gases, a gradual suppression of the involved two- and three-body correlations is evinced manifesting the impact of thermal effects. Moreover, spatial configurations of the distinct eigenstates ranging from localized structures to angular anisotropic patterns are captured. Our results provide valuable insights into the inherent correlation mechanisms of few-body mixtures which can be implemented in recent ultracold atom experiments and will be especially useful for probing the crossover from few- to many-atom systems.

**1. Introduction**

The advent of optical tweezers corroborates the experimental realization of few-body ultracold atom settings [1–3] in a controllable manner even at the level of two [4–7], and three [8] atoms. Moreover, advances in the relevant trapping techniques provide an exquisite variability of such systems, e.g. in terms of reduced dimensionality [1, 2] or tunable atomic interactions through Feshbach [9] and confinement induced resonances [10–13]. As such, strongly correlated few-body systems are nowadays accessible with a high fidelity in a prosaic way.

Three-particle systems in two-dimensions (2D) are of particular interest given that they yield insights into the stability properties of 2D gases in terms of their inherent three-body recombination processes [14–16], and are viewed as the fundamental building-blocks for understanding the crossover from few- to many atom systems [17–20]. Also, they constitute the minimal settings containing both two- and three-body correlations whose characteristics are essential for engineering many-body processes [18, 21, 22]. The reduced dimensionality plays a crucial role on the impact of correlations, namely they are more prominent in lower compared to three-dimensions (3D) [23–25]. Conventionally, correlation effects manifest in the asymptotic expansion of the momentum distribution of the one-body reduced density [26, 27] and are consecutively captured by the so-called two- and three-body contacts. The latter are

experimentally probed via radio-frequency spectroscopy, time-of-flight expansion, and subsequent measurement of the structure factor with the aid of Bragg spectroscopy [28–33]. Their investigation sheds light into the microscopic properties of the system, especially the formation of two- [34–37] and three-body bound states (trimers) [27, 34]. Importantly, the two-body contact satisfies universal relations regarding the energy, the two-body loss rate, and the radio-frequency spectra that hold regardless of the statistics and the dimensionality, in few- as well as in many-body settings [38–41].

Three-body correlations on the other hand, captured by the three-body contact, strongly depend on the dimensionality of the system [26, 27]. This behavior is attributed to the presence of the Efimov effect in 3D, which significantly affects the energy spectra of three-body systems [27, 42], and in particular the trimer states [19]. Interestingly, the experimental observation of the three-body contact in 2D settings remains, to the best of our knowledge, yet elusive. The important role of correlations in reduced dimensions however renders its study of immense interest, especially in trapped three-particle systems. This is further corroborated by the investigation of the two-body contact, in strongly interacting harmonically trapped two-component Fermi gases [43, 44], and more recently in a two-component bosonic gas confined in a 2D box potential [45], revealing enhanced two-body correlations in the BEC-BCS crossover.

Particularly, 2D binary set-ups consisting of two identical bosonic or fermionic atoms interacting with a third distinguishable one are known to possess a plethora of trimer states in terms of the 2D scattering lengths among the identical particles (intraspecies) and the two different atoms (interspecies), as well as the mass ratio [46, 47]. This holds in spite of the absence of the Efimov effect [48, 49], which is usually manifested as the appearance of an infinite progression of trimer states. Another crucial property is that when the identical bosons or fermions become heavier than the third particle, ancillary trimer states are created [46, 50]. Generally, studies in 3D have shown that the mass ratio can drastically affect the properties of the three-body complexes allowing, for example, more favorable experimental conditions to observe multiple successive Efimov states [51, 52], or resonant effects that are absent on equal mass three-body collisions [53–58]. Apart from that, the confinement of three-body systems in a 2D harmonic oscillator yields the presence of additional eigenstates in the energy spectrum aside from trimer ones. These consist of a dimer interacting with another trapped atom [17], as well as trap states characterizing three weakly interacting atoms confined in a harmonic potential.

Focusing on the problem of 2D three-particle binary settings, we unveil their emergent few-body correlation characteristics for a wide range of their intrinsic parameters such as the interspecies scattering lengths and the mass ratio, as well as for different particle statistics. An emphasis is placed on the impact of the above-described additional eigenstates originating from the presence of the trap which has not been studied so far [26]. Exploiting the utility of the adiabatic hyperspherical formalism [19, 59, 60], the corresponding few-body correlation measures are constructed and their behavior, as captured by the two- and three-body contacts, is systematically investigated over a vast parameter space which is comprised by the particles' statistics, the 2D scattering lengths and the mass ratio.

In particular, for trimer states we observe the same overall behavior of the corresponding two- and three-body correlations, as was shown in previous studies [26]. However, we explicate that despite the statistics, both the two- and three-body contacts of atom-dimer and trap states display an oscillatory pattern for varying scattering length. This behavior is attributed to the existent avoided-crossings between these two eigenstates in the energy spectra. By considering thermal gases, the amplitude of these oscillations decreases for larger temperatures, a phenomenon that holds equally for the magnitude of two- and three-body correlations. Interestingly, the atom-dimer states provide an upper bound for the two-body contact of all non-trimer states and a semi-analytical prediction is derived within the Jeffreys–Wentzel–Kramers–Brillouin (JWKB) method, regardless of the particle exchange symmetry. Such a bound is absent in the case of three-body correlations. Binary systems with bosonic majority species exhibit overall an increased degree of correlations, due to the existence of three-body ones, being absent in their fermionic counterpart. Moreover, the spatial configuration of the eigenstates is demonstrated via the experimentally accessible one-body reduced density in position space, an observable largely unexplored in 2D three-body systems [61].

This work is arranged as follows. In section 2, the Hamiltonian of the considered mixtures is introduced within the hyperspherical formalism whose main aspects are presented in detail. In section 3 we review the behavior of the adiabatic potential curves stemming from the hyperangular problem and the underlying energy spectra for different scattering lengths and mass ratios. Subsequently, the susceptibility of the contacts is unraveled with respect to the scattering lengths [section 4.1] and the mass ratios [section 4.2]. Furthermore, the spatial configuration of the binary 2D three-body systems is revealed via the reduced one-body density in section 5. We conclude and discuss future perspectives in section 6. Appendix A discusses the boundary condition of two colliding particles within the hyperspherical formalism while appendix B elaborates on the derivation of the reduced one-body density and its asymptotic expansion in

momentum space. Finally, in appendix C an analytic bound is established for the two-body contact of atom-dimer states for all binary mixtures.

## 2. Hamiltonian and hyperspherical framework

In the following, we focus on the three-body collisions of harmonically trapped binary mixtures in 2D. The three-body collisional complex mainly consists of two identical particles of either bosonic or fermionic symmetry and a third distinguishable one where their pairwise interactions are modeled via  $\delta$ -function pseudopotentials. This setup constitutes a straightforward generalisation of the analytically tractable trapped two-body problem [36, 62–64]. These particular considerations permit us to investigate the dependence of two-/three-body correlations on the scattering lengths, the mass ratio of the particles as well as the impact of particle symmetry. In view of the broad parameter space, three-body collisions in 2D are best treated in the theoretical framework of the adiabatic hyperspherical approach. One particular aspect of this method is that the particle symmetry can be postimposed. Therefore, following references [65, 66] the general scope of the hyperspherical approach is presented below whereas the particle symmetry is imposed at the end of this section.

In the laboratory (lab) frame the Hamiltonian of three-particles of mass  $m_i$  ( $i = 1, 2, 3$ ) in a 2D isotropic trap of frequency  $\omega$  reads:

$$\mathcal{H} = \sum_{i=1}^3 \left( -\frac{\hbar^2}{2m_i} \nabla_i^2 + \frac{1}{2} m_i \omega^2 \mathbf{r}_i^2 \right) + \sum_{i<j} V_{ij}(\mathbf{r}_i - \mathbf{r}_j), \quad (1)$$

where  $\mathbf{r}_i$  is the 2D position vector of the  $i$ -th particle with mass  $m_i$ . The regularized pseudopotential describing pairwise  $s$ -wave interactions in 2D [67] is given by

$$V_{ij}(\mathbf{r}_{ij}) = -\frac{\pi \hbar^2 \delta^{(2)}(\mathbf{r}_{ij})}{\mu_{ij} \ln(A\lambda a^{(k)})} \left[ 1 - \ln(A\lambda r_{ij}) r_{ij} \frac{\partial}{\partial r_{ij}} \right], \quad (2)$$

where  $\mathbf{r}_{ij} = \mathbf{r}_i - \mathbf{r}_j$  and the reduced two-body mass is given by  $\mu_{ij} = \frac{m_i m_j}{m_i + m_j}$ . The constant  $A$  is  $A = e^\gamma/2$  where  $\gamma \approx 0.577$  is the Euler–Mascheroni constant. Also,  $\lambda$  serves as an ultraviolet-cutoff for the zero-range pseudopotential and provides an upper bound in momentum, which, however, does not impact any observable [67].  $a^{(k)} \equiv a_{ij}$  refers to the 2D scattering length between the particles  $i$  and  $j$ , labeled in the odd-man-out notation [66]. Note that  $a^{(k)}$  is related to the 3D scattering length,  $a_{3D}^{(k)}$ , via the expression  $a^{(k)} = 2e^{-\gamma} \sqrt{\pi/0.915} l_0^{(k)} \exp\{-\sqrt{\pi/2} l_0^{(k)}/a_{3D}^{(k)}\}$  [68]. Here,  $l_0^{(k)} = \sqrt{\hbar/(\mu_{ij}\omega_z)}$  denotes the harmonic oscillator length in the  $z$ -direction perpendicular to the 2D plane. Experimentally,  $a_{3D}^{(k)}$  can be flexibly tuned by means of Feshbach resonances [9].

The number of degrees of freedom in the Hamiltonian of equation (1) can be reduced by changing from the lab-to the body-frame of reference. This permits us to separate  $\mathcal{H}$  into center-of-mass and relative Hamiltonian contributions. This can be achieved by transforming the lab coordinates  $\mathbf{r}_i$ , with  $i = 1, 2, 3$ , into a set of three equivalent mass-scaled Jacobi vectors [19, 69]. Namely

$$\mathbf{r}_{\text{CM}} = \frac{m_1 \mathbf{r}_1 + m_2 \mathbf{r}_2 + m_3 \mathbf{r}_3}{m_1 + m_2 + m_3}, \quad (3)$$

$$\boldsymbol{\rho}_1^{(k)} = \frac{\mathbf{r}_i - \mathbf{r}_j}{d_k}, \quad (4)$$

$$\boldsymbol{\rho}_2^{(k)} = d_k \left( \frac{m_i \mathbf{r}_i + m_j \mathbf{r}_j}{m_i + m_j} - \mathbf{r}_k \right), \quad (5)$$

where  $d_k^2 = \frac{m_k(m_i+m_j)}{\mu(m_1+m_2+m_3)}$  and  $\mu = \sqrt{\frac{m_1 m_2 m_3}{m_1+m_2+m_3}}$  is the three-body reduced mass. The superscript ( $k = 1, 2, 3$ ) labels the three sets of the relevant Jacobi vectors. The first vector,  $\boldsymbol{\rho}_1^{(k)}$ , links the particle pair  $i - j$  whereas  $\boldsymbol{\rho}_2^{(k)}$  relates the  $k$ -th particle with the center-of-mass of the pair [66], see also figure 1.

The separability of the center-of-mass and relative degrees of freedom permits us to consider that the center-of-mass part of the total wave function, namely  $\Psi_{\text{CM}}(\mathbf{r}_{\text{CM}})$ , resides in its ground state, i.e.  $\Psi_{\text{CM}}(\mathbf{r}_{\text{CM}}) = \sqrt{M\omega/\pi\hbar} e^{-M\omega\mathbf{r}_{\text{CM}}^2/2\hbar}$ , where  $M = m_1 + m_2 + m_3$  is the total mass of the system. However, the relative part of the wave function does not possess a simple expression as for the center-of-mass, since the corresponding Hamiltonian, i.e.  $\mathcal{H}_{\text{rel}}$ , contains all the relevant potential terms. In order to solve the Schrödinger equation of  $\mathcal{H}_{\text{rel}}$  we express the corresponding relative Jacobi vectors, i.e.  $\boldsymbol{\rho}_1^{(k)}$  and  $\boldsymbol{\rho}_2^{(k)}$ , in the hyperspherical coordinates that consist of the hyperradius  $R = \sqrt{(\boldsymbol{\rho}_1^{(k)})^2 + (\boldsymbol{\rho}_2^{(k)})^2}$  and a set of hyperangles

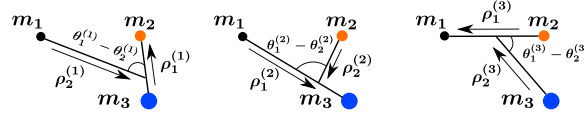


**Figure 1.** Sketch of the three possible sets of Jacobi vectors regarding three distinguishable atoms with masses  $m_1$ ,  $m_2$  and  $m_3$ .  $\theta_{1,2}^{(k)}$  are the polar angles corresponding to the  $\rho_{1,2}^{(k)}$  Jacobi vectors [equation (5)] which connect the atoms  $i$  and  $j$ ,  $\rho_1^{(k)}$ , and their center-of-mass with the third atom  $k$ ,  $\rho_2^{(k)}$ .

$\Omega^{(k)}$  [19, 66]. The hyperradius  $R$  indicates the entire system size whereas  $\Omega^{(k)}$  collectively denotes the hyperangles which track the orientation of the particles on the 2D plane [figure 1]. More specifically,  $\Omega^{(k)} = \{\alpha^{(k)}, \theta_1^{(k)}, \theta_2^{(k)}\}$ , where  $\theta_j^{(k)}$  are the polar angles associated to the  $\rho_j^{(k)}$  Jacobi vectors, and  $\alpha^{(k)}$  characterizes the length ratio between the two Jacobi vectors, i.e.  $\rho_1^{(k)} = R \sin \alpha^{(k)}$  and  $\rho_2^{(k)} = R \cos \alpha^{(k)}$ . The resulting relative Hamiltonian in this coordinate system takes the following form:

$$\mathcal{H}_{\text{rel}} = -\frac{\hbar^2}{2\mu R^{3/2}} \frac{\partial^2}{\partial R^2} R^{3/2} + \frac{3\hbar^2}{8\mu R^2} + \frac{1}{2}\mu\omega^2 R^2 + \mathcal{H}_{\text{ad}}(R; \Omega), \quad (6)$$

$$\mathcal{H}_{\text{ad}}(R; \Omega) = \frac{\hbar^2 \hat{\Lambda}^2}{2\mu R^2} + \sum_{i < j} V_{ij}(R; \Omega^{(k)}), \quad (7)$$

where in equation (6) the first three terms depend only on the hyperradius  $R$ , denoting the kinetic term and the trapping potential, respectively. In equation (7) the first term of  $\mathcal{H}_{\text{ad}}(R; \Omega)$  describes the centrifugal motion of the three particles where the hyperangular operator,  $\hat{\Lambda}^2$ , contains all the hyperangles  $\Omega^{(k)}$ , expressed in any of the three possible configurations  $k = 1, 2, 3$  [70, 71]. The second term of equation (7) refers to the three pairwise interactions which couple the hyperradial and hyperangular degrees of freedom.

In order to solve the corresponding three-body Schrödinger equation of equation (6) we choose the relative three-body wave function to obey the ansatz  $\Psi(R, \Omega) = R^{-3/2} \sum_{\nu} F_{\nu}(R) \Phi_{\nu}(R; \Omega)$ , where the hyperradius  $R$  is treated as an adiabatic parameter. This is the so-called adiabatic hyperspherical representation, where  $F_{\nu}(R)$  and  $\Phi_{\nu}(R; \Omega)$  denote the  $\nu$ -th hyperradial and hyperangular part of  $\Psi(R, \Omega)$ , respectively. In particular, the hyperangular  $\Phi_{\nu}(R; \Omega)$  is obtained by diagonalizing equation (7) at fixed  $R$ . Namely, the corresponding fixed- $R$  hyperangular Schrödinger equation reads:

$$\left[ \frac{2\mu R^2}{\hbar^2} \mathcal{H}_{\text{ad}}(R; \Omega) - (s_{\nu}^2(R) - 1) \right] \Phi_{\nu}(R; \Omega) = 0, \quad (8)$$

where  $s_{\nu}(R)$  indicate the eigenvalues of  $\mathcal{H}_{\text{ad}}(R; \Omega)$  for fixed  $R$ . Note that, in the following, for notation simplicity we drop the  $R$  dependence from the  $s_{\nu}(R) \equiv s_{\nu}$  eigenvalues. In order to tackle the hyperangular Schrödinger equation we exploit the fact that the two-body interactions are  $\delta$ -functions pseudopotentials. This allows us to semi-analytically solve equation (8) by employing the Green's function method [66] together with the corresponding two-body boundary conditions [for details see also appendix A]. Under these considerations, the hyperangular eigenfunction  $\Phi_{\nu}(R; \Omega^{(k)})$  for the  $k'$ -th Jacobi tree of equation (8) takes the form:

$$\begin{aligned} \Phi_{\nu}(R; \Omega^{(k')}) = & -\sum_{k=1}^3 \sum_{l=\pm L} C_{\nu,l}^{(k)}(R) Y_l(\theta_2^{(k)}) Y_0(\theta_1^{(k)}) \cos^{|l|} \alpha^{(k)} \\ & \times {}_2F_1 \left( \frac{\tilde{l} - s_{\nu}}{2}, \frac{s_{\nu} + \tilde{l}}{2}; \tilde{l}; \cos^2(\alpha^{(k)}) \right) \frac{\Gamma \left( \frac{s_{\nu} + \tilde{l}}{2} \right) \Gamma \left( \frac{\tilde{l} - s_{\nu}}{2} \right)}{2\Gamma(\tilde{l})}, \end{aligned} \quad (9)$$

where  ${}_2F_1(a, b; c; z)$  is the Gauss hypergeometric function,  $\Gamma(\cdot)$  is the gamma function [72],  $\tilde{l} = |l| + 1$ ,  $Y_l(\theta_2^{(k)}) = \frac{e^{il\theta_2^{(k)}}}{\sqrt{2\pi}}$  are plane-waves and  $L$  denotes the total angular momentum carried by the system. The sum is over the three possible Jacobi trees  $k = 1, 2, 3$  [see also figure 1], each weighted by the coefficients  $C_{\nu,l}^{(k)}(R)$ . The three Jacobi trees are connected to the specific  $k'$  tree on the left-hand side of equation (9) via a set of geometric relations [73]. It should be noted that by interrelating the  $C_{\nu,l}^{(k)}(R)$  coefficients of different  $k$  the bosonic or fermionic character of the particles can be specified [see also discussion below].

**Table 1.** The interrelation of  $C_{\nu,l}^{(k)}$  coefficients due to particle symmetry and the corresponding scattering lengths  $a^{(k)}$  in the case of two identical spin-polarized fermions (FFX) and two bosons (BBX), together with a third distinguishable particle. The table also connects the odd-man-out and the descriptive notation.

ABC	$C_{\nu,l}^{(1)}$	$a^{(1)}$	$C_{\nu,l}^{(2)}$	$a^{(2)}$	$C_{\nu,l}^{(3)}$	$a^{(3)}$
FFX	$C_{\nu,\pm 1}^{\text{FX}}$	$a_{\text{FX}}$	$-C_{\nu,\pm 1}^{\text{FX}}$	$a_{\text{FX}}$	0	0
BBX	$C_{\nu,0}^{\text{BX}}$	$a_{\text{BX}}$	$C_{\nu,0}^{\text{BX}}$	$a_{\text{BX}}$	$C_{\nu,0}^{\text{BB}}$	$a_{\text{BB}}$

By utilizing the analytic expression for  $\Phi_{\nu}(R; \Omega^{(k)})$  and the two-body boundary conditions we obtain a matrix equation for the  $C_{\nu,l}^{(k)}(R)$  coefficients [for details see also appendix A], which reads

$$\sum_k M_{k'k}^l C_{\nu,l}^{(k)}(R) = 0, \quad (10)$$

$$M_{k'k}^l = \begin{cases} \ln\left(\frac{d_k \text{Re}^{-\gamma}}{a^{(k)}}\right) - \frac{1}{2}\psi\left(\frac{\tilde{l} - s_{\nu}}{2}\right) - \frac{1}{2}\psi\left(\frac{\tilde{l} + s_{\nu}}{2}\right), & k' = k \\ (-1)^l \frac{\Gamma\left(\frac{s_{\nu} + \tilde{l}}{2}\right) \Gamma\left(\frac{\tilde{l} - s_{\nu}}{2}\right)}{2\Gamma(\tilde{l})} f(\beta_{k'k}), & k' \neq k, \end{cases} \quad (11)$$

$$f(\beta_{k'k}) = \cos^{|\tilde{l}|}(\beta_{k'k}) {}_2F_1\left(\frac{\tilde{l} - s_{\nu}}{2}, \frac{s_{\nu} + \tilde{l}}{2}; \tilde{l}; \cos^2 \beta_{k'k}\right), \quad (12)$$

where  $\beta_{k'k} = \arctan\left[\frac{(m_1 + m_2 + m_3)\mu}{m_k m_{k'}}\right]$ ,  $\tilde{l} = |l| + 1$ , and  $\psi(\cdot)$  is the digamma function. The hyperangular eigenvalues  $s_{\nu}$  are obtained by searching for zero-eigenvalues of the matrix  $\mathbf{M}^l$  at fixed  $R$  whereas the elements of the corresponding eigenvector determine the  $C_{\nu,l}^{(k)}(R)$  coefficients [14, 66, 73].

In equations (10) and (11) the particle symmetry is not specified and in principle refer to three-body systems where all particles are distinguishable with each other. As we mentioned at the beginning of this section we are primarily interested in three-body systems where two particles are identical obeying either bosonic or fermionic symmetry and the third one is distinguishable. Equations (10) and (11) in order to be symmetry adapted, additional constraints on the  $C_{\nu,l}^{(k)}$  coefficients must be imposed. Table 1 shows the symmetry adapted  $C_{\nu,l}^{(k)}(R)$  coefficients and the corresponding notation for the scattering lengths  $a^{(k)}$  of two spin-polarized fermions (FF) or two identical bosons (BB) interacting with a third distinguishable atom (X). For example, if the particles (1) and (2) are identical fermions, then only four coefficients are non-zero, namely  $C_{\nu,\pm 1}^{(1)} = -C_{\nu,\pm 1}^{(2)} = C_{\nu,\pm 1}^{\text{FX}}$ , and the third coefficient being zero due to the lack of  $p$ -wave interactions. The latter also implies that the  $s$ -wave interaction between the two fermions is zero, thus  $a_{\text{FF}} = 0$ , yielding thus one scattering length,  $a_{\text{FX}}$ , which describes the interaction between each fermion with the distinguishable atom [see also table 1].

Using the eigenvalues  $s_{\nu}$  and the eigenfunctions  $\Phi_{\nu}(R; \Omega)$  of equation (8), in the three-body Schrödinger equation belonging to the Hamiltonian  $\mathcal{H}_{\text{rel}}$ , and by integrating over all the hyperangular degrees of freedom, a system of coupled one-dimensional ordinary differential equations for the hyperradial degree-of-freedom is obtained.

$$\left\{-\frac{\hbar^2}{2\mu} \frac{d^2}{dR^2} + U_{\nu}(R)\right\} F_{\nu}(R) - \frac{\hbar^2}{2\mu} \sum_{\nu'} \left[2P_{\nu\nu'}(R) \frac{d}{dR} + Q_{\nu\nu'}(R)\right] F_{\nu'}(R) = EF_{\nu}(R). \quad (13)$$

Here,  $F_{\nu}(R)$  is the hyperradial part of the relative three-body wave function,  $U_{\nu}(R)$  indicates the  $\nu$ -th adiabatic potential that includes the trap, whereas the terms  $P_{\nu\nu'}(R)$  and  $Q_{\nu\nu'}(R)$  denote the non-adiabatic coupling matrix elements [19]. More specifically,  $U_{\nu}(R)$ ,  $P_{\nu\nu'}(R)$  and  $Q_{\nu\nu'}(R)$  are given by the following expressions:

$$U_{\nu}(R) = \frac{\hbar^2}{2\mu R^2} \left(s_{\nu}^2 - \frac{1}{4}\right) + \frac{1}{2}\mu\omega^2 R^2, \quad (14)$$

$$P_{\nu\nu'}(R) = \langle \Phi_{\nu}(R; \Omega^{(k)}) | \frac{\partial \Phi_{\nu'}(R; \Omega^{(k)})}{\partial R} \rangle_{\Omega}, \quad (15)$$

$$Q_{\nu\nu'}(R) = \langle \Phi_{\nu}(R; \Omega^{(k)}) | \frac{\partial^2 \Phi_{\nu'}(R; \Omega^{(k)})}{\partial R^2} \rangle_{\Omega}, \quad (16)$$

where the symbol  $\langle \dots \rangle_{\Omega}$  indicates that the integration is over the hyperangles only. Due to the zero-range interactions the  $P_{\nu\nu'}(R)$  and  $Q_{\nu\nu'}(R)$  matrix elements have semi-analytical expressions as shown in

**Table 2.** Representative cases of identical particles with fermionic and bosonic symmetry, which are lighter (LLH), roughly equal in mass (EM) and heavier than a third distinguishable particle (X).

ABC	LLH	EM	HHL
BBX	${}^7\text{Li} - {}^7\text{Li} - {}^{173}\text{Yb}$	${}^7\text{Li} - {}^7\text{Li} - {}^6\text{Li}$	${}^{133}\text{Cs} - {}^{133}\text{Cs} - {}^6\text{Li}$
FFX	${}^6\text{Li} - {}^6\text{Li} - {}^{133}\text{Cs}$	${}^6\text{Li} - {}^6\text{Li} - {}^7\text{Li}$	${}^{173}\text{Yb} - {}^{173}\text{Yb} - {}^7\text{Li}$

references [66, 74, 75]. This particular feature simplifies the numerical diagonalization of equation (13) where the hyperradial solutions  $F_\nu(R)$ , which are expanded in the basis of B-splines [76], obey the vanishing boundary conditions at the origin and asymptotically. The former is a result of the repulsive nature of the  $U_\nu(R)$  potentials at short hyperradii and the latter occurs due to the 2D harmonic trap. We should note that in the following sections and in the appendices the notation  $F_\nu^j(R)$  and  $E^j$  signifies the  $j$ th eigenvector and eigenvalue of equation (13) respectively.

In the following, we will mainly focus on two different types of three-body mixture systems. The first comprises two spin-polarized fermions interacting with a distinguishable particle. It will be termed FFX and exhibits total angular momentum  $L = 1$  with an antisymmetric wave function upon exchange of the two identical fermions i.e.  $L^\pi = 1^-$ , where  $\pi$  is the total parity of the system, a mass ratio  $\mathcal{M} = m_F/m_X$  and scattering length  $a_{FX}$ . The second setup consists of two identical interacting bosons coupled with a third atom. This setting is dubbed BBX and it is characterized by  $L^\pi = 0^+$ , a mass ratio  $\mathcal{M} = m_B/m_X$  as well as two scattering lengths  $a_{BB}$  and  $a_{BX}$  for the identical bosons and between the two different species respectively. For convenience, in the following, we will consider their ratio  $a_{BB}/a_{BX}$  as the relevant interaction parameter. Owing to the spherical symmetry of the interactions the total angular momentum  $L$  is conserved. However, the two-body angular momenta ( $l_1, l_2$ ) that construct the  $L$ -space are also decoupled in our case because we have only considered  $s$ -wave interactions [77]. Hereafter, harmonic oscillator units are adopted, meaning that  $\hbar = \omega = m_{B/F} = 1$ , where  $m_{B/F}$  denotes the mass of the majority species (two identical atoms), unless it is specified otherwise. It is also worth noting that considering a radial trapping frequency of  $\omega = 2\pi \times 20$  Hz, typical in 2D experiments [78, 79], then the harmonic oscillator length takes the values  $a_0 = 4.58, 9.22 \mu\text{m}$  when  ${}^{173}\text{Yb} - {}^{173}\text{Yb} - {}^7\text{Li}$  and  ${}^6\text{Li} - {}^6\text{Li} - {}^{133}\text{Cs}$  FFX settings are considered. Similarly,  $a_0$  takes the values  $a_0 = 5.29, 8.53 \mu\text{m}$  for  ${}^{133}\text{Cs} - {}^{133}\text{Cs} - {}^6\text{Li}$  and  ${}^7\text{Li} - {}^7\text{Li} - {}^{173}\text{Yb}$  BBX systems respectively.

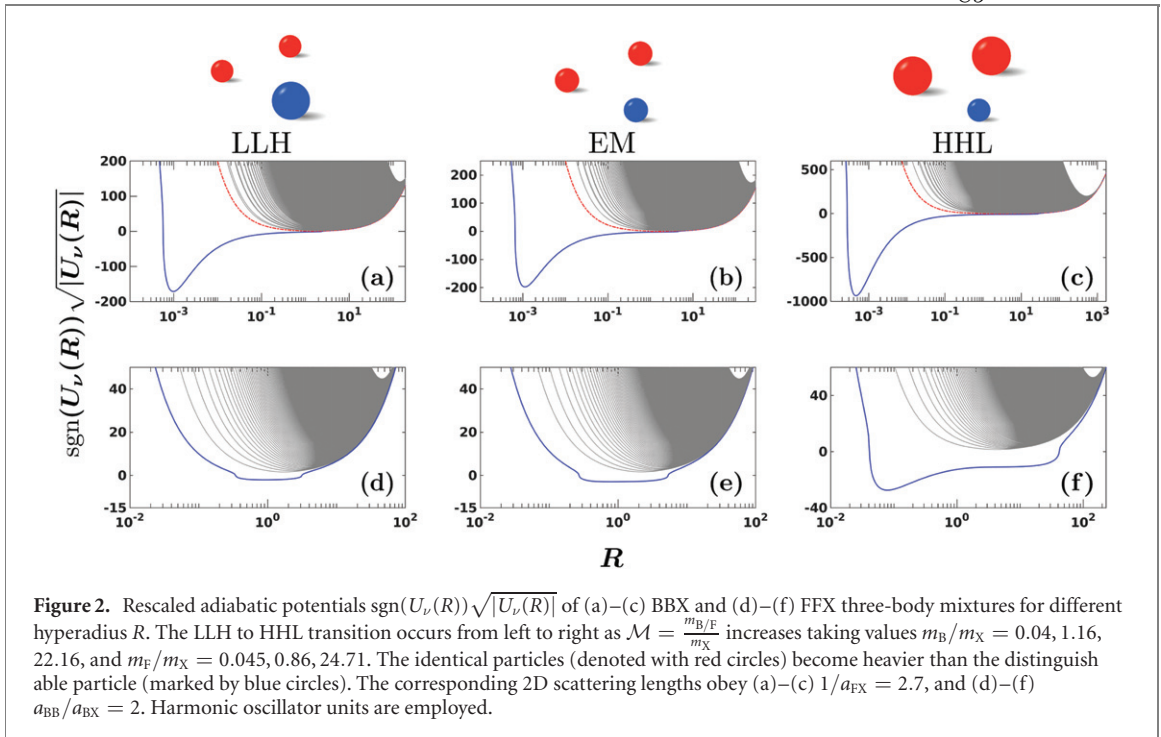
### 3. Adiabatic hyperspherical potentials and energy spectra

To shed light into the eigenspectrum of three-body mixtures and their microscopically allowed processes, in the following, we investigate the potential curves and the corresponding hyperradial spectrum for the FFX and BBX systems. More specifically, we consider three representative cases of different mass ratio, where the two identical particles, with either bosonic or fermionic symmetry, are lighter, roughly equal in mass, and heavier than the third distinguishable particle. These three distinct scenarios are referred to as light–light–heavy (LLH), equal-massed (EM) and heavy–heavy–light (HHL), respectively [19]. The adiabatic potential curves obtained via equation (14) for the above-described settings are depicted in figure 2. Note that the selection of the specific mass ratio corresponds to the experimentally relevant atomic species reported in table 2.

The two energetically lowest potential curves,  $U_1(R)$  (blue solid line) and  $U_2(R)$  (red dash-dotted line), shown in figures 2(a)–(c) represent the ones which in the absence of a trap approach asymptotically, i.e.  $R \rightarrow \infty$ , the BX + B and BB + X atom-dimer thresholds. The latter have energy  $E_{BX} = -2e^{-2\gamma}(1 + \mathcal{M})/a_{BX}^2$  and  $E_{BB} = -4e^{-2\gamma}/a_{BB}^2$  respectively [14]. However, here at large hyperradii the harmonic 2D trap dominates and thus these two potential curves coincide scaling as  $\sim R^2$  [65, 80]. In the limit of small hyperradius  $R$  (i.e.  $R \rightarrow 0$ ),  $U_1(R)$  and  $U_2(R)$  exhibit a repulsive potential ‘wall’ preventing in this manner the three atoms to approach together at short distances. Another notable feature of  $U_1(R)$  (blue line) is that independently of the mass ratio it possesses a classically allowed region at small  $R$  where the potential is deep enough in order to support trimer states. The remaining gray solid lines in figures 2(a)–(c) represent potential curves, with high hyperangular momentum  $s_\nu$ , which describe the effective centrifugal forces between the three atoms [14].

For FFX systems, the corresponding potential curves [see figures 2(d)–(f)] exhibit significantly altered characteristics from the BBX setting. Indeed, there is only one atom-dimer threshold, i.e. FX + F, since the two identical fermions do not interact. The associated potential curve is illustrated in panels (d)–(f) by the blue solid line. We remark that in the absence of a trapping potential this potential curve asymptotically saturates at an energy  $E_{FX} = -2e^{-2\gamma}(1 + \mathcal{M})/a_{FX}^2$  [14]. Moreover, in the classically allowed region, the

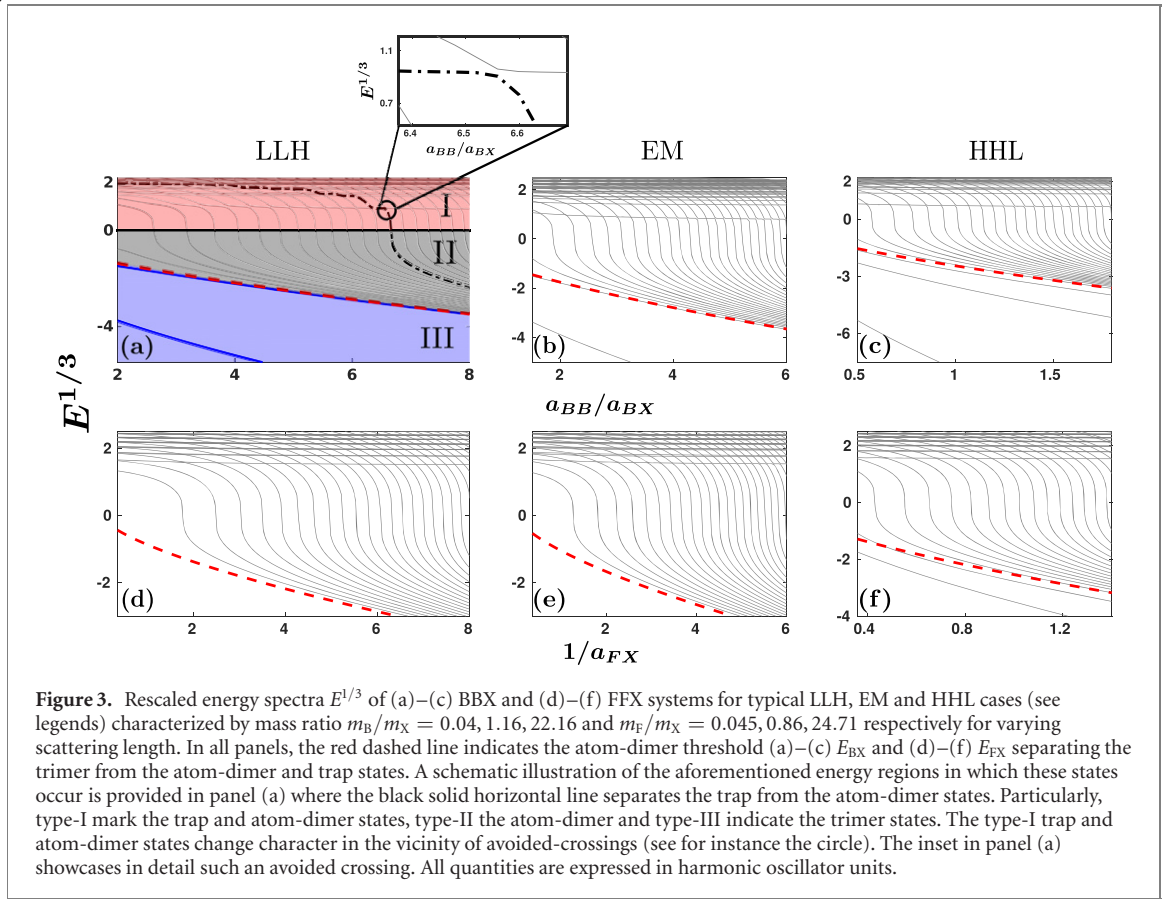




lowest potential is not deep enough to maintain trimer states for all mass ratios. Namely, only for systems with an adequately large mass ratio (HHL), the lower potential curve possesses a pronounced well [figure 2(f)] in contrast to BBX systems, where a deep well is always present [figures 2(a)–(c)].

The hyperradial spectra of the potential curves [figure 2] are provided in figure 3. Namely, panels in figures 3(a)–(c) [3(d)–(f)] refer to the adiabatic potential curves depicted in figures 2(a)–(c) [2(d)–(f)] and corresponding to the BBX [FFX] system at three different mass ratios. Evidently, three types of bound states are discernible: (I) trap states and atom-dimer states with energies  $E > 0$ , (II) purely atom-dimer states (black dash-dotted line) with dimer energies  $E_{\sigma\sigma'} \leq E < 0$ , where  $\sigma = B, F, X$  and  $\sigma \neq \sigma'$ , and (III) trimer bound states (blue solid line) with energies  $E < E_{\sigma\sigma'}$ . Note that the red dashed lines in figure 3 denote the  $\sigma\sigma'$ -dimer energies  $E_{\sigma\sigma'}$ , whereas the black solid horizontal line in panel (a) depicts  $E = 0$ . The trap states of type-I [figure 3(a)] correspond to three weakly interacting trapped atoms. They emerge at  $E > 0$  and are virtually independent of  $a_{BB}/a_{BX}$  or  $1/a_{FX}$  as depicted in figure 3(a) [65]. It is also important to mention that the energetically lowest trap state in BBX systems takes place at energies  $E > 0$  whereas for FFX they emerge for  $E > 1$ . The type-II states are associated with the formation of an atom and a dimer, while their energy lies between the dimer energy and 0. In the limit of  $a_{BB}/a_{BX} \gg 1$  [ $1/a_{FX} \gg 1$ ], the atom-dimer energies behave like  $-a_{BB}/a_{BX}^2$  ( $-1/a_{FX}^2$ ) for BBX [FFX], see in particular figures 3(a) and (d) [17, 65]. For large  $1/a_{FX}$  and  $a_{BB}/a_{BX}$ , the energy difference of two successive eigenstates, approaches  $\Delta E = 2$  [81], which is affected due to the employed scaling in figure 3. It is the excitation energy of the particle accompanying the dimer and stems from the harmonic trap. Due to the coupling between different adiabatic potentials via the  $P$  and  $Q$  non-adiabatic elements [equations (15) and (16)], the trap states change character in the vicinity of avoided-crossings, alternating between type-I atom-dimer and energetically lower trap states [see the circle in figure 3(a)]. The distinction between these two states in region I is more prominent in the case of sharp avoided-crossings [e.g. at  $a_{BB}/a_{BX} \simeq 7$  in figure 3(a)], compared to the case of broad avoided-crossings [e.g. at  $a_{BB}/a_{BX} \simeq 3$  in figure 3(a)].

The type-III states are related to trimers which energetically occur below the dimer energy  $E_{\sigma\sigma'}$ . More specifically, for the BBX system we observe in figures 3(a)–(c) that as the mass ratio increases the number of trimer states ranges from 2 to 4. This is an immediate effect of the corresponding potential curve, i.e.  $U_1(R)$  in figures 2(a)–(c) which deepens as we transition from a LLH scenario to a HHL one [61]. On the other hand, regarding the FFX system trimer states are visible only for a HHL case [figure 3(f)]. The aforementioned aspects of the 2D three-body collisions can be clearly inferred by inspecting figure 4. As can be seen, for the BBX system [figure 4(a)] at fixed  $a_{BB}/a_{BX} = 2$  there is at least one trimer state at *any* mass ratio, whilst for the FFX system [figure 4(b)] there are no trimer states at least within the regime of light identical fermions and a heavy spectator particle [50]. Indeed, a detailed calculation of the eigenvalues of equation (13) explicates that for a scattering length  $1/a_{FX} = 2$  the first trimer state occurs at a critical mass ratio  $\mathcal{M}^* = 3.817$ . This value is larger than  $\mathcal{M}^* = 3.34$  reported in reference [50], which treats the FFX



system in the absence of a trap. Note that a similar effect occurs in 3D FFX systems where the first trimer state appears at even larger mass ratio, i.e.  $\mathcal{M}^* = 8.17$  [82]. The fact that trimer states emerge at larger mass ratio compared to free space can be explained via the behavior of the first adiabatic potential,  $U_1(R)$  [figure 2(d)]. The trapping potential contribution [second term in equation (14)] shifts  $U_1(R)$  to more positive values, compared to the adiabatic potential term [first term in equation (14)] in free space. Accordingly,  $U_1(R)$  becomes shallower in the presence of a trap and therefore larger mass ratios deepen  $U_1(R)$ , favoring in turn the formation of trimer states.

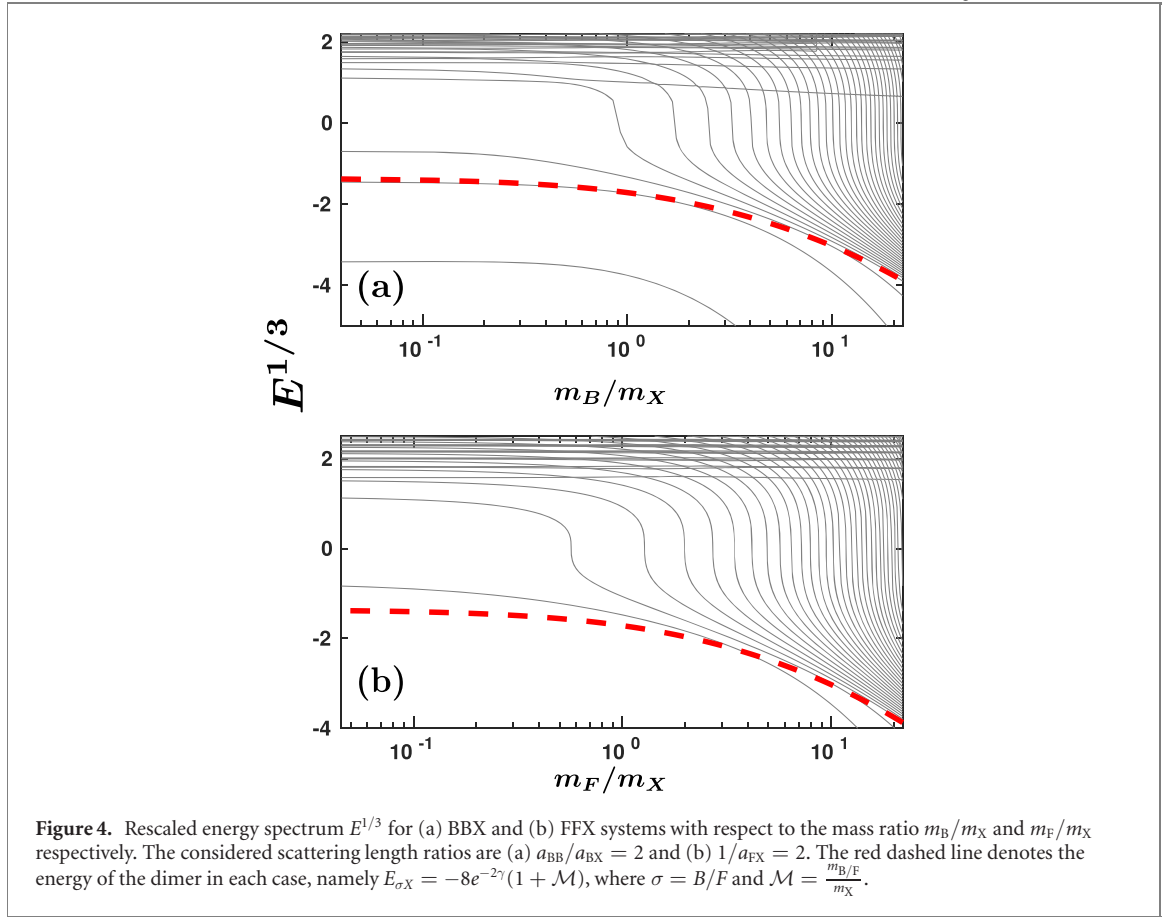
#### 4. Few-body correlations and Tan contacts

Few-body correlations of short-range interacting atomic ensembles are embedded in the momentum distribution of the reduced one-body density in the limit of large momenta [38, 83–85]. This observable can be routinely measured in ultracold atom experiments via time-of-flight measurements [30, 31]. For binary three-body mixtures this asymptotic expansion is related to the relevant short-range two- and three-body correlation functions [38] via the so-called two- and three-body contacts [26, 86]. In particular, the two-body contact has been directly measured via radio-frequency spectroscopy [29, 30]. More specifically, in the limit of large momenta the momentum distribution of the  $\sigma = B/F$  or  $X$  species reduced one-body density [see also appendices A and B] takes the form

$$n_\sigma(\mathbf{p}_\sigma) \approx n_\sigma^a(\mathbf{p}_\sigma) + n_\sigma^b(\mathbf{p}_\sigma), \quad (17)$$

where the single-particle momentum of the  $\sigma$  species  $\mathbf{p}_\sigma$  is larger than all the relevant momentum scales provided by the inverse scattering lengths  $1/a_{\sigma\sigma'}$ . Note that  $\sigma = \sigma'$  ( $\sigma' \neq \sigma$ ) denote the intraspecies (interspecies) interactions. Equation (17) shows that the momentum distribution of the one-body density possesses two main contributions, namely  $n_\sigma^a(\mathbf{p}_\sigma)$  and  $n_\sigma^b(\mathbf{p}_\sigma)$  which are attributed to the presence of two- [38] and three-body correlations [26, 27] respectively.

More specifically,  $n_\sigma^a(\mathbf{p}_\sigma)$  contains terms solely associated with intra- and interspecies two-body correlations of the  $\sigma$  species atom [see also appendix B]. For instance, the asymptotic expansion of the reduced density of B species involves both intra- and interspecies two-body correlations, whereas the density of X species involves only interspecies ones. Utilizing the hyperspherical approach,  $n_\sigma^a(\mathbf{p}_\sigma)$  can be expressed in terms of the hyperradial solutions  $F_\nu(R)$  and  $C_{\nu\sigma\sigma'}$  coefficients of the hyperangular part of the



three-body wave function in the descriptive notation [see also appendix B and table 1]

$$\begin{aligned}
 n_{\sigma}^a(\mathbf{p}_{\sigma}) &= \frac{4\pi}{\mu N_{\sigma} p_{\sigma}^4} \sum_{\sigma'} \mu_{\sigma\sigma'} \int_0^{\infty} \frac{dR}{R^2} \left| \sum_{\nu} F_{\nu}(R) \sum_{l=\pm L} C_{\nu,l}^{\sigma\sigma'}(R) \right|^2 \\
 &= \frac{1}{N_{\sigma} p_{\sigma}^4} \sum_{\sigma'} (1 + \delta_{\sigma\sigma'}) \mathcal{D}_2^{\sigma\sigma'}.
 \end{aligned} \tag{18}$$

Here,  $\mu_{\sigma\sigma'}$  is the two-body reduced mass between two atoms of the same species ( $\sigma = \sigma'$ ) or two atoms belonging to different species ( $\sigma \neq \sigma'$ ), while  $N_{\sigma}$  is the  $\sigma$  species particle number. Importantly,  $\mathcal{D}_2^{\sigma\sigma'}$  signifies the intra- ( $\sigma = \sigma'$ ) or interspecies ( $\sigma \neq \sigma'$ ) two-body contact [38]. On the other hand, the term  $n_{\sigma}^b(\mathbf{p}_{\sigma})$  is related to the product of inter- and intraspecies two-body correlations of the  $\sigma$  species particle giving rise to the three-body ones. In the hyperspherical framework  $n_{\sigma}^b(\mathbf{p}_{\sigma})$  reads:

$$\begin{aligned}
 n_{\sigma}^b(\mathbf{p}_{\sigma}) &= \frac{4\pi}{N_{\sigma} p_{\sigma}^4} \sum_{\sigma'} \frac{\mu_{\sigma\sigma'}}{\mu} \int_0^{\infty} \frac{dR}{R^2} \left\{ J_0 \left[ \frac{p_{\sigma} R \sqrt{\mu_{\sigma\sigma'}}}{\sqrt{\mu}} \right] (-1)^L + J_{2L} \left[ \frac{p_{\sigma} R \sqrt{\mu_{\sigma\sigma'}}}{\sqrt{\mu}} \right] (1 - \delta_{0,L}) \right\} \\
 &\times \sum_{\sigma'' \neq \sigma'} \sum_{l=\pm L} \left( \sum_{\nu} F_{\nu}(R) C_{\nu,l}^{\sigma\sigma'}(R) \right) \left( \sum_{\nu'} F_{\nu'}(R) C_{\nu',l}^{\sigma'\sigma''}(R) \right)^*,
 \end{aligned} \tag{19}$$

where  $J_{\nu}(\cdot)$  is the  $\nu$ -th Bessel function of the first kind and  $L$  is the total angular momentum of the three-body system. Note that in contrast to the two-body term  $n_{\sigma}^a(\mathbf{p}_{\sigma})$ , the single-particle momentum  $p_{\sigma}$  is also involved into the integration of  $n_{\sigma}^b(\mathbf{p}_{\sigma})$ . Hence, the scaling of the latter with the momentum is different than  $1/p_{\sigma}^4$ , see in particular the discussion in section 4.2.

#### 4.1. Scaling behavior of two-body correlations

The presence of two-body short-range correlations in binary mixtures, is captured by  $\mathcal{D}_2^{\sigma\sigma'}$  [equation (18)], i.e. the  $\sigma\sigma'$  two-body contact. Intuitively, the contact  $\mathcal{D}_2^{\sigma\sigma'}$  can, in principle, exhibit an increasing tendency as the  $\sigma\sigma'$  pair of particles comes closer relatively to the third particle. This enhancement of  $\mathcal{D}_2^{\sigma\sigma'}$  signals that the three-body is dominated by strong two-body correlations. Therefore, it is anticipated that  $\mathcal{D}_2^{\sigma\sigma'}$

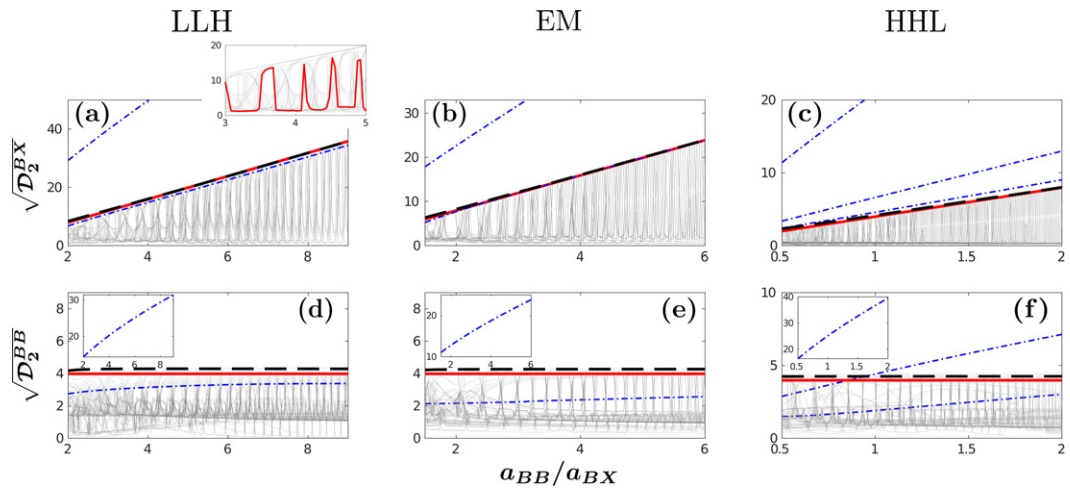


**Figure 5.** Two-body contact  $\sqrt{\mathcal{D}_2^{\sigma\sigma'}}$  among the (a)–(c) BX and (d)–(f) BB species for three body settings ranging from LLH ( $m_B/m_X = 0.04$ ), EM ( $m_B/m_X = 1.16$ ) to HHL ( $m_B/m_X = 22.16$ ) as a function of  $a_{BB}/a_{BX}$  [see also table 2]. The inset in panel (a) displays exemplarily the oscillatory behavior of  $\mathcal{D}_2^{BX}$  due to the change of character of type-I atom-dimer and trap states in the vicinity of avoided-crossings. The insets in panels (d)–(f) feature  $\sqrt{\mathcal{D}_2^{BB}}$  of the first trimer state. The bound stemming from the analytical expression described by equation (21), is shown with the red solid line, whereas the upper bound stemming from the JWKB method is depicted by the black dashed line. The two-body contact of (non) trimer states is illustrated with the (gray solid) blue dash-dotted lines.

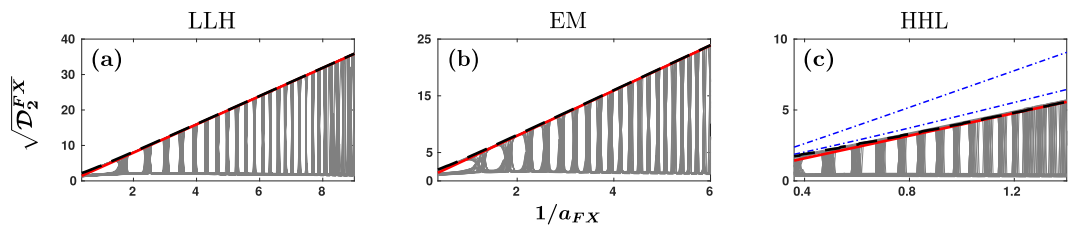


**Figure 6.** Two-body contact  $\sqrt{\mathcal{D}_2^{FX}}$  between FX species in (a) LLH ( $m_F/m_X = 0.045$ ), (b) EM ( $m_F/m_X = 0.86$ ) and (c) HHL ( $m_B/m_X = 24.71$ ) cases for different  $1/a_{FX}$ . The analytical expression for the upper bound [equation (21)] is shown with the red solid line, whereas the upper bound stemming from the JWKB method is denoted by the black dashed line. The two-body contact of (non) trimer states is showcased with (gray solid) blue dash-dotted lines.

possesses distinctive characteristics with respect to the particular type of eigenstate of the three-body system, i.e. referring to trimer, type-I/II atom-dimer and trap states.

For instance, the two-body contacts are strongly enhanced if the three particles are bounded in a trimer state, see in particular the blue dash-dotted lines in figures 5 and 6(c). Concretely, the two-body correlations of these states become substantial as  $a_{BB}/a_{BX}$  [figure 5] and  $1/a_{FX}$  [figure 6] increase. This holds for both inter- ( $\mathcal{D}_2^{BX}$ ) and intraspecies ( $\mathcal{D}_2^{BB}$ ) correlations in BBX as well for  $\mathcal{D}_2^{FX}$  in FFX settings. A general feature observed in both BBX [figure 5] and FFX [figure 6] systems is that the two-body contact of all the other eigenstates, that is atom-dimer and trap states showcased in gray lines, is confined within an envelope and oscillates between two values, see the red curve in the inset of figure 5(a) and also the discussion below for more details.

The lower value of the two-body contact is associated with highly excited trap states. This lower bound depends on the energy of the aforementioned eigenstates and eventually tends to zero as energetically higher excited trap states are taken into account. This is due to the fact that for highly excited trap states, the overall size of the three particles, as specified by the hyperradius  $R$ , increases compared to the size of the system residing in lower-lying energy states, yielding thus weak two-body correlations. This lower value of the contact is attained irrespectively of the value of the scattering length  $a_{BB}/a_{BX}$  and  $1/a_{FX}$ . On the other hand, the oscillatory behavior of the  $\mathcal{D}_2^{\sigma\sigma'}$ , as demonstrated by the red curve in the inset of figure 5(a), originates from the sharp avoided-crossings of the energy levels between the type-I atom-dimer and trap eigenstates [see the circle in figure 3(a)]. Indeed, in the vicinity of these narrow avoided-crossings the spatial configuration of the three particles alters significantly, e.g. from a delocalized trap state into a type-I atom-dimer, where at most two particles are close to each other. Therefore, if the system configuration is that of an atom-dimer (trap state) it leads to an enhanced (reduced) contact due to the strong (weak) pair

correlations. By tuning the scattering lengths  $a_{BB}/a_{BX}$  and  $1/a_{FX}$  towards the subsequent avoided-crossings this atom-dimer (trap) state becomes again a trap (atom-dimer) state, and  $\mathcal{D}_2^{\sigma\sigma'}$  approaches once more its lower (upper) value. Notice that in figure 5 the two-body contact of the energetically lower fifty eigenstates is presented. A larger number of energy states results in the filling of the envelope by atom-dimer and trap states (gray lines) which exhibit an oscillatory behavior. Moreover, the lower bound of  $\mathcal{D}_2^{\sigma\sigma'}$  has a value closer to zero compared to the case with fewer considered eigenstates.

The upper value of the two-body contact is attributed to the presence of two-body correlations stemming from type-II purely atom-dimer states. In particular, the upper value of  $\mathcal{D}_2^{BX}$  [figures 5(a)–(c)] and  $\mathcal{D}_2^{FX}$  [figure 6] becomes larger for increasing scattering lengths,  $a_{BB}/a_{BX}$  and  $1/a_{FX}$ . This is associated to the behavior of type-II purely atom-dimer states [see also the energy spectra in figure 3(a)] whose energy increases in absolute value for larger scattering length. As a consequence, the dimer becomes strongly bound, leading to an enhanced  $\mathcal{D}_2^{\sigma\sigma'}$ . However, the upper value of  $\mathcal{D}_2^{BB}$  [figures 5(d)–(f)] remains almost constant when varying  $a_{BB}/a_{BX}$ . This occurs since  $a_{BB} = 1$ . The latter implies that the second adiabatic potential  $U_2(R)$  [red dash-dotted line in figures 2(a)–(c)], which is associated with the BB + X atom-dimer threshold, is insensitive to variations of  $a_{BB}/a_{BX}$ . Hence the upper bound of  $\mathcal{D}_2^{BB}$ , being determined by the BB dimer states, is constant with respect to  $a_{BB}/a_{BX}$ . However, two-body correlations between the identical bosons are substantially enhanced for increasing  $a_{BB}/a_{BX}$  when the BBX system resides in trimer states [blue dash-dotted lines in figures 5(d)–(f)]. This becomes more prominent in the HHL case [figure 5(f)], where comparatively deeper bound trimer states are formed [61] [see also figure 3(c)]. In these deep trimer states, the overall size of both species, as captured by the hyperradius  $R$  decreases for larger  $a_{BB}/a_{BX}$ . Therefore, the two identical bosons approach each other and become strongly correlated.

To address the aforementioned upper bound in the two-body correlations for non-trimer states in BBX and FFX systems, the JWKB method (see also the review of reference [87] and references therein) is employed. Specifically, the hyperradial part of the three-body wave function [equation (13)] of the atom-dimer states reads

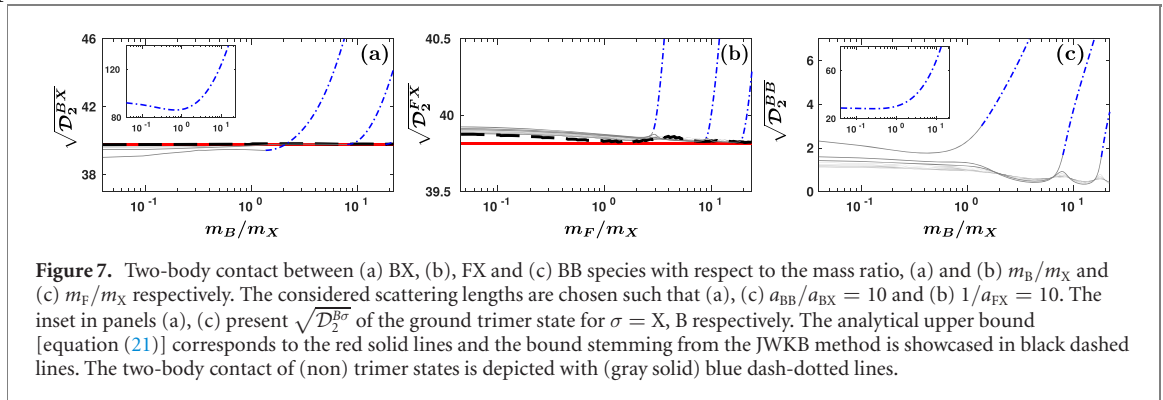
$$F_\nu^{\text{JWKB}}(R) = \begin{cases} \frac{1}{\sqrt{p(R)}} \exp\left(-\left|\int_{R_{\text{ctp}}}^R p(R')dR'\right|\right), & E < U_\nu(R) \\ \frac{2}{\sqrt{p(R)}} \cos\left(\int_{R_{\text{ctp}}}^R p(R')dR' - \phi\right), & E > U_\nu(R). \end{cases} \quad (20)$$

In the above equation,  $\phi = \pi/2 + \pi(s_\nu - \sqrt{s_\nu^2 - 1/4})$ ,  $p(R) = \sqrt{2\mu|E - U_\nu(R)|}$  is the local momentum of a fictitious particle with mass  $\mu$  and  $R_{\text{ctp}}$  is the classical turning point, where  $E = U_\nu(R_{\text{ctp}})$ . Moreover, we focus only on the adiabatic hyperspherical potential curves that support atom-dimer states. In this way, we neglect all the involved non-adiabatic couplings such that we can neatly attribute the upper bound of the contact to type-II atom-dimer states supported by the potentials featuring an atom-dimer threshold. Evidently, the two-body contact [equation (18)], derived within the JWKB method [equation (20)] both for BBX and FFX systems [black dashed lines in figures 5 and 6], accounts well for the upper bound of  $\mathcal{D}_2^{\sigma\sigma'}$  independently of the value of the scattering length.

In order to demonstrate the physical origin of the upper bound in  $\mathcal{D}_2^{\sigma\sigma'}$ , an approximation for the two-body contact of type-II atom-dimer states is employed in the limit of large inverse inter- and intraspecies scattering lengths  $1/a_{\sigma\sigma'}$  [for details see also appendix C]. More specifically, and similarly to the approximation employed within the JWKB method, we single out only the adiabatic hyperspherical potential curves supporting atom-dimer states, neglecting the corresponding non-adiabatic couplings. Under these considerations, the two-body contact between the  $\sigma\sigma'$  species ( $\sigma\sigma' = B, F, X$ ) which characterize only atom-dimer eigenstates acquires the following compact form

$$\mathcal{D}_2^{\sigma\sigma'} \approx \frac{16\pi e^{-2\gamma}}{a_{\sigma\sigma'}^2}. \quad (21)$$

The prediction of the preceding analytical expression is indeed in good agreement with the upper bound of  $\mathcal{D}_2^{BX}$  and  $\mathcal{D}_2^{FX}$  within 1%–2%, except for small scattering lengths  $a_{BB}/a_{BX}$  [see the red solid lines in figures 5(a)–(c)] and  $1/a_{FX}$  [red solid lines in figures 6(a)–(c)] respectively. Deviations larger than 10% occur up to  $a_{BB}/a_{BX} = 3$  for LLH and EM, and  $a_{BB}/a_{BX} = 1.5$  for HHL BBX systems. Likewise, similar deviations are found in the range  $1/a_{FX} = [0.36, 2]$  for LLH and EM, and  $1/a_{FX} = [0.36, 1.4]$  for HHL FFX mixtures. This discrepancy originates from the fact that the analytical expression [equation (21)] stems from a treatment of the atom-dimer state as a product of the BX (FX) dimer and the third particle. This approach becomes more accurate for large  $a_{BB}/a_{BX}$  ( $1/a_{FX}$ ), where the third particle is far away from the strongly bound dimer. However, it fails for small  $a_{BB}/a_{BX}$  ( $1/a_{FX}$ ), where a product state is not adequate anymore, since the third particle approaches the bound dimer and affects the BX (FX) two-body



correlations. In this regime, the JWKB method [equation (20)] accounts well for the upper bound. Thus, as suggested by equation (21), two-body correlations between the BX and FX species depend quadratically on  $a_{BB}/a_{BX}$  and  $1/a_{FX}$ , respectively, in the limit where the latter two are large. This is a manifestation of the universal relation connecting the energy change of an eigenstate with respect to the scattering length and the two-body contact of this state [38, 39].

Interestingly, the analytically obtained upper bound [equation (21)], suggests that  $D_2^{\sigma\sigma'}$  of the atom-dimer states does not depend on the mass ratio of the two identical particles (B,F) with respect to the distinguishable one (X) in the limit where large scattering lengths  $a_{BB}/a_{BX}$  and  $1/a_{FX}$  are considered. To further address this point, the two-body contact versus  $\mathcal{M} = \frac{m_{B/F}}{m_X}$  between the BX, BB and FX species is unraveled for large values of the involved scattering lengths i.e.  $a_{BB}/a_{BX}, 1/a_{FX} = 10$  [figure 7]. Furthermore, we investigate not only the two-body contact of the atom-dimer states but also of the trimer ones [blue dashed-dotted lines in figure 7]. The latter are naturally included since atom-dimer states convert to trimers in the transition from LLH to HHL of BBX and FFX settings [see also figure 4].

In the case of trimer states, the two-body contacts increase with  $\mathcal{M}$ , see the blue dash-dotted lines in figure 7. This behavior is expected since in the HHL scenario the trimer states become deeply bound for both BBX and FFX systems [figures 3(c) and (f)] as  $\mathcal{M}$  increases. Moreover, for large mass ratio additional trimer states are formed [figure 4], whose two-body correlations subsequently shoot up [figure 7]. Indeed, for increasing mass ratio the repulsive wall present at small  $R$  [figure 2], recedes to even smaller hyperradii  $R$ , and so the overall system size of these newly formed trimers decreases, resulting in enhanced two-body correlations. Turning to the two-body contact of atom-dimer states between the BX and FX species, depicted with gray solid lines in figures 7(a) and (b), we observe a good agreement between the derived analytical expression [red solid lines in figures 7(a) and (b)] and  $D_2^{BX}, D_2^{FX}$ , as well as with the two-body contact obtained via the JWKB method [black dashed lines in figures 7(a) and (b)]. Hence, the two-body contact of atom-dimer states in these systems is almost insensitive to a change in the mass ratio,  $m_B/m_X$  and  $m_F/m_X$ .

Moreover, the response of the intraspecies two-body correlations of atom-dimer states in BBX systems as captured by  $D_2^{BB}$  is studied with respect to the mass ratio [depicted with gray solid lines in figure 7(c)]. Due to the large energy separation of the first and second adiabatic potentials [blue solid and red dash-dotted lines respectively in figures 2(a)–(c)] at this large scattering length ratio  $a_{BB}/a_{BX} = 10$ , we investigate the two-body contact of those eigenstates that lay below the BB + X atom-dimer threshold, exhibited by  $U_2(R)$ . In order to observe the upper bound in the BB two-body contact,  $\sqrt{D_2^{BB}} \simeq 4$ , derived in equation (21), a larger number of excited eigenstates is required. The intraspecies two-body contact varies mainly in the HHL scenario. At the mass ratio where new trimer states are formed,  $\sqrt{D_2^{BB}}$  of atom-dimer states is enhanced, and subsequently decreases [figure 7(c)]. This behavior can be attributed to a slight energy attraction and consequent repulsion of the atom-dimer states towards the BX + B atom-dimer threshold as  $m_B/m_X$  approaches and further departs from the value where new trimer states are formed. Whenever this slight attraction occurs, and the three-particle system approaches the threshold of trimer state formation, the probability cloud of both species, as captured by  $R$ , shrinks. Hence, the two identical bosons come closer signaling the increase of  $\sqrt{D_2^{BB}}$ . Notice that this pattern emerges also in the interspecies two-body contact,  $\sqrt{D_2^{BX}}$  [figure 7(a)], being however less pronounced than in the case of the intraspecies one. Since  $a_{BB} = 1$ , the second adiabatic potential  $U_2(R)$  with a BB + X atom-dimer threshold is shallower than the first one which possesses a BX + B threshold, and thus it is more sensitive to the mass ratio. This sensitivity is reflected to the hyperradial part of the wave function,  $F_2(R)$ , which in turn determines the two-body contact between the identical bosons [see also equation (18)].

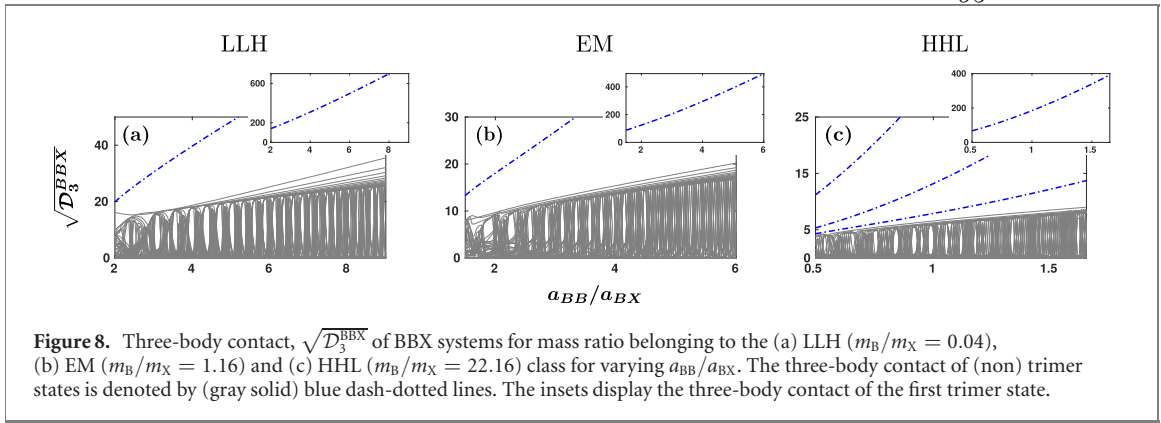


**Figure 8.** Three-body contact,  $\sqrt{\mathcal{D}_3^{\text{BBX}}}$  of BBX systems for mass ratio belonging to the (a) LLH ( $m_B/m_X = 0.04$ ), (b) EM ( $m_B/m_X = 1.16$ ) and (c) HHL ( $m_B/m_X = 22.16$ ) class for varying  $a_{\text{BB}}/a_{\text{BX}}$ . The three-body contact of (non) trimer states is denoted by (gray solid) blue dash-dotted lines. The insets display the three-body contact of the first trimer state.

#### 4.2. Response of the three-body correlations

As argued above [see equation (17)], in the asymptotic expansion of the  $\sigma$  species reduced one-body density in momentum space there is a contribution related to three-body correlations having an explicit dependence on the single-particle momentum  $p_\sigma$  [equation (19)]. Indeed, as it has also been demonstrated in references [26, 27] treating the three-body problem in momentum space, the next-to-leading order term in the asymptotic expansion of the reduced one-body density in momentum space reads

$$n_\sigma^b(\mathbf{p}_\sigma) = \frac{\ln^3 p_\sigma}{p_\sigma^6} \mathcal{D}_3. \quad (22)$$

In this expression,  $\mathcal{D}_3$  is the three-body contact which captures the three-body correlations between all particles that participate in the binary 2D mixture. Herein, the three-body contact is derived by linear fitting to  $n_\sigma^b(\mathbf{p}_\sigma)/\ln^3 p_\sigma$  stemming from the numerical solution of equation (19) for large  $p_\sigma$ . For the binary mixtures that we consider, the only relevant three-body contact is the one of BBX systems, denoted hereafter by  $\mathcal{D}_3^{\text{BBX}}$ . For the FFX setting, the three-body correlations are predominantly suppressed due to the Pauli exclusion principle between the identical fermions [26].

Three-body correlations are greatly enhanced when two identical bosons and the third distinguishable particle reside in a trimer state independently of the considered mass ratio [blue dash-dotted lines in figure 8]. More specifically, in the transition from LLH to the HHL scenario, the first trimer state [insets of figure 8] displays a substantially enhanced three-body contact,  $\sqrt{\mathcal{D}_3^{\text{BBX}}}$ . This is due to the fact that for heavier identical bosons than the third particle, trimer states become deeply bound as shown in figures 3(a)–(c). Hence, all three particles are confined within a small hyperradius which results into large valued three-body contacts. However, in the EM case, the three-body contact of the first trimer state is slightly suppressed compared to the one in the LLH setting [e.g. see the insets in figures 8(a) and (b) at  $a_{\text{BB}}/a_{\text{BX}} = 2$ ]. This behavior will be further addressed below arguing on the dependence of  $\sqrt{\mathcal{D}_3^{\text{BBX}}}$  with respect to the mass ratio. Even though three-body correlations are significantly pronounced for trimer states, the asymptotic expansion of the  $\sigma$  species one-body density  $n_\sigma(\mathbf{p}_\sigma)$  in momentum space [equation (17)] is mainly dominated by the first term attributed to two-body correlations [equation (18)]. Deviations from the first term occur at  $p_\sigma \simeq 100$ , and especially by considering large scattering length ratios  $a_{\text{BB}}/a_{\text{BX}} > 6$ , where three-body correlations of the trimer states are more pronounced [see insets of figure 8].

Furthermore, three-body correlations of highly excited trap states are greatly reduced, more than two orders of magnitude compared to the three-body contact of trimer states. The large suppression of  $\sqrt{\mathcal{D}_3^{\text{BBX}}}$  is due to the fact that the system size (captured by the hyperradius  $R$ ) in each of these excited trap states is large. As such, the simultaneous collisions of all three particles at small distances become very improbable. In contrast, atom-dimer states showcase prominent three-body correlations, especially by tuning  $a_{\text{BB}}/a_{\text{BX}}$  to large values. In this regime, the atom-dimers [figure 3(a)] consist of a deeply bound BX dimer accompanied by the second identical bosonic particle. Due to the bosonic symmetry, the BX dimer involves both B atoms, and hence  $\sqrt{\mathcal{D}_3^{\text{BBX}}}$  increases with the ratio  $a_{\text{BB}}/a_{\text{BX}}$ , similarly to the two-body contact. Let us note that in the case of atom-dimer and trap states, the asymptotic expansion of  $n_\sigma(\mathbf{p}_\sigma)$  for large  $p_\sigma$  is practically dominated solely by the first term described by equation (18) being associated with two-body correlations.

Similarly to the behavior of the two-body contact, the three-body one of type-I atom-dimer and trap states displays oscillations due to the character change of the latter at the location of the avoided-crossings taking place at specific scattering lengths in the three-body eigenspectrum [see circle in figure 3(a)]. The lower bound eventually approaches zero for higher lying excited trap eigenstates. Recall that an equivalent

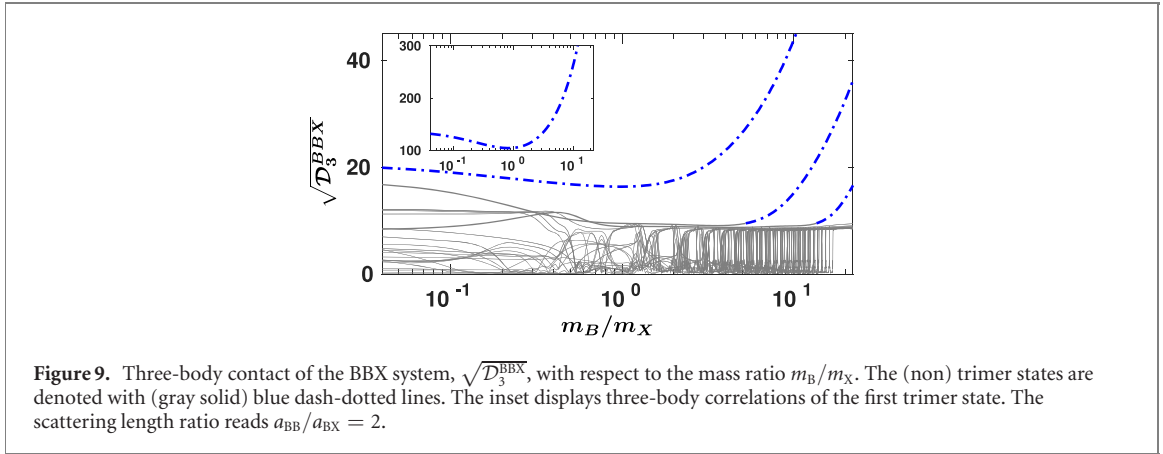


**Figure 9.** Three-body contact of the BBX system,  $\sqrt{\mathcal{D}_3^{\text{BBX}}}$ , with respect to the mass ratio  $m_B/m_X$ . The (non) trimer states are denoted with (gray solid) blue dash-dotted lines. The inset displays three-body correlations of the first trimer state. The scattering length ratio reads  $a_{\text{BB}}/a_{\text{BX}} = 2$ .

behavior is observed for the two-body contact  $\sqrt{\mathcal{D}_2^{\text{BBX}}}$  [see figures 5(a)–(c)]. However, in contrast to  $\sqrt{\mathcal{D}_2^{\text{BBX}}}$ , the type-II purely atom-dimer states do not provide a well defined upper bound for  $\sqrt{\mathcal{D}_3^{\text{BBX}}}$ . As the ratio  $a_{\text{BB}}/a_{\text{BX}}$  increases, three-body correlations of purely atom-dimer states exhibit a state dependent growth rate [figure 8]. The latter is larger for purely atom-dimer states lying close to the  $\text{BX} + \text{B}$  dimer threshold. The three particles residing in these atom-dimer states, are confined within a smaller hyperradius  $R$  when compared to excited atom-dimers, and as such they feature an enhanced three-body contact. Energetically higher atom-dimer eigenstates are more delocalized, thus possessing a smaller  $\sqrt{\mathcal{D}_3^{\text{BBX}}}$ .

The dependence of  $\sqrt{\mathcal{D}_3^{\text{BBX}}}$  with respect to the mass ratio of (non) trimer states denoted by blue dash-dotted lines (gray solid lines) is provided in figure 9 exemplarily for  $a_{\text{BB}}/a_{\text{BX}} = 2$ . In particular, we observe that an enhancement of three-body correlations takes place in the LLH to the HHL transition for trimer states [blue dash-dotted lines in figure 9], as discussed previously. For sufficiently large  $m_B/m_X$ , atom-dimer states [denoted by gray lines in figure 9] change character to trimers [figure 4(a)], whose three-body correlations subsequently become dominant [see for instance figure 9 at  $m_B/m_X \simeq 6$ ]. This is similar to the enhancement of two-body correlations between both BX and BB species of atom-dimer states when transitioning to trimers as manifested in figures 7(a) and (c). In particular, the first atom-dimer state, possesses a dominant  $\sqrt{\mathcal{D}_3^{\text{BBX}}}$ , in the LLH regime ( $m_B/m_X \simeq 0.04$ ), similarly to the second trimer state [figure 9]. Later on, three-body correlations become substantial at the mass ratio where this atom-dimer state transits into a trimer [figure 9 at  $m_B/m_X \simeq 6$ ]. This behavior is caused by an energy shift of both the first atom-dimer and second trimer states towards the  $\text{BX} + \text{B}$  dimer threshold when  $m_B/m_X \simeq 0.04$  (LLH), leading to an increased (reduced) three-body contact. Notice that the aforementioned energy shift towards the  $\text{BX} + \text{B}$  dimer threshold takes place also for the first trimer state in the LLH to EM transition, resulting in a slight decrease of  $\sqrt{\mathcal{D}_3^{\text{BBX}}}$  [see the insets of figures 9 and 8(a) and (b)]. It is also worth mentioning that  $\sqrt{\mathcal{D}_3^{\text{BBX}}}$  exhibits oscillations, due to the conversion of trap to type-I atom-dimer states [gray lines in figure 9] and vice versa nearby the avoided-crossings.

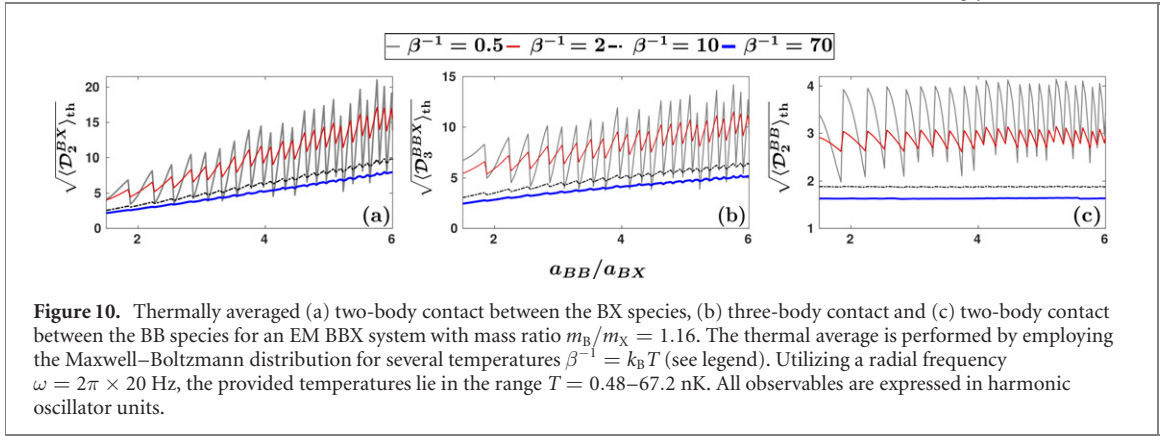
### 4.3. Impact of thermal effects on the correlations

In the previous subsections, we investigated how two- and three-body correlations depend on the scattering length and mass ratio, as well as, the statistics of the atoms. Another important issue of immense experimental relevance is the impact of the gas temperature. Indeed, it has been experimentally and theoretically evinced that temperature effects play a crucial role on few-body correlation properties of bosonic and two-component fermionic thermal gases [45, 88–92]. For this reason, in the following, the temperature dependence of the two- and three-body contacts with respect to the involved scattering lengths is investigated exemplarily for BBX systems.

The temperature effect, in our system, can be taken into account by simply considering an ensemble of type-I atom-dimer and trap states which are populated according to a Maxwell–Boltzmann distribution [88]. This means that states with energy  $E > 0$  are those which can be thermally averaged whereas type-II atom-dimer and trimer states are excluded [see also section 3 for the classification of the participating states]. This stems from the fact that initially a binary thermal gas consists of unbound atoms with energy larger than zero [93]. Note that in the limit of a zero trapping frequency we recover the thermally averaged contacts in free space. Under these considerations, any thermally averaged observable  $\langle \mathcal{O} \rangle_{\text{th}}$  is given by

$$\langle \mathcal{O} \rangle_{\text{th}} = \frac{\sum_j e^{-\beta E_j} \mathcal{O}_j}{\sum_j e^{-\beta E_j}} \quad \text{with} \quad \beta^{-1} = k_B T, \quad (23)$$





where  $T$  is the temperature of the gas and  $k_B$  is the Boltzmann's constant.  $\mathcal{O}^j$  is the observable associated with the  $j$ th eigenstate of our system having an eigenvalue  $E^j$ , while the summation is performed over eigenstates with  $E^j > 0$ . Additionally, the range of temperatures that we consider in the following is up to 70 nK referring to an experimentally relevant radial trapping frequency  $\omega = 2\pi \times 20$  Hz [78, 79]. In this temperature regime  $s$ -wave interactions are adequate for describing thermal effects of few-body correlation observables [45].

The thermally averaged two- and three-body contacts, capturing the imprint of temperature on the behavior of the two- and three-body correlations respectively, are illustrated in figure 10. We focus on a BBX system with fixed mass ratio  $m_B/m_X = 1.16$  (EM) and inspect different values of temperature within the interval  $T = 0.48\text{--}67.2$  nK. However, we note that mass-imbalanced BBX or FFX systems display a qualitatively similar behavior. For all  $\beta^{-1}$  presented in figures 10(a) and (b), there is an increasing tendency of two- ( $\sqrt{\langle \mathcal{D}_2^{\text{BX}} \rangle_{\text{th}}}$ ) and three-body ( $\sqrt{\langle \mathcal{D}_3^{\text{BBX}} \rangle_{\text{th}}}$ ) correlations between the BX species and the BBX atoms respectively, for a larger scattering length ratio  $a_{\text{BB}}/a_{\text{BX}}$ . This overall behavior stems from the growth observed in the two- and three-body zero temperature contacts [see figures 5(b) and 8(b)] associated with type-I atom-dimer states, lying close to the zero energy threshold. These eigenstates possess energy larger than zero and thus similarly to the zero temperature scenario they contribute to the growth of the thermally averaged two-body contact.

In particular,  $\sqrt{\langle \mathcal{D}_2^{\text{BX}} \rangle_{\text{th}}}$  features an oscillatory behavior with respect to  $a_{\text{BB}}/a_{\text{BX}}$ , whose amplitude decreases as  $\beta^{-1}$  becomes larger. These oscillations originate from the undulations present in the  $\sqrt{\mathcal{D}_2^{\text{BX}}}$  [see inset of figure 5(a)]. They are bounded above by the two-body contact of type-II atom-dimer states and below eventually by zero, in the limit where infinitely many trap states are taken into account. In contrast, as the temperature increases, a larger number of eigenstates contributes to the thermal average [equation (23)] resulting in an  $\sqrt{\langle \mathcal{D}_2^{\text{BX}} \rangle_{\text{th}}}$  free from the oscillatory fringes. Indeed, in figure 10(a), the  $\sqrt{\langle \mathcal{D}_2^{\text{BX}} \rangle_{\text{th}}}$  at low temperature, i.e.  $\beta^{-1} = 0.5$  (gray solid line), exhibits prominent oscillations. However, as the temperature increases, e.g.  $\beta^{-1} = 70$  (blue solid line), more type-I atom-dimer and trap states participate in the thermal average smearing out any interference feature. The same mechanism is responsible for the decay of the oscillation fringes present in  $\sqrt{\langle \mathcal{D}_3^{\text{BBX}} \rangle_{\text{th}}}$  for larger temperatures [figure 10(b)].

Moreover, we observe that the magnitude of the thermally averaged two-body contact between the BX species shown in figure 10(a) decreases as the temperature of the gas increases [88]. For example, focusing on  $a_{\text{BB}}/a_{\text{BX}} = 6$ ,  $\sqrt{\langle \mathcal{D}_2^{\text{BX}} \rangle_{\text{th}}}$  is approximately one order of magnitude smaller than the upper bound of  $\sqrt{\mathcal{D}_2^{\text{BX}}}$  [figure 5(b)] at  $\beta^{-1} = 70$ . Similarly, the amount of three-body correlations, quantified by  $\sqrt{\langle \mathcal{D}_3^{\text{BBX}} \rangle_{\text{th}}}$ , also becomes suppressed with increasing temperature. In particular, at  $\beta^{-1} = 70$ , the thermally averaged three-body correlations are reduced by almost a factor of four compared to  $\sqrt{\mathcal{D}_3^{\text{BBX}}}$  of the first atom-dimer state at  $a_{\text{BB}}/a_{\text{BX}} = 6$  [figure 8(b)]. Note also that both the thermally averaged two- and three-body contacts at  $\beta^{-1} = 70$  are suppressed by two orders of magnitude compared to the respective correlation measures of the first trimer state. This behavior occurs due to the fact that for increasing temperature the likelihood that the three particles occupy trap states becomes larger. These trap states possess fairly small two- and three-body correlations. Thus, the thermal average over such states significantly decreases the magnitude of both  $\sqrt{\langle \mathcal{D}_2^{\text{BX}} \rangle_{\text{th}}}$  and  $\sqrt{\langle \mathcal{D}_3^{\text{BBX}} \rangle_{\text{th}}}$ .

A similar qualitative behavior is observed for  $\sqrt{\langle \mathcal{D}_2^{\text{BB}} \rangle_{\text{th}}}$ , where again two-body correlations are suppressed for increasing  $\beta^{-1}$  [figure 10(c)]. In particular, the oscillation amplitude of  $\sqrt{\langle \mathcal{D}_2^{\text{BB}} \rangle_{\text{th}}}$  reduces with increasing temperature ( $\beta^{-1}$ ). Also,  $\sqrt{\langle \mathcal{D}_2^{\text{BB}} \rangle_{\text{th}}}$  remains almost constant as a function of  $a_{\text{BB}}/a_{\text{BX}}$  for  $\beta^{-1} > 10$ . This stems from the fact that the zero-temperature  $\mathcal{D}_2^{\text{BB}}$  of type-I atom-dimer and trap states does not show an increasing tendency with respect to the tuning of  $a_{\text{BB}}/a_{\text{BX}}$  [see figures 5(d)–(f)], in

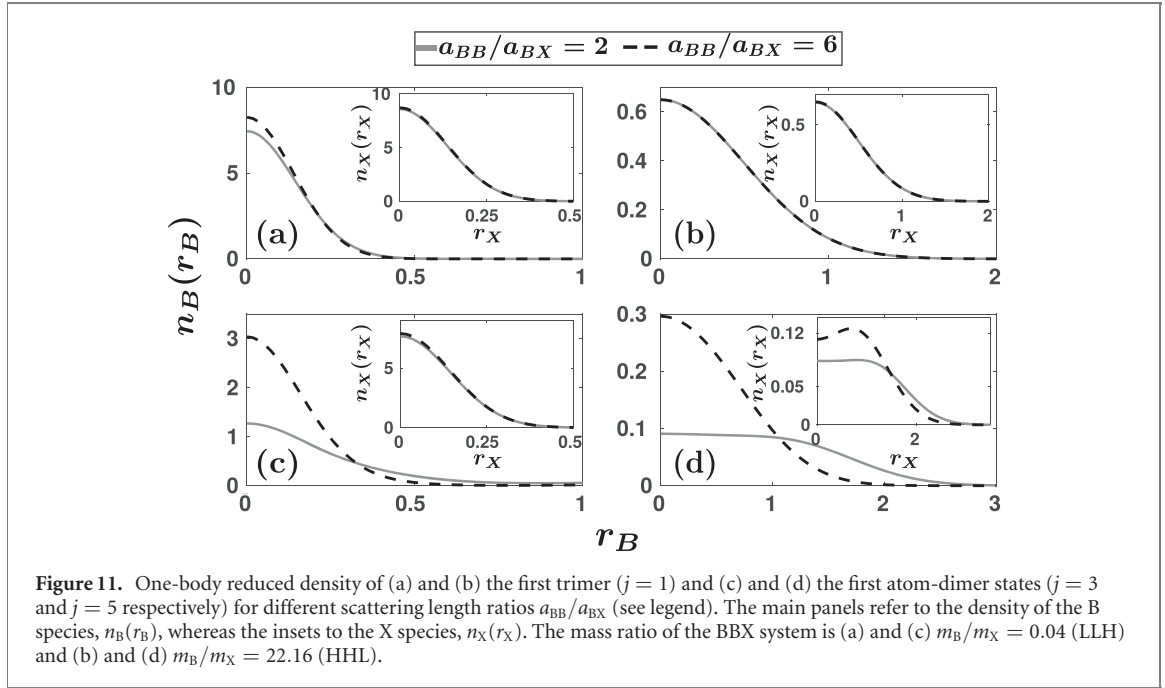


**Figure 11.** One-body reduced density of (a) and (b) the first trimer ( $j = 1$ ) and (c) and (d) the first atom-dimer states ( $j = 3$  and  $j = 5$  respectively) for different scattering length ratios  $a_{BB}/a_{BX}$  (see legend). The main panels refer to the density of the B species,  $n_B(r_B)$ , whereas the insets to the X species,  $n_X(r_X)$ . The mass ratio of the BBX system is (a) and (c)  $m_B/m_X = 0.04$  (LLH) and (b) and (d)  $m_B/m_X = 22.16$  (HHL).

contrast to the zero-temperature contact of the BX species. Upon increasing the temperature,  $\beta^{-1}$ , the oscillations of  $\mathcal{D}_2^{BB}$  are smeared out [see also the relevant discussion on  $\sqrt{\langle \mathcal{D}_2^{BX} \rangle_{th}}$ ], yielding thus a constant  $\sqrt{\langle \mathcal{D}_2^{BB} \rangle_{th}}$ . Similarly to the case of two-body correlations between the BX species, as the temperature increases the magnitude of the thermally averaged two-body correlations between the identical bosonic particles is further suppressed. In particular, at  $\beta^{-1} = 70$  [blue solid line in figure 10(c)], the magnitude of  $\sqrt{\langle \mathcal{D}_2^{BB} \rangle_{th}}$  is smaller by a factor of two than the upper bound of two-body correlations between the identical bosonic particles for  $a_{BB}/a_{BX} = [1.5, 6]$  [figure 5(e)].

## 5. Spatial configurations of the three-body states

Next, we explore the underlying spatial structure of the few-body binary systems via the corresponding  $\sigma$  species one-body reduced density. This quantity is a common experimental observable which can be measured by averaging over a sample of different single-shot realizations [6, 94, 95], shedding light into the static and dynamical properties of a system [31, 96]. Within the used descriptive notation [see also table 1 and appendix B for details] the reduced one-body density acquires the form

$$n_\sigma(\mathbf{r}_\sigma) = \frac{M}{\pi} \int dR d\Omega^{\sigma''\sigma'} e^{-G(\mathbf{r}_\sigma, R, \Omega^{\sigma''\sigma'})} \times \left| \sum_\nu F_\nu \Phi_\nu(R; \Omega^{\sigma''\sigma'}) \right|^2, \quad (24)$$

where  $\sigma' \neq \sigma$ ,  $\sigma'' = B/F$  depending on the mixture and  $(r_\sigma, \phi)$  are the polar coordinates of the  $\mathbf{r}_\sigma$  2D vector. Moreover the expression  $G(\mathbf{r}_\sigma, R, \Omega^{\sigma''\sigma'})$  reads

$$G(\mathbf{r}_\sigma, R, \Omega^{\sigma''\sigma'}) = Mr_\sigma^2 + (m_{\sigma''} + m_{\sigma'})^2 \frac{R^2 \cos^2 \alpha^{\sigma''\sigma'} \mu_{\sigma''\sigma'}}{M\mu} + 2 \frac{(m_{\sigma''} + m_{\sigma'}) \sqrt{\mu_{\sigma''\sigma'}}}{\sqrt{\mu}} r_\sigma R \cos \alpha^{\sigma''\sigma'} \times \cos(\theta_2^{\sigma''\sigma'} - \phi). \quad (25)$$

Note that the  $\sigma$  species one-body reduced density is normalized to unity.

Initially, we consider a BBX system with a small mass ratio  $m_B/m_X$  i.e. a LLH case. Characteristic one-body densities of trimer states are provided in figure 11(a) for two representative scattering length ratios  $a_{BB}/a_{BX}$ . Since the X particle is heavier than the identical bosons, it is located close to the trap center while being insensitive to scattering length alterations as can be seen from the Gaussian profile of  $n_X(r_X)$  in the inset of figure 11(a). The reduced density of the bosonic species closely resembles and encloses the one of the distinguishable particle while it slightly shrinks as  $a_{BB}/a_{BX}$  becomes larger, compare  $n_B(r_B = 0)$  for  $a_{BB}/a_{BX} = 6$  and  $a_{BB}/a_{BX} = 2$  in figure 11(a). This behavior signifies that the light bosons come very close to the heavier distinguishable particle, which is a feature of the trimer state.

Similar density profiles occur for trimer states in the HHL scenario [figure 11(b)]. Evidently, the one-body densities are wider for HHL [figure 11(b)] than LLH [figure 11(a)] settings. Indeed, as  $m_B/m_X$  increases the trapping potential becomes more shallow [see equation (14)] and thus it leads to a larger spatial extent of the one-body density. Contrary to the LLH case, here the bosons are placed near the center of the trap due to their heavier mass. Apart from this difference both  $n_B(r_B)$  and  $n_X(r_X)$  possess a Gaussian form being almost unaffected by  $a_{BB}/a_{BX}$ . All particles reside close to each other since the system occupies deep trimer states.

Turning to the first type-II atom-dimer state, see figures 11(c) and (d), we deduce that in contrast to trimer states [figures 11(a) and (b)] the corresponding reduced one-body densities are strongly impacted by scattering length variations. For example, in the case of a LLH BBX system [inset of figure 11(c)],  $n_X(r_X)$  features a narrow Gaussian distribution which is not altered when tuning  $a_{BB}/a_{BX}$  due to the large mass of the X particle. However,  $n_B(r_B)$  depends strongly on  $a_{BB}/a_{BX}$  exhibiting a large spatial extent at  $a_{BB}/a_{BX} = 2$ , whereas at  $a_{BB}/a_{BX} = 6$  tends to a Gaussian of small width comparable with the one of  $n_X(r_X)$  [inset of figure 11(c)]. This occurs since in this regime ( $a_{BB}/a_{BX} = 6$ ) the configuration of the type-II atom-dimer state consists of a strongly bound BX dimer [see also figure 3(a)] which results into having a boson localized at the trap center and lying close to the X particle. An analogous behavior of the density takes place for the first type-II atom-dimer state in the HHL case [figure 11(d)]. Namely, for increasing scattering length ratio ( $a_{BB}/a_{BX} = 6$ ), the density profiles show a narrower spatial configuration.

The reduced one-body densities of FFX systems presented in figure 12 for small mass ratios ( $m_F/m_X = 0.0451$ , LLH) evince a remarkable angular dependence. This is in sharp contrast to the densities of BBX systems which are isotropic and their involved mass and scattering length ratios impact only their radial part. This difference between the one-body densities of FFX and BBX systems mainly stems from the fact that the total angular momentum and parity of FFX systems is  $L^\pi = 1^-$  whereas for BBX is equal to  $L^\pi = 0^+$ . Paradigmatic densities of an FFX system occupying the eigenstates of the first atom-dimer [see panels (a) and (b)] and two excited trap states [see panels (c) and (d)] at two different scattering lengths  $1/a_{FX}$  are showcased in figure 12. We should note that figure 12 presents only the fermionic density since the one of the X particle features an angular isotropic configuration localized close to the trap center similarly to the structure illustrated in figure 12(b). This angular isotropy originates from the fact that the X particle interacts with an  $s$ -wave zero-range pseudopotential with the identical particles and is not constrained by any symmetry as is the case with the identical fermions. In contrast, apart from symmetric  $s$ -wave interactions, particle exchange antisymmetry constraints induce the angular dependence of  $n_F(x_F, y_F)$  by introducing a non-zero angular momentum [97].

Focusing on the first atom-dimer state [figures 12(a) and (b)],  $n_F(x_F, y_F)$  displays an angular dependent pattern which tends to an isotropic configuration as the interspecies scattering length  $1/a_{FX}$  is tuned to a larger value [figure 12(b)]. In particular, for  $1/a_{FX} = 0.36$  a small anisotropy is present in the angular direction and  $n_F(x_F, y_F)$  extends to larger distances compared to  $1/a_{FX} = 6$  [figure 12(b)]. This is caused by the smaller binding energy of this state compared to the type-II atom-dimer state considered at  $1/a_{FX} = 6$  [see also figure 3(d)]. Therefore, the densities of type-II atom-dimer states exhibit a configuration where the F particles reside in the vicinity of the trap center, at the location of the X particle, with a larger probability than the respective type-I states [figure 12(a)].

The angular deformation of the densities  $n_F(x_F, y_F)$  of trap states [figures 12(c) and (d)], becomes even more pronounced. Specifically, for  $1/a_{FX} = 0.36$  [figure 12(c)], the presented eigenstate ( $j = 15$ ) is a superposition of an atom-dimer and an excited trap state, since its energy lies close to an avoided-crossing [figure 3(d)]. As can be seen this is directly reflected in the fermionic density which displays a peak close to the trap center, at the location of the distinguishable particle. However, away from the peak ( $x_F = 0, y_F = 0$ ) the density shows prominent undulations in the angular direction. Strikingly, by singling out a particular  $\nu$  in the summation of equation (24), one can assign the observed patterns in the reduced densities to specific states that are associated with the  $\nu$ -th adiabatic hyperspherical potential [figure 2(d)]. In this way, these undulations are attributed to the specific density patterns building upon states of the higher-lying adiabatic hyperspherical potentials  $U_\nu(R)$  [figure 2(d)] with  $\nu > 1$ . The configuration of the three particles associated with these potentials consist of the X particle being located between the two fermions, which are further separated by the former. Similarly, the lowest adiabatic hyperspherical potential  $U_1(R)$ , supporting atom-dimer states, is responsible for the density peak close to the trap center [figure 12(c)].

A different angular pattern appears in the fermionic density of a trap eigenstate ( $j = 14$ ) [figure 12(d)] for larger interspecies scattering lengths e.g.  $1/a_{FX} = 6$ , whose energy lies away from avoided-crossings. Here, the fermions are repelled from the trap center, where the heavy X particle is positioned. Since this is a trap state, the attraction between the X particle and the fermions is not strong enough to localize both species at the trap center as is the case for atom-dimer states [figures 12(a) and (b)]. Thus, the fermions form a shell structure [98, 99] surrounding the X particle [figure 12(d)], a process being reminiscent of the

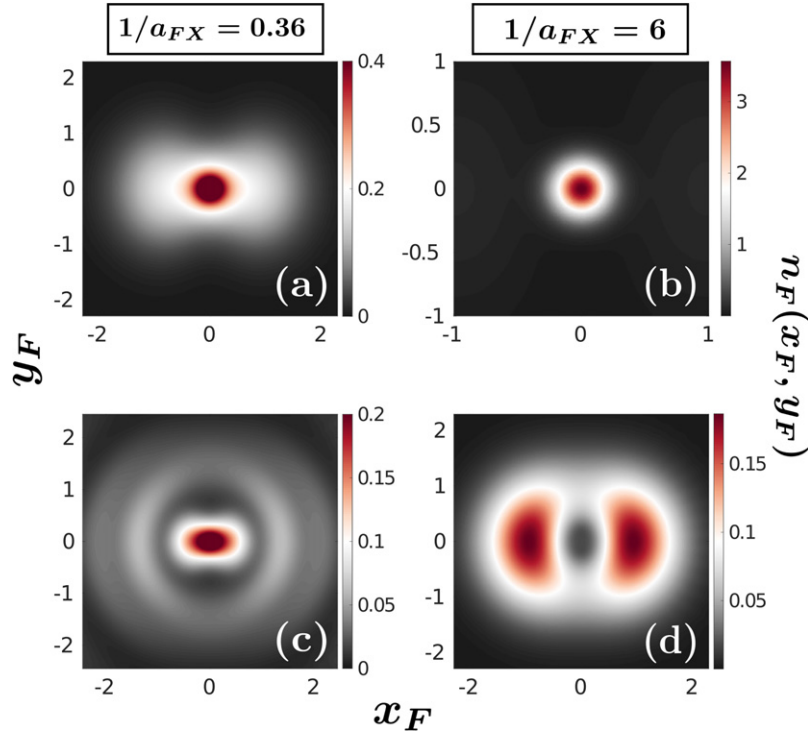


**Figure 12.** One-body reduced density,  $n_F(x_F, y_F)$  of (a) and (b) the first atom-dimer ( $j = 1$ ) and (c) and (d) excited trap states ( $j = 15$  and  $14$  respectively) of a LLH FFX system ( $m_F/m_X = 0.0451$ ). The considered interspecies scattering lengths  $1/a_{FX}$  read (a) and (c)  $1/a_{FX} = 0.36$  and (b) and (d)  $1/a_{FX} = 6$ .

phase separation mechanism emerging in many-body Bose–Fermi mixtures [100–102]. Here, this configuration is attributed to adiabatic hyperspherical potentials with  $\nu > 1$  as can be deduced by focusing on specific  $\nu$ 's in equation (24). Notice that this pattern characterizes also other highly excited trap states as well.

## 6. Summary and outlook

We have provided insights into the behavior of few-body correlations emerging in arbitrary mass-imbalanced three-body binary mixtures confined in a 2D harmonic trap. In particular, the considered mixtures consist of either two identical bosonic (BB) or fermionic (FF) atoms interacting with a third distinguishable one (X) yielding two distinct physical systems, i.e. BBX and FFX respectively. Utilizing the hyperspherical formalism we discuss the properties of the individual energy spectra and explicate that they can be classified according to three types of energy hyperradial eigenstates. Namely, trap states describing three weakly interacting atoms, a dimer accompanied by a spectator atom (atom-dimers), and trimer configurations. The few-body correlation properties, as captured by the two- and three-body contacts, are studied with respect to both the 2D scattering lengths of BBX ( $a_{BB}/a_{BX}$ ) and FFX ( $1/a_{FX}$ ) setups as well as the mass ratio between the species. These correlation measures are investigated for all above mentioned energy eigenstates, distinguishing thus our treatment from previous works in 2D where correlation properties of only the trimer states were considered for three-body binary mixtures in free space [26].

Inspecting the characteristics of two-body intra- (BB) and interspecies (BX, FX) correlations, as encapsulated in the respective two-body contacts, we exemplify a distinction between the aforementioned energy eigenstates. Indeed, if the system lies in deep trimer states substantial two-body correlations emerge, which become stronger for increasing scattering lengths (either  $a_{BB}/a_{BX}$  or  $1/a_{FX}$ ) or larger mass ratio  $m_B/m_X$  and  $m_F/m_X$ . Interestingly, in the case of atom-dimer and trap states the two-body correlations feature an upper and a lower bound while exhibiting an oscillatory behavior with respect to the scattering length ratio. This response originates from the fact that atom-dimer and trap states change character in the vicinity of avoided-crossings present in the energy spectra. Qualitatively, these characteristics of the two-body correlations are of universal nature regardless the atomic species or particle exchange symmetry.

In particular, the lower bound is attributed to the presence of highly excited trap states and approaches zero when a larger number of them is taken into account in the two-body contacts. On the other hand, the upper bound is associated with pure atom-dimer states. This upper bound is successfully addressed by

employing the semi-classical JWKB method, tackling both BBX and FFX systems for all considered scattering length ratios. For large scattering lengths ( $a_{\text{BB}}/a_{\text{BX}}$  or  $1/a_{\text{FX}}$ ) an analytical expression for this upper bound is derived, stemming from the approximation of the atom-dimer wave function as a product state describing a deep dimer and the remaining trapped particle. Interestingly, the values of the upper bound depends solely on the considered scattering lengths  $a_{\text{BB}}/a_{\text{BX}}$  or  $1/a_{\text{FX}}$ . By comparing with the semi-classical JWKB formula, it is possible to infer the effect of the third particle to the two-body correlations of the dimer, especially at small scattering lengths  $a_{\text{BB}}/a_{\text{BX}}$  or  $1/a_{\text{FX}}$ . Moreover, the two-body contact of atom-dimer states with respect to the mass ratio for large fixed  $a_{\text{BB}}/a_{\text{BX}}$  or  $1/a_{\text{FX}}$ , shows a saturation tendency towards the analytically predicted value.

Turning to BBX mixtures a similar oscillatory behavior of three-body correlations occurs as a function of the scattering length for atom-dimer and trap states as manifested in the three-body contact. The corresponding lower bound is caused by the existence of energetically higher-lying trap states. Antithetically to two-body correlations, the three-body contact of the atom-dimer states lacks an upper bound, exhibiting a state-dependent growth rate. Three-body correlations are more enhanced for atom-dimer states residing close to the trimer formation threshold, compared to states lying further away from it. Proceeding one step further, the impact of thermal effects on the two- and three-body correlations of the 2D binary mixtures is also investigated. Concretely, for thermal gases we observe that a thermally averaged two- or three-body contact possesses an oscillatory pattern with a reduced peak-to-peak amplitude as the temperature increases, whereas their overall magnitude is also suppressed. This behavior is attributed to a superposition of highly excited trap and atom-dimer states weighted according to the Boltzmann distribution, which destroys the oscillatory patterns present for zero temperature.

To comprehend the spatially resolved structure of the species in the different eigenstates we employ the respective reduced one-body densities, an observable that has not been extensively studied in 2D three-body binary systems [61]. For trimer and atom-dimer states of BBX systems the reduced density displays an isotropic configuration in the angular direction, with a spatial extent characterized by the binding energy of the state. On the other hand, for FFX systems patterns with an angular dependence appear in the fermionic reduced density due to the non-zero total angular momentum of the system, which is particularly more prominent for excited trap states. However, the density of the distinguishable X particle features an isotropic configuration in the angular direction, since it is not constrained by any symmetry contrary to the case of the fermionic particles and similarly to the distinguishable particle in BBX systems.

Concluding, there are many interesting future perspectives that are worth being studied. For instance, the investigation of the dynamical formation of trimer and atom-dimer states [103] and in particular the interplay and transfer efficiency of the involved two- and three-body correlations [104] by e.g. applying interaction quenches or time-dependent pulses will yield insight into the early-time dynamics of Bose and Fermi gases in 2D. Another aspect regards the inclusion of finite-range corrections [14] that would possibly alter the upper bound of the two-body contact for atom-dimer states in the regime of large inverse scattering lengths. Indeed, the adiabatic potential curves can exhibit higher-order corrections for finite-range two-body potentials as discussed in reference [77]. For example, in the case of the EM FFX system, finite-range effects are important in the region of  $1/a_{\text{FX}} \gtrsim 55$  for a trapping frequency  $\omega = 2\pi \times 20$  Hz, and in the interval  $1/a_{\text{FX}} \gtrsim 8$  for  $\omega = 2\pi \times 1$  kHz [14]. An additional possibility for future studies concerns the stationary properties of fermionic mixtures featuring  $p$ -wave interactions [77, 105, 106] which will permit the exploration of unitary Fermi gases from a few-body perspective.

## Acknowledgments

The authors thank A G Volosniev for insightful comments. GB kindly acknowledges financial support by the State Graduate Funding Program Scholarships (Hmb-NFG). SIM gratefully acknowledges financial support in the framework of the Lenz-Ising Award of the University of Hamburg. This work is supported by the Cluster of Excellence ‘CUI: Advanced Imaging of Matter’ of the Deutsche Forschungsgemeinschaft (DFG)-EXC 2056-project ID 390715994.

## Data availability statement

The data that support the findings of this study are available upon reasonable request from the authors.

## Appendix A. Boundary condition of the hyperangular part in the hyperspherical formalism

The boundary condition whenever two particles collide is expressed within the hyperspherical formalism. Since the interparticle interaction is modelled by a delta pseudopotential [equation (2)] the hyperangular wave functions satisfying equation (8) can be written in a closed analytical form whenever the particles  $i$  and  $j$  collide [66], i.e.  $\rho_1^{(k)} \rightarrow 0$ ,

$$\lim_{\rho_1^{(k)} \rightarrow 0} \Phi_\nu(R; \Omega) = \sum_{l=\pm L} C_{\nu,l}^{(k)}(R) Y_l(\theta_2^{(k)}) Y_0(\theta_1^{(k)}) \ln \left( \frac{d_k \rho_1^{(k)}}{a^{(k)}} \right). \quad (\text{A1})$$

The above equation can be rewritten in the following form,

$$\begin{aligned} \sum_{l=\pm L} Y_l(\theta_2^{(k')}) C_{\nu,l}^{(k')} &= - \lim_{\rho_1^{(k')} \rightarrow 0} \frac{1}{\ln(A\Lambda a^{(k')})} \\ &\times \left[ 1 - \ln(A\Lambda d_k \rho_1^{(k')}) \rho_1^{(k')} \frac{\partial}{\partial \rho_1^{(k')}} \right] \Phi_\nu(R; \Omega), \end{aligned} \quad (\text{A2})$$

an expression which will ultimately determine the eigenvalues  $s_\nu$  and the  $C_\nu^{(k)}$  coefficients.

## Appendix B. Asymptotic expansion of the reduced one-body density

The expansion of the reduced one-body density at large single-particle momenta is derived first in a general form in the lab frame. Subsequently, a coordinate transformation is employed so that this asymptotic expansion is expressed within the hyperspherical formalism.

### B.1. Reduced one-body density in the lab frame

The reduced one-body density of the  $\sigma = \text{B, F or X}$  species containing  $N_\sigma$  particles reads in momentum space

$$n_\sigma(\mathbf{p}_\sigma) = \frac{1}{N_\sigma} \sum_{i=1}^{N_\sigma} \int \prod_{j \neq i} d\mathbf{r}_j \left| \tilde{\Psi}_\sigma(\mathbf{p}_\sigma, \mathbf{r}_{j \neq i}) \right|^2, \quad (\text{B1})$$

with  $\tilde{\Psi}_\sigma(\mathbf{p}_\sigma, \mathbf{r}_{j \neq i})$  being

$$\tilde{\Psi}_\sigma(\mathbf{p}_\sigma, \mathbf{r}_{j \neq i}) = \int d\mathbf{r}_i e^{-i\mathbf{p}_\sigma \cdot \mathbf{r}_i} \Psi_{\text{tot}}(\mathbf{r}_i, \mathbf{r}_j, \mathbf{r}_k). \quad (\text{B2})$$

In the last expression  $p_\sigma$  is the single-particle momentum of the  $\sigma$ -species, and  $\Psi_{\text{tot}}$  is the total wave function in the lab frame, including the center-of-mass contribution. Similarly, the reduced one-body density in position space reads

$$n_\sigma(\mathbf{r}_\sigma) = \int d\mathbf{r}_j d\mathbf{r}_k \left| \Psi_{\text{tot}}(\mathbf{r}_\sigma, \mathbf{r}_j, \mathbf{r}_k) \right|^2. \quad (\text{B3})$$

$n_\sigma(\mathbf{p}_\sigma)$  can be decomposed into a part where the  $i$ -th and  $j$ -th particles approach each other while  $j \neq i$  and another part where the integration is performed in the remaining space [107, 108]. In the first part, the following 2D boundary condition is employed [38]

$$\Psi_{\text{tot}}(\mathbf{r}_i, \mathbf{r}_j, \mathbf{r}_k) \xrightarrow{r_i \simeq r_j} \ln \left( \frac{r_{ij}}{a_{ij}} \right) A_{ij}(\mathbf{c}_{ij}, \mathbf{r}_{k \neq i,j}), \quad (\text{B4})$$

where  $\mathbf{c}_{ij} = \frac{m_i \mathbf{r}_i + m_j \mathbf{r}_j}{m_i + m_j}$  is the center-of-mass of the  $i$ -th and  $j$ -th particles,  $\mathbf{r}_{ij} = \mathbf{r}_i - \mathbf{r}_j$  denotes their relative position,  $A_{ij}(\mathbf{c}_{ij}, \mathbf{r}_{k \neq i,j})$  is a regular function and  $a_{ij}$  signifies the scattering length corresponding to the interaction of the  $i - j$  pair. Thus, the reduced one-body density in momentum space acquires the following asymptotic expansion,

$$n_\sigma(\mathbf{p}_\sigma) \approx n_\sigma^a(\mathbf{p}_\sigma) + n_\sigma^b(\mathbf{p}_\sigma), \quad (\text{B5})$$

which is valid for  $p_\sigma$  larger than all the momentum scales provided by the scattering lengths  $a_{ij}^{-1}$  between the  $i - j, j \neq i$ , particle pairs. The two terms read explicitly

$$n_\sigma^a(\mathbf{p}_\sigma) = \frac{4\pi^2}{N_\sigma p_\sigma^4} \sum_{i=1}^{N_\sigma} \sum_{k \neq i} \int \prod_{j \neq i} d\mathbf{r}_j \left| A_{ik}(\mathbf{c}_{ik}, \mathbf{r}_{j \neq i,k}) \right|^2 \quad (\text{B6})$$

and

$$n_\sigma^b(\mathbf{p}_\sigma) = \frac{4\pi^2}{N_\sigma p_\sigma^4} \sum_{i=1}^{N_\sigma} \sum_{\substack{kj \\ k \neq j \neq i}} \int \prod_{l \neq i} d\mathbf{r}_l \exp[-i\mathbf{p}_\sigma \cdot (\mathbf{r}_k - \mathbf{r}_j)] A_{ik}(\mathbf{c}_{ik}, \mathbf{r}_{j \neq i, k}) A_{ij}^*(\mathbf{c}_{ij}, \mathbf{r}_{k \neq i, j}). \quad (\text{B7})$$

**B.2. Transformation to the body-frame**

In order to transform equations (B6) and (B7) to the body-frame, the following coordinate transformation is employed [109]

$$\int d\mathbf{r}_j d\mathbf{r}_k = \frac{1}{d_j^2} \int d\mathbf{r}_{\text{CM}} d\rho_2^{(j)} = \frac{1}{d_j^2} \int d\mathbf{r}_{\text{CM}} d\theta_2^{(j)} dR, \quad (\text{B8})$$

where  $\rho_2^{(j)} = d_k(\mathbf{r}_k - \mathbf{r}_j)$  and  $\mathbf{r}_{\text{CM}}$  is the center-of-mass of the three particles. The norm of the second Jacobi vector in equation (B8),  $\rho_2^{(j)}$  is substituted by the hyperradius  $R$ , since the first Jacobi vector vanishes due to the boundary condition [see also appendix A].

The boundary condition equation (B4) can be also expressed in the hyperspherical formalism, making use of the descriptive notation  $\sigma\sigma'$ , denoting the species B, F or X [see also table 1]. Thus, whenever a  $\sigma$  species particle collides with a  $\sigma'$  species one ( $\alpha^{\sigma\sigma'} \rightarrow 0$ )

$$\Psi_{\text{CM}}(\mathbf{r}_{\text{CM}})\Psi(R; \Omega) \xrightarrow{\alpha^{\sigma\sigma'} \rightarrow 0} \Psi_{\text{CM}}(\mathbf{r}_{\text{CM}}) \ln \left( \frac{\sqrt{\mu}R\alpha^{\sigma\sigma'}}{\sqrt{\mu_{\sigma\sigma'}}a_{\sigma\sigma'}} \right) \times \sum_{\nu} \frac{F_{\nu}(R)}{R^{3/2}} \sum_{l=\pm L} C_{\nu,l}^{\sigma\sigma'}(R) Y_l(\theta_2^{\sigma\sigma'}) Y_0(\theta_1^{\sigma\sigma'}). \quad (\text{B9})$$

Here,  $\mu_{\sigma\sigma'}$  and  $a_{\sigma\sigma'}$  denote the two-body reduced mass and scattering length respectively between the  $\sigma\sigma'$  species. By integrating the center-of-mass, the first term,  $n_\sigma^a(\mathbf{p}_\sigma)$  is expressed as follows

$$n_\sigma^a(\mathbf{p}_\sigma) = \frac{4\pi}{\mu N_\sigma p_\sigma^4} \sum_{\sigma'} \mu_{\sigma\sigma'} \int_0^\infty \frac{dR}{R^2} \left| \sum_{\nu} F_{\nu}(R) \sum_{l=\pm L} C_{\nu,l}^{\sigma\sigma'}(R) \right|^2 = \frac{1}{N_\sigma p_\sigma^4} \sum_{\sigma'} (1 + \delta_{\sigma\sigma'}) \mathcal{D}_2^{\sigma\sigma'}, \quad (\text{B10})$$

where  $\mathcal{D}_2^{\sigma\sigma'}$  is the two-body contact between the species  $\sigma\sigma'$ . Similarly, the second term  $n_\sigma^b(\mathbf{p}_\sigma)$  yields,

$$n_\sigma^b(\mathbf{p}_\sigma) = \frac{4\pi}{N_\sigma p_\sigma^4} \sum_{\sigma'} \frac{\mu_{\sigma\sigma'}}{\mu} \int_0^\infty \frac{dR}{R^2} \left\{ J_0 \left[ \frac{p_\sigma R \sqrt{\mu_{\sigma\sigma'}}}{\sqrt{\mu}} \right] (-1)^L + J_{2L} \left[ \frac{p_\sigma R \sqrt{\mu_{\sigma\sigma'}}}{\sqrt{\mu}} \right] (1 - \delta_{0,L}) \right\} \times \sum_{\sigma'' \neq \sigma'} \sum_{l=\pm L} \left( \sum_{\nu} F_{\nu}(R) C_{\nu,l}^{\sigma\sigma'}(R) \right) \left( \sum_{\nu'} F_{\nu'}(R) C_{\nu',l}^{\sigma'\sigma''}(R) \right)^* \quad (\text{B11})$$

where  $J_\nu(\cdot)$  is the  $\nu$ -th Bessel function of the first kind, and  $L$  is the total angular momentum of the system.

Regarding the reduced one-body density in position space, by employing the transformation from the lab to the body-frame,  $\int \prod_{j \neq i} d\mathbf{r}_j = \int d\rho_1^{(i)} d\rho_2^{(i)}$  and the descriptive notation, one gets

$$n_\sigma(\mathbf{r}_\sigma) = \frac{M}{\pi} \int dR d\Omega^{\sigma''\sigma'} e^{-G(r_\sigma, R, \Omega^{\sigma''\sigma'})} \times \left| \sum_{\nu} F_{\nu} \Phi_{\nu}(R; \Omega^{\sigma''\sigma'}) \right|^2, \quad (\text{B12})$$

where

$$G(\mathbf{r}_\sigma, R, \Omega^{\sigma''\sigma'}) = Mr_\sigma^2 + (m_{\sigma''} + m_{\sigma'})^2 \frac{R^2 \cos^2 \alpha^{\sigma''\sigma'} \mu_{\sigma''\sigma'}}{M\mu} + 2 \frac{(m_{\sigma''} + m_{\sigma'}) \sqrt{\mu_{\sigma''\sigma'}}}{\sqrt{\mu}} r_\sigma R \cos \alpha^{\sigma''\sigma'} \times \cos(\theta_2^{\sigma''\sigma'} - \phi). \quad (\text{B13})$$

In the above expressions,  $\sigma' \neq \sigma$ ,  $\sigma'' = B/F$  depending on the mixture and  $(r_\sigma, \phi)$  are the polar coordinates of the  $\mathbf{r}_\sigma$  2D vector.

## Appendix C. Derivation of the upper bound of the two-body contact

In the limit of large inter- and intraspecies scattering lengths  $1/a_{\sigma\sigma'}$ , an approximate analytical form of the corresponding two-body contact of atom-dimer states is derived. The adiabatic potentials  $U_\nu(R)$  with  $\nu = 1$  ( $\nu = 1, 2$ ) at large hyperradius  $R$  and in the absence of a trap asymptote to an atom-dimer threshold in the case of FFX (BBX) systems. This behavior is reflected to the eigenvalues  $s_\nu(R)$ , which obey the following relations [14, 74],

$$s_1(R) \xrightarrow{R>R_0} i \frac{2e^{-\gamma} R \sqrt{1 + \mathcal{M}}}{a_{\sigma X} \sqrt{2\mathcal{M} + 1}} \quad (\text{C1})$$

$$s_2(R) \xrightarrow{R>R_0} i \frac{2\sqrt{2}e^{-\gamma} R}{a_{\text{BB}} \sqrt{2\mathcal{M} + 1}}, \quad (\text{C2})$$

where  $\mathcal{M} = \frac{m_{\text{F/B}}}{m_X}$ ,  $\sigma = B/F$  and  $i$  is the imaginary unit. The value of  $R_0$  is proportional to the scattering lengths, and so for large  $1/a_{\text{FX}}$ ,  $1/a_{\text{BX}}$ , and  $1/a_{\text{BB}}$ , the parameter  $R_0$  becomes small. In these regimes, the two-body contact between  $\sigma\sigma'$  species can be decomposed into two parts

$$\begin{aligned} \mathcal{D}_2^{\sigma\sigma'} &= \frac{2\pi\mu_{\sigma\sigma'}(2 - \delta_{\sigma\sigma'})}{\mu} \int_0^{R_0} \frac{dR}{R^2} \left| F_\nu(R) \sum_{l=\pm L} C_{\nu,l}^{\sigma\sigma'}(R) \right|^2 \\ &+ \frac{2\pi\mu_{\sigma\sigma'}(2 - \delta_{\sigma\sigma'})}{\mu} \int_{R_0}^{\infty} \frac{dR}{R^2} \left| F_\nu(R) \sum_{l=\pm L} C_{\nu,l}^{\sigma\sigma'}(R) \right|^2. \end{aligned} \quad (\text{C3})$$

In the above expression we take into account only the first potential ( $\nu = 1$ ) for FFX or the two lowest potentials ( $\nu = 1, 2$ ) for BBX systems, which support atom-dimer states and neglect all the other coupling elements with the remaining adiabatic potentials.

The  $C_{\nu,l}^{\sigma\sigma'}$  coefficients satisfy a semi-analytical expression [66, 74, 75], valid in the case of a zero-range pseudopotential, relating the coefficients with the derivatives of the eigenvalues  $s_\nu$ . By employing these expressions we end up with the following relations in the limit where  $1/a_{\text{FX}}, 1/a_{\text{BX}}, 1/a_{\text{BB}} \gg 1$ ,

$$\mathcal{D}_2^{\sigma X} = \frac{4\pi\sqrt{2\mathcal{M} + 1}}{1 + \mathcal{M}} \int_0^{R_0} \frac{dR}{R^2} \left| F_1(R) \sum_{l=\pm L} C_{1,l}^{\sigma X}(R) \right|^2 + \frac{16\pi e^{-2\gamma}}{a_{\sigma X}^2} \int_{R_0}^{\infty} dR |F_1(R)|^2 \approx \frac{16\pi e^{-2\gamma}}{a_{\sigma X}^2}. \quad (\text{C4})$$

$$\mathcal{D}_2^{\text{BB}} = \frac{2\pi\sqrt{2\mathcal{M} + 1}}{2} \int_0^{R_0} \frac{dR}{R^2} \left| F_2(R) \sum_{l=\pm L} C_{2,l}^{\text{BB}}(R) \right|^2 + \frac{16\pi e^{-2\gamma}}{a_{\text{BB}}^2} \int_{R_0}^{\infty} dR |F_2(R)|^2 \approx \frac{16\pi e^{-2\gamma}}{a_{\text{BB}}^2}, \quad (\text{C5})$$

where  $\sigma = B/F$ . In the last steps of equations (C4) and (C5), we have kept only the dominant second term. The second integral is approximated by unity since  $R_0$  is small. Hence, this yields the normalization condition for the hyperradial part  $F_\nu(R)$ , where  $\nu = 1, 2$ .

## ORCID iDs

S I Mistakidis  <https://orcid.org/0000-0002-5118-5792>

P Giannakeas  <https://orcid.org/0000-0002-1164-0201>

P Schmelcher  <https://orcid.org/0000-0002-2637-0937>

## References

- [1] Bayha L, Holten M, Klemm R, Subramanian K, Bjerlin J, Reimann S M, Bruun G M, Preiss P M and Jochim S 2020 *Nature* **587** 583
- [2] Holten M, Bayha L, Subramanian K, Heintze C, Preiss P M and Jochim S 2021 *Phys. Rev. Lett.* **126** 020401
- [3] Blume D 2012 *Rep. Prog. Phys.* **75** 046401
- [4] Xu P et al 2015 *Nat. Commun.* **6** 7803
- [5] Sompet P, Carpentier A V, Fung Y H, McGovern M and Andersen M F 2013 *Phys. Rev. A* **88** 051401
- [6] Anderegg L, Cheuk L W, Bao Y, Burchesky S, Ketterle W, Ni K-K and Doyle J M 2019 *Science* **365** 1156
- [7] Guan Q, Klinkhamer V, Klemm R, Becher J H, Bergschneider A, Preiss P M, Jochim S and Blume D 2019 *Phys. Rev. Lett.* **122** 083401
- [8] Reynolds L A, Schwartz E, Ebling U, Weyland M, Brand J and Andersen M F 2020 *Phys. Rev. Lett.* **124** 073401
- [9] Chin C, Grimm R, Julienne P and Tiesinga E 2010 *Rev. Mod. Phys.* **82** 1225



- [10] Olshanii M 1998 *Phys. Rev. Lett.* **81** 938
- [11] Bergeman T, Moore M G and Olshanii M 2003 *Phys. Rev. Lett.* **91** 163201
- [12] Haller E, Mark M J, Hart R, Danzl J G, Reichsöllner L, Melezhik V, Schmelcher P and Nägerl H-C 2010 *Phys. Rev. Lett.* **104** 153203
- [13] Giannakeas P, Diakonou F and Schmelcher P 2012 *Phys. Rev. A* **86** 042703
- [14] D’Incao J P, Anis F and Esry B D 2015 *Phys. Rev. A* **91** 062710
- [15] Helfrich K and Hammer H-W 2011 *Phys. Rev. A* **83** 052703
- [16] Pricoupenko L and Olshanii M 2007 *J. Phys. B: At. Mol. Opt. Phys.* **40** 2065
- [17] Liu X-J, Hu H and Drummond P D 2010 *Phys. Rev. B* **82** 054524
- [18] Daily K M, Wooten R E and Greene C H 2015 *Phys. Rev. B* **92** 125427
- [19] Greene C H, Giannakeas P and Pérez-Ríos J 2017 *Rev. Mod. Phys.* **89** 035006
- [20] Gharashi S E, Daily K M and Blume D 2012 *Phys. Rev. A* **86** 042702
- [21] Kirk T and Parish M M 2017 *Phys. Rev. A* **96** 053614
- [22] Bermudez A, Porras D and Martin-Delgado M A 2009 *Phys. Rev. A* **79** 060303
- [23] Lang G 2018 *Correlations in Low-Dimensional Quantum Gases (Springer Theses)* (Berlin: Springer)
- [24] Lindgren E J, Rotureau J, Forssén C, Volosniev A G and Zinner N T 2014 *New J. Phys.* **16** 063003
- [25] Zinner N T, Volosniev A G, Fedorov D V, Jensen A S and Valiente M 2014 *Europhys. Lett.* **107** 60003
- [26] Bellotti F F, Frederico T, Yamashita M T, Fedorov D V, Jensen A S and Zinner N T 2014 *New J. Phys.* **16** 013048
- [27] Bellotti F F, Frederico T, Yamashita M T, Fedorov D V, Jensen A S and Zinner N T 2013 *Phys. Rev. A* **87** 013610
- [28] Fletcher R J, Lopes R, Man J, Navon N, Smith R P, Zwierlein M W and Hadzibabic Z 2017 *Science* **355** 377
- [29] Wild R J, Makotyn P, Pino J M, Cornell E A and Jin D S 2012 *Phys. Rev. Lett.* **108** 145305
- [30] Sagi Y, Drake T E, Paudel R and Jin D S 2012 *Phys. Rev. Lett.* **109** 220402
- [31] Stewart J T, Gaebler J P, Drake T E and Jin D S 2010 *Phys. Rev. Lett.* **104** 235301
- [32] Kuhnle E D, Hu H, Liu X-J, Dyke P, Mark M, Drummond P D, Hannaford P and Vale C J 2010 *Phys. Rev. Lett.* **105** 070402
- [33] Hoinka S, Lingham M, Fenech K, Hu H, Vale C J, Drut J E and Gandolfi S 2013 *Phys. Rev. Lett.* **110** 055305
- [34] Sykes A G, Corson J P, D’Incao J P, Koller A P, Greene C H, Rey A M, Hazzard K R A and Bohn J L 2014 *Phys. Rev. A* **89** 021601
- [35] Corson J P and Bohn J L 2015 *Phys. Rev. A* **91** 013616
- [36] Bougas G, Mistakidis S I and Schmelcher P 2019 *Phys. Rev. A* **100** 053602
- [37] Bougas G, Mistakidis S I, Alshalan G M and Schmelcher P 2020 *Phys. Rev. A* **102** 013314
- [38] Werner F and Castin Y 2012 *Phys. Rev. A* **86** 053633
- [39] Valiente M, Zinner N T and Mølmer K 2011 *Phys. Rev. A* **84** 063626
- [40] Valiente M, Zinner N T and Mølmer K 2012 *Phys. Rev. A* **86** 043616
- [41] Werner F and Castin Y 2012 *Phys. Rev. A* **86** 013626
- [42] Castin Y and Werner F 2011 *Phys. Rev. A* **83** 063614
- [43] Fröhlich B, Feld M, Vogt E, Koschorreck M, Köhl M, Berthod C and Giamarchi T 2012 *Phys. Rev. Lett.* **109** 130403
- [44] Bertaina G and Giorgini S 2011 *Phys. Rev. Lett.* **106** 110403
- [45] Zou Y-Q, Bakkali-Hassani B, Maury C, Le Cerf É, Nascimbene S, Dalibard J and Beugnon J 2021 *Nat. Commun.* **12** 760
- [46] Bellotti F F, Frederico T, Yamashita M T, Fedorov D V, Jensen A S and Zinner N T 2013 *J. Phys. B: At. Mol. Opt. Phys.* **46** 055301
- [47] Bellotti F F, Frederico T, Yamashita M T, Fedorov D V, Jensen A S and Zinner N T 2011 *J. Phys. B: At. Mol. Opt. Phys.* **44** 205302
- [48] Lim T K and Shimer B 1980 *Z. Phys. A* **297** 185
- [49] Bruch L W and Tjon J A 1979 *Phys. Rev. A* **19** 425
- [50] Pricoupenko L and Pedri P 2010 *Phys. Rev. A* **82** 033625
- [51] Tung S-K, Jiménez-García K, Johansen J, Parker C V and Chin C 2014 *Phys. Rev. Lett.* **113** 240402
- [52] Pires R, Ulmanis J, Häfner S, Repp M, Arias A, Kuhnle E D and Weidemüller M 2014 *Phys. Rev. Lett.* **112** 250404
- [53] Ulmanis J, Häfner S, Pires R, Kuhnle E D, Wang Y, Greene C H and Weidemüller M 2016 *Phys. Rev. Lett.* **117** 153201
- [54] Johansen J, DeSalvo B J, Patel K and Chin C 2017 *Nat. Phys.* **13** 731
- [55] Wacker L J, Jørgensen N B, Birkmose D, Winter N, Mikkelsen M, Sherson J, Zinner N and Arlt J J 2016 *Phys. Rev. Lett.* **117** 163201
- [56] Giannakeas P and Greene C H 2018 *Phys. Rev. Lett.* **120** 023401
- [57] Mikkelsen M, Jensen A S, Fedorov D V and Zinner N T 2015 *J. Phys. B: At. Mol. Opt. Phys.* **48** 085301
- [58] Petrov D S and Werner F 2015 *Phys. Rev. A* **92** 022704
- [59] Naidon P and Endo S 2017 *Rep. Prog. Phys.* **80** 056001
- [60] D’Incao J P 2018 *J. Phys. B: At. Mol. Opt. Phys.* **51** 043001
- [61] Sandoval J H, Bellotti F F, Jensen A S and Yamashita M T 2016 *Phys. Rev. A* **94** 022514
- [62] Busch T, Englert B-G, Rzazewski K and Wilkens M 1998 *Found. Phys.* **28** 549
- [63] Budewig L, Mistakidis S I and Schmelcher P 2019 *Mol. Phys.* **117** 2043
- [64] Farrell A and van Zyl B P 2009 *J. Phys. A: Math. Theor.* **43** 015302
- [65] Rittenhouse S T, Wray A and Johnson B L 2016 *Phys. Rev. A* **93** 012511
- [66] Rittenhouse S T, Mehta N P and Greene C H 2010 *Phys. Rev. A* **82** 022706
- [67] Olshanii M and Pricoupenko L 2001 *Phys. Rev. Lett.* **88** 010402
- [68] Petrov D S and Shlyapnikov G V 2001 *Phys. Rev. A* **64** 012706
- [69] Whitten R C and Smith F T 1968 *J. Math. Phys.* **9** 1103
- [70] Smirnov Y F and Shitikova K V 1977 *Sov. J. Part. Nucl.* **8** 44
- [71] Avery J 1989 *Hyperspherical Harmonics: Applications in Quantum Theory* (Dordrecht: Kluwer)
- [72] Abramowitz M and Stegun I 1965 *Handbook of Mathematical Functions, with Formulas, Graphs, and Mathematical Tables* (New York: Dover)
- [73] Nielsen E, Fedorov D V, Jensen A S and Garrido E 2001 *Phys. Rep.* **347** 373
- [74] Kartavtsev O I and Malykh A V 2006 *Phys. Rev. A* **74** 042506
- [75] Kartavtsev O I and Malykh A V 2007 *JETP Lett.* **86** 625
- [76] De Boor C 1978 *A Practical Guide to Splines* vol 27 (New York: Springer)
- [77] Volosniev A G, Fedorov D V, Jensen A S and Zinner N T 2014 *J. Phys. B: At. Mol. Opt. Phys.* **47** 185302
- [78] Holten M, Bayha L, Klein A C, Murthy P A, Preiss P M and Jochim S 2018 *Phys. Rev. Lett.* **121** 120401
- [79] Murthy P A, Defenu N, Bayha L, Holten M, Preiss P M, Enss T and Jochim S 2019 *Science* **365** 268

106

- [80] Blume D and Daily K M 2010 *Phys. Rev. A* **82** 063612
- [81] Portegies J and Kokkelmans S 2011 *Few-Body Syst.* **51** 219
- [82] Kartavtsev O I and Malykh A V 2007 *J. Phys. B: At. Mol. Opt. Phys.* **40** 1429
- [83] Tan S 2008 *Ann. Phys., NY* **323** 2952
- [84] Tan S 2008 *Ann. Phys., NY* **323** 2971
- [85] Tan S 2008 *Ann. Phys., NY* **323** 2987
- [86] Braaten E, Kang D and Platter L 2011 *Phys. Rev. Lett.* **106** 153005
- [87] Friedrich H 2013 *Scattering Theory (Lecture Notes in Physics)* vol 872 (Berlin: Springer)
- [88] Yan Y and Blume D 2013 *Phys. Rev. A* **88** 023616
- [89] Sant'Ana F T, Hébert F, Rousseau V G, Albert M and Vignolo P 2019 *Phys. Rev. A* **100** 063608
- [90] Rakhimov A, Abdurakhmonov T and Tanatar B 2021 arXiv:2104.11894
- [91] Hoffman M D, Javernick P D, Loheac A C, Porter W J, Anderson E R and Drut J E 2015 *Phys. Rev. A* **91** 033618
- [92] Capuzzi P and Vignolo P 2020 *Phys. Rev. A* **101** 013633
- [93] Braaten E and Hammer H-W 2013 *J. Phys. B: At. Mol. Opt. Phys.* **46** 215203
- [94] Bergschneider A, Klinkhamer V M, Becher J H, Klemt R, Zürn G, Preiss P M and Jochim S 2018 *Phys. Rev. A* **97** 063613
- [95] Mistakidis S I, Katsimiga G C, Kevrekidis P G and Schmelcher P 2018 *New J. Phys.* **20** 043052
- [96] Katsimiga G C, Mistakidis S I, Koutentakis G M, Kevrekidis P G and Schmelcher P 2017 *New J. Phys.* **19** 123012
- [97] Xie W F and Bao C G 1997 *Commun. Theor. Phys.* **27** 185
- [98] Papp S B, Pino J M and Wieman C E 2008 *Phys. Rev. Lett.* **101** 040402
- [99] Maity D K, Mukherjee K, Mistakidis S I, Das S, Kevrekidis P G, Majumder S and Schmelcher P 2020 *Phys. Rev. A* **102** 033320
- [100] Lous R S, Fritsche I, Jag M, Lehmann F, Kirilov E, Huang B and Grimm R 2018 *Phys. Rev. Lett.* **120** 243403
- [101] Viverit L, Pethick C J and Smith H 2000 *Phys. Rev. A* **61** 053605
- [102] Mistakidis S I, Hilbig L and Schmelcher P 2019 *Phys. Rev. A* **100** 023620
- [103] D'Incao J P, Wang J and Colussi V E 2018 *Phys. Rev. Lett.* **121** 023401
- [104] Colussi V E, Corson J P and D'Incao J P 2018 *Phys. Rev. Lett.* **120** 100401
- [105] Kanjilal K and Blume D 2006 *Phys. Rev. A* **73** 060701
- [106] Nishida Y, Moroz S and Son D T 2013 *Phys. Rev. Lett.* **110** 235301
- [107] Olshanii M and Dunjko V 2003 *Phys. Rev. Lett.* **91** 090401
- [108] Pătu O I and Klümper A 2017 *Phys. Rev. A* **96** 063612
- [109] Colussi V 2019 *Atoms* **7** 19

**4.1.4 Dynamical excitation processes and correlations of three-body two-dimensional mixtures**

## Dynamical excitation processes and correlations of three-body two-dimensional mixtures

G. Bougas,<sup>1,\*</sup> S. I. Mistakidis<sup>2,3</sup>, P. Giannakeas,<sup>4</sup> and P. Schmelcher<sup>1,5</sup>

<sup>1</sup>*Center for Optical Quantum Technologies, Department of Physics, University of Hamburg, Luruper Chaussee 149, 22761 Hamburg, Germany*

<sup>2</sup>*ITAMP, Center for Astrophysics | Harvard & Smithsonian, Cambridge, Massachusetts 02138, USA*

<sup>3</sup>*Department of Physics, Harvard University, Cambridge, Massachusetts 02138, USA*

<sup>4</sup>*Max-Planck-Institut für Physik komplexer Systeme, Nöthnitzer Strasse 38, D-01187 Dresden, Germany*

<sup>5</sup>*The Hamburg Centre for Ultrafast Imaging, University of Hamburg, Luruper Chaussee 149, 22761 Hamburg, Germany*



(Received 4 May 2022; accepted 12 October 2022; published 31 October 2022)

A scheme is proposed to dynamically excite distinct eigenstate superpositions in three-body Bose-Fermi mixtures confined in a two-dimensional harmonic trap. The system is initialized in a noninteracting state with a variable spatial extent, and the scattering lengths are subsequently quenched spanning the regime from weak to strong interactions. For spatial widths smaller than the three-body harmonic oscillator length, a superposition of trimers and atom-dimers is dynamically attained, otherwise trap states are predominantly populated, as inferred from the frequency spectrum of the fidelity. Accordingly, the Tan contacts evince the buildup of short-range two- and three-body correlations in the course of the evolution. A larger spatial extent of the initial state leads to a reduction of few-body correlations, endowed, however, with characteristic peaks at the positions of the avoided crossings in the energy spectra, thereby signaling the participation of atom-dimers. Our results expose ways to dynamically excite selectively trimers, atom-dimers, and trapped few-body states characterized by substantial correlations, and they are likely to be accessible within current experiments.

DOI: [10.1103/PhysRevA.106.043323](https://doi.org/10.1103/PhysRevA.106.043323)

### I. INTRODUCTION

The appealing feature of ultracold physics is the controllability of interactions, which enables us to study a plethora of phenomena, such as the formation of droplets [1–3] and polarons [4,5], and to understand in depth the buildup of few- and many-body correlations [6]. More specifically, the few-body correlations can be quantified by Tan contacts. These stem from the short-range character of the interatomic interactions [7–15], and they are experimentally probed through radiofrequency (rf) spectroscopy [16–18], time-of-flight expansion [19], or Bragg spectroscopy [20,21]. Contacts interrelate macroscopic observables at equilibrium, such as the energy and pressure of a gas, in terms of few-body microscopic mechanisms [11,22] addressing the properties of a gas universally, regardless of the atom number, the statistics, or the interaction strength.

The recent realization of three-dimensional (3D) unitary Bose gases offers the possibility to investigate the dynamical formation of few-body correlations in strongly interacting ultracold matter [23–26]. Quenching the scattering length from the noninteracting case to unitarity enables the experimental observation of few-body states such as the Efimov states, i.e., an infinite geometric progression of three-body bound levels comprised of unbound two-body subsystems [27,28]. In addition, theoretical efforts demonstrated that the quenched dynamics of such three-body systems exhibits unique features

in the population growth of Efimov trimers and atom-dimers [29–33]. For example, in Ref. [29] it was argued that the two-body Tan contact is enhanced during the early stages of the dynamics, whereas the three-body contact increases appreciably only when the interparticle spacing matches the size of an Efimov state [30]. However, the latter are typically short-lived due to three-body recombination processes [34].

Promising candidates to mitigate such losses while maintaining a high fraction of trimer states are two-dimensional (2D) gases [35,36]. There the corresponding trimer wave functions have a small amplitude at short distances suppressing three-body recombination processes [36,37] as compared to 3D systems. Additionally, theoretical studies in 2D three-body systems [38–44] have addressed their time-independent attributes in terms of their eigenspectrum as well as their corresponding few-body correlations via Tan contacts [41,45–47]. In particular, it was shown that mass-imbalanced mixtures support a multitude of trimer states with amplified two- and three-body correlations compared to the mass-balanced case [41,45].

In contrast to the 3D systems [29–31,48,49], the dynamical response including the underlying excitation processes and accompanying correlation mechanisms of 2D three-body systems is not well-understood. Importantly, the study of these systems has thus far been restricted to their stationary correlation properties [38,40,45,46] in the absence of external confinement. In this work, a protocol is proposed for triggering specific excitation branches in 2D harmonically trapped mixtures of two identical bosons or fermions interacting with another atom. Apart from the particle statistics, our study

\*gbougas@physnet.uni-hamburg.de

addresses the effect of unequal massed three-body collisions. In 3D gases, it is known that highly mass-imbalanced systems exhibit rich resonant effects [50–55], or they favor the observation of multiple successive Efimov states [56–58], while offering unique platforms to study reaction rates in atom-dimer and molecule-molecule collisions [59–65]. Therefore, the inclusion of unequal masses here provides a comprehensive description of the dynamic properties of 2D three-body collisions ranging from light-light-heavy (LLH) to heavy-heavy-light (HHL) systems.

Initially, the three-body mixture is considered in a non-interacting state characterized by a parameter  $w$  describing its spatial extent. Subsequently, the interactions are turned on abruptly (interaction quench), resulting in distinct dynamical response regimes characterized by specific excitation mechanisms and correlations being imprinted in the fidelity spectrum. The Hilbert space of the postquench three-body system, at the final values of the scattering lengths, is mainly partitioned into three generic types of eigenstates: trimers, atom-dimers, and trap states. For widths  $w$  of the initial state smaller than the harmonic-oscillator lengthscale, we observe that the dominant excitation branches identified in the fidelity spectrum correspond to trimers and atom-dimers. In the case of HHL systems, however, these states are prevalent over a relatively smaller range of scattering lengths. For an increasing width  $w$  of the initial state, the trap states are predominantly populated.

Furthermore, we show that the participation of distinct eigenstates impacts strongly the dynamics of short-range correlations quantified by the Tan contacts. In particular, both the two- and three-body correlations become enhanced for initial-state widths smaller than the spatial extent of the trap. The correlations are suppressed as the width of the initial configuration is increased since the population of trap states becomes more dominant. In addition, distinct peaks in the few-body correlations are observed as the scattering lengths vary. This structure arises from the narrow avoided crossings in the eigenspectrum where the atoms are in a superposition of trap and atom-dimer states. The above-mentioned features occur for both LLH and HHL settings regardless of the exchange symmetry of the particles. However, the enhancements in the few-body contacts become narrower in the HHL case, as compared to the LLH one, due to the existence of sharp avoided crossings in the respective energy spectrum [41].

This work proceeds as follows: In Sec. II the adiabatic hyperspherical formalism is briefly outlined, and in Sec. III the initial ansatz of the three-body system and the time-evolved wave function are introduced. Subsequently, the excitation spectra, associated modes, and correlation dynamics based on the fidelity spectrum and Tan contacts are unveiled for both LLH systems in Sec. IV and HHL ones in Sec. V. In Sec. VI we briefly comment on the possible experimental realization of our setup. Section VII lays out our conclusions and provides an outlook. Moreover, Appendix A introduces the adiabatic Hamiltonian and the 2D zero-range pseudopotential. Appendix B provides the form of the hyperangular wave function for the noninteracting initial state. In Appendix C, we elaborate on the excitation spectrum of the LLH BBX system for widths of the initial state equal to the three-body harmonic-oscillator length.

## II. ADIABATIC HYPERSPHERICAL REPRESENTATION OF THE THREE-BODY MIXTURE

In the following, we consider three-body binary mass-imbalanced mixtures trapped in a 2D harmonic oscillator of frequency  $\omega$ . They typically consist of either two identical bosons (BBX) or two identical noninteracting spin-polarized fermions (FFX) interacting with a third distinguishable particle. The underlying pairwise interactions are modeled with  $s$ -wave zero-range pseudopotentials [66] characterized by 2D scattering lengths  $a_{FX}$  and  $a_{BB}, a_{BX}$  for the FFX and BBX systems, respectively. Here,  $a_{\sigma\sigma'}$  denotes the 2D scattering length between a particle of species  $\sigma$  and  $\sigma'$ , where  $\sigma = B, X$  or  $\sigma = F, X$ . Below, for simplicity, we typically consider variations of  $1/a_{FX}$  and  $a_{BB}/a_{BX}$  where in the latter case  $a_{BB}$  is kept fixed. The magnitude of the 2D scattering lengths can in principle be adjusted via standard Fano-Feshbach resonances [67], since they parametrically depend on their 3D counterparts [68]. Let us note that by definition the 2D scattering lengths can only be positive, a property stemming from the existence of a two-body bound state always in 2D, and the noninteracting limit occurs when they are either 0 or  $+\infty$  [69]. Moreover, depending on the mass ratio between the identical atom and the third particle, i.e.,  $m_{B/F}/m_X$ , we distinguish between LLH and HHL cases. In particular, the employed mass ratios are  $m_B/m_X = 0.04, 22.16$  for BBX referring to mixtures of  ${}^7\text{Li} - {}^7\text{Li} - {}^{173}\text{Yb}$ ,  ${}^{133}\text{Cs} - {}^{133}\text{Cs} - {}^6\text{Li}$ , and  $m_F/m_X = 0.0451, 24.71$  for FFX corresponding to  ${}^6\text{Li} - {}^6\text{Li} - {}^{133}\text{Cs}$ ,  ${}^{173}\text{Yb} - {}^{173}\text{Yb} - {}^7\text{Li}$  systems.

The stationary properties of these mixtures are straightforwardly addressed within the adiabatic hyperspherical framework [27, 34, 70–72], with the pairwise interactions modeled via contact pseudopotentials. Due to the decoupling of the center of mass, the hyperspherical coordinates representation is employed and the relative position of the atoms is described by a set of three hyperangles (which collectively are denoted by  $\Omega$ ) and the hyperradius  $R$  that controls the overall size of the system. Hence, by employing the hyperspherical coordinates, the relative three-body Hamiltonian [41] reads

$$H_{\text{rel}} = -\frac{\hbar^2}{2\mu R^{3/2}} \frac{\partial^2}{\partial R^2} R^{3/2} + \frac{1}{2} \mu \omega^2 R^2 + H_{\text{ad}}(R; \Omega). \quad (1)$$

The first term refers to the kinetic energy, while the second one is the external trapping potential.  $H_{\text{ad}}(R; \Omega)$  describes the centrifugal motion of the three particles, and it contains the pairwise  $s$ -wave contact interactions, depending on the aforementioned 2D scattering lengths (for more details, see Appendix A). Also,  $\mu = m_{B/F}/\sqrt{2m_{B/F}/m_X + 1}$  is the three-body reduced mass and  $m_{B/F}$  stands for the mass of bosons or fermions. Note that in the following, we employ as a characteristic lengthscale of the three-body system the quantity  $a_{\text{ho}} = \sqrt{\hbar/\mu\omega}$ , i.e., the three-body harmonic-oscillator length.

The eigenstates of the three-body system are determined as follows: First,  $H_{\text{ad}}(R; \Omega)$  is diagonalized at a fixed hyperradius  $R$  [72] where the eigenvalues  $s_\nu(R)$  are associated with the adiabatic potential curves  $\hbar^2(s_\nu^2(R) - 1/4)/2\mu R^2$ , and the corresponding eigenfunctions, i.e.,  $\Phi_\nu(R; \Omega)$ , are used as a basis set for the three-body relative wave function. The latter in the adiabatic hyperspherical representation is given by the

expression  $\Psi(R, \Omega) = R^{-3/2} \sum_{\nu} F_{\nu}(R) \Phi_{\nu}(R; \Omega)$ .<sup>1</sup>  $F_{\nu}(R)$  denotes the hyperradial component of  $\Psi(R, \Omega)$ , which satisfies the following system of coupled ordinary differential equations:

$$\begin{cases} -\frac{\hbar^2}{2\mu} \frac{d^2}{dR^2} + U_{\nu}(R) \Big\} F_{\nu}(R) \\ -\frac{\hbar^2}{2\mu} \sum_{\nu'} \left[ 2P_{\nu\nu'}(R) \frac{d}{dR} + Q_{\nu\nu'}(R) \right] F_{\nu'}(R) = E F_{\nu}(R). \end{cases} \quad (2)$$

Here,  $U_{\nu}(R)$  represents the  $\nu$ th adiabatic potential curve including the trap, whereas the  $P_{\nu\nu'}(R)$  and  $Q_{\nu\nu'}(R)$  terms denote the nonadiabatic coupling matrix elements. More specifically, the adiabatic potential curves and the nonadiabatic coupling matrix elements are given by the following expressions [41,43,72]:

$$U_{\nu}(R) = \frac{\hbar^2}{2\mu R^2} \left( s_{\nu}^2(R) - \frac{1}{4} \right) + \frac{1}{2} \mu \omega^2 R^2, \quad (3)$$

$$P_{\nu\nu'}(R) = \left\langle \Phi_{\nu}(R; \Omega) \left| \frac{\partial \Phi_{\nu'}(R; \Omega)}{\partial R} \right\rangle_{\Omega}, \quad (4)$$

$$Q_{\nu\nu'}(R) = \left\langle \Phi_{\nu}(R; \Omega) \left| \frac{\partial^2 \Phi_{\nu'}(R; \Omega)}{\partial R^2} \right\rangle_{\Omega}, \quad (5)$$

where the symbol  $\langle \dots \rangle_{\Omega}$  indicates that the integration is over the hyperangles only. In the following, harmonic-oscillator units are adopted, unless stated otherwise, i.e.,  $m_{B/F} = \hbar = \omega = 1$ , where  $m_{B/F}$  is the mass of the identical bosons or spin-polarized fermions.

### III. INITIALIZATION AND QUENCH PROTOCOL

Initially the three atoms are prepared in a noninteracting state. This situation in 2D translates to a scattering length either 0 or  $+\infty$ , which in the case of two harmonically trapped atoms is shown to reproduce the corresponding noninteracting energy spectra [69,73,74]. The state is characterized by  $1/a_{BX} = 1/a_{BB} = 0$  for BBX or  $1/a_{FX} = 0$  for FFX systems, while its spatial extent is parametrized by  $w$ ; see Fig. 1(a). The initial three-body wave function in the hyperspherical coordinate frame reads

$$\Psi(R, \Omega, t=0) = \frac{R^L \sqrt{2}}{\sqrt{\Gamma(2+L)w^{2+L}}} e^{-\frac{R^2}{2w^2}} \Phi_0^{(0)}(\Omega), \quad (6)$$

where  $\Gamma(\cdot)$  is the gamma function. Also,  $\Phi_0^{(0)}(\Omega)$  is the noninteracting ground state of  $H_{\text{ad}}(R; \Omega)$  [Eq. (1)] [denoted by the (0) superscript] taking into account the total angular momentum  $L$  and parity  $\pi$  of the system  $L^{\pi}$ . In particular,  $L^{\pi} = 0^{+}$  ( $L^{\pi} = 1^{-}$ ) for BBX (FFX) systems. The independence of  $\Phi_0^{(0)}(\Omega)$  on  $R$  stems from the independence of the hyperangular eigenvalues of the noninteracting adiabatic

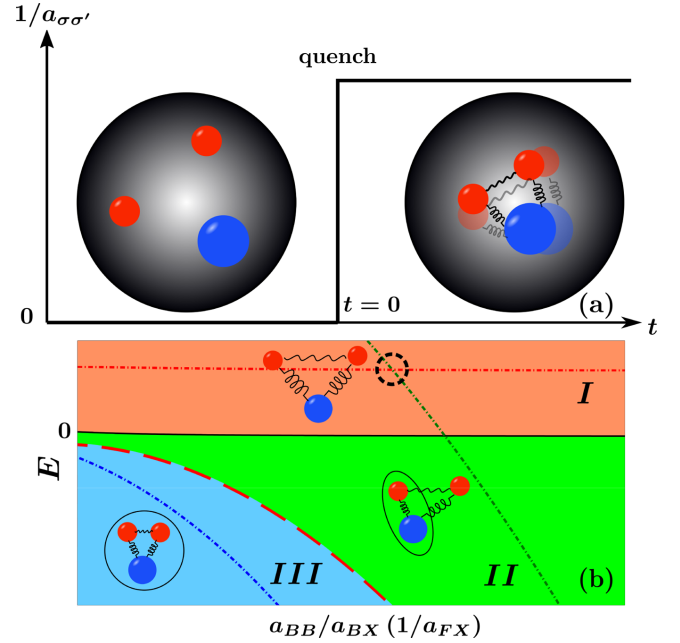


FIG. 1. (a) Cartoon of the quench scenario. The system consists of either two (red particles) identical bosons (BBX) or fermions (FFX) and a distinguishable atom (blue particle). They are initialized ( $t = 0$ ) in a noninteracting state with spatial extent  $w$ . The dynamics is induced by a sudden change of the scattering lengths (interspecies denoted by springs and intraspecies by wiggly lines) from their noninteracting to finite values. (b) Schematic representation of a typical three-body energy spectrum. In region III, below the BX or FX bare dimer threshold (red dashed line), trimer states can be formed, denoted by a circle. Region II signals the presence of atom-dimers (dimers are marked by an ellipse), and in region I, trap states appear along with atom-dimers. These two latter eigenstates feature avoided-crossings; see, for instance, the dashed circle. The energy dependence of the trimers, atom-dimers, and trap states on the scattering length is schematically presented by the blue, green, and red dash-dotted lines, respectively. Note that the horizontal axis corresponds to a wide range of considered scattering lengths, but it does not reach the zero limit.

Hamiltonian on this parameter; for more details, see Appendix B. The hyperradial part of  $\Psi(R, \Omega, t=0)$  is the ground state of the hyperradial equation [Eq. (2)] with zero nonadiabatic coupling matrix elements, due to the independence of  $\Phi_0^{(0)}(\Omega)$  on  $R$ , and one potential curve, associated to this ground hyperangular state,  $U(R) = 1/(2\mu R^2)[(L+1)^2 - 1/4] + 1/(2\mu w^4)R^2$ . Its energy reads  $(2+L)/(\mu w^2)$ , where  $L = 0$  (1) refers to the total angular momentum for the BBX (FFX) system.

It should be noted that Eq. (6) is an eigenstate of the noninteracting Hamiltonian Eq. (1) only in the case of  $w = a_{\text{ho}}$  coinciding with the noninteracting ground trap state. The spatial extent  $w$  can be adjusted experimentally, e.g., by means of a trap frequency quench (see Sec. VI for a more detailed discussion), however in the following we treat it as a free parameter. This permits us to investigate the role of the spatial extent of the initial wave function on the postquench dynamics. However, a detailed argumentation on the interval of values of the width  $w$  is provided in Sec. VI. Nevertheless,

<sup>1</sup>We note that in the following sections and Appendices, the wave functions with the superscripts  $\Psi(R, \Omega, t)$  or  $\Psi^f(R, \Omega)$  indicate the time-evolved wave function at time  $t$  or the postquench  $f$ -th eigenstate, respectively (see also Sec. III).

for typical LLH settings that we shall consider below these bounds yield,  $w \geq 0.46$  while for HHL ones,  $w \geq 1.16$ .

### A. Time evolution of the wave function

To trigger the nonequilibrium dynamics of the three-body mixture, we perform quenches of the relevant 2D scattering lengths  $a_{\sigma,\sigma'}$ . Accordingly, their values are suddenly reduced at  $t = 0$  from their initial noninteracting ones. Recall that this is experimentally feasible via appropriate Feshbach resonances (for more details, see also Sec. VI). Specifically, a different quench scheme is applied for the BBX and FFX systems since the former (latter) possesses two (one) scattering lengths, i.e.,  $a_{BB}$  and  $a_{BX}$  ( $a_{FX}$ ). In the case of FFX mixtures, solely  $1/a_{FX}$  is quenched and the consequent dynamics is explored over a wide range of postquench  $1/a_{FX}$  [Fig. 1(a)]. On the other hand, for the BBX system both the  $1/a_{BB}$  and  $1/a_{BX}$  are changed abruptly at  $t = 0$  from their noninteracting values [Fig. 1(a)] towards different postquench  $1/a_{BX}$  and fixed  $1/a_{BB} = 1$ . It is worth mentioning that by tuning the magnetic field for the quench in the experiment, both  $a_{BX}$  and  $a_{BB}$  are affected, and hence broad (narrow) intraspecies (interspecies) resonances are required such that the variation of  $a_{BB}$  is very small compared to that of  $a_{BX}$  (see also Sec. VI). We remark that  $a_{BB} = 1$  is chosen such that the bosonic atoms have an intermediate repulsive interaction strength.<sup>2</sup> However, we have checked that the dynamical processes and response of the LLH and HHL BBX systems that are presented below (Secs. IV and V) do not change substantially closer to the noninteracting limit, i.e.,  $a_{BB} > 1$ . The fact that the qualitative features of the results remain the same towards the noninteracting limit permits us to expose the role of the particle statistics between BBX and FFX systems.

To describe the quenched dynamics of the three-body system, the time-evolved wave function is expressed as a projection of the initial state [Eq. (6)] onto the interacting eigenstates of the postquench 2D scattering lengths. Specifically, it acquires the form

$$\Psi(R, \Omega, t) = \sum_f e^{-iE_f t} c_{f,\text{in}} \Psi^f(R, \Omega), \quad (7)$$

where  $\Psi^f(R, \Omega) = R^{-3/2} \sum_v F_v^f(R) \Phi_v(R; \Omega)$  are the postquench interacting eigenstates, and  $E_f$  are their eigenenergies. Also,  $c_{f,\text{in}} = \int dR d\Omega R^3 \Psi(R, \Omega, t=0) [\Psi^f(R, \Omega)]^*$  denote the overlap coefficients between the initial and the postquench eigenstates. The overlap coefficients are explicitly determined by the initial state and hence its width  $w$  for a fixed postquench scattering length. This leads to a  $w$ -dependent participation of specific postquench eigenstates, i.e., depending on  $w$ , different eigenstates contribute in the dynamics, whose distinct features dictate the dynamical

response of the system, as will be demonstrated below (Secs. IV and V).

### B. Classification of postquench three-body eigenstates

Detailed knowledge of the three-body energy spectra [41,69,76] will allow an in-depth understanding of the emergent nonequilibrium dynamics of both the BBX and FFX mixtures. The postquench interacting eigenstates can be categorized into the so-called trimers, atom-dimers, and trap states [77,78]. Trimers are three-body bound states that exist below the BX or FX dimer energies; see, in particular, the red-dashed line and region III in Fig. 1(b). In Ref. [35] it was shown that in the absence of a trap the BX or FX dimer energy is given by  $E_{\sigma X} = -2e^{-2\gamma}(1 + \mathcal{M})/a_{\sigma X}^2$ . Here,  $\sigma = B, F$ ,  $\gamma = 0.577$ , and  $\mathcal{M} = m_\sigma/m_X$ . For BBX systems there is also the BB dimer energy determined by  $E_{BB} = -4e^{-2\gamma}/a_{BB}^2$ , which is constant since  $a_{BB} = 1$  remains fixed for all the postquench  $a_{BX}$  scattering lengths.<sup>3</sup>

Region II of Fig. 1(b) indicates the energies of the atom-dimer states, which are two-body bound states interacting with a third particle. The atom-dimer states depend strongly on  $a_{BB}/a_{BX}$  ( $1/a_{FX}$ ) in the case of the BBX (FFX) systems having a BX+B (FX+F) character. Moreover, the region I of Fig. 1(b) depicts the energy regime of the trap states that are almost insensitive to scattering length variations [see the straight lines in Fig. 1(b)] referring to three weakly interacting particles. Apparently, avoided crossings occur between BX+B or FX+F atom-dimers, also encountered in region I, and trap states, designated by dashed circles in Fig. 1(b). For BBX systems, apart from the aforementioned states appearing in region I, BB+X atom-dimers arise as well. Their eigenenergies experience only small variations with respect to  $a_{BB}/a_{BX}$ , similarly to the trap states, since the postquench  $a_{BB}$  is kept fixed. A way to distinguish them from trap states is by inspecting their stationary two-body BB short-range correlations, e.g., through the two-body BB contact. In Ref. [41] it was shown that the latter is more pronounced in the case of BB+X atom-dimers than for trap states.

Notably, all three types of eigenstates display a different spatial extent in terms of the hyperradius  $R$ . Therefore, the initial state described by Eq. (6) will eventually screen out particular states or superpositions in the time evolution for different widths  $w$ , and this information is encoded in the overlap coefficients  $c_{f,\text{in}}$  (see also Secs. IV and V).

## IV. QUENCH DYNAMICS OF LLH SETTINGS

To obtain an overview of the system's dynamical response for different widths of the initial state and postquench scattering lengths, we employ the time-averaged fidelity [73,80,81]

$$\langle |F| \rangle = \lim_{T \rightarrow \infty} \frac{\int_0^T dt |F(t)|}{T}. \quad (8)$$

<sup>2</sup>The two-body interaction strength between the  $\sigma = B, F$  and  $\sigma'$  species [73–75] is defined as  $g_{\sigma\sigma'} = [\ln(2e^{-2\gamma}(1 + m_\sigma/m_{\sigma'})/a_{\sigma\sigma'}^2)]^{-1}$ , where  $\gamma = 0.577$ . This implies that when  $a_{\sigma\sigma'} > (<)e^{-\gamma}\sqrt{2}\sqrt{1 + \frac{m_\sigma}{m_{\sigma'}}}$ , attractive (repulsive) effective interaction regimes arise.

<sup>3</sup>These relations are altered in the presence of a trap only for scattering lengths comparable to or larger than the lengthscale  $\ell = \sqrt{\hbar/\mu_{2B}\omega}$  (with  $\mu_{2B}$  being the two-body reduced mass) [79]. This effect depends also on the mass ratio of the three-body system.

The total time evolution  $T$  is considered to be long enough such that  $\langle |F| \rangle$  is converged.<sup>4</sup> The fidelity, which essentially estimates the deviation of the time-evolved state [Eq. (7)] from the initial one, reads

$$\begin{aligned} F(t) &= \langle \Psi(R, \Omega, t) | \Psi(R, \Omega, t = 0) \rangle \\ &= \sum_f |c_{f,\text{in}}|^2 e^{-iE_f t}. \end{aligned} \quad (9)$$

Here,  $c_{f,\text{in}}$  are the overlap coefficients introduced in Eq. (7), and  $E_f$  refer to the energies of the postquench eigenstates. As a function of the postquench scattering length, the dynamical response of the three-body system exhibits two distinct regimes mainly determined by the width of the initial state with respect to the three-body harmonic-oscillator length,  $a_{\text{ho}}$ . In this section, the LLH setups that are considered have a mass ratio  $m_{B/F}/m_X = 0.04$  yielding a three-body harmonic-oscillator length  $a_{\text{ho}} = 1.02$ .

Regarding the LLH BBX system, the time-averaged fidelity  $\langle |F| \rangle$  in terms of  $a_{BB}/a_{BX}$  is depicted in Fig. 2(a) for various widths of the initial state. Apparently, the qualitative behavior of  $\langle |F| \rangle$  depends strongly on  $w$ . For instance, in the case of  $w/a_{\text{ho}} = 0.78$  the deviation from the initial state becomes larger for increasing  $a_{BB}/a_{BX}$ . Such a decrease of  $\langle |F| \rangle$  holds also when  $w/a_{\text{ho}} = 1$  as long as  $a_{BB}/a_{BX} < 4$ , and beyond this interval it shows a saturation trend, due to the amplified population of trap states; see also Appendix C. The latter renders the response of the system more enhanced compared to the  $w/a_{\text{ho}} = 0.78$  case, since a larger number of postquench eigenstates contributes in the dynamics (see also Appendix C). However, considering an initial state with a width at  $w/a_{\text{ho}} = 4.9$ , the response of the system is substantially enhanced as compared to the previous case, and in particular it is almost independent of  $a_{BB}/a_{BX}$ . This pattern, as will be explained in Sec. IV A, originates from the significant population of trap states. In this sense, it becomes evident that there are two characteristic response regimes of the system with respect to  $a_{\text{ho}}$ .

A similar qualitative behavior of  $\langle |F| \rangle$  occurs also for LLH FFX settings [Fig. 2(b)] at  $w/a_{\text{ho}} < 1$  or  $w/a_{\text{ho}} > 1$ . Notably, for  $w/a_{\text{ho}} = 0.78$ ,  $\langle |F| \rangle$  is almost constant in the region  $1/a_{FX} > 3$ . Such a response can also be observed for other widths  $w/a_{\text{ho}} < 1$ , due to the participation of trap states for large  $1/a_{FX}$ . For an initial state with  $w/a_{\text{ho}} = 1$ , we observe that the response of the LLH FFX system is decreased for  $1/a_{FX} > 3$ , meaning that the deviation from the initial state reduces progressively. This mainly occurs due to the smaller number of contributing states in the course of the evolution (as thoroughly discussed in the Appendix A of Ref. [82]), since the participation of the first two atom-dimers reduces as  $1/a_{FX}$  is further tuned to larger values (see also Appendix C). For  $w/a_{\text{ho}} = 4.9$ , the time-averaged fidelity is practically constant due to the participation of trap states during the dynamics, whose overlap coefficients do not depend strongly on  $1/a_{FX}$  (see also Sec. IV B). Note that the considered postquench

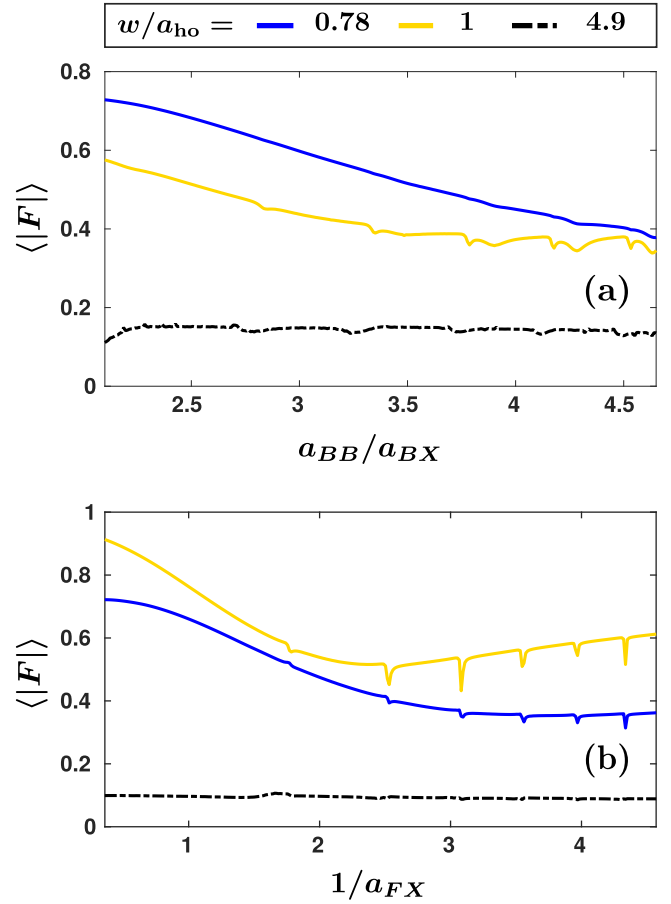


FIG. 2. Average dynamical response, as captured by the time-averaged fidelity  $\langle |F| \rangle$ , with respect to the scattering length ratio (a)  $a_{BB}/a_{BX}$  for the BBX and (b)  $1/a_{FX}$  for the FFX LLH systems. Cases of different widths  $w$  (see legend) of the initial state are presented. Apparently, in both settings the response is changed for widths smaller or larger than  $a_{\text{ho}} = 1.02$ . In particular, it is enhanced for wider initial states having  $w > a_{\text{ho}}$ .

$1/a_{FX}$  values do not include 0, and  $\langle |F| \rangle$  therefore deviates from unity in the leftmost part in Fig. 2(b) at  $w/a_{\text{ho}} = 1$ . However, when  $w \neq a_{\text{ho}}$ , even at  $1/a_{FX} = 0$  the deviation would persist, since the initial state is not a noninteracting eigenstate.

Evidently, regardless of the particle statistics, we observe that the width of the initial state plays a crucial role on the dynamical response of the three-body system. Thus, in order to further address the physical origin of this behavior in the following we will analyze the involved excitations, in terms of the postquench eigenstates, that contribute in the nonequilibrium dynamics. Their identification is indeed, in general, tractable in few-body setups [83,84]. For this purpose, we utilize the fidelity spectrum

$$|F(\tilde{\omega})| = \left| \int \frac{dt}{\sqrt{2\pi}} e^{-i\tilde{\omega}t} |F(t)| \right|. \quad (10)$$

It discloses information regarding the predominantly contributing final eigenstates in the dynamics via the energy differences  $\tilde{\omega}_{f,f'} = E_f - E_{f'}$  [recall that we work with

<sup>4</sup>Here we consider total evolution times  $T = 800$ , while the time-averaged fidelity for the LLH (HHL) settings saturates already from  $T = 300$  ( $T = 500$ ).



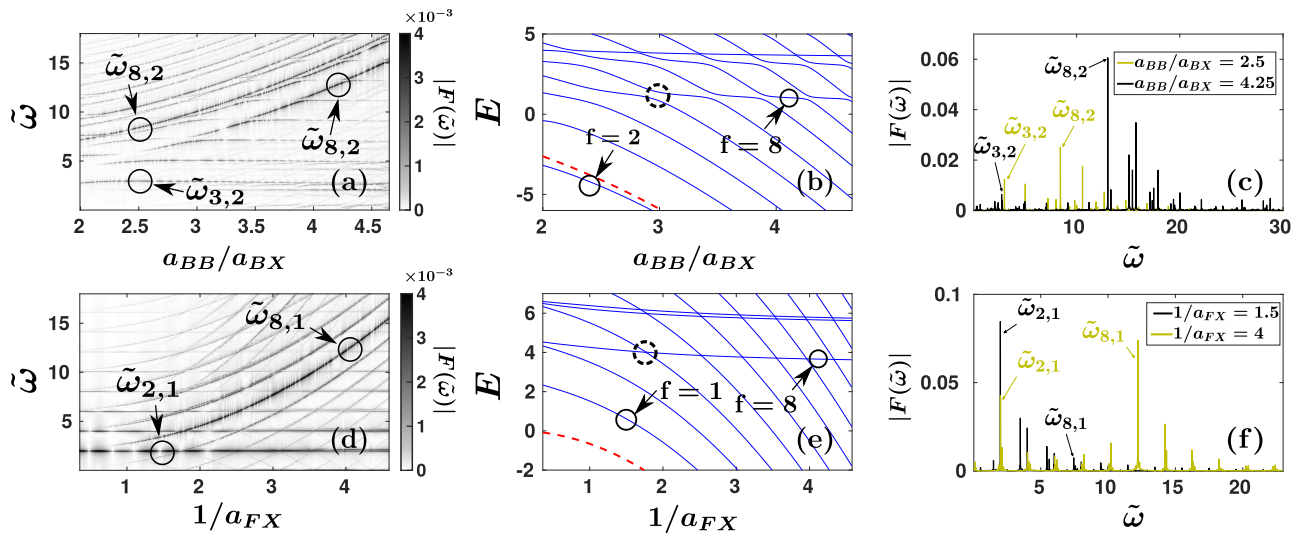


FIG. 3. Fidelity spectra of the quenched (a) BBX and (d) FFX LLH systems with a narrow prequench state of  $w/a_{\text{ho}} = 0.78$ . The circles denote frequencies associated with specific postquench eigenstates. The interaction-dependent excitation branches signal the dominant participation of trimer and atom-dimer states in the dynamics, and they refer to their energy differences with respect to trap states. Almost constant branches are related to trap excitations. The energy spectra of the (b) BBX and (e) FFX LLH systems, where a series of avoided crossings among atom-dimers and trap states occurs, are marked by the dashed circles. The red dashed line indicates the bare BX or FX dimer threshold. (c),(f) Profiles of the fidelity spectrum for the (c) BBX and (f) FFX mixture at different scattering lengths (see the legend).

dimensionless units (Sec. II)], which are identified from the energy spectra of BBX and FFX systems [41]. Below, we elaborate on the excitation spectrum of both LLH BBX and FFX systems in the two above-mentioned distinct response regimes.

#### A. Excitations from narrow initial states with $w < a_{\text{ho}}$

As a prototype LLH setup with an initial state width  $w < a_{\text{ho}}$ , we use the case of  $w/a_{\text{ho}} = 0.78$ . To understand the excitation processes of the quenched system, we inspect the respective fidelity spectrum together with the energy eigen-spectrum and the overlap coefficients. For the BBX system, the fidelity spectrum  $|F(\tilde{\omega})|$  and the three-body postquench eigenenergies are shown in Figs. 3(a) and 3(b), respectively. Note that the indexing of the eigenenergies, e.g., in Fig. 3(b) starts from the ground state, which possesses an energy way below the displayed range, and increases as we climb the energy ladder.

In Fig. 3, for  $a_{\text{BB}}/a_{\text{BX}} < 4$  the excited frequency branches appearing in  $|F(\tilde{\omega})|$  mainly refer to energy differences between the second trimer state (first excited trimer)  $f = 2$ , and either the first atom-dimer ( $f = 3$ ) or the trap states ( $f = 8$ ); see, e.g.,  $\tilde{\omega}_{3,2}$  and  $\tilde{\omega}_{8,2}$ , respectively, in Fig. 3(a) at  $a_{\text{BB}}/a_{\text{BX}} = 2.5$ . In these frequency branches, the most dominant contribution in the coefficients  $c_{f,\text{in}}$  stems mainly from the second trimer. This occurs since both the initial state and the second trimer are well localized at small values of the hyperradius, i.e., for  $R < a_{\text{ho}}$ , yielding thus a large overlap. In particular, for the frequency  $\tilde{\omega}_{3,2}$  we observe that it remains constant as the scattering length ratio  $a_{\text{BB}}/a_{\text{BX}}$  varies. This arises from the fact that the scattering length dependence of the second trimer and first atom-dimer eigenenergies is similar as shown

in Fig. 3(b), thus their energy difference results into an almost constant frequency  $\tilde{\omega}$ .

As  $a_{\text{BB}}/a_{\text{BX}}$  is tuned to larger values, the spatial extent of the postquench eigenstates changes drastically [Fig. 3(b)], thus affecting their overlap with the initial configuration. Indeed, the participation of the second trimer state ( $f = 2$ ) decreases for  $a_{\text{BB}}/a_{\text{BX}} > 4$ . For these scattering length ratios, the trimer and the atom-dimer states become tightly bound [see Fig. 3(b)]. Accordingly, their wave functions are much narrower than the initial one, which reduces the corresponding overlap coefficients. In return, this results in a smaller amplitude of  $\tilde{\omega}_{3,2}$ ; see Fig. 3(c) at  $a_{\text{BB}}/a_{\text{BX}} = 4.25$ . This reduced contribution in the fidelity spectrum is counterbalanced by the enhanced population of more trap states giving rise to excitation branches whose values increase with larger  $a_{\text{BB}}/a_{\text{BX}}$ ; see, e.g., the scaling of  $\tilde{\omega}_{8,2}$  in Fig. 3(a).<sup>5</sup> Their increasing behavior reflects the growing energy difference between the second trimer and trap states for  $a_{\text{BB}}/a_{\text{BX}} > 3$  [Fig. 3(b)]. Also, the amplitude  $\tilde{\omega}_{8,2}$  increases with  $a_{\text{BB}}/a_{\text{BX}}$  since the substantial spatial extent of the trap wave functions yields larger overlap with the initial state. Furthermore, a larger number of branches arises in the fidelity spectrum as can be seen by comparing the profiles of  $|F(\tilde{\omega})|$  at  $a_{\text{BB}}/a_{\text{BX}} = 4.25$  and  $a_{\text{BB}}/a_{\text{BX}} = 2.5$  illustrated in Fig. 3(c). As a result, the response of the time-averaged fidelity for  $w/a_{\text{ho}} = 0.78$  is more enhanced (smaller value of  $\langle |F| \rangle$ ) for larger ratios of  $a_{\text{BB}}/a_{\text{BX}}$  [Fig. 2(a)]. Let us remark that time-dependent variation protocols of the scattering lengths would be of great interest, since they could result

<sup>5</sup>Note that even if the labels of the postquench eigenstates are the same, the frequency associated with them,  $\tilde{\omega}_{8,2}$ , acquires different values depending on the scattering length [Fig. 3(a)], since the energy spectrum changes drastically with respect to  $a_{\text{BB}}/a_{\text{BX}}$ .

in a significant population of trimer states, even at the regimes where trap states acquire a large contribution.

For the dynamical response of the LLH FFX system, we observe the appearance of a larger number of excitations in the fidelity spectrum [Fig. 3(d)] as  $1/a_{FX}$  increases. Notice that this behavior is already anticipated from the enhanced response of  $\langle |F| \rangle$  presented in Fig. 2(b) for  $w/a_{ho} = 0.78$ . However, the microscopic mechanisms behind this response are different from the ones in the BBX system due to the distinct eigenenergy spectra, compare in particular Figs. 3(b) and 3(e). Evidently, in the case of the LLH FFX system trimers do not form. Here, the major contribution for  $1/a_{FX} < 2$  is shared among the first two atom-dimer states,  $f = 1, 2$ , possessing a small spatial extent and mostly localized at  $R < a_{ho}$ . This claim can be verified by the corresponding frequency peak  $\tilde{\omega}_{2,1}$  of  $|F(\tilde{\omega})|$  shown in Figs. 3(d) and 3(f) as well as the contribution of the relevant overlap coefficients (with a total contribution 90–60% for  $1/a_{FX} \in [0.36, 2]$ ). For large scattering lengths ( $1/a_{FX} > 2$ ), the participation of atom-dimers diminishes since their spatial extent further decreases. This results in their reduced overlap with the initial state and consequently to a smaller amplitude of  $\tilde{\omega}_{2,1}$  as shown in Fig. 3(f) for  $1/a_{FX} = 4$ . In this case, trap states acquire a non-negligible population leading to interaction-dependent frequency branches which grow with respect to  $1/a_{FX}$ ; see, e.g.,  $\tilde{\omega}_{8,1}$  in Fig. 3(d).

### B. Response for wide initial configurations of $w > a_{ho}$

Next, we examine the susceptibility of LLH three-body setups to quenches for initial configurations characterized by  $w > a_{ho}$ . As a representative example of this kind, we choose  $w/a_{ho} = 4.9$  and first investigate BBX mixtures. Recall that in this scenario, the time-averaged response captured by  $\langle |F| \rangle$  [Fig. 2(a)] is drastically enhanced as compared to  $w/a_{ho} = 0.78$  and experiences small variations with respect to  $a_{BB}/a_{BX}$ .

To determine the microscopic origin of the involved excitations, we resort again to the fidelity spectrum  $|F(\tilde{\omega})|$  provided in Fig. 4(a). The almost horizontal frequency branches stem from energy differences between trap states, e.g.,  $\tilde{\omega}_{12,8}$ . This is verified by calculating the respective overlap coefficients and monitoring the energy spectrum [Fig. 3(b)]. Additionally, since  $w/a_{ho} = 4.9 \gg 1$ , the postquench atom-dimers and trimers, being naturally narrow, exhibit a reduced overlap with the initial state. The dominant contribution in the course of the evolution originates from the trap states whose overlap with  $\Psi(R, \Omega, t = 0)$  is appreciable. Indeed, a multitude of trap states is populated as can be inferred from the several frequency peaks of comparable amplitude appearing in  $|F(\tilde{\omega})|$  [Fig. 4(a)]. This fact, in turn, induces the enhanced response identified in  $\langle |F| \rangle$  [Fig. 2(a)] for  $w/a_{ho} = 4.9$ .

A similar overall phenomenology takes place also for LLH FFX systems; see Fig. 4(b). Evidently, also here the respective excitation branches are almost insensitive to  $1/a_{FX}$  variations [Fig. 4(b)]. Notably, the postquench eigenstates responsible for this behavior are again trap states, e.g.,  $\tilde{\omega}_{6,3}$ , although they are not the same as those identified in the BBX scenario [Fig. 4(a)]. The reason for this change can be traced back to the different structure of the eigenspectrum between BBX and FFX LLH systems; compare Figs. 3(b) and 3(e).

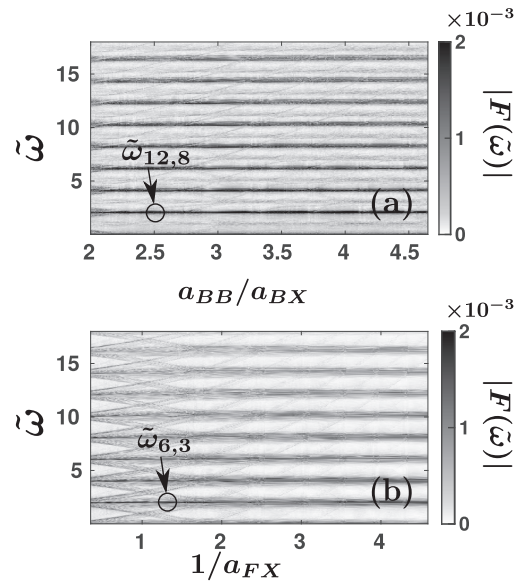


FIG. 4. Fidelity spectra of a wide initial state, i.e.,  $w/a_{ho} = 4.9$ , for the (a) BBX and (b) FFX LLH systems following a quench of the scattering length. The circles designate specific frequency peaks corresponding to different postquench eigenstates. The atoms reside in a superposition consisting predominantly of trap states. The latter are imprinted as excitation branches being insensitive to scattering length variations.

Focusing on the underlying selection processes according to which specific postquench eigenstates are populated, it is instructive to carefully study the respective overlap coefficients. Of immediate interest here are the ones referring to pairs of postquench eigenstates that experience avoided crossings [dashed circles in Figs. 3(b) and 3(e)], namely atom-dimers and trap states, and in particular we illuminate their dependence on the width  $w$  of the initial states. In the vicinity of the avoided crossings, the spatial extent of the involved eigenstates changes abruptly, since their character alters between trap and atom-dimer states.

For a BBX setup, a characteristic example regarding the dependence of the overlap coefficients between the initial state and the  $f = 5, 6$  eigenstates as a function of  $w$  and  $a_{BB}/a_{BX}$  is displayed in Fig. 5(a). A transition between the different types of eigenstates is apparent by the complementary behavior of the respective overlap coefficients [30]. On the left of the first avoided crossing shown in Fig. 3(b) at  $a_{BB}/a_{BX} \simeq 3$  (dashed circle), the occupation of the trap state  $f = 5$  [see the red color gradient in Fig. 5(a)] prevails for a larger  $w$  when compared to the atom-dimer  $f = 6$  [see the green color gradient in Fig. 5(a)]. This behavior arises from the mere fact that the atom-dimer has a smaller spatial extent compared to the trap state, thus the latter yields larger overlap compared to the former. The opposite behavior takes place within  $a_{BB}/a_{BX} \in [3, 3.5]$ , since then the  $f = 5, 6$  states interchange their character. After the second avoided crossing at  $a_{BB}/a_{BX} \simeq 3.5$ , these states are substantially occupied only for  $0.19 < w/a_{ho} < 0.39$ , since then both of them are atom-dimers [Fig. 3(b)]. For larger  $w/a_{ho} \simeq 1$  and around  $a_{BB}/a_{BX} \in [3.5, 4]$ , a significant contribution stems from a trap eigenstate ( $f = 7$ ), not shown

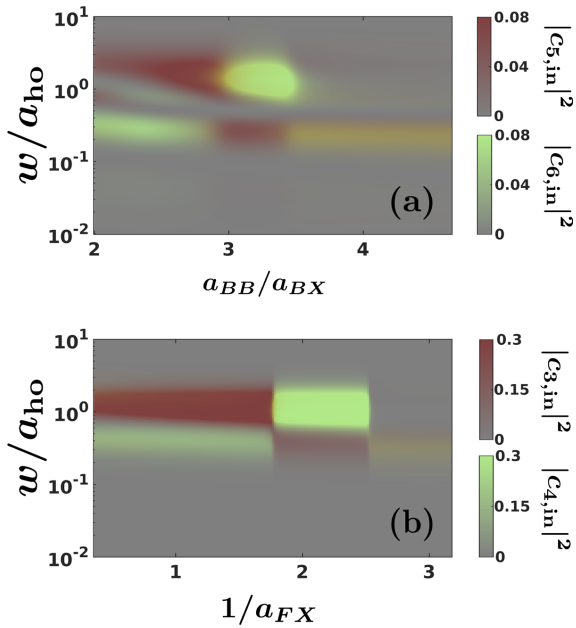


FIG. 5. Overlap coefficients  $|c_{f,\text{in}}|^2$  between the initial state of width  $w$  and two postquench eigenstates  $f$  as a function of  $w/a_{\text{ho}}$  and the scattering length for the (a) BBX ( $f = 5, 6$ ) and (b) FFX ( $f = 3, 4$ ) LLH system. In each case, the presented pair of postquench eigenstates experiences an avoided crossing in the respective energy spectra [Figs. 3(b) and 3(e) with dashed circles]. A change of the character of the state from a trap to an atom-dimer (atom-dimer to trap) state is signified by a shift of its major contribution to smaller (larger) values of the width of the prequench state  $w/a_{\text{ho}}$ .

in Fig. 5(a). Similar transitions occur also for the FFX LLH system [Fig. 5(b)], where in this case the pair of eigenstates  $f = 3, 4$  exchange character from a trap to an atom-dimer and vice versa through the avoided crossing at  $1/a_{\text{FX}} \simeq 1.77$  [Fig. 3(e) designated with a dashed circle].

Concluding, it is worth mentioning that upon considering a width of the initial state being the same as the three-body harmonic-oscillator length, namely  $w = a_{\text{ho}}$ , the original configuration corresponds to the noninteracting ground trap state (Sec. III). For this reason, the role of trimers and atom-dimers is less important during the time evolution, and as expected trap states have a somewhat larger population (for more details, see Appendix C). This behavior holds for both BBX and FFX systems.

### C. Buildup of two- and three-body correlations

Having established an understanding regarding the contributing eigenstates for different widths of the initial state, an intriguing question that arises is how these states influence the associated short-range few-body correlations in the course of the evolution. These correlations can be addressed by the experimentally measurable [17,19] two- and three-body contacts [9,11,13,41,47,85]. The latter are defined as coefficients in a high momentum expansion of the  $\sigma$ -species one-body density

in momentum space,

$$n_{\sigma}(\mathbf{p}_{\sigma}, t) \simeq \frac{1}{N_{\sigma} p_{\sigma}^4} \sum_{\sigma'} (1 + \delta_{\sigma\sigma'}) \mathcal{D}_2^{\sigma\sigma'}(t) + \frac{\ln^3 p_{\sigma}}{p_{\sigma}^6} \mathcal{D}_3(t). \quad (11)$$

This expansion pertains to the case in which  $p_{\sigma}$  is significantly larger than the momentum scales provided by the inverse scattering lengths [41]. Here,  $N_{\sigma}$  is the atom number belonging to the  $\sigma$ -species, while  $\mathcal{D}_2^{\sigma\sigma'}(t)$  denotes the time-dependent two-body contact between the species  $\sigma$  and  $\sigma'$ . Note that only the three-body contact  $\mathcal{D}_3(t)$  of BBX systems [ $\mathcal{D}_3^{\text{BBX}}(t)$ ] is finite, since for FFX systems three-body correlations are suppressed<sup>6</sup> due to the Pauli exclusion principle [45]. The main features of these few-body correlation observables are captured by their time-averaged measure. Namely, the time-averaged two-body contacts are described by the following expressions:

$$\langle \mathcal{D}_2^{\sigma X} \rangle = \lim_{T \rightarrow \infty} \frac{1}{T} \int_0^T dt \mathcal{D}_2^{\sigma X}(t), \quad \sigma = B, F \quad (12)$$

and the three-body ones read

$$\langle \mathcal{D}_3^{\text{BBX}} \rangle = \lim_{T \rightarrow \infty} \frac{1}{T} \int_0^T dt \mathcal{D}_3^{\text{BBX}}(t). \quad (13)$$

These quantities assess the overall degree of dynamical correlations for various widths of the initial state and postquench scattering lengths; see Fig. 6. A detailed analysis of the stationary three-body FFX and BBX setups reveals a hierarchy in terms of the degree of few-body correlations for the different types of eigenstates. Namely, as shown in Refs. [41,85,86], trimer states possess more enhanced two- and three-body correlations than those of the BX or FX atom-dimer states, and, similarly, the atom-dimer contacts are larger than those of the trap states. This hierarchy will also be apparent here as the width of the initial state changes and different eigenstates contribute in the dynamical response. Indeed, as the width of the initial state [Eq. (6)] increases, the magnitude of all the aforementioned correlations at any scattering length is reduced (Fig. 6). This occurs because for larger widths, a superposition of trap states is predominantly populated (see also Fig. 4).

On the contrary, for  $w/a_{\text{ho}} = 0.78$ , the first two atom-dimers (second trimer) provide the main contribution to the postquench wave function Eq. (7) of the FFX (BBX) system. This is confirmed through their dominant overlap coefficients (see Sec. IV A), enhancing few-body correlations compared to cases in which  $w > a_{\text{ho}}$  (Fig. 6). Therefore, in the limit of small  $w < a_{\text{ho}}$ , correlations at the two- and three-body level are, generically, enhanced due to the non-negligible involvement of trimer and atom-dimer states. This amplification was also observed for a three-boson setup in the quench dynamics at unitarity in 3D [29], especially when the width of the initial state matched the size of an Efimov trimer.

<sup>6</sup>The three-body contact yields the probability to detect three particles in close vicinity. As such, it is zero by construction for FFX systems within the  $s$ -wave zero-range interaction model, where the two identical and noninteracting fermions cannot approach one another due to the Pauli principle.

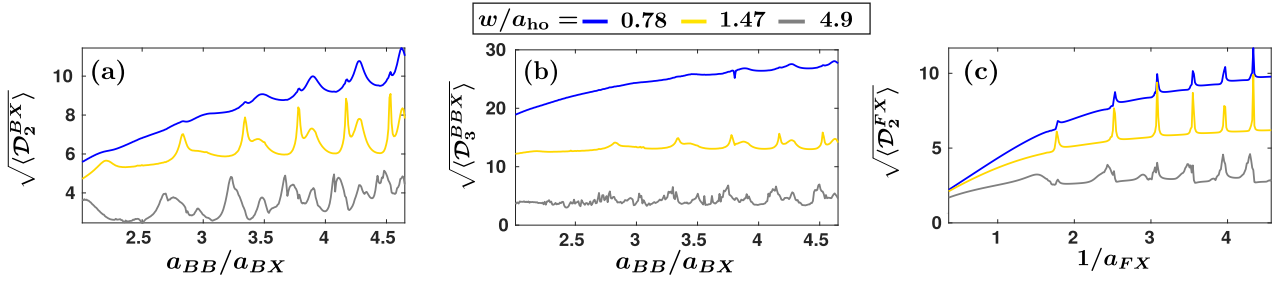


FIG. 6. Time-averaged (a) two-body  $\sqrt{\langle \mathcal{D}_2^{BBX} \rangle}$  and (b) three-body contact  $\sqrt{\langle \mathcal{D}_3^{BBX} \rangle}$  of the BBX LLH setting, and (c) two-body contact  $\sqrt{\langle \mathcal{D}_2^{FFX} \rangle}$  of the FFX setup. Correlations at all levels increase for larger  $a_{BB}/a_{BX}$  or  $1/a_{FX}$ , and their magnitude reduces for larger widths. The peak structure at specific scattering lengths is an imprint of the participation of atom-dimers. The widths of the initial state are provided in the legend.

Another remarkable feature of the correlations is their magnification at particular scattering lengths for fixed  $w$ ; see the individual peaks displayed in Fig. 6. Their amplitudes become more prominent from the overall two- and three-body contacts for increasing width  $w$ , where trap states contribute substantially (see Sec. IV B). These peaks occur in the vicinity of avoided crossings present in Figs. 3(b) and 3(e), where the corresponding three-body wave function is predominantly in a superposition of a trap and an atom-dimer state. Therefore, in this range of scattering length ratios, the overall character of the wave function abruptly changes, yielding in this manner an enhanced  $\langle \mathcal{D}_2^{BBX} \rangle$ ,  $\langle \mathcal{D}_3^{BBX} \rangle$ , and  $\langle \mathcal{D}_2^{FFX} \rangle$ . This particular property of the time-averaged two- and three-body contacts can be utilized as an experimental probe for the formation of atom-dimers in a 2D gas.

Furthermore, the appearance of enhanced peaks in the two-body contacts at the avoided-crossings due to the atom-dimer component in the time-evolved wave function is also a manifestation of the universal Tan relations. These universal relations exemplify that the short-range two-body correlations are proportional to the variation of the stationary energy spectra with respect to the scattering length [11,46]. Therefore, close to the avoided-crossings the eigenenergies of the three-body system [see Figs. 3(b) and 3(e)] strongly vary with the scattering length, thus yielding narrow peaked two-body correlations [Figs. 6(a) and 6(c)]. By this token, we can address the main difference between the two-body contacts of BBX and FFX systems in Figs. 6(a) and 6(c), respectively, where the former exhibits broader peaks than the latter. This occurs because in the FFX eigenspectra shown in Fig. 3(e) we observe much sharper avoiding crossings than in the BBX ones [see Fig. 3(b)]. Such a universal relation is absent in the case of the three-body contact [47] in 2D, and the peak structure is attributed to the enhanced stationary three-body correlations [41] of the atom-dimer component of the time-evolved wave function.

Moreover, it is also worth mentioning that a broadening of these correlation peaks is evident for larger widths; see, e.g.,  $w/a_{ho} = 4.9$  in Fig. 6. In this case, as already discussed and observed in the fidelity spectrum (Fig. 4), a large amount of trap states participates in the three-body time-evolved wave function. This results in an agglomeration of avoided crossings contributing to the dynamics, which are slightly displaced horizontally from one another at a fixed scattering length [see Figs. 3(b) and 3(e)]. The aforementioned displacement

then yields a range of scattering lengths over which the Tan contacts display an enhanced behavior, manifested as a peak broadening.

## V. DYNAMICAL RESPONSE OF HHL MIXTURES

In this section, we address the role of the masses on the dynamical build up of few-body correlations by considering HHL three-body mixtures. The intrinsic dynamical behavior of this system is explored, for widths  $w$  of the initial state smaller or larger than the characteristic three-body harmonic-oscillator length  $a_{ho} = 2.6$  [Eq. (6)]. As in the LLH case in Sec. IV, we remark that initial states with a spatial extent smaller (larger) than  $a_{ho}$  favor the participation of trimer and/or atom-dimer (trap) states. Our analysis on the response of the 2D mixtures is based on the time-averaged fidelity  $\langle |F| \rangle$  given in Eq. (8).

The overall response of a HHL BBX system characterized by  $m_B/m_X = 22.16$  is intensified in the case of  $w/a_{ho} = 0.57$  [Fig. 7(a)] as compared to  $w > a_{ho}$  within  $a_{BB}/a_{BX} \in [0.5, 3]$ . This is in contrast to the susceptibility of LLH mixtures [Fig. 2(a)]. Moreover, for  $w/a_{ho} = 1$  a strong dependence of  $\langle |F| \rangle$  is observed with respect to the scattering length ratio. This feature of  $\langle |F| \rangle$  differs dramatically from the response for  $w/a_{ho} = 1.92$ , where it is arguably almost insensitive within the interaction interval  $a_{BB}/a_{BX} \in [2, 3]$ . This behavior is related to the prominent contribution of trap states. For  $w/a_{ho} = 1$ , the system becomes less susceptible to the quench as compared to the case of  $w/a_{ho} = 1.92$ , since fewer trap states contribute, especially for large  $a_{BB}/a_{BX} > 2$ . Notably, there are a series of peaks appearing in  $\langle |F| \rangle$  at specific scattering lengths, where avoided crossings among atom-dimer and trap states exist in the few-body eigenspectrum [see also Figs. 8(b) and 8(e)]. Their importance, especially in the relevant few-body correlations, will be discussed below.

Subsequently, the susceptibility of a HHL FFX system with  $m_F/m_X = 24.71$  is illustrated in Fig. 7(b). Apparently, the FFX mixture becomes more perturbed when considering  $w/a_{ho} = 0.57$ . For larger widths, e.g.,  $w/a_{ho} = 1.92$ , the system experiences a weak dependence on the scattering length within the range  $1/a_{FX} \in [1.5, 2]$ . This is linked to the dominant presence of trap states during the time evolution due to their large spatial extent. Moreover, we note that similarly to the BBX HHL case [Fig. 7(a)], the FFX mixture is less perturbed for  $w/a_{ho} = 1.92$  than in the  $w/a_{ho} = 0.57$  scenario.

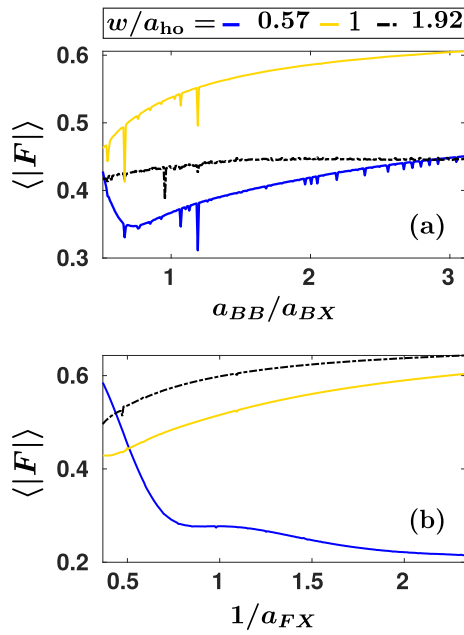


FIG. 7. Time-averaged fidelity  $\langle |F| \rangle$  of the three-body (a) BBX and (b) FFX HHL mixture subjected to quenches of the interspecies scattering length. Different widths of the initial state are considered (see the legend) whose values in terms of the oscillator length ( $a_{ho} = 2.6$ ) determine the degree of the system's response. The substantial population of atom-dimer and trimer (trap) states for  $w < a_{ho}$  ( $w > a_{ho}$ ) leads to a strongly (weakly) interaction-dependent response. In contrast to the LLH case, trap states also have a small contribution for  $w < a_{ho}$  in addition to trimers and atom-dimers, and the larger number of participating eigenstates compared to the  $w > a_{ho}$  scenario enhances the response of the system.

However, in contrast to the HHL BBX system, for  $w/a_{ho} = 1$  the mixture develops a stronger response in comparison to  $w/a_{ho} = 1.92$ , due to the more prominent population of trimers and atom-dimers.

#### A. Excitation processes for $w < a_{ho}$

Prequenched states with a spatial extent smaller than the three-body harmonic-oscillator length apparently exhibit a larger overlap with the trimers and atom-dimer states of the BBX and FFX HHL systems. The latter contribute significantly in the underlying dynamics compared to the case in which  $w > a_{ho}$ . In the opposite regime ( $w > a_{ho}$ ), trap states become substantially populated in the postquench dynamics (see also Sec. IV B), a mechanism pertaining also to the HHL mixtures. The frequency spectra will be analyzed for the  $w < a_{ho}$  scenario, since for  $w > a_{ho}$ , the underlying microscopic mechanisms resemble those presented in Sec. IV B. However, the differences present in  $\langle |F| \rangle$  between LLH (Fig. 2) and HHL setups (Fig. 7) for  $w > a_{ho}$  stem mostly from the different number of participating trap states in the postquench dynamics. Moreover, in the HHL scenario, in addition to the participation of trap states, there are a few contributing atom-dimer and trimer states especially for small values of  $1/a_{FX}$  and  $a_{BB}/a_{BX}$ . This results in further perturbation of the system from the initial state compared to larger scattering lengths.

Recall also here the relevant discussion in Sec. IV concerning LLH mixtures.

Inspecting the fidelity spectrum  $|F(\tilde{\omega})|$  [Fig. 8(a)] together with the overlap coefficients and the energy spectrum [Fig. 8(b)] for the HHL BBX system, we can infer that for  $a_{BB}/a_{BX} < 1$ , the second and third trimer states are significantly populated. This gives rise to excitation branches such as  $\tilde{\omega}_{8,3}$ , indicating the participation of the third trimer and the  $f = 8$  trap state [Fig. 8(a)] for small  $a_{BB}/a_{BX} < 1$ . This frequency branch shows an appreciable growth with larger  $a_{BB}/a_{BX}$  due to the accompanied increasing energy difference between trimer and trap states [Figs. 8(a) and 8(b)]. Note that the energies of the  $f = 2, 3$  trimers are large in magnitude and negative and therefore lie below the energy window presented in Fig. 8(b). Apart from trimer states, trap ones, e.g.,  $f = 8, 10$ , are occupied as well, but their respective energy differences depend weakly on changes of  $a_{BB}/a_{BX}$ ; see, e.g.,  $\tilde{\omega}_{10,8}$  in Fig. 8(a).

A further increase of the scattering length ratio  $a_{BB}/a_{BX} > 1$  leads to a reduction of the amplitude and number of the higher-lying excitation frequencies in comparison to  $a_{BB}/a_{BX} < 1$ . This behavior can be readily seen in the relevant profiles of the fidelity spectra depicted in Fig. 8(c) for  $a_{BB}/a_{BX} = 2.5$  and  $0.8$ . It stems from the suppressed contribution of the two trimer states for  $a_{BB}/a_{BX} > 1$ , resulting in a less perturbed system as also reflected in  $\langle |F| \rangle$  [Fig. 7(a)] for  $w = 1.5$ . Similarly to the case of  $a_{BB}/a_{BX} < 1$ , trap states are also populated here, imprinted in the spectrum as distinct almost horizontal frequency branches, e.g.,  $\tilde{\omega}_{52,50}$  in Fig. 8(c).<sup>7</sup>

A qualitatively similar dynamical response to the BBX mixture is also observed for the HHL FFX system; see  $|F(\tilde{\omega})|$  illustrated in Fig. 8(d) for  $w/a_{ho} = 0.57$ . Here, the heavy fermions with respect to the third particle favor trimer formation [39], a result that is in contrast to the corresponding LLH case. These trimer states possess large negative energies [38,41], lying beyond the values depicted in the energy spectrum provided in Fig. 8(e). Particularly, a superposition of the first two trimer states ( $f = 1$  and  $2$ ) is prevalent in the course of the evolution for  $1/a_{FX} < 1$ , leading to excitation branches such as  $\tilde{\omega}_{2,1}$  [Fig. 8(d)]. Moreover, similar to the BBX HHL system, trap states are also present in the dynamical response of the corresponding FFX mixture, as identified by the energy spectrum and the overlap coefficients. The frequency branches associated with energy differences between these states are almost independent of  $1/a_{FX}$  [Fig. 8(d)].

Tuning the inverse scattering length to larger values  $1/a_{FX} > 1$ , a plethora of trap states contributes in the time-evolved three-body wave function. Accordingly, a multitude of excitation branches arise in  $|F(\tilde{\omega})|$  whose location is almost constant with varying  $1/a_{FX}$  [Fig. 8(d)] and are clustering at

<sup>7</sup>Apart from the horizontal excitation branches within  $a_{BB}/a_{BX} \in [2, 3]$ , there exist also faint ones having a V-shape dependence on the scattering length with tipping points located at  $a_{BB}/a_{BX} = 2.25$  and  $2.57$  [Fig. 8(a)]. These are attributed to energy differences between trap and atom-dimer states. At the tipping point of these V-shaped branches, the energies of participating states come close together due to the avoided crossings and are thus associated with small  $\tilde{\omega}$  in  $|F(\tilde{\omega})|$ .

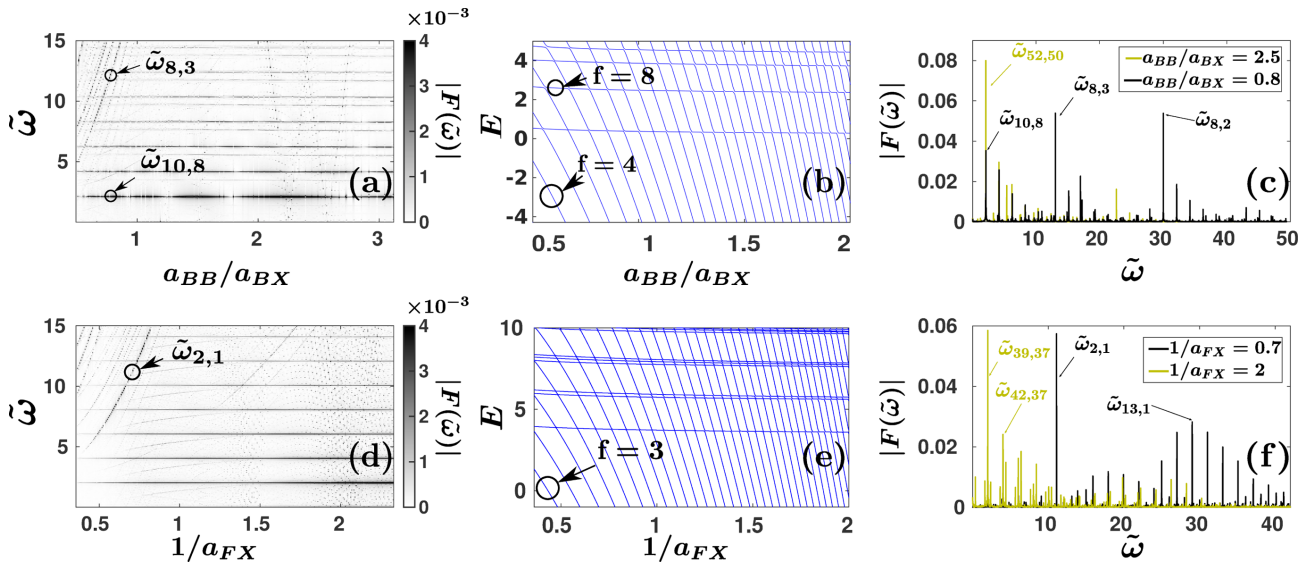


FIG. 8. Fidelity spectrum of the (a) BBX and (d) FFX HHL systems performing an interaction quench of an initial state where  $w/a_{\text{ho}} = 0.57$ . The arrows mark characteristic frequency branches  $\tilde{\omega}_{f,f'}$ . Excitation branches that alter with respect to the scattering length (see the top left corners) correspond to energy differences between trimers, atom-dimers, and trap states. Otherwise, the almost fixed frequency branches refer to trap states. Energy spectra of (b) BBX and (e) FFX HHL mixtures. Particular eigenstates are denoted by circles and arrows. Specific profiles of the fidelity spectrum of the (c) BBX and (f) FFX system at distinct scattering lengths (see the legends).

low  $\tilde{\omega}$  as shown in Fig. 8(f). The large number of contributing trap states for  $1/a_{FX} > 1$  is linked to the enhanced response of the HHL FFX system, e.g., captured by the time-averaged fidelity displayed in Fig. 7(b) for  $w/a_{\text{ho}} = 0.57$ .

### B. Dynamical formation of few-body correlations

As already demonstrated in Sec. IV C for LLH systems, the buildup of few-body correlations regardless of the particle statistics exhibits a peak structure for scattering lengths in the vicinity of avoided crossings appearing in the postquench eigenspectrum (see also Fig. 6). Similarly, in this section we focus on HHL systems in order to showcase the role of increased mass ratio on the time-averaged Tan contacts as illustrated in Fig. 9. In particular, the two-body BX species contact [Fig. 9(a)] exhibits sequences of narrow peaks at specific scattering length ratios in agreement with Tan's universal relation [7, 10, 11]. Namely, at these postquench scattering lengths, the corresponding eigenspectrum possesses narrow avoided crossings among trap states and atom-dimers [Fig. 8(b)], thus resulting into the strong amplification of the two-body correlations. Moreover, the amplitude of the peaks in the  $\langle \mathcal{D}_2^{BX} \rangle$  decreases for large  $a_{BB}/a_{BX}$  independently of  $w$ . This suppression occurs for large  $a_{BB}/a_{BX}$  where the avoided crossings become increasingly narrow [Fig. 8(b)]. In this sense, they cannot be well resolved, leading to less pronounced peaks compared to smaller  $a_{BB}/a_{BX}$ .

In the case of the three-body contact [Fig. 9(b)], a multitude of peaks with tiny amplitude appears as  $w$  increases. This holds even for large  $a_{BB}/a_{BX}$  as  $w$  increases, despite the narrow avoided crossings present in the HHL eigenspectra [Fig. 8(b)]. Particularly, for increasing  $w$ , trap states are predominantly populated, but in the vicinity of avoided crossings

atom-dimers contribute as well. Therefore, the amplification of stationary three-body correlations of the atom-dimer postquench eigenstates compared to trap states leads to the rise of peaks in  $\sqrt{\langle \mathcal{D}_3^{BBX} \rangle}$  at the locations of the avoided crossings. Moreover, equivalently to the two-body BX species contact [Fig. 9(a)], the time-averaged three-body contact is reduced for larger  $w$ , due to the significant participation of trap states, whose stationary three-body correlations are greatly suppressed.

Furthermore,  $\sqrt{\langle \mathcal{D}_3^{BBX} \rangle}$  at  $w/a_{\text{ho}} = 0.57$  has an overall maximum around  $a_{BB}/a_{BX} \simeq 1.2$ , and then decreases for larger values of  $a_{BB}/a_{BX}$ . This behavior is related to the significant population of the second trimer which specifically possesses a population up to 16% until  $a_{BB}/a_{BX} \simeq 1.2$ . Subsequently, the corresponding overlap coefficient with the initial state decreases for  $a_{BB}/a_{BX} > 1.2$ , since in this range of scattering length ratios the second trimer state is narrower than the initial one. HHL BBX systems favor the existence of strongly bound trimer states, due to the increased mass ratio [38]. The contribution of such a trimer state (second) for  $w < a_{\text{ho}}$  results in an augmented three-body contact, in contrast to the one presented in LLH setups [Fig. 6(b),  $w/a_{\text{ho}} = 0.78$ ], where the small mass ratio inhibits the creation of strongly bound trimers.

In an equal fashion to the time-averaged two-body BX contact,  $\sqrt{\langle \mathcal{D}_2^{FX} \rangle}$  [Fig. 9(c)] showcases small amplitude peaks, arising mostly for  $w/a_{\text{ho}} = 0.57$ . Their magnitude again drops for increasing scattering length ratio  $1/a_{FX}$  since sharper avoided crossings are encountered in the eigenspectrum of the HHL FFX system than the ones appearing in the LLH case [compare Fig. 3(e) and Fig. 8(e)].

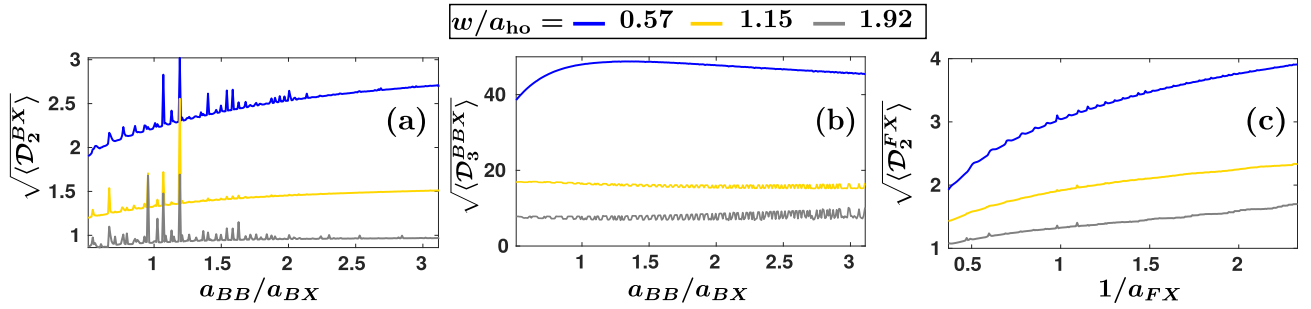


FIG. 9. Time-averaged contacts revealing the enhancement of short range (a), (c) two-body and (b) three-body correlations for larger inverse interspecies scattering lengths of HHL (a), (b) BBX and (c) FFX settings. The existence of peaks at individual scattering length ratios reveals the population of atom-dimers due to the sharp avoided crossing taking place at the eigenspectrum [Figs. 8(b) and 8(e)]. The widths of the initial state are shown in the legend.

## VI. EXPERIMENTAL PARAMETERS FOR THE REALIZATION OF THE DYNAMICS OF THE THREE-BODY MIXTURE

In an experimental environment, 2D gases are realized in quasi-2D trapping potentials where the confinement in the transversal direction of the 2D plane is tighter than the radial one. This transversal trapping component is characterized by a frequency  $\omega_{\perp}$  chosen such that the atomic motion is energetically restricted to the radial confinement potential with frequency  $\omega_r$  [68,87]. A comparison of the low-lying energy states of two interacting particles in 3D and in a pure 2D geometry [79] revealed that the aspect ratio in a quasi-2D setup required to attain the 2D character of the relative motion of the two particles [68] should satisfy  $\omega_r/\omega_{\perp} < 1/10$ . This is corroborated by typical quasi-2D experiments [88–90]. For our setup, this energy requirement translates to  $1/(\mu w^2) \leq 0.1\omega_{\perp}$ , and furthermore assuming  $\omega_{\perp} = 50$  [91], it reduces to  $w \geq 1/\sqrt{5\mu}$ . As such, for the typical LLH settings that we have considered, this condition yields  $w \geq 0.4559$ , while for HHL settings it yields  $w \geq 1.16$ .

The dynamical protocol outlined in Sec. III relies on the realization of a noninteracting three-body system with a tunable spatial extent  $w$ , and the subsequent quench of the relevant 2D scattering lengths. The latter are related to their 3D counterparts [68], which can be tuned by means of Feshbach resonances [67]. For the BBX systems, in particular, the coexistence of broad and narrow intra- and interspecies resonances in a magnetic field window ensures a regime where the postquench scattering length  $a_{BB}$  remains almost constant while  $a_{BX}$  varies in magnitude and sign. For instance, for the HHL BBX system of  $^{133}\text{Cs} - ^{133}\text{Cs} - ^6\text{Li}$ , such a magnetic field window exists for [840, 845] G, i.e., around the interspecies resonance [92–94]. Also, in the vicinity of  $\simeq 880$  G, both 3D scattering lengths vanish, thus materializing a noninteracting state.

The parameters of interest for the trapping potential are  $\omega_r = 2\pi \times 65$  kHz and  $\omega_{\perp} = 50\omega_r$  [91]. Also, regarding the 3D counterparts of the 2D postquench scattering lengths used herein, we discern the following values displayed in Table I. Note that in the considered intervals of the 3D scattering length (in atomic units), there is a sign change due to a resonance.

Our analysis in the previous sections illustrated the role of the width  $w$  of the initial state in the dynamical response of the three-body system. This  $w$  parameter can be experimentally adjusted by the following procedure. The two identical particles ( $B$  or  $F$ ) together with the third distinguishable atom ( $X$ ) are confined in a trap with a planar frequency  $\omega_{\text{in}}$ , which are initialized in their noninteracting ground state. A simple relation can be established between the initial state's width and the planar frequency, i.e.,  $\mu\omega_{\text{in}} = w^{-2}$ , where  $\mu$  is the three-body reduced mass (see also Sec. III). Prior to the quench on the scattering lengths, a quench on the trap frequency from  $\omega_{\text{in}}$  to  $\omega_f$  is performed. This allows for the preparation of initial states that possess widths different from the lengthscale of the trap with final frequency  $\omega_f$  where the interaction quench dynamics will take place. By setting the final radial trapping frequency at  $\omega_f = 2\pi \times 65$  kHz, the initial frequency is determined from the relation  $\omega_{\text{in}} = \omega_f a_{\text{ho}}^2/w^2$ . Thus, for the LLH settings in Sec. IV, the widths  $w/a_{\text{ho}} = 0.78, 4.9$  correspond to  $\omega_{\text{in}} = 2\pi \times (105.5, 2.7)$  kHz. For the HHL setup (Sec. V), the initial widths  $w/a_{\text{ho}} = 0.57, 1.92$  are obtained for  $\omega_{\text{in}} = 2\pi \times (194.5, 17.5)$  kHz.

TABLE I. Mapping of the 2D BX, FX, and BB postquench scattering lengths to their 3D counterparts (in atomic units with  $a_0$  denoting the Bohr radius) for both LLH and HHL setups. The radial and transversal trapping frequencies utilized herein are  $\omega_r = 2\pi \times 65$  kHz and  $\omega_{\perp} = 50\omega_r$ .

	$1/a_{FX}$	$a_{FX}^{3D} (a_0)$
LLH	[0.36, 2.77] ([4, 5])	[−246, −3000] ([3000, 1343])
HHL	[0.36, 6] ([0.82, 2.5])	[−715, −2976] ([2991, 380])
	$1/a_{BX}$	$a_{BX}^{3D} (a_0)$
LLH	[2, 2.81] ([3.94, 4.65])	[−994, 3000] ([2995, 1497])
HHL	[0.85, 3]	[3000, 380]
	$a_{BB}$	$a_{BB}^{3D} (a_0)$
LLH	1	−421
HHL	1	1578

## VII. SUMMARY AND OUTLOOK

The quench dynamics of mass-imbalanced three-body mixtures with either bosonic or fermionic constituents interacting with a third atom is investigated. Depending on the mass ratio, we distinguish between the LLH and HHL cases. Initially the mixture is confined in a 2D harmonic trap and assumed to be noninteracting. The spatial extent of the initial state and the postquench scattering length are exploited as parameters in order to map out the buildup of two- and three-body correlations via distinct microscopic excitation mechanisms.

In particular, the interactions are abruptly switched on triggering a distinct dynamical response depending on the width of the initial state. A complete knowledge of the energy spectra in conjunction with the fidelity spectrum allows us to identify the prevalent microscopic mechanisms in terms of specific postquench eigenstates. It is found that if the initial state width is smaller than the three-body harmonic-oscillator length  $a_{ho}$ , trimers and atom-dimers contribute predominantly in the dynamics. In contrast, for larger widths trap states are those that are significantly populated regardless of the mass imbalance of the system. However, in HHL ensembles for narrow widths, the participation of trimers and atom-dimers prevails in a relatively smaller range of scattering lengths as compared to LLH mixtures.

Interestingly, the participating eigenstates have a distinct imprint on the dynamics of the underlying few-body short-range correlations, as captured by the Tan contacts. It is explicated that for an increasing width of the initial state, the magnitude of both the overall time-averaged two- and three-body correlations decreases for a fixed 2D scattering length. For small widths, these correlations are found to be enhanced as a result of the involvement of trimer states and atom-dimers. The respective amplification of the Tan contacts, due to the participation of such states, was also independently reported following the quench dynamics of three-body systems at unitarity in 3D [29]. Strikingly, for widths larger than the three-body harmonic-oscillator length, few-body correlations display sharp peaks at certain scattering lengths. This behavior is directly linked to the presence of avoided crossings among trap and atom-dimer states taking place in the few-body eigenspectrum, and it signifies the non-negligible cooperation of atom-dimers in the time evolution.

Overall, our work proposes a scheme to dynamically excite distinct superpositions of eigenstates in three-body mixtures. Specifically, it was demonstrated that depending on the interplay between the three-body harmonic-oscillator length and the width of the initial state, all three types of eigenstates, that is, trimers, atom-dimers, and trap states, may be dominantly populated during the nonequilibrium dynamics. Moreover, temperature effects are expected to mitigate few-body correlations, as shown in [41,95]. In this sense, the investigation of possible smearing effects of the identified peak structures building upon the time-averaged contacts for large  $w > a_{ho}$  is a compelling perspective for further research.

In addition, an interesting question that arises for future studies is how to efficiently populate individual target states, and in particular trimers. Their properties, such as lifetimes, are usually studied indirectly via three-body recombination

loss mechanisms [50,57]. However, many questions remain open, especially regarding their dynamical formation in a gas [23]. A promising route towards achieving this goal would be to utilize time-dependent protocols in order to activate individual target states instead of superpositions of them generated by quenches. There is currently active research for the dynamical creation of the macroscopic population of trimer states in cold gases [23,29,33]. A first step has already been accomplished in Ref. [23], where an abrupt tuning of interactions to unitarity and a subsequent sweep to weak repulsion were shown to be able to produce an 8% population of trimers.

## ACKNOWLEDGMENTS

G.B. acknowledges financial support by the State Graduate Funding Program Scholarships (Hmb-NFG). S.I.M. acknowledges support from the NSF through a grant for ITAMP at Harvard University. This work is supported (P.S.) by the Cluster of Excellence ‘‘The Hamburg Center for Ultrafast Imaging’’ of the Deutsche Forschungsgemeinschaft (DFG)-EXC 1074- project ID 194651731. The authors thank G. M. Koutentakis for insightful discussions, M.T. Eiles for his comments on the manuscript, and Lydia Schollmeier for the collaboration and discussions in the early stages of this project.

## APPENDIX A: ADIABATIC HAMILTONIAN AND $s$ -WAVE PSEUDOPOTENTIAL IN TWO DIMENSIONS

The adiabatic Hamiltonian  $H_{ad}(R; \mathbf{\Omega})$  as introduced in Eq. (1) is expressed in the following way [72]:

$$H_{ad}(R; \mathbf{\Omega}) = \frac{\hbar^2 \Lambda^2(\mathbf{\Omega})}{2\mu R^2} + \frac{3\hbar^2}{8\mu R^2} + \sum_k V_k(R; \mathbf{\Omega}^{(k)}), \quad (\text{A1})$$

where  $\Lambda^2(\mathbf{\Omega})$  is the hyperangular operator referring to the centrifugal motion of the three particles [96,97]. Also, the three-body reduced mass is  $\mu = m_{B/F} / \sqrt{2m_{B/F}/m_X + 1}$ , with  $m_{B/F}$  denoting the mass of the bosons or the fermions depending on the type of the mixture.

The last term of Eq. (A1) stands for the three (two) pairwise  $s$ -wave contact interactions among the particles in a BBX (FFX) system. The  $V_k$  potential refers to the interaction between the  $i$  and  $j$  particles (also known as odd-man-out notation, where the  $i$ ,  $j$ , or  $k$  indices refer to interaction pairs of the remaining two indices [72]). In particular, the  $V_k$  interaction is modeled by a 2D pseudopotential, which reads [66,98]

$$V_k(R; \mathbf{\Omega}^{(k)}) = -\frac{\hbar^2 \delta(\alpha^{(k)})}{\mu \sin(2\alpha^{(k)}) R^2 \ln(A\lambda\alpha^{(k)})} \times \left[ 1 - \ln(A\lambda\sqrt{\mu/\mu_k} R \sin(\alpha^{(k)})) \alpha^{(k)} \frac{\partial}{\partial \alpha^{(k)}} \right], \quad (\text{A2})$$

where  $\alpha^{(k)} \in [0, \pi/2]$  is the hyperangle describing the relative position of two particles compared to the third one. For instance, if  $\alpha^{(k)} = 0$ , then the particles  $i$  and  $j$  are on top of each other, whereas for  $\alpha^{(k)} = \pi/2$ , all three particles are collinear.



Moreover,  $\mu_k = \frac{m_i m_j}{m_i + m_j}$  is the reduced two-body mass and  $A = 0.5 e^\gamma$ , with  $\gamma \approx 0.577$  being the Euler-Mascheroni constant. Importantly,  $a^{(k)} \equiv a_{ij}$  is the 2D scattering length between the  $(i, j)$  pair of particles. The factor  $\lambda$  is an ultraviolet cutoff

for the zero-range pseudopotential, setting an upper bound in momentum space. However, it does not affect any observable as argued in Refs. [66,99].

## APPENDIX B: HYPERANGULAR WAVE FUNCTION OF THE NONINTERACTING INITIAL STATE

The hyperangular wave function of the noninteracting initial state [denoted by the (0) superscript] can be expressed [27,100] as follows:

$$\Phi_n^{(0)}(\Omega) = \sum_{k=1}^3 \sum_{\substack{m_1, m_2 \\ |m_1 + m_2| = L}} C^{(k)} \mathcal{N}_n^{(m_1, m_2)} \sin^{|m_1|} \alpha^{(k)} \cos^{|m_2|} \alpha^{(k)} Y_{m_1}(\theta_1^{(k)}) Y_{m_2}(\theta_2^{(k)}) \frac{\Gamma(1+n+|m_1|)}{\Gamma(1+|m_1|)n!} \times {}_2F_1(1+|m_1|+|m_2|+n, -n; |m_1|+1; \sin^2 \alpha^{(k)}), \quad (\text{B1})$$

where  $\mathcal{N}_n^{(m_1, m_2)} = \sqrt{\frac{(2n+1+|m_1|+|m_2|)\Gamma(n+1)\Gamma(n+1+|m_1|+|m_2|)}{2\Gamma(n+1+|m_1|)\Gamma(n+1+|m_2|)}}$  are normalization coefficients. The above eigenfunction is the  $n$ th eigenstate ( $n$  is a non-negative integer) of the hyperangular operator  $\Lambda^2(\Omega)$  [96,97] with eigenvalues  $\lambda_n(\lambda_n + 2)$ , where

$$\lambda_n = 2n + |m_1| + |m_2|, \quad (\text{B2})$$

and  $L = |m_1 + m_2|$  is the total angular momentum of the three-body system. It is expressed in terms of the angular quantum numbers  $m_1, m_2$  related to the polar angles  $\theta_1^{(k)}$  and  $\theta_2^{(k)}$ . The polar angles  $\theta_1^{(k)}$  and  $\theta_2^{(k)}$  refer to the orientation of the Jacobi vectors  $\rho_1^{(k)}, \rho_2^{(k)}$  in the 2D plane, respectively, where  $\rho_1^{(k)}$  is the relative distance of the  $(i, j)$  pair, and  $\rho_2^{(k)}$  is the relative vector of the  $k$  spectator particle relative to the  $(i, j)$  pair's center of mass. The summation running over these angular quantum numbers is restricted by the condition  $L = |m_1 + m_2|$ . Note that in the case of three identical particles,  $n = 1$  gives an unphysical solution and therefore it is not allowed [101]. Additionally,  ${}_2F_1(a, b; c; \cdot)$  is the Gauss hypergeometric function [102], and  $Y_m(x) = e^{imx}/\sqrt{2\pi}$  are plane waves. The angle  $\alpha^{(k)}$  determines the ratio of the measure of the two Jacobi vectors via the relation  $\tan \alpha^{(k)} = \rho_1^{(k)}/\rho_2^{(k)}$  (see also Appendix A).

The particle statistics of the above wave function is properly taken into account by the first summation and the  $C^{(k)}$  coefficients. These read explicitly  $(C_1, -C_1, 0)$  and  $(C_1, C_1, C_2)$  for FFX and BBX systems, respectively, with the  $C_1$  and  $C_2$  terms being normalization coefficients. The hyperangular wave functions  $\Phi_v(R; \Omega)$  [which are eigenstates of  $H_{\text{ad}}(R; \Omega)$ ] correspond to the interacting postquench eigenstates and have angular quantum numbers  $(m_1, m_2) = (0, \pm L)$  due to the  $s$ -wave zero-range pseudopotential. As such, the relevant subset in the summation [Eq. (B1)] will also be  $(0, \pm L)$ . Indeed, the remaining terms in the summation have a zero contribution in the overlap coefficients,  $c_{f,\text{in}}$ , since the plane waves  $Y_m(\cdot)$  are orthonormal. Here, we focus on  $n = 0$ , that is, the ground state. Note that the hyperangular wave function does not depend on the hyperradius  $R$  since in the noninteracting case  $H_{\text{ad}}(R; \Omega)$  does not depend on  $R$ , as all interaction terms  $V_k(R; \Omega^{(k)})$  drop (see also Appendix A).

## APPENDIX C: QUENCH DYNAMICS OF THE LLH BBX MIXTURE FOR INITIAL STATES WITH $w = a_{\text{ho}}$

For completeness, we shall also analyze the excitation spectrum of three-body mixtures starting from a prequench state of width  $w = a_{\text{ho}}$ . As characteristic system for this investigation, we consider a LLH BBX system whose fidelity spectrum [Eq. (10)] is illustrated in Fig. 10 for varying postquench  $a_{\text{BB}}/a_{\text{BX}}$ .

Recall that for  $w/a_{\text{ho}} = 0.78$ , the second trimer state  $f = 2$  contributes the most in the quench dynamics of the LLH BBX setting; see also the discussion in Sec. IV A. The predominant population of the second trimer yields, in particular, excitation

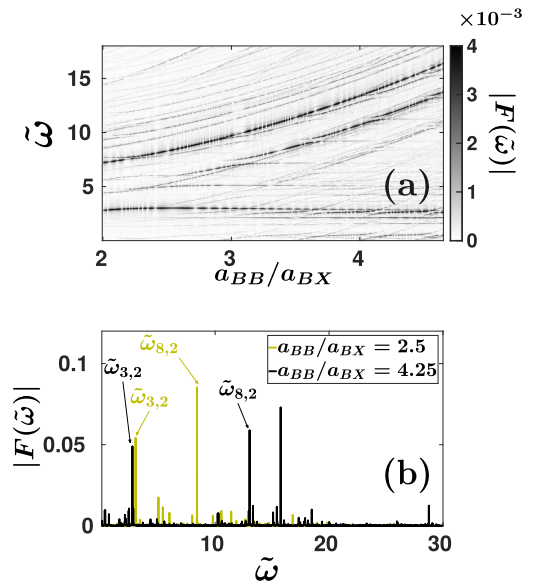


FIG. 10. (a) Fidelity spectrum  $[|F(\tilde{\omega})|]$  for the LLH BBX system subjected to a quench of  $a_{\text{BB}}/a_{\text{BX}}$  from an initial noninteracting state with  $w/a_{\text{ho}} = 1$ . (b) Profiles of  $|F(\tilde{\omega})|$  at different scattering length ratios  $a_{\text{BB}}/a_{\text{BX}}$  (see the legend). The excitation processes involve majorly trimer and atom-dimer states which are imprinted in the spectrum as branches that are sensitive to the scattering length. Notice that the participation of the second trimer is reduced compared to the  $w/a_{\text{ho}} = 0.78$  case, resulting in different branches than in  $|F(\tilde{\omega})|$  depicted in Fig. 3(c).

branches that are strongly influenced by  $a_{BB}/a_{BX}$  [Fig. 3(a)]. This is a consequence of the fact that the branches associated with these transitions refer to energy differences between the  $f = 2$  trimer and the trap states, and they are increasing as  $a_{BB}/a_{BX}$  is tuned to larger values.

These excitation branches are still present even for an initial state width  $w/a_{ho} = 1$  as shown in Fig. 10(a). Here, the almost constant frequency branch located around  $\tilde{\omega} \simeq 2$ , stemming from the transition among the second trimer ( $f = 2$ ) and the first atom-dimer ( $f = 3$ ) states, is more enhanced than in the case where  $w/a_{ho} = 0.78$  [compare  $\tilde{\omega}_{3,2}$  in Fig. 10(b) and Fig. 3(c)]. This difference is attributed to the fact that the occupation of the first atom-dimer state is larger when  $w = a_{ho}$ , while the one from the second trimer is reduced, a result that is supported by the corresponding overlap coefficients  $c_{f,in}$ . To be more precise, the population of the  $f = 2$  trimer as long as  $w/a_{ho} = 0.78$  ( $w/a_{ho} = 1$ ) ranges from 73% (57%) to 35% (21%) within the interval  $a_{BB}/a_{BX} \in [2, 4.6]$ . Apart from the enhanced population of the first atom-dimer, the contribution of trap states, similar to the ones

populated also for  $w/a_{ho} = 0.78$ , increases as well with respect to  $w/a_{ho} = 0.78$ . This is imprinted in the spectrum by the larger number of faint excitation branches; compare, in particular, Fig. 10(a), where  $w/a_{ho} = 1$  with Fig. 3(a) for which  $w/a_{ho} = 0.78$ .

Similar observations to the above can be made for the other types of mixtures utilized in the main text. Regarding the LLH FFX system, the contribution of the first two atom-dimer states at  $w/a_{ho} = 1$  remains the same in comparison to  $w/a_{ho} = 0.78$  for  $1/a_{FX} < 1$ . Otherwise, it reduces further from the value obtained for  $w/a_{ho} = 0.78$  (18% versus 25% at  $1/a_{FX} = 4.5$ ). This reduction is compensated by an increasing population of a few trap states. Due to the reduced number of participating postquench eigenstates compared to smaller  $1/a_{FX}$ , the time-averaged fidelity possesses a smaller magnitude for  $1/a_{FX} > 3$  [see Fig. 2(b) for  $w/a_{ho} = 1$ ]. In a similar way, the population of trimers and first atom-dimers also drops when considering  $w/a_{ho} = 1$  for the HHL mixtures (both BBX and FFX systems) as compared to the scenario in which  $w/a_{ho} = 0.57$ .

- 
- [1] D. S. Petrov, *Phys. Rev. Lett.* **115**, 155302 (2015).
- [2] Z.-H. Luo, W. Pang, B. Liu, Y.-Y. Li, and B. A. Malomed, *Front. Phys.* **16**, 32201 (2021).
- [3] L. Chomaz, I. Ferrier-Barbut, F. Ferlaino, B. Laburthe-Tolra, B. L. Lev, and T. Pfau, [arXiv:2201.02672](https://arxiv.org/abs/2201.02672).
- [4] P. Massignan, M. Zaccanti, and G. M. Bruun, *Rep. Prog. Phys.* **77**, 034401 (2014).
- [5] G. Ness, C. Shkedrov, Y. Florshaim, O. K. Diessel, J. von Milczewski, R. Schmidt, and Y. Sagi, *Phys. Rev. X* **10**, 041019 (2020).
- [6] S. I. Mistakidis, A. G. Volosniev, R. E. Barfknecht, T. Fogarty, T. Busch, A. Foerster, P. Schmelcher, and N. T. Zinner, [arXiv:2202.11071](https://arxiv.org/abs/2202.11071).
- [7] S. Tan, *Ann. Phys.* **323**, 2952 (2008).
- [8] S. Tan, *Ann. Phys.* **323**, 2987 (2008).
- [9] S. Tan, *Ann. Phys.* **323**, 2971 (2008).
- [10] E. Braaten, D. Kang, and L. Platter, *Phys. Rev. Lett.* **106**, 153005 (2011).
- [11] F. Werner and Y. Castin, *Phys. Rev. A* **86**, 053633 (2012).
- [12] M. Valiente, N. T. Zinner, and K. Mølmer, *Phys. Rev. A* **86**, 043616 (2012).
- [13] M. Olshanii and V. Dunjko, *Phys. Rev. Lett.* **91**, 090401 (2003).
- [14] M. He, S. Zhang, H. M. Chan, and Q. Zhou, *Phys. Rev. Lett.* **116**, 045301 (2016).
- [15] S.-L. Zhang, M. He, and Q. Zhou, *Phys. Rev. A* **95**, 062702 (2017).
- [16] R. J. Fletcher, R. Lopes, J. Man, N. Navon, R. P. Smith, M. W. Zwierlein, and Z. Hadzibabic, *Science* **355**, 377 (2017).
- [17] Y. Sagi, T. E. Drake, R. Paudel, and D. S. Jin, *Phys. Rev. Lett.* **109**, 220402 (2012).
- [18] R. J. Wild, P. Makotyn, J. M. Pino, E. A. Cornell, and D. S. Jin, *Phys. Rev. Lett.* **108**, 145305 (2012).
- [19] J. T. Stewart, J. P. Gaebler, T. E. Drake, and D. S. Jin, *Phys. Rev. Lett.* **104**, 235301 (2010).
- [20] S. Hoinka, M. Lingham, K. Fenech, H. Hu, C. J. Vale, J. E. Drut, and S. Gandolfi, *Phys. Rev. Lett.* **110**, 055305 (2013).
- [21] E. D. Kuhnle, H. Hu, X.-J. Liu, P. Dyke, M. Mark, P. D. Drummond, P. Hannaford, and C. J. Vale, *Phys. Rev. Lett.* **105**, 070402 (2010).
- [22] E. Braaten, D. Kang, and L. Platter, *Phys. Rev. A* **78**, 053606 (2008).
- [23] C. E. Klauss, X. Xie, C. Lopez-Abadia, J. P. D’Incao, Z. Hadzibabic, D. S. Jin, and E. A. Cornell, *Phys. Rev. Lett.* **119**, 143401 (2017).
- [24] P. Makotyn, C. E. Klauss, D. L. Goldberger, E. A. Cornell, and D. S. Jin, *Nat. Phys.* **10**, 116 (2014).
- [25] C. Eigen, J. A. P. Glidden, R. Lopes, N. Navon, Z. Hadzibabic, and R. P. Smith, *Phys. Rev. Lett.* **119**, 250404 (2017).
- [26] C. Eigen, J. A. P. Glidden, R. Lopes, E. A. Cornell, R. P. Smith, and Z. Hadzibabic, *Nature* **563**, 221 (2018).
- [27] E. Nielsen, D. V. Fedorov, A. S. Jensen, and E. Garrido, *Phys. Rep.* **347**, 373 (2001).
- [28] V. N. Efimov, *Sov. J. Nucl. Phys.* **12**, 589 (1971).
- [29] V. E. Colussi, J. P. Corson, and J. P. D’Incao, *Phys. Rev. Lett.* **120**, 100401 (2018).
- [30] J. P. D’Incao, J. Wang, and V. E. Colussi, *Phys. Rev. Lett.* **121**, 023401 (2018).
- [31] V. E. Colussi, B. E. van Zwol, J. P. D’Incao, and S. J. J. M. F. Kokkelmans, *Phys. Rev. A* **99**, 043604 (2019).
- [32] V. E. Colussi, H. Kurkjian, M. Van Regemortel, S. Musolino, J. van de Kraats, M. Wouters, and S. J. J. M. F. Kokkelmans, *Phys. Rev. A* **102**, 063314 (2020).
- [33] S. Musolino, H. Kurkjian, M. Van Regemortel, M. Wouters, S. J. J. M. F. Kokkelmans, and V. E. Colussi, *Phys. Rev. Lett.* **128**, 020401 (2022).
- [34] C. H. Greene, P. Giannakeas, and J. Pérez-Ríos, *Rev. Mod. Phys.* **89**, 035006 (2017).
- [35] J. P. D’Incao, F. Anis, and B. D. Esry, *Phys. Rev. A* **91**, 062710 (2015).

- [36] J. Levinsen, P. Massignan, and M. M. Parish, *Phys. Rev. X* **4**, 031020 (2014).
- [37] T. Kirk and M. M. Parish, *Phys. Rev. A* **96**, 053614 (2017).
- [38] F. F. Bellotti, T. Frederico, M. T. Yamashita, D. V. Fedorov, A. S. Jensen, and N. T. Zinner, *J. Phys. B* **46**, 055301 (2013).
- [39] L. Pricoupenko and P. Pedri, *Phys. Rev. A* **82**, 033625 (2010).
- [40] F. F. Bellotti, T. Frederico, M. T. Yamashita, D. V. Fedorov, A. S. Jensen, and N. T. Zinner, *J. Phys. B* **44**, 205302 (2011).
- [41] G. Bougas, S. I. Mistakidis, P. Giannakeas, and P. Schmelcher, *New J. Phys.* **23**, 093022 (2021).
- [42] J. H. Sandoval, F. F. Bellotti, A. S. Jensen, and M. T. Yamashita, *Phys. Rev. A* **94**, 022514 (2016).
- [43] O. I. Kartavtsev and A. V. Malykh, *Phys. Rev. A* **74**, 042506 (2006).
- [44] L. W. Bruch and J. A. Tjon, *Phys. Rev. A* **19**, 425 (1979).
- [45] F. F. Bellotti, T. Frederico, M. T. Yamashita, D. V. Fedorov, A. S. Jensen, and N. T. Zinner, *New J. Phys.* **16**, 013048 (2014).
- [46] M. Valiente, N. T. Zinner, and K. Mølmer, *Phys. Rev. A* **84**, 063626 (2011).
- [47] F. F. Bellotti, T. Frederico, M. T. Yamashita, D. V. Fedorov, A. S. Jensen, and N. T. Zinner, *Phys. Rev. A* **87**, 013610 (2013).
- [48] A. D. Kerin and A. M. Martin, [arXiv:2207.09091](https://arxiv.org/abs/2207.09091).
- [49] A. D. Kerin and A. M. Martin, [arXiv:2208.05666](https://arxiv.org/abs/2208.05666).
- [50] J. Ulmanis, S. Häfner, R. Pires, E. D. Kuhnle, Y. Wang, C. H. Greene, and M. Weidemüller, *Phys. Rev. Lett.* **117**, 153201 (2016).
- [51] P. Giannakeas and C. H. Greene, *Atoms* **9**, 110 (2021).
- [52] P. Giannakeas and C. H. Greene, *Phys. Rev. Lett.* **120**, 023401 (2018).
- [53] M. Mikkelsen, A. S. Jensen, D. V. Fedorov, and N. T. Zinner, *J. Phys. B* **48**, 085301 (2015).
- [54] L. J. Wacker, N. B. Jørgensen, D. Birkmose, N. Winter, M. Mikkelsen, J. Sherson, N. Zinner, and J. J. Arlt, *Phys. Rev. Lett.* **117**, 163201 (2016).
- [55] J. Johansen, B. J. DeSalvo, K. Patel, and C. Chin, *Nat. Phys.* **13**, 731 (2017).
- [56] S.-K. Tung, K. Jiménez-García, J. Johansen, C. V. Parker, and C. Chin, *Phys. Rev. Lett.* **113**, 240402 (2014).
- [57] R. Pires, J. Ulmanis, S. Häfner, M. Repp, A. Arias, E. D. Kuhnle, and M. Weidemüller, *Phys. Rev. Lett.* **112**, 250404 (2014).
- [58] A. D. Kerin and A. M. Martin, [arXiv:2204.09205](https://arxiv.org/abs/2204.09205).
- [59] C. Gao and P. Zhang, *Phys. Rev. A* **97**, 042701 (2018).
- [60] M. A. Shalchi, M. T. Yamashita, T. Frederico, and L. Tomio, *Phys. Rev. A* **102**, 062814 (2020).
- [61] M. A. Shalchi, A. Delfino, T. Frederico, and L. Tomio, *Phys. Rev. A* **98**, 032705 (2018).
- [62] J. Rui, H. Yang, L. Liu, D.-C. Zhang, Y.-X. Liu, J. Nan, Y.-A. Chen, B. Zhao, and J.-W. Pan, *Nat. Phys.* **13**, 699 (2017).
- [63] H. Yang, D.-C. Zhang, L. Liu, Y.-X. Liu, J. Nan, B. Zhao, and J.-W. Pan, *Science* **363**, 261 (2019).
- [64] D. K. Hoffmann, T. Paintner, W. Limmer, D. S. Petrov, and J. H. Denschlag, *Nat. Commun.* **9**, 5244 (2018).
- [65] C. Makrides, D. S. Barker, J. A. Fedchak, J. Scherschligt, S. Eckel, and E. Tiesinga, *Phys. Rev. A* **101**, 012702 (2020).
- [66] M. Olshanii and L. Pricoupenko, *Phys. Rev. Lett.* **88**, 010402 (2001).
- [67] C. Chin, R. Grimm, P. Julienne, and E. Tiesinga, *Rev. Mod. Phys.* **82**, 1225 (2010).
- [68] D. S. Petrov and G. V. Shlyapnikov, *Phys. Rev. A* **64**, 012706 (2001).
- [69] X.-J. Liu, H. Hu, and P. D. Drummond, *Phys. Rev. B* **82**, 054524 (2010).
- [70] P. Naidon and S. Endo, *Rep. Prog. Phys.* **80**, 056001 (2017).
- [71] J. P. D’Incao, *J. Phys. B* **51**, 043001 (2018).
- [72] S. T. Rittenhouse, N. P. Mehta, and C. H. Greene, *Phys. Rev. A* **82**, 022706 (2010).
- [73] G. Bougas, S. I. Mistakidis, and P. Schmelcher, *Phys. Rev. A* **100**, 053602 (2019).
- [74] T. Busch, B.-G. Englert, K. Rzazewski, and M. Wilkens, *Found. Phys.* **28**, 549 (1998).
- [75] R. A. Doganov, S. Klaiman, O. E. Alon, A. I. Streltsov, and L. S. Cederbaum, *Phys. Rev. A* **87**, 033631 (2013).
- [76] S. E. Gharashi, K. M. Daily, and D. Blume, *Phys. Rev. A* **86**, 042702 (2012).
- [77] D. Blume and C. H. Greene, *Phys. Rev. A* **66**, 013601 (2002).
- [78] J. Portegies and S. Kokkelmans, *Few-Body Syst.* **51**, 219 (2011).
- [79] Z. Idziaszek and T. Calarco, *Phys. Rev. A* **74**, 022712 (2006).
- [80] G. Bougas, S. I. Mistakidis, G. M. Alshalan, and P. Schmelcher, *Phys. Rev. A* **102**, 013314 (2020).
- [81] L. Budewig, S. I. Mistakidis, and P. Schmelcher, *Mol. Phys.* **117**, 2043 (2019).
- [82] T. Gorin, T. Prosen, T. H. Seligman, and M. Žnidarič, *Phys. Rep.* **435**, 33 (2006).
- [83] S. I. Mistakidis, L. Cao, and P. Schmelcher, *J. Phys. B* **47**, 225303 (2014).
- [84] S. I. Mistakidis and P. Schmelcher, *Phys. Rev. A* **95**, 013625 (2017).
- [85] V. E. Colussi, *Atoms* **7**, 19 (2019).
- [86] D. Blume, M. W. C. Sze, and J. L. Bohn, *Phys. Rev. A* **97**, 033621 (2018).
- [87] M. He and Q. Zhou, *Phys. Rev. A* **100**, 012701 (2019).
- [88] K. Kwon, K. Mukherjee, S. J. Huh, K. Kim, S. I. Mistakidis, D. K. Maity, P. G. Kevrekidis, S. Majumder, P. Schmelcher, and J.-y. Choi, *Phys. Rev. Lett.* **127**, 113001 (2021).
- [89] M. Holten, L. Bayha, A. C. Klein, P. A. Murthy, P. M. Preiss, and S. Jochim, *Phys. Rev. Lett.* **121**, 120401 (2018).
- [90] P. A. Murthy, N. Defenu, L. Bayha, M. Holten, P. M. Preiss, T. Enss, and S. Jochim, *Science* **365**, 268 (2019).
- [91] V. Makhalov, K. Martiyanov, and A. Turlapov, *Phys. Rev. Lett.* **112**, 045301 (2014).
- [92] M. Berninger, A. Zenesini, B. Huang, W. Harm, H.-C. Nägerl, F. Ferlaino, R. Grimm, P. S. Julienne, and J. M. Hutson, *Phys. Rev. A* **87**, 032517 (2013).
- [93] R. Pires, M. Repp, J. Ulmanis, E. D. Kuhnle, M. Weidemüller, T. G. Tiecke, C. H. Greene, B. P. Ruzic, J. L. Bohn, and E. Tiemann, *Phys. Rev. A* **90**, 012710 (2014).
- [94] M. Repp, R. Pires, J. Ulmanis, R. Heck, E. D. Kuhnle, M. Weidemüller, and E. Tiemann, *Phys. Rev. A* **87**, 010701(R) (2013).
- [95] Y. Yan and D. Blume, *Phys. Rev. A* **88**, 023616 (2013).
- [96] J. Avery, *Hyperspherical Harmonics: Applications in Quantum Theory* (Kluwer Academic, Norwell, MA, 1989).
- [97] T. K. Das, *Hyperspherical Harmonics Expansion Techniques: Application to Problems in Physics* (Springer India, New Delhi, 2016), pp. 17–32.

- [98] K. Kanjilal and D. Blume, *Phys. Rev. A* **73**, 060701(R) (2006).
- [99] L. Pricoupenko and M. Olshanii, *J. Phys. B* **40**, 2065 (2007).
- [100] A. G. Volosniev, D. V. Fedorov, A. S. Jensen, and N. T. Zinner, *J. Phys. B* **47**, 185302 (2014).
- [101] J. P. D’Incao and B. D. Esry, *Phys. Rev. A* **90**, 042707 (2014).
- [102] M. Abramowitz and I. Stegun, *Handbook of Mathematical Functions, With Formulas, Graphs, and Mathematical Tables* (Dover, New York, 1965).

**4.1.5 Interferometry of Efimov states in thermal gases by modulated magnetic fields**

## Interferometry of Efimov states in thermal gases by modulated magnetic fields

G. Bougas,<sup>1,\*</sup> S. I. Mistakidis,<sup>2,3</sup> P. Schmelcher,<sup>1,4</sup> C. H. Greene,<sup>5,6</sup> and P. Giannakeas<sup>7</sup>

<sup>1</sup>*Center for Optical Quantum Technologies, Department of Physics,  
University of Hamburg, Luruper Chaussee 149, 22761 Hamburg Germany*

<sup>2</sup>*ITAMP, Center for Astrophysics | Harvard & Smithsonian, Cambridge, MA 02138 USA*

<sup>3</sup>*Department of Physics, Harvard University, Cambridge, Massachusetts 02138, USA*

<sup>4</sup>*The Hamburg Centre for Ultrafast Imaging, University of Hamburg,  
Luruper Chaussee 149, 22761 Hamburg, Germany*

<sup>5</sup>*Department of Physics and Astronomy, Purdue University, West Lafayette, Indiana 47907, USA*

<sup>6</sup>*Purdue Quantum Science and Engineering Institute,  
Purdue University, West Lafayette, Indiana 47907, USA*

<sup>7</sup>*Max-Planck-Institut für Physik komplexer Systeme, Nöthnitzer Str. 38, D-01187 Dresden, Germany*

We demonstrate that an interferometer based on modulated magnetic field pulses enables precise characterization of the energies and lifetimes of Efimov trimers irrespective of the magnitude and sign of the interactions in  $^{85}\text{Rb}$  thermal gases. Despite thermal effects, interference fringes develop when the dark time between the pulses is varied. This enables the selective excitation of coherent superpositions of trimer, dimer and free atom states. The interference patterns possess two distinct damping timescales at short and long dark times that are either equal to or twice as long as the lifetime of Efimov trimers, respectively. Specifically, this behavior at long dark times provides an interpretation of the unusually large damping timescales reported in a recent experiment with  $^7\text{Li}$  thermal gases [Phys. Rev. Lett. **122**, 200402 (2019)]. Apart from that, our results constitute a stepping stone towards a high precision few-body state interferometry for dense quantum gases.

Efimovian trimers constitute an infinite set of particle triplets occurring in the absence of two-body binding [1–7]. Owing to their universal character, they have been explored in both nuclear and atomic physics [4, 8–11] and in the context of many-body physics as the binding mechanism for magnons [12] and polaritons [13]. Furthermore, the role of Efimov states is pivotal for some ultracold gases in equilibrium, e.g. polarons [14–17] and in some out-of-equilibrium [18–23], despite their short lifetime due to collisional decay, i.e. three-body recombination processes. Recent investigations in dense gas mixtures demonstrate that such processes can be suppressed due to medium effects [24]. Specifically, putting forward the idea that the intrinsic properties of Efimov states, i.e. the binding energies and lifetimes, are potentially modified. Hence, dynamically probing simultaneously both intrinsic properties of Efimov trimers could provide alternative ways to study the impact of an environment.

To address such effects, a promising dynamical protocol is to expose a many-body system in a double sequence of magnetic field modulations (pulses). The latter has been used successfully to precisely measure the binding energies and lifetimes of dimers [25] near a Feshbach resonance [26]. Beyond two-body physics, employing this Ramsey-type protocol for a thermal gas of  $^7\text{Li}$  atoms, Yudkin *et al.* precisely probed Efimov molecules even near the atom-dimer threshold [27, 28]; an experimentally challenging region. Specifically, the surviving atom number exhibited damped Ramsey fringes that were robust against thermal effects. However, the corresponding damping timescale was found to exceed the typical lifetime of Efimov trimers even for  $^{85}\text{Rb}_3$  [22]. In this regard, it has remained elusive how the lifetime of Efimov

trimers emerges in the interference fringes induced by magnetic field pulses. To address the intricate dynamics of a three-body system requires a time-dependent theoretical framework establishing also a systematic pathway to explore the role of few-body physics in out-of-equilibrium many-body systems [20, 22].

In this Letter, such an approach is developed to investigate the three-body dynamics of a thermal gas. We consider  $^{85}\text{Rb}$  atoms since the lifetimes of the ensuing trimers and dimers are known experimentally [22] in contrast to  $^7\text{Li}$  [27]. Our study establishes that, by implementing double magnetic field pulses, the intrinsic properties of Efimov trimers are readily probed regardless of the sign or magnitude of the scattering length; at which these states occur. Rich interferometric spectra exhibit both low- and high-frequencies independent of the gas temperature. The low-frequency components originate from the coherent superposition of the trimer with the dimer state, consistent with the observations in Ref. [27]. The additional high-frequencies arise from the coherent population of the trimer or dimer states with the ones lying at the “at break-up” threshold. The characteristic damping time of the field generated interference fringes is shown to be twice the lifetime of the Efimov trimers, providing an explanation for the unusually long decay times observed in Ref. [27].

Our paradigm system consists of three  $^{85}\text{Rb}$  atoms of mass  $m$  confined in a spherically symmetric harmonic trap with radial frequency  $\omega_r$ . Following the prescription of Refs. [29–34], we set  $\omega_r = 2\pi \times 350\text{Hz}$  yielding a single atom trap length  $a_r = \sqrt{\hbar/(m\omega_r)}$ , that compares to the interparticle spacing ( $\sim \langle n \rangle^{-1/3}$ ) used in Ref. [22] for a

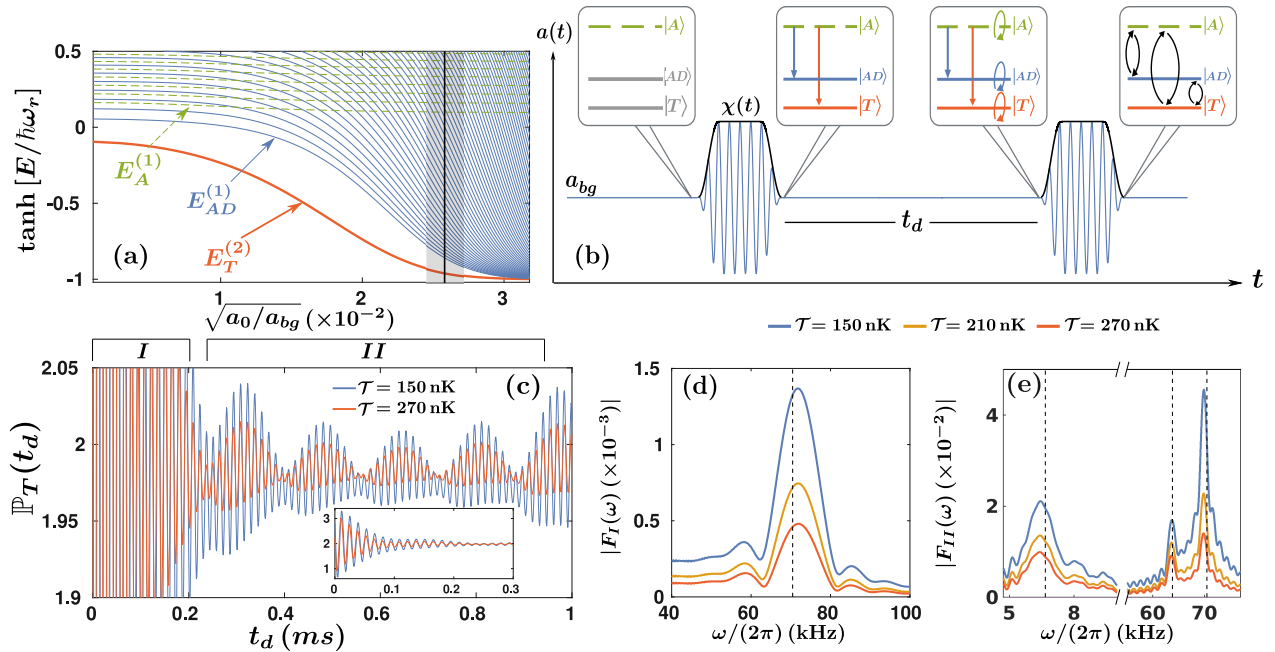


Figure 1. (a) Energy spectrum of three harmonically trapped  $^{85}\text{Rb}$  particles with  $\omega_r/(2\pi) = 350\text{Hz}$ . Efimov trimer (T), atom-dimer (AD) and trap (A) states are depicted. Initially the scattering length is set at  $a_{bg} = 819a_0$  (dashed vertical line), then modulated with amplitude  $a_m$  (gray region). Note  $a_0$  is the Bohr radius. (b) A schematic illustration of the Ramsey-type interferometer: A first pulse with envelope  $\chi(t)$  associates atom-dimers and Efimov states out of trap states (first and second sub-graphs in (b)), the system then evolves freely during the dark time  $t_d$  (third sub-graph in (b)), while a second pulse further admixes the states together with their dynamical phases that were accumulated during  $t_d$  (fourth sub-graph in (b)). (c) The ratio of thermally averaged (RTA) probabilities,  $\mathbb{P}_T(t_d)$  at  $a_{bg} = 819a_0$  and distinct temperatures (see legend). Inset: A zoom out plot of RTA at early  $t_d$ . (d) [(e)] Frequency spectra referring to region I [II] of the RTA quantifying its single [multifrequency] behavior at different values of temperature  $\mathcal{T}$ . The vertical dotted lines correspond to the three-level model (TLM) predictions for  $E_T^{(2)}$ ,  $E_{AD}^{(1)}$  and a trap state (see text).

local peak density  $n_0 = 5 \cdot 10^{12} \text{cm}^{-3}$ . The dynamics and the universal characteristics of the three-body system are addressed by employing contact interactions with a time-dependent  $s$ -wave scattering length, i.e.  $a(t)$ . The three-body Hamiltonian reads:

$$\mathcal{H}(t) = \sum_{i=1}^3 \left( \frac{-\hbar^2 \nabla_i^2}{2m} + \frac{m\omega_r^2}{2} r_i^2 \right) + \sum_{i<j} \frac{4\pi\hbar^2 a(t)}{m} \delta(\mathbf{r}_{ij}) \hat{O}_{ij}, \quad (1)$$

where  $\mathbf{r}_i$  denotes the position of the  $i$ -th atom, and  $\hat{O}_{ij} = \partial_{r_{ij}}(r_{ij} \cdot)$  is the Fermi-Huang regularization operator with  $r_{ij} = |\mathbf{r}_i - \mathbf{r}_j|$ . Fig. 1(b) depicts the dynamical profile of  $a(t)$  determined by the double pulse magnetic field sequence used in Ref. [27], namely

$$a(t) = a_{bg} + a_m \cos(\Omega t) \left[ \chi(t) + \chi(t - t_d - 2t_0 - \tau) \right], \quad (2)$$

$$\text{with } \chi(t) = \begin{cases} \sin^2\left(\frac{\pi t}{2t_0}\right), & 0 \leq t < t_0 \\ 1, & t_0 \leq t < t_0 + \tau \\ \sin^2\left(\frac{\pi(t-\tau)}{2t_0}\right), & t_0 + \tau \leq t \leq 2t_0 + \tau \\ 0, & \text{otherwise} \end{cases} \quad (3)$$

Here,  $a_{bg}$  indicates the background scattering length of the time-independent system, and  $a_m$  is the pulse's amplitude yielding  $\sim 20\%$  change to  $a_{bg}$ .  $\Omega$  is the driving frequency and  $\chi(t)$  denotes the envelope of the pulse where  $t_0$  and  $\tau$  are the ramp on/off times and length of the pulse envelope, respectively. The time between the two pulses is represented by  $t_d$ , i.e. *dark time*, where the system freely evolves.

The spectrum of the field-free Hamiltonian versus the scattering length obtained via the adiabatic hyperspherical approach [4–7, 35] is provided in Fig. 1(a). The corresponding eigenstates,  $|n\rangle$ , fall into three classes: Efimov trimers (T), atom-dimers (AD) and trap (A) states [red, blue and green lines in Fig. 1(a)]. Furthermore, this approach allows to express the time-dependent wave function of Eq. (1) in terms of the field-free eigenstates, i.e.  $|\Psi_{3b}^{(\alpha)}(t)\rangle = \sum_n c_n^{(\alpha)}(t) |n\rangle$  with  $c_n^{(\alpha)}(t)$  being the probability amplitude of the  $n$ -th stationary state. The initial boundary condition is  $c_n^{(\alpha)}(0) = \delta_{n\alpha}$  where the index  $\alpha$  enumerates solely trap states, i.e.  $\alpha \in A$ . Owing to Eq. (2), it suffices to simulate the corresponding time-dependent Schrödinger equation in the center-of-mass of the three-body system [details in Supplemental Material

(SM) [36]].

According to Fig. 1(b), initially the three particles interact with  $a(t=0) = a_{bg} = 819 a_0$  [see black solid line in Fig. 1(a)] residing in a specific trap state. Similar to Ref. [27], at  $a_{bg}$  the system supports two Efimov trimer states, with the second (excited) one at energy  $E_T^{(2)}$  lying close to the first atom-dimer energy in the trap,  $E_{AD}^{(1)}$ , which represents the atom-dimer threshold. At  $t \neq 0$  the first pulse turns on with an envelope  $\chi(t)$  of amplitude  $a_m$  [gray region in Fig. 1 (a)], where  $a(t)$  modulates with angular frequency  $\Omega$  [27, 37]. The latter is equal to the energy difference between the first trap and atom-dimer states, i.e.  $\Omega/2\pi = (E_A^{(1)} - E_{AD}^{(1)})/h = 63.8$  kHz, as in the experiment of Ref. [27]. Furthermore, the pulse's full-width-at-half-maximum is  $27 \mu\text{s}$  providing an energy bandwidth of 6.5 kHz matching the energy difference between the second trimer and first atom-dimer states,  $|E_T^{(2)} - E_{AD}^{(1)}|/h$ . This implies that the first excited trimer  $E_T^{(2)}$  and atom-dimer  $E_{AD}^{(1)}$  states are coherently populated since the pulse cannot energetically resolve them. After the first pulse, the system occupies several  $|n\rangle$  eigenstates which freely evolve during the dark time  $t_d$ , each accumulating a dynamic phase [see Fig. 1(b)]. At  $t = t_d$ , a second pulse, identical to the first one, is applied, admixing different stationary eigenstates and their corresponding dynamical phases. By the end of the second pulse, we extract the probability to occupy the Efimov trimer state as a function  $t_d$ .

In a typical experiment, the three-body dynamics takes place in a thermal gas at temperature  $\mathcal{T}$  [27, 28]. Hence, after the double pulse sequence the probability density to occupy the Efimov trimer needs to be thermally averaged over a Maxwell-Boltzmann ensemble of initial trap states. For our purposes, we introduce a ratio of thermally averaged (RTA) probabilities,  $\mathbb{P}_T(t_d)$ , to populate Efimov trimer states after two pulses (numerator) versus one pulse (denominator),

$$\mathbb{P}_T(t_d) = \frac{\sum_{\alpha \in A} \sum_{j \in T} e^{-\frac{E_A^{(\alpha)}}{k_B \mathcal{T}}} \left| c_j^{(\alpha)}(2\tilde{\tau} + t_d) \right|^2}{\sum_{\alpha \in A} \sum_{j \in T} e^{-\frac{E_A^{(\alpha)}}{k_B \mathcal{T}}} \left| c_j^{(\alpha)}(\tilde{\tau}) \right|^2}, \quad (4a)$$

$$c_j^{(\alpha)}(2\tilde{\tau} + t_d) = \sum_n U_{jn}(2\tilde{\tau} + t_d, \tilde{\tau} + t_d) e^{-iE^{(n)}t_d/h} U_{n\alpha}(\tilde{\tau}, 0), \quad (4b)$$

where  $k_B$  is the Boltzmann constant,  $\tilde{\tau} = 2t_0 + \tau$  is the pulse duration, and  $U_{ij}(\cdot, \cdot)$  represents the three-body evolution operator during a single pulse, expressed in the field-free basis.

Fig. 1(c) depicts  $\mathbb{P}_T(t_d)$  for two characteristic temperatures  $\mathcal{T}$ , where oscillatory fringes are observed that persist after thermal averaging. Namely,  $\mathbb{P}_T(t_d)$  exhibits fast oscillations throughout regions I and II, and additional slow ones only in region II. The contributing frequencies are identified in the Fourier spectra of

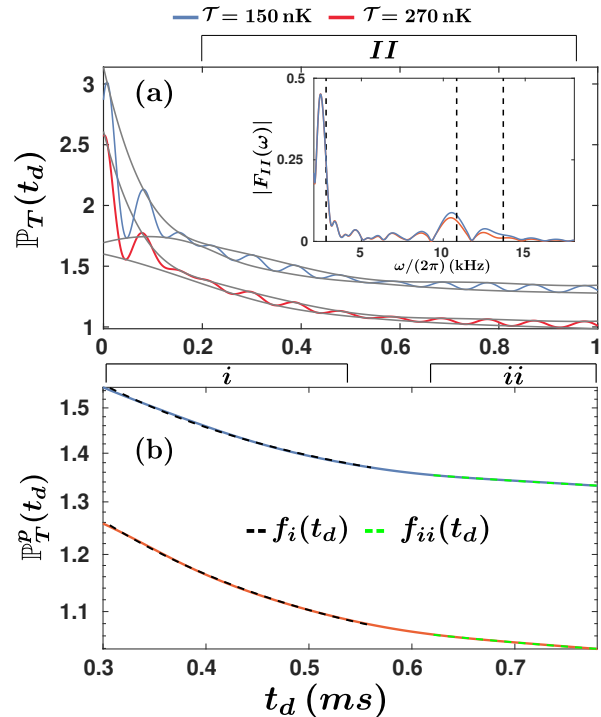


Figure 2. (a)  $\mathbb{P}_T(t_d)$  for different temperatures (see legend), taking into account the decay width,  $\Gamma^{(2)}/h = 748$  Hz of the first excited Efimov state at  $a_{bg} = 2030 a_0$ . The gray solid lines outline the upper and lower peak envelopes. The inset presents the frequency spectrum pertaining to region II,  $|F_{II}(\omega)|$ . (b) The mean peak-to-peak envelope,  $\mathbb{P}_T^p(t_d)$  is fitted with the exponentials  $f_{i/ii}(t_d) = g_{i/ii} e^{-\Gamma_{i/ii}(t_d - t_{i/ii}^0)/h} + w_{i/ii}$  at dark time intervals  $i$  and  $ii$  (black and green dashed lines) with  $g_{i/ii}$ ,  $w_{i/ii}$  representing fitting constants. The characteristic decay time of the oscillations at long  $t_d$  is twice as long as the intrinsic Efimov lifetime  $\hbar/\Gamma^{(2)}$ .

RTA demonstrated in panels (d) and (e) for regions I and II, respectively. In region I, independently of the temperature, a single frequency dominates in  $\mathbb{P}_T(t_d)$  at  $\omega/(2\pi) = 71.8$  kHz [Fig. 1 (d)] corresponding to the energy difference  $|E_A^{(1)} - E_T^{(2)}|/h$ . For longer dark times (region II), three distinct frequencies occur, Fig. 1(e), with the high ones, i.e.  $\omega/(2\pi) = 63.7$  and  $69.9$  kHz, referring to the superposition of the first trap state with the first atom-dimer and excited Efimov states, respectively. The low-frequency peak at  $\omega/(2\pi) = 6.5$  kHz originates from interfering amplitudes between the first atom-dimer and first excited Efimov state pathways. Note that region II ( $\sim 1.2$  kHz) shows better frequency resolution than region I ( $\sim 10$  kHz), which results in small deviations between the highest frequencies in both regions. Due to the finite resolution, a small mismatch also occurs between the difference  $69.9 - 63.7$  kHz and the low frequency peak in region II. Similar low-frequency and temperature independent oscillatory fringes were also experimentally observed for  $^7\text{Li}$  atoms [27, 28]. However, the present



analysis reveals that *high-frequency interferences* are also imprinted in the RTA probability, where the *early dark time fringes* can be experimentally utilized to measure the Efimov binding energy at a given  $a_{bg}$ .

The fact that  $\mathbb{P}_T(t_d)$  features three main frequencies, irrespectively of  $\mathcal{T}$ , is traced back to the incoherent sum of the trimer probability [see Eq. (4a)]. Namely, all contributions involving higher-lying trap states peter out, except for three arising from the ground trap state  $E_A^{(1)}$ , the first atom-dimer  $E_{AD}^{(1)}$  and the first excited Efimov state  $E_T^{(2)}$ . This particular set of eigenstates survives upon the thermal average due to the specifics of the pulse and its envelope. Recall that the driving frequency is in resonance between the  $E_A^{(1)}$  and  $E_{AD}^{(1)}$  stationary eigenstates, whereas the duration of the pulse is short in order to coherently populate only the first atom-dimer and first excited Efimov states. Focusing on this aspect, a three-level model (TLM) Hamiltonian containing  $E_T^{(2)}$ ,  $E_{AD}^{(1)}$  and a single trap state is constructed, and treated within first-order perturbation theory (see details in [36]). The TLM predictions, illustrated as vertical dotted lines in Figs. 1 (d), (e), are found to be in excellent agreement with the full numerical calculations.

In Fig. 1(c)-(e), our analysis neglects the decay of the Efimov trimers and dimer states. However, in thermal gases three-body recombination or relaxation processes are present resulting in finite lifetimes of the trimers and dimers. In the following, we choose  $a_{bg} = 2030 a_0$  that is significantly larger than the van der Waals length scale  $l_{vdW} = 82.5 a_0$  for  $^{85}\text{Rb}$ , yielding negligible finite range effects [26]. Therefore, in this universal regime, the zero-range theory predicts that the lifetime of the first excited Efimov state is  $\hbar/\Gamma^{(2)} = 212 \mu\text{s}$  ( $\Gamma^{(2)}$  denotes the decay width) [22, 38–40]. Also, since the decay of dimers lie within the range 2-9 *ms*, for local peak density  $n_0 = 5 \cdot 10^{12} \text{cm}^{-3}$  [41–43], they can be safely neglected within the considered range,  $t_d \leq 1$  *ms*, rendering the lifetime of Efimov trimers the most relevant decay mechanism. Furthermore, the pulse frequency is  $\Omega/2\pi = 10.8$  *kHz* over a time span  $2t_0 + \tau = 134.7 \mu\text{s}$  ensuring that the Efimov trimers do not decay during the pulse. Under these considerations, it suffices after the first pulse to multiply the amplitude of the  $E_T^{(2)}$  state with the factor  $e^{-\Gamma^{(2)}t_d/(2\hbar)}$ , as was employed in Refs. [44, 45].

The interference fringes of the RTA probability including the effect of the decay at 150 and 270 *nK* are provided in Fig. 2(a). Owing to the large  $a_{bg}$ , the frequencies are in the range of tenths of *kHz* adequately agreeing with the TLM calculations [see dashed lines in the inset Fig. 2 (a)]. Isolating the impact of the Efimov states decay on the RTA probability, Fig. 2 (b) shows the mean peak-to-peak envelopes of  $\mathbb{P}_T(t_d)$ , i.e.  $\mathbb{P}_T^p(t_d)$ . Fitting  $\mathbb{P}_T^p(t_d)$  with  $f_{i/ii}(t_d) = g_{i/ii}e^{-\Gamma_{i/ii}(t_d-t_{i/ii}^0)/\hbar} + w_{i/ii}$  at the

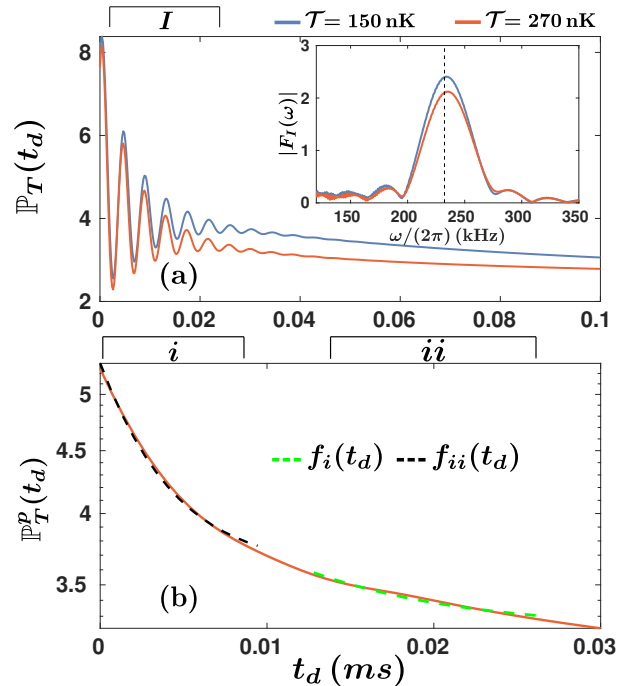


Figure 3. (a)  $\mathbb{P}_T(t_d)$  at  $a_{bg} = -2030 a_0$  and various temperatures (see legend). The driving frequency is resonant with the transition between the ground Efimov and the first trap state, and the decay width of the former  $\Gamma^{(1)}/\hbar = 41$  *kHz*. The inset presents the frequency spectrum of region I,  $|F_T(\omega)|$ . (b) The mean peak-to-peak envelope,  $\mathbb{P}_T^p(t_d)$  at  $\mathcal{T} = 270$  *nK* is fitted with  $f_{i/ii}(t_d) = g_{i/ii}e^{-\Gamma_{i/ii}(t_d-t_{i/ii}^0)/\hbar} + w_{i/ii}$  at the dark time intervals *i* and *ii*. Even at attractive interactions the energy and lifetime of Efimov states can be simultaneously assessed.

dark time intervals *i* and *ii* [see dashed lines in Fig. 2 (b)] reveals two distinct decay widths independent of the temperature. Namely,  $\Gamma_i/\hbar = 749.925(1.47)$  *Hz* close to  $\Gamma^{(2)}/\hbar$ , while at later  $t_d$ ,  $\Gamma_{ii}/\hbar = 375.03(1.63)$  *Hz*, approximately  $\Gamma^{(2)}/(2\hbar)$ . This means that at early dark times  $\mathbb{P}_T(t_d)$  falls off according to the intrinsic lifetime of the  $E_T^{(2)}$  Efimov trimer. In region II, where the interference between the first atom-dimer and the first excited trimer is pronounced, the decay of the RTA probability is *nearly twice* the lifetime of the  $E_T^{(2)}$  state. This effect can in principle explain the unusually long decay times observed in the experiment [27].

Including the trimer's lifetime in the TLM allows to gain insights on the decay of the RTA probability, where  $\mathbb{P}_T(t_d)$  becomes proportional to

$$\mathbb{P}_T(t_d) \propto [\mathbb{B}_{T,A}(t_d) + \mathbb{B}_{T,AD}(t_d)]e^{-\frac{\Gamma^{(2)}t_d}{2\hbar}} + \mathbb{B}_{AD,A}(t_d) + e^{-\frac{\Gamma^{(2)}t_d}{\hbar}}. \quad (5)$$

The terms  $\mathbb{B}_{i,j}(t_d) = A_{i,j}(t_d) \sin[(E_i^{(\sigma)} - E_j^{(1)})t_d/\hbar]$  with  $\sigma = 1 + \delta_{i,T}$  originate from the superposition of states *i*, *j*, and  $A_{i,j}(t_d)$  refer to their amplitudes (see SM [36]). The

first three terms correspond to the three dominant frequencies shown as dashed lines in the inset of Fig. 2 (a). The mixed contributions that involve  $E_T^{(2)}$  with another state, contain only the factor  $e^{-\Gamma^{(2)}t_d/(2\hbar)}$ . Therefore, within region II where the coherent admixture between the  $E_{AD}^{(1)}$  and  $E_T^{(2)}$  states is manifested, the decay time of  $\mathbb{P}_T(t_d)$  is virtually twice as long as the intrinsic Efimov lifetime. The last non-oscillatory term in Eq. (5) involves only the Efimov state and thus decays according to  $e^{-\Gamma^{(2)}t_d/\hbar}$ . The above expression *holds in general* for any atomic species and  $a_{bg} > 0$ , provided that both the first excited Efimov and first atom-dimer are coherently populated.

As a generalization, the RTA probability is demonstrated in Fig. 3 at negative scattering lengths, e.g.  $a_{bg} = -2030 a_0$ , where the atom-dimer pathways are intrinsically absent since no universal dimer exists. The pulse frequency  $\Omega/2\pi = |E_T^{(1)} - E_A^{(1)}|/\hbar = 232.2$  kHz and its duration is  $2t_0 + \tau = 3.7 \mu\text{s}$ . Note that here the pulse resonantly couples the first trap and the Efimov *ground* state, whereas the pulse's length is shorter than the ground Efimov state lifetime  $\hbar/\Gamma^{(1)} = 3.9 \mu\text{s}$  [46]. As expected, the  $\mathbb{P}_T(t_d)$  in Fig. 3(a) oscillates with a single frequency, i.e.  $\omega/(2\pi) = |E_T^{(1)} - E_A^{(1)}|/\hbar = 233.5$  kHz, only in region I and vanishes fast due to the large  $\Gamma^{(1)}$  decay width. Moreover, Fig. 3(b) showcases the mean peak-to-peak amplitude  $\mathbb{P}_T^p(t_d)$  and their fittings at the dark time intervals  $i$  and  $ii$  [see dashed lines in Fig. 3 (b)]. Similar to Fig. 2 (b), we extract two decay widths with their values being  $\Gamma_i/\hbar = 41.35(5.35)$  kHz and  $\Gamma_{ii}/\hbar = 17.56(7.02)$  kHz at  $\mathcal{T} = 270$  nK, which within error bars are close to  $\Gamma^{(1)}/\hbar$  and  $\Gamma^{(1)}/(2\hbar)$ , respectively. These findings are in accordance to the description of Eq. (5), omitting terms associated with atom-dimer transitions.

In summary, the present theory demonstrates that the double magnetic field interferometer has broad applicability. Namely, it permits the simultaneous extraction of the binding energy and the lifetime of Efimov states regardless the sign/magnitude of the scattering length and the temperature of the gas. Going beyond previous studies, our analysis demonstrates that the Ramsey fringes possess long damping times equal to twice the intrinsic lifetime of Efimov trimers. This relation in particular provides also an upper bound to the lifetime of  ${}^7\text{Li}$  Efimov trimers which has remained unknown to date.

Owing to the sensitivity of the Ramsey-type dynamical protocol, the corresponding interferometric signals could provide a stringent test for the Efimov universality [47–52]. Furthermore, recent experiments explore the modifications of three-body recombination processes in mixtures of a bosonic thermal gas with a degenerate fermion gas [24]. Hence, creation of dynamically coherent superpositions between few-body states can reveal the influence of a dense many-body environment on them.

We are grateful to H.R. Sadeghpour and J. P. D’Incao for fruitful discussions. G. B. acknowledges financial support by the State Graduate Funding Program Scholarships (Hmb-NFG). S.I.M. acknowledges support from the NSF through a grant for ITAMP at Harvard University. The Purdue research has been supported in part by the U.S. National Science Foundation, Grant No. PHY-2207977. This work has been supported by the Cluster of Excellence ‘The Hamburg Center for Ultrafast Imaging’ of the Deutsche Forschungsgemeinschaft (DFG)-EXC 1074- project ID 194651731.

\* gbougas@physnet.uni-hamburg.de

- [1] V. Efimov, Phys. Lett. B **33**, 563 (1970).
- [2] V. Efimov, Nucl. Phys. A **210**, 157 (1973).
- [3] V. N. Efimov, Sov. J. Nucl. Phys. **12**, 589 (1971).
- [4] C. H. Greene, P. Giannakeas, and J. Pérez-Ríos, Rev. Mod. Phys. **89**, 035006 (2017).
- [5] E. Nielsen, D. V. Fedorov, A. S. Jensen, and E. Garrido, Phys. Rep. **347**, 373 (2001).
- [6] P. Naidon and S. Endo, Rep. Prog. Phys. **80**, 056001 (2017).
- [7] J. P. D’Incao, J. Phys. B: At. Mol. Opt. Phys. **51**, 043001 (2018).
- [8] T. Kraemer, M. Mark, P. Waldburger, J. G. Danzl, C. Chin, B. Engeser, A. D. Lange, K. Pilch, A. Jaakkola, H.-C. Nägerl, and R. Grimm, Nature **440**, 315 (2006).
- [9] M. Kunitski, S. Zeller, J. Voigtsberger, A. Kalinin, L. P. H. Schmidt, M. Schöffler, A. Czasch, W. Schöllkopf, R. E. Grisenti, T. Jahnke, D. Blume, and R. Dörner, Science **348**, 551 (2015).
- [10] S. Endo, A. M. García-García, and P. Naidon, Phys. Rev. A **93**, 053611 (2016).
- [11] A. Kievsky, M. Gattobigio, L. Girlanda, and M. Viviani, Annu. Rev. Nucl. Part. Sci. **71**, 465 (2021).
- [12] Y. Nishida, Y. Kato, and C. D. Batista, Nature Phys. **9**, 93 (2013).
- [13] M. Gullans, S. Diehl, S. Rittenhouse, B. Ruzic, J. D’Incao, P. Julienne, A. Gorshkov, and J. Taylor, Phys. Rev. Lett. **119**, 233601 (2017).
- [14] B. Tran, M. Rautenberg, M. Gerken, E. Lippi, B. Zhu, J. Ulmanis, M. Drescher, M. Salmhofer, T. Enss, and M. Weidemüller, Braz J Phys **51**, 316 (2021).
- [15] A. Christianen, J. I. Cirac, and R. Schmidt, Phys. Rev. A **105**, 053302 (2022).
- [16] P. Naidon, J. Phys. Soc. Jpn. **87**, 043002 (2018).
- [17] M. Sun and X. Cui, Phys. Rev. A **99**, 060701 (2019).
- [18] S. Musolino, H. Kurkjian, M. Van Regemortel, M. Wouters, S. J. J. M. F. Kokkelmans, and V. E. Colussi, Phys. Rev. Lett. **128**, 020401 (2022).
- [19] V. E. Colussi, S. Musolino, and S. J. J. M. F. Kokkelmans, Phys. Rev. A **98**, 051601 (2018).
- [20] P. Makotyn, C. E. Klauss, D. L. Goldberger, E. A. Cornell, and D. S. Jin, Nature Phys. **10**, 116 (2014).
- [21] C. Eigen, J. A. P. Glidden, R. Lopes, E. A. Cornell, R. P. Smith, and Z. Hadzibabic, Nature **563**, 221 (2018).
- [22] C. E. Klauss, X. Xie, C. Lopez-Abadia, J. P. D’Incao, Z. Hadzibabic, D. S. Jin, and E. A. Cornell, Phys. Rev. Lett. **119**, 143401 (2017).
- [23] R. J. Fletcher, R. Lopes, J. Man, N. Navon, R. P. Smith,

- M. W. Zwierlein, and Z. Hadzibabic, *Science* **355**, 377 (2017).
- [24] X.-Y. Chen, M. Duda, A. Schindewolf, R. Bause, I. Bloch, and X.-Y. Luo, *Phys. Rev. Lett.* **128**, 153401 (2022).
- [25] E. A. Donley, N. R. Claussen, S. T. Thompson, and C. E. Wieman, *Nature* **417**, 529 (2002).
- [26] C. Chin, R. Grimm, P. Julienne, and E. Tiesinga, *Rev. Mod. Phys.* **82**, 1225 (2010).
- [27] Y. Yudkin, R. Elbaz, P. Giannakeas, C. H. Greene, and L. Khaykovich, *Phys. Rev. Lett.* **122**, 200402 (2019).
- [28] Y. Yudkin, R. Elbaz, and L. Khaykovich, *arXiv:2004.02723* (2020).
- [29] K. Góral, T. Köhler, S. A. Gardiner, E. Tiesinga, and P. S. Julienne, *J. Phys. B: At. Mol. Opt. Phys.* **37**, 3457 (2004).
- [30] A. G. Sykes, J. P. Corson, J. P. D’Incao, A. P. Koller, C. H. Greene, A. M. Rey, K. R. A. Hazzard, and J. L. Bohn, *Phys. Rev. A* **89**, 021601 (2014).
- [31] J. P. Corson and J. L. Bohn, *Phys. Rev. A* **91**, 013616 (2015).
- [32] B. Borca, D. Blume, and C. H. Greene, *New J. Phys.* **5**, 111 (2003).
- [33] J. P. D’Incao, J. Wang, and V. Colussi, *Phys. Rev. Lett.* **121**, 023401 (2018).
- [34] J. von Stecher and C. H. Greene, *Phys. Rev. Lett.* **99**, 090402 (2007).
- [35] S. T. Rittenhouse, N. P. Mehta, and C. H. Greene, *Phys. Rev. A* **82**, 022706 (2010).
- [36] See Supplemental Material for more details regarding the solution of the TDSE in the center-of-mass frame, the matrix elements of the interaction potential with the field-free eigenstates, and the RTA probability derived from the TLM in conjunction with perturbation theory.
- [37] P. Giannakeas, L. Khaykovich, J.-M. Rost, and C. H. Greene, *Phys. Rev. Lett.* **123**, 043204 (2019).
- [38] F. Werner and Y. Castin, *Phys. Rev. Lett.* **97**, 150401 (2006).
- [39] D. S. Petrov, C. Salomon, and G. V. Shlyapnikov, *Phys. Rev. Lett.* **93**, 090404 (2004).
- [40] E. Nielsen, H. Suno, and B. D. Esry, *Phys. Rev. A* **66**, 012705 (2002).
- [41] E. Braaten and H.-W. Hammer, *Phys. Rev. A* **70**, 042706 (2004).
- [42] N. R. Claussen, S. J. J. M. F. Kokkelmans, S. T. Thompson, E. A. Donley, E. Hodby, and C. E. Wieman, *Phys. Rev. A* **67**, 060701 (2003).
- [43] T. Köhler, E. Tiesinga, and P. S. Julienne, *Phys. Rev. Lett.* **94**, 020402 (2005).
- [44] V. Colussi, J. Corson, and J. D’Incao, *Phys. Rev. Lett.* **120**, 100401 (2018).
- [45] V. E. Colussi, B. E. van Zwol, J. P. D’Incao, and S. J. J. M. F. Kokkelmans, *Phys. Rev. A* **99**, 043604 (2019).
- [46] E. Braaten and H. W. Hammer, *Phys. Rep.* **428**, 259 (2006).
- [47] J. c. v. Etrych, G. Martirosyan, A. Cao, J. A. P. Glidden, L. H. Dogra, J. M. Hutson, Z. Hadzibabic, and C. Eigen, *Phys. Rev. Res.* **5**, 013174 (2023).
- [48] X. Xie, M. J. Van de Graaff, R. Chapurin, M. D. Frye, J. M. Hutson, J. P. D’Incao, P. S. Julienne, J. Ye, and E. A. Cornell, *Phys. Rev. Lett.* **125**, 243401 (2020).
- [49] M. Berninger, A. Zenesini, B. Huang, W. Harm, H.-C. Nägerl, F. Ferlaino, R. Grimm, P. S. Julienne, and J. M. Hutson, *Phys. Rev. Lett.* **107**, 120401 (2011).
- [50] J. Johansen, B. J. DeSalvo, K. Patel, and C. Chin, *Nature Phys.* **13**, 731 (2017).
- [51] P. Naidon, S. Endo, and M. Ueda, *Phys. Rev. Lett.* **112**, 105301 (2014).
- [52] J. Wang, J. P. D’Incao, B. D. Esry, and C. H. Greene, *Phys. Rev. Lett.* **108**, 263001 (2012).

## Supplemental Material: Interferometry of Efimov states in thermal gases by modulated magnetic fields

G. Bougas,<sup>1</sup> S. I. Mistakidis,<sup>2,3</sup> P. Schmelcher,<sup>1,4</sup> C. H. Greene,<sup>5,6</sup> and P. Giannakeas<sup>7</sup>

<sup>1</sup>Center for Optical Quantum Technologies, Department of Physics,  
University of Hamburg, Luruper Chaussee 149, 22761 Hamburg Germany

<sup>2</sup>ITAMP, Center for Astrophysics | Harvard & Smithsonian, Cambridge, MA 02138 USA

<sup>3</sup>Department of Physics, Harvard University, Cambridge, Massachusetts 02138, USA

<sup>4</sup>The Hamburg Centre for Ultrafast Imaging, University of Hamburg,  
Luruper Chaussee 149, 22761 Hamburg, Germany

<sup>5</sup>Department of Physics and Astronomy, Purdue University, West Lafayette, Indiana 47907, USA

<sup>6</sup>Purdue Quantum Science and Engineering Institute,  
Purdue University, West Lafayette, Indiana 47907, USA

<sup>7</sup>Max-Planck-Institut für Physik komplexer Systeme, Nöthnitzer Str. 38, D-01187 Dresden, Germany

In this supplemental material further information is provided regarding the following aspects of the main text:

- Details on the three-body time-dependent Schrödinger equation using the split-step operator method.
- Evaluation of the matrix elements of the contact interaction potential pertaining to the pulse amplitude scattering length with respect to the field-free eigenstates.
- Derivation of the ratio of the thermally averaged probability within the three-level model in conjunction with first-order time-dependent perturbation theory.

### THE THREE-BODY TIME-DEPENDENT SCHRÖDINGER EQUATION

According to Eq. (1) in the main text, the three-body Hamiltonian in the laboratory frame reads

$$\mathcal{H}(t) = \sum_{i=1}^3 \left( \frac{-\hbar^2 \nabla_i^2}{2m} + \frac{m\omega_r^2}{2} \mathbf{r}_i^2 \right) + \sum_{i<j} \frac{4\pi\hbar^2 a(t)}{m} \delta(\mathbf{r}_{ij}) \hat{O}_{ij}, \quad (\text{S1})$$

where  $a(t) = a_{bg} + a_m f(t)$ ,  $f(t) = \cos(\Omega t)[\chi(t) + \chi(t - t_d - 2t_0 + \tau)]$ , [see Eqs. (2) and (3) in the main text].  $a_{bg}$  is the background scattering length,  $a_m$  is the pulse amplitude, and  $\Omega$  is the driving frequency. For the pulse, we consider  $t_0$  as the ramp on/off time, whereas  $\tau$  is the length of the pulse envelope, and  $t_d$  is the dark time between the two pulses. Finally,  $\omega_r$  denotes the radial frequency of the spherically symmetric trap. The  $\mathbf{r}_i$  indicates the position of the  $i$ -th particle and  $\mathbf{r}_{ij} = \mathbf{r}_i - \mathbf{r}_j$  is the relative distance between the  $(i, j)$  pair of particles.

In order to simplify Eq. (S1) we perform a transformation from the laboratory to the center-of-mass frame. This will allow to eliminate the three degrees of freedom associated to the center-of-mass Hamiltonian. More

specifically,  $\mathcal{H}(t)$  splits into a time-independent part describing the center-of-mass and a time-dependent part for the relative degrees of freedom, i.e.  $\mathcal{H}(t) = \mathcal{H}_{cm} + \mathcal{H}_{rel}(t)$ . Evidently,  $\mathcal{H}_{rel}(t)$  encapsulates the relevant three-body dynamics, which we express in hyperspherical coordinates, [S1–S3] yielding the expression

$$\mathcal{H}_{rel}(t) = -\frac{\hbar^2}{2\mu} \frac{1}{R^{5/2}} \frac{\partial^2}{\partial R^2} (R^{5/2} \cdot) + \frac{15\hbar^2}{8\mu R^2} + \frac{\hbar^2 \Lambda^2}{2\mu R^2} + \frac{1}{2} \mu \omega_r^2 R^2 + V_{bg}(R; \boldsymbol{\varpi}) + V(R; \boldsymbol{\varpi}) f(t). \quad (\text{S2})$$

In this coordinate system,  $R$  describes the overall system size, and the five hyperangles collectively indicated by  $\boldsymbol{\varpi}$  address the relative particle positions.  $V_{bg}(R; \boldsymbol{\varpi})$  and  $V(R; \boldsymbol{\varpi})$  are the contact interaction potentials associated to the background ( $a_{bg}$ ) and amplitude scattering length ( $a_m$ ) respectively, expressed in hyperspherical coordinates.  $\Lambda^2$  is the grand angular momentum operator describing the total angular momentum of the three atoms [S4], and  $\mu$  is the three-body reduced mass.

According to Eq. (S2),  $\mathcal{H}_{rel}(t)$  splits into a field-free Hamiltonian that describes three particles interacting with  $a_{bg}$  scattering length and a time-dependent part which contains the pulse field, i.e.  $\mathcal{H}_{rel}(t) = \mathcal{H}_{bg} + V(R; \boldsymbol{\varpi}) f(t)$ . This particular structure of  $\mathcal{H}_{rel}(t)$  suggests that the time-dependent three-body relative wave function can be conveniently expanded on a basis such that  $\mathcal{H}_{bg}$  is a diagonal matrix. Therefore, in order to obtain the eigenstates  $\{|n\rangle\}$  of  $\mathcal{H}_{bg}$ , we employ the adiabatic hyperspherical representation [S2, S5], where the hyperradius  $R$  is treated as an adiabatic parameter. For completeness reasons, below will provide a brief description on the calculation of  $|n\rangle$  in this formalism. Namely,  $\mathcal{H}_{bg}$  is recasted as follows:

$$\mathcal{H}_{bg} = -\frac{\hbar^2}{2\mu} \frac{1}{R^{5/2}} \frac{\partial^2}{\partial R^2} (R^{5/2}) + \underbrace{\frac{15\hbar^2}{8\mu R^2} + \frac{\hbar^2 \Lambda^2}{2\mu R^2} + \frac{1}{2} \mu \omega_r^2 R^2 + V_{bg}(R; \boldsymbol{\varpi})}_{\mathcal{H}_{ad}(R; \boldsymbol{\varpi})}, \quad (\text{S3})$$

where  $\mathcal{H}_{ad}(R; \boldsymbol{\varpi})$  refers to the adiabatic hyperangular Hamiltonian which parametrically depends on the hyper-radius  $R$ . In addition, the eigenstates  $|n\rangle$  are expressed by the ansatz

$$\langle R, \boldsymbol{\varpi} | n \rangle = R^{-5/2} \sum_{\nu} F_{\nu}^{(n)}(R) \Phi_{\nu}(R; \boldsymbol{\varpi}), \quad (\text{S4})$$

where  $F_{\nu}^{(n)}(R)$   $[\Phi_{\nu}(R; \boldsymbol{\varpi})]$  denotes the hyperradial (hyperangular) component of  $|n\rangle$ . More specifically,  $\Phi_{\nu}(R; \boldsymbol{\varpi})$  are obtained by diagonalizing  $\mathcal{H}_{ad}(R; \boldsymbol{\varpi})$  at fixed hyperradius  $R$  [S1, S3] according to the expression

$$\mathcal{H}_{ad}(R; \boldsymbol{\varpi}) \Phi_{\nu}(R; \boldsymbol{\varpi}) = U_{\nu}(R) \Phi_{\nu}(R; \boldsymbol{\varpi}), \quad (\text{S5})$$

where  $U_{\nu}(R)$  represents the  $\nu$ -th hyperspherical potential curve that depends only on  $R$ . The hyperradial functions  $F_{\nu}^{(n)}(R)$  are determined by acting with  $\mathcal{H}_{bg}$  on  $|n\rangle$  and integrating over all the hyperangles  $\boldsymbol{\varpi}$ . This yields a system of coupled hyperradial equations that include the non-adiabatic couplings [S1, S2]. By diagonalizing the resulting matrix equations we obtain the eigenenergies  $E^{(n)}$  and hyperradial wave functions  $F_{\nu}^{(n)}(R)$  [S1, S2].

According to the above mentioned prescription the eigenstates  $|n\rangle$  are uniquely defined and they fall into three classes: Efimov trimer, atom-dimer and trap states [see the discussion regarding Fig. 1 (a) in the main text]. Expanding the time-dependent three-body wave function in terms of  $|n\rangle$  yields the following relation:

$$|\Psi_{3b}^{(\alpha)}(t)\rangle = \sum_n c_n^{(\alpha)}(t) |n\rangle, \quad (\text{S6})$$

where the time-dependent coefficients initially satisfy  $c_n^{(\alpha)}(t=0) = \delta_{n\alpha}$ , and the  $\alpha$  index refers to an initial trap state.

Plugging Eq. (S6) into the TDSE under the Hamiltonian of Eq. (S2) leads to a matrix differential equation for the time-dependent expansion coefficients,

$$i\hbar \frac{d\mathbf{c}^{(\alpha)}(t)}{dt} = (\mathcal{H}_{bg} + f(t)\mathbf{V}) \cdot \mathbf{c}^{(\alpha)}(t). \quad (\text{S7})$$

Eq. (S7) is solved numerically by utilizing the second-order split-operator method [S6]. Namely, the propagator of the  $\mathbf{c}^{(\alpha)}(t)$  vectors within the time interval  $(t, t+dt)$  reads

$$\mathbf{c}^{(\alpha)}(t+dt) = e^{-i\mathcal{H}_{bg}dt/(2\hbar)} e^{-i\mathbf{V}/\hbar \int_t^{t+dt} dt' f(t')} e^{-i\mathcal{H}_{bg}dt/(2\hbar)} \times \mathbf{c}^{(\alpha)}(t) + \mathcal{O}(dt^3). \quad (\text{S8})$$

### MATRIX ELEMENTS OF THE INTERACTION POTENTIAL WITH THE FIELD-FREE EIGENSTATES

Having at hand the set of field-free eigenstates  $\{|n\rangle\}$ , obtained from the adiabatic hyperspherical formalism, the matrix elements of the interaction potential associated to  $a_m, \mathbf{V}_{n'n}$ , can be evaluated as

$$\mathbf{V}_{n'n} = \sum_{\nu, \nu'} \int dR F_{\nu'}^{(n')*}(R) \mathcal{M}_{\nu'\nu}(R) F_{\nu}^{(n)}(R), \quad (\text{S9})$$

$$\mathcal{M}_{\nu'\nu}(R) = \langle \Phi_{\nu'}(R) | V | \Phi_{\nu}(R) \rangle_{\boldsymbol{\varpi}}, \quad (\text{S10})$$

where  $\langle \cdot \rangle_{\boldsymbol{\varpi}}$  indicates that the integral is performed over the hyperangles.

Eq. (S10) can be recasted in a simple form by exploiting the property  $V(R; \boldsymbol{\varpi}) = -(a_m/a_{bg}) \frac{R}{3} \partial_R V_{bg}(R; \boldsymbol{\varpi})$  between the contact potentials and utilizing the Hellman-Feynman theorem [S7]. Namely, for  $\nu \neq \nu'$  the relation  $\mathcal{M}_{\nu'\nu}(R) = -(a_m/a_{bg}) R \langle \Phi_{\nu'}(R) | \partial_R \Phi_{\nu}(R) \rangle_{\boldsymbol{\varpi}} [U_{\nu'}(R) - U_{\nu}(R)]$  holds. Similar expressions are derived for  $\nu = \nu'$  which can be regrouped as follows

$$\mathcal{M}_{\nu'\nu}(R) = \frac{a_m}{a_{bg}} \frac{\hbar^2}{2\mu R} (-)^{1+\text{sgn}(\nu-\nu')} \sqrt{\partial_R s_{\nu}^2(R) \partial_R s_{\nu'}^2(R)}. \quad (\text{S11})$$

Here,  $s_{\nu}^2(R)$  are related to the potential curves, i.e.  $2\mu R^2/\hbar^2 U_{\nu}(R) = s_{\nu}^2(R) - 1/4$ , and  $\text{sgn}(\cdot)$  denotes the sign function.

### THREE-LEVEL MODEL AND PERTURBATION THEORY

To provide a simplified picture of the full dynamics of the few-body bound states we next construct an effective three-level model [S8]. Within this model, we consider only three field-free eigenstates, the first excited Efimov trimer (T), the first atom-dimer (AD) and an initial trap state  $\alpha$ . The system is initialized in the single trap state and we apply square pulses of the scattering length [see Eqs. (2), (3) in the main text] to trigger the nonequilibrium dynamics of the three-body system.

At the end of the first pulse, the probability amplitude to occupy the  $T$  state,  $\bar{c}_T^{(\alpha)}$ , within first-order time-dependent perturbation theory [S9], reads

$$\bar{c}_T^{(\alpha)}(t_0 + \tau) = \mathbf{V}_{T,\alpha} R_{T,\alpha}(t_0 + \tau), \quad (\text{S12a})$$

$$R_{n,m}(t_0 + \tau) = \frac{-e^{i(\omega_{n,m} + \Omega)(t_0 + \tau)/2} \sin[(\omega_{n,m} + \Omega) \frac{t_0 + \tau}{2}]}{\hbar(\omega_{n,m} + \Omega)} - (\Omega \leftrightarrow -\Omega), \quad (\text{S12b})$$

where  $\omega_{n,m} \equiv (E^{(n)} - E^{(m)})/\hbar$ .

During the dark time  $t_d$ , the probability amplitude of the  $n$ -th state acquires the phase factor

$e^{-iE^{(n)}t_d/\hbar}\bar{c}_n^{(\alpha)}(t_0 + \tau)$ . In particular, the amplitude of the first excited Efimov state is supplemented with the factor  $e^{-\Gamma^{(2)}t_d/(2\hbar)}$ , due to the width  $\Gamma^{(2)}$  of the Efimov state, leading to the decay of the latter during  $t_d$ .

The second pulse mixes all states together, and the probability amplitude to occupy the  $T$  state at the end of this pulse reads,

$$\begin{aligned} \bar{d}_T^{(\alpha)}(2t_0 + 2\tau + t_d) &= \sum_{j=T,AD} \left[ \mathbf{V}_{T,j} R_{T,j}(t_0 + \tau) \right. \\ &\quad \left. \times \bar{c}_j^{(\alpha)}(t_0 + \tau) e^{-iE_j^{(\sigma)}t_d/\hbar - \Gamma^{(2)}t_d/(2\hbar)\delta_{T,j}} \right] \\ &+ \mathbf{V}_{T,\alpha} R_{T,\alpha}(t_0 + \tau) \bar{c}_A^{(\alpha)}(t_0 + \tau) e^{-iE_A^{(\alpha)}t_d/\hbar}, \end{aligned} \quad (\text{S13})$$

where  $\sigma = 1 + \delta_{j,T}$ .

To obtain the ratio of the thermally averaged probability  $\mathbb{P}_T(t_d)$ , we weight the probabilities  $|\bar{d}_T^{(\alpha)}(2t_0 + 2\tau + t_d)|^2$  and  $|\bar{c}_T^{(\alpha)}(t_0 + \tau)|^2$  according to the Maxwell-Boltzmann distribution for the trap states of energy  $E_A^{(\alpha)}$  at temperature  $\mathcal{T}$ ,

$$\mathbb{P}_T(t_d) = \frac{\sum_{\alpha \in A} e^{-\frac{E_A^{(\alpha)}}{k_B \mathcal{T}}} |\bar{d}_T^{(\alpha)}(2t_0 + 2\tau + t_d)|^2}{\sum_{\alpha \in A} e^{-\frac{E_A^{(\alpha)}}{k_B \mathcal{T}}} |\bar{c}_T^{(\alpha)}(t_0 + \tau)|^2}, \quad (\text{S14})$$

$$\mathbb{P}_T(t_d) \propto [\mathbb{B}_{T,A}(t_d) + \mathbb{B}_{T,AD}(t_d)] e^{-\Gamma^{(2)}t_d/(2\hbar)} + \mathbb{B}_{AD,A}(t_d) + e^{-\Gamma^{(2)}t_d/\hbar}, \quad (\text{S15})$$

where the  $\mathbb{B}$ -terms are given by the expressions

$$\mathbb{B}_{T,A}(t_d) = C_1 \Im \left[ e^{-i\Delta\phi_1} \Phi \left( e^{f(k_B \mathcal{T}, t_d, \omega_r)}, -0.5, \frac{E_A^{(1)}}{2\hbar\omega_r} \right) \right] \quad (\text{S16a})$$

$$\mathbb{B}_{T,AD}(t_d) = \sum_{\pm} (-)^{\pm} C_2^{\pm} \sin \left[ (E_T^{(2)} - E_{AD}^{(1)})t_d/\hbar \pm \Omega(t_0 + \tau)/2 \right] \quad (\text{S16b})$$

$$\mathbb{B}_{AD,A}(t_d) = \sum_{\pm} C_3^{\pm} \Re \left[ e^{-i\Delta\phi_2 \pm i\Omega(t_0 + \tau)/2} \Phi \left( e^{f(k_B \mathcal{T}, t_d, \omega_r)}, -0.5, \frac{E_A^{(1)}}{2\hbar\omega_r} \right) \right] \quad (\text{S16c})$$

$$f(k_B \mathcal{T}, t_d, \omega_r) = -\frac{2\hbar\omega_r}{k_B \mathcal{T}} + 2i\omega_r[t_d + 1.5(t_0 + \tau)]. \quad (\text{S16d})$$

$\Phi(a, b, z)$  is the Hurwitz-Lersch zeta function [S10] and the phases  $\Delta\phi_1$  and  $\Delta\phi_2$  are defined as follows,

$$\Delta\phi_1 \equiv \frac{(E_T^{(2)} - E_A^{(1)})t_d}{\hbar} - 3E_A^{(1)} \frac{t_0 + \tau}{2\hbar} \quad (\text{S17})$$

$$\Delta\phi_2 \equiv \frac{(E_{AD}^{(1)} - E_A^{(1)})t_d}{\hbar} - 3E_A^{(1)} \frac{t_0 + \tau}{2\hbar}. \quad (\text{S18})$$

The explicit form of the prefactors  $C_1, C_2^{\pm}, C_3^{\pm}$  is given by,

where  $k_B$  is the Boltzmann constant.

In order to derive an analytical expression for Eq. (S14) additional approximations are used. Namely, the expressions for  $\bar{d}_T^{(\alpha)}(2t_0 + 2\tau + t_d)$  and  $\bar{c}_T^{(\alpha)}(t_0 + \tau)$  can be further simplified by employing the rotating-wave approximation [S9].

Furthermore, the energy of the  $\alpha$ -th trap state is roughly approximated by the non-interacting energy spectrum,  $E_A^{(\alpha)} = E_A^{(1)} + 2\alpha\hbar\omega_r$ , where  $E_A^{(1)}$  is the energy of the first trap state. In addition, we approximate the  $\mathbf{V}_{T,\alpha}$  matrix elements with a quartic root of the energy of the  $\alpha$ -th trap state, a dependence corroborated by a fitting procedure. Under these considerations, Eq. (S14) obtains the same form as Eq. (5) in the main text,

$$C_1 = \frac{\hbar\Omega}{\mathbf{V}_{T,T}} \frac{\Phi^{-1} \left( e^{-2\hbar\omega_r/(k_B \mathcal{T})}, -0.5, \frac{E_A^{(1)}}{2\hbar\omega_r} \right)}{\sin^2[\Omega(t_0 + \tau)/2]}, \quad (\text{S19})$$

$$\begin{aligned} C_2^{\pm} &= \frac{\mathbf{V}_{T,AD}}{\mathbf{V}_{T,T}} \frac{\hbar\Omega}{\sin^2[\Omega(t_0 + \tau)/2]} \\ &\times \frac{\sin[(\omega_{T,AD} \pm \Omega)(t_0 + \tau)/2]}{\hbar(\omega_{T,AD} \pm \Omega)}, \end{aligned} \quad (\text{S20})$$

$$C_3^\pm = (-)^\pm \frac{\mathbf{V}_{T,AD}}{|\mathbf{V}_{T,T}|^2} \frac{\sin[(\omega_{T,AD} \pm \Omega)(t_0 + \tau)/2]}{2\hbar(\omega_{T,AD} \pm \Omega)} \frac{\hbar^2 \Omega^2}{\sin^4[\Omega(t_0 + \tau)/2]} \times \Phi^{-1} \left( e^{-2\hbar\omega_r/(k_B T)}, -0.5, \frac{E_A^{(1)}}{2\hbar\omega_r} \right), \quad (\text{S21})$$

Note that there are revivals of the oscillatory signals  $\mathbb{B}_{T,A}(t_d)$  and  $\mathbb{B}_{AD,A}(t_d)$  at later dark times  $\frac{n\pi}{\omega_r} - 1.5(t_0 + \tau)$ , which are attributed to the trap [S11].

---

[S1] S. T. Rittenhouse, N. P. Mehta, and C. H. Greene, Phys. Rev. A **82**, 022706 (2010).


- [S2] C. H. Greene, P. Giannakeas, and J. Pérez-Ríos, Rev. Mod. Phys. **89**, 035006 (2017).
- [S3] G. Bougas, S. I. Mistakidis, P. Giannakeas, and P. Schmelcher, New J. Phys. **23**, 093022 (2021).
- [S4] J. Avery, *Hyperspherical Harmonics: Applications in Quantum Theory* (Kluwer Academic Publishers, Norwell, MA, 1989).
- [S5] E. Nielsen, D. V. Fedorov, A. S. Jensen, and E. Garrido, Phys. Rep. **347**, 373 (2001).
- [S6] S. Z. Burstein and A. A. Mirin, J. Comput. Phys. **5**, 547 (1970).
- [S7] R. P. Feynman, Phys. Rev. **56**, 340 (1939).
- [S8] P. Lambropoulos, *Fundamentals of quantum optics and quantum information* (Springer, 2007).
- [S9] J. J. Sakurai, *Advanced quantum mechanics* (Pearson Education India, 1967).
- [S10] I. S. Gradshteyn, I. M. Ryzhik, D. Zwillinger, and V. Moll, *Table of integrals, series, and products; 8th ed.* (Academic Press, Amsterdam, 2015).
- [S11] J. P. D’Incao, J. Wang, and V. Colussi, Phys. Rev. Lett. **121**, 023401 (2018).

## 4.2 Dynamics of few particles in a many-body environment

### 4.2.1 Pattern formation of correlated impurities subjected to an impurity-medium interaction pulse



## Pattern formation of correlated impurities subjected to an impurity-medium interaction pulse

G. Bougas,<sup>1</sup> S. I. Mistakidis ,<sup>1</sup> and P. Schmelcher<sup>1,2</sup>

<sup>1</sup>*Center for Optical Quantum Technologies, Department of Physics, University of Hamburg,  
Luruper Chaussee 149, 22761 Hamburg, Germany*

<sup>2</sup>*The Hamburg Centre for Ultrafast Imaging, University of Hamburg, Luruper Chaussee 149, 22761 Hamburg, Germany*



(Received 18 September 2020; accepted 27 January 2021; published 9 February 2021)

We study the correlated dynamics of few interacting bosonic impurities immersed in a one-dimensional harmonically trapped bosonic environment. The mixture is exposed to a time-dependent impurity-medium interaction pulse moving it across the relevant phase-separation boundary. For modulation frequencies smaller than the trapping one, the system successively transits through the miscible and immiscible phases according to the driving of the impurity-medium interactions. For strong modulations, and driving from the miscible to the immiscible regime, a significant fraction of the impurities is expelled to the edges of the bath. They exhibit a strong localization behavior and tend to equilibrate. Following the reverse driving protocol, the impurities perform a breathing motion while featuring a two-body clustering and the bath is split into two incoherent parts. Interestingly, in both driving scenarios, dark-bright solitons are nucleated in the absence of correlations. A localization of the impurities around the trap center for weak impurity-impurity repulsions is revealed, which subsequently disperse into the bath for increasing interactions.

DOI: [10.1103/PhysRevA.103.023313](https://doi.org/10.1103/PhysRevA.103.023313)

### I. INTRODUCTION

Ultracold atoms serve as an excellent platform to monitor the nonequilibrium dynamics of quantum many-body (MB) systems [1], due to the extraordinary experimental tunability of their intrinsic parameters. For instance, the interparticle interactions can be adjusted by means of Feshbach [2,3] or confinement induced resonances [4–6], and it is possible to realize systems of different dimensionality with arbitrarily shaped trapping potentials [7]. Moreover, remarkable progress has been achieved in realizing multicomponent quantum gases [8–12]. A particular focus has been placed on mobile impurities immersed in a MB environment which are consecutively dressed with the collective excitations of the latter thereby forming quasiparticles [13–17]. The stationary properties of impurity atoms in a Bose or a Fermi medium [18–23], such as their effective mass [21,23,24], lifetime [14,17], and induced interactions [25–27], have been extensively studied. Recently the emergent dynamics of these settings has been investigated [28–34], e.g., by dragging impurities in a MB environment [35,36], quenching the impurity-medium interaction strength [33,37], and modifying the external potential experienced by the impurities [38,39]. The aforementioned quench protocols have led to dynamical phenomena such as entropy exchange processes between the impurity and the bath [38], dissipative motion of impurities inside Bose-Einstein condensates (BECs) [31,36], slow relaxation dynamics [35,40], the breakdown of the quasiparticle picture for near resonant impurity-bath interactions [41], and the emergence of temporal orthogonality catastrophe phenomena [33,34].

Independently and in a completely different context, nonequilibrium periodic driving protocols of the involved

scattering lengths or the trapping potential have been utilized in order to generate and stabilize nonlinear excitations such as solitons in one-dimensional (1D) single [42–45], and two-component BECs [46–48], as well as higher-dimensional settings [49,50], and also unravel their collisions in a controllable manner [46,48]. Interestingly, it has been showcased that the periodic modulation of the interatomic interactions leads to parametrically excited resonant modes and pattern formation in BECs, such as Faraday waves [51–57], resembling the response of fluids subjected to a vertical oscillatory force. Moreover, a plethora of additional intriguing phenomena have been exemplified, including the ejection of matter-wave jets in a two-dimensional (2D) cesium BEC [58–60], which carry information regarding the phase of the condensate [60], and the emission of correlated atom jets from a bright soliton [61].

Motivated by the above-described phenomena the periodic driving of the impurity-medium interactions provides an interesting avenue to unravel the dynamical response of both subsystems. Given the advances that have been put forward with time-periodic quench protocols, we expect to identify a variety of dynamical response regimes depending on the characteristics of the driving, where for instance spatial localization of the impurities might occur [62], phase-separation phenomena can be manifested, and specific patterns can be imprinted in the bath, being inherently related to its coherence properties [63]. For instance, it has been shown that shaking the impurities harmonic trap and depending on the driving frequency leads to intriguing collisional aspects with their host such as a distorted collective dipole motion, their effective trapping, or escape from the medium [39]. In this sense, nonlinear structures can be spontaneously generated [23,64], with the time-periodic driving favoring pattern formation in both

components of the system [54]. Additionally the response of few instead of one or two impurities during the dynamics is certainly an interesting aspect. In the present paper a pulse of the impurity-medium interactions is employed in order to study the nonequilibrium correlated dynamics of few interacting bosonic impurities embedded in a MB bosonic gas, driving the mixture across its miscibility-immiscibility phase boundary. We track the correlated dynamics of the bosonic mixture by utilizing a variational approach, namely, the multilayer multiconfiguration time-dependent Hartree method for atomic mixtures (ML-MCTDHX) [65–67].

First, the particle imbalanced system is driven from the miscible to the immiscible phase and two distinct response regimes are identified. For modulation frequencies smaller than the trapping one, the impurities and the bath successively transit in time through the miscible and immiscible phases according to the temporal driving of their mutual interactions. Turning to larger modulation frequencies, dark-bright (DB) soliton pairs emerge in the absence of correlations forming after half an oscillation period an almost steady bound state around the trap center [43,64]. Taking correlations into account, these pairs travel towards the edges of the cloud of their environment, where they remain while oscillating [33,36,37]. Simultaneously they feature a spatial localization tendency and are two-body correlated between each other. Moreover a density dip (hump) around the trap center is formed for the bath (impurities). Two-body correlations develop for bath particles residing between the two distinct spatial regions separated by the central hump. Employing an effective potential picture [33,36], it is found that the impurities reside in a superposition of its lowest-lying eigenstates. In the opposite modulation scenario, where the system is driven to its miscible phase, the two previously mentioned regimes can still be captured. For modulation frequencies larger than the trapping one, oscillating DB solitons emerge within the mean-field (MF) framework [64], which at long evolution times gradually fade away. In sharp contrast within the MB scenario a splitting of the quantum DB soliton pair [68] into two fragments occurs at the initial stages of the dynamics which subsequently fluctuate near the trap center. Accordingly, coherence is almost completely lost for the MB environment. The impurities exhibit a breathing motion, the frequency of which is in good agreement with the predictions of the effective potential, and for longer times they exhibit a two-body clustering [15,25,33].

Moreover, we inspect the role of impurity-impurity interactions for the cases of two and ten impurity atoms following an impurity-bath interaction pulse from the immiscible to the miscible phase and vice versa. For weak repulsions, the impurities majorly reside in both cases around the trap center, occupying predominantly the ground state of their effective potential [39]. Outer density branches become pronounced only when the particle number or the impurity-impurity repulsion increases.

This paper unfolds as follows. Section II introduces our system, and describes the employed driving protocol, the used MB *Ansatz*, and the observables which will be employed to track the dynamics. Subsequently, in Sec. III the nonequilibrium dynamics of the bath-impurity system is explored for a driving from the miscible to the immiscible phase and the reverse scenario is deployed in Sec. IV. Section V elaborates

on the dynamical response of the impurities for different particle numbers and impurity-impurity interactions, in both driving scenarios. Finally, in Sec. VI we summarize our main results and suggest possible future extensions of our paper. In Appendix A we briefly discuss the energy exchange processes taking place between the two components, while in Appendix B, the breathing frequency of the impurities is investigated as a function of the modulation frequency within the MF approach for a driving to the miscible phase.

## II. THEORETICAL FRAMEWORK

### A. Hamiltonian and driving protocol

We consider a particle imbalanced bosonic mixture containing  $N_A = 100$  atoms forming the environment and  $N_B = 10$  impurities. The system is mass balanced, i.e.,  $M_A = M_B = M$ , and it is confined within an elongated harmonic trap of frequency  $\omega_A = \omega_B = \omega$ . Such a mixture can be realized experimentally, by employing two hyperfine states of  $^{87}\text{Rb}$ , e.g., the  $|F = 1, m_F = -1\rangle$  for the environment and  $|F = 2, m_F = 1\rangle$  for the impurities [10]. The MB Hamiltonian of this system reads

$$\begin{aligned} \mathcal{H} = & \sum_{\sigma=A,B} \sum_{i=1}^{N_\sigma} \left[ -\frac{\hbar^2}{2M_\sigma} \frac{\partial^2}{\partial (x_i^\sigma)^2} + \frac{1}{2} M_\sigma \omega_\sigma^2 (x_i^\sigma)^2 \right] \\ & + \sum_{\sigma=A,B} g_{\sigma\sigma} \sum_{i<j} \delta(x_i^\sigma - x_j^\sigma) \\ & + g_{AB}(t) \sum_{i=1}^{N_A} \sum_{j=1}^{N_B} \delta(x_i^A - x_j^B), \end{aligned} \quad (1)$$

where  $g_{\sigma\sigma}$  denotes the two involved intraspecies interaction strengths,  $g_{AB}(t)$  is the impurity-medium coupling, and  $\mathbf{x}^\sigma = (x_1^\sigma, \dots, x_{N_\sigma}^\sigma)$  are the spatial coordinates of the  $\sigma = A, B$  species. The mixture consists of ultracold  $^{87}\text{Rb}$  atoms, and hence its interparticle interactions occur predominantly via  $s$ -wave scattering [2]. All the involved effective coupling strengths can be expressed in terms of the corresponding three-dimensional  $s$ -wave scattering lengths,  $a_{\sigma\sigma'}$ , and the harmonic oscillator length in the transverse direction  $a_\perp = \sqrt{\hbar/\mu\omega_\perp}$  [4,5]. Namely,  $g_{\sigma\sigma'} = \frac{2\hbar^2 a_{\sigma\sigma'}}{\mu a_\perp^2} [1 - |\zeta(1/2)| \frac{a_{\sigma\sigma'}}{a_\perp}]^{-1}$ , where  $\mu = M/2$  is the two-body reduced mass and  $\zeta$  is the Riemann zeta function. It is convenient to recast the MB Hamiltonian of Eq. (1) in terms of  $\hbar\omega_\perp$ , and in what follows we express all the relevant length, time, and coupling strength scales in units of  $\sqrt{\hbar/M\omega_\perp}$ ,  $\omega_\perp^{-1}$ , and  $\sqrt{\hbar^3\omega_\perp/M}$ , respectively. The trapping frequency is  $\omega_A = \omega_B = \omega = 0.1$  and the involved intraspecies coupling constants  $g_{AA} = 1.004$  and  $g_{BB} = 0.9544$  are kept fixed to mimic the experimentally relevant interactions of the above-mentioned  $^{87}\text{Rb}$ , unless it is stated otherwise. To limit the spatial extent of our system, we impose hard-wall boundary conditions at  $x = \pm 40$ , thereby ensuring that their location does not affect the emergent dynamics. It is also worth commenting that experimentally using for instance  $\omega \simeq 2\pi \times 100$  Hz the 1D description holds for  $\omega_\perp \simeq 2\pi \times 5$  kHz whereas temperature effects are negligible for  $k_B T \ll 1.5\mu\text{K}$ .

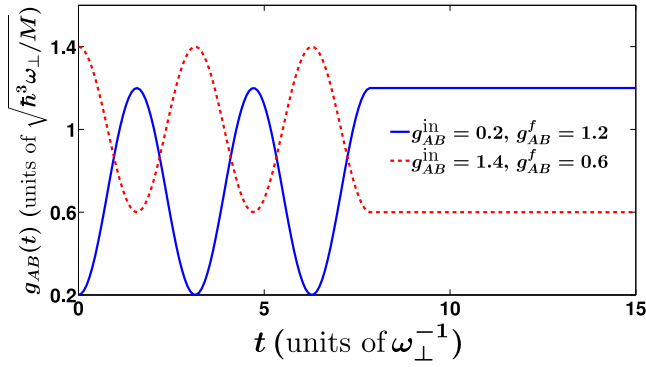


FIG. 1. Time-periodic modulation protocol of the impurity-medium interaction strength  $g_{AB}(t)$  [Eq. (2)] for the two relevant driving scenarios across the phase-separation boundary, namely, starting from  $g_{AB}^{\text{in}} = 0.2$  to  $g_{AB}^{\text{f}} = 1.2$  and from  $g_{AB}^{\text{in}} = 1.4$  to  $g_{AB}^{\text{f}} = 0.6$ .

The employed time-periodic pulse protocol involves solely  $g_{AB}(t)$ , which is sinusoidally modulated in time (for  $t \geq 0$ ), according to

$$g_{AB}(t) = [g_{AB}^{\text{in}} + (g_{AB}^{\text{f}} - g_{AB}^{\text{in}}) \sin^2(\Omega t)] \theta\left(\frac{5\pi}{2\Omega} - t\right) + g_{AB}^{\text{f}} \theta\left(t - \frac{5\pi}{2\Omega}\right), \quad (2)$$

for a time span of  $T = 5\pi/(2\Omega)$ , with an amplitude of  $|g_{AB}^{\text{f}} - g_{AB}^{\text{in}}|$  and frequency  $\Omega$  starting from  $g_{AB}(0) = g_{AB}^{\text{in}}$ . Subsequently  $g_{AB}(t)$  is held constant at  $g_{AB}(t) = g_{AB}^{\text{f}}$ , for  $t > T$ , while  $\theta(x)$  is the Heaviside function. For  $T \rightarrow 0$ , the driving of  $g_{AB}(t)$  occurs only at small time scales, and the protocol effectively reduces to a simple interaction quench, whereas in the limit  $T \rightarrow \infty$ , the bosonic system is subjected to a continuous driving of a small frequency. Furthermore, if  $\Omega > \omega$  the system is strongly driven, whereas for  $\Omega < \omega$ , the pulse lies in the weak driving regime.

The considered interaction pulse is schematically shown in Fig. 1 when crossing the miscible to the immiscible phase and vice versa. In the following, we will consider two interaction pulse scenarios, both of them driving the impurity-medium interaction strength across the phase-separation boundary. For this reason we choose a fixed driving amplitude, namely,  $|g_{AB}^{\text{f}} - g_{AB}^{\text{in}}| = 1$ . Naturally, a larger driving amplitude crossing the phase-separation boundary leads to the same behavior as below, while a smaller amplitude which does not cross the relevant threshold is another interesting case which we do not address in the present paper. Recall that phase separation occurs whenever  $g_{AB} > \sqrt{g_{AA}g_{BB}}$ , a condition that is also adequate in the trapped scenario, and then the wave functions of the two species have minimal spatial overlap [69,70]. In our case, the threshold takes place at  $g_{AB} = 0.9789$ . In Sec. III, the dynamics is explored as the impurity-medium coupling strength is driven according to Eq. (2) to the immiscible phase ( $g_{AB}^{\text{f}} = 1.2$ ) starting from the system's ground state in the miscible regime, characterized by  $g_{AB}^{\text{in}} = 0.2$ . Subsequently, in Sec. IV the reverse driving scenario is investigated, and in particular  $g_{AB}^{\text{in}} = 1.4$  with the system being initialized in

its ground state is modulated to  $g_{AB}^{\text{f}} = 0.6$ , i.e., towards the miscible regime. More precisely, we aim to understand the driven phase-separation process and associated pattern formation in both species depending on the initial phase and the related driving frequency. We shall also briefly comment on the impact of different pulse durations and large modulation frequencies on the driven dynamics. However, a more thorough analysis on this issue, leading possibly to the control of the participating correlations of the emergent patterns, is desirable, and is left for future investigations.

## B. Many-body wave-function Ansatz

In order to simulate the nonequilibrium driven dynamics of the bosonic mixture, as the impurity-medium interaction strength is sinusoidally modulated, the wave function is expanded in a time-dependent and variationally optimized basis, deploying the ML-MCTDHX variational method [65–67]. Importantly, this wave-function Ansatz involves two major stages in order to adequately capture the system's correlations. The full wave function residing in the composite Hilbert space  $\mathcal{H}^{AB} = \mathcal{H}^A \otimes \mathcal{H}^B$ , with  $\mathcal{H}_A$  and  $\mathcal{H}_B$  being the Hilbert spaces of the environment and the impurities, respectively, is expressed in the form of a truncated Schmidt decomposition of rank  $D$  [71]:

$$\Psi_{\text{MB}}(\mathbf{x}^A, \mathbf{x}^B; t) = \sum_{k=1}^D \sqrt{\lambda_k(t)} \Psi_k^A(\mathbf{x}^A; t) \Psi_k^B(\mathbf{x}^B; t). \quad (3)$$

Here  $D \leq \min(\dim(\mathcal{H}^A), \dim(\mathcal{H}^B))$  and  $\lambda_k(t)$  are the well-known time-dependent Schmidt coefficients. The species functions  $\Psi_k^\sigma(\mathbf{x}^\sigma; t)$  serve as an orthonormal basis for the  $\sigma = A, B$  species and signify the  $k$ th mode of entanglement between the two subsystems. If at least two distinct Schmidt coefficients  $\lambda_k(t)$  are nonzero, then the two species are entangled since the MB wave function  $\Psi_{\text{MB}}$  of Eq. (3) cannot be expressed as a direct product of two states [71,72] as for instance in the MF case (see below).

At a next step each species function is accordingly expanded in terms of the permanents of  $d_\sigma$  time-dependent single-particle functions (SPFs)  $\varphi_i$ , as follows:

$$\begin{aligned} \Psi_k^\sigma(\mathbf{x}^\sigma; t) &= \sum_{\substack{n_1, \dots, n_{d_\sigma} \\ \sum n_i = N_\sigma}} C_{k, (n_1, \dots, n_{d_\sigma})}(t) \\ &\times \sum_{i=1}^{N_\sigma!} \mathcal{P}_i \left[ \prod_{j=1}^{n_1} \varphi_1(x_j^\sigma; t) \cdots \prod_{j=1}^{n_{d_\sigma}} \varphi_{d_\sigma}(x_{n_1+\dots+n_{d_\sigma-1}+j}^\sigma; t) \right]. \end{aligned} \quad (4)$$

Here  $C_{k, (n_1, \dots, n_{d_\sigma})}(t)$  denotes the time-dependent expansion coefficients, with  $n_i$  being the population of particles occupying the  $i$ th SPF,  $\varphi_i$ . The species function,  $\Psi_k^\sigma(\mathbf{x}^\sigma; t)$ , is thus expanded over all  $\binom{N_\sigma + d_\sigma - 1}{d_\sigma - 1}$  permanents, subject to the constraint  $\sum_{i=1}^{d_\sigma} n_i = N_\sigma$ .  $\mathcal{P}$  is the permutation operator, exchanging two particles among the SPFs. The above-described variational Ansatz captures the presence of interspecies [Eq. (3)] and intraspecies [Eq. (4)] correlations, thus testifying

the appearance of MB effects that are naturally absent, e.g., in a MF treatment.

Employing the Dirac-Frenkel variational principle [73,74] for the above-described MB variational *Ansatz* [see Eqs. (3) and (4)], the ML-MCTDHX equations of motion are derived [67]. These equations consist of  $D^2$  linear differential equations for  $\lambda_k(t)$ , which are coupled to  $D[\sum_{\sigma} \binom{N_{\sigma}+d_{\sigma}-1}{d_{\sigma}-1}]$  nonlinear integrodifferential equations for the coefficients  $C_{k,(n_1,\dots,n_{d_{\sigma}})}(t)$ , and  $(m_A + m_B)$  nonlinear integrodifferential equations for the SPFs. For further details regarding the derivation of the ML-MCTDHX equations of motion, we refer the reader to Refs. [65–67]. We should note that employing only a single Schmidt coefficient,  $\lambda_1(t) = 1$ , i.e., using  $D = 1$ , and one SPF per species, i.e.,  $d_{\sigma} = 1$ , results in a product MF state among the two species [68,72]. In this sense all particles of a particular species occupy solely a single wave function, namely,

$$\begin{aligned} \Psi_{\text{MF}}(\mathbf{x}^A, \mathbf{x}^B; t) &= \Psi_{\text{MF}}^A(\mathbf{x}^A; t) \Psi_{\text{MF}}^B(\mathbf{x}^B; t) \\ &= \prod_{j=1}^{N_A} \varphi^A(x_j^A; t) \prod_{k=1}^{N_B} \varphi^B(x_k^B; t). \end{aligned} \quad (5)$$

This yields a set of coupled Gross-Pitaevskii equations for the bosonic mixture [72]. Evidently, within this framework all particle correlations are ignored. Therefore, the comparison of the dynamics of the mixture between the above MF state and the variational *Ansatz* as described by Eqs. (3) and (4) sheds light onto the impact of interparticle correlations. Herein we explicate their role in the different driving regions defined with respect to the trap frequency. Note that since the bosonic bath consists of  $N_A = 100$  atoms its initial (ground state) density profile has a Thomas-Fermi (TF) shape, which is well captured by the MF product state. In this way, at least for the used interaction parameters, the dominant effect of correlations is expected to manifest during the dynamics due to their buildup.

### C. Relevant correlation measures

In order to monitor the overall dynamical response of the impurities and their environment as well as to identify their emergent pattern formation, we employ the  $\sigma$ -species one-body reduced density matrix [75]:

$$\begin{aligned} \rho^{(1),\sigma}(x, x'; t) &= N_{\sigma} \int \prod_{j=1}^{N_{\sigma}-1} d\tilde{x}_j^{\sigma} \prod_{k=1}^{N_{\bar{\sigma}}} dx_k^{\bar{\sigma}} \Psi_{\text{MB}}^*(x, \tilde{\mathbf{x}}^{\sigma}, \mathbf{x}^{\bar{\sigma}}; t) \\ &\quad \times \Psi_{\text{MB}}(x', \tilde{\mathbf{x}}^{\sigma}, \mathbf{x}^{\bar{\sigma}}; t), \end{aligned} \quad (6)$$

where  $\sigma = A, B$  and  $\tilde{\mathbf{x}}^{\sigma} = (x_1^{\sigma}, \dots, x_{N_{\sigma}-1}^{\sigma})$ , and  $\sigma \neq \bar{\sigma}$ . Accordingly, the one-body density of the  $\sigma$  species is the diagonal of the one-body reduced density matrix, i.e.,  $\rho^{(1),\sigma}(x; t) = \rho^{(1),\sigma}(x, x' = x; t)$ , and herein it is normalized such that  $\int dx \rho^{(1),\sigma}(x; t) = N_{\sigma}$ . This observable is experimentally accessible via averaging over several single-shot realizations [76,77]. The eigenfunctions of  $\rho^{(1),\sigma}(x, x'; t)$ ,  $\phi_j^{\sigma}(x; t)$ ,  $j = 1, \dots, d_{\sigma}$ , are termed natural orbitals [67], and they are normalized to their corresponding eigenvalues dubbed natural populations  $n_j^{\sigma}$ , i.e.,  $\int dx |\phi_j^{\sigma}(x; t)|^2 = n_j^{\sigma}$ . Recall that in the MF case  $n_1^A = n_1^B = 1$ ,  $n_{j>1}^B = n_{j>1}^A = 0$ , and hence the

population of more than a single natural orbital manifests the existence of intraspecies correlations [72].

To evince the occurrence of intraspecies correlations of the bath and the impurities we invoke the first-order coherence function [72,75,78]:

$$g^{(1),\sigma}(x, x'; t) = \frac{\rho^{(1),\sigma}(x, x'; t)}{\sqrt{\rho^{(1),\sigma}(x; t) \rho^{(1),\sigma}(x'; t)}}. \quad (7)$$

It takes values in the interval  $[0,1]$ , and provides a measure of the proximity of the MB state to a MF product state, for a specific set of spatial coordinates,  $x$  and  $x'$ . Two distinct spatial regions are dubbed fully coherent or perfectly incoherent if  $|g^{(1),\sigma}(x, x'; t)| = 1$  or  $0$ , respectively. When  $0 < g^{(1),\sigma} < 1$ , we can infer the presence of intraspecies correlations [72,78]. Recall that for a MF product state [Eq. (5)]  $g^{(1),\sigma}(x, x'; t) = 1$ ,  $\forall x, x'$  and  $\forall t$ .

To capture the appearance of two-body impurity-impurity and bath correlations in a time-resolved manner, we inspect the second-order noise correlation function,  $g^{(2),\sigma\sigma}(x, x'; t)$  [78–80], defined as

$$\begin{aligned} g^{(2),\sigma\sigma}(x, x'; t) &= \rho^{(2),\sigma\sigma}(x, x'; t) \\ &\quad - \rho^{(1),\sigma}(x; t) \rho^{(1),\sigma}(x'; t). \end{aligned} \quad (8)$$

Here, in second quantization  $\rho^{(2),\sigma\sigma}(x, x'; t) = \langle \Psi_{\text{MB}}(t) | \hat{\Psi}^{\dagger,\sigma}(x') \hat{\Psi}^{\dagger,\sigma}(x) \hat{\Psi}^{\sigma}(x) \hat{\Psi}^{\sigma}(x') | \Psi_{\text{MB}}(t) \rangle$  is the diagonal two-body density matrix, and  $\hat{\Psi}^{\sigma}(x) [\hat{\Psi}^{\dagger,\sigma}(x)]$  is the bosonic operator that annihilates [creates] one particle of species  $\sigma$  at position  $x$ . The diagonal two-body density matrix  $\rho^{(2),\sigma\sigma}(x, x'; t)$  provides the probability of simultaneously finding two particles of species  $\sigma$  at positions  $x$  and  $x'$ , respectively. Accordingly, the noise correlation function quantifies the presence of two-body correlations between two particles of species  $\sigma$  at positions  $x$  and  $x'$ , respectively. The  $\sigma$ -species MB state is termed two-body correlated [anticorrelated], when  $g^{(2),\sigma\sigma}(x, x'; t) > 0$ , [ $g^{(2),\sigma\sigma}(x, x'; t) < 0$ ]. If  $g^{(2),\sigma\sigma}(x, x'; t) = 0$ , then perfect second-order coherence can be inferred. We remark that  $g^{(2),\sigma\sigma}(x, x'; t)$  is experimentally probed via *in situ* density-density fluctuation measurements [81]. Moreover, let us note that a MF product state ensures that  $g^{(2),\sigma\sigma}(x, x'; t) = 0 \forall x, x'$  and  $\forall t$ .

Another important observable, which yields information regarding the spatial extent of each species cloud and thus for its breathing motion, is the position variance [82]:

$$\langle (x^{\sigma})^2 \rangle = \int \prod_{j=1}^{N_{\sigma}} dx_j^{\sigma} \prod_{k=1}^{N_{\bar{\sigma}}} dx_k^{\bar{\sigma}} (x^{\sigma})^2 |\Psi_{\text{MB}}(\mathbf{x}^{\sigma}, \mathbf{x}^{\bar{\sigma}}; t)|^2, \quad (9)$$

where  $\bar{\sigma} \neq \sigma$ . This quantity is experimentally accessible via time-of-flight imaging [83].

### III. DRIVEN DYNAMICS TO THE IMMISCIBLE PHASE

Below, we discuss the nonequilibrium periodically driven dynamics of the bosonic mixture consisting of a bath with  $N_A = 100$  atoms and  $N_B = 10$  impurities. The mixture is initialized in its ground state characterized by  $g_{AA} = 1.004$ ,  $g_{BB} = 0.9544$ , and  $g_{AB}^{\text{in}} = 0.2$ . Then, the impurity-medium interaction strength is sinusoidally modulated with frequency  $\Omega$  for a time span of  $T = \frac{5\pi}{2\Omega}$  according to the protocol

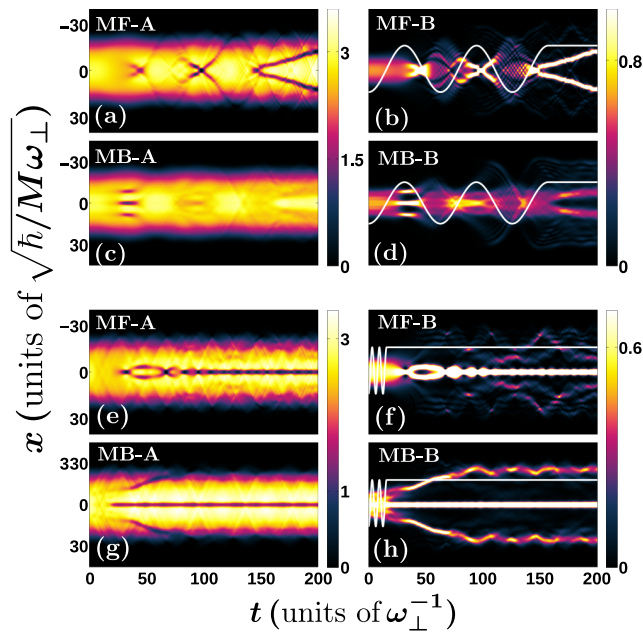


FIG. 2. Spatiotemporal evolution of the one-body density  $\rho^{(1),\sigma}(x;t)$  of the impurities (B) and the bosonic bath (A) considering a time-periodic modulation of the impurity-medium coupling [depicted with the solid line in (b), (d), (f), and (g)] from  $g_{AB}^{\text{in}} = 0.2$  to  $g_{AB}^{\text{f}} = 1.2$  for driving frequencies (a–d)  $\Omega = 0.05$  and (e–h)  $\Omega = 0.5$ . The driven dynamics is showcased in the MF approximation in (a), (b), (e), and (f) and in the MB approach in (c), (d), (g), and (h). The mixture consists of  $N_A = 100$  and  $N_B = 10$  particles while it is initialized in its ground state with  $g_{AA} = 1.004$ ,  $g_{BB} = 0.9544$ , and  $g_{AB}^{\text{in}} = 1.2$ .

introduced in Eq. (2). The modulation drives the mixture into its immiscible phase since the final interaction is  $g_{AB}^{\text{f}} = 1.2$ . To unveil the correlated character of the dynamics we utilize the variational *Ansätze* of Eqs. (3) and (4), and compare with the MF approximation within the ML-MCTDHX framework.

### A. One-body density evolution for a pulse with $\Omega < \omega$

The dynamical response of the bosonic bath and the impurities as captured by the corresponding density evolution is shown in Figs. 2 and 3 for some exemplary modulation frequencies of the impurity-medium pulse protocol of Eq. (2). As we shall argue below the systems' response is significantly altered for modulation frequencies above ( $\Omega > \omega$ ) and below ( $\Omega < \omega$ ) the trapping frequency. First, we focus on the weak pulse case with  $\Omega = 0.05 < \omega$ , presented in Figs. 2(a)–2(d). The dynamics within the MF approach [Figs. 2(a) and 2(b)] can be divided into two temporal regimes: one where  $g_{AB}(t)$  is modulated across the miscibility threshold (which occurs here at  $g_{AB} = 0.9789$ ) for  $t \lesssim 157$  and the other for  $t > 157$ , where  $g_{AB}^{\text{f}} = 1.2$  is constant and the mixture lies in its immiscible phase. In the first regime the impurities and the bath develop simultaneously density humps and dips, respectively, when  $g_{AB}(t) > 1$ , i.e., within the immiscible phase [see, e.g., Fig. 2(b) at  $85 < t < 108$ ]. In contrast, the impurities feature a diffusive behavior when the bosonic mixture lies in its miscible phase [e.g., at  $117 < t < 138$  in Fig. 2(b)]. As long as the

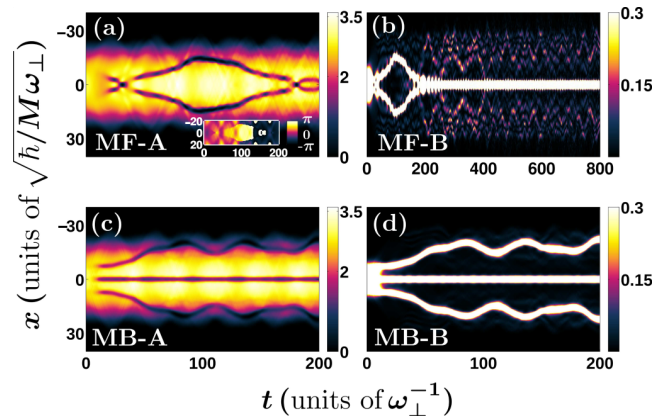


FIG. 3. Temporal evolution of the density  $\rho^{(1),\sigma}(x;t)$  of the bath (A) and the impurities (B) following a modulation of the impurity-medium interaction strength from  $g_{AB}^{\text{in}} = 0.2$  to  $g_{AB}^{\text{f}} = 1.2$  with driving frequency  $\Omega = 1.5$ . The dynamics is compared between (a, b) the MF approach and (c, d) the MB method. The inset of (a) illustrates the phase of the bath in the course of the dynamics. The long-time evolution of the impurities for the same modulation and within the MF approximation is presented in (b).

modulation is terminated, i.e.,  $t > \frac{5\pi}{2\Omega}$ , we observe the emission of two counterpropagating impurity density branches, which travel towards the edges of the bath cloud. At later evolution times  $t > 300$  (not shown here), these branches turn back and collide, forming a density dip at the trap center. Accordingly, since  $g_{AB}^{\text{f}} = 1.2$ , the bath density exhibits dips at the locations of the impurities branches as a result of the impurity-medium phase separation [72] [see Fig. 2(a)].

In the presence of correlations [Figs. 2(c) and 2(d)], the density of both components exhibits the same qualitative behavior as for the MF evolution, but with some differences which are mainly manifested at later evolution times ( $t > 40$ ). Density humps and dips form on top of the density profiles of the impurities and the bath, respectively. These structures differ in their number, position, and amplitude from the ones identified within the MF approach as can be seen by comparing Figs. 2(a) and 2(c) as well as Figs. 2(b) and 2(d), e.g., at  $t \simeq 100$ .

More precisely the aforementioned dips and humps present in the MF scenario [see, e.g., Figs. 2(a) and 2(b) at  $t = 98$ ] resemble the formation of DB solitons in binary mixtures, where the bright solitons are effectively trapped by the dark ones building upon the bath density [84–89]. To further support this argument, we perform a fit on the densities of both species at  $t = 98$  with  $\Omega = 0.05$ , i.e., in the immiscible phase, using the exact single DB soliton wave function in the limit where all interactions among and within the species are equal, i.e., the so-called Manakov limit [89,90]. The corresponding *Ansatz* for the dark soliton reads

$$\Psi_{DS}^{\pm}(x, t) = \cos \varphi \tanh \{d[x \pm x_0(t)]\} + i \sin \varphi, \quad (10)$$

while for the bright component it has the following form:

$$\Psi_{BS}^{\pm}(x, t) = B \operatorname{sech} \{d[x \pm x_0(t)]\} e^{ikx + i\theta(t)}. \quad (11)$$

In these expressions  $\pm x_0(t)$  are the positions of the dark and bright solitons;  $\cos \varphi$  and  $B$  denote the amplitudes of dark

and bright entities, respectively; whereas  $d$  is their common inverse width. Moreover,  $\sin \varphi$  denotes the dark soliton's velocity,  $k = d \tan \varphi$  is the constant wave number of the bright soliton, and  $\theta(t)$  is its phase. For the fitting of these waveforms to our data we employ  $\rho^{(1),A}(x; t) = Q(R^2 - x^2)\theta(R^2 - x^2)|\Psi_{DS}^+(x, t)|^2|\Psi_{DS}^-(x, t)|^2$  for the bosonic medium, where we assume that the dark solitons are formed on top of a TF profile and  $\rho^{(1),B}(x; t) = |\Psi_{BS}^+(x; t)|^2 + |\Psi_{BS}^-(x, t)|^2$  for the impurity subsystem. The agreement between the theoretical *Ansatz* and the MF calculations at  $t = 98$  is adequate, having a standard deviation of the order of 0.038 42 for the dark soliton fit and 0.0847 for the bright component. At later evolution times  $t > 150$  [Figs. 2(a) and 2(b)], the density profiles are again reminiscent of DB solitons, however on top of a distorted TF background.

Interestingly, after the termination of the modulation, the density humps (dips) building on top of the density of the impurities (bath) in the MB case [Figs. 2(c) and 2(d)] are less pronounced than the corresponding ones within the MF approach [Figs. 2(a) and 2(b)]. A similar effect, induced by MB correlations, has been reported in the case of quantum DB solitons imprinted on BECs, where depleted atoms fill the notch of the dark soliton [91–96].

### B. Density evolution for modulations characterized by $\Omega > \omega$

As the modulation frequency becomes larger than the trapping one, the patterns appearing in the one-body density of each component are significantly altered compared to the  $\Omega \leq \omega$  case. Characteristic case examples are showcased in Figs. 2(e)–2(h) and Fig. 3 for  $\Omega = 0.5$  and 1.5, respectively. This difference to the  $\Omega \leq \omega$  scenario is in part due to the fact that the modulation of  $g_{AB}(t)$  occurs at very short timescales and the system cannot adjust to its very fast external perturbation. Indeed, during the modulation, e.g., until  $t \lesssim 15$  in Figs. 2(e)–2(h) and  $t \lesssim 5$  in Fig. 3,  $\rho^{(1),\sigma}(x; t)$  exhibits a weak amplitude expansion compared to  $\rho^{(1),\sigma}(x; 0)$ . The magnitude of this expansion is of the order of 3 and 9% for the bath and the impurities, respectively, for  $\Omega = 1.5$  which is in sharp contrast to the  $\Omega = 0.05$  case [Figs. 2(a)–2(d)].

In particular, within the MF approach and for  $\Omega = 0.5$  [Figs. 2(e) and 2(f)] a central density hump forms on top of  $\rho^{(1),B}$  at the initial stages of the dynamics ( $0 < t < 20$ ) and subsequently ( $t > 34$ ) splits into two density branches, which later on ( $t > 66$ ) merge into a central branch propagating undistorted for long evolution times. During the latter process small density portions are emitted traveling towards the edges of the cloud of the bath and back to the trap center. As a consequence of the underlying phase-separation mechanism,  $\rho^{(1),A}$  displays density dips at the very same positions where the impurities density branches appear [Fig. 2(e)]. Turning to a larger driving frequency [Fig. 3(b),  $\Omega = 1.5$ ], the impurities density exhibits a two hump structure after  $t \gtrsim 12$ , the humps of which subsequently collide around  $t \approx 33$ , and afterwards again split moving towards the edges of the bath. These branches collide again at a much later time instant [ $t \approx 180$  in Figs. 3(b) and 4(c)]. In this case a significant portion of energy is pumped into the system and thus both species gain more energy from the modulation compared to the  $\Omega = 0.5$  scenario, resulting in a larger amount of

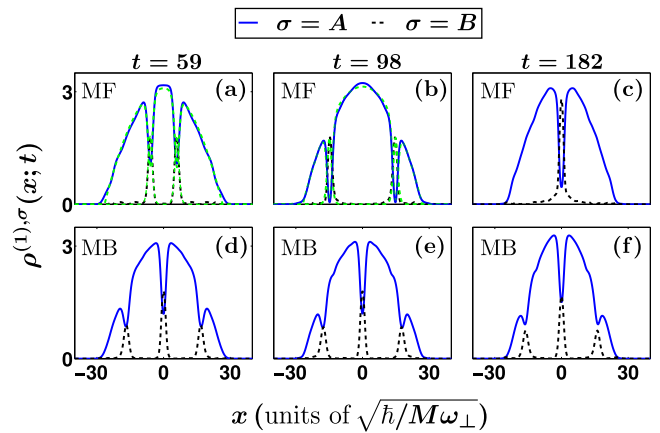


FIG. 4. Profile snapshots of the one-body density of the impurities (B) and the bath (A) following a time-periodic modulation of the impurity-bath coupling with frequency  $\Omega = 1.5$  within the (a–c) MF and (d–f) MB approach (see legend). The dashed green lines in (a) and (b) represent fittings of the DB soliton *Ansatz* [Eqs. (10) and (11)] on  $\rho^{(1),\sigma}(x; t)$ .

excitations (see also Appendix A). As a consequence, for instance, the impurities have enough energy to reach the edges of the bath before colliding again at the trap center. It is also worth mentioning that in the long-time dynamics [see Fig. 3(b)] the impurities density branches merge after  $t \approx 180$  into a single central hump, which stays unperturbed throughout evolution. This hump comes along with small fluctuating emitted density branches, which diffuse within the background density of the medium [hardly visible in Fig. 3(b)]. We note that the aforementioned merger of the impurities density branches occurs at earlier times accompanied by a larger amount of excitations in the BEC background as the pulse duration increases since more energy is pumped into the system.

The above-described density dips (peaks) displayed in the bath cloud (impurities) [see Figs. 3(a) and 3(b)] are once more reminiscent of the dynamical formation of DB solitons. Indeed, the DB soliton waveform [Eqs. (10) and (11)] serves as a good candidate to the density profiles of both components [see the dashed green lines in Figs. 4(a) and 4(b)] with the corresponding fit exhibiting a standard deviation of the order of 0.07. Moreover, the spatiotemporal evolution of the phase of the MF bath wave function displays jumps being multiples of  $\pi$ , as can be seen in the inset of Fig. 3(a) at  $t > 100$ , which is a characteristic feature of dark solitons.

The inclusion of correlations leads to a drastically different time evolution of both the impurities and the medium than in the MF approach [see Figs. 2(g), 2(h), 3(c), and 3(d) for  $t > 5$ ]. Indeed the impurities density branches formed after the modulation move to the edges of the bath cloud, where they perform a weak amplitude oscillatory motion having an equilibration tendency. We remark that an analogous response of the impurities has been demonstrated in the impurity-medium interaction quench dynamics of two spin-polarized fermions inside a Bose gas [64]. Also similar dynamical phase-separation phenomena have been shown to occur for strong impurity-medium interactions signifying temporal orthogonality catastrophe phenomena of the Bose

polaron [33,36,37]. Moreover, there is a central density hump (dip) in the density of the impurities (bath). The major difference between  $\Omega = 0.5$  and 1.5 within the MB framework is that the density branches in the former case [Fig. 2(h)] reach the edges of the bosonic medium, their amplitude decreases, and they undergo smaller amplitude oscillations than the ones for  $\Omega = 1.5$  [Fig. 3(d)]. Inspecting the instantaneous MB density profiles  $\rho^{(1),\sigma}(x;t)$  [Figs. 4(d)–4(f)] when  $\Omega = 1.5$ , we observe that the side humps (dips) for the impurities (bath) appearing around  $x \simeq 16$  have a smaller amplitude and are displaced with respect to the ones emerging within the MF approach. Another difference occurring between the MF and the MB evolution is the formation of a central density hump (dip) for the impurities (bath), in addition to the side humps and dips when correlations are present, as can be seen in Figs. 4(d)–4(f). We should note that as we increase the modulation frequency  $\Omega$  and thus tend to the abrupt quench scenario [Eq. (2)], a similar dynamics to the one illustrated in Figs. 3(c) and 3(d) for  $\Omega = 1.5$  takes place for both components. The most notable difference is that the separation of the outer  $\rho^{(1),B}(x;t)$  branches becomes slightly larger.

An intuitive understanding of the response of the impurities is provided by constructing an effective potential picture [33,97]. The latter is derived from the impurities external trapping potential, and the one-body density of their bosonic medium [33,97,98], namely,

$$V_{\text{eff}}(x;t) = \frac{1}{2}M\omega^2x^2 + g_{AB}(t)\rho^{(1),A}(x;t). \quad (12)$$

Evidently  $V_{\text{eff}}(x;t)$  is a time-dependent single-particle potential, which is in general different from the external harmonic trap due to its second contribution accounting for the bath and the impurity-medium interactions. Before proceeding we should clarify that  $V_{\text{eff}}(x;t)$  is not able to account for impurity-medium correlations and as a consequence it does not provide insights into, e.g., two-body mechanisms such as the emergent impurity-impurity induced correlations as has been argued in Refs. [33,37]. Of course, all these processes are naturally included within our MB treatment performed within the ML-MCTDHX approach.

For instance,  $V_{\text{eff}}(x;t)$  for  $\Omega = 1.5$  features a deep central well, present throughout the evolution, and additional shallower side wells the depths and positions of which change with time [Figs. 5(a) and 5(c)]. These potential wells are a manifestation of the density dips of the bath displayed for instance in Fig. 3(c). Even though the effective potential yields a single-particle picture, one can readily see that  $\rho^{(1),B}(x;t = 182)$  in Fig. 3(d) mainly resides in a superposition of the ground and the first two excited states of  $V_{\text{eff}}(x;t)$ , with corresponding participation weights 41, 23.6, and 23.6%, respectively. There are also additional density modulations [hardly visible in Fig. 3(d)], which suggest the occupation of higher-lying excited states as well, with a small nonvanishing population up to the 18th excited state. At other time instants [Fig. 5(c)], the depth of the central well of  $V_{\text{eff}}(x;t)$  changes slightly with time and the outer wells are displaced, accounting thus for the oscillations of the outer density branches shown in Fig. 3(d). Apart from the aforementioned undulations during the time evolution, the effective potential changes also with respect to the driving frequency  $\Omega$ , since the density profile of the medium is accordingly

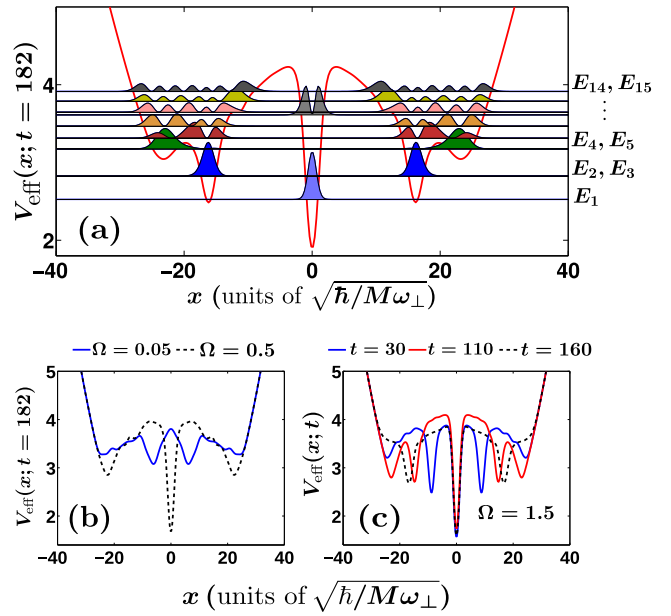


FIG. 5. (a) Instantaneous effective potential at  $t = 182$  for a modulation frequency  $\Omega = 1.5$ . On top of  $V_{\text{eff}}(x;t)$  its single-particle eigenstates are depicted together with their energies. (b) The effective potential for other driving frequencies (see legends) at  $t = 182$ . (c)  $V_{\text{eff}}(x;t)$  at distinct time instants for  $\Omega = 1.5$ . The effective potential is measured in units of  $\hbar\omega_{\perp}$ .

modified. For instance, the central potential dip is absent in the case of  $\Omega = 0.05$  [Fig. 5(b)] and the effective potential displays a double-well structure accounting for the impurities density peaks [Fig. 2(d)]. For  $\Omega = 0.5$ , the central density dip of  $\rho^{(1),A}$  forms, which mainly attracts the impurity atoms since its depth is larger than the one of the outer wells.

### C. Correlation dynamics and impurities antibunching

Having explicated the imprint of correlations in the density evolution of both the impurities and the bath we subsequently inspect the first- and second-order correlation functions as introduced in Eqs. (7) and (8), respectively. In this way, we will be able to demonstrate from  $g^{(1),\sigma}$  the possibly emergent coherence losses of each species when  $g^{(1),\sigma} < 1$ . Along the same lines, utilizing  $g^{(2),\sigma\sigma}$  the two-body correlation properties of the impurities and the bath can be identified for  $g^{(2),\sigma\sigma} \neq 0$ . Initially, the first-order coherence  $g^{(1),\sigma}(x, x'; t)$  is examined [Eq. (7)], from which one can infer the proximity of a MB to a MF product state for a specific set of spatial coordinates  $x$  and  $x'$  at time  $t$ . Instantaneous profile snapshots of  $g^{(1),A}(x, x'; t)$  and  $g^{(1),B}(x, x'; t)$  are shown in Fig. 6 exemplarily for  $\Omega = 0.5$ .

At early evolution times ( $t \leq 40$ ), where the two impurity density branches travel to the edges of the bath cloud [Figs. 2(g) and 2(h)], the BEC background exhibits relatively small coherence losses; see the off-diagonal of  $g^{(1),A}$  [Fig. 6(a)]. Indeed, it appears that the two separate spatial intervals of the medium enclosed by the central and the outer density dips [see Fig. 2(g)], namely,  $D^+ = (0, +10.56)$  and  $D^- = (-10.56, 0)$ , are slightly off-coherent between each other as well as with the regions from the outer

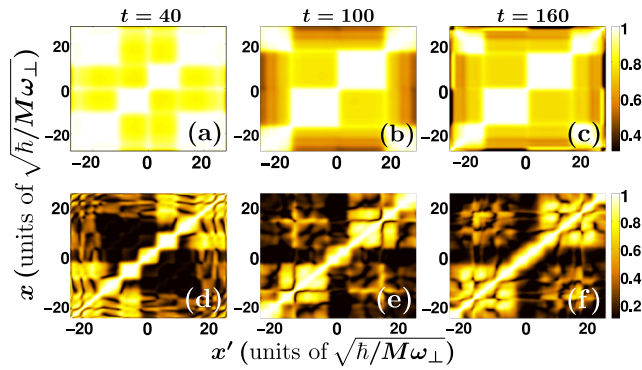


FIG. 6. Snapshots of the first-order coherence function of the (a–c) bath  $g^{(1),A}$  and the (d–f) impurities  $g^{(1),B}$  for a driving frequency  $\Omega = 0.5$ . Other system parameters are the same as in Figs. 2(g) and 2(h).

density dips until the edges of the bath cloud; see, e.g.,  $g^{(1),A}(6.02, -6.02; t = 40) \simeq 0.8$  [Fig. 6(a)]. At later times [see for instance Figs. 6(b) and 6(c)], the spatial domains separated by the central dip at  $x = 0$ , namely,  $D^+ = (0, 19)$  and  $D^- = (-19, 0)$ , become less coherent with respect to one another and, e.g.,  $g^{(1),A}(12.17, -12.17; t = 160) \simeq 0.75$ . On the other hand, the two density branches of the impurities [Fig. 2(h)] are entirely noncoherent throughout the time evolution [see in particular Figs. 6(d)–6(f) where  $g^B(x, x' \neq x; t > 40)$  is vanishing]. Therefore, the impurities develop Mott-like correlations, suggesting their spatial localization tendency in the two separate density branches [72,99]. When the impurity density branches lie at the edges of their background for  $t \gtrsim 62$  and are weakly oscillating, a small amount of coherence is restored, e.g.,  $g^{(1),B}(12.17, -12.17; t = 100) \simeq 0.4$  between the emitted faint density peaks located in the spatial regions  $x \in [9, 13]$ ,  $x' \in [-13, -9]$  [Fig. 2(h)]. We remark that a similar coherence behavior occurs also for other modulation frequencies larger than the trapping one. For  $\Omega < \omega$  the medium remains almost perfectly coherent throughout the time evolution and the impurities are localized either in  $x > 0$  or  $x < 0$ .

Next, we discuss the two-body correlation characteristics of the impurities and their BEC background, by monitoring  $g^{(2),AA}$  and  $g^{(2),BB}$ , respectively (Fig. 7), for  $\Omega = 0.5$ . Focusing on the BEC medium, we observe that for  $t \leq 100$  where the impurities density humps travel to the edges of the medium cloud [Figs. 7(a) and 7(b)], two particles of the environment tend to avoid each other within the two spatial intervals enclosed by the central and outer density dips of  $\rho^{(1),A}(x; t)$ , i.e.,  $D_+ \simeq (0, 20)$  and  $D_- \simeq (-20, 0)$  [Fig. 2(g)], since  $g^{(2),AA}(x, x' = x; t \leq 100) < 0$ . However, there is an increased probability of finding one of the particles in one of those intervals, e.g., in  $D_+$ , and the other particle being symmetrically placed with respect to the trap center, e.g., in  $D_-$ . This behavior persists at later evolution times, as can be seen in Figs. 7(b) and 7(c), where two-body correlations build up for particles residing in opposite spatial regions with respect to the trap center; see the antidiagonal of  $g^{(2),AA}(x; t)$ . Moreover, a two-body anticorrelation tendency occurs between  $D_+$  and  $D_-$  since  $g^{(2),AA}(x, x' \neq x; t) < 0$ .

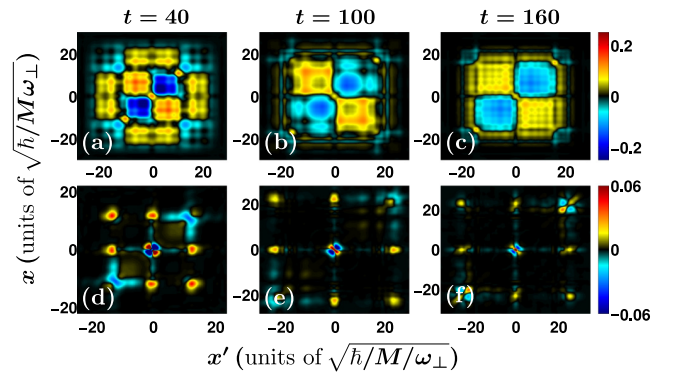


FIG. 7. Instantaneous profiles of the second-order noise correlation of (a–c) the bath particles  $g^{(2),AA}(x, x'; t)$  and (d–f) the impurities  $g^{(2),BB}(x, x'; t)$ . In all cases the modulation frequency is  $\Omega = 0.5$ , while other system parameters are the same as in Figs. 2(g) and 2(h).

Turning to the impurities, anticorrelations appear for particles occupying the same position for  $t \leq 100$  where the impurities move to the edges of the background cloud [Figs. 7(d) and 7(e)]. However, two particles residing in different density branches [Fig. 7(d)] display a correlated character, e.g.,  $g^{(2),BB}(-10.84, -10.84; 40) \simeq -0.0345$  and  $g^{(2),BB}(-10.84, 10.84; 40) \simeq 0.012$ . For longer evolution times [Fig. 7(f)] two-body correlations build among particles occupying the three distinct density branches; see for instance  $g^{(2),BB}(22.61, 22.61; t = 160) \simeq 0.01$  [72,82,100]. In contrast, two particles are anticorrelated when they both lie in the same density hump, e.g., the one close to the trap center where  $g^{(2),BB}(-0.94, -0.94; 160) \simeq -0.05$ .

#### IV. DRIVEN DYNAMICS TO THE MISCIBLE PHASE

We proceed by analyzing the reverse pulse driving scenario, namely, the one where the mixture is driven from the immiscible to the miscible phase, according to the time-dependent protocol of Eq. (2). More specifically, the mixture is initially prepared in its ground state, characterized by  $g_{AA} = 1.004$ ,  $g_{BB} = 0.9544$ , and  $g_{AB}^{\text{in}} = 1.4$ . The final impurity-medium interaction strength is  $g_{AB}^f = 0.6$ . As before, the nonequilibrium dynamics is investigated, while it is compared and contrasted between the MF and the MB framework.

##### A. Dynamical response for $\Omega < \omega$

As explicated in Sec. III, monitoring the one-body density evolution of the participating components, it is possible to distinguish two driving related response regimes, namely,  $\Omega < \omega$  and  $\Omega > \omega$  (see Figs. 8 and 9, respectively). First, let us focus on the case of  $\Omega = 0.05 < \omega$  [Figs. 8(a) and 8(b)], and inspect the dynamical behavior of the bath and the impurities within the MF framework. As it can be readily seen in Fig. 8(b),  $\rho^{(1),B}(x; t)$  exhibits density humps filling the dips of the bosonic medium, within the time intervals where  $g_{AB} > 1$ , and diffusive patterns as the system is driven to its miscible phase [39], i.e.,  $g_{AB} < 1$ . To facilitate this observation, a white solid line indicating the modulation of the impurity-medium coupling is depicted in Fig. 8(b). The inclusion of correlations results in a similar dynamical response of the mixture



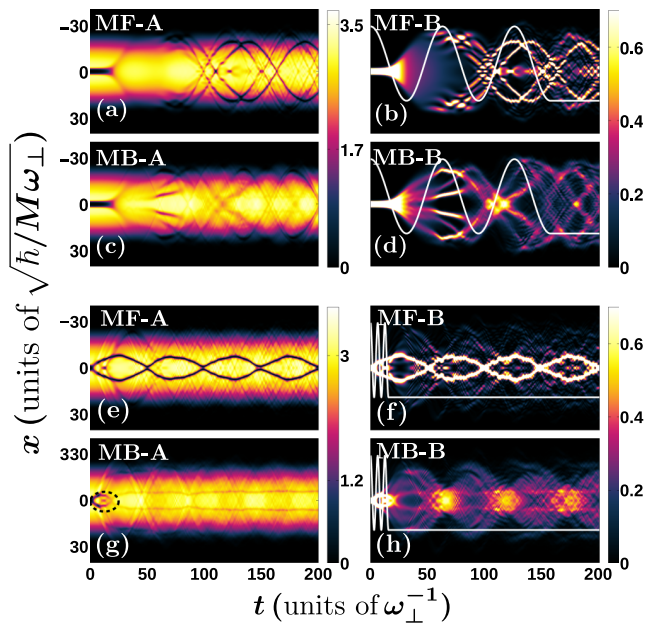


FIG. 8. Time evolution of the one-body density of (a, c, e, g) the bosonic bath and (b, d, f, h) the impurities following a modulation of the impurity-medium coupling from  $g_{AB}^{\text{in}} = 1.4$  to  $g_{AB}^{\text{f}} = 0.6$ . The modulation is exemplarily depicted with the white solid line in (b), (d), (f), and (h). The dynamics is tracked for two driving frequencies (a–d)  $\Omega = 0.05$  and (e–h)  $\Omega = 0.5$  within the (a, b, e, f) MF approach and (c, d, g, h) the MB method. The mixture is composed of  $N_A = 100$  bath and  $N_B = 10$  impurity atoms, characterized initially (ground state) by  $g_{AA} = 1.004$ ,  $g_{BB} = 0.9544$ , and  $g_{AB}^{\text{in}} = 1.4$ .

at early evolution times ( $t < 40$ ) but subsequently significant alterations take place [Figs. 8(c) and 8(d)].

Concretely, in the MB approach [Figs. 8(c) and 8(d)] a smaller number of generated density dips and humps in

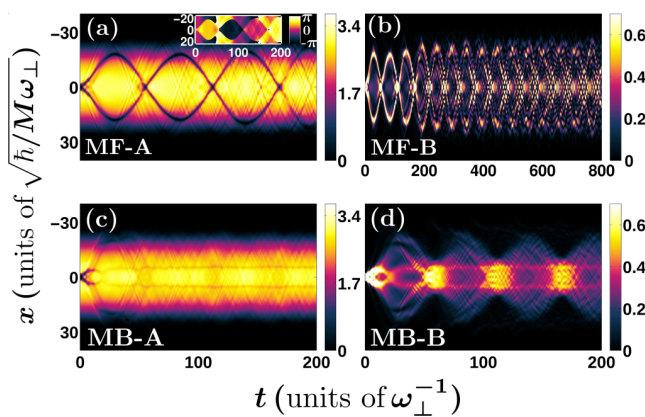


FIG. 9. Spatiotemporal evolution of the one-body density of (a, c) the bosonic environment and (b, d) the impurities applying a modulation of the impurity-medium interaction from  $g_{AB}^{\text{in}} = 1.4$  to  $g_{AB}^{\text{f}} = 0.6$  with frequency  $\Omega = 1$ . The dynamics is displayed both within the (a, b) MF and (c, d) MB approaches. The inset of (a) showcases the phase of the bath throughout the time evolution. The long-time evolution of the impurities within the MF approach is presented in (b).

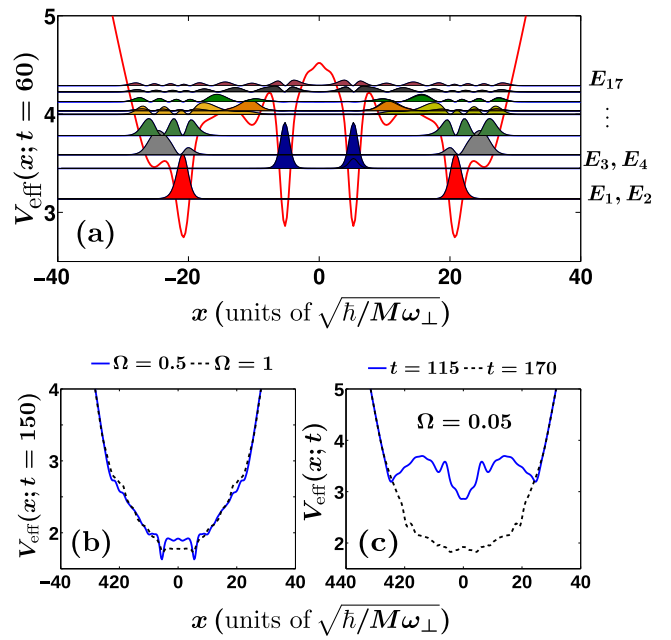


FIG. 10. (a) Instantaneous effective potential at  $t = 60$  and modulation frequency  $\Omega = 0.05$ . On top of  $V_{\text{eff}}(x; t)$ , its eigenstates are displayed together with their energy. (b) The effective potential for other driving frequencies (see legends) at  $t = 150$ . (c)  $V_{\text{eff}}(x; t)$  at other time instants for  $\Omega = 0.05$ . The effective potential is measured in units of  $\hbar\omega_{\perp}$ .

$\rho^{(1),A}(x; t)$  and  $\rho^{(1),B}(x; t)$ , respectively, is observed compared to the MF case [72,100,101]; see, e.g.,  $\rho^{(1),B}(x; t)$  at  $t \simeq 97$ . Later on, the diffusive character of  $\rho^{(1),B}(x; t)$  is more pronounced than within the MF treatment; compare for instance Figs. 8(b) and 8(d) around  $t \simeq 157$ . When correlations are present, the impurities are effectively trapped at the density dips developed in the bosonic bath [Fig. 8(d)]. The medium thus provides an effective potential experienced by the impurities, and their density profile can be understood by resorting to the potential defined in Eq. (12). As shown in Fig. 10(a), the underlying  $V_{\text{eff}}(x; t = 60)$  features four deep wells, caused by the density profile of the medium. Inspecting the density profile of the impurities [Fig. 8(d)] and the form of the effective potential [Fig. 10(a)], one can infer that  $\rho^{(1),B}(x; t = 60)$  mainly resides in a superposition of the four lowest-lying eigenstates,  $E_1, \dots, E_4$  of  $V_{\text{eff}}(x; t)$  [33]. At later time instants  $\rho^{(1),B}(x; t = 150)$  presents a diffusive behavior throughout the environment, with a small portion of its density lying outside of the cloud of the bath [Fig. 8(d)]. The density of the latter resembles a distorted TF profile, in sharp contrast to the MF case [Fig. 8(a)], where  $\rho^{(1),A}$  develops a three-dip structure which suggests a significantly more excited background than the MB case. The distorted TF profile then provides an effective potential for the impurities, which resembles a harmonic trap, as can be seen in Fig. 10(c) at later times  $t = 170$ . The absence of any potential wells is a signature of the miscible character of the impurity-medium interactions. In that case a superposition of many excited states is needed in order to properly account for the density profiles similar to those displayed in Fig. 8(d) [37,97].

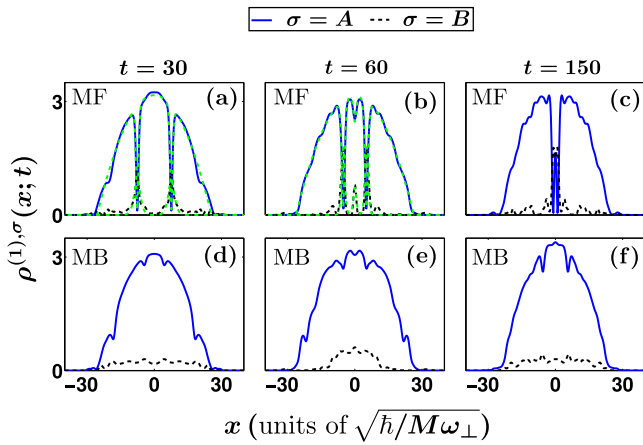


FIG. 11. Profile snapshots of the one-body density of the bath (A) and the impurities (B) following a modulation of the impurity-medium coupling with  $\Omega = 0.5$  within the (a–c) MF and (d–f) MB frameworks. The dashed green lines in (a) and (b) present DB soliton fits on the density of both components.

### B. Dynamical response for $\Omega > \omega$

Turning to larger modulation frequencies, the dynamical response of both components is substantially different from the previous case where  $\Omega < \omega$ . More precisely, the spontaneously generated patterns emerging in the course of the MF evolution clearly resemble DB solitons, as is presented in Figs. 8(e) and 8(f) for  $\Omega = 0.5$ . Recall that similar structures have been shown to be nucleated in the reverse driving scenario for strong driving frequencies, however they were shown to be not as robust as here and to form a bound pair (Sec. III). Moreover, the oscillation frequency of these structures is much larger than the one associated to the entities in the reverse driving scenario [see Figs. 3(a) and 3(b)], and importantly it crucially depends on  $\Omega$ , as can be easily deduced by inspecting Figs. 8(e) and 8(f) ( $\Omega = 0.5$ ) and Figs. 9(a) and 9(b) ( $\Omega = 1$ ). Also, their oscillation amplitude changes with respect to  $\Omega$  and in particular it increases from  $\Omega = 0.5$  to 1 by approximately 59%. Another difference that occurs with the respective structure formation within the MF approach for  $\Omega > \omega$  compared to the reverse modulation discussed in Sec. III [Figs. 3(a) and 3(b)] is the existence of a larger amount of excitations, which consequently alter the shape of the pronounced oscillating humps during the time evolution [Fig. 9(b)]. For sufficiently long evolution times ( $t > 300$ ), these oscillating density humps increase in amplitude and gradually fade away, as a result of the prominent interference processes caused by the miscible nature of the bosonic mixture, as can be seen in Fig. 9(b).

To further support our argument regarding the character of these structures, we employ the known DB soliton waveforms [Eqs. (10) and (11)], denoted by dashed green lines in Figs. 11(a) and 11(b). As already mentioned, however, there are excitations on top of  $\rho^{(1),B}(x; t)$ , which render the fitting of the bright soliton waveform not so accurate. Regarding the bath, the spatiotemporal evolution of its phase [inset of Fig. 9(a)] displays phase jumps at the positions of the density dips. These jumps, being multiples or less than  $\pi$ , are of

course indicative of the presence of moving dark (i.e., gray) solitons [43, 89, 90]. Moreover, the oscillation period of the DB structures that we obtain for  $\Omega = 1$  is  $T^{\text{osc}} = 112.4$ , whereas the theoretical prediction yields  $T^{\text{DB}} = 108.7154$  [85, 89]. This discrepancy is predominantly attributed to the interactions among the solitons and the background excitations of the impurities [43]. Let us finally mention that for a larger pulse duration the period and amplitude of the above-described DB solitons remain almost unaffected while the background becomes more excited because a larger amount of energy is introduced into the system.

Incorporating correlations, the behavior of the density of the bath and the impurities for  $\Omega = 0.5$  and 1 [Figs. 8(g) and 8(h) and Figs. 9(c) and 9(d)], is evidently altered from the respective MF time evolution for  $t > 5$ . Focusing on the impurities,  $\rho^{(1),B}(x; t)$  displays initially a density hump for both modulation frequencies close to the trap center, which reflects the immiscible character of the system since at  $t = 0$   $g_{AB}^{\text{in}} = 1.4$ , and later on it diffuses within the medium suffering enhanced interference phenomena due to the miscible character of the system. The initial density hump subsequently splits, a process which is more prominent in the case of the initial density dip of the bath, as we shall discuss later on [Figs. 8(g) and 9(c)]. The impurities cloud undergoes a large amplitude breathing motion with frequency  $\omega^{\text{br}} \simeq 0.157$  for both  $\Omega = 0.5$  and 1. This frequency is extracted by calculating the impurities position variance,  $\langle (x^B)^2 \rangle$  [25, 31]. To explain such a breathing frequency, we resort to the effective potential experienced by the impurities due to the presence of the bath [Eq. (12)]. By inspecting the density snapshots of the bosonic environment in Figs. 11(d)–11(f), the time-averaged profile  $\bar{\rho}^{(1),A}(x) = \frac{1}{T} \int_0^T g_{AB}(t) \rho^{(1),A}(x; t)$  smears out small density fluctuations and resembles a TF profile,  $\bar{\rho}^{(1),A}(x) = Q(R^2 - x^2)\theta(R^2 - x^2)$ , with  $\theta(x)$  being the Heaviside function and  $T = 200$ . Therefore, the small density undulations caused by the impurity motion, present in the instantaneous profiles of  $\rho^{(1),A}(x; t)$ , are now eliminated. We remark that in the case of  $\Omega = 0.5$  ( $\Omega = 1$ )  $\bar{\rho}^{(1),A}$  saturates for  $T > 195$  ( $T > 180$ ). On top of the time-averaged density of the medium there are small density humps at  $x = \pm 5$ , which will be discussed later on. The effective potential is a deformed harmonic trap with a renormalized frequency  $\omega_{\text{eff}} = \sqrt{\omega^2 - \frac{2Q}{M}}$  [37, 98, 101]. Therefore, the corresponding effective breathing frequency is  $\omega_{\text{eff}}^{\text{br}} = 2\omega_{\text{eff}} = 0.1328$  for  $\Omega = 1$ , with a 1% relative deviation for  $\Omega = 0.5$ . The discrepancy between  $\omega^{\text{br}}$  and  $\omega_{\text{eff}}^{\text{br}}$  arises due to the presence of correlations [68], which alter the TF profile and are imprinted as small density humps on top of  $\rho^{(1),A}(x; t)$  at  $x = \pm 5$  [Figs. 8(g) and 9(c)].

Turning to the dynamical response of the bath,  $\rho^{(1),A}(x; t)$  features structural changes compared to its MF analog [Figs. 8(e) and 9(a)] especially right after the termination of the impurities-bath interaction modulation, namely, at  $t \simeq 15$  for  $\Omega = 0.5$  and at  $t \simeq 7$  for  $\Omega = 1$ . Initially ( $0 < t < 2.5$ ) there is a density dip localized at  $x = 0$ , which splits into two repelling density branches; see the black-dashed ellipses in Figs. 8(g) and 9(c). Subsequently each of these branches splits further into two shallower density dips, with one traveling towards the edges of the medium and the other one having a significantly smaller amplitude, and remaining almost un-

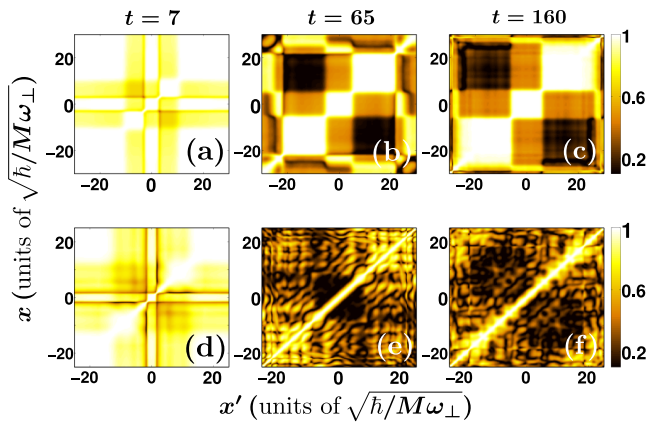


FIG. 12. Snapshots of the first-order coherence of (a–c) the bath,  $g^{(1),A}(x, x'; t)$ , and (d–f) the impurities,  $g^{(1),B}(x, x'; t)$ . The modulation frequency is  $\Omega = 0.5$  and all other system parameters are the same as in Figs. 8(g) and 8(h).

affected throughout time evolution. The amplitude of these dips increases slightly in time but their position stays the same at  $x \simeq \pm 5$ , as can be seen in Figs. 11(d)–11(f). This process together with the splitting of the bright component is reminiscent of the splitting of a quantum DB soliton pair in the presence of correlations, into a fast and a slower moving solitary wave, as reported in Ref. [68]. A similar to the above-described phenomenology occurs for larger modulation frequencies  $\Omega$  and therefore also for the case of an impurity-medium interaction quench; see Eq. (2). However, in the latter case the outer  $\rho^{(1),A}$  shallow dips when reaching the trap edges are reflected back and robustly propagate within the medium displaced from the trap center while the inner  $\rho^{(1),A}$  dips collide at  $t \approx 80$  and merge into a single one. Moreover, the impurities exhibit a somewhat larger spatial extent.

The small density dips which remain almost unaffected in the course of the time evolution manifest themselves in the effective potential [Eq. (12)] for both modulation frequencies [Fig. 10(b)]. They form shallow potential wells, and in their positions the impurities showcase small amplitude humps; see for instance Fig. 11(f). Apart from these dips, the density of the bosonic medium resembles a TF profile as we have discussed before, and therefore  $V_{\text{eff}}(x; t)$  is similar to a harmonic trap. Hence a multitude of its eigenstates is needed in order to at least qualitatively account for the impurities density profiles in the course of the evolution [Fig. 11(f)].

### C. Correlation patterns and the bunching of impurities

To expose the role of correlations for the bath and the impurities subsystems, in the driven dynamics to the miscible regime, we employ the first-order coherence function [Eq. (7)], measuring the underlying coherence losses, and the second-order noise correlation function [Eq. (8)], capturing the emergent two-body correlation processes. Initially, the first-order coherence  $g^{(1),\sigma}(x, x'; t)$  is exemplarily studied during the time evolution for  $\Omega = 0.5$  (Fig. 12). At the early stages of the dynamics ( $0 < t < 10$ ) the two narrow density dips at  $x \simeq \pm 3$  [see Fig. 8(g)] experience a localization trend; see for instance  $g^{(1),A}(3.3, -3.6; t = 7) \simeq 0.47$  [Fig. 12(a)].

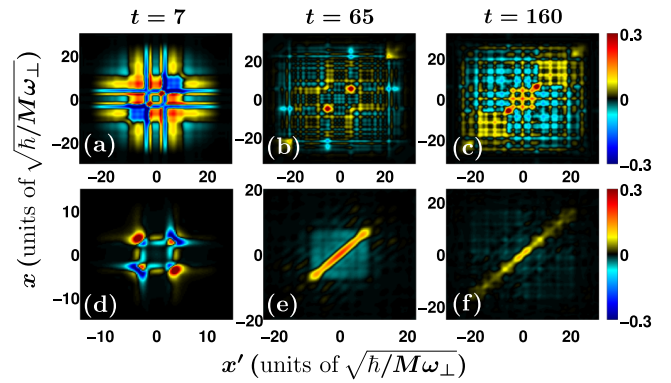


FIG. 13. Instantaneous profiles of the second-order coherence of (a–c) the bath particles and (d–f) the impurities. In all cases the modulation frequency is  $\Omega = 0.5$ , while all other parameters are the same as in Figs. 8(g) and 8(h).

At later evolution times [Figs. 12(b) and 12(c)], coherence is almost completely lost for the two symmetric spatial intervals  $D^+ = (5, 22)$  and  $D^- = (-22, -5)$  delimited by the mainly stationary density dips, located at  $x \simeq \pm 5$  and the outer edges of the medium cloud, with  $g^{(1),A}(-15.9, 14.6; t = 160) \simeq 0.1$ . The aforementioned behavior signals the appearance of Mott correlations meaning that the bath particles tend to be localized in either one of those spatial intervals. Turning to the impurities, we observe that at short evolution times, similarly to the bosonic medium, coherence is significantly reduced between the spatial regions corresponding to the density humps [Fig. 8(h) at  $t \simeq 7$ ], with  $g^{(1),B}(2.54, -3; t = 7) \simeq 0.53$  [Fig. 12(d)]. Later on, the impurities undergo a breathing motion. Upon contraction of the impurity cloud, e.g., at  $t = 65$  [Fig. 8(h)], the impurity particles are localized in either of the two spatial intervals  $D_+ \simeq (0, 12)$  and  $D_- \simeq (-12, 0)$ , with  $g^{(1),B}(5, -5.5; t = 65) \simeq 0.01$  [Fig. 12(e)]. However, when the impurity cloud expands, e.g., at  $t = 160$ , there is still a loss of coherence between the spatial regions away from the trap center, with  $g^{(1),B}(-8.7, 7.6; t = 160) \simeq 0.15$ . It is also worth mentioning that for  $\Omega < \omega$  the same qualitative picture holds and there is loss of coherence between the outer spatial regions delimited by the small density dips of the bosonic medium cloud.

Moving to the investigation of two-body correlations, we invoke the second-order noise correlation function  $g^{(2)}(x, x'; t)$  [Eq. (8)], for the same driving frequency, namely,  $\Omega = 0.5$ . Initially, e.g., at  $t = 7$ , there is a probability for two particles of the environment to cluster together in the density dips located at  $x \simeq \pm 3$ ; see, e.g.,  $g^{(2),AA}(2.5, -2.8; t = 7) \simeq 0.65$  [Fig. 13(a)]. Moreover, anticorrelations build up for particles occupying the same spatial regions enclosed by the density dips and the edges of the cloud of the bath, e.g.,  $g^{(2),AA}(-6.56, -6.56; t = 7) \simeq -0.17$ . Later on, two particles of the bath residing in the two shallow and almost stationary density dips of  $\rho^{(1),A}$  located at  $x \simeq \pm 5$  exhibit two-body correlations since  $g^{(2),AA}(-5.217, -5.217; t = 65) \simeq 0.58$  and  $g^{(2),AA}(-5.8, -5.8; t = 160) \simeq 0.64$  [Figs. 13(b) and 13(c), respectively], while opposite spatial regions between the density dips at  $x \simeq \pm 5$  and the edges of the medium cloud are anticorrelated [Fig. 12(c),  $g^{(2),AA}(-9, 8.7; t = 160) \simeq$

–0.12]. Turning to the impurity atoms, we observe that initially two-body correlations build up for particles lying on top of the  $\rho^{(1),B}$  density humps at  $x \simeq \pm 3$ , similarly to the case of the bosonic medium, with  $g^{(2),BB}(-3.08, -3.08; t = 7) \simeq 0.15$  [Fig. 13(d)]. Moreover, anticorrelations develop among impurity atoms occupying each of the two distinct density humps, for instance  $g^{(2),BB}(-2.54, 2.54; t = 7) \simeq -0.21$ . At later time instants, impurities cluster [25,26,37] and tend to occupy the same position inside the impurity cloud [Figs. 13(e) and 13(f)],  $g^{(2),BB}(-0.14, -0.14; t = 65) \simeq 0.21$ . The second-order noise correlation acquires small negative values (anticorrelations), when the impurities do not reside in the same position, for instance  $g^{(2),BB}(1.74, -6.29; t = 160) \simeq -0.01$ .

### V. IMPACT OF THE IMPURITIES INTERACTIONS AND CONCENTRATION

Having addressed the impurity-medium pulse dynamics we now demonstrate its dependence on the number of impurities and the impurity-impurity interaction strength. The remaining system parameters are considered to be the same as in the two previous sections (Secs. III and IV), i.e.,  $N_A = 100$  while  $g_{AA} = 1.004$ . The impurity-bath interaction strength  $g_{AB}$  is driven first from  $g_{AB}^{\text{in}} = 0.2$  to  $g_{AB}^{\text{f}} = 1.2$ , with modulation frequency  $\Omega = 1.5$ , and subsequently from  $g_{AB}^{\text{in}} = 1.4$  to  $g_{AB}^{\text{f}} = 0.6$  with  $\Omega = 1$ , according to the pulse protocol introduced in Eq. (2).

Initially, we explore the impurities dynamical response by considering  $N_B = 2$  noninteracting ( $g_{BB} = 0$ ) ones while driving the impurities-bath interaction strength to the immiscible phase, i.e., from  $g_{AB}^{\text{in}} = 0.2$  to  $g_{AB}^{\text{f}} = 1.2$  exemplarily with  $\Omega = 1.5$ . The two impurities display mainly a Gaussian profile during the time evolution and reside around the trap center [Fig. 14(a)], where a density dip is present in  $\rho^{(1),A}(x; t)$  of the bosonic medium. Moreover, faint density branches of  $\rho^{(1),B}(x; t)$  are emitted and subsequently disperse within the medium [39]. Employing the effective potential picture [Eq. (12)], we deduce that the two particles occupy its ground state with a probability of 93%. For an increasing number of impurities, the time-evolved density of  $N_B = 10$  noninteracting ones [Fig. 14(b)] is different from the density of  $N_B = 10$  interacting impurity atoms [Fig. 3(d)]. Indeed, for  $g_{BB} = 0$  there are no prominent outer density humps but rather fragmented faint ones, which after their emission from the central branch oscillate back and forth from the trap center to the edges of the bosonic medium diffusing within the latter. Recall that in the case of  $N_B = 10$  interacting impurities [Fig. 3(d)], the corresponding humps, possessing a significant population, travel away from the trap center and remain at the edges of the environment while oscillating with a small amplitude. This distinct behavior is due to the presence of repulsive impurity-impurity interactions. The central density hump, which corresponds to the ground state of the effective potential, is present both in the interacting and the noninteracting case. The outer faint humps when  $g_{BB} = 0$  [Fig. 14(b)] refer to higher-lying excited states of  $V_{\text{eff}}(x; t)$ , localized in its respective outer potential wells, which are shallower com-

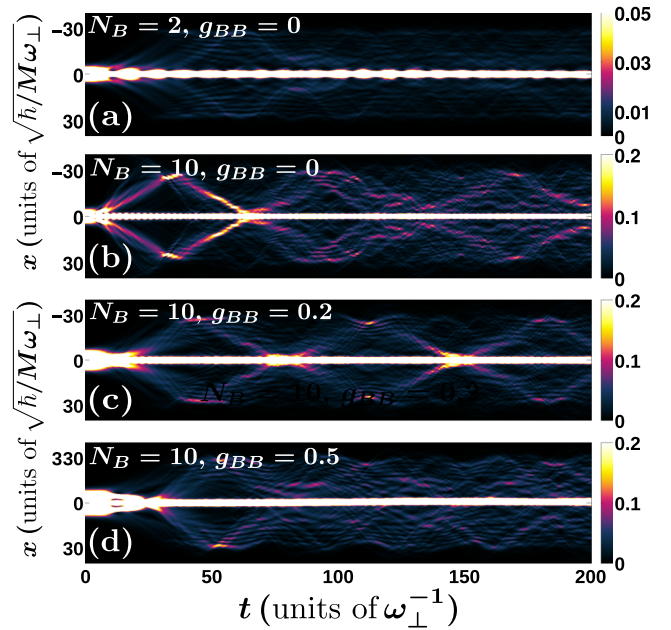


FIG. 14. Time evolution of the one-body density for (a)  $N_B = 2$  and (b)  $N_B = 10$  noninteracting impurity atoms, and density evolution for  $N_B = 10$  impurities with (c)  $g_{BB} = 0.2$  and (d)  $g_{BB} = 0.5$  impurity-impurity interactions. The impurity-bath interaction strength is driven from  $g_{AB}^{\text{in}} = 0.2$  to  $g_{AB}^{\text{f}} = 1.2$  with frequency  $\Omega = 1.5$  according to Eq. (2).

pared to the ones of  $V_{\text{eff}}(x; t)$  in the interacting case due to the different shape of  $\rho^{(1),A}(x; t)$  [Fig. 5(a)].

We then move on to study the effect of impurity-impurity interactions on the dynamics in the presence of the pulse [39]. The cases of  $g_{BB} = 0.2$  [Fig. 14(c)] and  $g_{BB} = 0.5$  [Fig. 14(d)] with  $N_B = 10$  feature a similar dynamical behavior to the noninteracting ( $g_{BB} = 0$ ) scenario [Fig. 14(b)]. Upon increasing  $g_{BB}$ , the ground state of  $\rho^{(1),B}(x; t)$  exhibits a larger spatial extent due to the stronger repulsion [see, e.g., Fig. 14(d) with  $g_{BB} = 0.5$  and Fig. 3(d) with  $g_{BB} = 0.9544$ ] and the impurities ground state displays a TF profile. The dynamical response of the impurities as quantified by  $\rho^{(1),B}(x; t)$  is very similar for  $g_{BB} = 0$  and  $0.2$  in the sense that there exist faint emitted density branches that oscillate back and forth between the edges of the bosonic bath and  $x = 0$ . These are emitted at later evolution times for a stronger  $g_{BB}$ , e.g.,  $g_{BB} = 0.2$  [Fig. 14(c)] compared to  $g_{BB} = 0$  [Fig. 14(b)]. After their creation, they immediately disperse within the cloud of the bath while stronger repulsive interactions lead to larger portions of the impurities occupying the outer density branches [Figs. 14(b) and 14(c)].

Furthermore we investigate the impurities response in the reverse pulse scenario, i.e., when the impurity-bath interaction strength drives the system into the miscible phase, with  $g_{AB}^{\text{in}} = 1.4$  to  $g_{AB}^{\text{f}} = 0.6$ , and  $\Omega = 1$ . Focusing on  $N_B = 2$  and  $10$  noninteracting impurities [Figs. 15(a) and 15(b), respectively], a breathing motion is apparent with the most prominent frequency being  $\omega^{\text{br}} = 0.157$  in both cases. Note that the latter coincides with  $\omega^{\text{br}}$  for  $N_B = 10$  and  $g_{BB} = 0.9544$  [Fig. 9(d)]. Moreover, there is a central density hump

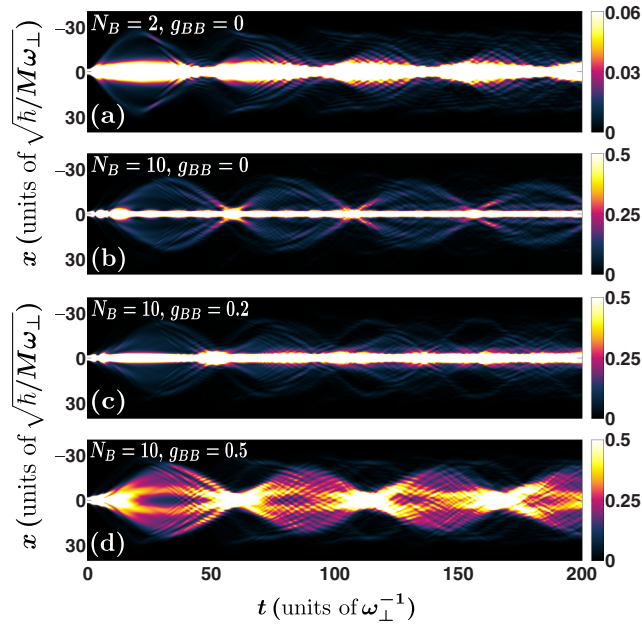


FIG. 15. Spatiotemporal evolution of the one-body density for (a)  $N_B = 2$  and (b)  $N_B = 10$  noninteracting impurities, and density evolution for  $N_B = 10$  impurities with (c)  $g_{BB} = 0.2$  and (d)  $g_{BB} = 0.5$ . The impurity-bath interaction is driven from  $g_{AB}^{\text{in}} = 1.4$  to  $g_{AB}^{\text{f}} = 0.6$  with the modulation frequency  $\Omega = 1$  according to Eq. (2).

building upon  $\rho^{(1),B}(x; t)$ , which is especially pronounced for  $N_B = 2$  [Fig. 15(a)]. This density structure is similar to the case of  $N_B = 2$  impurities in the reverse pulse scenario, i.e., from the miscible to the immiscible phase [Fig. 14(a)], where the two impurities are predominantly localized around the trap center. In this latter case, however, the two particles exhibit a weaker breathing motion compared to the one triggered by the driven dynamics to the miscible regime [Fig. 15(a)]. This is due to the immiscible character of the system following the reverse pulse scenario. Utilizing once more the effective potential picture [Eq. (12)], we can infer that both the  $N_B = 2$  and 10 impurities occupy predominantly its ground state, a result that is manifested by the presence of the central density hump in  $\rho^{(1),B}(x; t)$  [Figs. 15(a) and 15(b)].

As the interactions increase, i.e.,  $g_{BB} = 0.2$  and  $g_{BB} = 0.5$  [Figs. 15(c) and 15(d), respectively],  $\rho^{(1),B}$  shows similar patterns to the one emerging for  $g_{BB} = 0.9544$ , especially for  $g_{BB} = 0.5$  [Fig. 9(d)]. Note that this is in contrast to the reverse scenario to the immiscible phase [Figs. 14(c) and 14(d)], where there is a generic diffusive pattern being apparently different from the localized outer density branches when  $g_{BB} = 0.9544$  [Fig. 9(d)]. The central density hump present for  $g_{BB} = 0$  and 0.2 [Figs. 15(b) and 15(c)] corresponds again to the ground state of the respective  $V_{\text{eff}}(x; t)$ , and becomes less prominent for a larger  $g_{BB}$  as depicted in Fig. 15(d). In the latter case, the effective potential resembles the structure illustrated in Fig. 10(b), displaying two shallow wells accounting for the two density humps close to the trap center in the case of  $g_{BB} = 0.5$  [Fig. 15(d)]. Furthermore, both for  $g_{BB} = 0.2$  and 0.5 [Figs. 15(c) and 15(d)], the cloud performs a breathing motion, with the most prominent frequency being

$\omega^{\text{br}} = 0.157$ , i.e., the same as in the noninteracting case [see Fig. 15(b)].

## VI. SUMMARY AND CONCLUSIONS

We have investigated the nonequilibrium quantum dynamics of few repulsively interacting harmonically trapped bosonic impurities immersed in a MB bosonic bath, subjected to a time-periodic pulse of the impurity-bath interaction strength. Importantly, the effect of the driving frequency on the emergent dynamical response of both components is studied in detail ranging from weak to strong driving. The amplitude of the modulation is large enough to drive the two-component system across its phase-separation boundary. In this sense, we examine the driven impurity-medium dynamics from the miscible to the immiscible phase and vice versa.

Focusing on the driving to the immiscible phase, two distinct response regimes are identified. Namely, if the modulation frequency is smaller than the trapping one, the system transits successively in the course of time from the miscible to the immiscible regime, according to the phase in which it is driven by the impurity-bath coupling. Turning to larger modulation frequencies than the trapping one, DB soliton pairs emerge within the MF approach, which subsequently merge after half of an oscillation period forming a bound state around the trap center. Taking correlations into account, these pairs are expelled towards the edges of the bath cloud, where they equilibrate by performing small-amplitude oscillations. In particular, by comparing the MF and the MB dynamics we conclude that at early evolution times both descriptions yield similar results, but subsequently correlations become important and hence the MF product state does not provide an adequate description. Interestingly, for an increasing modulation frequency we demonstrate that the MF framework is valid only at the very initial stages of the dynamics. The impurity atoms exhibit Mott-like correlations, thus being spatially localized in these outer density branches, which develop two-body correlations among each other. Moreover, a stable density dip (hump) is formed around the trap center in the bath (impurities). This dip splits the bath into two spatial regions which feature two-body correlations. The impurities motion can be intuitively understood in terms of an effective potential picture, unveiling that they predominantly reside in a superposition of its ground and first two excited states.

In the reverse driving scenario, i.e., following an interaction pulse from the immiscible to the miscible phase, we again capture two distinct dynamical regimes, depending on the modulation frequency. For small driving frequencies, the mixture transits consecutively in time from the immiscible to the miscible phase according to the modulation of the impurity-bath coupling. In the time interval that the system lies into its immiscible phase, the impurities reside in a superposition of their lowest-lying effective potential eigenstates. For larger modulation frequencies DB soliton pairs are generated within the MF framework possessing a larger oscillation frequency compared to the previous driving scenario. Incorporating correlations, the impurities perform a breathing motion, the frequency of which is in good agreement with the one predicted by their effective potential. We also argue that the dynamical response of the mixture can be well described

within the MF approximation only at early evolution times, a result that becomes more pronounced for an increasing modulation frequency where correlation effects are more enhanced. Furthermore, it is found that a multitude of excited eigenstates of their effective potential participate in the dynamics. Regarding the bosonic bath, two small density dips are nucleated, originating from the splitting of the spontaneously generated quantum DB soliton pairs, which are symmetric with respect to the trap center and are almost stable throughout the time evolution. These dips split the bath into two incoherent parts featuring two-body anticorrelations.

The role of different impurity particle numbers and impurity-impurity interactions is also explored. It is found that for weak repulsions, the impurities are mainly trapped by the bath around the trap center, occupying predominantly the ground state of their effective potential. This behavior is especially pronounced for two noninteracting particles. By increasing the impurity-impurity interactions or their particle number, weak amplitude emitted density humps form and oscillate between the edges of the cloud of the bath and the trap center. They also exhibit a dispersion within the bath density, mostly for strong repulsions. In particular, when driving the impurity-bath interactions from the immiscible to the miscible phase, it is showcased that the impurities perform a breathing motion with the same prominent frequency regardless of their inherent repulsion.

The present paper can inspire several promising and interesting future research directions. An extension of immediate interest is to consider the 2D analog of the current setup, where the ejection of correlated jet structures [58–60] and the emergence of star-shaped patterns has been reported upon modulating the scattering length [54]. Additionally, the driving of the impurity-bath coupling strength in the presence of fermionic impurities immersed in a Bose or Fermi gas is an interesting prospect for studying the induced interactions between the impurities and the impact of their flavor in the dynamical response of the system. In a similar vein, the dynamics of bosonic impurities embedded in a fermionic bath with a similar driving protocol will highlight the role of induced correlations mediated by the fermionic bath [102]. Certainly, the study of modulated interaction pulses in the presence of dipolar couplings is highly desirable.

#### ACKNOWLEDGMENTS

G.B. kindly acknowledges financial support by the State Graduate Funding Program Scholarships (HmbNFG). S.I.M. gratefully acknowledges financial support in the framework of the Lenz-Ising Award of the Department of Physics of the University of Hamburg. P.S. is grateful for financial support by the Deutsche Forschungsgemeinschaft (DFG, German Research Foundation) – SFB-925 – project 170620586.

#### APPENDIX A: ENERGY EXCHANGE PROCESSES

To elucidate the underlying energy exchange processes between the different components [22,36,38] of the system in both driving scenarios addressed in Secs. III and IV we invoke the corresponding energy contributions of three different com-

ponents, namely, the one of the bath ( $E_A$ ), the impurities ( $E_B$ ), and their mutual interactions ( $E_{AB}$ ). In particular the energy of the bath is given by

$$E_A(t) = \langle \Psi_{\text{MB}}(t) | \hat{T}_A + \hat{V}_A(x) + \hat{H}_{AA} | \Psi_{\text{MB}}(t) \rangle - \langle \Psi_{\text{MB}}(0) | \hat{T}_A + \hat{V}_A(x) + \hat{H}_{AA} | \Psi_{\text{MB}}(0) \rangle, \quad (\text{A1})$$

while the energy of the impurities is

$$E_B(t) = \langle \Psi_{\text{MB}}(t) | \hat{T}_B + \hat{V}_B(x) + \hat{H}_{BB} | \Psi_{\text{MB}}(t) \rangle, \quad (\text{A2})$$

and the impurity-medium interaction energy reads

$$E_{AB}(t) = \langle \Psi_{\text{MB}}(t) | \hat{H}_{AB}(t) | \Psi_{\text{AB}}(t) \rangle. \quad (\text{A3})$$

In these expressions, the kinetic, potential, and impurity-bath interaction operators have the form  $\hat{T}_\sigma = -\frac{\hbar^2}{2M} \int dx \hat{\Psi}^{\sigma\dagger} \frac{d^2}{dx^2} \hat{\Psi}^\sigma(x)$ ,  $\hat{V}_\sigma(x) = \frac{1}{2} M \omega^2 \int dx \hat{\Psi}^{\sigma\dagger}(x) x^2 \hat{\Psi}^\sigma(x)$ , and  $\hat{H}_{\sigma\sigma'}(t) = g_{\sigma\sigma'}(t) \int dx \hat{\Psi}^{\sigma\dagger}(x) \hat{\Psi}^{\sigma'\dagger}(x) \hat{\Psi}^\sigma(x) \hat{\Psi}^{\sigma'}(x)$ , respectively, with  $\sigma = A, B$ . Also,  $\hat{\Psi}^\sigma(x) [\hat{\Psi}^{\sigma\dagger}(x)]$  denotes the operator that annihilates [creates] a  $\sigma$ -species particle at position  $x$ . Note that the initial energy of the bath, which is large due to its substantial spatial extent and particle number, is subtracted in order to render  $E_A$  comparable with the other energy contributions.

Focusing on the driving of the system from the miscible to the immiscible phase with modulation frequency  $\Omega = 1.5$ , the interaction energy  $E_{AB}(t)$  initially oscillates according to the quench protocol of Eq. (2) and subsequently decreases [Fig. 16(a)]. Since energy is pumped into the system after the pulse the energy of both components,  $E_A$  and  $E_B$ , increases. The impurities acquire more energy than the bath and this reflects the fact that the outer impurity density branches [Fig. 3(d)] reach the edges of the cloud of the bath and remain there while oscillating [39,64]. At later time instants  $E_B$  features maxima whenever the outer density branches of  $\rho^{(1),B}$  [see Figs. 3(d) and 16(a) at  $t \approx 85$ ] tend to the edges of the bath cloud, acquiring thus maximal potential energy, and minima when the  $\rho^{(1),B}$  branches approach the trap center [Fig. 16(a),  $t \approx 111$ ].  $E_A$  exhibits a similar behavior and its minima and maxima occur simultaneously with the minima and maxima of  $E_B$ , since the dips formed in the bath density move in phase with the outer impurity density branches. The impurity-bath interaction energy exhibits out-of-phase oscillations with  $E_A$  and  $E_B$ , which is a manifestation of the energy exchange process between the two components [33,64]. To infer the behavior of the bath energy with respect to  $\Omega$  we present  $E_A$  for  $\Omega = 0.05, 0.5$ , and  $1.5$  [inset of Fig. 16(a)]. Evidently, there is a growth tendency of  $E_A$  with increasing  $\Omega$ , since for larger modulation frequencies more energy is pumped into the system. However for  $\Omega = 1.5$ ,  $E_A$  is energetically close to the case  $\Omega = 0.5$ . For even larger modulation frequencies, the energy of the bath displays a similar behavior as for  $\Omega = 1.5$  because for large driving frequencies the effect of the pulse is averaged out [39]. Turning to small  $\Omega$  [ $\Omega = 0.05$  in the inset of Fig. 16(a)],  $E_A$  performs small amplitude oscillations, which are in phase with the oscillations of  $E_{AB}(t)$  and consequently with the modulation of  $g_{AB}(t)$ .

Turning to the reverse pulse scenario, namely, from  $g_{AB}^{\text{in}} = 1.4$  to  $g_{AB}^f = 0.6$  with  $\Omega = 1$ , the impurity-bath interaction energy  $E_{AB}(t)$  now increases and afterwards oscillates around a mean value. This behavior is attributed to the fact that the

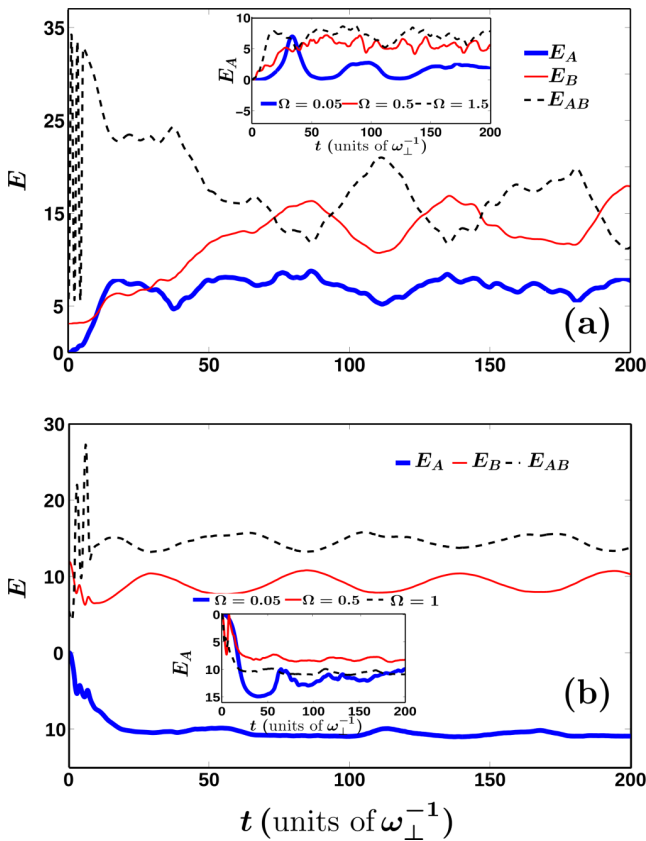


FIG. 16. (a) Energy contributions of the bath ( $E_A$ ), the impurities ( $E_B$ ), and their mutual interaction ( $E_{AB}$ ) following a time-periodic pulse of the impurity-bath coupling from  $g_{AB}^{\text{in}} = 0.2$  to  $g_{AB}^{\text{f}} = 1.2$  with  $\Omega = 1.5$ . (b) The same as in (a) but for  $g_{AB}^{\text{in}} = 1.4$ ,  $g_{AB}^{\text{f}} = 0.6$ , and modulation frequency  $\Omega = 1$ . The insets display the energy of the bath for other modulation frequencies (see legend). The energies are given in terms of  $\hbar\omega_{\perp}$ .

system is driven into the miscible phase where the overlap between the two components is large, compared to the driving to the immiscible regime. The energy of the impurities oscillates around a mean value reflecting their breathing motion [see Fig. 9(d)], with maxima at the positions where  $\rho^{(1),B}(x;t)$  expands [Fig. 9(d) at  $t \simeq 25$ ], possessing maximal potential energy, and minima at the locations where  $\rho^{(1),B}(x;t)$  contracts [see Fig. 9(d) at  $t \simeq 60$ ]. Since the impurities energy remains roughly the same and oscillates around a mean value while  $E_{AB}$  increases with time due to the miscible character of the system, the bath energy decreases due to energy conservation until  $t \simeq 25$  and thereafter oscillates with a small amplitude around a constant value. As can be seen from the inset of Fig. 16(b),  $E_A$  becomes negative for other modulation frequencies as well.

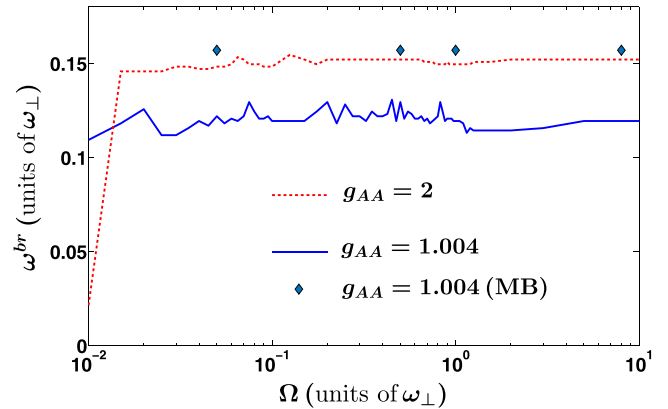


FIG. 17. Impurities breathing frequency following a pulse to the miscible phase, i.e.,  $g_{AB}^{\text{in}} = 1.4$  and  $g_{AB}^{\text{f}} = 0.6$  when varying  $g_{AA}$  while keeping  $g_{BB} = 0.9544$  fixed (see legend). The rhombi present the numerically obtained breathing frequency in the MB evolution with  $g_{AA} = 1.004$ .

#### APPENDIX B: IMPURITIES BREATHING FREQUENCY FOLLOWING A PULSE TO THE MISCIBLE REGIME

For consistency, let us finally investigate within the MF approximation the role of the driving frequency on the impurities breathing frequency  $\omega^{\text{br}}$  as the system is driven from the immiscible to the miscible phase, i.e.,  $g_{AB}^{\text{in}} = 1.4$  and  $g_{AB}^{\text{f}} = 0.6$ . The breathing frequency is derived by examining the impurities position variance,  $\langle (x_B)^2 \rangle$  [31,101]. Apart from  $\Omega$  the impact of different bath interactions is also explored (Fig. 17). By fixing  $g_{BB} = 0.9544$ ,  $\omega^{\text{br}}$  eventually saturates for sufficiently large driving frequencies ( $\Omega > 5$ ). More precisely,  $\omega^{\text{br}} = 0.1194$  in the case of  $g_{AA} = 1.004$  and  $\omega^{\text{br}} = 0.1521$  in the case of  $g_{AA} = 2$  (Fig. 17). Indeed for large  $\Omega$ , the effect of the pulse is averaged out (Sec. II A) and hence the dynamical response of the impurities is unaffected. To explain these breathing frequency values we resort to the effective potential experienced by the impurities for large  $\Omega$  [Eq. (12)]. A time averaging is performed on the medium density,  $\bar{\rho}^{(1),A}(x) = \frac{1}{T} \int_0^T g_{AB}(t) \rho^{(1),A}(x;t) dt$  for sufficiently long evolution times  $T$ , in order to eliminate small density fluctuations [36,37]. For  $g_{AA} = 1.004$  and 2, the time-averaged density resembles a TF profile  $\bar{\rho}^{(1),A}(x) = Q(R^2 - x^2)\theta(R^2 - x^2)$ , and the breathing frequency is then given by  $\omega^{\text{br}} = 2\sqrt{\omega^2 - \frac{2Q}{M}}$  [101]. According to the theoretical predictions [37,98,101] the latter provides  $\omega^{\text{br}} = 0.13$  and 0.1689 for  $g_{AA} = 1.004$  and 2, respectively, when  $\Omega = 10$ . The relative error of these theoretically anticipated values with the numerically predicted values is of the order of 10% in both cases. Taking correlations into account for  $g_{AA} = 1.004$ , already from  $\Omega = 0.05$ ,  $\omega^{\text{br}}$  saturates to 0.157 (rhombi in Fig. 17), a value well above the MF case where  $\omega^{\text{br}} = 0.1194$ , thus suggesting the importance of impurity-impurity correlations [25,37].

[1] I. Bloch, J. Dalibard, and W. Zwerger, *Rev. Mod. Phys.* **80**, 885 (2008).

[2] C. Chin, R. Grimm, P. Julienne, and E. Tiesinga, *Rev. Mod. Phys.* **82**, 1225 (2010).

- [3] S. Inouye, M. R. Andrews, J. Stenger, H. J. Miesner, D. M. Stamper-Kurn, and W. Ketterle, *Nature (London)* **392**, 151 (1998).
- [4] M. Olshanii, *Phys. Rev. Lett.* **81**, 938 (1998).
- [5] T. Bergeman, M. G. Moore, and M. Olshanii, *Phys. Rev. Lett.* **91**, 163201 (2003).
- [6] E. Haller, M. J. Mark, R. Hart, J. G. Danzl, L. Reichsöllner, V. Melezhik, P. Schmelcher, and H.-C. Nägerl, *Phys. Rev. Lett.* **104**, 153203 (2010).
- [7] A. Görlitz, J. M. Vogels, A. E. Leanhardt, C. Raman, T. L. Gustavson, J. R. Abo-Shaer, A. P. Chikkatur, S. Gupta, S. Inouye, T. Rosenband, and W. Ketterle, *Phys. Rev. Lett.* **87**, 130402 (2001).
- [8] G. Modugno, M. Modugno, F. Riboli, G. Roati, and M. Inguscio, *Phys. Rev. Lett.* **89**, 190404 (2002).
- [9] C. J. Myatt, E. A. Burt, R. W. Ghrist, E. A. Cornell, and C. E. Wieman, *Phys. Rev. Lett.* **78**, 586 (1997).
- [10] M. Egorov, B. Opanchuk, P. Drummond, B. V. Hall, P. Hannaford, and A. I. Sidorov, *Phys. Rev. A* **87**, 053614 (2013).
- [11] K. Pilch, A. D. Lange, A. Prantner, G. Kerner, F. Ferlino, H.-C. Nägerl, and R. Grimm, *Phys. Rev. A* **79**, 042718 (2009).
- [12] A. Burchianti, C. D'Errico, S. Rosi, A. Simoni, M. Modugno, C. Fort, and F. Minardi, *Phys. Rev. A* **98**, 063616 (2018).
- [13] A. Schirotzek, C.-H. Wu, A. Sommer, and M. W. Zwierlein, *Phys. Rev. Lett.* **102**, 230402 (2009).
- [14] C. Kohstall, M. Zaccanti, M. Jag, A. Trenkwalder, P. Massignan, G. M. Bruun, F. Schreck, and R. Grimm, *Nature (London)* **485**, 615 (2012).
- [15] P. Massignan, M. Zaccanti, and G. M. Bruun, *Rep. Prog. Phys.* **77**, 034401 (2014).
- [16] N. B. Jørgensen, L. Wacker, K. T. Skalmstang, M. M. Parish, J. Levinsen, R. S. Christensen, G. M. Bruun, and J. J. Arlt, *Phys. Rev. Lett.* **117**, 055302 (2016).
- [17] M.-G. Hu, M. J. Van de Graaff, D. Kedar, J. P. Corson, E. A. Cornell, and D. S. Jin, *Phys. Rev. Lett.* **117**, 055301 (2016).
- [18] L. A. Peña Ardila, N. B. Jørgensen, T. Pohl, S. Giorgini, G. M. Bruun, and J. J. Arlt, *Phys. Rev. A* **99**, 063607 (2019).
- [19] A. G. Volosniev and H.-W. Hammer, *Phys. Rev. A* **96**, 031601(R) (2017).
- [20] N.-E. Guenther, P. Massignan, M. Lewenstein, and G. M. Bruun, *Phys. Rev. Lett.* **120**, 050405 (2018).
- [21] J. Tempere, W. Casteels, M. K. Oberthaler, S. Knoop, E. Timmermans, and J. T. Devreese, *Phys. Rev. B* **80**, 184504 (2009).
- [22] L. A. Peña Ardila and S. Giorgini, *Phys. Rev. A* **94**, 063640 (2016).
- [23] F. Grusdt, G. E. Astrakharchik, and E. Demler, *New J. Phys.* **19**, 103035 (2017).
- [24] L. A. Peña Ardila and S. Giorgini, *Phys. Rev. A* **92**, 033612 (2015).
- [25] S. I. Mistakidis, A. G. Volosniev, and P. Schmelcher, *Phys. Rev. Research* **2**, 023154 (2020).
- [26] A. S. Dehkharghani, A. G. Volosniev, and N. T. Zinner, *Phys. Rev. Lett.* **121**, 080405 (2018).
- [27] J. Chen, J. M. Schurer, and P. Schmelcher, *Phys. Rev. Lett.* **121**, 043401 (2018).
- [28] N. Spethmann, F. Kindermann, S. John, C. Weber, D. Meschede, and A. Widera, *Phys. Rev. Lett.* **109**, 235301 (2012).
- [29] N. J. Robinson, J.-S. Caux, and R. M. Konik, *Phys. Rev. Lett.* **116**, 145302 (2016).
- [30] R. Schmidt, M. Knap, D. A. Ivanov, J.-S. You, M. Cetina, and E. Demler, *Rep. Prog. Phys.* **81**, 024401 (2018).
- [31] J. Catani, G. Lamporesi, D. Naik, M. Gring, M. Inguscio, F. Minardi, A. Kantian, and T. Giamarchi, *Phys. Rev. A* **85**, 023623 (2012).
- [32] T. Fukuhara, A. Kantian, M. Endres, M. Cheneau, P. Schauss, S. Hild, D. Bellem, U. Schollwöck, T. Giamarchi, C. Gross, I. Bloch, and S. Kuhr, *Nat. Phys.* **9**, 235 (2013).
- [33] S. I. Mistakidis, G. C. Katsimiga, G. M. Koutentakis, Th. Busch, and P. Schmelcher, *Phys. Rev. Lett.* **122**, 183001 (2019).
- [34] M. Knap, A. Shashi, Y. Nishida, A. Imambekov, D. A. Abanin, and E. Demler, *Phys. Rev. X* **2**, 041020 (2012).
- [35] D. Boyanovsky, D. Jasnow, X.-L. Wu, and R. C. Coalson, *Phys. Rev. A* **100**, 043617 (2019).
- [36] S. I. Mistakidis, F. Grusdt, G. M. Koutentakis, and P. Schmelcher, *New J. Phys.* **21**, 103026 (2019).
- [37] S. I. Mistakidis, G. M. Koutentakis, G. C. Katsimiga, Th. Busch, and P. Schmelcher, *New J. Phys.* **22**, 043007 (2020).
- [38] J. Catani, G. Barontini, G. Lamporesi, F. Rabatti, G. Thalhammer, F. Minardi, S. Stringari, and M. Inguscio, *Phys. Rev. Lett.* **103**, 140401 (2009).
- [39] K. Mukherjee, S. I. Mistakidis, S. Majumder, and P. Schmelcher, *Phys. Rev. A* **101**, 023615 (2020).
- [40] T. Lausch, A. Widera, and M. Fleischhauer, *Phys. Rev. A* **97**, 023621 (2018).
- [41] Z. Z. Yan, Y. Ni, C. Robens, and M. W. Zwierlein, *Science* **368**, 190 (2020).
- [42] P. G. Kevrekidis, G. Theocharis, D. J. Frantzeskakis, and B. A. Malomed, *Phys. Rev. Lett.* **90**, 230401 (2003).
- [43] *Emergent Nonlinear Phenomena in Bose-Einstein Condensates. Theory and Experiment*, edited by P. G. Kevrekidis, D. J. Frantzeskakis, and R. Carretero-González (Springer-Verlag, Berlin, 2008).
- [44] H. Sakaguchi and B. A. Malomed, *Phys. Rev. E* **70**, 066613 (2004).
- [45] S. Rajendran, P. Muruganandam, and M. Lakshmanan, *Physica D* **239**, 366 (2010).
- [46] C.-Y. Ding, X.-F. Zhang, D. Zhao, H.-G. Luo, and W. M. Liu, *Phys. Rev. A* **84**, 053631 (2011).
- [47] S. Rajendran, P. Muruganandam, and M. Lakshmanan, *J. Phys. B* **42**, 145307 (2009).
- [48] T. Kanna, R. B. Mareeswaran, F. Tsitoura, H. E. Nistazakis, and D. J. Frantzeskakis, *J. Phys. A: Math. Theor.* **46**, 475201 (2013).
- [49] H. Saito and M. Ueda, *Phys. Rev. Lett.* **90**, 040403 (2003).
- [50] F. Kh. Abdullaev, J. G. Caputo, R. A. Kraenkel, and B. A. Malomed, *Phys. Rev. A* **67**, 013605 (2003).
- [51] P. Engels, C. Atherton, and M. A. Hofer, *Phys. Rev. Lett.* **98**, 095301 (2007).
- [52] J. H. V. Nguyen, M. C. Tsatsos, D. Luo, A. U. J. Lode, G. D. Telles, V. S. Bagnato, and R. G. Hulet, *Phys. Rev. X* **9**, 011052 (2019).
- [53] W. Cairncross and A. Pelster, *Eur. Phys. J. D* **68**, 106 (2014).
- [54] D. K. Maity, K. Mukherjee, S. I. Mistakidis, S. Das, P. G. Kevrekidis, S. Majumder, and P. Schmelcher, *Phys. Rev. A* **102**, 033320 (2020).




- [55] A. I. Nicolin, R. Carretero-González, and P. G. Kevrekidis, *Phys. Rev. A* **76**, 063609 (2007).
- [56] K. Staliunas, S. Longhi, and G. J. de Valcárcel, *Phys. Rev. Lett.* **89**, 210406 (2002).
- [57] D. Kobayakov, V. Bychkov, E. Lundh, A. Bezett, and M. Marklund, *Phys. Rev. A* **86**, 023614 (2012).
- [58] L. W. Clark, A. Gaj, L. Feng, and C. Chin, *Nature (London)* **551**, 356 (2017).
- [59] H. Fu, L. Feng, B. M. Anderson, L. W. Clark, J. Hu, J. W. Andrade, C. Chin, and K. Levin, *Phys. Rev. Lett.* **121**, 243001 (2018).
- [60] H. Fu, Z. Zhang, K.-X. Yao, L. Feng, J. Yoo, L. W. Clark, K. Levin, and C. Chin, *Phys. Rev. Lett.* **125**, 183003 (2020).
- [61] T. Mežnaršič, R. Žitko, T. Arh, K. Gosar, E. Zupanič, and P. Jeglič, *Phys. Rev. A* **101**, 031601(R) (2020).
- [62] F. Kh. Abdullaev, M. S. A. Hadi, M. Salerno, and B. A. Umarov, *J. Phys. B* **50**, 165301 (2017).
- [63] Z. Li and L.-M. Kuang, *Quantum Inf. Process* **19**, 188 (2020).
- [64] S. I. Mistakidis, L. Hilbig, and P. Schmelcher, *Phys. Rev. A* **100**, 023620 (2019).
- [65] L. Cao, S. Krönke, O. Vendrell, and P. Schmelcher, *J. Chem. Phys.* **139**, 134103 (2013).
- [66] S. Krönke, L. Cao, O. Vendrell, and P. Schmelcher, *New J. Phys.* **15**, 063018 (2013).
- [67] L. Cao, V. Bolsinger, S. I. Mistakidis, G. M. Koutentakis, S. Krönke, J. Schurer, and P. Schmelcher, *J. Chem. Phys.* **147**, 044106 (2017).
- [68] G. C. Katsimiga, G. M. Koutentakis, S. I. Mistakidis, P. G. Kevrekidis, and P. Schmelcher, *New J. Phys.* **19**, 073004 (2017).
- [69] P. Ao and S. T. Chui, *Phys. Rev. A* **58**, 4836 (1998).
- [70] E. Timmermans, *Phys. Rev. Lett.* **81**, 5718 (1998).
- [71] R. Horodecki, P. Horodecki, M. Horodecki, and K. Horodecki, *Rev. Mod. Phys.* **81**, 865 (2009).
- [72] S. I. Mistakidis, G. C. Katsimiga, P. G. Kevrekidis, and P. Schmelcher, *New J. Phys.* **20**, 043052 (2018).
- [73] J. Frenkel, in *Wave Mechanics*, 1st ed. (Clarendon, Oxford, 1934), pp. 423–428.
- [74] P. A. Dirac, *Proc. Camb. Philos. Soc.* **26**, 376 (1930).
- [75] K. Sakmann, A. I. Streltsov, O. E. Alon, and L. S. Cederbaum, *Phys. Rev. A* **78**, 023615 (2008).
- [76] A. Bergschneider, V. M. Klinkhamer, J. H. Becher, R. Klemt, G. Zürn, P. M. Preiss, and S. Jochim, *Phys. Rev. A* **97**, 063613 (2018).
- [77] G. C. Katsimiga, S. I. Mistakidis, G. M. Koutentakis, P. G. Kevrekidis, and P. Schmelcher, *New J. Phys.* **19**, 123012 (2017).
- [78] M. Naraschewski and R. J. Glauber, *Phys. Rev. A* **59**, 4595 (1999).
- [79] E. Altman, E. Demler, and M. D. Lukin, *Phys. Rev. A* **70**, 013603 (2004).
- [80] L. Mathey, A. Vishwanath, and E. Altman, *Phys. Rev. A* **79**, 013609 (2009).
- [81] P. E. S. Tavares, A. R. Fritsch, G. D. Telles, M. S. Hussein, F. Impens, R. Kaiser, and V. S. Bagnato, *Proc. Natl. Acad. Sci. USA* **114**, 12691 (2017).
- [82] J. Kwasniok, S. I. Mistakidis, and P. Schmelcher, *Phys. Rev. A* **101**, 053619 (2020).
- [83] J. P. Ronzheimer, M. Schreiber, S. Braun, S. S. Hodgman, S. Langer, I. P. McCulloch, F. Heidrich-Meisner, I. Bloch, and U. Schneider, *Phys. Rev. Lett.* **110**, 205301 (2013).
- [84] P. G. Kevrekidis and D. J. Frantzeskakis, [arXiv:1512.06754](https://arxiv.org/abs/1512.06754).
- [85] Th. Busch and J. R. Anglin, *Phys. Rev. Lett.* **87**, 010401 (2001).
- [86] S. Middelkamp, J. Chang, C. Hamner, R. Carretero-González, P. G. Kevrekidis, V. Achilleos, D. Frantzeskakis, P. Schmelcher, and P. Engels, *Phys. Lett. A* **375**, 642 (2011).
- [87] A. Álvarez, J. Cuevas, F. R. Romero, C. Hamner, J. J. Chang, P. Engels, P. G. Kevrekidis, and D. J. Frantzeskakis, *J. Phys. B* **46**, 065302 (2013).
- [88] A. Romero-Ros, G. C. Katsimiga, P. G. Kevrekidis, and P. Schmelcher, *Phys. Rev. A* **100**, 013626 (2019).
- [89] D. Yan, J. J. Chang, C. Hamner, P. G. Kevrekidis, P. Engels, V. Achilleos, D. J. Frantzeskakis, R. Carretero-González, and P. Schmelcher, *Phys. Rev. A* **84**, 053630 (2011).
- [90] G. C. Katsimiga, J. Stockhofe, P. G. Kevrekidis, and P. Schmelcher, *Phys. Rev. A* **95**, 013621 (2017).
- [91] J. Dziarmaga, Z. P. Karkuszewski, and K. Sacha, *J. Phys. B* **36**, 1217 (2003).
- [92] D. Delande and K. Sacha, *Phys. Rev. Lett.* **112**, 040402 (2014).
- [93] J. Dziarmaga and K. Sacha, *Phys. Rev. A* **66**, 043620 (2002).
- [94] J. Dziarmaga, Z. P. Karkuszewski, and K. Sacha, *Phys. Rev. A* **66**, 043615 (2002).
- [95] S. Burger, K. Bongs, S. Dettmer, W. Ertmer, K. Sengstock, A. Sanpera, G. V. Shlyapnikov, and M. Lewenstein, *Phys. Rev. Lett.* **83**, 5198 (1999).
- [96] S. Krönke and P. Schmelcher, *Phys. Rev. A* **91**, 053614 (2015).
- [97] F. Theel, K. Keiler, S. I. Mistakidis, and P. Schmelcher, *New J. Phys.* **22**, 023027 (2020).
- [98] I. Ferrier-Barbut, M. Delehaye, S. Laurent, A. T. Grier, M. Pierce, B. S. Rem, F. Chevy, and C. Salomon, *Science* **345**, 1035 (2014).
- [99] F. Sherson, C. Weitenberg, M. Endres, M. Cheneau, I. Bloch, and S. Kuhr, *Nature (London)* **467**, 68 (2010).
- [100] J. Erdmann, S. I. Mistakidis, and P. Schmelcher, *Phys. Rev. A* **99**, 013605 (2019).
- [101] H. Kiehn, S. I. Mistakidis, G. C. Katsimiga, and P. Schmelcher, *Phys. Rev. A* **100**, 023613 (2019).
- [102] K. Mukherjee, S. I. Mistakidis, S. Majumder, and P. Schmelcher, *Phys. Rev. A* **102**, 053317 (2020).



## Chapter 5

# Conclusions and Outlook

he present cumulative thesis dealt with the correlated dynamics of few atoms in the ultracold regime by considering time-dependent protocols such as quenches or modulations of the interaction strengths. First, we have employed two- and three atom setups trapped in harmonic oscillators, and utilized the available analytical solutions to obtain further insights about their dynamical response. Second, the correlated dynamics of few interacting impurities embedded in a mesoscopic cold bosonic environment has been investigated, induced by the driving of the impurity-medium interaction strength. In this section we briefly summarize the main findings of the above investigations and outline interesting future perspectives.

### Correlations and dynamical response of few-body trapped systems

The stationary properties of two trapped ultracold atoms in two dimensions have been thoroughly examined in [B1, B2]. In particular we have provided analytical expressions for the short-range two-body correlations for all eigenstates and interaction strengths. Moreover, by tightly confining the atoms along a single dimension, we were able to probe the not so explored crossover from two dimensions to one [408]. Analytical expressions were derived for the relative wavefunctions in real and momentum space. We have also determined the energy level structure over a wide range of the aspect ratios between the trapping frequencies.

Subsequently, these analytical solutions were employed to track the correlated dynamics of two particles in a harmonic trap in two dimensions, by considering interaction quenches. In three dimensions [245], but mostly in one [244, 376], the response of two particles to such protocols has been explored extensively. In two dimensions however, their out-of-equilibrium dynamics has not been so far studied, despite the inherent differences with other dimensionalities, such as the existence of a two-body bound state regardless of the interaction. Indeed, by inspecting the post-quench populations we have observed a significant contribution of the two-body bound state for quenches from the repulsive to the attractive regime and vice versa. Signatures of this state have also been unveiled by the evolution of the two-body contact, which exhibited an oscillatory behavior with a plethora of frequencies present in the Fourier spectra analysis. Overall, it was found that the system of two atoms was efficiently driven out-of-equilibrium by initializing it in the two-body bound state compared to other initializations such as the ground atom-atom eigenstate. Moreover, the setup exhibited an enhanced dynamical response when considering quenches from finite interaction strengths, either repulsive or attractive, towards the vicinity of zero interactions.

The same response was also observed when considering interaction quenches of two particles confined in an anisotropic two dimensional harmonic oscillator. The system was perturbed the most for small trapping frequency aspect ratio, i.e. close to an isotropic two dimensional harmonic oscillator. This occurred independently of

the post-quench interaction strength. For larger trapping frequency aspect ratio, i.e. close to the one dimensional case, the dynamics along the strongly confined dimension was essentially frozen. Such behavior was clearly illustrated in the evolution of the one-body reduced density, which exhibited a breathing pattern only along the weakly confined direction.

An intriguing extension of the quench dynamics of two ultracold atoms would be to consider particles possessing long range interactions, such as dipole-dipole interactions. Ultracold dipolar gases are being currently explored [409–413] and the competition between the dipolar and the  $s$ -wave scattering length results in a rich phase diagram [414–416]. In the two atom level, the energy spectrum in a trap is far more rich than considering solely short-range interactions [417]. A multitude of two-body bound states appears, displaying avoided crossings with atom-atom eigenstates, reminiscent of the three particle energy structure. Moreover, recently there was an extension of the two-body contact for dipolar interactions [418], and a set of new universal relations was derived. These involved a generalized form of the two-body contact, but also a new one associated to the dipolar length. Exploring the dynamical behavior of these generalized contacts for two dipoles following an interaction quench is an interesting research path. The time evolution of the contacts could reveal dynamical regimes where two-body bound states with a long range character are efficiently populated.

Another promising research path would be to investigate the recently explored two dimensional breathers in box potentials [419–422] from a few-body perspective. The two atoms are initialized such that their density obtains a triangular or circular shape, enforced by a box potential. Subsequently, the latter is turned off and the atoms perform breathing dynamics in a loose harmonic trap in two dimensions. It would certainly be interesting to explore whether the dynamical breathing symmetry persists or not on the two-body level.

Extending our analysis of two cold particles, we have then considered three-body binary mixtures confined in two dimensional harmonic traps [B3]. The mixtures consist of either two bosonic particles or two spin polarized fermions, interacting with a third distinguishable one. We have examined their short-range two- and three-body correlation properties for a wide range of interspecies scattering lengths and for all classes of eigenstates. In order to do so, we have developed a theoretical framework for examining the three-body contact in trapped three-particle binary mixtures at any interaction strength in two dimensions. This is an extension of the usual description of the three-body contact, relying on the Faddeev components formalism in free space [302, 303].

It is found that the contacts of atom-dimer and atom-atom-atom eigenstates display an oscillatory behavior with respect to the interspecies scattering length. This behavior is attributed to the avoided crossings present in the energy spectra, where atom-dimers are converted to atom-atom-atom eigenstates and vice versa. These two types of states feature different correlation properties. Atom-dimers exhibit larger values of two- and three-body contacts compared to atom-atom-atom eigenstates, due to the strongly correlated nature of the dimer. In the vicinity of an avoided crossing these differences are manifested as a sharp increase or decrease of the contacts, induced by transitions among these two classes of eigenstates as one tunes the interspecies scattering length. This behavior holds independently of the statistics of the identical particles or the mass ratio with respect to the third distinguishable atom.

At the limit of small interspecies scattering lengths we are able to derive analytical expressions for the two-body contact of atom-dimers. These expressions stem from the separation of the three-body wavefunction into a part treating the strongly bound dimers, and another one taking into account the third atom. These analytical limits

provide an upper bound for the two-body contact of atom-dimers. For large inverse scattering lengths the contacts of all of these states saturate the bound. Larger values of the two-body contact than these limits correspond to three-body bound states, exhibiting enhanced two-body correlations. Turning to the three-body contact of atom-dimers, such an upper bound is absent. At small interspecies scattering lengths, the atom-dimers lying energetically close to the atom-dimer threshold feature stronger three-body contacts compared to atom-dimers further away from the threshold. The strongest three-body correlations are displayed by trimers, and this occurs for any interspecies scattering length.

As mentioned in Sec. 2.4.2, the two dimensional three-body contact does not satisfy any universal relation, in stark contrast to the three dimensional one. As an extension of our theoretical treatment of short-range three-body correlations in two dimensions, we could further explore the asymptotic expansion of the one-body density in momentum space from where the three-body contact is defined. For instance, an expression could be derived relating the number of trimers in a gas to the three-body contact, in analogy to the already existing formulas in three dimensions [123, 423]. The fact that there is no need to introduce any additional length scale to describe three-body physics in two dimensions, could lead to a formula that depends only on a few parameters, such as the three-body contact and the two dimensional scattering length.

Having at hand the correlation properties of trapped three-body binary mixtures, we set on to investigate their out-of-equilibrium dynamics by quenching the interspecies scattering lengths [B4]. The few-body setups are initialized in a non-interacting eigenstate with a variable spatial extent. An interaction quench is performed subsequently, and the system evolves in a two dimensional harmonic trap. Its dynamical response is evaluated for spatial extents smaller or larger than the three-body harmonic oscillator length. It is found that when the initial extent is smaller than the oscillator length, a superposition of trimers and atom-dimers is dynamically generated. These states are identified both from the overlap coefficients of the initial with the final state, and the Fourier spectra of the fidelity. For initial widths larger than the oscillator length, mostly atom-atom-atom eigenstates are contributing in the quench dynamics. This behavior is independent of the quantum statistics of the mixture.

This selective excitation process relies on the following observation. The three classes of three-body eigenstates possess distinct spatial extents. The width of atom-atom-atom states is essentially of the order of the oscillator length. In contrast, trimers and atom-dimers are localized to much smaller distances, due to their bound state characteristics. By tuning the spatial extent of the initial three-body wavefunction, we maximize the overlap of the initial state with certain classes of eigenstates, hence the observed superpositions.

The signatures of few-body bound states are readily appreciated by the evolution of the contacts. For small initial spatial widths, the latter are substantially enhanced in comparison to the other scenario. For spatial extents larger than the oscillator length, the contacts feature a peak structure with respect to the post-quench inverse interspecies scattering lengths. At certain values of the latter, the time-evolved contacts acquire very large values, and subsequently decrease as the inverse scattering lengths are tuned further away. This enhancement stems from the participation of atom-dimers in the vicinity of avoided crossings. In these regions, the predominantly populated atom-atom-atom eigenstates change character, transitioning to atom-dimers. The latter as we know already from [B3] exhibit greater two-body short-range correlations compared to the other eigenstate type. The peaked structure of the contacts is therefore an indication of the contribution of atom-dimers in the dynamics.

As discussed earlier, this selective dynamical excitation process is similar for both identical bosonic and fermionic particles. Differences however occur when considering different mass ratio between the identical atoms and the distinguishable one. For heavy identical particles, atom-atom-atom eigenstates are also populated when the initial spatial extent is smaller than the oscillator length. Moreover, the peaks in the contacts with respect to the scattering lengths are more sharp compared to the case of light identical atoms. This discrepancy can be traced back to the different energy structure around the avoided crossings [B3]. For heavy bosons or fermions, the avoided crossings between atom-dimers and atom-atom-atom eigenstates are sharper compared to the case of light identical particles.

By varying the initial spatial extent of the three-body wavefunction, we were able to selectively excite distinct classes of eigenstates, such as trimers or atom-atom-atom eigenstates. In all scenarios however, a superposition of eigenstates belonging to a certain class was dynamically generated. In [424] selective eigenstates of a three-body binary mixture trapped in one dimension were dynamically populated with high fidelity by considering time-dependent interaction strengths. This process relied on shortcut-to-adiabaticity protocols [425–430] for driving the interaction strengths such that the final target state is reached. Employing such protocols could help us populate specific few-body bound eigenstates for our two dimensional three-body binary mixtures.

Time-dependent protocols of interaction strengths were very successful in creating a coherent superposition of the first excited Efimov trimer with atom-dimers in three dimensional thermal gases with repulsive interactions [118, 119]. Such superposition was achieved by considering a sequence of modulated magnetic fields (pulses) delayed by a variable free evolution time (dark time), in analogy to the Ramsey scheme. The binding energy of the Efimov trimer was measured with high precision from the particle loss signal, which displayed interference fringes. Moreover, the signal displayed a decay, that could not be properly identified. In [B5] we solve the time-dependent three boson problem in a trap to provide insights about the association and decay mechanisms of the aforementioned dynamical protocol.

We start our analysis by investigating solely the impact of thermal effects. By inspecting the scaled probability to populate Efimov trimers at the end of the second magnetic field pulse, two regimes can be identified. The first one occurs at early dark times, where high amplitude high frequency oscillations are observed. The Fourier analysis reveals a single dominant frequency matching the energy difference of the first excited Efimov trimer and the first atom-atom-atom eigenstate. The frequency is robust against high temperatures. At later dark times the amplitude of oscillations drastically drops, and the decay is assigned to the temperature of the system. The Fourier spectra however now reveal three prevailing frequencies. The highest one corresponds to the one identified in the early dark time regime. The other two stem from the energy gap between the first atom-atom-atom eigenstate and first atom-dimer, and between the latter and the Efimov trimer. The frequency between such two states was measured in the experimental works for  $^7\text{Li}$  thermal gases [118, 119]. In addition to that we find that higher frequencies involving the first atom-atom-atom eigenstate also persist despite thermal effects.

We now set to investigate the role of the decay width of the Efimov state. In order to accurately assess it within the zero-range model, we park at a large scattering (positive) scattering length. The width is taken into account only during the dark time because the length of the pulses is shorter than the lifetime of the Efimov trimers. It is found that the signal stemming from the probability to occupy Efimov trimers possesses two distinct decay widths. At early dark times, the oscillatory signal decays

according to the inherent decay width of the Efimov trimer. At later dark times however, the signal has a characteristic decay time, being twice as long as the Efimov lifetime. This behavior originates from the coherent superposition of the Efimov trimer with the first atom-dimer and atom-atom-atom eigenstate. The decay widths of the two latter eigenstates are at least one order of magnitude smaller than the one of the trimer and can be safely neglected. The identified factor of two in the decay width sets a new perspective on the decay mechanisms reported in [118].

Moreover, we extend the dynamical protocol to associate Efimov trimers at attractive interactions as well. Despite the absence of atom-dimers, the first atom-atom-atom eigenstate is sufficient for creating a coherent superposition of the latter with the Efimov trimer. As expected, this single superposition manifests in a single dominant frequency in the frequency spectrum. Similarly to the case of repulsive interactions, the oscillatory signal of the trimer probability at later dark times possesses a decay time twice as long as the lifetime of the Efimov state.

Overall, the results stemming from the time-dependent three-body problem with modulated interactions lead to two conclusions. First, that the Efimov trimer is indeed associated by the protocol for all interaction strengths despite thermal effects. Second, that the manifested interference fringes of the Efimov trimer probability possess a decay time which is twice as long as the lifetime of the Efimov trimer. Therefore, apart from the binding energy, the lifetime of the trimer can also be assessed.

Our work sets new perspectives for assessing the properties of Efimov trimers in a precise way. The dynamical protocol with modulated magnetic fields can be employed to measure the binding energy and lifetime of Efimov trimers at all interaction strengths. It can be especially utilized in the attractive regime, providing high precision tests of the Efimov universality [112, 431–433]. The latter refers to the observation, and later theoretical vindication [434–436], that the negative scattering length at which the ground Efimov state dissociates, depends solely on the van der Waals length, and not on the interaction characteristics of the considered species.

Moreover, the shape of the pulses employed in the dynamical protocol can be optimized so that a higher population of associated Efimov trimers can be achieved, compared to the one reported in [118], or even in the experiment employing quenches to strong interactions [79]. In that regard, one could generate a gas with a macroscopic fraction of Efimov trimers at finite negative or positive scattering lengths, without the additional complications arising from a strongly interacting quantum gas. Apart from observing trimers, one could investigate the possibility of creating dressed Efimov states. This could be achieved by driving the interactions sinusoidally, resulting in dressing of their properties, such as the lifetime. Such prospect could lead to long-lived dressed Efimov trimers, bypassing the problem of strong losses due to their inherently short lifetimes. Signatures of dressing and lifetime modification have already been observed in mass imbalanced settings [437].

### Dynamics of few particles in a many-body environment

Turning to the problem of interacting impurities in a many-body environment, we have investigated their correlated dynamics upon modulating the interspecies interactions. We have considered 10 impurities in a mesoscopic medium, consisting of 100 bosons, all of the setups trapped in a one dimensional harmonic oscillator. We have examined two scenarios, one in which the system lies initially in its miscible phase and is driven to the immiscible phase, and one where the reverse transition takes place. In all cases, it is found that when the interspecies interaction is driven with a smaller frequency compared to the trapping one, the system goes through a sequence of dynamical

transitions from the miscible to the immiscible phase and vice versa. The frequency of these transitions matches the driving frequency. However, when the latter is larger than the trapping frequency, the initial condition plays a major role.

When the system is initialized in its miscible phase, a significant fraction of impurities is expelled from the medium, performing small amplitude oscillations at the edges of the bosonic cloud. The remaining impurities are simultaneously localized at the trap center with a considerable probability. To better grasp their behavior, an effective potential is constructed, taking into account the trapping one, and the instantaneous density of the majority species weighted with the interspecies interaction. We see that during the time evolution the impurities reside mostly at the three lowest eigenstates. To evaluate the degree of correlations, we have also determined the dynamics of the impurities within a strict mean-field approximation. It is found that pairs of dark-bright solitons are formed. After a quarter of an oscillation period, the two pairs merge at the trap center, in a single solitonic bound state.

When the system lies initially in its immiscible phase, a breathing motion of the impurities is observed. Employing the effective potential once again, we can reproduce the breathing frequency of that motion to a very good extent. The bath also performs a breathing movement, but most importantly, two small symmetric dips develop in the vicinity of the trap center. These structures separate the bath into two disjoint regions, where one-body coherence is lost, meaning that one particle is localized on either sides of these regions. In the absence of correlations, pairs of dark-bright solitons form similarly to the opposite driving scenario. The difference is that the pairs perform a breathing motion of much smaller period and do not merge at the trap center, even at very large evolution times. The breathing frequency lies very close to the theoretical prediction for such pairs of solitonic structures confined in a trap.

Subsequently, we study the effect of the impurity number as well as their intraspecies interactions in their dynamical behavior. For two non-interacting impurities we observe that they mainly reside at the trap center throughout the entire time evolution, regardless of the initialization protocol. This is the case even for 10 non-interacting impurities. Only by increasing the intraspecies repulsion do we start discerning differences between the two initializations. In particular, when the system lies initially in its miscible phase, signatures of the expelled impurities at the edges of the bosonic cloud appear in their one-body reduced density. For the inverse initialization, the breathing motion of the impurities becomes visible upon increasing their intraspecies repulsion.

Considering binary ultracold mixtures, there is a challenging regime where the interspecies attraction is slightly dominating over the intraspecies repulsion. From a mean-field perspective, the binary mixture is unstable due to the net attraction, and the whole system collapses [47, 438, 439]. Quantum fluctuations however arrest this collapse from happening, and the binary mixture forms a quantum droplet. One of the main tell-tale signatures of droplet formation is the flat-top profile appearing in the one-body density. A challenging yet exciting direction is to investigate the dynamics of these quantum droplets in low dimensions. In two dimensions for instance, one can study whether embedding soliton stripes on top of the quantum droplet will result in the so-called snake instability [440–444]. This is the process of vortex pair formation, each with opposite circulation. Furthermore, the recent realization of dipolar binary mixtures [445, 446] sets the stage for exploring novel aspects of quantum droplets [447], this time occurring due to the competition of the dipolar and the scattering length.



## *Acknowledgements*

This has been a long journey with an equal share of good and bad times, lots of thrill and excitement, frustration and disappointment. The majority of the (scientific related) things I learned during this process ended up in this thesis, finalizing an episode of this journey. Even though it seems like the effort of a single man, this is far from the truth. There are a lot of people who did their own part, large or small, in having this thesis printed in black and white (or color), whom I would like to thank here in this section.

First and foremost I would like to thank my supervisor, Peter, for providing the means to expand my knowledge, investigate all of these beautiful topics, participate in conferences, and work in a pleasant environment. I am grateful for his advice, his feedback and his trust. I would like to thank Simos for his guidance, support throughout the years, his patience in focusing my scattered efforts, and setting an example on how to pursue scientific ideas. I am also very grateful for giving me the opportunity to even continue this journey. I would like also to thank Panos for his support, trust, knowledge, and for teaching me the importance of concise and consistent argumentation. I am grateful for his constant flow of ideas, and his willingness and patience to explain any topic. I would also like to thank my professors, who even though didn't have an active say in my Ph.D., had a significant contribution in the prior formative years. I would like to thank my professors in the University of Athens, Prof. Fotis Diakonou and Alexandros Karanikas for planting the seeds of curiosity, and being sources of motivation. Special thanks go also to my professors from my masters, DDR Christos Charmousis and Prof. Marios Petropoulos for their support and advice. I would like to thank Prof. Chris Greene for the discussions and the nice collaboration that we had. I am also grateful to Prof. Hossein Sadeghpour for the discussions and for hosting me twice at ITAMP. Special thanks go to Dr. Christoph Becker, Dr. Benjamin Abeln for the fruitful conversations. I am grateful for having had the opportunity to work together with Ghadah, Lydia, Jan, William, Henryk, and having learned new things with them.

I want to express my gratitude to my friends and colleagues in the office, Giorgis, Alexandra, Lia, Simos, Christian M., Ilias, Fanis, Dimitris, Zeki, Koushik, Rohan, Kapil, Friethjof, Frederic, Alejandro, Rick, Maxim, Kevin, Malte, Fabian, Jie, Aritra, Iqra, Christian F., Jenny, Andrea, Ansgar, Felipe, Dan, André, Judith, Samir, Antonio, for providing a very nice working environment, having fun in and out of office, exchanging ideas and thoughts. Special thanks go to Anja, for consistently slaying the bureaucratic Leviathan.

I would also like to thank José, partner in crime in drilling holes in the wall and disentangling resistors during the praktikum move. I am grateful to Giorgos for teaming up in kicker and constantly beating Ilias and Fanis. I am also grateful to Torsten, Gundolf, Hans-Christoff, and the whole DESY table tennis team for teaching me the importance of consistently losing, yet persisting. I am grateful to Herr Michael for all the german courses. Special thanks go to Marion and her cat, Catzalcoatl, for the hospitality in Boston.

I am very grateful to Eugenia for her love, support, and all the lessons that we learned together. I would like to thank Nicolas, Sebastian, Tuan, Melih, Javier for the reunion. I am also very grateful to Manos, Alexandros, Emmanouela, Dimitris, Mitsos, Antonis, Elisavet for their friendship, the time spent together, and for always helping me consider things from a different perspective.

Finally, but most importantly, I would like to thank my parents for their love, support, guidance, and for always setting an example through their actions. I am

grateful that they always stand by me no matter what, and that they have provided me with the tools to stand up in this crazy world.

# Bibliography

- [1] C. Cohen-Tannoudji and D. Guéry-Odelin, *Advances in atomic physics: an overview* (World Scientific, 2011).
- [2] R. Grimm, M. Weidemüller, and Y. B. Ovchinnikov, in *Advances in atomic, molecular, and optical physics*, Vol. 42 (Elsevier, 2000), pp. 95–170.
- [3] C. E. Wieman, D. E. Pritchard, and D. J. Wineland, “Atom cooling, trapping, and quantum manipulation”, *Rev. Mod. Phys.* **71**, S253 (1999).
- [4] W. D. Phillips, “Nobel lecture: laser cooling and trapping of neutral atoms”, *Rev. Mod. Phys.* **70**, 721 (1998).
- [5] C. J. Foot, “Laser cooling and trapping of atoms”, *Contemporary Physics* **32**, 369 (1991).
- [6] H. J. Metcalf and P. van der Straten, “Laser cooling and trapping of atoms”, *J. Opt. Soc. Am. B* **20**, 887 (2003).
- [7] M. H. Anderson, J. R. Ensher, M. R. Matthews, C. E. Wieman, and E. A. Cornell, “Observation of bose-einstein condensation in a dilute atomic vapor”, *Science* **269**, 198 (1995).
- [8] K. B. Davis, M. -O. Mewes, M. R. Andrews, N. J. van Druten, D. S. Durfee, D. M. Kurn, and W. Ketterle, “Bose-einstein condensation in a gas of sodium atoms”, *Phys. Rev. Lett.* **75**, 3969 (1995).
- [9] B. DeMarco and D. S. Jin, “Onset of fermi degeneracy in a trapped atomic gas”, *Science* **285**, 1703 (1999).
- [10] G. Roati, F. Riboli, G. Modugno, and M. Inguscio, “Fermi-bose quantum degenerate  $^{40}\text{K}$ - $^{87}\text{Rb}$  mixture with attractive interaction”, *Phys. Rev. Lett.* **89**, 150403 (2002).
- [11] A. G. Truscott, K. E. Strecker, W. I. McAlexander, G. B. Partridge, and R. G. Hulet, “Observation of fermi pressure in a gas of trapped atoms”, *Science* **291**, 2570 (2001).
- [12] C. J. Pethick and H. Smith, *Bose-einstein condensation in dilute gases*, 2nd ed. (Cambridge University Press, 2008).
- [13] L. Pitaevskii and S. Stringari, *Bose-Einstein Condensation and Superfluidity* (Oxford University Press, Jan. 2016).
- [14] W. Ketterle and M. W. Zwierlein, “Making, probing and understanding ultracold fermi gases”, *La Rivista del Nuovo Cimento* **31**, 247 (2008).
- [15] C. Chin, R. Grimm, P. Julienne, and E. Tiesinga, “Feshbach resonances in ultracold gases”, *Rev. Mod. Phys.* **82**, 1225 (2010).
- [16] S. Inouye, M. R. Andrews, J. Stenger, H.-J. Miesner, D. M. Stamper-Kurn, and W. Ketterle, “Observation of feshbach resonances in a bose-einstein condensate”, *Nature* **392**, 151 (1998).

- [17] T. Loftus, C. A. Regal, C. Ticknor, J. L. Bohn, and D. S. Jin, “Resonant control of elastic collisions in an optically trapped fermi gas of atoms”, *Phys. Rev. Lett.* **88**, 173201 (2002).
- [18] P. Makotyn, C. E. Klauss, D. L. Goldberger, E. A. Cornell, and D. S. Jin, “Universal dynamics of a degenerate unitary Bose gas”, en, *Nature Phys* **10**, 116 (2014).
- [19] T. Bourdel, L. Khaykovich, J. Cubizolles, J. Zhang, F. Chevy, M. Teichmann, L. Tarruell, S. J. J. M. F. Kokkelmans, and C. Salomon, “Experimental study of the bec-bcs crossover region in lithium 6”, *Phys. Rev. Lett.* **93**, 050401 (2004).
- [20] K. M. O’Hara, S. L. Hemmer, M. E. Gehm, S. R. Granade, and J. E. Thomas, “Observation of a strongly interacting degenerate fermi gas of atoms”, *Science* **298**, 2179 (2002).
- [21] R. J. Fletcher, A. L. Gaunt, N. Navon, R. P. Smith, and Z. Hadzibabic, “Stability of a unitary bose gas”, *Phys. Rev. Lett.* **111**, 125303 (2013).
- [22] U. Eismann, L. Khaykovich, S. Laurent, I. Ferrier-Barbut, B. S. Rem, A. T. Grier, M. Delehaye, F. Chevy, C. Salomon, L.-C. Ha, and C. Chin, “Universal loss dynamics in a unitary bose gas”, *Phys. Rev. X* **6**, 021025 (2016).
- [23] B. S. Rem, A. T. Grier, I. Ferrier-Barbut, U. Eismann, T. Langen, N. Navon, L. Khaykovich, F. Werner, D. S. Petrov, F. Chevy, and C. Salomon, “Lifetime of the Bose Gas with Resonant Interactions”, *Phys. Rev. Lett.* **110**, 163202 (2013).
- [24] M. Lewenstein, A. Sanpera, V. Ahufinger, B. Damski, A. Sen(De), and U. Sen, “Ultracold atomic gases in optical lattices: mimicking condensed matter physics and beyond”, *Advances in Physics* **56**, 243 (2007).
- [25] M. Greiner, I. Bloch, O. Mandel, T. W. Hänsch, and T. Esslinger, “Exploring phase coherence in a 2d lattice of bose-einstein condensates”, *Phys. Rev. Lett.* **87**, 160405 (2001).
- [26] I. Bloch, “Ultracold quantum gases in optical lattices”, *Nature Phys.* **1**, 23 (2005).
- [27] I. Bloch, J. Dalibard, and W. Zwerger, “Many-body physics with ultracold gases”, *Rev. Mod. Phys.* **80**, 885 (2008).
- [28] Z. Hadzibabic and J. Dalibard, “Two-dimensional Bose fluids: An atomic physics perspective”, en, *Riv. Nuovo Cim.* **34**, 389 (2011).
- [29] D. Petrov, D. M. Gangardt, and G. V. Shlyapnikov, “Low-dimensional trapped gases”, in *Journal de physique iv (proceedings)*, Vol. 116 (EDP sciences, 2004), pp. 5–44.
- [30] Z. Hadzibabic, P. Krüger, M. Cheneau, B. Battelier, and J. Dalibard, “Berezinskii–kosterlitz–thouless crossover in a trapped atomic gas”, *Nature* **441**, 1118 (2006).
- [31] B. Paredes, A. Widera, V. Murg, O. Mandel, S. Fölling, I. Cirac, G. V. Shlyapnikov, T. W. Hänsch, and I. Bloch, “Tonks–girardeau gas of ultracold atoms in an optical lattice”, *Nature* **429**, 277 (2004).
- [32] E. Haller, M. Gustavsson, M. J. Mark, J. G. Danzl, R. Hart, G. Pupillo, and H.-C. Nägerl, “Realization of an excited, strongly correlated quantum gas phase”, *Science* **325**, 1224 (2009).
- [33] G. Modugno, M. Modugno, F. Riboli, G. Roati, and M. Inguscio, “Two atomic species superfluid”, *Phys. Rev. Lett.* **89**, 190404 (2002).

- [34] C. J. Myatt, E. A. Burt, R. W. Ghrist, E. A. Cornell, and C. E. Wieman, “Production of two overlapping bose-einstein condensates by sympathetic cooling”, *Phys. Rev. Lett.* **78**, 586 (1997).
- [35] M. Egorov, B. Opanchuk, P. Drummond, B. V. Hall, P. Hannaford, and A. I. Sidorov, “Measurement of  $s$ -wave scattering lengths in a two-component bose-einstein condensate”, *Phys. Rev. A* **87**, 053614 (2013).
- [36] K. Pilch, A. D. Lange, A. Prantner, G. Kerner, F. Ferlaino, H.-C. Nägerl, and R. Grimm, “Observation of interspecies feshbach resonances in an ultracold rb-cs mixture”, *Phys. Rev. A* **79**, 042718 (2009).
- [37] A. Burchianti, C. D’Errico, S. Rosi, A. Simoni, M. Modugno, C. Fort, and F. Minardi, “Dual-species bose-einstein condensate of 41K and 87Rb in a hybrid trap”, *Phys. Rev. A* **98**, 063616 (2018).
- [38] P. Ao and S. T. Chui, “Binary bose-einstein condensate mixtures in weakly and strongly segregated phases”, *Phys. Rev. A* **58**, 4836 (1998).
- [39] E. Timmermans, “Phase separation of bose-einstein condensates”, *Phys. Rev. Lett.* **81**, 5718 (1998).
- [40] T. Busch and J. R. Anglin, “Dark-bright solitons in inhomogeneous bose-einstein condensates”, *Phys. Rev. Lett.* **87**, 010401 (2001).
- [41] S. Middelkamp, J. Chang, C. Hamner, R. Carretero-González, P. Kevrekidis, V. Achilleos, D. Frantzeskakis, P. Schmelcher, and P. Engels, “Dynamics of dark-bright solitons in cigar-shaped bose-einstein condensates”, *Phys. Lett. A* **375**, 642 (2011).
- [42] A. Álvarez, J. Cuevas, F. R. Romero, C. Hamner, J. J. Chang, P. Engels, P. G. Kevrekidis, and D. J. Frantzeskakis, “Scattering of atomic dark-bright solitons from narrow impurities”, *J. Phys. B: At., Mol. Opt. Phys.* **46**, 065302 (2013).
- [43] A. Romero-Ros, G. C. Katsimiga, P. G. Kevrekidis, and P. Schmelcher, “Controlled generation of dark-bright soliton complexes in two-component and spinor bose-einstein condensates”, *Phys. Rev. A* **100**, 013626 (2019).
- [44] D. Yan, J. J. Chang, C. Hamner, P. G. Kevrekidis, P. Engels, V. Achilleos, D. J. Frantzeskakis, R. Carretero-González, and P. Schmelcher, “Multiple dark-bright solitons in atomic bose-einstein condensates”, *Phys. Rev. A* **84**, 053630 (2011).
- [45] Z.-H. Luo, W. Pang, B. Liu, Y.-Y. Li, and B. A. Malomed, “A new form of liquid matter: quantum droplets”, *Frontiers of Physics* **16**, 32201 (2020).
- [46] D. S. Petrov, “Quantum mechanical stabilization of a collapsing bose-bose mixture”, *Phys. Rev. Lett.* **115**, 155302 (2015).
- [47] C. R. Cabrera, L. Tanzi, J. Sanz, B. Naylor, P. Thomas, P. Cheiney, and L. Tarruell, “Quantum liquid droplets in a mixture of bose-einstein condensates”, *Science* **359**, 301 (2018).
- [48] G. Semeghini, G. Ferioli, L. Masi, C. Mazzinghi, L. Wolswijk, F. Minardi, M. Modugno, G. Modugno, M. Inguscio, and M. Fattori, “Self-bound quantum droplets of atomic mixtures in free space”, *Phys. Rev. Lett.* **120**, 235301 (2018).
- [49] C. D’Errico, A. Burchianti, M. Prevedelli, L. Salasnich, F. Ancilotto, M. Modugno, F. Minardi, and C. Fort, “Observation of quantum droplets in a heteronuclear bosonic mixture”, *Phys. Rev. Res.* **1**, 033155 (2019).

- [50] F. Böttcher, J.-N. Schmidt, J. Hertkorn, K. S. H. Ng, S. D. Graham, M. Guo, T. Langen, and T. Pfau, “New states of matter with fine-tuned interactions: quantum droplets and dipolar supersolids”, *Reports on Progress in Physics* **84**, 012403 (2020).
- [51] F. Serwane, G. Zürn, T. Lompe, T. B. Ottenstein, A. N. Wenz, and S. Jochim, “Deterministic Preparation of a Tunable Few-Fermion System”, *Science* **332**, 336 (2011).
- [52] A. N. Wenz, G. Zürn, S. Murmann, I. Brouzos, T. Lompe, and S. Jochim, “From few to many: observing the formation of a fermi sea one atom at a time”, *Science* **342**, 457 (2013).
- [53] M. Holten, L. Bayha, K. Subramanian, S. Brandstetter, C. Heintze, P. Lunt, P. M. Preiss, and S. Jochim, “Observation of cooper pairs in a mesoscopic two-dimensional fermi gas”, *Nature* **606**, 287 (2022).
- [54] L. Bayha, M. Holten, R. Klemt, K. Subramanian, J. Bjerlin, S. M. Reimann, G. M. Bruun, P. M. Preiss, and S. Jochim, “Observing the emergence of a quantum phase transition shell by shell”, en, *Nature* **587**, 583 (2020).
- [55] A. M. Kaufman and K.-K. Ni, “Quantum science with optical tweezer arrays of ultracold atoms and molecules”, *Nat. Phys.* **17**, 1324 (2021).
- [56] M. Endres, H. Bernien, A. Keesling, H. Levine, E. R. Anschuetz, A. Krajenbrink, C. Senko, V. Vuletic, M. Greiner, and M. D. Lukin, “Atom-by-atom assembly of defect-free one-dimensional cold atom arrays”, *Science* **354**, 1024 (2016).
- [57] L. R. Liu, J. D. Hood, Y. Yu, J. T. Zhang, N. R. Hutzler, T. Rosenband, and K.-K. Ni, “Building one molecule from a reservoir of two atoms”, *Science* **360**, 900 (2018).
- [58] L. Anderegg, L. W. Cheuk, Y. Bao, S. Burchesky, W. Ketterle, K.-K. Ni, and J. M. Doyle, “An optical tweezer array of ultracold molecules”, *Science* **365**, 1156 (2019).
- [59] L. A. Reynolds, E. Schwartz, U. Ebling, M. Weyland, J. Brand, and M. F. Andersen, “Direct Measurements of Collisional Dynamics in Cold Atom Triads”, *Phys. Rev. Lett.* **124**, 073401 (2020).
- [60] G. Zürn, F. Serwane, T. Lompe, A. N. Wenz, M. G. Ries, J. E. Bohn, and S. Jochim, “Fermionization of two distinguishable fermions”, *Phys. Rev. Lett.* **108**, 075303 (2012).
- [61] Q. Guan, V. Klinkhamer, R. Klemt, J. H. Becher, A. Bergschneider, P. M. Preiss, S. Jochim, and D. Blume, “Density Oscillations Induced by Individual Ultracold Two-Body Collisions”, *Phys. Rev. Lett.* **122**, 083401 (2019).
- [62] T. Stöferle, H. Moritz, K. Günter, M. Köhl, and T. Esslinger, “Molecules of fermionic atoms in an optical lattice”, *Phys. Rev. Lett.* **96**, 030401 (2006).
- [63] Y. Yu, N. R. Hutzler, J. T. Zhang, L. R. Liu, J. D. Hood, T. Rosenband, and K.-K. Ni, “Motional-ground-state cooling outside the lamb-dicke regime”, *Phys. Rev. A* **97**, 063423 (2018).
- [64] A. M. Kaufman, B. J. Lester, and C. A. Regal, “Cooling a single atom in an optical tweezer to its quantum ground state”, *Phys. Rev. X* **2**, 041014 (2012).
- [65] J. D. Thompson, T. G. Tiecke, A. S. Zibrov, V. Vuletić, and M. D. Lukin, “Coherence and raman sideband cooling of a single atom in an optical tweezer”, *Phys. Rev. Lett.* **110**, 133001 (2013).

- [66] C. H. Greene, P. Giannakeas, and J. Pérez-Ríos, “Universal few-body physics and cluster formation”, *Rev. Mod. Phys.* **89**, 035006 (2017).
- [67] W. Zwerger, *The bcs-bec crossover and the unitary fermi gas*, Vol. 836 (Springer Science & Business Media, 2011).
- [68] J. von Stecher and C. H. Greene, “Spectrum and Dynamics of the BCS-BEC Crossover from a Few-Body Perspective”, *Phys. Rev. Lett.* **99**, 090402 (2007).
- [69] T. Busch, B.-G. Englert, K. Rzazewski, and M. Wilkens, “Two cold atoms in a harmonic trap”, *Foundations of Physics* **28**, 549 (1998).
- [70] Z. Idziaszek and T. Calarco, “Analytical solutions for the dynamics of two trapped interacting ultracold atoms”, *Phys. Rev. A* **74**, 022712 (2006).
- [71] N. T. Zinner, “Universal two-body spectra of ultracold harmonically trapped atoms in two and three dimensions”, *Journal of Physics A: Mathematical and Theoretical* **45**, 205302 (2012).
- [72] F. Werner and Y. Castin, “Unitary Quantum Three-Body Problem in a Harmonic Trap”, *Phys. Rev. Lett.* **97**, 150401 (2006).
- [73] T. Sowiński and M. Á. García-March, “One-dimensional mixtures of several ultracold atoms: a review”, *Reports on Progress in Physics* **82**, 104401 (2019).
- [74] S. I. Mistakidis, A. G. Volosniev, R. E. Barfknecht, T. Fogarty, T. Busch, A. Foerster, P. Schmelcher, and N. T. Zinner, *Cold atoms in low dimensions – a laboratory for quantum dynamics*, 2022.
- [75] P. Naidon and S. Endo, “Efimov physics: a review”, *Rep. Prog. Phys.* **80**, 056001 (2017).
- [76] Z. Idziaszek and T. Calarco, “Two atoms in an anisotropic harmonic trap”, *Phys. Rev. A* **71**, 050701 (2005).
- [77] M. Köhl, K. Günter, T. Stöferle, H. Moritz, and T. Esslinger, “Strongly interacting atoms and molecules in a 3d optical lattice”, *J. Phys. B: At., Mol. and Opt. Phys.* **39**, S47 (2006).
- [78] F. Deuretzbacher, K. Plassmeier, D. Pfannkuche, F. Werner, C. Ospelkaus, S. Ospelkaus, K. Sengstock, and K. Bongs, “Heteronuclear molecules in an optical lattice: theory and experiment”, *Phys. Rev. A* **77**, 032726 (2008).
- [79] C. E. Klauss, X. Xie, C. Lopez-Abadia, J. P. D’Incao, Z. Hadzibabic, D. S. Jin, and E. A. Cornell, “Observation of Efimov Molecules Created from a Resonantly Interacting Bose Gas”, *Phys. Rev. Lett.* **119**, 143401 (2017).
- [80] R. Schmitz, S. Krönke, L. Cao, and P. Schmelcher, “Quantum breathing dynamics of ultracold bosons in one-dimensional harmonic traps: unraveling the pathway from few- to many-body systems”, *Phys. Rev. A* **88**, 043601 (2013).
- [81] X. Y. Yin, H. Hu, and X.-J. Liu, “Few-body perspective of a quantum anomaly in two-dimensional fermi gases”, *Phys. Rev. Lett.* **124**, 013401 (2020).
- [82] S. I. Mistakidis, A. G. Volosniev, and P. Schmelcher, “Induced correlations between impurities in a one-dimensional quenched bose gas”, *Phys. Rev. Res.* **2**, 023154 (2020).
- [244] L. Budewig, S. I. Mistakidis, and P. Schmelcher, “Quench dynamics of two one-dimensional harmonically trapped bosons bridging attraction and repulsion”, *Molecular Physics* **117**, 2043 (2019).
- [245] A. D. Kerin and A. M. Martin, “Two-body quench dynamics of harmonically trapped interacting particles”, *Phys. Rev. A* **102**, 023311 (2020).

- [83] A. Galea, T. Zielinski, S. Gandolfi, and A. Gezerlis, “Fermions in two dimensions: scattering and many-body properties”, *Journal of Low Temperature Physics* **189**, 451 (2017).
- [84] M. A. Cirone, K. Rzazewski, W. P. Schleich, F. Straub, and J. Wheeler, “Quantum anticentrifugal force”, *Phys. Rev. A* **65**, 022101 (2001).
- [85] J. P. D’Incao, F. Anis, and B. D. Esry, “Ultracold three-body recombination in two dimensions”, *Phys. Rev. A* **91**, 062710 (2015).
- [86] J. Levinsen, P. Massignan, and M. M. Parish, “Efimov Trimers under Strong Confinement”, *Phys. Rev. X* **4**, 031020 (2014).
- [87] T. Köhler, K. Góral, and P. S. Julienne, “Production of cold molecules via magnetically tunable Feshbach resonances”, *Rev. Mod. Phys.* **78**, 1311 (2006).
- [88] K. Góral, T. Köhler, S. A. Gardiner, E. Tiesinga, and P. S. Julienne, “Adiabatic association of ultracold molecules via magnetic-field tunable interactions”, *J. Phys. B: At., Mol. and Opt. Phys.* **37**, 3457 (2004).
- [89] J. Herbig, T. Kraemer, M. Mark, T. Weber, C. Chin, H.-C. Nägerl, and R. Grimm, “Preparation of a pure molecular quantum gas”, *Science* **301**, 1510 (2003).
- [90] C. A. Regal, C. Ticknor, J. L. Bohn, and D. S. Jin, “Creation of ultracold molecules from a fermi gas of atoms”, *Nature* **424**, 47 (2003).
- [91] K. E. Strecker, G. B. Partridge, and R. G. Hulet, “Conversion of an atomic fermi gas to a long-lived molecular bose gas”, *Phys. Rev. Lett.* **91**, 080406 (2003).
- [92] S. Dürr, T. Volz, A. Marte, and G. Rempe, “Observation of molecules produced from a bose-einstein condensate”, *Phys. Rev. Lett.* **92**, 020406 (2004).
- [93] R. Elbaz, Y. Yudkin, P. Giannakeas, J.-M. Rost, C. H. Greene, and L. Khaykovich, “Observation of coherent oscillations in the association of dimers from a thermal gas of ultracold atoms”, *Phys. Rev. A* **107**, L031304 (2023).
- [94] N. R. Claussen, S. J. J. M. F. Kokkelmans, S. T. Thompson, E. A. Donley, E. Hodby, and C. E. Wieman, “Very-high-precision bound-state spectroscopy near a  $^{85}\text{Rb}$  Feshbach resonance”, *Phys. Rev. A* **67**, 060701 (2003).
- [95] S. T. Thompson, E. Hodby, and C. E. Wieman, “Ultracold molecule production via a resonant oscillating magnetic field”, *Phys. Rev. Lett.* **95**, 190404 (2005).
- [96] E. A. Donley, N. R. Claussen, S. T. Thompson, and C. E. Wieman, “Atom–molecule coherence in a Bose–Einstein condensate”, en, *Nature* **417**, 529 (2002).
- [97] B. Borca, D. Blume, and C. H. Greene, “A two-atom picture of coherent atom–molecule quantum beats”, *New J. Phys.* **5**, 111 (2003).
- [98] E. Hodby, S. T. Thompson, C. A. Regal, M. Greiner, A. C. Wilson, D. S. Jin, E. A. Cornell, and C. E. Wieman, “Production Efficiency of Ultracold Feshbach Molecules in Bosonic and Fermionic Systems”, *Phys. Rev. Lett.* **94**, 120402 (2005).
- [99] P. Giannakeas, L. Khaykovich, J.-M. Rost, and C. H. Greene, “Nonadiabatic Molecular Association in Thermal Gases Driven by Radio-Frequency Pulses”, *Phys. Rev. Lett.* **123**, 043204 (2019).
- [100] T. M. Hanna, T. Köhler, and K. Burnett, “Association of molecules using a resonantly modulated magnetic field”, *Phys. Rev. A* **75**, 013606 (2007).



- [101] Y. Ding, J. P. D’Incao, and C. H. Greene, “Effective control of cold collisions with radio-frequency fields”, *Phys. Rev. A* **95**, 022709 (2017).
- [102] J. P. D’Incao, M. Krutzik, E. Elliott, and J. R. Williams, “Enhanced association and dissociation of heteronuclear feshbach molecules in a microgravity environment”, *Phys. Rev. A* **95**, 012701 (2017).
- [103] K. Waiblinger, J. R. Williams, and J. P. D’Incao, “Quenched magneto-association of ultracold Feshbach molecules”, *Phys. Rev. A* **104**, 033310 (2021).
- [104] R. J. Fletcher, R. Lopes, J. Man, N. Navon, R. P. Smith, M. W. Zwierlein, and Z. Hadzibabic, “Two- and three-body contacts in the unitary Bose gas”, *Science* **355**, 377 (2017).
- [105] J. P. Corson and J. L. Bohn, “Bound-state signatures in quenched Bose-Einstein condensates”, *Phys. Rev. A* **91**, 013616 (2015).
- [106] A. G. Sykes, J. P. Corson, J. P. D’Incao, A. P. Koller, C. H. Greene, A. M. Rey, K. R. A. Hazzard, and J. L. Bohn, “Quenching to unitarity: Quantum dynamics in a three-dimensional Bose gas”, *Phys. Rev. A* **89**, 021601 (2014).
- [107] T. Kraemer, M. Mark, P. Waldburger, J. G. Danzl, C. Chin, B. Engeser, A. D. Lange, K. Pilch, A. Jaakkola, H.-C. Nägerl, and R. Grimm, “Evidence for Efimov quantum states in an ultracold gas of caesium atoms”, *Nature* **440**, 315 (2006).
- [108] M. Zaccanti, B. Deissler, C. D’Errico, M. Fattori, M. Jona-Lasinio, S. Müller, G. Roati, M. Inguscio, and G. Modugno, “Observation of an efimov spectrum in an atomic system”, *Nature Phys.* **5**, 586 (2009).
- [109] N. Gross, Z. Shotan, S. Kokkelmans, and L. Khaykovich, “Observation of Universality in Ultracold  $^7\text{Li}$  Three-Body Recombination”, *Phys. Rev. Lett.* **103**, 163202 (2009).
- [110] S.-K. Tung, K. Jiménez-García, J. Johansen, C. V. Parker, and C. Chin, “Geometric Scaling of Efimov States in a  $^6\text{Li}$ - $^{133}\text{Cs}$  Mixture”, *Phys. Rev. Lett.* **113**, 240402 (2014).
- [111] R. Pires, J. Ulmanis, S. Häfner, M. Repp, A. Arias, E. D. Kuhnle, and M. Weidemüller, “Observation of Efimov Resonances in a Mixture with Extreme Mass Imbalance”, *Phys. Rev. Lett.* **112**, 250404 (2014).
- [112] J. Johansen, B. J. DeSalvo, K. Patel, and C. Chin, “Testing universality of Efimov physics across broad and narrow Feshbach resonances”, *Nature Phys.* **13**, 731 (2017).
- [113] V. E. Colussi, J. P. Corson, and J. P. D’Incao, “Dynamics of Three-Body Correlations in Quenched Unitary Bose Gases”, *Phys. Rev. Lett.* **120**, 100401 (2018).
- [114] J. P. D’Incao, J. Wang, and V. E. Colussi, “Efimov Physics in Quenched Unitary Bose Gases”, *Phys. Rev. Lett.* **121**, 023401 (2018).
- [115] V. E. Colussi, B. E. van Zwol, J. P. D’Incao, and S. J. J. M. F. Kokkelmans, “Bunching, clustering, and the buildup of few-body correlations in a quenched unitary Bose gas”, *Phys. Rev. A* **99**, 043604 (2019).
- [116] V. E. Colussi, H. Kurkjian, M. Van Regemortel, S. Musolino, J. van de Kraats, M. Wouters, and S. J. J. M. F. Kokkelmans, “Cumulant theory of the unitary Bose gas: Prethermal and Efimovian dynamics”, *Phys. Rev. A* **102**, 063314 (2020).

- [117] S. Musolino, H. Kurkjian, M. Van Regemortel, M. Wouters, S. J. J. M. F. Kokkelmans, and V. E. Colussi, “Bose-einstein condensation of efimovian triples in the unitary bose gas”, *Phys. Rev. Lett.* **128**, 020401 (2022).
- [118] Y. Yudkin, R. Elbaz, P. Giannakeas, C. H. Greene, and L. Khaykovich, “Coherent Superposition of Feshbach Dimers and Efimov Trimers”, *Phys. Rev. Lett.* **122**, 200402 (2019).
- [119] Y. Yudkin, R. Elbaz, and L. Khaykovich, “Efimov energy level rebounding off the atom-dimer continuum”, [arXiv:2004.02723](https://arxiv.org/abs/2004.02723) [cond-mat, physics:physics, physics:quant-ph] (2020).
- [120] S. Tan, “Large momentum part of a strongly correlated Fermi gas”, en, *Annals of Physics* **323**, 2971 (2008).
- [121] S. Tan, “Energetics of a strongly correlated Fermi gas”, en, *Annals of Physics* **323**, 2952 (2008).
- [122] S. Tan, “Generalized virial theorem and pressure relation for a strongly correlated Fermi gas”, en, *Annals of Physics* **323**, 2987 (2008).
- [123] F. Werner and Y. Castin, “General relations for quantum gases in two and three dimensions. II. Bosons and mixtures”, *Phys. Rev. A* **86**, 053633 (2012).
- [124] M. Barth and W. Zwerger, “Tan relations in one dimension”, *Annals of Physics* **326**, 2544 (2011).
- [125] M. Valiente, N. T. Zinner, and K. Mølmer, “Universal properties of Fermi gases in arbitrary dimensions”, *Phys. Rev. A* **86**, 043616 (2012).
- [126] F. Werner and Y. Castin, “General relations for quantum gases in two and three dimensions: two-component fermions”, *Phys. Rev. A* **86**, 013626 (2012).
- [127] Y. Castin and F. Werner, “Single-particle momentum distribution of an Efimov trimer”, *Phys. Rev. A* **83**, 063614 (2011).
- [128] E. Braaten, D. Kang, and L. Platter, “Universal relations for a strongly interacting Fermi gas near a Feshbach resonance”, *Phys. Rev. A* **78**, 053606 (2008).
- [129] D. H. Smith, E. Braaten, D. Kang, and L. Platter, “Two-Body and Three-Body Contacts for Identical Bosons near Unitarity”, *Phys. Rev. Lett.* **112**, 110402 (2014).
- [130] J. T. Stewart, J. P. Gaebler, T. E. Drake, and D. S. Jin, “Verification of Universal Relations in a Strongly Interacting Fermi Gas”, *Phys. Rev. Lett.* **104**, 235301 (2010).
- [131] R. J. Wild, P. Makotyn, J. M. Pino, E. A. Cornell, and D. S. Jin, “Measurements of Tan’s Contact in an Atomic Bose-Einstein Condensate”, *Phys. Rev. Lett.* **108**, 145305 (2012).
- [132] Y. Sagi, T. E. Drake, R. Paudel, and D. S. Jin, “Measurement of the Homogeneous Contact of a Unitary Fermi Gas”, *Phys. Rev. Lett.* **109**, 220402 (2012).
- [133] F. Werner, “Virial theorems for trapped cold atoms”, *Phys. Rev. A* **78**, 025601 (2008).
- [134] D. T. Son and E. G. Thompson, “Short-distance and short-time structure of a unitary fermi gas”, *Phys. Rev. A* **81**, 063634 (2010).
- [135] H. Hu, X.-J. Liu, and P. D. Drummond, “Static structure factor of a strongly correlated fermi gas at large momenta”, *Europhysics Letters* **91**, 20005 (2010).

- [136] W. D. Goldberger and I. Z. Rothstein, “Structure-function sum rules for systems with large scattering lengths”, *Phys. Rev. A* **85**, 013613 (2012).
- [137] E. Taylor and M. Randeria, “Viscosity of strongly interacting quantum fluids: spectral functions and sum rules”, *Phys. Rev. A* **81**, 053610 (2010).
- [138] E. Braaten, D. Kang, and L. Platter, “Short-time operator product expansion for rf spectroscopy of a strongly interacting fermi gas”, *Phys. Rev. Lett.* **104**, 223004 (2010).
- [139] W. Schneider and M. Randeria, “Universal short-distance structure of the single-particle spectral function of dilute Fermi gases”, *Phys. Rev. A* **81**, 021601 (2010).
- [140] J. Hofmann, “Quantum anomaly, universal relations, and breathing mode of a two-dimensional fermi gas”, *Phys. Rev. Lett.* **108**, 185303 (2012).
- [141] M. Holten, L. Bayha, A. C. Klein, P. A. Murthy, P. M. Preiss, and S. Jochim, “Anomalous Breaking of Scale Invariance in a Two-Dimensional Fermi Gas”, *Phys. Rev. Lett.* **121**, 120401 (2018).
- [142] P. A. Murthy, N. Defenu, L. Bayha, M. Holten, P. M. Preiss, T. Enss, and S. Jochim, “Quantum scale anomaly and spatial coherence in a 2D Fermi superfluid”, *Science* **365**, 268 (2019).
- [143] T. Peppler, P. Dyke, M. Zamorano, I. Herrera, S. Hoinka, and C. J. Vale, “Quantum anomaly and 2d-3d crossover in strongly interacting fermi gases”, *Phys. Rev. Lett.* **121**, 120402 (2018).
- [144] E. Vogt, M. Feld, B. Fröhlich, D. Pertot, M. Koschorreck, and M. Köhl, “Scale invariance and viscosity of a two-dimensional fermi gas”, *Phys. Rev. Lett.* **108**, 070404 (2012).
- [145] G. B. Partridge, K. E. Strecker, R. I. Kamar, M. W. Jack, and R. G. Hulet, “Molecular probe of pairing in the bec-bcs crossover”, *Phys. Rev. Lett.* **95**, 020404 (2005).
- [146] F. Werner, L. Tarruell, and Y. Castin, “Number of closed-channel molecules in the bec-bcs crossover”, *The European Physical Journal B* **68**, 401 (2009).
- [147] S. Zhang and A. J. Leggett, “Universal properties of the ultracold fermi gas”, *Phys. Rev. A* **79**, 023601 (2009).
- [148] J. Wang, X.-J. Liu, and H. Hu, “Photoexcitation measurement of Tan’s contact for a strongly interacting Fermi gas”, *Phys. Rev. A* **104**, 063309 (2021).
- [149] S. Pekar, “Autolocalization of the electron in an inertially polarizable dielectric medium”, *Zh. Eksp. Teor. Fiz* **16**, 335 (1946).
- [150] S. Pekar, “Theory of colored crystals”, *Zh. Eksp. Teor. Fiz* **17**, 868 (1947).
- [151] H. Fröhlich, “Electrons in lattice fields”, *Advances in Physics* **3**, 325 (1954).
- [152] L. Landau and S. Pekar, “Effective mass of a polaron”, *Zh. Eksp. Teor. Fiz* **18**, 419 (1948).
- [153] A. Schirotzek, C.-H. Wu, A. Sommer, and M. W. Zwierlein, “Observation of fermi polarons in a tunable fermi liquid of ultracold atoms”, *Phys. Rev. Lett.* **102**, 230402 (2009).
- [154] C. Kohstall, M. Zaccanti, M. Jag, A. Trenkwalder, P. Massignan, G. M. Bruun, F. Schreck, and R. Grimm, “Metastability and coherence of repulsive polarons in a strongly interacting fermi mixture”, *Nature* **485**, 615 (2012).

- [155] P. Massignan, M. Zaccanti, and G. M. Bruun, “Polarons, dressed molecules and itinerant ferromagnetism in ultracold fermi gases”, *Rep. Prog. Phys.* **77**, 034401 (2014).
- [156] N. B. Jørgensen, L. Wacker, K. T. Skalmstang, M. M. Parish, J. Levinsen, R. S. Christensen, G. M. Bruun, and J. J. Arlt, “Observation of attractive and repulsive polarons in a bose-einstein condensate”, *Phys. Rev. Lett.* **117**, 055302 (2016).
- [157] M.-G. Hu, M. J. Van de Graaff, D. Kedar, J. P. Corson, E. A. Cornell, and D. S. Jin, “Bose polarons in the strongly interacting regime”, *Phys. Rev. Lett.* **117**, 055301 (2016).
- [158] J. Tempere, W. Casteels, M. K. Oberthaler, S. Knoop, E. Timmermans, and J. T. Devreese, “Feynman path-integral treatment of the bec-impurity polaron”, *Phys. Rev. B* **80**, 184504 (2009).
- [159] L. P. Ardila and S. Giorgini, “Impurity in a bose-einstein condensate: study of the attractive and repulsive branch using quantum monte carlo methods”, *Physical Review A* **92**, 033612 (2015).
- [160] F. Grusdt, G. E. Astrakharchik, and E. Demler, “Bose polarons in ultracold atoms in one dimension: beyond the fröhlich paradigm”, *New J. Phys.* **19**, 103035 (2017).
- [161] A. S. Dehkharghani, A. G. Volosniev, and N. T. Zinner, “Coalescence of two impurities in a trapped one-dimensional bose gas”, *Phys. Rev. Lett.* **121**, 080405 (2018).
- [162] J. Chen, J. M. Schurer, and P. Schmelcher, “Entanglement induced interactions in binary mixtures”, *Phys. Rev. Lett.* **121**, 043401 (2018).
- [163] P. Naidon, “Two impurities in a bose-einstein condensate: from yukawa to efimov attracted polarons”, *Journal of the Physical Society of Japan* **87**, 043002 (2018).
- [164] T. Enss, B. Tran, M. Rautenberg, M. Gerken, E. Lippi, M. Drescher, B. Zhu, M. Weidemüller, and M. Salmhofer, “Scattering of two heavy fermi polarons: resonances and quasibound states”, *Phys. Rev. A* **102**, 063321 (2020).
- [165] A. Klein and M. Fleischhauer, “Interaction of impurity atoms in bose-einstein condensates”, *Phys. Rev. A* **71**, 033605 (2005).
- [166] A. Petković and Z. Ristivojević, “Mediated interaction between polarons in a one-dimensional bose gas”, *Phys. Rev. A* **105**, L021303 (2022).
- [167] A. Camacho-Guardian, L. A. Peña Ardila, T. Pohl, and G. M. Bruun, “Bipolarons in a bose-einstein condensate”, *Phys. Rev. Lett.* **121**, 013401 (2018).
- [168] W. Casteels, J. Tempere, and J. T. Devreese, “Bipolarons and multipolarons consisting of impurity atoms in a bose-einstein condensate”, *Phys. Rev. A* **88**, 013613 (2013).
- [169] A. Camacho-Guardian and G. M. Bruun, “Landau effective interaction between quasiparticles in a bose-einstein condensate”, *Phys. Rev. X* **8**, 031042 (2018).
- [170] M. Will, G. E. Astrakharchik, and M. Fleischhauer, “Polaron interactions and bipolarons in one-dimensional bose gases in the strong coupling regime”, *Phys. Rev. Lett.* **127**, 103401 (2021).
- [171] J. Jäger and R. Barnett, “The effect of boson-boson interaction on the bipolaron formation”, *New J. Phys.* **24**, 103032 (2022).

- [172] D. S. Petrov, “The few-atom problem”, [arXiv:1206.5752 \[cond-mat\]](https://arxiv.org/abs/1206.5752) (2012).
- [173] Y. Wang, J. Wang, J. P. D’Incao, and C. H. Greene, “Universal Three-Body Parameter in Heteronuclear Atomic Systems”, *Phys. Rev. Lett.* **109**, 243201 (2012).
- [174] B. Tran, M. Rautenberg, M. Gerken, E. Lippi, B. Zhu, J. Ulmanis, M. Drescher, M. Salmhofer, T. Enss, and M. Weidemüller, “Fermions Meet Two Bosons—the Heteronuclear Efimov Effect Revisited”, en, *Braz J Phys* **51**, 316 (2021).
- [175] Y. Nishida, “Casimir interaction among heavy fermions in the bcs-bec crossover”, *Phys. Rev. A* **79**, 013629 (2009).
- [176] R. Combescot, A. Recati, C. Lobo, and F. Chevy, “Normal state of highly polarized fermi gases: simple many-body approaches”, *Phys. Rev. Lett.* **98**, 180402 (2007).
- [177] M. A. Ruderman and C. Kittel, “Indirect exchange coupling of nuclear magnetic moments by conduction electrons”, *Phys. Rev.* **96**, 99 (1954).
- [178] J. Friedel, “Xiv. the distribution of electrons round impurities in monovalent metals”, *The London, Edinburgh, and Dublin Philosophical Magazine and Journal of Science* **43**, 153 (1952).
- [179] S. I. Mistakidis, G. C. Katsimiga, G. M. Koutentakis, T. Busch, and P. Schmelcher, “Quench dynamics and orthogonality catastrophe of bose polarons”, *Phys. Rev. Lett.* **122**, 183001 (2019).
- [180] S. I. Mistakidis, G. M. Koutentakis, G. C. Katsimiga, T. Busch, and P. Schmelcher, “Many-body quantum dynamics and induced correlations of bose polarons”, *New J. Phys.* **22**, 043007 (2020).
- [181] S. I. Mistakidis, F. Grusdt, G. M. Koutentakis, and P. Schmelcher, “Dissipative correlated dynamics of a moving impurity immersed in a bose–einstein condensate”, *New J. Phys.* **21**, 103026 (2019).
- [182] D. Boyanovsky, D. Jasnow, X.-L. Wu, and R. C. Coalson, “Dynamics of relaxation and dressing of a quenched bose polaron”, *Phys. Rev. A* **100**, 043617 (2019).
- [183] J. Catani, G. Barontini, G. Lamporesi, F. Rabatti, G. Thalhammer, F. Minardi, S. Stringari, and M. Inguscio, “Entropy exchange in a mixture of ultracold atoms”, *Phys. Rev. Lett.* **103**, 140401 (2009).
- [184] K. Mukherjee, S. I. Mistakidis, S. Majumder, and P. Schmelcher, “Pulse- and continuously driven many-body quantum dynamics of bosonic impurities in a bose-einstein condensate”, *Phys. Rev. A* **101**, 023615 (2020).
- [185] M. Knap, A. Shashi, Y. Nishida, A. Imambekov, D. A. Abanin, and E. Demler, “Time-dependent impurity in ultracold fermions: orthogonality catastrophe and beyond”, *Phys. Rev. X* **2**, 041020 (2012).
- [186] Z. Z. Yan, Y. Ni, C. Robens, and M. W. Zwierlein, “Bose polarons near quantum criticality”, *Science* **368**, 190 (2020).
- [187] T. Lausch, A. Widera, and M. Fleischhauer, “Prethermalization in the cooling dynamics of an impurity in a bose-einstein condensate”, *Phys. Rev. A* **97**, 023621 (2018).
- [188] J. T. M. Walraven, “Quantum Gases lectures, University of Amsterdam”, <https://staff.fnwi.uva.nl/j.t.m.walraven/walraven/Lectures.htm> (2019).
- [189] M. Kardar, *Statistical physics of particles* (Cambridge University Press, 2007).

- [190] F. Reif, *Fundamentals of statistical and thermal physics* (McGraw-Hill, Tokyo, 1965).
- [191] J. O. Andersen, “Theory of the weakly interacting bose gas”, *Rev. Mod. Phys.* **76**, 599 (2004).
- [192] H. T. C. Stoof, M. Bijlsma, and M. Houbiers, “Theory of interacting quantum gases”, *J Res Natl Inst Stand Technol* **101**, 443 (1996).
- [193] P. G. Kevrekidis, D. J. Frantzeskakis, and R. Carretero-González, *Emergent nonlinear phenomena in bose-einstein condensates: theory and experiment*, Vol. 45 (Springer, 2008).
- [194] N. P. Proukakis and B. Jackson, “Finite-temperature models of bose–einstein condensation”, *J. Phys. B: At., Mol. Opt. Phys.* **41**, 203002 (2008).
- [195] J. Dalibard, *Collisional dynamics of ultra-cold atomic gases* (Bose-Einstein Condensation in Gases, IOS Press, 1999).
- [196] L. D. Landau and E. M. Lifshitz, *Quantum mechanics: non-relativistic theory*, Vol. 3 (Elsevier, 2013).
- [197] C. J. Joachain, *Quantum collision theory* (North-Holland, 1975).
- [198] H. Friedrich, *Scattering theory*, Vol. 872 (Springer, 2013).
- [199] P. Giannakeas, “Higher partial wave and dipolar confinement-induced resonances”, PhD thesis (Staats-und Universitätsbibliothek Hamburg Carl von Ossietzky, 2013).
- [200] H. Bethe and R. Peierls, “Quantum theory of the diplon”, *Proceedings of the Royal Society of London. Series A-Mathematical and Physical Sciences* **148**, 146 (1935).
- [201] E. Fermi, “Sopra lo spostamento per pressione delle righe elevate delle serie spettrali”, *Il Nuovo Cimento* (1924-1942) **11**, 157 (1934).
- [202] K. Huang and C. N. Yang, “Quantum-mechanical many-body problem with hard-sphere interaction”, *Phys. Rev.* **105**, 767 (1957).
- [203] A. Farrell and B. P. van Zyl, “Universality of the energy spectrum for two interacting harmonically trapped ultra-cold atoms in one and two dimensions”, *Journal of Physics A: Mathematical and Theoretical* **43**, 015302 (2009).
- [204] S. K. Adhikari, W. G. Gibson, and T. K. Lim, “Effective-range theory in two dimensions”, *J. Chem. Phys.* **85**, 5580 (1986).
- [205] D. S. Petrov and G. V. Shlyapnikov, “Interatomic collisions in a tightly confined Bose gas”, *Phys. Rev. A* **64**, 012706 (2001).
- [206] B. J. Verhaar, J. P. H. W. van den Eijnde, M. A. J. Voermans, and M. M. J. Schaffrath, “Scattering length and effective range in two dimensions: application to adsorbed hydrogen atoms”, *Journal of Physics A: Mathematical and General* **17**, 595 (1984).
- [207] X.-J. Liu, H. Hu, and P. D. Drummond, “Exact few-body results for strongly correlated quantum gases in two dimensions”, *Phys. Rev. B* **82**, 054524 (2010).
- [208] S. K. Adhikari, “Quantum scattering in two dimensions”, *American Journal of Physics* **54**, 362 (1986).
- [209] T. K. Lim and P. A. Maurone, “Nonexistence of the efimov effect in two dimensions”, *Phys. Rev. B* **22**, 1467 (1980).

- [210] M. Olshanii and L. Pricoupenko, “Rigorous Approach to the Problem of Ultra-violet Divergencies in Dilute Bose Gases”, *Phys. Rev. Lett.* **88**, 010402 (2001).
- [211] K. Kanjilal and D. Blume, “Coupled-channel pseudopotential description of the Feshbach resonance in two dimensions”, *Phys. Rev. A* **73**, 060701 (2006).
- [212] K. Wódkiewicz, “Fermi pseudopotential in arbitrary dimensions”, *Phys. Rev. A* **43**, 68 (1991).
- [213] M. Li, H. Fu, Y.-Z. Wang, J. Chen, L. Chen, and C. Chen, “Pseudopotential operator for hard-sphere interactions in any-dimensional space”, *Phys. Rev. A* **66**, 015601 (2002).
- [214] M. Abramowitz and I. A. Stegun, “Handbook of mathematical functions with formulas, graphs, and mathematical tables”, Washington: US Govt. Print (2006).
- [215] L. Pricoupenko and M. Olshanii, “Stability of two-dimensional Bose gases in the resonant regime”, en, *J. Phys. B: At. Mol. Opt. Phys.* **40**, 2065 (2007).
- [216] J. Levinsen and M. M. Parish, “Strongly interacting two-dimensional fermi gases”, *Annual review of cold atoms and molecules*, 1 (2015).
- [217] V. E. Barlette, M. M. Leite, and S. K. Adhikari, “Quantum scattering in one dimension”, *European Journal of Physics* **21**, 435 (2000).
- [218] J. P. Corson and J. L. Bohn, “Ballistic quench-induced correlation waves in ultracold gases”, *Phys. Rev. A* **94**, 023604 (2016).
- [219] D. S. Petrov, M. Holzmann, and G. V. Shlyapnikov, “Bose-einstein condensation in quasi-2d trapped gases”, *Phys. Rev. Lett.* **84**, 2551 (2000).
- [220] L. Pricoupenko, “Resonant scattering of ultracold atoms in low dimensions”, *Phys. Rev. Lett.* **100**, 170404 (2008).
- [221] S. R. Beane and M. Jafry, “Dimensional crossover in non-relativistic effective field theory”, *J. Phys. B: At., Mol. Opt. Phys.* **52**, 035001 (2019).
- [222] B. M. Faigle-Cedzich, J. M. Pawłowski, and C. Wetterich, “Dimensional crossover in ultracold fermi gases from functional renormalization”, *Phys. Rev. A* **103**, 033320 (2021).
- [223] S. Lammers, I. Boettcher, and C. Wetterich, “Dimensional crossover of nonrelativistic bosons”, *Phys. Rev. A* **93**, 063631 (2016).
- [224] M. Olshanii, “Atomic Scattering in the Presence of an External Confinement and a Gas of Impenetrable Bosons”, *Phys. Rev. Lett.* **81**, 938 (1998).
- [225] T. Bergeman, M. G. Moore, and M. Olshanii, “Atom-atom scattering under cylindrical harmonic confinement: numerical and analytic studies of the confinement induced resonance”, *Phys. Rev. Lett.* **91**, 163201 (2003).
- [226] I. S. Gradshteyn and I. M. Ryzhik, *Table of integrals, series, and products* (Academic press, 2014).
- [227] V. A. Yurovsky, M. Olshanii, and D. S. Weiss, in , Vol. 55, edited by E. Arimondo, P. R. Berman, and C. C. Lin, *Advances In Atomic, Molecular, and Optical Physics* (Academic Press, 2008), pp. 61–138.
- [228] E. Haller, M. J. Mark, R. Hart, J. G. Danzl, L. Reichsöllner, V. Melezhik, P. Schmelcher, and H.-C. Nägerl, “Confinement-induced resonances in low-dimensional quantum systems”, *Phys. Rev. Lett.* **104**, 153203 (2010).
- [229] V. S. Melezhik and P. Schmelcher, “Multichannel effects near confinement-induced resonances in harmonic waveguides”, *Phys. Rev. A* **84**, 042712 (2011).

- [230] P. Giannakeas, F. K. Diakonov, and P. Schmelcher, “Coupled  $\ell$ -wave confinement-induced resonances in cylindrically symmetric waveguides”, *Phys. Rev. A* **86**, 042703 (2012).
- [231] R. Duine and H. Stoof, “Atom–molecule coherence in bose gases”, *Physics Reports* **396**, 115 (2004).
- [232] U. Fano, “Sullo spettro di assorbimento dei gas nobili presso il limite dello spettro d’arco”, *Il Nuovo Cimento (1924-1942)* **12**, 154 (1935).
- [233] U. Fano, “Effects of configuration interaction on intensities and phase shifts”, *Phys. Rev.* **124**, 1866 (1961).
- [234] H. Feshbach, “Unified theory of nuclear reactions”, *Annals of Physics* **5**, 357 (1958).
- [235] H. Feshbach, “A unified theory of nuclear reactions. ii”, *Annals of Physics* **19**, 287 (1962).
- [236] E. Tiesinga, B. J. Verhaar, and H. T. C. Stoof, “Threshold and resonance phenomena in ultracold ground-state collisions”, *Phys. Rev. A* **47**, 4114 (1993).
- [237] C. Eigen, J. A. P. Glidden, R. Lopes, N. Navon, Z. Hadzibabic, and R. P. Smith, “Universal Scaling Laws in the Dynamics of a Homogeneous Unitary Bose Gas”, *Phys. Rev. Lett.* **119**, 250404 (2017).
- [238] E. Nicklas, H. Strobel, T. Zibold, C. Gross, B. A. Malomed, P. G. Kevrekidis, and M. K. Oberthaler, “Rabi flopping induces spatial demixing dynamics”, *Phys. Rev. Lett.* **107**, 193001 (2011).
- [239] P. Engels, C. Atherton, and M. A. Hofer, “Observation of faraday waves in a bose-einstein condensate”, *Phys. Rev. Lett.* **98**, 095301 (2007).
- [240] M. Theis, G. Thalhammer, K. Winkler, M. Hellwig, G. Ruff, R. Grimm, and J. H. Denschlag, “Tuning the scattering length with an optically induced feshbach resonance”, *Phys. Rev. Lett.* **93**, 123001 (2004).
- [241] J. T. Zhang, Y. Yu, W. B. Cairncross, K. Wang, L. R. B. Picard, J. D. Hood, Y.-W. Lin, J. M. Hutson, and K.-K. Ni, “Forming a Single Molecule by Magnetoassociation in an Optical Tweezer”, *Phys. Rev. Lett.* **124**, 253401 (2020).
- [242] W. B. Cairncross, J. T. Zhang, L. R. B. Picard, Y. Yu, K. Wang, and K.-K. Ni, “Assembly of a Rovibrational Ground State Molecule in an Optical Tweezer”, *Phys. Rev. Lett.* **126**, 123402 (2021).
- [243] D. Blume, “Few-body physics with ultracold atomic and molecular systems in traps”, *Reports on Progress in Physics* **75**, 046401 (2012).
- [246] M. A. Cirone, K. Góral, K. Rzazewski, and M. Wilkens, “Bose-einstein condensation of two interacting particles”, *Journal of Physics B: Atomic, Molecular and Optical Physics* **34**, 4571 (2001).
- [247] Y. Chen, D.-W. Xiao, R. Zhang, and P. Zhang, “Analytical solution for the spectrum of two ultracold atoms in a completely anisotropic confinement”, *Phys. Rev. A* **101**, 053624 (2020).
- [248] R. A. Doganov, S. Klaiman, O. E. Alon, A. I. Streltsov, and L. S. Cederbaum, “Two trapped particles interacting by a finite-range two-body potential in two spatial dimensions”, *Phys. Rev. A* **87**, 033631 (2013).
- [249] L. Delves, “Tertiary and general-order collisions”, *Nuclear Physics* **9**, 391 (1958).
- [250] E. Nielsen, D. V. Fedorov, A. S. Jensen, and E. Garrido, “The three-body problem with short-range interactions”, *en, Physics Reports* **347**, 373 (2001).



- [251] J. P. D’Incao, “Few-body physics in resonantly interacting ultracold quantum gases”, en, *J. Phys. B: At. Mol. Opt. Phys.* **51**, 043001 (2018).
- [252] A. G. Volosniev, D. V. Fedorov, A. S. Jensen, and N. T. Zinner, “Borromean ground state of fermions in two dimensions”, en, *J. Phys. B: At. Mol. Opt. Phys.* **47**, 185302 (2014).
- [253] L. Delves, “Tertiary and general-order collisions (ii)”, *Nuclear Physics* **20**, 275 (1960).
- [254] R. C. Whitten and F. T. Smith, “Symmetric Representation for Three-Body Problems. II. Motion in Space”, *J. Math. Phys.* **9**, 1103 (1968).
- [255] B. R. Johnson, “On hyperspherical coordinates and mapping the internal configurations of a three body system”, *The Journal of Chemical Physics* **73**, 5051 (1980).
- [256] A. G. Volosniev, D. V. Fedorov, A. S. Jensen, and N. T. Zinner, “Hyperspherical treatment of strongly-interacting few-fermion systems in one dimension”, *The European Physical Journal Special Topics* **224**, 585 (2015).
- [257] J. S. Avery, *Hyperspherical harmonics: applications in quantum theory*, Vol. 5 (Springer Science & Business Media, 2012).
- [258] T. K. Das, *Hyperspherical harmonics expansion techniques*, Vol. 170 (Springer, 2016).
- [259] J. Macek, “Properties of autoionizing states of he”, *Journal of Physics B: Atomic and Molecular Physics* **1**, 831 (1968).
- [260] U. Fano, “Unified treatment of collisions”, *Phys. Rev. A* **24**, 2402 (1981).
- [261] U. Fano, “Dynamics of electron excitation”, *Physics Today* **29**, 32 (1976).
- [262] S. T. Rittenhouse, N. P. Mehta, and C. H. Greene, “Green’s functions and the adiabatic hyperspherical method”, *Phys. Rev. A* **82**, 022706 (2010).
- [263] M. Fabre de La Ripelle, “Green function and scattering amplitudes in many-dimensional space”, *Few-Body Systems* **14**, 1 (1993).
- [264] R. Szmytkowski, “Closed form of the generalized green’s function for the helmholtz operator on the two-dimensional unit sphere”, *Journal of mathematical physics* **47**, 063506 (2006).
- [265] M. Mikkelsen, A. S. Jensen, D. V. Fedorov, and N. T. Zinner, “Three-body recombination of two-component cold atomic gases into deep dimers in an optical model”, *Journal of Physics B: Atomic, Molecular and Optical Physics* **48**, 085301 (2015).
- [266] P. Giannakeas and C. H. Greene, “Ultracold Heteronuclear Three-Body Systems: How Diabaticity Limits the Universality of Recombination into Shallow Dimers”, *Phys. Rev. Lett.* **120**, 023401 (2018).
- [267] S. T. Rittenhouse, A. Wray, and B. L. Johnson, “Hyperspherical approach to a three-boson problem in two dimensions with a magnetic field”, *Phys. Rev. A* **93**, 012511 (2016).
- [268] L. H. Thomas, “The interaction between a neutron and a proton and the structure of  $h^3$ ”, *Phys. Rev.* **47**, 903 (1935).
- [269] V. Efimov, “Energy levels of three resonantly interacting particles”, *Nuclear Physics A* **210**, 157 (1973).

- [270] O. I. Kartavtsev and A. V. Malykh, “Universal low-energy properties of three two-dimensional bosons”, *Phys. Rev. A* **74**, 042506 (2006).
- [271] O. I. Kartavtsev and A. V. Malykh, “Low-energy three-body dynamics in binary quantum gases”, en, *J. Phys. B: At. Mol. Opt. Phys.* **40**, 1429 (2007).
- [272] H. Bachau, E. Cormier, P. Decleva, J. Hansen, and F. Martín, “Applications of b-splines in atomic and molecular physics”, *Rep. Prog. Phys.* **64**, 1815 (2001).
- [273] C. De Boor, *A practical guide to splines*, Vol. 27 (springer-verlag New York, 1978).
- [274] J. Portegies and S. Kokkelmans, “Efimov Trimers in a Harmonic Potential”, en, *Few-Body Syst* **51**, 219 (2011).
- [275] D. Blume and C. H. Greene, “Three particles in an external trap: Nature of the complete  $J = 0$  spectrum”, *Phys. Rev. A* **66**, 013601 (2002).
- [276] A. D. Kerin and A. M. Martin, “Energetics and efimov states of three interacting bosons and mass-imbalanced fermions in a three-dimensional spherical harmonic trap”, *Journal of Physics B: Atomic, Molecular and Optical Physics* **56**, 055201 (2023).
- [277] N. L. Harshman, “Symmetries of three harmonically trapped particles in one dimension”, *Phys. Rev. A* **86**, 052122 (2012).
- [278] D. Blume, J. Von Stecher, and C. H. Greene, “Universal properties of a trapped two-component fermi gas at unitarity”, *Physical Review Letters* **99**, 233201 (2007).
- [279] J. Kestner and L.-M. Duan, “Level crossing in the three-body problem for strongly interacting fermions in a harmonic trap”, *Physical Review A* **76**, 033611 (2007).
- [280] K. M. Daily and D. Blume, “Energy spectrum of harmonically trapped two-component fermi gases: three- and four-particle problem”, *Phys. Rev. A* **81**, 053615 (2010).
- [281] E. J. Lindgren, J. Rotureau, C. Forssén, A. G. Volosniev, and N. T. Zinner, “Fermionization of two-component few-fermion systems in a one-dimensional harmonic trap”, en, *New J. Phys.* **16**, 063003 (2014).
- [282] M. A. Garcia-March, B. Juliá-Díaz, G. E. Astrakharchik, J. Boronat, and A. Polls, “Distinguishability, degeneracy, and correlations in three harmonically trapped bosons in one dimension”, *Phys. Rev. A* **90**, 063605 (2014).
- [283] L. Pricoupenko and P. Pedri, “Universal (1 + 2)-body bound states in planar atomic waveguides”, *Phys. Rev. A* **82**, 033625 (2010).
- [284] F. F. Bellotti, T. Frederico, M. T. Yamashita, D. V. Fedorov, A. S. Jensen, and N. T. Zinner, “Mass-imbalanced three-body systems in two dimensions”, en, *J. Phys. B: At. Mol. Opt. Phys.* **46**, 055301 (2013).
- [285] F. F. Bellotti, T. Frederico, M. T. Yamashita, D. V. Fedorov, A. S. Jensen, and N. T. Zinner, “Scaling and universality in two dimensions: three-body bound states with short-ranged interactions”, en, *J. Phys. B: At. Mol. Opt. Phys.* **44**, 205302 (2011).
- [286] M. Olshanii and V. Dunjko, “Short-Distance Correlation Properties of the Lieb-Liniger System and Momentum Distributions of Trapped One-Dimensional Atomic Gases”, *Phys. Rev. Lett.* **91**, 090401 (2003).

- [287] E. Braaten and L. Platter, “Exact relations for a strongly interacting fermi gas from the operator product expansion”, *Phys. Rev. Lett.* **100**, 205301 (2008).
- [288] M. Valiente, N. T. Zinner, and K. Mølmer, “Universal relations for the two-dimensional spin-1/2 Fermi gas with contact interactions”, *Phys. Rev. A* **84**, 063626 (2011).
- [289] E. Braaten and H.-W. Hammer, “Universal relation for the inelastic two-body loss rate”, *Journal of Physics B: Atomic, Molecular and Optical Physics* **46**, 215203 (2013).
- [290] O. I. Pâțu and A. Klümper, “Universal tan relations for quantum gases in one dimension”, *Phys. Rev. A* **96**, 063612 (2017).
- [291] E. Braaten, D. Kang, and L. Platter, “Universal Relations for Identical Bosons from Three-Body Physics”, *Phys. Rev. Lett.* **106**, 153005 (2011).
- [292] V. E. Colussi, “Two-Body and Three-Body Contacts for Three Bosons in the Unitary Regime: Analytic Expressions and Limiting Forms”, en, *Atoms* **7**, 19 (2019).
- [293] V. Efimov, “Energy levels arising from resonant two-body forces in a three-body system”, *Physics Letters B* **33**, 563 (1970).
- [294] V. N. Efimov, “Weakly-Bound States Of 3 Resonantly-Interacting particles”, *Sov. J. Nucl. Phys.* **12**, 589 (1971).
- [295] E. Braaten and H. -W. Hammer, “Universality in few-body systems with large scattering length”, *Physics Reports* **428**, 259 (2006).
- [296] R. Grimm, “Efimov states in an ultracold gas: how it happened in the laboratory”, *Few-Body Systems* **60**, 23 (2019).
- [297] F. Ferlaino and R. Grimm, “Forty years of efimov physics: how a bizarre prediction turned into a hot topic”, *Physics* **3**, 9 (2010).
- [298] C. H. Greene, “Universal insights from few-body land”, *Physics Today* **63**, 40 (2010).
- [299] J. Wang, J. P. D’Incao, and C. H. Greene, “Numerical study of three-body recombination for systems with many bound states”, *Phys. Rev. A* **84**, 052721 (2011).
- [300] M. Kunitski, S. Zeller, J. Voigtsberger, A. Kalinin, L. P. H. Schmidt, M. Schöffler, A. Czasch, W. Schöllkopf, R. E. Grisenti, T. Jahnke, D. Blume, and R. Dörner, “Observation of the efimov state of the helium trimer”, *Science* **348**, 551 (2015).
- [301] L. W. Bruch and J. A. Tjon, “Binding of three identical bosons in two dimensions”, *Phys. Rev. A* **19**, 425 (1979).
- [302] F. F. Bellotti, T. Frederico, M. T. Yamashita, D. V. Fedorov, A. S. Jensen, and N. T. Zinner, “Dimensional effects on the momentum distribution of bosonic trimer states”, *Phys. Rev. A* **87**, 013610 (2013).
- [303] F. F. Bellotti, T. Frederico, M. T. Yamashita, D. V. Fedorov, A. S. Jensen, and N. T. Zinner, “Contact parameters in two dimensions for general three-body systems”, en, *New J. Phys.* **16**, 013048 (2014).
- [304] P. G. Kevrekidis, D. J. Frantzeskakis, and R. Carretero-González, *The defocusing nonlinear schrödinger equation: from dark solitons to vortices and vortex rings* (SIAM, 2015).

- [305] Bose, “Plancks gesetz und lichtquantenhypothese”, *Zeitschrift für Physik* **26**, 178 (1924).
- [306] A. Einstein, “Sitzungsberichte der preussischen akademie der wissenschaften”, Physikalisch-mathematische Klasse **261**, 1925 (1924).
- [307] E. P. Gross, “Structure of a quantized vortex in boson systems”, *Il Nuovo Cimento (1955-1965)* **20**, 454 (1961).
- [308] E. P. Gross, “Hydrodynamics of a superfluid condensate”, *Journal of Mathematical Physics* **4**, 195 (1963).
- [309] L. P. Pitaevskii, “Vortex lines in an imperfect bose gas”, *Sov. Phys. JETP* **13**, 451 (1961).
- [310] D. Frantzeskakis, “Dark solitons in atomic bose–einstein condensates: from theory to experiments”, *Journal of Physics A: Mathematical and Theoretical* **43**, 213001 (2010).
- [311] M. R. Matthews, B. P. Anderson, P. Haljan, D. Hall, C. Wieman, and E. A. Cornell, “Vortices in a bose-einstein condensate”, *Physical Review Letters* **83**, 2498 (1999).
- [312] K. E. Strecker, G. B. Partridge, A. G. Truscott, and R. G. Hulet, “Formation and propagation of matter-wave soliton trains”, *Nature* **417**, 150 (2002).
- [313] L. Khaykovich, F. Schreck, G. Ferrari, T. Bourdel, J. Cubizolles, L. D. Carr, Y. Castin, and C. Salomon, “Formation of a matter-wave bright soliton”, *Science* **296**, 1290 (2002).
- [314] E. A. L. Henn, J. A. Seman, E. R. F. Ramos, M. Caracanhas, P. Castilho, E. P. Olimpio, G. Roati, D. V. Magalhães, K. M. F. Magalhães, and V. S. Bagnato, “Observation of vortex formation in an oscillating trapped bose-einstein condensate”, *Phys. Rev. A* **79**, 043618 (2009).
- [315] A. Weller, J. Ronzheimer, C. Gross, J. Esteve, M. Oberthaler, D. Frantzeskakis, G. Theocharis, and P. Kevrekidis, “Experimental observation of oscillating and interacting matter wave dark solitons”, *Physical review letters* **101**, 130401 (2008).
- [316] K. W. Madison, F. Chevy, W. Wohlleben, and J. Dalibard, “Vortex formation in a stirred bose-einstein condensate”, *Physical review letters* **84**, 806 (2000).
- [317] T. W. Neely, E. C. Samson, A. S. Bradley, M. J. Davis, and B. P. Anderson, “Observation of vortex dipoles in an oblate bose-einstein condensate”, *Physical review letters* **104**, 160401 (2010).
- [318] J. R. Abo-Shaeer, C. Raman, J. M. Vogels, and W. Ketterle, “Observation of vortex lattices in bose-einstein condensates”, *Science* **292**, 476 (2001).
- [319] Y. S. Kivshar, T. J. Alexander, and S. K. Turitsyn, “Nonlinear modes of a macroscopic quantum oscillator”, *Physics Letters A* **278**, 225 (2001).
- [320] V. M. Pérez-García, H. Michinel, and H. Herrero, “Bose-einstein solitons in highly asymmetric traps”, *Phys. Rev. A* **57**, 3837 (1998).
- [321] A. D. Jackson, G. M. Kavoulakis, and C. J. Pethick, “Solitary waves in clouds of bose-einstein condensed atoms”, *Phys. Rev. A* **58**, 2417 (1998).
- [322] L. Salasnich, A. Parola, and L. Reatto, “Effective wave equations for the dynamics of cigar-shaped and disk-shaped bose condensates”, *Phys. Rev. A* **65**, 043614 (2002).

- [323] D. R. Hartree, “The wave mechanics of an atom with a non-coulomb central field. part i. theory and methods”, *Math. Proc. Cambridge* **24**, 89 (1928).
- [324] V. Fock, “Näherungsmethode zur lösung des quantenmechanischen mehrkörperproblems”, *Z. Physik* **61**, 126 (1930).
- [325] J. Mitroy, S. Bubin, W. Horiuchi, Y. Suzuki, L. Adamowicz, W. Cencek, K. Szalewicz, J. Komasa, D. Blume, and K. Varga, “Theory and application of explicitly correlated gaussians”, *Reviews of modern physics* **85**, 693 (2013).
- [326] J. von Stecher and C. H. Greene, “Correlated gaussian hyperspherical method for few-body systems”, *Phys. Rev. A* **80**, 022504 (2009).
- [327] A. Christianen, J. I. Cirac, and R. Schmidt, “Bose polaron and the efimov effect: a gaussian-state approach”, *Physical Review A* **105**, 053302 (2022).
- [328] A. Christianen, J. I. Cirac, and R. Schmidt, “Chemistry of a light impurity in a bose-einstein condensate”, *Physical Review Letters* **128**, 183401 (2022).
- [329] T. Shi, E. Demler, and J. I. Cirac, “Variational study of fermionic and bosonic systems with non-gaussian states: theory and applications”, *Annals of Physics* **390**, 245 (2018).
- [330] S. R. White, “Density matrix formulation for quantum renormalization groups”, *Physical review letters* **69**, 2863 (1992).
- [331] S. R. White, “Density-matrix algorithms for quantum renormalization groups”, *Physical review b* **48**, 10345 (1993).
- [332] U. Schollwöck, “The density-matrix renormalization group”, *Reviews of modern physics* **77**, 259 (2005).
- [333] U. Schollwöck, “The density-matrix renormalization group in the age of matrix product states”, *Annals of physics* **326**, 96 (2011).
- [334] G. Astrakharchik and S. Giorgini, “Quantum monte carlo study of the three-to one-dimensional crossover for a trapped bose gas”, *Physical Review A* **66**, 053614 (2002).
- [335] W. Krauth, *Statistical mechanics: algorithms and computations*, Vol. 13 (OUP Oxford, 2006).
- [336] N. V. Prokof’ev, B. V. Svistunov, and I. S. Tupitsyn, “Exact, complete, and universal continuous-time worldline monte carlo approach to the statistics of discrete quantum systems”, *Journal of Experimental and Theoretical Physics* **87**, 310 (1998).
- [337] L. Cao, S. Krönke, O. Vendrell, and P. Schmelcher, “The multi-layer multi-configuration time-dependent hartree method for bosons: theory, implementation, and applications”, *The Journal of Chemical Physics* **139** (2013).
- [338] L. Cao, V. Bolsinger, S. Mistakidis, G. Koutentakis, S. Krönke, J. Schurer, and P. Schmelcher, “A unified ab initio approach to the correlated quantum dynamics of ultracold fermionic and bosonic mixtures”, *The Journal of chemical physics* **147** (2017).
- [339] V. Bolsinger, S. Krönke, and P. Schmelcher, “Beyond mean-field dynamics of ultra-cold bosonic atoms in higher dimensions: facing the challenges with a multi-configurational approach”, *Journal of Physics B: Atomic, Molecular and Optical Physics* **50**, 034003 (2017).

- [340] S. Krönke, L. Cao, O. Vendrell, and P. Schmelcher, “Non-equilibrium quantum dynamics of ultra-cold atomic mixtures: the multi-layer multi-configuration time-dependent hartree method for bosons”, *New Journal of Physics* **15**, 063018 (2013).
- [341] G. C. Katsimiga, S. I. Mistakidis, G. M. Koutentakis, P. G. Kevrekidis, and P. Schmelcher, “Many-body quantum dynamics in the decay of bent dark solitons of bose–einstein condensates”, *New J. Phys.* **19**, 123012 (2017).
- [342] V. J. Bolsinger, S. Krönke, and P. Schmelcher, “Ultracold bosonic scattering dynamics off a repulsive barrier: coherence loss at the dimensional crossover”, *Phys. Rev. A* **96**, 013618 (2017).
- [343] F. Theel, S. I. Mistakidis, and P. Schmelcher, *Crossover from attractive to repulsive induced interactions and bound states of two distinguishable bose polarons*, 2023.
- [344] G. C. Katsimiga, G. M. Koutentakis, S. I. Mistakidis, P. G. Kevrekidis, and P. Schmelcher, “Dark–bright soliton dynamics beyond the mean-field approximation”, *New J. Phys.* **19**, 073004 (2017).
- [345] G. M. Koutentakis, S. I. Mistakidis, and P. Schmelcher, “Probing ferromagnetic order in few-fermion correlated spin-flip dynamics”, *New J. Phys.* **21**, 053005 (2019).
- [346] S. I. Mistakidis, G. C. Katsimiga, P. G. Kevrekidis, and P. Schmelcher, “Correlation effects in the quench-induced phase separation dynamics of a two species ultracold quantum gas”, *New J. Phys.* **20**, 043052 (2018).
- [347] D. J. Bosworth, M. Pyzh, and P. Schmelcher, “Spectral properties of a three-body atom-ion hybrid system”, *Phys. Rev. A* **103**, 033303 (2021).
- [348] M. Pyzh and P. Schmelcher, “Phase separation of a bose-bose mixture: impact of the trap and particle-number imbalance”, *Phys. Rev. A* **102**, 023305 (2020).
- [349] J. Erdmann, S. I. Mistakidis, and P. Schmelcher, “Correlated tunneling dynamics of an ultracold fermi-fermi mixture confined in a double well”, *Phys. Rev. A* **98**, 053614 (2018).
- [350] J. Erdmann, S. I. Mistakidis, and P. Schmelcher, “Phase-separation dynamics induced by an interaction quench of a correlated fermi-fermi mixture in a double well”, *Phys. Rev. A* **99**, 013605 (2019).
- [351] F. Theel, K. Keiler, S. I. Mistakidis, and P. Schmelcher, “Entanglement-assisted tunneling dynamics of impurities in a double well immersed in a bath of lattice trapped bosons”, *New J. Phys.* **22**, 023027 (2020).
- [352] G. M. Koutentakis, S. I. Mistakidis, and P. Schmelcher, “Interplay of phase separation and itinerant magnetism for correlated few fermions in a double-well”, *New Journal of Physics* **22**, 063058 (2020).
- [353] F. Theel, K. Keiler, S. I. Mistakidis, and P. Schmelcher, “Many-body collisional dynamics of impurities injected into a double-well trapped bose-einstein condensate”, *Phys. Rev. Res.* **3**, 023068 (2021).
- [354] J. Chen, S. I. Mistakidis, and P. Schmelcher, “Intra- and interband excitations induced residue decay of the bose polaron in a one-dimensional double-well”, *New J. Phys.* **24**, 033004 (2022).
- [355] F. Theel, S. I. Mistakidis, K. Keiler, and P. Schmelcher, “Counterflow dynamics of two correlated impurities immersed in a bosonic gas”, *Phys. Rev. A* **105**, 053314 (2022).

- [356] J. Becker, M. Pyzh, and P. Schmelcher, “Interaction-controlled impurity transport in trapped mixtures of ultracold bosons”, *Phys. Rev. A* **106**, 053314 (2022).
- [357] S. I. Mistakidis and P. Schmelcher, “Mode coupling of interaction quenched ultracold few-boson ensembles in periodically driven lattices”, *Phys. Rev. A* **95**, 013625 (2017).
- [358] S. I. Mistakidis, L. Cao, and P. Schmelcher, “Interaction quench induced multimode dynamics of finite atomic ensembles”, *Journal of Physics B: Atomic, Molecular and Optical Physics* **47**, 225303 (2014).
- [359] P. Siegl, S. I. Mistakidis, and P. Schmelcher, “Many-body expansion dynamics of a bose-fermi mixture confined in an optical lattice”, *Phys. Rev. A* **97**, 053626 (2018).
- [360] K. Keiler, S. I. Mistakidis, and P. Schmelcher, “Doping a lattice-trapped bosonic species with impurities: from ground state properties to correlated tunneling dynamics”, *New Journal of Physics* **22**, 083003 (2020).
- [361] M. Pyzh, K. Keiler, S. I. Mistakidis, and P. Schmelcher, “Entangling lattice-trapped bosons with a free impurity: impact on stationary and dynamical properties”, *Entropy* **23**, 10.3390/e23030290 (2021).
- [362] K. Keiler and P. Schmelcher, “Interaction-induced single-impurity tunneling in a binary mixture of trapped ultracold bosons”, *Phys. Rev. A* **100**, 043616 (2019).
- [363] G. Koutentakis, “Probing the correlated spin-dynamics of ultracold atoms: magnetic and polaronic properties”, PhD thesis (Staats-und Universitätsbibliothek Hamburg Carl von Ossietzky, 2021).
- [364] S. Mystakidis, “Non-equilibrium correlated quantum dynamics of lattice trapped finite bosonic ensembles”, PhD thesis (Staats-und Universitätsbibliothek Hamburg Carl von Ossietzky, 2019).
- [365] K. Keiler, “Static and dynamical quantum correlations of ultracold bosonic mixtures”, PhD thesis (Staats-und Universitätsbibliothek Hamburg Carl von Ossietzky, 2021).
- [366] M. Pyzh, “Spectral properties and breathing dynamics of a few-body trapped bosonic mixture”, PhD thesis (Staats-und Universitätsbibliothek Hamburg Carl von Ossietzky, 2022).
- [367] V. J. Bolsinger, “Correlated dynamics of ultracold bosonic atoms in three dimensions. facing the challenge with a multi-configurational approach”, (2017).
- [368] J. H. V. Nguyen, M. C. Tsatsos, D. Luo, A. U. J. Lode, G. D. Telles, V. S. Bagnato, and R. G. Hulet, “Parametric excitation of a bose-einstein condensate: from faraday waves to granulation”, *Phys. Rev. X* **9**, 011052 (2019).
- [369] R. Lin, C. Georges, J. Klinder, P. Mognini, M. Büttner, A. U. J. Lode, R. Chitra, A. Hemmerich, and H. Keßler, “Mott transition in a cavity-boson system: A quantitative comparison between theory and experiment”, *SciPost Phys.* **11**, 030 (2021).
- [370] R. Horodecki, P. Horodecki, M. Horodecki, and K. Horodecki, “Quantum entanglement”, *Rev. Mod. Phys.* **81**, 865 (2009).
- [371] J. Broeckhove, L. Lathouwers, E. Kesteloot, and P. Van Leuven, “On the equivalence of time-dependent variational principles”, *Chem. Phys. Lett.* **149**, 547 (1988).

- [372] I. A. Englezos, S. I. Mistakidis, and P. Schmelcher, “Correlated dynamics of collective droplet excitations in a one-dimensional harmonic trap”, *Phys. Rev. A* **107**, 023320 (2023).
- [373] G. M. Koutentakis, S. I. Mistakidis, and P. Schmelcher, “Pattern formation in one-dimensional polaron systems and temporal orthogonality catastrophe”, *Atoms* **10**, 10.3390/atoms10010003 (2022).
- [374] P. Mujal, E. Sarlé, A. Polls, and B. Juliá-Díaz, “Quantum correlations and degeneracy of identical bosons in a two-dimensional harmonic trap”, *Phys. Rev. A* **96**, 043614 (2017).
- [375] M. Á. García-March, T. Fogarty, S. Campbell, T. Busch, and M. Paternostro, “Non-equilibrium thermodynamics of harmonically trapped bosons”, *New J. Phys.* **18**, 103035 (2016).
- [376] L. M. A. Kehrberger, V. J. Bolsinger, and P. Schmelcher, “Quantum dynamics of two trapped bosons following infinite interaction quenches”, *Phys. Rev. A* **97**, 013606 (2018).
- [377] T. Gorin, T. Prosen, T. H. Seligman, and M. Žnidarič, “Dynamics of loschmidt echoes and fidelity decay”, *Phys. Rep.* **435**, 33 (2006).
- [378] L. Tonks, “The complete equation of state of one, two and three-dimensional gases of hard elastic spheres”, *Phys. Rev.* **50**, 955 (1936).
- [379] M. Girardeau, “Relationship between Systems of Impenetrable Bosons and Fermions in One Dimension”, *Journal of Mathematical Physics* **1**, 516 (1960).
- [380] P. Mujal, A. Polls, and B. Juliá-Díaz, “Fermionic properties of two interacting bosons in a two-dimensional harmonic trap”, *Condensed Matter* **3**, 10.3390/condmat3010009 (2018).
- [381] S. I. Mistakidis, L. Cao, and P. Schmelcher, “Negative-quench-induced excitation dynamics for ultracold bosons in one-dimensional lattices”, *Phys. Rev. A* **91**, 033611 (2015).
- [382] J. Neuhaus-Steinmetz, S. I. Mistakidis, and P. Schmelcher, “Quantum dynamical response of ultracold few-boson ensembles in finite optical lattices to multiple interaction quenches”, *Phys. Rev. A* **95**, 053610 (2017).
- [383] S. Mistakidis, G. Koutentakis, and P. Schmelcher, “Bosonic quantum dynamics following a linear interaction quench in finite optical lattices of unit filling”, *Chem. Phys.* **509**, 106 (2018).
- [384] J. Decamp, M. Albert, and P. Vignolo, “Tan’s contact in a cigar-shaped dilute bose gas”, *Phys. Rev. A* **97**, 033611 (2018).
- [385] M. He and Q. Zhou, “ $s$ -wave contacts of quantum gases in quasi-one-dimensional and quasi-two-dimensional traps”, *Phys. Rev. A* **100**, 012701 (2019).
- [386] K. Helfrich and H.-W. Hammer, “Resonant three-body physics in two spatial dimensions”, *Phys. Rev. A* **83**, 052703 (2011).
- [387] J. H. Sandoval, F. F. Bellotti, A. S. Jensen, and M. T. Yamashita, “Mean-square radii of two-component three-body systems in two spatial dimensions”, *Phys. Rev. A* **94**, 022514 (2016).
- [388] Y.-Q. Zou, B. Bakkali-Hassani, C. Maury, É. Le Cerf, S. Nascimbene, J. Dalibard, and J. Beugnon, “Tan’s two-body contact across the superfluid transition of a planar bose gas”, *Nature Comm.* **12**, 760 (2021).



- [389] Y. Yan and D. Blume, “Harmonically trapped Fermi gas: Temperature dependence of the Tan contact”, *Phys. Rev. A* **88**, 023616 (2013).
- [390] M. D. Hoffman, P. D. Javernick, A. C. Loheac, W. J. Porter, E. R. Anderson, and J. E. Drut, “Universality in one-dimensional fermions at finite temperature: density, pressure, compressibility, and contact”, *Phys. Rev. A* **91**, 033618 (2015).
- [391] P. Capuzzi and P. Vignolo, “Finite-temperature contact for a SU(2) Fermi gas trapped in a one-dimensional harmonic confinement”, *Phys. Rev. A* **101**, 013633 (2020).
- [392] X.-Y. Chen, M. Duda, A. Schindewolf, R. Bause, I. Bloch, and X.-Y. Luo, “Suppression of Unitary Three-Body Loss in a Degenerate Bose-Fermi Mixture”, *Phys. Rev. Lett.* **128**, 153401 (2022).
- [393] L. A. Peña Ardila, N. B. Jørgensen, T. Pohl, S. Giorgini, G. M. Bruun, and J. J. Arlt, “Analyzing a bose polaron across resonant interactions”, *Phys. Rev. A* **99**, 063607 (2019).
- [394] A. G. Volosniev and H.-W. Hammer, “Analytical approach to the bose-polaron problem in one dimension”, *Phys. Rev. A* **96**, 031601 (2017).
- [395] N.-E. Guenther, P. Massignan, M. Lewenstein, and G. M. Bruun, “Bose polarons at finite temperature and strong coupling”, *Phys. Rev. Lett.* **120**, 050405 (2018).
- [396] C.-Y. Ding, X.-F. Zhang, D. Zhao, H.-G. Luo, and W. M. Liu, “Matter-wave solitons in heteronuclear atomic bose-einstein condensates with synchronously controllable interactions and potentials”, *Phys. Rev. A* **84**, 053631 (2011).
- [397] S. Rajendran, P. Muruganandam, and M. Lakshmanan, “Interaction of dark–bright solitons in two-component bose–einstein condensates”, *J. Phys. B: At., Mol. and Opt. Phys.* **42**, 145307 (2009).
- [398] T. Kanna, R. B. Mareswaran, F. Tsitoura, H. E. Nistazakis, and D. J. Frantzeskakis, “Non-autonomous bright–dark solitons and Rabi oscillations in multi-component Bose–Einstein condensates”, *J. Phys. A: Math. Theor.* **46**, 475201 (2013).
- [399] W. Cairncross and A. Pelster, “Parametric resonance in bose-einstein condensates with periodic modulation of attractive interaction”, *The European Physical Journal D* **68**, 106 (2014).
- [400] D. K. Maity, K. Mukherjee, S. I. Mistakidis, S. Das, P. G. Kevrekidis, S. Majumder, and P. Schmelcher, “Parametrically excited star-shaped patterns at the interface of binary bose-einstein condensates”, *Phys. Rev. A* **102**, 033320 (2020).
- [401] A. I. Nicolin, R. Carretero-González, and P. G. Kevrekidis, “Faraday waves in bose-einstein condensates”, *Phys. Rev. A* **76**, 063609 (2007).
- [402] K. Staliunas, S. Longhi, and G. J. de Valcárcel, “Faraday patterns in bose-einstein condensates”, *Phys. Rev. Lett.* **89**, 210406 (2002).
- [403] D. Kobayakov, V. Bychkov, E. Lundh, A. Bezett, and M. Marklund, “Parametric resonance of capillary waves at the interface between two immiscible bose-einstein condensates”, *Phys. Rev. A* **86**, 023614 (2012).
- [404] M. Naraschewski and R. J. Glauber, “Spatial coherence and density correlations of trapped bose gases”, *Phys. Rev. A* **59**, 4595 (1999).
- [405] E. Altman, E. Demler, and M. D. Lukin, “Probing many-body states of ultracold atoms via noise correlations”, *Phys. Rev. A* **70**, 013603 (2004).

- [406] L. Mathey, A. Vishwanath, and E. Altman, “Noise correlations in low-dimensional systems of ultracold atoms”, *Phys. Rev. A* **79**, 013609 (2009).
- [407] I. Ferrier-Barbut, M. Delehaye, S. Laurent, A. T. Grier, M. Pierce, B. S. Rem, F. Chevy, and C. Salomon, “A mixture of bose and fermi superfluids”, *Science* **345**, 1035 (2014).
- [408] Y. Guo, H. Yao, S. Ramanjanappa, S. Dhar, M. Horvath, L. Pizzino, T. Giamarchi, M. Landini, and H.-C. Nägerl, *Experimental observation of the 2d-1d dimensional crossover in strongly interacting ultracold bosons*, 2023.
- [409] E. Poli, T. Bland, C. Politi, L. Klaus, M. A. Norcia, F. Ferlaino, R. N. Bisset, and L. Santos, “Maintaining supersolidity in one and two dimensions”, *Phys. Rev. A* **104**, 063307 (2021).
- [410] M. A. Norcia, C. Politi, L. Klaus, E. Poli, M. Sohmen, M. J. Mark, R. N. Bisset, L. Santos, and F. Ferlaino, “Two-dimensional supersolidity in a dipolar quantum gas”, *Nature* **596**, 357 (2021).
- [411] L. Klaus, T. Bland, E. Poli, C. Politi, G. Lamporesi, E. Casotti, R. N. Bisset, M. J. Mark, and F. Ferlaino, “Observation of vortices and vortex stripes in a dipolar condensate”, *Nature Phys.* **18**, 1453 (2022).
- [412] J. Hertkorn, J.-N. Schmidt, M. Guo, F. Böttcher, K. S. H. Ng, S. D. Graham, P. Uerlings, H. P. Büchler, T. Langen, M. Zwierlein, and T. Pfau, “Supersolidity in two-dimensional trapped dipolar droplet arrays”, *Phys. Rev. Lett.* **127**, 155301 (2021).
- [413] T. Bland, G. Lamporesi, M. J. Mark, and F. Ferlaino, *Vortices in dipolar bose-einstein condensates*, 2023.
- [414] L. Chomaz, I. Ferrier-Barbut, F. Ferlaino, B. Laburthe-Tolra, B. L. Lev, and T. Pfau, “Dipolar physics: a review of experiments with magnetic quantum gases”, *Rep. Prog. Phys.* **86**, 026401 (2022).
- [415] T. Lahaye, C. Menotti, L. Santos, M. Lewenstein, and T. Pfau, “The physics of dipolar bosonic quantum gases”, *Rep. Prog. Phys.* **72**, 126401 (2009).
- [416] M. A. Baranov, M. Dalmonte, G. Pupillo, and P. Zoller, “Condensed matter theory of dipolar quantum gases”, *Chem. Rev.* **112**, 5012 (2012).
- [417] B. Schulz, S. Sala, and A. Saenz, “Resonances in ultracold dipolar atomic and molecular gases”, *New J. Phys.* **17**, 065002 (2015).
- [418] J. Hofmann and W. Zwerger, “Universal relations for dipolar quantum gases”, *Phys. Rev. Res.* **3**, 013088 (2021).
- [419] R. Saint-Jalm, P. C. M. Castilho, É. Le Cerf, B. Bakkali-Hassani, J.-L. Ville, S. Nascimbene, J. Beugnon, and J. Dalibard, “Dynamical symmetry and breathers in a two-dimensional bose gas”, *Phys. Rev. X* **9**, 021035 (2019).
- [420] C. Lv, R. Zhang, and Q. Zhou, “ $su(1, 1)$  echoes for breathers in quantum gases”, *Phys. Rev. Lett.* **125**, 253002 (2020).
- [421] J. Torrents, V. Dunjko, M. Gonchenko, G. Astrakharchik, and M. Olshanii, “The origin of the period- $2t/7$  quasi-breathing in disk-shaped gross-pitaevskii breathers”, *SciPost Phys.* **12**, 092 (2022).
- [422] M. Olshanii, D. Deshommes, J. Torrents, M. Gonchenko, V. Dunjko, and G. E. Astrakharchik, “Triangular gross-pitaevskii breathers and damski-chandrasekhar shock waves”, *SciPost Phys.* **10**, 114 (2021).

- [423] F. Werner and X. Leyronas, *Three-body contact for fermions. i. general relations*, 2022.
- [424] A. Kahan, T. Fogarty, J. Li, and T. Busch, “Driving interactions efficiently in a composite few-body system”, *Universe* **5**, 10.3390/universe5100207 (2019).
- [425] J.-F. ç. Schaff, X.-L. Song, P. Vignolo, and G. Labeyrie, “Fast optimal transition between two equilibrium states”, *Phys. Rev. A* **82**, 033430 (2010).
- [426] J.-F. Schaff, X.-L. Song, P. Capuzzi, P. Vignolo, and G. Labeyrie, “Shortcut to adiabaticity for an interacting bose-einstein condensate”, *Europhys. Lett.* **93**, 23001 (2011).
- [427] J.-F. Schaff, P. Capuzzi, G. Labeyrie, and P. Vignolo, “Shortcuts to adiabaticity for trapped ultracold gases”, *New Journal of Physics* **13**, 113017 (2011).
- [428] W. Rohringer, D. Fischer, F. Steiner, I. E. Mazets, J. Schmiedmayer, and M. Trupke, “Non-equilibrium scale invariance and shortcuts to adiabaticity in a one-dimensional bose gas”, *Scientific Reports* **5**, 9820 (2015).
- [429] S. Deng, P. Diao, Q. Yu, A. del Campo, and H. Wu, “Shortcuts to adiabaticity in the strongly coupled regime: nonadiabatic control of a unitary fermi gas”, *Phys. Rev. A* **97**, 013628 (2018).
- [430] P. Diao, S. Deng, F. Li, S. Yu, A. Chenu, A. del Campo, and H. Wu, “Shortcuts to adiabaticity in fermi gases”, *New Journal of Physics* **20**, 105004 (2018).
- [431] J. ř. Etrych, G. Martirosyan, A. Cao, J. A. P. Glidden, L. H. Dogra, J. M. Hutson, Z. Hadzibabic, and C. Eigen, “Pinpointing feshbach resonances and testing efimov universalities in  $^{39}\text{K}$ ”, *Phys. Rev. Res.* **5**, 013174 (2023).
- [432] M. Berninger, A. Zenesini, B. Huang, W. Harm, H.-C. Nägerl, F. Ferlaino, R. Grimm, P. S. Julienne, and J. M. Hutson, “Universality of the three-body parameter for efimov states in ultracold cesium”, *Phys. Rev. Lett.* **107**, 120401 (2011).
- [433] X. Xie, M. J. Van de Graaff, R. Chapurin, M. D. Frye, J. M. Hutson, J. P. D’Incao, P. S. Julienne, J. Ye, and E. A. Cornell, “Observation of efimov universality across a nonuniversal feshbach resonance in  $^{39}\text{K}$ ”, *Phys. Rev. Lett.* **125**, 243401 (2020).
- [434] J. Wang, J. P. D’Incao, B. D. Esry, and C. H. Greene, “Origin of the Three-Body Parameter Universality in Efimov Physics”, *Phys. Rev. Lett.* **108**, 263001 (2012).
- [435] P. Naidon, S. Endo, and M. Ueda, “Microscopic Origin and Universality Classes of the Efimov Three-Body Parameter”, *Phys. Rev. Lett.* **112**, 105301 (2014).
- [436] P. Naidon, S. Endo, and M. Ueda, “Physical origin of the universal three-body parameter in atomic Efimov physics”, *Phys. Rev. A* **90**, 022106 (2014).
- [437] A. G. Sykes, H. Landa, and D. S. Petrov, “Two- and three-body problem with Floquet-driven zero-range interactions”, *Phys. Rev. A* **95**, 062705 (2017).
- [438] E. A. Donley, N. R. Claussen, S. L. Cornish, J. L. Roberts, E. A. Cornell, and C. E. Wieman, “Dynamics of collapsing and exploding bose–einstein condensates”, *Nature* **412**, 295 (2001).
- [439] J. M. Gerton, D. Strekalov, I. Prodan, and R. G. Hulet, “Direct observation of growth and collapse of a bose–einstein condensate with attractive interactions”, *Nature* **408**, 692 (2000).

- [440] J. Denschlag, J. E. Simsarian, D. L. Feder, C. W. Clark, L. A. Collins, J. Cubizolles, L. Deng, E. W. Hagley, K. Helmerson, W. P. Reinhardt, S. L. Rolston, B. I. Schneider, and W. D. Phillips, “Generating solitons by phase engineering of a bose-einstein condensate”, *Science* **287**, 97 (2000).
- [441] Z. Dutton, M. Budde, C. Slowe, and L. V. Hau, “Observation of quantum shock waves created with ultra- compressed slow light pulses in a bose-einstein condensate”, *Science* **293**, 663 (2001).
- [442] J. Brand and W. P. Reinhardt, “Solitonic vortices and the fundamental modes of the “snake instability”: possibility of observation in the gaseous bose-einstein condensate”, *Phys. Rev. A* **65**, 043612 (2002).
- [443] A. Muryshev, G. V. Shlyapnikov, W. Ertmer, K. Sengstock, and M. Lewenstein, “Dynamics of dark solitons in elongated bose-einstein condensates”, *Phys. Rev. Lett.* **89**, 110401 (2002).
- [444] B. P. Anderson, P. C. Haljan, C. A. Regal, D. L. Feder, L. A. Collins, C. W. Clark, and E. A. Cornell, “Watching dark solitons decay into vortex rings in a bose-einstein condensate”, *Phys. Rev. Lett.* **86**, 2926 (2001).
- [445] A. Trautmann, P. Ilzhöfer, G. Durastante, C. Politi, M. Sohmen, M. J. Mark, and F. Ferlaino, “Dipolar quantum mixtures of erbium and dysprosium atoms”, *Phys. Rev. Lett.* **121**, 213601 (2018).
- [446] G. Durastante, C. Politi, M. Sohmen, P. Ilzhöfer, M. J. Mark, M. A. Norcia, and F. Ferlaino, “Feshbach resonances in an erbium-dysprosium dipolar mixture”, *Phys. Rev. A* **102**, 033330 (2020).
- [447] R. N. Bisset, L. A. P. Ardila, and L. Santos, “Quantum droplets of dipolar mixtures”, *Phys. Rev. Lett.* **126**, 025301 (2021).

# Eidesstattliche Versicherung / Declaration of oath

Hiermit versichere ich an Eides statt, die vorliegende Dissertationsschrift selbst verfasst und keine anderen als die angegebenen Hilfsmittel und Quellen benutzt zu haben. Die eingereichte schriftliche Fassung entspricht der auf dem elektronischen Speichermedium.

Die Dissertation wurde in der vorgelegten oder einer ähnlichen Form nicht schon einmal in einem früheren Promotionsverfahren angenommen oder als ungenügend beurteilt.

*Hamburg, den 25/08/2023*

*Γεώργιος Μπουγας*

---

Georgios Bougas